

NASA Conference Publication 3079

Fire Science Results 1989

(NASA-CP-3079) 1989
(NASA) 434 2

1989-28306
Unclas

H1/47 0290954

Fire Science Results 1989

Edited by
David S. McDougal
NASA Langley Research Center
Hampton, Virginia

Proceedings of a conference sponsored by
the National Aeronautics and Space Administration,
the National Science Foundation, the Office of Naval
Research, the Department of Energy, the Air Force
Geophysics Laboratory, and the National Oceanic and
Atmospheric Administration, and held in
Monterey, California
July 10–14, 1989



National Aeronautics and
Space Administration
Office of Management
Scientific and Technical
Information Division

1990

PREFACE

FIRE (First ISCCP Regional Experiment) is a U.S. cloud-radiation research program formed in 1984 to increase our basic understanding of cirrus and marine stratocumulus cloud systems, to develop realistic parameterizations for these cloud systems, and to validate and improve ISCCP cloud product retrievals. A FIRE Science Meeting was held in Monterey, California, July 10-14, 1989, to highlight presentations of results culminating 5 years of FIRE Phase I research activities that focused on these objectives.

This Conference Publication contains the full text of the papers presented at the FIRE Science Meeting. The presentations describe important elements of the 1986 Cirrus Intensive Field Observations (IFO), the 1987 Marine Stratocumulus IFO, the Extended Time Observations (ETO), and modeling activities. A number of papers describe collaborative efforts involving the comparison of multiple data sets (i.e. satellite, airborne, and surface), incorporation of data measurements into modeling activities, validation of ISCCP cloud parameters, and development of parameterization schemes for GCMs.

In order to keep this volume to a manageable size and to encourage authors to complete their papers and submit them to refereed journals, summaries were restricted to a maximum of 5 pages.

The managers of the sponsoring agencies wish to express their thanks and appreciation to the FIRE investigators, not only for their conscientious and skillful efforts in preparation for and displayed at this meeting, but also for their dedication, cooperation, and scientific excellence that they have performed throughout the years of FIRE Phase I.

I am pleased to acknowledge the contributions of the session chairmen: Bruce A. Albrecht, James A. Coakley, Stephen K. Cox, Howard P. Hanson, Michael D. King, Pat Minnis, David A. Randall, Kenneth Sassen, David O. C. Starr, and Graeme Stephens. It is with grateful appreciation that I recognize the talents and efforts of Doris Stroup, STX, for the excellent logistics in planning, preparing, and conducting this meeting and, with Ginanna Karalfa, STX, for the administrative and secretarial assistance in preparing this document.

AGENDA

FIRE SCIENCE MEETING

July 10-14, 1989
Hyatt Regency Monterey
Monterey, California

MONDAY, JULY 10, 1989

MARINE STRATOCUMULUS

M01: Physical Properties	King
M02: Optical Properties	Stephens
M03: Radiative Properties	Hanson
M04: Dynamic and Thermodynamic Properties	Hanson

TUESDAY, JULY 11, 1989

M05: Microphysical Properties	Stephens
M06: Transport Mechanisms and Modeling	Albrecht
M07: FIRE Phase II	Randall
M08: Poster Session	Randall

WEDNESDAY, JULY 12, 1989

EXTENDED TIME

E01: Satellite Studies	Coakley
E02: Surface-Based Studies	Coakley
E03: Large-Scale Environment and Modeling	Coakley

CIRRUS

C01: Physical and Microphysical Properties	Starr
C02: Case Studies	Sassen

THURSDAY, JULY 13, 1989

C03:	Large-Scale Environment and Modeling	Starr
C04:	Radiative/Optical Properties	Minnis
C05:	FIRE Phase II	Cox
C06:	Focused IFOs	Starr
C07:	Poster Session	Cox

FRIDAY, JULY 14, 1989

C08:	Midlatitude Cirrus IFO	Starr
------	------------------------	-------

TABLE OF CONTENTS

	PAGE
MARINE STRATOCUMULUS	
SESSION M01: Physical Properties	Michael D. King
M01.01 Comparative Climatology of Four Stratocumulus Regimes Hanson, Howard P.	3
M01.02 Large-Scale Variability in Marine Stratocumulus Clouds Defined from Simultaneous Aircraft and Satellite Measurements Albrecht, Bruce A., and Roy W. Barlow	9
M01.03 On Estimating Scale Invariance in Stratocumulus Cloud Fields Seze, Genevieve, and Leonard A. Smith	15
M01.04 Inhomogeneities of Stratocumulus Liquid Water Cahalan, Robert F., and Jack B. Snider	21
M01.05 Intercomparisons of GOES-Derived Cloud Parameters and Surface Observations Over San Nicolas Island Minnis, P., C. W. Fairall, and D. F. Young	27
M01.06 Stratocumulus Cloud Height Variations Determined from Surface and Satellite Observations Minnis, P., D. F. Young, R. Davies, M. Blaskovic, and B. A. Albrecht	33
M01.07 Cloud Top Entrainment Instability and Cloud Top Distributions Boers, Reinout, and James D. Spinhirne	39
M01.08 July 16, 1987 Revisited: Lessons for Modelers Hanson, Howard P.	45
M01.09 An Eight-Month Climatology of Marine Stratocumulus Cloud Fraction, Albedo, and Integrated Liquid Water <u>Fairall, C. W.</u> , J. E. Hare, and J. B. Snider	51
M01.10 Mesoscale Variability of Free Tropospheric Humidity Near San Nicolas Island During FIRE <u>White, A. B.</u> , C. W. Fairall, and D. W. Thomson	57
M01.11 The Above-Inversion Moisture Structure Observed During FIRE Kloesel, Kevin A.	63
SESSION M02: Optical Properties	
	Graeme L. Stephens
M02.01 Reflectivities of Uniform and Broken Stratiform Clouds--An Update Coakley, Jr., J. A., and B. P. Briegleb	71

TABLE OF CONTENTS

	PAGE
M02.02 Observed Cloud Reflectivities and Liquid Water Paths--An Update Coakley, Jr., J. A., and J. B. Snider	75
M02.03 Spectral Absorption of Marine Stratocumulus Clouds Derived from <i>In Situ</i> Cloud Radiation Measurements King, Michael D., Lawrence F. Radke, and Peter V. Hobbs	79
M02.04 Cloud Optical Parameters as Derived from the Multispectral Cloud Radiometer Nakajima, Teruyuki, and Michael D. King	85
 SESSION M03: Radiative Properties	 Howard P. Hanson
M03.01 Satellite-Derived Cloud and Radiation Fields Over the Marine Stratocumulus IFO Young, David F., Patrick Minnis, and Edwin F. Harrison	95
M03.02 Analysis of ER-2 Radiometer and Lidar Observations from the 1987 Marine Stratus Experiment Spinhirne, J. D., R. Boers, T. Nakajima, and W. D. Hart	101
M03.03 The Radiation Budget of Stratocumulus Clouds Measured by Tethered Balloon Instrumentation: Variability of Flux Measurements Duda, David P., Graeme L. Stephens, and Stephen K. Cox	103
 SESSION M04: Dynamic and Thermodynamic Properties	 Howard P. Hanson
M04.01 Structural Analysis of Stratocumulus Convection <u>Siems, S. T.</u> , M. B. Baker, and C. S. Bretherton	107
M04.02 On the Dynamic and Thermodynamic Structures of Marine Stratocumulus Lauferweiler, Mark J., and <u>Hampton N. Shirer</u>	113
M04.03 A Stratocumulus Thermodynamic Analysis: July 5 Case Study <u>Austin, Philip</u>	119
M04.04 Turbulence Spectra of the FIRE Stratocumulus-Topped Boundary Layers Young, G. S., J. J. Nucciarone, and B. A. Albrecht	125
M04.05 Turbulence Structure in Clear and Cloudy Regions of the 7 July 1987 Electra Mission Khalsa, Siri Jodha Singh	131
M04.06 Diurnal Variation in the Turbulent Structure of the Cloudy Marine Boundary Layer During FIRE 1987 <u>Hignett, Phillip</u>	137

TABLE OF CONTENTS

	PAGE
SESSION M05: Microphysical Properties	Graeme L. Stephens
M05.01 Supersaturation, Droplet Spectra, and Turbulent Mixing in Clouds <u>Gerber, H.</u>	145
M05.02 The Influence of Continental Sources of Aerosols on the Marine Stratocumulus During FIRE IFO-I Durkee, Philip A.	151
M05.03 Observations of Anthropogenic Cloud Condensation Nuclei Hudson, James G.	157
M05.04 Direct and Remote Sensing Observations of the Effects of Ships on Clouds Radke, Lawrence F., Peter V. Hobbs, James A. Coakley, Jr., and Michael D. King	163
M05.05 Optical Properties of Marine Stratocumulus Clouds Modified by Ship Track Effluents King, Michael D., and Teruyuki Nakajima	165
SESSION M06: Transport Mechanisms and Modeling	Bruce A. Albrecht
M06.01 A Unified View of Convective Transports by Stratocumulus Clouds, Shallow Cumulus Clouds, and Deep Convection Randall, David A.	173
M06.02 STRATUS: An Interactive Steady State Mixed Layer Model for Personal Computers Guinn, Thomas A., and Wayne H. Schubert	179
M06.03 A Case Study of Cumulus Formation Beneath a Stratocumulus Sheet: Its Structure and Effect on Boundary Layer Budgets <u>Barlow, R. W.</u> , and S. Nicholls (deceased)	185
M06.04 Verification of the Naval Oceanic Vertical Aerosol Model During FIRE Davidson, K. L., <u>G. de Leeuw</u> , S. G. Gathman, and D. R. Jensen	191
M06.05 Modification of the Background Flow by Roll Vortices <u>Shirer, Hampton N.</u> , and Tracy Haack	197
M06.06 A Cloudiness Transition in a Marine Boundary Layer Betts, Alan K., and Reinout Boers	203
M06.07 Analysis of Marine Stratocumulus Clearing Events During FIRE Kloesel, Kevin A.	211
M06.08 FIRE Aircraft Observations of Horizontal and Vertical Transport in Marine Stratocumulus Paluch, Ilga R., and <u>Donald H. Lenschow</u>	213

TABLE OF CONTENTS

	PAGE
M06.09 Vertical-Velocity Skewness in the Marine Stratus-Topped Boundary Layer <u>Moeng, Chin-Hoh</u> , Richard Rotunno, and Ilga Paluch	219
M06.10 Laboratory Experiments on Stability and Entrainment of Oceanic Stratocumulus-- Part I: Instability Experiment Shy, Shenqyang S.	225
SESSION M07: FIRE Phase II David A. Randall	
M07.01 Overview Randall, David A.	***
M07.02 Objectives Randall, David A.	***
M07.03 Management Plan McDougal, David S.	***
M07.04 FIRE Central Archive Olsen, Lola M.	***
M07.05 General Discussion Cox, Stephen K.	***
SESSION M08: Poster Session David A. Randall	
M08.01 On the Dynamic and Thermodynamic Structures of Marine Stratocumulus Lauferweiler, M. J., and Hampton N. Shirer	***
M08.02 Analysis of Marine Stratocumulus Clearing Events During FIRE Kloesel, Kevin A.	***
M08.03 Cloud Top Distributions and Cloud Top Entrainment Instability Boers, Reinout, and James D. Spinhirne	***
M08.04 Comparative Climatology of Four Stratocumulus Regimes Hanson, Howard P.	***
M08.05 Laboratory Experiments on Stability and Entrainment of Oceanic Stratocumulus-- Part II: Entrainment Experiment Shy, Shenqyang S.	235
M08.06 High Resolution Infrared Measurements Kessler, B., and Robert Cawley	241
M08.07 On Estimating Scale Invariance of Stratocumulus Cloud Fields Seze, Genevieve, and L. A. Smith	***

TABLE OF CONTENTS

	PAGE
M08.08 Spectral Absorption of Marine Stratocumulus Clouds Derived from In Situ Cloud Radiation Measurements King, Michael D., Lawrence F. Radke, and Peter V. Hobbs	***
M08.09 Turbulent Statistics in the Vicinity of an SST Front: A North Wind Case, FASINEX February 16, 1986 Stage, Stephen A., and Chris Herbster	247

EXTENDED TIME

SESSION E01: Satellite Studies		James A. Coakley
E01.01 A Comparison of ISCCP and FIRE Satellite Cloud Parameters Gibson, Gary G., Patrick W. Heck, David F. Young, Patrick Minnis, and Edwin F. Harrison		257
E01.02 Comparison of Satellite Based Cloud Retrieval Methods for Cirrus and Stratocumulus Parker, Lindsay, and Bruce A. Wielicki		263
E01.03 Retrievals, Validation, and Analysis of Cloud Properties from AVHRR Data Arking, Albert, et al		***
SESSION E02: Surface-Based Studies		James A. Coakley
E02.01 ETO Lidar Studies of Cirrostratus Altocumulogenitus: Another Role for Super-Cooled Liquid Water in Cirrus Cloud Formation <u>Sassen, Kenneth</u>		271
E02.02 Impact of Cirrus on the Surface Radiative Environment at the FIRE ETLA Palisades, NY Site Robinson, David A., <u>George Kukla</u> , and Allan Frei		275
SESSION E03: Large-Scale Environment and Modeling		James A. Coakley
E03.01 The Effects of Clouds on CO ₂ Forcing Randall, David A.		283
E03.02 Seasonal and Interannual Changes in Cirrus Wylie, Donald		289
E03.03 Relationship Between the Longwave Cloud Radiative Forcing at the Surface and the Top of the Atmosphere <u>Harshvardhan</u>		295

TABLE OF CONTENTS

	PAGE
E03.04 Comparison of 30 Day Integrations With and Without Interactive Clouds Gordon, C. T.	301
CIRRUS	
SESSION C01: Physical and Microphysical Properties	David O'C. Starr
C01.01 Spatial Scales of Cirrus Cloud Properties Hein, Paul F., and Stephen K. Cox	311
C01.02 Interpretation of Cirrus Cloud Properties Using Coincident Satellite and Lidar Data During the FIRE Cirrus IFO Minnis, Patrick, Joseph M. Alvarez, David F. Young, Kenneth Sassen, and Christian J. Grund	317
C01.03 Properties of Cirrus from Multispectral AVHRR Imagery Data Coakley, Jr., J. A.	323
C01.04 Summary of Results and Conclusions Based on Analysis of Volume Imaging and High Spectral Resolution Lidar Data Acquired During FIRE Phase I: Part I Grund, C. J., and <u>E. W. Eloranta</u>	327
C01.05 Moisture and Heat Budgets of a Cirrus Cloud from Aircraft Measurements During FIRE <u>Gultepe, Ismail</u> , and Andrew Heymsfield	333
SESSION C02: Case Studies	Kenneth Sassen
C02.01 The 27-28 October 1986 FIRE Cirrus Case Study: Meteorology and Clouds Starr, David O'C., and Donald P. Wylie	341
C02.02 Satellite-Derived Cloud Fields During the FIRE Cirrus IFO Case Study Heck, Patrick W., Gary G. Gibson, Patrick Minnis, and Edwin F. Harrison	345
C02.03 Comparison of Surface-Derived and ISCCP Cloud Optical Properties <u>Whitlock, C. H.</u> , L. R. Poole, S. R. LeCroy, W. B. Rossow, K. L. Bell, D. A. Robinson, and C. Grund	351
C02.04 The October 27-28, 1986, FIRE Cirrus Case Study: Cloud Microstructure Miller, Karen M., Andrew J. Heymsfield, and James D. Spinhirne	357
C02.05 Cirrus Microphysics and Radiative Transfer: Cloud Field Study on October 28 th , 1986 Kinne, Stefan, Thomas P. Ackerman, Andrew J. Heymsfield, Francisco P. J. Valero, Kenneth Sassen, and James D. Spinhirne	363

TABLE OF CONTENTS

	PAGE
C02.06 The 27-28 October 1986 FIRE IFO Cirrus Case Study: Comparison of Satellite and Aircraft Derived Particle Size Wielicki, Bruce A., J. T. Suttles, Andrew J. Heymsfield, Ronald M. Welch, James D. Spinhirne, Man-Li C. Wu, David O'C. Starr, Lindsay Parker, and Robert F. Arduini	369
C02.07 Cirrus Radiative Characteristics and the Radiative Impact of Small Particles <u>Stackhouse, Jr. Paul W.</u> , Graeme L. Stephens, and S. K. Cox	375
C02.08 Regional Conditions During the 25 October 1986 FIRE Cirrus/Alto cumulus Case Study Starr, David O'C., and Kenneth Sassen	381
 SESSION C03: Large-Scale Environment and Modeling	 David O'C. Starr
C03.01 Cirrus Clouds and Climate Feedback: Is the Sky Falling and Should We Go Tell the King? Stephens, Graeme L.	389
C03.02 Low-Frequency Cloud-Radiation Interactions Randall, David A.	395
C03.03 Preliminary Simulations of the Large-Scale Environment During the FIRE Cirrus IFO <u>Westphal, Douglas L.</u> , and Owen B. Toon	401
C03.04 Microphysical Fundamentals Governing Cirrus Cloud Growth: Modeling Studies <u>Sassen, Kenneth</u> , Gregory C. Dodd, and David O'C. Starr	407
C03.05 A Scheme for Parameterizing Cirrus Cloud Ice Water Content in General Circulation Models Heymsfield, Andrew J., and Leo J. Donner	411
C03.06 Radiative Diffusivity Factors in Cirrus and Stratocumulus Clouds--Applications to Two-Stream Models Stephens, G. L., P. J. Flatau, S.-C. Tsay, and P. Hein	415
 SESSION C04: Radiative/Optical Properties	 Patrick Minnis
C04.01 A Comparative Study of Infrared Radiance Measurements by an ER-2 Based Radiometer and the Landsat 5 Thematic Mapper (TM-6) <u>Hammer, Philip D.</u> , Francisco P. J. Valero, and Stefan Kinne	423
C04.02 Radiative Properties of Cirrus Clouds Inferred from Broadband Measurements During FIRE <u>Smith, Jr., William L.</u> , and Stephen K. Cox	429
C04.03 Remote Sounding Through Semi-Transparent Cirrus Cloud <u>Smith, William L.</u> , Steven A. Ackerman, and Allan H.-L. Huang	435

TABLE OF CONTENTS

	PAGE
C04.04 IR Spectral Characteristics of Cirrus Clouds <u>Ackerman, Steven A.</u> , and William L. Smith	441
C04.05 Airborne Lidar/Radiometric Measurements of Cirrus Cloud Parameters and Their Application to Lowtran Radiance Evaluations Uthe, Edward E.	447
SESSION C05: FIRE Phase II	Stephen K. Cox
C05.01 Objectives Cox, Stephen K.	***
C05.02 Future Plans Cox, Stephen K.	***
SESSION C06: Focused IFO	David O'C. Starr
C06.01 The May-June 1989 Wisconsin Focused IFO Eloranta, Edwin W., Christian J. Grund, and Donald Wylie	***
C06.02 The Colorado/Missouri 1989 Mini Cirrus IFO Heymsfield, Andrew J., and Donald Hagen	457
C06.03 The Central Pennsylvania Focused IFO: Utilization of a Surface-Based Cloud Observing System Ackerman, Thomas P., Bruce A. Albrecht, and Christopher W. Fairall	***
C06.04 Utah Focused IFO Sassen, Kenneth	***
C06.05 TOGA Stephens, Graeme L.	***
C06.06 A Tropical Cirrus Mini IFO at Kwajalein, Marshall Islands Heymsfield, Andrew J.	***
C06.07 General Discussion Cox, Stephen K.	***

TABLE OF CONTENTS

	PAGE
SESSION C07: Poster Session	Stephen K. Cox
C07.01 Summary of Results and Conclusions Based on Analysis of Volume Imaging and High Spectral Resolution Lidar Data Acquired During FIRE Phase I: Part II Grund, C. J., and <u>E. W. Eloranta</u>	463
C07.02 A System for Recording Physical Properties of Clouds Purgold, G. C., and C. H. Whitlock	467
C07.03 Cirrus Parameterization from the FIRE ER-2 Observations Spinhirne, J. D.	473
C07.04 1973-1974 Lidar Observations of Cirrus Clouds at Kwajalein Uthe, Edward E.	477
C07.05 The Use of an Airborne Lidar for Mapping Cirrus Clouds in FIRE II Radke, Lawrence F., and Peter V. Hobbs	481
C07.06 On the Use of IR Lidar and Ka-Band Radar for Observing Cirrus Clouds <u>Eberhard, Wynn L.</u> , R. Michael Hardesty, and Robert A. Kropfli	487
C07.07 Intercomparison of Standard Resolution and High Resolution TOVS Soundings with Radiosonde, Lidar, and Surface Temperature/Humidity Data Wheeler, R. J., C. H. Whitlock, J. M. Alvarez, D. O'C. Starr, and D. P. Wylie	491
C07.08 The October 27-28, 1986 FIRE Case Study: A Lidar Compendium from Fort McCoy Alvarez, J. M., W. H. Hunt, J. G. Moore, and M. A. Vaughn	***
SESSION C08: Midlatitude Cirrus IFO	David O'C. Starr
C08.01 Objectives Cox, Stephen K.	***
C08.02 Climatology Wylie, Donald	***
C08.03 Methodology Starr, David O'C.	***
C08.04 General Discussion Starr, David O'C.	***

	PAGE
M01.01 Comparative Climatology of Four Stratocumulus Regimes Hanson, Howard P.	3
M01.02 Large-Scale Variability in Marine Stratocumulus Clouds Defined from Simultaneous Aircraft and Satellite Measurements Albrecht, Bruce A., and Roy W. Barlow	9
M01.03 On Estimating Scale Invariance in Stratocumulus Cloud Fields Seze, Genevieve, and Leonard A. Smith	15
M01.04 Inhomogeneities of Stratocumulus Liquid Water Cahalan, Robert F., and Jack B. Snider	21
M01.05 Intercomparisons of GOES-Derived Cloud Parameters and Surface Observations Over San Nicolas Island Minnis, P., C. W. Fairall, and D. F. Young	27
M01.06 Stratocumulus Cloud Height Variations Determined from Surface and Satellite Observations Minnis, P., D. F. Young, R. Davies, M. Blaskovic, and B. A. Albrecht	33
M01.07 Cloud Top Entrainment Instability and Cloud Top Distributions Boers, Reinout, and James D. Spinhirne	39
M01.08 July 16, 1987 Revisited: Lessons for Modelers Hanson, Howard P.	45
M01.09 An Eight-Month Climatology of Marine Stratocumulus Cloud Fraction, Albedo, and Integrated Liquid Water <u>Fairall, C. W.</u> , J. E. Hare, and J. B. Snider	51
M01.10 Mesoscale Variability of Free Tropospheric Humidity Near San Nicolas Island During FIRE <u>White, A. B.</u> , C. W. Fairall, and D. W. Thomson	57
M01.11 The Above-Inversion Moisture Structure Observed During FIRE Kloesel, Kevin A.	63

Comparative Climatology of Four Marine Stratocumulus Regimes

HOWARD P. HANSON

Atmospheric and Climate Dynamics Program

Cooperative Institute for Research in Environmental Sciences

University of Colorado at Boulder 80309-0216

1. Introduction

Much has been made of clouds in the climate system of late, including a Symposium on the Role of Clouds and Chemistry in Global Climate at the 1989 Annual Meeting of the AMS and a special session on Clouds and Climate at the Spring, 1989, AGU Meeting. On top of this high visibility in the *scientific* community, there seems to be the *popular* perception that, as climate warms, clouds will tend to occur more often—i.e., their time/space areal coverage will increase—thus helping to ameliorate the problem of global warming. Of course, the FSET community is unlikely to take such a stand, for at least two reasons. First, it is overly simplified: if *cirrus* cloud coverage increases, the problem of global warming is likely to be exacerbated. Second, the relationship of cloud coverage to average temperature is not at all obvious. One of the reasons to continue FIRE toward Phase II is to attempt to develop a quantitative understanding of just this question.

As currently envisioned, the second set of FIRE IFO's will again be process-oriented, using a coordinated observational approach to examine the behavior of cloud systems on the time and space scales of the individual cloud elements composing the systems. A complementary approach, embodied by the large-scale, long-term FIRE components, is the analysis of existing climate data sets

without specific concern about the behavior of the individual cloud elements. One such study is the topic of this paper. The focus here is on the climatology of MSc cloud regimes off the west coasts of California, Peru, Morocco, and Angola. The material presented here complements the brief climatology of July that appears in the "Grey Book", the FIRE Phase II Research Plan (FIRE Project Office, 1989)¹. This abstract, due to space limitations, presents the long-term, annual averages of several quantities of interest in the four MSc regimes.

The climatologies presented here were constructed using the Comprehensive Ocean-Atmosphere Data Set—COADS (Woodruff et al., 1987). A 40-year time series of the observations (1948-1987) was extracted for 32°x32° analysis domains in the four MSc regimes; the figures to follow are simply averages of these data sets. The data were taken from the monthly-averaged, 2° product, and the resolution of the analysis is therefore limited to scales of greater than about 200 km with sub-monthly variability not resolved. Background maps for the four areas of interest are shown in Fig. 1, with 2° squares superimposed. In contrast to actual coastlines, the COADS land squares

¹ The July SST and cloud cover figure captions in the Grey Book were inadvertently transposed.

(dark in Fig. 1) provide only a crude estimate of geography. Consequently, contours near the coast are not necessarily accurate; this point is underscored by the contamination of coastal squares by observations made near shore. In addition, the plotting package shifts data to the centers of the 2° squares; therefore the coastal observations do not represent open ocean conditions well. The figures to follow therefore take the expedient approach of blanking out the near-shore COADS data. In addition, the observations in the southwest corner of the domain off Peru are sparse (the hatched squares were omitted from the analysis), and the resulting analyses are often noisy.

The averages of total cloud cover, SST, and surface pressure are presented

here. "Cloud cover" in COADS is total cloudiness, as observed from the surface. For the regions under consideration, it correlates well with low cloud cover, i.e., marine stratocumulus, broken stratus, and trade cumulus.

Acknowledgments: This research is supported by the National Aeronautics and Space Administration and the Office of Naval Research.

REFERENCES

- FIRE Project Office, 1989: FIRE Phase II Research Plan: *An Omnibus Proposal*. NASA Langley Research Center, 114pp
- Woodruff, S.D., R.J. Slutz, R.L. Jenne, and P.M. Steurer, A comprehensive ocean-atmosphere data set. *Bull. Amer. Meteor. Soc.*, **69**, 1239-1250.

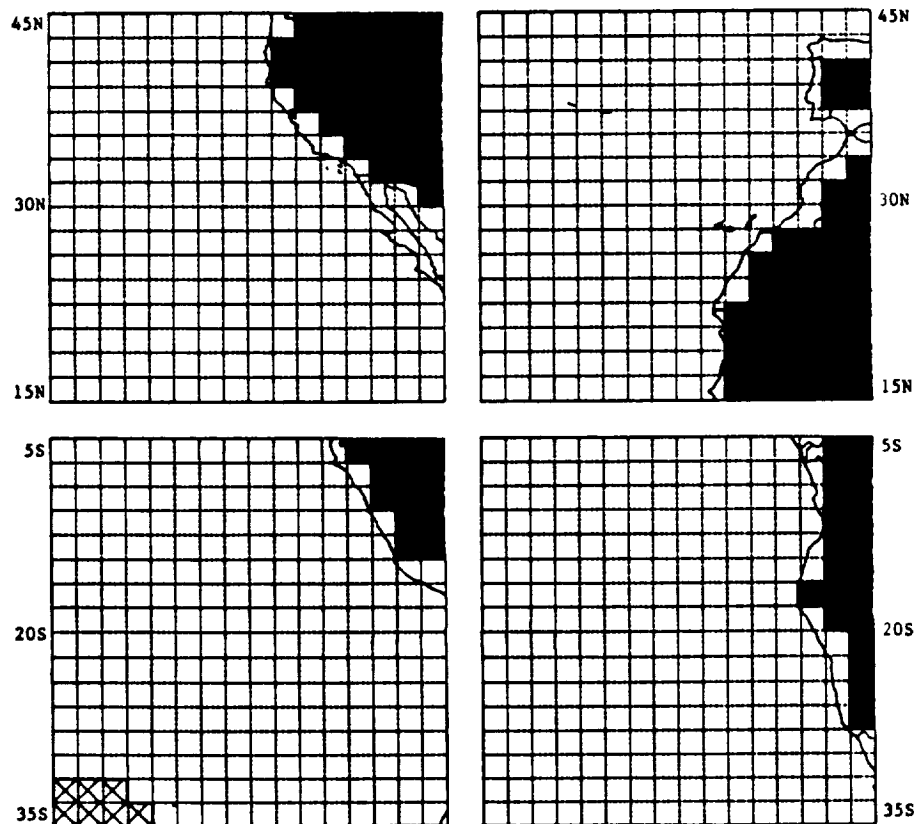
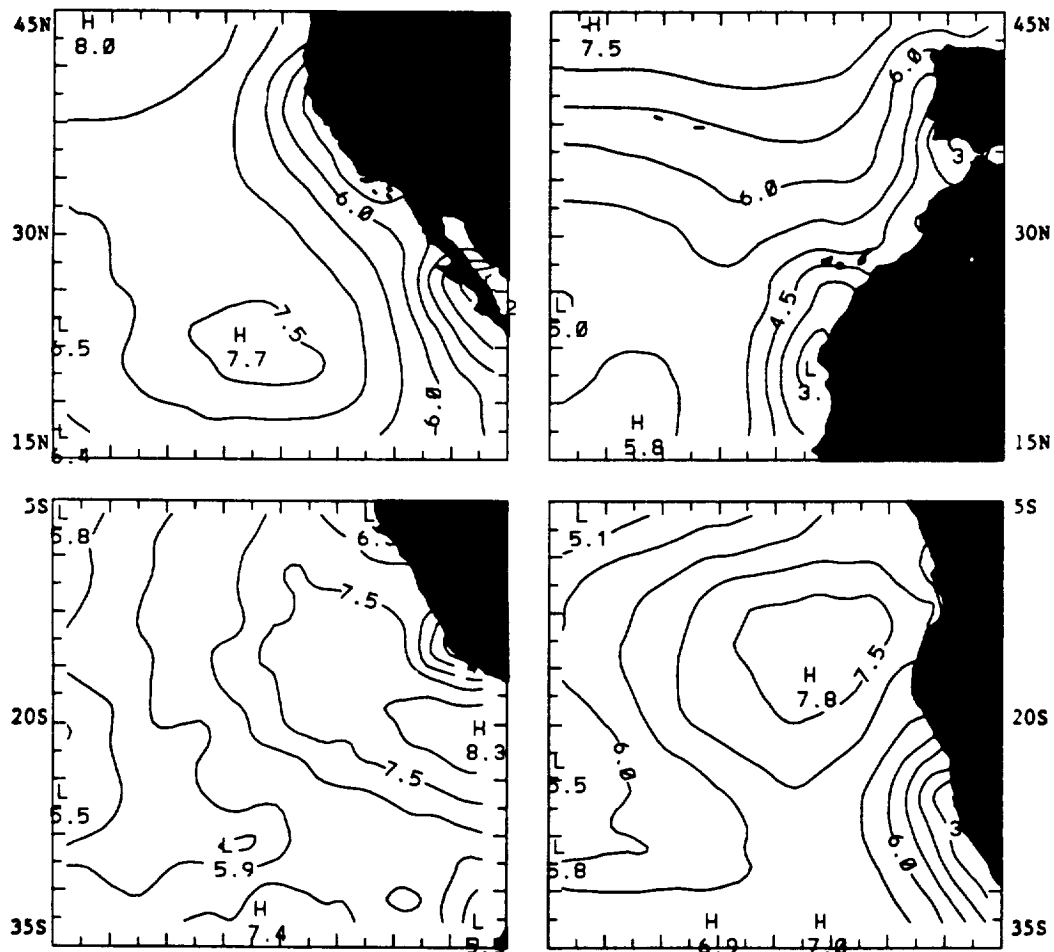


Fig. 1. Analysis domains for the four MSc regimes under consideration. Dark squares are COADS continents; 2° grid is superimposed. Hatched squares in the South Pacific were excluded from the analysis.

2. Cloudiness

The long-term average of total cloud cover (in tenths—below) is surprisingly similar to that of July (shown in Appendix B of the Grey Book [p.B-15]), with the off-shore maxima of cloudiness having somewhat lower values in the annual mean. Although very noisy, the data off Peru indicate that, both for July and for the annual mean, the maximum cloud cover occurs over the southeast

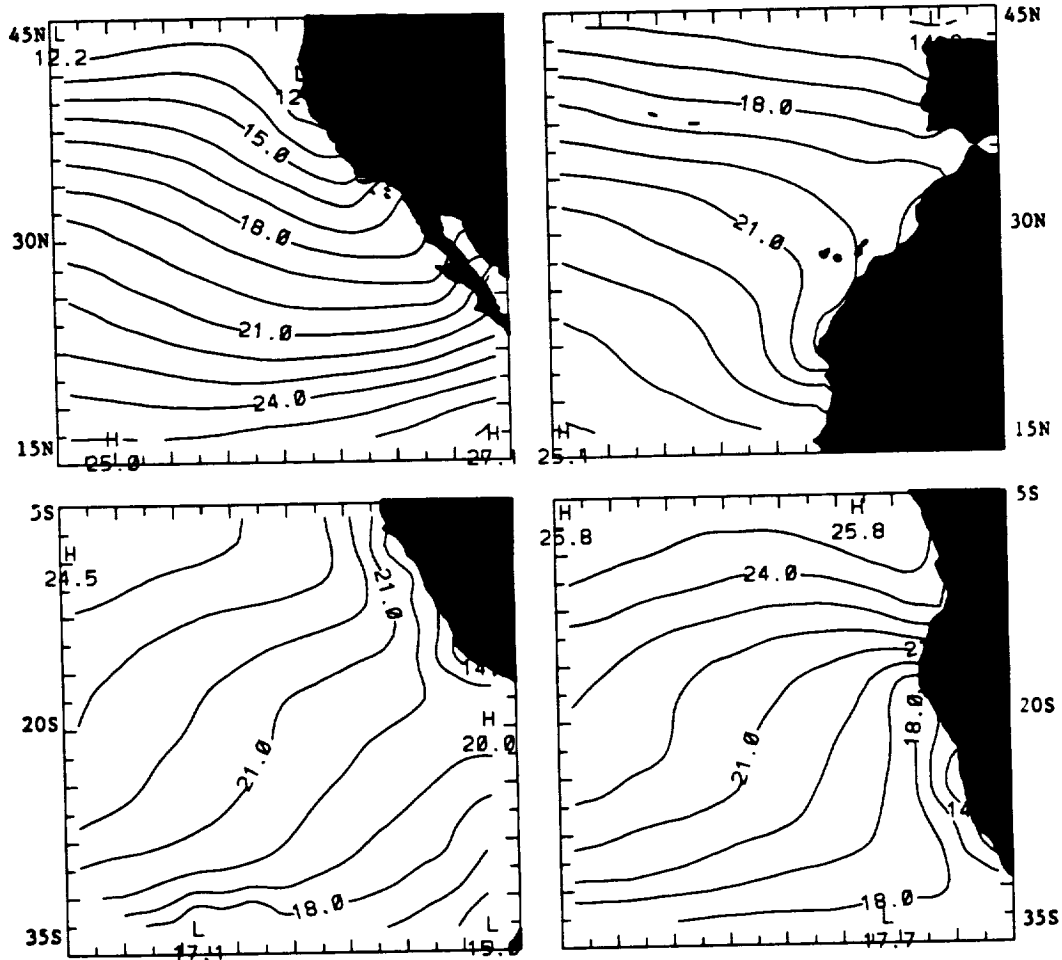
Pacific, with a large area just off shore exhibiting coverage of more than 90% in July and more than 75% in the annual average. The least cloudiness occurs off Morocco; in fact, the larger values to the north of the Morocco domain are associated with frontal activity, and the subtropical cloudiness, in the annual average, is shifted to the far southwest of the domain.



3. Sea-Surface Temperature

As with the cloud cover, the annual mean SST ($^{\circ}\text{C}$ —below) is quite similar to the July average (Appendix B [p. B-13]), although, naturally, the July temperatures are somewhat higher in the Northern Hemisphere and cooler in the Southern Hemisphere. Note that the coa-

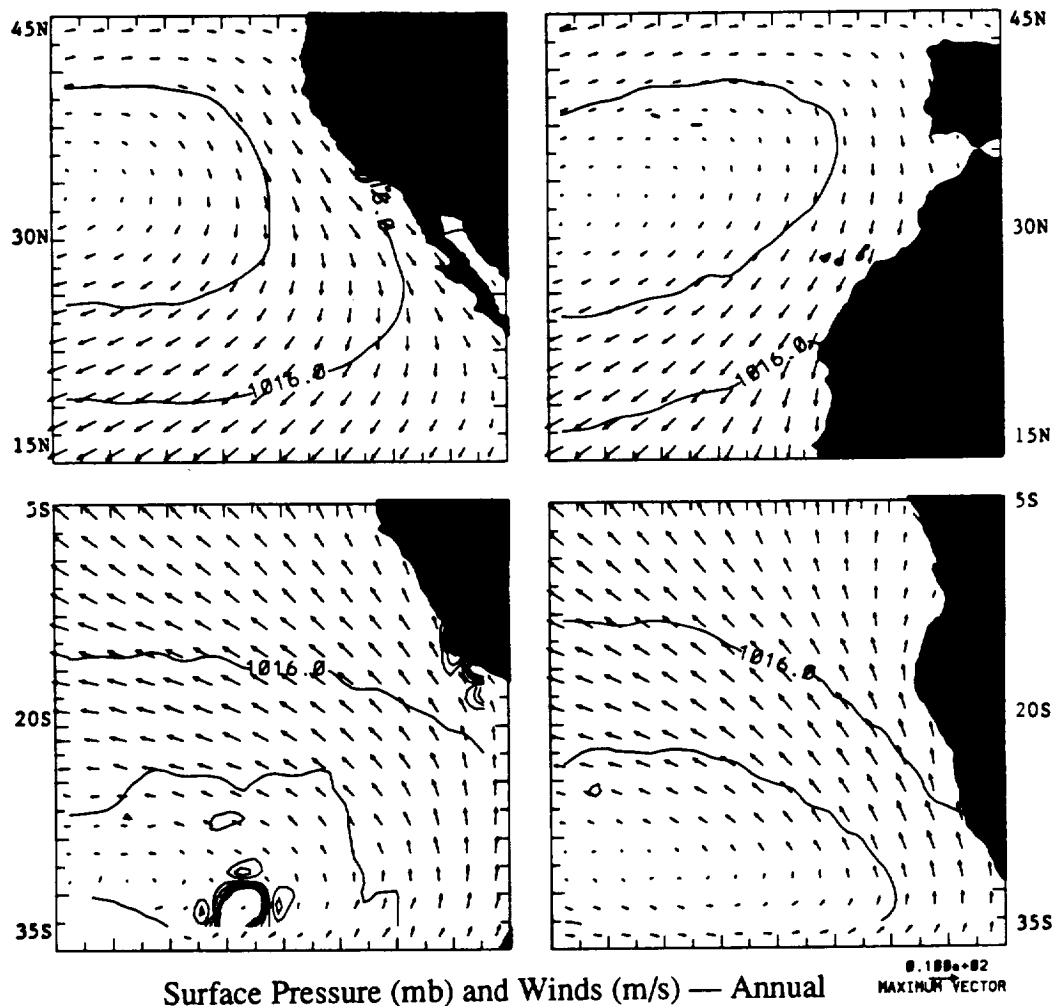
stal upwelling is evident in all four regimes even in the annual average, and that the bias of the temperatures off Morocco by about $+3^{\circ}\text{C}$ over the other areas holds in the annual average as well as for July. Also of interest is the much stronger N-S SST gradient off California compared to the other regimes.



4. Surface Pressure

The surface pressure and wind fields (below) for the annual average reflect seasonality to a greater degree than does the cloud field, but there are still large similarities between the annual average and the July average (Appendix B [p. B-14]). The subtropical highs are stronger—in both hemispheres—in July and shifted northward slightly, but the

wind fields in the areas of maximum cloud cover are remarkably similar. There is an apparent correlation of the areas of maximum cloudiness with stronger winds, suggesting that either or both advective effects and strong surface fluxes play a strong role in cloud maintenance, at least from the climatological perspective.



Large-scale Variability in Marine Stratocumulus Clouds Defined from
Simultaneous Aircraft and Satellite Measurements

Bruce A. Albrecht
Penn State University
University Park, PA 16802

and

Roy W. Barlow
Cloud Physics Branch
Meteorological Office, London Road, Berks RG12 2SZ, UK

Satellite images often show significant variations in the structure of marine stratocumulus clouds on scales ranging from 10 km to 1000 km. This is illustrated in Fig. 1 where a GOES West satellite image shows a well-defined variation in cloud structure near 32 N, 122 W on 30 June 1987. Aircraft measurements were made with the UK C-130 and the NCAR Electra on this day as part of the FIRE Marine Stratocumulus IFO. The UK C-130 made measurements in a solid cloud area at approximately 32.5 N, 123.5 W and just north of a more textured cloud area sampled by the Electra at approximately 31 N, 122 W. In this paper we compare the mean, turbulent, and the microphysical structure of the clouds sampled in these two areas and attempt to explain the differences in cloud structure at regions E and B in Fig. 1.

The two aircraft used in this study were comparably instrumented and both flew along-wind and cross-wind legs of about 60 km in length at several levels in the boundary layer to make estimates of turbulent quantities. Mean profiles of temperature, mixing ratio, winds, and microphysical quantities were obtained during slow ascents and descents.

In an attempt to identify any systematic differences between the measurements made with the two aircraft, we analyzed data that were collected on 14 July 1987 with the C-130 and the Electra flying in close formation at an altitude of 250 m. In general, both the mean and the standard deviation of the temperature, moisture, pressure and the sea surface temperature were in good agreement during the intercomparison. The mean temperature from the two aircraft differed by about 0.2°C and the mixing ratio differed by about 0.1 g/kg.

The mean flow in the regions sampled by the C-130 and the Electra on 30 June was weak. A 1028 mb high was centered about 1500 km west of the Oregon and Washington coast and resulted in relatively weak pressure gradients off the coast of southern California (Kloesel et al., 1988). Boundary layer winds were about 4 m/s from the northwest. The sea surface temperature was about 18°C in the area of the Electra compared with 16°C at the more northerly location of the C-130. These differences in temperature are reflected in the potential temperature profiles made during the early part of the mission (1100 LST) shown in Fig. 2. The boundary layer temperature at the Electra's location is about 2°C warmer than that at the C-130. The C-130 sounding is about 1-1.5 g/kg drier than the Electra as shown by the mixing ratio profiles in Fig. 3. Although the cloud thickness is about the same in the two regions,

the cloud liquid water content measured from the C-130 is about 0.2 gm^{-3} greater than that measured with the Electra (Fig. 4). Soundings taken later in the experiment from 1600-1800 LST show similar differences in the boundary layer temperature and moisture (Fig. 5 and 6).

The thermodynamic structures at the two locations are similar. The inversion is at a height of about 900 m at both sites and varies little with time. The air just above the inversion, however, is drier in the area sampled by the Electra than it is in the area sampled by the C-130. This results in a 10 K decrease in equivalent potential temperature (THETA_E) across the inversion in the Electra sounding with no jump in THETA_E at the inversion for the C-130. A well-defined moist layer extends from about 1250-1750 m in the C-130 sounding. This moist layer is capped by a weak inversion. Evidence of a moist layer is also present in the Electra sounding. These soundings indicate that the relatively complicated moisture stratification above the inversion on this day appears to have a large areal extent.

The soundings at both locations show a stable layer at about 450 m, which indicates some decoupling (Nicholls, 1984). This stable layer is better defined later in the day (Fig. 5), which is consistent with the diurnal variations described by Nicholls. Although small cumuli were observed beneath and sometimes penetrated into the main stratus deck in both areas sampled, the stable layer is better defined in the Electra sounding than in the C-130 sounding. Lidar observations from the Electra indicate a cumulus cloud base near the weak stable layer at 450 m, which is about 200 m below the stratus deck. In addition, the moisture structure clearly shows the decoupling (Fig. 6). The lower layer is shallower in the late afternoon sounding than in the earlier sounding. This may be due to the moistening of the low levels and a drying of the cloud layer associated with the decoupling.

The microphysical and turbulence data are being compared in an attempt to explain the differences in the cloud liquid water content obtained with the two aircraft and the differences in cloud structure shown by the GOES image. In addition, data are being analyzed for three other days during the experiment when coordinated downstream flights were made with the Electra and the C-130.

Acknowledgments: We gratefully acknowledge the cooperation and support of the British Meteorological Research Flight and the NCAR Research Aviation Facility. One of us (BAA) was supported by the National Science Foundation Grant ATM-8619854) and the Office of Naval Research (N000014-86-K-06880) for this work.

References:

Kloesel, K.A., B.A. Albrecht, and D.P. Wylie, 1988: FIRE marine stratocumulus observations--Summary of operations and synoptic conditions. Penn State University, Department of Meteorology, FIRE Technical Report No. 1, University Park, PA 16802, 171 pp.

Nicholls, S., 1984: The dynamics of stratocumulus: Aircraft observations and comparisons with a mixed layer model. Quart. J. Roy. Meteor. Soc., 110, 783-820.

ORIGINAL PAGE
BLACK AND WHITE PHOTOGRAPH

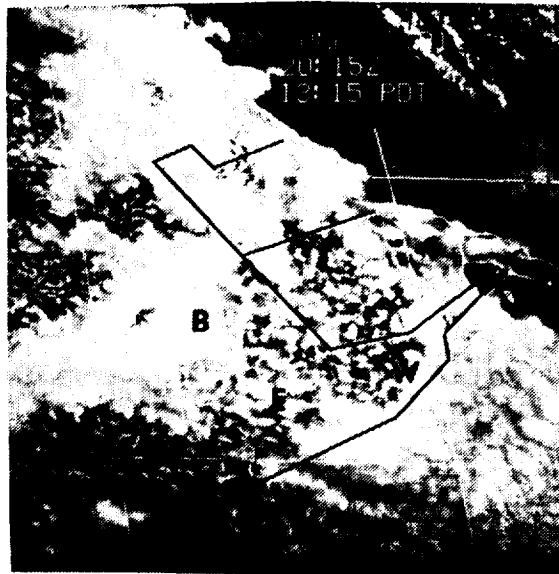


Figure 1. GOES West visible image for 30 June 1987 at 2015 UTC. The 'B' marks the general area sampled by the UK C-130 and the 'E' marks the region sampled by the NCAR Electra.

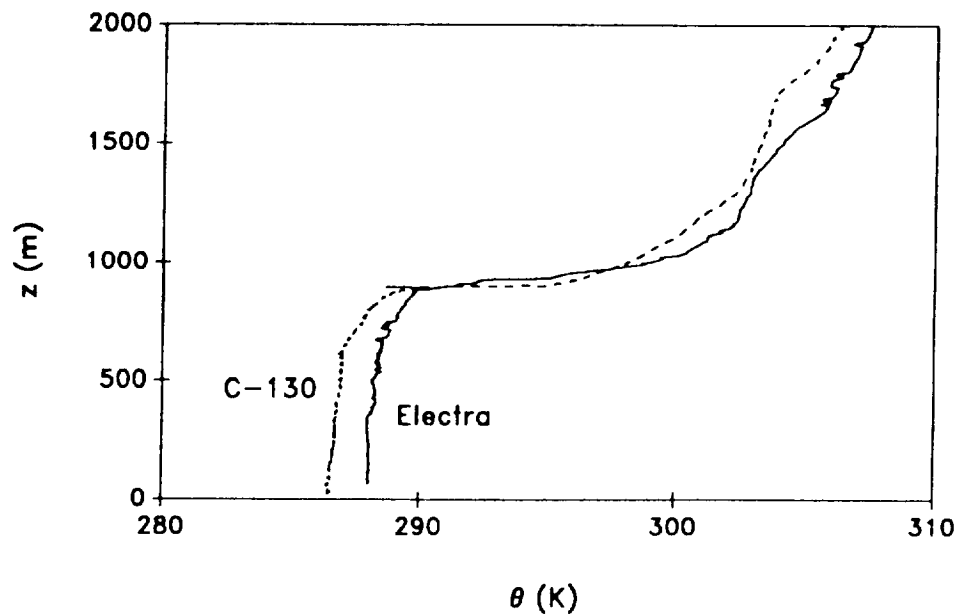


Figure 2. Potential temperature profile from the C-130 at approximately 9:45 UTC and the NCAR Electra at approximately 19:10 UTC on 30 June 1987.

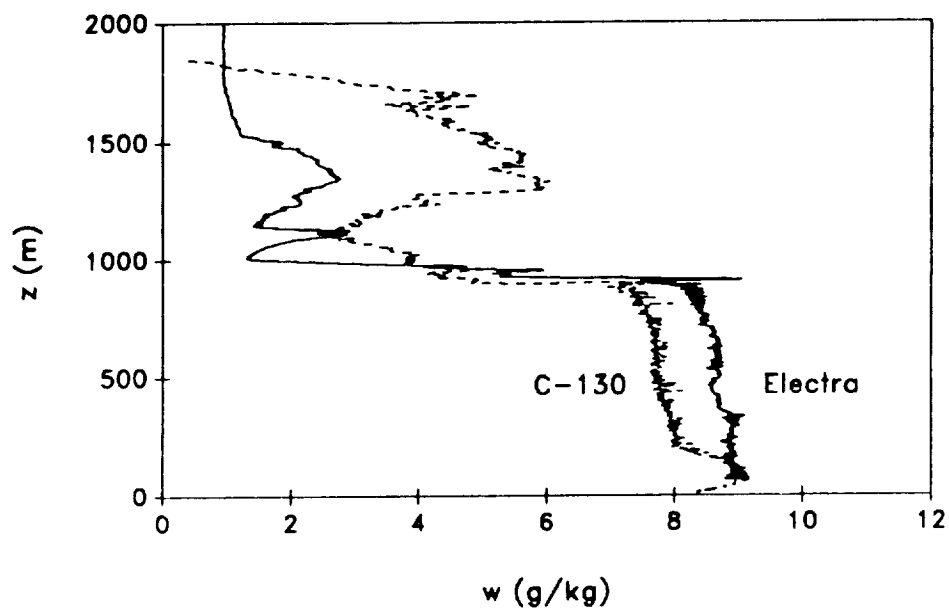


Figure 3. Same as Fig. 2 but for mixing ratio.

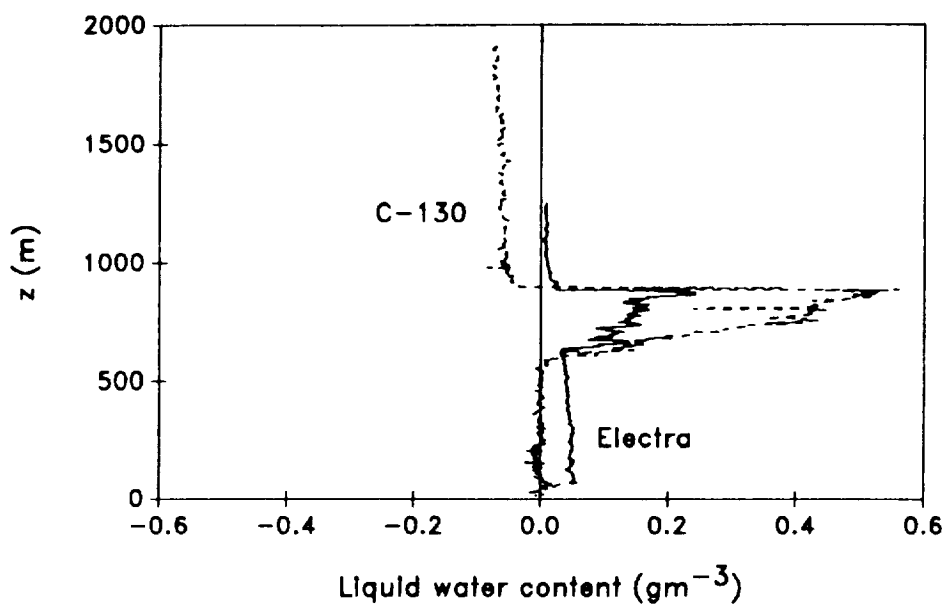


Figure 4. Same as Fig. 2 but for liquid water. Offsets have not been removed.

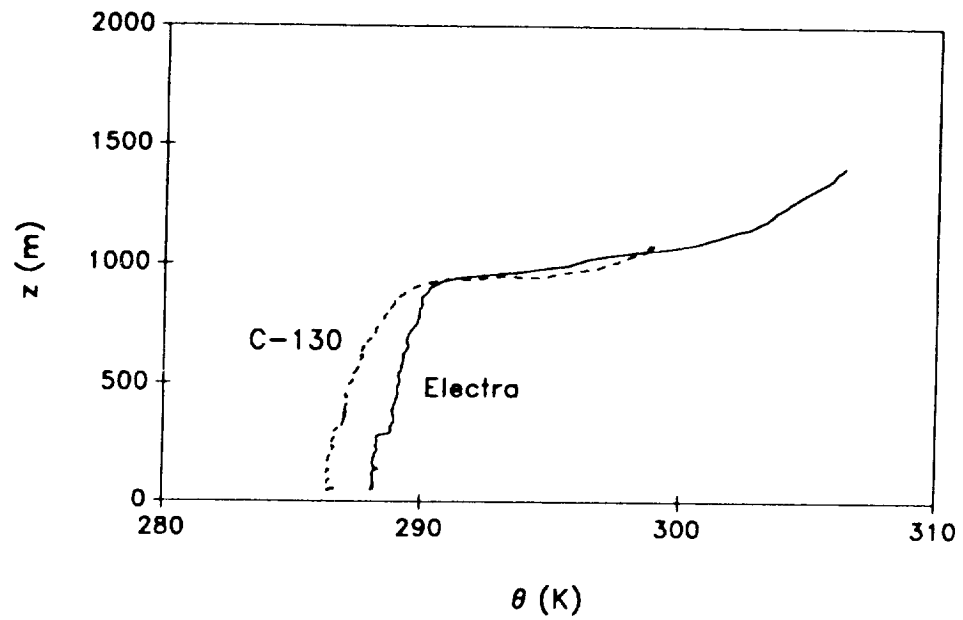


Figure 5. Potential temperature profile for the C-130 at approximately 22:35 UTC and the NCAR Electra at 23:29.

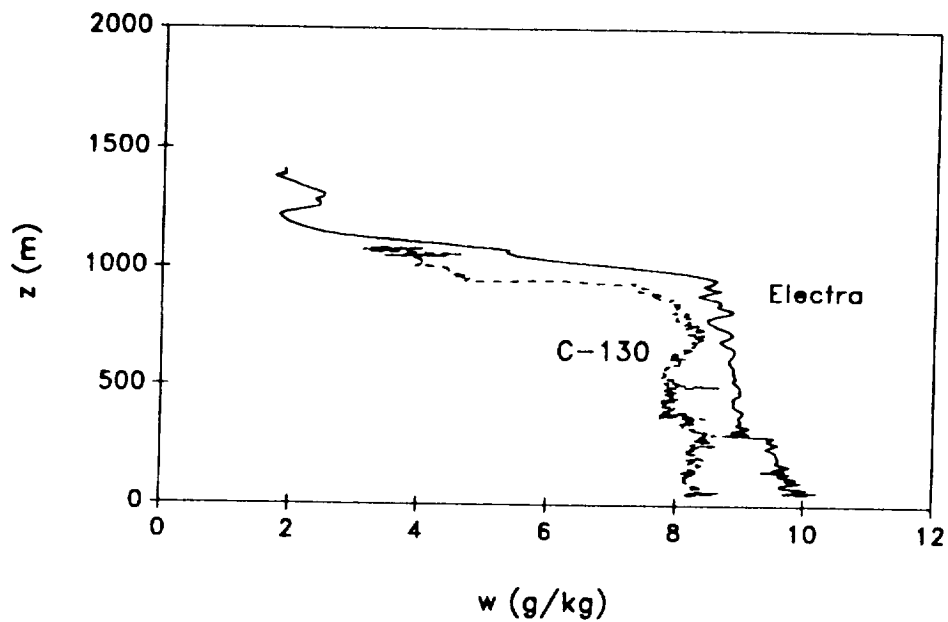


Figure 6. Same as Fig. 5 but for mixing ratio.

ON ESTIMATING SCALE INVARIANCE IN STRATOCUMULUS CLOUD FIELDS

Genevieve Seze[°] and Leonard A. Smith^{°°}[°]LMD/Ecole Polytechnique 91128 Palaiseau Cedex (France)^{°°}DAMTP, Cambridge University Cambridge CB3 9EW (UK)

Examination of cloud radiance fields derived from satellite observations sometimes indicates the existence of a range of scales over which the statistics of the field are scale invariant. Many methods have been developed to quantify this scaling behavior in geophysics. The usefulness of such techniques depends both on the physics of the process being robust over a wide range of scales and on the availability of high resolution, low noise observations over these scales. The present paper applies these techniques (area perimeter relation, distribution of areas, estimation of the capacity, d_0 , through box counting, correlation exponent) to the high resolution satellite data taken during the FIRE experiment and provides initial estimates of the quality of data required by analysing simple sets. We proceed by contrasting the results of the observed fields with those of images of objects with known characteristics (e.g. dimension) where the details of the constructed image simulate current observational limits. Throughout we shall speak of cloud elements and cloud boundaries; it should be clearly understood that by this we mean structures in the radiance field: all the boundaries considered here are defined by simple threshold arguments.

DATA

The satellite images considered here are Spot images (see Figure 1), covering approximately 60km by 70km, which were taken during the FIRE experiment on stratocumulus on June 7th, 8th and 19th in the panchromatic mode (10m resolution at visible wavelengths) and the multispectral mode (20m resolution at visible and near infrared wavelengths). The results presented here are for the 10m resolution images unless otherwise stated. Two of the scenes, those from the 7th and the 8th, show overcast conditions while the scene on the 19th is almost clear with only small cumulus clouds present. For each image, several thresholds are chosen and the corresponding binary images constructed. In order to test the reliability of the methods defined below, we construct similar binary images of known scaling structure. Our aim is to determine the effect of reasonable amounts of variation in the large scale structure; here we report initial studies considering only the observational effects on the common Koch island. This set is constructed by repeated replacement of a sample pattern at smaller and smaller scales and is shown in Figure 2. In this case we know the boundary is a homogenous fractal with dimension(s) equal to $\log(4)/\log(3)$.

INDIVIDUAL ELEMENT ANALYSIS

Historically, the first approach to analysing the scaling behavior in cloud boundaries (Lovejoy, 1982) was through techniques which quantified the properties of individual cloud elements via area-perimeter studies. This approach is very appealing and we begin with it.

i) Area-Perimeter Studies

When self-similar objects are viewed under increasing magnification, details in the boundaries appear in a rate determined by the dimension of the boundary. In a similar way, one expects a relation between the area and perimeter of a collection of similar objects of different size all observed at the same resolution (Mandelbrot, 1982). In an image the area is simply defined as the number of pixels forming the cloud; the perimeter may be defined in one of two ways either (1) as the number of pixels on the cloud boundary, or (2) as the number of pixel edges on the cloud boundary.

To estimate the effects of finite resolution in the most optimal case, Koch islands of various sizes and orientations relative to a 4096x4096 grid were constructed and their areas and perimeters

were computed. The results are shown on a log-log plot of the square root of area versus the perimeter (Figure 3). The linear relation is evident. Note the variability due to the grid; this would be the expected error if every cloud had exactly the same macroscopic structure; it is, effectively, the smallest possible error level. A more complete study using clouds with homogeneous boundary dimensions but different macroscopic characteristics will be presented in a more detailed report. As expected the "scatter" in this area-perimeter graph is greater due to macroscopic structure in the observations.

The area and perimeter of the cloud elements from the SPOT images were computed for a variety of different subscenes of size 1024×1024 to 6000×7000 pixels. To avoid finite length scale effects clouds smaller than 16 pixels in area were not included in the analysis. Figure 3 shows the observed power law relation between these area and perimeters. The exponents found are almost independent of the threshold and of the size of the sub-scene and were generally similar for both the 10m and the 20m resolution images. For the stratocumulus deck this exponent is between (1.35-1.40); for the fair weather cumulus (19th) this exponent is between 1.30-1.32. A similar behavior was found by Cahalan and by Welch et al. using Landsat images. We do not, however, see the increase in these exponents with increasing threshold observed by Cahalan.

The variability found for clouds is larger than that for the Koch islands. This is in part due to the different macroscopic structure of the various cloud elements. We are also concerned that high ellipticity clouds are selectively removed from the sample because they are more likely to cross the boundary of the image. Such a bias could result in lowering the spread of observed areas for a given perimeter and producing a misleading result.

Using definition (2) for the perimeter results in changes as large as 0.8 in the estimated value of the power law exponent. This change remains if the inner cutoff (i.e. the size of the smallest clouds taken included in the estimate) is changed, such an effect does not occur in the scaling of the Koch island and indicates the presence of macroscopic effects.

i) The distribution of observed areas

For the SPOT scenes, taking reasonable thresholds, our observations are in agreement with those of Cahalan (1988) and Welch et al. (1988). Specifically, we observe that the rate at which the number of cells of a given surface area decreases with increasing surface area is well approximated by a power law over a range of scales compatible with the scene size. This result is clear on the 1024×1024 scenes but not so evident from the 2048 scene compared to the 6000 scene. Again in agreement with Cahalan, the fair weather cumulus fields appear, in general, less fragmented (exponent value smaller than 1) than the stratocumulus fields (exponent value larger than 1). The results obtained from the 3 simultaneous 20m resolution scenes appear quite consistent while they exhibit some differences between these results and those obtained with the 10m resolution scene. The extent to which these differences are due to resolution, threshold, and changes in cloud properties is not certain; however, resolution effect seems to dominate.

FULL FIELD ANALYSIS

Both the strength and the weakness of the area-perimeter method is that it does not consider the interaction of the different elements which compose the field. An alternative approach to individual element analysis is to consider the scaling properties of the boundary set of the entire field as a whole. Once the behavior of the full field is considered, the potential complexity of the structures observed increases greatly. As pointed out by Schertzer and Lovejoy (1989), the disparity in the scaling exponents reported by different groups may be due to differences in the absolute calibration and resolution of the instruments involved. Given a gridded field of fractal boundaries, it is not yet clear how much data is required to estimate the dimension. The range of scales, and hence the data requirements, will clearly depend on the complexity of the boundary. Below we give an indication of data range required by analysing a single Koch curve.

BOX COUNTING: COMPUTING THE D0 OF BOUNDARIES

For the boundary sets, the estimated capacity or fractal dimension, d_0 , is obtained by assuming that the number of boxes (aligned with the grid) required to cover the set is related to their size (side length) by a power law. The capacity is the exponent of this power law. When dealing with finitely resolved sets, it is useful to consider the variations of this exponent with length scale. We denote this quantity $d_0(l)$; d_0 is then the limiting value of $d_0(l)$ as l tends to zero.

Figure 5 shows this function for a single Koch island which fills the initial frame. Note the slow transition to the asymptotic value; effectively scales greater than 2^{16} times (or however many data points are bad) the size of the element must be treated as a transition zone. This makes the analysis of a field composed of a variety of distinct elements of various sizes difficult. For the SPOT images, for the cloud boundaries, the same estimation of d_0 has been done for both 1024, 2048 and 4096 square scenes (Fig 5). The continuity of the boundary on the grid can induce a value close to 1 for the smallest scales while the outer effects produce $d_0(l) = 2$ for the largest. The lack of a range of scales with a flat plateau makes it impossible to reliably estimate d_0 from these curves. We note however, that near the smallest scales the slope is roughly independent of the threshold; as the sub-scene size increases this range of this scaling increases. This indicates that the technique might converge if observations over a slightly longer range of scales were available.

POINT DISTRIBUTIONS: CORRELATION INTEGRAL

The correlation integral (Grassberger and Procaccia, 1983) has become a standard measure of the geometry of scaling point sets. This quantity has been computed for the boundary sets. The integral is defined as

$$C_2(l) = \frac{\text{Number of pairs of points separated by less than } l}{\text{Total Number of Pairs of points.}}$$

When C_2 is a power law in l , d_2 quantifies this scaling in the limit of zero length scales. As with $d_0(l)$ we consider $d_2(l)$, the local slope of C_2 , as a function of l .

For the cloud boundaries, at the smallest scales $d_2(l)$ shows variability due to finite (quantized) length of the smallest scales used, while at large scales finite size effects bias $d_2(l)$ to smaller values (see Smith, 1988). At intermediate length scales, some sub-scenes (and thresholds) show a region in which $d_2(l)$ varies around a mean value. In general, the mean value decreases as the threshold increases. However, this variation around a mean value is not always present, and increasing the size of the image considered does not always resolve this problem. In general, increasing the true area considered is not expected to clarify the analysis if it results in the inclusion of clouds with different scaling properties (or, for example, a cloud free region!). One method for improving the statistics is to analyse several images of similar radiation fields, for example of the same region at the same time of day on different days. Cumulating the data in this way (instead of increasing the area size) appears to yield good results. We are investigating whether this approach will make it possible to use observations with lower spacial resolution data sets which are extended in time.

CONCLUSION

We have quantified the scaling behavior of the terrestrial radiance field during the FIRE experiment using observations from the SPOT satellite, noting the constraints and uncertainty imposed by the range of scales available in the data set. SPOT provides data at 10 meter resolution with an outer length scale of 100 km - the longest scaling range yet considered from a single instrument. Nevertheless the effects of a finite range of length scales and the outer boundary cutoff are clearly visible in our results. An idea of the quantity and quality of data required to ascertain reliable estimates from grid point data has been determined by examining the scaling of simple sets. Finally, the correlation exponent has been computed for the radiation field data with promising results.

References

- Cahalan, 1988: Overview of fractal clouds. *Advances in Remote Sensing*. Deepark Pub, 1988.
- Lovejoy, S. , 1982: The area-perimeter relation-ship for rain and cloud areas. *Science*, 216.
- Grassberger, P. and I. Procaccia, 1983: Characterization of strange attractors. *Phys. Rev. Lett.* 50, 346-349.
- Lovejoy, S. and D. Schertzer, 1989: Multifractal analysis techniques and the rain and cloud fields from 10-3 to 106m. *Scaling, fractal and Nonlinear Variability in Geophysics*, edited by D. Schertzer and S. Lovejoy, Kluwer.
- Mandelbrot, B, 1982: *The Fractal Geometry of Nature*. Freeman, 465pp.
- Smith, L.A., 1988: Intrinsic limits on dimension calculations, *Phys. Lett. A* 133, 6, 283.
- Welch, R.W., K.S. Kuo, B.A. Wielicki, S.K. Sengupta, L. Parker, 1988: Marine stratocumulus cloud fields off the coast of southern California observed using Landsat imagery. Part I: Structural characteristics. *J. Appl. Meteor.*, 27, 341-362.

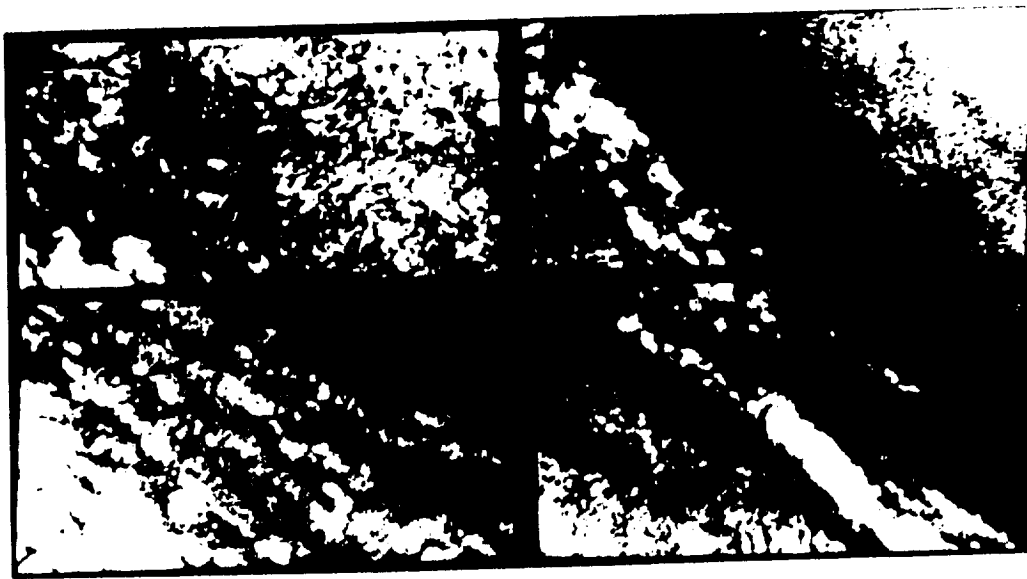


Fig 1. 7th of July SPOT scene

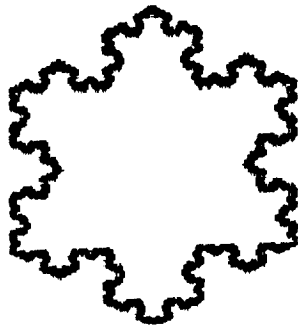


Fig 2. Koch Island

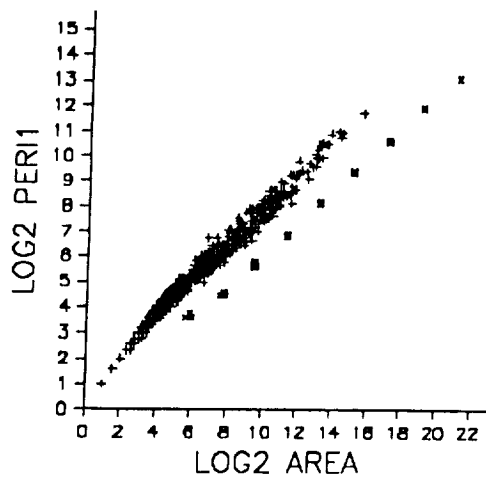


Fig 3. perimeter versus area for Koch islands (x symbol), for clouds extracted from a 4096 square scene on the 7th of July (+ symbol). For clarity, the Koch island results are displaced in x (area) by a factor of 2.

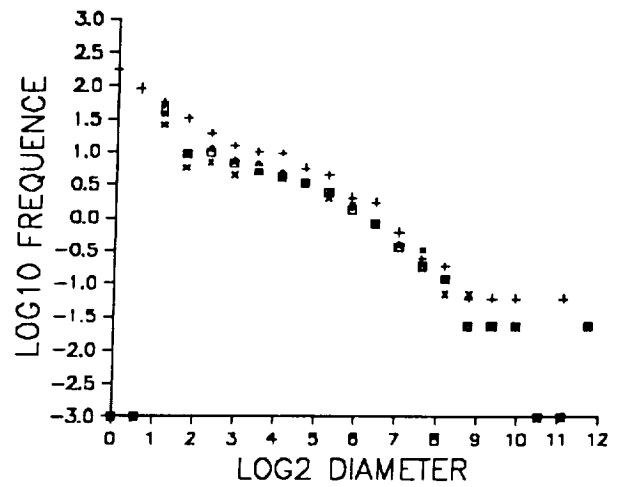


Fig 4: area distribution for a 4096 square scene on the 7th of July (+ curve) and the 3 corresponding 20m resolution scene (x, \square and \triangle symbols)

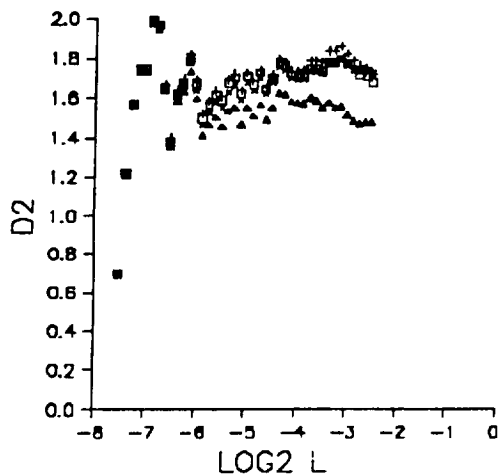


Fig 6: d2 versus scale for a cloud scene on the 8th of July for 4 different thresholds.

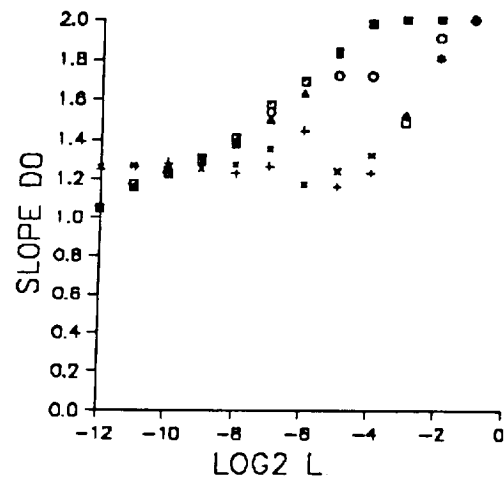


Fig5: d0 versus scale eps for two 4096 square koch islands (+ and x symbols), for one 4096 square Spot scene on the 7th of July for 3 different thresholds (\square , \triangle , \circ symbols)

Inhomogeneities of Stratocumulus Liquid Water

Robert F. Cahalan

Laboratory for Atmospheres, Goddard Space Flight Center

Jack B. Snider

NOAA/ERL/Wave Propagation Laboratory

There is a growing body of observational evidence on inhomogeneous cloud structure, most recently from the extensive measurements of the FIRE field program (Albrecht et al., 1988). Knowledge of cloud structure is important because it strongly influences the cloud radiative properties, one of the major factors in determining the global energy balance. Current atmospheric circulation models use plane-parallel radiation, so that the liquid water in each gridbox is assumed to be uniform, which gives an unrealistically large albedo, forcing the models to divide the liquid water by a "fudge factor" to get the albedo right (Harshvardhan and Randall, 1985). In reality cloud liquid water occupies only a subset of each gridbox, greatly reducing the mean albedo. If future climate models are to treat the hydrological cycle in a manner consistent with energy balance, a better treatment of cloud liquid water will be needed.

FIRE concentrated upon two cloud types of special interest: cirrus and marine stratocumulus. Cirrus tend to be high and optically thin, thus reducing the effective radiative temperature without increasing the albedo significantly, leading to an enhanced greenhouse heating. In contrast, marine stratocumulus are low and optically thick, thus producing a large increase in reflected radiation with a small change in emitted radiation, giving a net cooling which could potentially mitigate the expected greenhouse warming. The FIRE measurements in California stratocumulus during June and July of 1987 show variations in cloud liquid water on all scales. Boers and Betts (1988) describe the vertical structure, while Cahalan and Snider (1989, hereafter CS) discuss horizontal variations, which is our focus here. Such variations are associated with inhomogeneous entrainment, in which entrained dry air, rather than mixing uniformly with cloudy air, remains intact in blobs of all sizes, which decay only slowly by invasion of cloudy air. The following paragraphs describe two important stratocumulus observations, then follows a simple fractal model which reproduces these properties, and the paper concludes by briefly discussing the model radiative properties.

Vertically integrated liquid water was measured at 10 Hz and averaged over

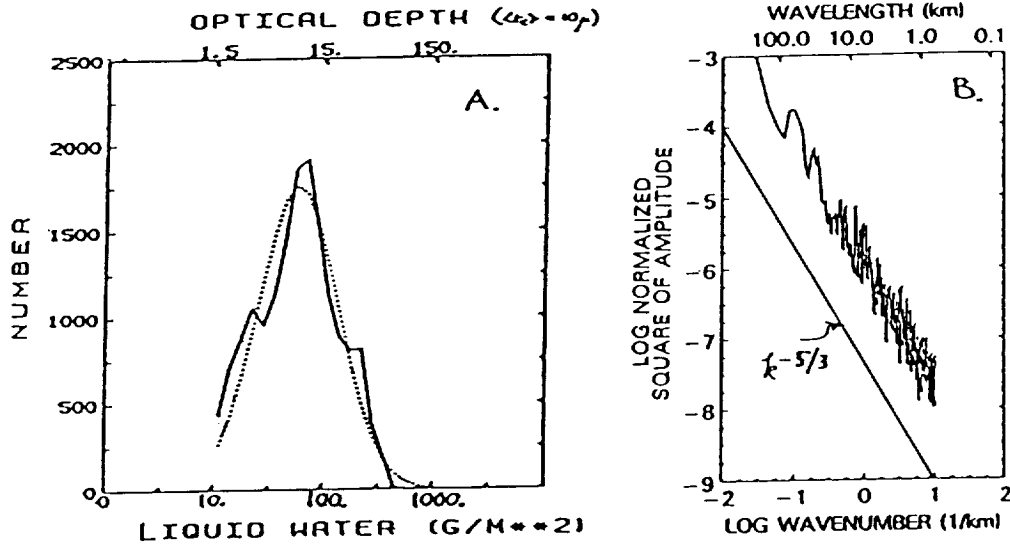


Figure 1: (a) Histogram of logarithm of vertically integrated stratocumulus liquid water in mm along with a lognormal fit. The equivalent optical depth scale shown at the top assumes a 10 micron effective radius. (b) Wavenumber spectrum of integrated liquid water computed from time series assuming 5 m/s frozen turbulence.

1 minute intervals during a 3-week period on San Nicolas Island. The histogram of this data is shown in the first figure on a log-linear scale, with a lognormal fit plotted for comparison. The lognormal roughly follows the data, while differing in detail. The “shoulders” seen to each side of the observed central peak are a reminder that individual days often show a bimodal distribution.

The liquid water wavenumber spectrum shown in the second figure was estimated from the frequency spectra computed from several 1-day time series from the same 19-day data set used for the histogram. Results were translated from frequency to wavenumber assuming frozen turbulence with a 5 m/s mean advection. The least-squares fit over the mesoscale regime from about 400 km down to about 400 m gives $S(k) \sim k^{-5/3}$.

This is the spectrum expected from a “passive” scalar (i.e. a scalar field whose variations in space and time are due only to advection.) when energy from a small-scale source (convection) is being transferred to larger scales by 2-dimensional homogeneous turbulence (Kraichnan, 1967; Lilly, 1989). This mesoscale $5/3$ power spectrum was previously observed in velocity and potential temperature spectra from commercial aircraft data (Gage and Nastrom, 1986). The fact that the mesoscale liquid water spectrum is that expected for a 2-dimensional passive scalar — one being forced by small-scale convection — suggests that the total integrated liquid water in stratocumulus clouds fluctuates with the mesoscale-averaged vertical velocity, being large in updrafts and

small in downdrafts. This kind of behavior has been observed in fine-resolution numerical simulations (MacVean and Nicholls, 1988), though they do not reproduce the highly irregular fractal structure described above. At scales smaller than the cloud thickness (about 200 m) the spectrum drops off more rapidly, the slope being closer to -3 (CS). This within-cloud regime is still poorly understood, but is apparently not consistent with a 3-dimensional homogeneous cascade of energy from larger scales, which would also give a 5/3. The steep falloff could be related to the distribution of energy sources and sinks, including the active role of condensation, or to the inhomogeneity of the transfer process. More work is needed on the within-cloud regime, but the following focuses upon the mesoscale structure because of its greater impact on the large-scale energy balance.

In order to simulate the mesoscale fractal structure of stratocumulus liquid water, a procedure is needed to generate a random function having the probability and spectrum shown above. As a first step, variations in only one horizontal direction will be allowed, forming fractal streets, a simplified version of the cloud streets observed in the July 7 Landsat scene during FIRE (CS). Consider a stratocumulus cloud forming an infinitely long slab of horizontal width $L \approx 100\text{km}$ and a typical optical depth of, say, $\tau_0 = 10$. Divide this into two slabs of width $L/2$, and transfer a fraction f_1 of the liquid water from one half to the other, with the direction chosen at random. The optical depth in one half is then increased (by increasing the density — thickness is assumed unchanged), and the other half is correspondingly thinned. This may be written $\tau_1^{(\pm)} = (1 \pm f_1)\tau_0$, where the superscript on the left indicates whether the brighter or darker half is being considered.

To continue the process, each half is itself divided in half, and a fraction of liquid water, f_2 , is transferred, again in a random direction. After iterating for n cascade steps, there are 2^n segments, each with an optical depth of the form

$$\tau_n^{(\pm \dots \pm)} = \prod_{k=1}^n (1 \pm f_k) \tau_0, \quad (1)$$

where $0 < f_k < 1$. Any of the possible combinations of signs in (1) may be found somewhere among the 2^n segments. An upper bound on the optical depth of the optically thickest segment may be found from

$$\tau_{max} = \prod_{k=1}^n (1 + f_k) < \prod_{k=1}^n \exp(f_k) = \exp\left(\sum_{k=1}^n f_k\right). \quad (2)$$

Consider two cases: a “singular model” in which the fraction does not change with k (i.e. $f_k = f$), and a “bounded model” in which the fraction decreases (i.e. $f_k = fc^k$, where f and c are both constants between 0 and 1). The upper bound given by (2) diverges for the singular model, and one can show that the liquid water becomes concentrated on a fractal set of singularities as $n \rightarrow \infty$.

The upper bound for the bounded model is $\exp(fc/(1-c))\tau_0$, and is close to τ_{max} . It is possible to show that both models have a wavenumber spectrum of the form $S(k) \sim k^{-\alpha}$, where

$$\alpha = \begin{cases} 1 - \ln_2(1 + f^2), & \text{(singular model)} \\ 1 - \ln_2(c^2), & \text{(bounded model)} \end{cases} \quad (3)$$

Note that as $f \rightarrow 1$, the exponent of the singular model approaches zero, giving a flat spectrum, while as $f \rightarrow 0$ the spectrum steepens to k^{-1} . No value of f allows the singular model to fit the observed $k^{-5/3}$ spectrum. The exponent of the bounded model, on the other hand, gives $\alpha = 5/3$ if we choose $c = 2^{-1/3}$. The probability density is sensitive to c , and often shows considerable structure, but when $c = 2^{-1/3}$ it is close to lognormal, and similar to the first figure.

These simple models of one-dimensional fractal cloud streets can be generalized to allow variations in three dimensions and tuned to simulate other cloud types. The albedo and other radiation properties are computed by Monte Carlo techniques, and results are parameterized to provide alternatives to plane parallel theory. For the stratocumulus models the redistribution of liquid water at each iteration decreases the mean albedo from the plane parallel case, since the albedo of optically thick regions saturates for large optical depths, so that realistic amounts of cloud liquid water lead to realistic albedos (Cahalan, 1989). Much remains to be done both in documenting the global climatology of cloud fractal structure and in understanding the physical processes underlying this structure, but improved observations and more appropriate analytical tools are finally allowing the great complexity of cloud liquid water to be approximated as something other than a uniform distribution.

References

- Albrecht, B. A., D. A. Randall, and S. Nicholls (1988), Observations of marine stratocumulus clouds during FIRE, *Bull. Amer. Meteor. Soc.*, **69**, 618-626.
- Boers, R., and A. K. Betts (1988), Saturation point structure of marine stratocumulus clouds, *J. Atmos. Sci.*, **45**, 1156-1175.
- Cahalan, R. F. (1989), Overview of fractal clouds, in **Advances in Remote Sensing Retrieval Methods**, A. Deepak Publishing, pp. 371-389, xxiv + 519 pp.
- Cahalan, R. F., and J. H. Joseph (1989), Fractal statistics of cloud fields, *Mon. Wea. Rev.*, **117**, 261-272.
- Cahalan, R. F., and J. B. Snider (1989), Marine stratocumulus structure during FIRE, *Remote Sens. Environ.*, **28**, 95-107.

Gage, K. S. and G. D. Nastrom (1986), Theoretical interpretation of atmospheric wavenumber spectra of wind and temperature observed by commercial aircraft during GASP, *J. Atmos. Sci.*, **43**, 729-740.

Harshvardhan and D. A. Randall (1985), Comments on "The parameterization of radiation for numerical weather prediction and climate models", *Mon. Wea. Rev.*, **113**, 1832-1833.

Kraichnan, R. H. (1967), Inertial ranges in two-dimensional turbulence, *Phys. Fluids*, **10**, 1417-1423.

Lilly, D. K. (1989), Two-dimensional turbulence generated by energy sources at two scales, *J. Atmos. Sci.*, **46**, 2026-2030.

MacVean, M. K., and S. Nicholls (1988), A fine-resolution, two-dimensional numerical study of a cloud-capped boundary layer, Proceedings of the 10th International Cloud Physics Conference, Bad-Hamburg, FRG, August 15-20, pp. 425-427.

INTERCOMPARISONS OF GOES-DERIVED CLOUD PARAMETERS AND SURFACE OBSERVATIONS OVER SAN NICOLAS ISLAND

P. Minnis
Atmospheric Sciences Division, NASA Langley Research Center
Hampton, Virginia 23665-5225

C. W. Fairall
Department of Meteorology, Pennsylvania State University
University Park, Pennsylvania 16802

D. F. Young
Aerospace Technologies Division, Planning Research Corporation
Hampton, Virginia 23666

1. Introduction

The spatial sampling limitations of surface measurement systems necessitate the use of satellite data for the investigation of large-scale cloud processes. Understanding the information contained in the satellite-observed radiances, however, requires a connection between the remotely sensed cloud properties and those more directly observed within the troposphere. Surface measurements taken during the First ISCCP Regional Experiment (FIRE) Marine Stratocumulus Intensive Field Observations (IFO) are compared here to cloud properties determined from Geostationary Operational Environmental Satellite (GOES) data in order to determine how well the island measurements represent larger areas and to verify some of the satellite-measured parameters.

2. Data

Total cloud amounts and visible ($0.65 \mu\text{m}$) top-of-the-atmosphere cloud albedos were derived with the hybrid bispectral threshold method (HBTM; Minnis et al., 1987) from hourly GOES-West data (Young et al., 1989) over two 0.5° regions between 119°W and 120°W and 33°N and 33.5°N for July 1-19, 1987. Cloud albedos, cloud fractions, and integrated cloud liquid water contents were determined from measurements taken nearly continuously over San Nicolas Island (Fairall et al., 1989) with a variety of instrumentation during this same time period. San Nicolas Island (SNI) is located near the center of the east-west boundary of two satellite regions. Results from both the microwave and solar radiometer cloud liquid water content (LWC) measurements are compared to the satellite albedos. These preliminary comparisons match relatively large areal averages to essentially linear averages of the cloud fields advecting over a fixed point.

3. Results and Discussion

Mean hourly cloud fractions are shown in Fig. 1 for the SNI and HBTM results. The SNI cloud amounts, on average, are 0.045 ± 0.076 greater than the HBTM total cloud amounts. The diurnal variations are similar with early morning maxima and late afternoon or evening minima. The HBTM diurnal range, however, is 0.50 compared to 0.30 for the SNI data. Peak cloud cover occurs ~ 1 hour earlier for the HBTM results. The differences in the cloud amounts may arise for several reasons. Cloud cover over the island may not be representative of the larger area. Since the clouds generally

pass over the island, there may be some surface heating during the day which affects the cloud deck. During the night, the local heating ceases. Radiative cooling of the island is limited by the large-scale cloud field so that there should be little island effect at night. Sampling differences may also affect the comparison. A visual examination of the data using the video imagery developed by D. Wylie and P. Grimm (University of Wisconsin, unpublished, 1988) revealed that of the 19 days, the cloud cover over the island and surrounding regions appeared to vary the same during only 7 days. During 5 of the days, a V-shaped clearing formed around and downwind of the island during the afternoon. During another 5 days, the regions surrounding the island showed considerable clearing while a strip centered on the island remained overcast. The clouds cleared around the island and over the island itself during the remaining 2 days, however, the clouds cleared over the island last. In nearly all cases in the imagery, the cloud cover over the island and surrounding regions was very similar at the beginning of each day during the IFO. These visual findings are consistent with the means shown in Fig. 1 and with SNI time series of cloud amount. The HBTM and SNI results show good agreement after midnight until sunrise. Faster and more extensive clearing occurs around the island than over the island itself. This apparent island effect may also be responsible for the differences in satellite and island cloud-top heights observed during the day (Minnis et al., 1989).

A comparison of the satellite visible and SNI broadband shortwave cloud albedos is shown in Fig. 2. The narrowband albedo is considerably lower than the island-derived albedo values. Spectral differences, sampling, and the atmospheric effects included in the satellite results are primarily responsible for the differences. To minimize the spectral differences, the visible albedos were converted to broadband shortwave albedos using an empirical solar-zenith angle dependent ratio. The resulting albedos were then corrected for atmospheric effects using the simple model of Chen and Ohring (1984). Since the clouds are so low, it was assumed that they could be treated like the surface. The resulting cloud albedos derived from those in Fig. 2 are shown in Fig. 3. Cloud albedos were averaged without any weighting by cloud amount for all cases with cloud amounts greater than 10%. The dashed line represents a mirror image of the morning satellite results. It is shown to demonstrate the sizable decrease in cloud albedo during the afternoon. Despite the broadband and atmospheric corrections, the SNI cloud albedos are still higher by ~5% on average. If it is assumed that the SNI clouds are more like those over the surrounding regions when there is more cloudiness, then mean satellite cloud albedos derived by weighting the albedo by the cloud fraction should be more similar to the SNI results than those derived using a simple averaging technique. This approach was implemented with the results shown in Fig. 4. In this instance, the mean cloud albedo differences are only ~2% with greater errors near the terminator as expected (Chen and Ohring, 1984). The remaining discrepancies may be due to sampling and technique differences, bidirectional reflectance model biases, and island effects. Though visual examination of albedo is unreliable, the clouds were distinctly brighter over the island than over the adjacent areas during at least 2 days, July 5 and 8. An island effect which results in more cloud cover may also alter the cloud composition relative to the large scale.

The LWC values derived from the SNI microwave and solar measurements are correlated with the satellite visible albedos in Figs. 5 and 6, respectively. Two curves are shown in each figure. The lower curve which levels at an albedo of $\sim 55\%$ is based on the results of Coakley and Snider (1989). Their regression is

$$1/\rho = 1.74 + 48\mu_0/\text{LWC}, \quad (1)$$

where ρ is the visible reflectance, μ_0 is the cosine of the solar zenith angle, and LWC is given in gm^{-2} . The second curve shown in these figures is a regression fit to the observed data using the relationship,

$$\ln(1 - \alpha) = a + b\text{LWC}/\mu_0. \quad (2)$$

The cloud albedo is $\alpha = \rho / \chi$, where χ is an anisotropic reflectance correction factor. The coefficients a and b are -0.44 and -0.0016 , respectively, for the microwave data. The coefficients for the solar data are $a = -0.46$ and $b = -0.0016$. The curve for (2) is tangential to the knee of the curve for (1). The latter seems to fit the data well for $\text{LWC}/\mu_0 < 100 \text{ gm}^{-2}$, but does not provide for any albedos greater than $\sim 55\%$. Thus, the curve is unrealistic for higher values of albedo. Equation (2), however, shows no skill for matching the lower albedos, but it allows for additional increases in cloud albedos beyond 50% . It is concluded, therefore, that a combination of these two functions would provide a more complete representation of the relationship between albedo and LWC. This combination is accomplished by matching the curves at $\alpha = 45\%$.

4. Concluding Remarks

It appears that the SNI-observed clouds may be affected by the island. Additional support for this thesis will require analysis of satellite data over a small region centered on the instrument site. Accounting for these potential effects, the satellite-derived cloud amounts and albedos are very similar to those observed over SNI. The diurnal variations in cloud amount and cloud albedo are also comparable to those seen over other areas (e.g., Minnis and Harrison, 1984). These preliminary results have also provided a relationship which may be utilized during the day to determine cloud LWC over other parts of the IFO area.

REFERENCES

- Chen, T. S., and G. Ohring, 1984: On the relationship between planetary and surface albedos. J. Atmos. Sci., **41**, 156-158.
- Coakley, J. A., Jr., and J. B. Snider, 1989: Observed reflectivities and liquid water content for marine stratocumulus. Proc. AMS Symp., Role of Clouds in Atmospheric Chemistry and Global Climate, Anaheim, CA, Jan. 30-Feb. 3, 175-177.
- Fairall, C. W., J. E. Heve, and J. B. Snider, 1989: An 8-month climatology of marine stratocumulus cloud fraction, albedo, and integrated liquid water. Presented at FIRE Annual Meeting/ASTEX Workshop, Monterey, CA, July 10-14.

- Minnis, P., and E. F. Harrison, 1984: Diurnal variability of regional cloud and clear-sky radiative parameters derived from GOES data, Part III: November 1978 radiation parameters. *J. Clim. Appl. Meteor.*, 23, 1032-1051.
- Minnis, P., E. F. Harrison, and G. G. Gibson, 1987: Cloud cover over the eastern equatorial Pacific derived from July 1983 ISCCP data using a hybrid bispectral threshold method. *J. Geophys. Res.*, 92, 4051- 4073.
- Minnis, P., D. F. Young, R. Davies, M. Blaskovic, and B. A. Albrecht, 1989: Stratocumulus cloud height variations determined from surface and satellite measurements. Presented at FIRE Annual Meeting/ASTEX Workshop, Monterey, CA, July 10-14.
- Young, D. F., P. Minnis, and E. F. Harrison, 1989: Satellite-derived cloud and radiative parameters over the marine stratocumulus IFO. Presented at FIRE Annual Meeting/ASTEX Workshop, Monterey, CA, July 10-14.

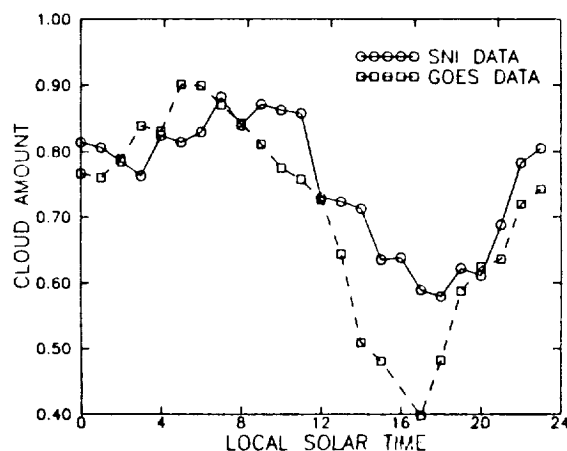


Fig. 1. Mean IFO cloud amounts derived from GOES over a $0.5^\circ \times 1.0^\circ$ region centered on San Nicolas Island and from island observations.

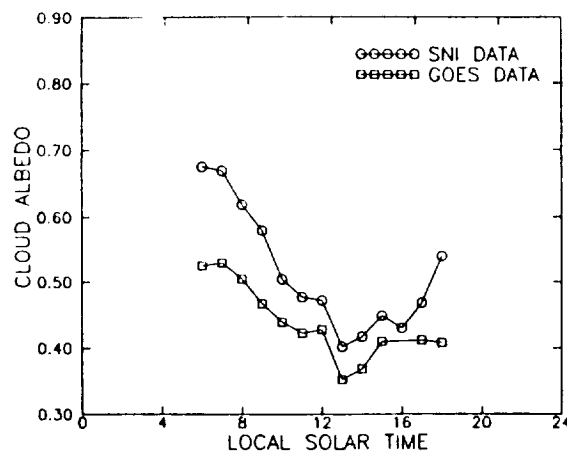


Fig. 2. Same as Fig. 1, except for GOES visible cloud albedos at the top of the atmosphere and island broadband shortwave cloud albedos.

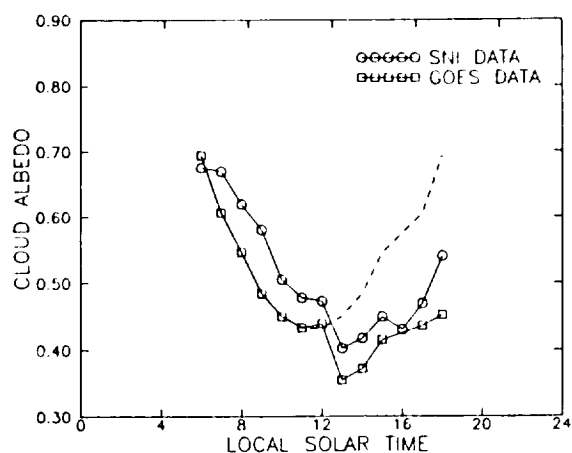


Fig. 3. Same as Fig. 2, except for broadband, atmosphere-corrected GOES cloud albedos.

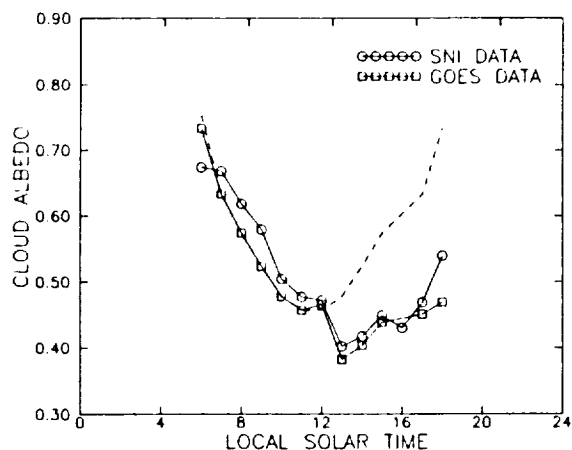


Fig. 4. Same as Fig. 3, except for cloud-amount weighted averaging of GOES cloud albedos.

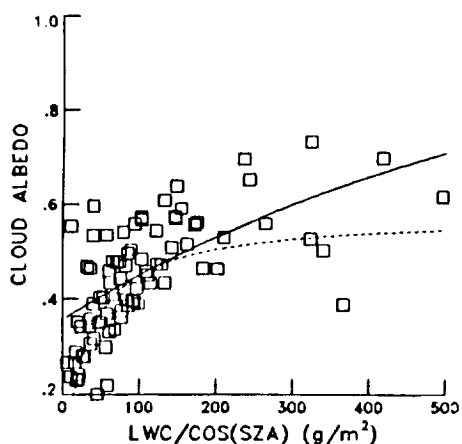


Fig. 5. Correlation of GOES visible cloud albedos and LWC derived from island microwave measurements (see text for discussion of curves).

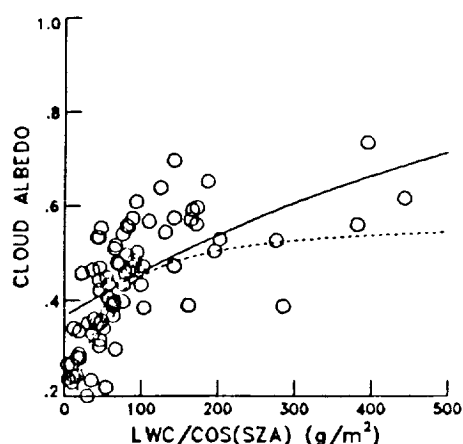


Fig. 6. Correlation of GOES visible cloud albedos and LWC derived from island solar radiation data (see text for discussion of curves).

**STRATOCUMULUS CLOUD HEIGHT VARIATIONS
DETERMINED FROM SURFACE AND SATELLITE OBSERVATIONS**

P. Minnis
Atmospheric Sciences Division, NASA Langley Research Center
Hampton, Virginia 23665-5225

D. F. Young
Planning Research Corporation
Hampton, Virginia 23666

R. Davies and M. Blaskovic
Department of Meteorology, McGill University
Montreal PQ, Canada H3A2K6

B. A. Albrecht
Department of Meteorology, Pennsylvania State University
University Park, Pennsylvania 16802

1. Introduction

Determination of cloud-top heights from satellite-inferred cloud-top temperatures is a relatively straightforward procedure for a well-behaved troposphere. The assumption of a monotonically decreasing temperature with increasing altitude is commonly used to assign a height to a given cloud-top temperature. In the hybrid bispectral threshold method, or HBTM, Minnis et al. (1987) assume that the lapse rate for the troposphere is -6.5 K km^{-1} and that the surface temperature which calibrated this lapse rate is the 24-hour mean of the observed or modeled clear-sky, equivalent blackbody temperature. The International Satellite Cloud Climatology Project (ISCCP) algorithm (Rossow et al., 1988) attempts a more realistic assignment of height by utilizing interpolations of analyzed temperature fields from the National Meteorological Center (NMC) to determine the temperature at a given level over the region of interest. Neither these nor other techniques have been tested to any useful extent. The First ISCCP Regional Experiment (FIRE) Intensive Field Observations (IFO) provide an excellent opportunity to assess satellite-derived cloud height results because of the availability of both direct and indirect cloud-top altitude data of known accuracy. This paper examines the variations of cloud-top altitude during the Marine Stratocumulus IFO (MSIFO, June 29 - July 19, 1987) derived from surface, aircraft, and satellite data.

2. Data

The soundings taken by the NCAR Electra during the IFO are used to characterize the vertical temperature and moisture structure of the lower troposphere (surface to 850 mb) over the California marine stratocumulus (MS) area. These soundings also reveal the location of the cloud top by providing the altitude of the inversion base. The Electra flights used here were confined to the Pacific between 30°N and 34°N and 119.5°W and 125.1°W . A nominal low-level lapse rate, Γ_{BL} , was constructed by averaging the lapse rates between 1000 mb and the inversion base. Average temperatures, T , and specific humidities, q , were computed for each of six levels: the surface

(1000 mb), inversion base, inversion top, 850 mb, 700 mb, and 500 mb. NMC analyses from the IFO time period were used to determine T and q at 700 and 500 mb. The six levels define five layers which are simplified to three for discussion purposes: the boundary layer BL (surface to inversion base), the above-cloud layer AL (inversion base to 850 mb), and the upper layer UL (850 mb - 500 mb). The mean temperature and humidity of each layer are the averages of T and q at the boundaries of the layer.

Continuous data taken from San Nicolas Island (SNI) with the Pennsylvania State University sodar were used to measure cloud-top altitude over the island. The instantaneous data were first averaged over all cloudy, 30-minute intervals between July 1 and 19. A mean diurnal cycle of cloud-top altitude, z_c , was computed from these interval averages.

Cloud amount C , cloud-top temperature T_c , cloud albedo, and clear-sky temperature T_{cs} , were derived from hourly GOES data using the HBTM on a 0.5° grid (Young et al., 1989). Surface temperature, T_g , was derived from T_{cs} using a simple five-layer radiative transfer model employing the parameterization for absorption in the $11.5 \mu\text{m}$ window region used by the ISCCP (Rossow et al., 1988). It is assumed that attenuation by the atmosphere above 500 mb is negligible for this area. The resulting values of T_g were generally 1.5 to 2.5 K warmer than those for T_{cs} . The effect of atmospheric attenuation on cloud-top temperature was also examined with the model. In general, the warm AL increased the outgoing radiance canceling the attenuation by the UL so that the resulting value of T_c was ~ 0.1 K colder than the original value. Therefore, it is assumed that the satellite-measured value of T_c is representative of the actual radiating temperature of the cloud top. Satellite cloud-top altitude, z_{sc} , was determined by two techniques: (1) using Γ_{BL} and the 24-hour average of T_s to compute the variation of T with height and (2) using the HBTM approach.

3. Results

Average soundings derived from the Electra results and corresponding NMC data are shown in Fig. 1. The NMC data lack the vertical resolution necessary to detect the BL inversion. In general, the NMC humidities are higher than expected from the aircraft data, but the 1000- and 850-mb temperatures were within ± 2 K of the Electra data. It was found that Γ_{BL}

$= 7.1 \text{ Kkm}^{-1}$ with a standard deviation of $\pm 1.5 \text{ Kkm}^{-1}$ for 23 soundings. Satellite-derived cloud-top heights using methods (1) and (2) are compared to the inversion base heights from the Electra in Fig. 2. The values of z_{sc} are taken from the 0.5° region containing the flight track of the Electra. The average difference in cloud-top heights are 0.2 ± 0.2 km and 0.3 ± 0.2 km for methods (1) and (2), respectively. The average value of T_c is quite close to the mean temperature of the inversion base.

The average diurnal variations of z_c and cloud-base altitude over SNI during the IFO are shown in Fig. 3. Maximum cloud-top height occurs near 1000 LST with a broad minimum around sunset. The cloud base is lowest around 0430 LST before rising steadily to a peak value of ~ 0.5 km shortly

after noon. Cloud thickness is relatively constant at ~ 0.25 km between 0200 and 1000 LST. The clouds thin rapidly to about half the maximum thickness by late afternoon before thickening again during the night. Diurnal variations of z_{sc} from both methods are superimposed on the SNI results in Fig. 4. SNI is situated between two of the 0.5° regions. The results shown in Fig. 4 were derived from the combined averages for the two regions. Data from hours with $C < 10$ percent were not used in these comparisons. The relative changes in z_{sc} are similar to those for z_c , except for the minimum in z_{sc} near 1400 LST. The diurnal range in cloud-top height is greater for the satellite data. The satellite data also appear to be noisier. Some of the noise may be due to missing data (up to 7 days of data were lost at some hours) and navigation errors (Young et al., 1989). Average cloud heights from (1) are 0.08 ± 0.1 km lower than the SNI results, while the method (2) heights are 0.15 ± 0.8 km lower than z_c . Between 0 and 10 LST, the mean values of z_{sc} are within ± 0.02 km of the sodar results. During the day, the differences increase steadily while the cloud depths decrease (Fig. 2). After sunset, the differences decrease.

4. Discussion

The differences in cloud-top heights shown in Fig. 2 appear to be due to a 0.8-K underestimate in the derived surface temperature. It is not known, however, if the actual surface temperature is the same as the 1000-mb temperature. Over SNI at night (Fig. 4), there is excellent agreement suggesting that there is no problem with the satellite-derived surface temperature. During the day, the underestimate of cloud-top height may be due to several factors. Clear-sky contamination of the cloudy radiances is more likely during the day when the clouds break up. This effect would be manifest in lower values of T_{cs} during the day. The observed clear-sky temperatures, though, increase during the day. Since the clouds thicken at night and thin during the day (Fig. 3), there may be some variation in the cloud infrared opacity. Figure 5 shows a correlation of cloud thickness and the difference between the sodar and method-1 cloud-top altitudes. These data reveal that the two height values agree for cloud thicknesses greater than 250 m. The differences increase almost linearly with decreasing thickness. The diurnal variation of the mean visible cloud albedo (Minnis et al., 1989) is also consistent with the cloud thinning during the day. Initial estimates, however, indicate that the reduced opacity can account for only ~ 0.02 km of the observed daytime differences. Other potential effects include sampling differences and island heating during the day.

5. Concluding Remarks

The results presented here clearly show the problems associated with using temperature soundings with low vertical resolution to convert cloud-top temperature to cloud-top altitude over regions with significant inversions. It is clear that the average value of z_{sc} would have been closer to 680 mb instead of 913 mb if the NMC data had been used in the analysis. Estimation of the vertical profile using a simple lapse rate and a measurement of surface temperature appears to be an effective solution to the difficulties of boundary-layer inversions. The differences between the island and satellite-derived cloud-top heights are currently unresolved. A

closer comparison using a smaller area corresponding to SNI and one-to-one sampling is required to properly examine the differences.

Diurnal variations of cloud-top height and thickness deduced from the satellite data are reasonably representative of the changes actually occurring in the cloud field over the course of the day. The clouds thicken and rise during the night and sink and break up while they thin out during the day. This diurnal variation in cloud structure was also observed by Minnis and Harrison (1984) from similar satellite measurements taken over the southeastern Pacific during November 1978 as well as over other parts of the California marine stratocumulus area (Young et al., 1989). These intercomparisons are encouraging for the capabilities of satellite retrieval algorithms to accurately determine low-level cloud properties.

REFERENCES

- Minnis, P., and E. F. Harrison, 1984: Diurnal variability of regional cloud and clear-sky radiative parameters derived from GOES data, Part II: November 1978 cloud parameters. J. Clim. Appl. Meteor., **23**, 1012-1031.
- Minnis, P., E. F. Harrison, and G. G. Gibson, 1987: Cloud cover over the eastern equatorial Pacific derived from July 1983 ISCCP data using a hybrid bispectral threshold method. J. Geophys. Res., **92**, 4051-4073.
- Minnis, P., C. W. Fairall, and D. F. Young, 1989: Intercomparisons of GOES-derived cloud parameters and surface observations over San Nicolas Island. Presented at FIRE Annual Meeting/ASTEX Workshop, Monterey, CA, July 10-14.
- Rosow, W. B., L. C. Garder, P. Lu, and A. Walker, 1988: International Satellite Cloud Climatology Project (ISCCP), Documentation of cloud data. WCRP Report, August, 78 pp.
- Young, D. F., P. Minnis, and E. F. Harrison, 1989: Satellite-derived cloud and radiative parameters over the marine stratocumulus IFO. Presented at FIRE Annual Meeting/ASTEX Workshop, Monterey, CA, July 10-14.

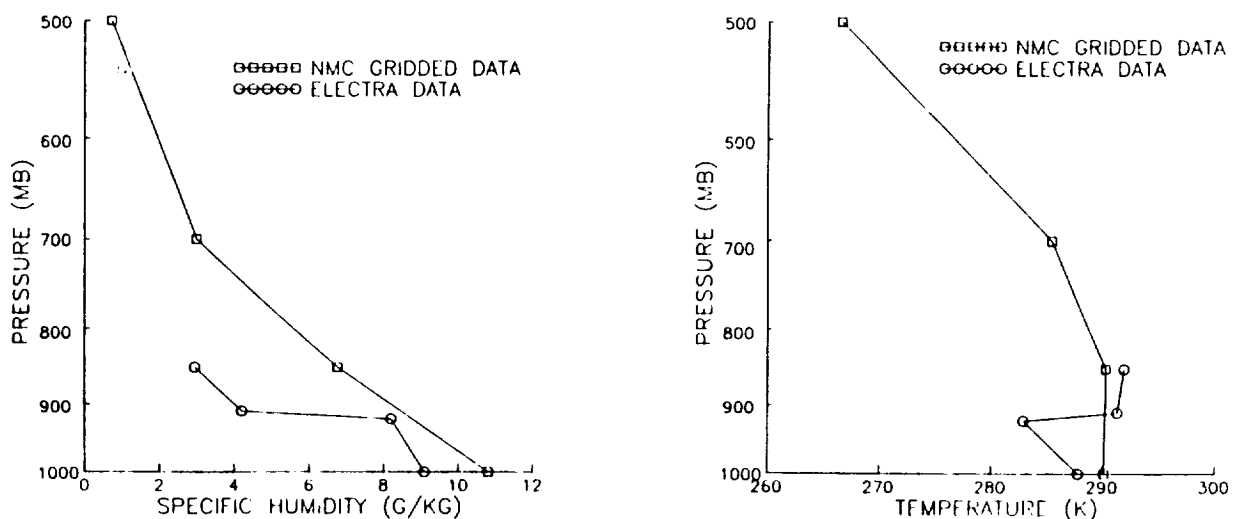


Fig. 1. Comparison of mean temperatures and humidities for IFO Electra flights and corresponding NMC analyses.

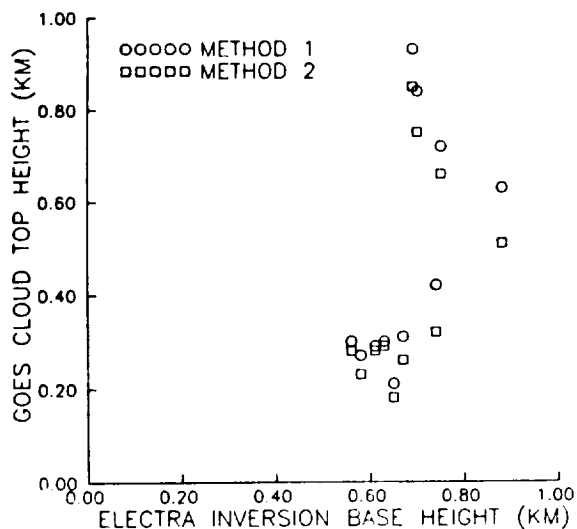


Fig. 2. Comparison of Electra-derived inversion base heights and corresponding satellite-derived cloud-top heights during IFO period.

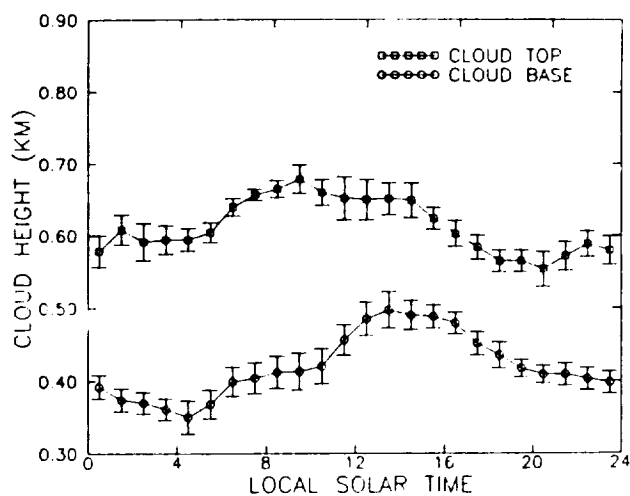


Fig. 3. Diurnal variations of mean sodar-derived cloud-base and cloud-top heights over SNI for July 1-19, 1987.

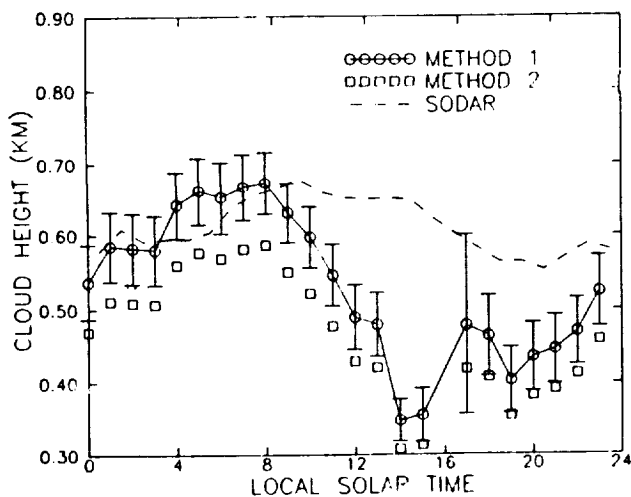


Fig. 4. Comparison of mean GOES-derived cloud-top heights over $1.0^\circ \times 0.5^\circ$ region centered on SNI and mean sodar-derived cloud-top altitudes over SNI for July 1-19, 1987.

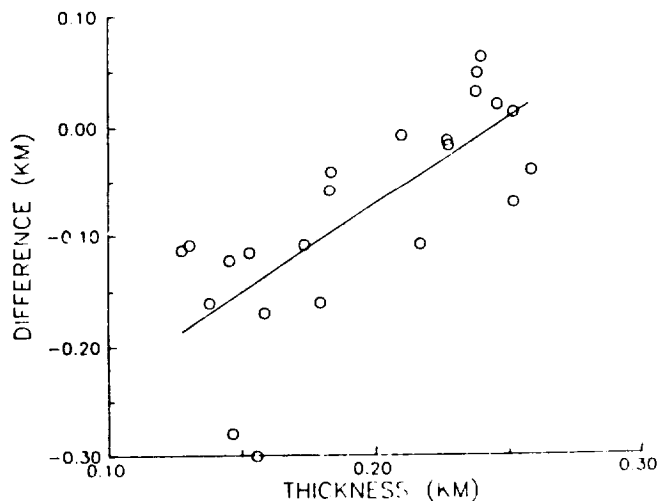


Fig. 5. Correlation of mean sodar-derived cloud thicknesses and differences in satellite-island-derived cloud-top altitudes over SNI for July 1-19, 1987.

Cloud Top Entrainment Instability and Cloud Top Distributions

Reinout Boers

James D. Spinhirne

NASA/GSFC, code 617

Greenbelt, Maryland 20771

The classical cloud top entrainment instability condition is commonly formulated as

$$g \Delta\theta_e + h \Delta q_t < 0 \quad (1)$$

where g, h are slowly varying parameters taken to be constant, $\Delta\theta_e, \Delta q_t$ the jumps in equivalent potential temperature and total water mixing ratio at the cloud top.

Plotted in θ_e, q_t coordinates the entrainment instability criterion (EI) for a collection of different atmospheric conditions appears as a highly elliptical point cluster as a result of the strong correlation between θ_e and q_t . More independent coordinates are θ_ℓ and q_t , where θ_ℓ is the liquid water potential temperature or saturation point potential temperature. In this paper we examine EI in θ_ℓ, q_t coordinates. Rather than focussing on jump conditions we will emphasize the gradients $\delta\theta_\ell/\delta q_t$. EI occurs when

$$\delta\theta_\ell/\delta q_t < (\delta\theta_\ell/\delta q_t)_{\text{crit}} \quad (2)$$

where the critical value represents the gradient along the moist virtual adiabat. (2) is entirely consistent with (1), however the manner in which EI is shown by (2) reveals that additional parameters need to be considered in the entrainment of negatively buoyant parcels. For simplicity we neglect radiation.

Figure 1 shows a θ_ℓ, q_t plot typical of 6/29/87 (C130-data). M corresponds to the in-cloud parcel, T to the parcel above the cloud. Cloud top appears at 870 hPa. Mixtures of T and M fall along the straight line TM. This diagram can be interpreted in pressure (p) and saturation point pressure (p_*) coordinates. The $p=870$ hPa line shows the mixing level and whether M, or T or both are cloudy or clear. Other mixing levels can be arbitrarily defined by simply shifting the p -line up or down. If a point, say M falls below that p -line it means that at that pressure level a parcel with the coordinates M is cloudy. If it falls above that line, it is clear. The p_* -lines indicate how much lifting or lowering is needed to make M or T just saturated. For example if the cloudy boundary layer would be well mixed, it would be

represented by M and the cloud thickness would be $(937-870)= 67$ hPa. In Figure 1 the moist virtual adiabat falls to the right of the mixing line MT. This means that all cloudy mixtures (below the level $p=870$ hPa) are denser than the unmixed cloudy parcel M.

Additional information about the mixing process is available if we draw dry virtual adiabats on this plot as in Figure 2. The moist virtual adiabat through M kinks at the $p=870$ hPa line at point c and then follows the dry adiabat of $\theta_{vu}=291.72$ K. T lies on the dry virtual adiabat marked as 299.27 K. Therefore there is a difference of $\Delta\theta_v = 7.55$ K between the dry air and the cloud top so that the cloud is statically very stable. In order to make the cloud statically unstable it would have to be raised several hundred hPa's until point c would be above the dry virtual adiabat through T. Entrainment at pressure level $p=870$ hPa takes parcels with $p_*=566$ hPa at T and mixes them with parcels at $p_*=937$ hPa. During the mixing process the saturation point coordinates of the mixture slide from T along the mixing line MT towards M. Entrainment will increase p_* of the mixture until it gains the same buoyancy as the cloudy parcel M at point a, where the dry virtual adiabat $\theta_{vu}=291.72$ K intersects the mixing line. At a the parcel is still clear. Subsequent mixing from a to b decreases the mixture buoyancy below that of the cloudy parcel. At b where $p_{\text{mixture}}=p_{\text{mixing level}}$ the mixture becomes cloudy. Below b on the mixing line, lines of equal buoyancy are represented by lines parallel to the moist virtual adiabat. In continuing the mixing process from b to M the buoyancy will increase again until it becomes the same as that of the cloudy parcel M.

Four points can be immediately recognized from this plot: First, the densest mixture is just cloudy (point b). Although this is well known from the literature, the actual buoyancy difference can be immediately read from this graph by drawing the dry virtual adiabat through point b ($\theta_{vu}=291.45$ K) and computing the difference with θ_{vu} through a and c (0.27 K); Second, the fraction of dense buoyant mixtures to all possible mixtures is given by $(a-T)/(T-M)$; Third, the buoyancy difference of cloudy mixtures with M can be increased if the unmixed dry parcel would be cooler or dryer than represented by point T; Fourth, the fraction of buoyant mixtures can be increased if the mixing level is raised (pressure lowered). Lidar cloud top data shows that over a 30 km flight leg cloud top variability of several hundred meters (several tens of hPa's) is not uncommon. The two dashed lines parallel to the $p=870$ hPa line indicate how variations in the mixing level changes the fraction of potentially positively buoyant parcels.

Neglecting radiation we can derive the virtual potential temperature flux from this diagram as follows: Let F_{MT} be the convective flux in $(\theta_e, \theta_l, q_t)$ and ω_e be the entrainment

velocity, then

$$F_{MT} = (T - M) \omega_e = (T - b) \omega_e + (b - M) \omega_e \quad (3)$$

$$\begin{aligned} \text{where } T &= (\theta_e, \theta_l, q_t)_T \\ M &= (\theta_e, \theta_l, q_t)_M \end{aligned}$$

then the virtual potential temperature flux is defined as

$$\begin{aligned} F_{\theta v} &= g_u (\theta_{lT} - \theta_{lb}) \omega_e + h_u (q_{tT} - q_{tb}) \omega_e + \\ &g_c (\theta_{lb} - \theta_{lM}) \omega_e + h_c (q_{tb} - q_{tM}) \omega_e \quad (4) \end{aligned}$$

where g_u , h_u , g_c , h_c are the appropriate factors for clear and cloudy conditions. From (4) it is immediately clear that although a portion of the buoyancy flux (in cloud) is indeed positive by virtue of the slope of the mixing line MT, this flux is very small in comparison to the flux necessary to create the cloudy mixture in the first place. We believe that this is a point that is commonly overlooked in EI-studies. The energy necessary to create the cloudy mixture is very much greater (proportional to the difference 299.27-291.45 K) than the energy created by mixing inside the cloud (proportional to the difference 291.72-291.45 K). It is therefore not surprising that recent studies have shown that in many cases where condition (1) or (2) was satisfied, the clouds appeared to be stable.

So far we only considered mixing at pressure level p . However a dry parcel from above the cloud is drawn into the cloud and acquires a downward speed representative of the in-cloud circulation. Let this speed be indicated by ω_T . ω_T is responsible for lowering the mixing level of the parcel, increasing the pressure level. On the other hand ω_e , the entrainment velocity is responsible for increasing the saturation point pressure of the mixture. The process of entrainment and vertical movement of the parcel is schematically represented in Figure 3. Assume that the highest cloud tops are at point b, and that at that level the dry unmixed parcels have their saturation level at T (566 hPa). As the parcel is drawn into the layer the mixing pressure level is increased from point b to say point a. If point a corresponds to the lowest cloud top we know that at point a all mixtures are cloudy. This means that in moving an unmixed parcel at point b to point a the saturation level of the mixture has increased from its unmixed value at T to the actual pressure level at a. Simple geometry on Figure 3 reveals the following constraint:

$$f = \omega_T / \omega_e < (P_a - P_b) / (P_a - P_T) \quad (5)$$

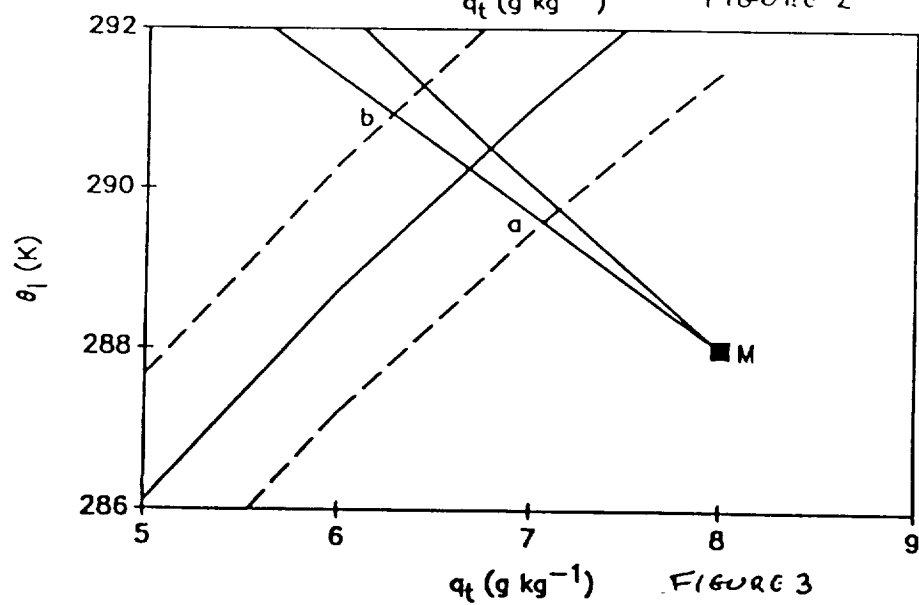
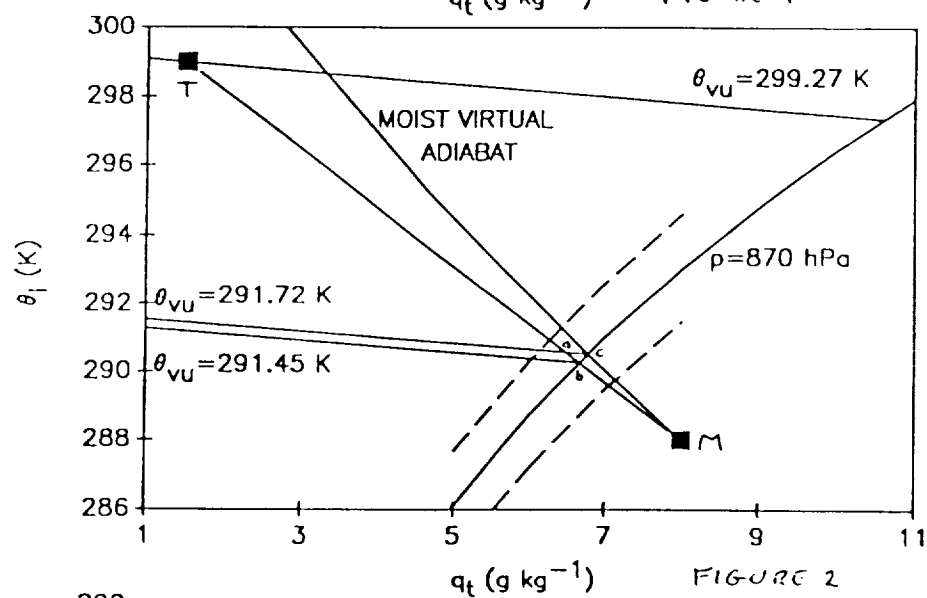
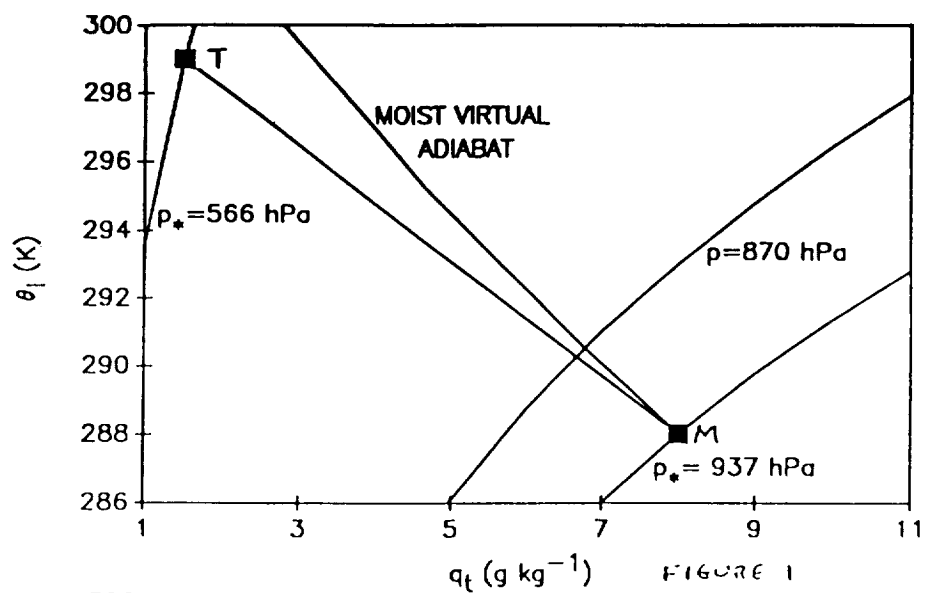
For typical cloud top variations of 15 hPa we find $f < 0.05$. It means that the entrainment velocity needs to be very much

higher than the translation velocity in order to get dense sinking cloud parcels. This statement means that cloud top entrainment instability is unlikely to break up a cloud in case the circulation speed near the cloud top is large; in such cases the strength of the circulation merely draws unmixed parcels into the layer that do not have the chance to become cloudy in their downward transport. Below the mean cloud base those parcels will always be less dense than the mixed layer environment.

In conclusion we have shown that a saturation point diagram can be used to investigate the details of mixing in cases where the cloud top entrainment instability criterion is satisfied. We find that for typical situations found during FIRE, where the EI condition is satisfied clouds are likely to be stable because the energy required to create a cloudy mixture is much greater than the energy which is released once the parcel has become cloudy. The mixing level is crucially important in determining the fraction of cool cloudy mixtures. The vertical levels at which cloud tops can be found (derived from cloud top lidar data) puts a constraint on the entrainment velocity and the transport velocity of the mixture in such a way that the entrainment velocity needs to be an order of magnitude higher than the transport velocity in order to get any cloudy sinking mixtures. If the transport velocity is too large, clouds will break up, however mixtures will remain less dense than their environment. Radiation was neglected in this analysis, but is likely to enhance the instability, as it cools the parcels once they become cloudy. A complete analysis then involves another velocity scale representing the speed at which a mixture moves along lines of equal θ_e . The mixing process will deviate from the simple mixing line structure as shown in this paper and is the subject of further research.

Acknowledgement.

The authors are sponsored by the Mesoscale and Climate Research Office at NASA.



July 16, 1987 Revisited: Lessons for Modelers

HOWARD P. HANSON

*Atmospheric and Climate Dynamics Program
Cooperative Institute for Research in Environmental Sciences
University of Colorado at Boulder 80309-0216*

1. Introduction

At last summer's FSET Workshop in Vail, I presented preliminary results from 16 July 1987, the day that the NCAR Electra was allowed in the restricted air space around San Nicolas Island (NSI). We flew a cross pattern, with one leg approximately NW-SE between NSI and the R/V *Pt. Sur*, about 50 km "upstream" (although the surface winds were weak and variable), and the other leg at approximately right angles (Fig. 1). There was a LANDSAT image coincident with this mission as well. This paper discusses one interesting aspect of the "cross-stream" flight legs, i.e., the legs between points "D" and "E" in Fig. 1.

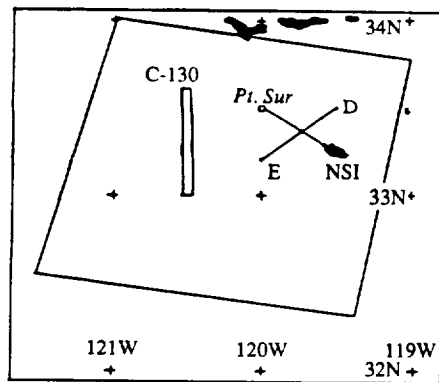


Fig. 1 FIRE operations, 16 July 1987. The NCAR Electra flew the cross pattern; the inset trapezoid is the LANDSAT scene.

The LANDSAT images (not reproduced here) show a distinct difference in cloud reflectance between the two halves

of the flight leg from D (which is at the less reflective end) to E. Figure 2, which shows IR lidar observations of the cloud-top height and the reflectance calculated from the Electra's pyranometers, confirms this. Note also that the temperature of the upwelling IR radiation is actually higher where the cloud top is higher, suggesting that the cloud is thinner there (and hence radiation from the sea surface is being transmitted). This corresponds to the less reflective part of the cloud.

What I will discuss here is the apparent reason for the variability of cloud thickness along this flight track. The evidence points to *variability in the water vapor content above the inversion* as the controlling factor. This compounds the difficulty of parameterizing these clouds in GCM's.

2. Mixing Diagram

Figure 3, which summarizes relevant Electra data taken just above and within the cloud-topped boundary layer, is sufficiently rich in information that the remainder of this abstract will discuss it in some detail. This is a mixing diagram, plotted using total water mixing ratio and liquid water potential temperature, constructed using 1-second averages of Electra data from various altitudes. Because the two variables used are conservative to water phase changes, mixing occurs along straight lines unless there are

significant diabatic effects (due to, e.g., radiative transfer or precipitation).

The ellipses summarize data from the individual runs below cloud top, with the center of each ellipse positioned at the average values for each run and the axes determined using ± 2 standard deviations. Each run has been broken into two segments, corresponding to the less (segments 1) and more (segments 2) reflective parts of the cloud. The surface data ellipse (labeled "S") was determined

using the radiometric sea-surface temperature (SST) and the associated saturation vapor mixing ratio (the SST varied little between D & E, and this is not segmented). Proceeding generally down and to the right, the other data ellipses are from flight legs at 60m, 475m (the base of the cloud layer), and 675m (in the middle of the cloud layer). The asterisks (circles) are 1-second data points from the cloud top run corresponding to segment 1 (2), during which we "porpoised"

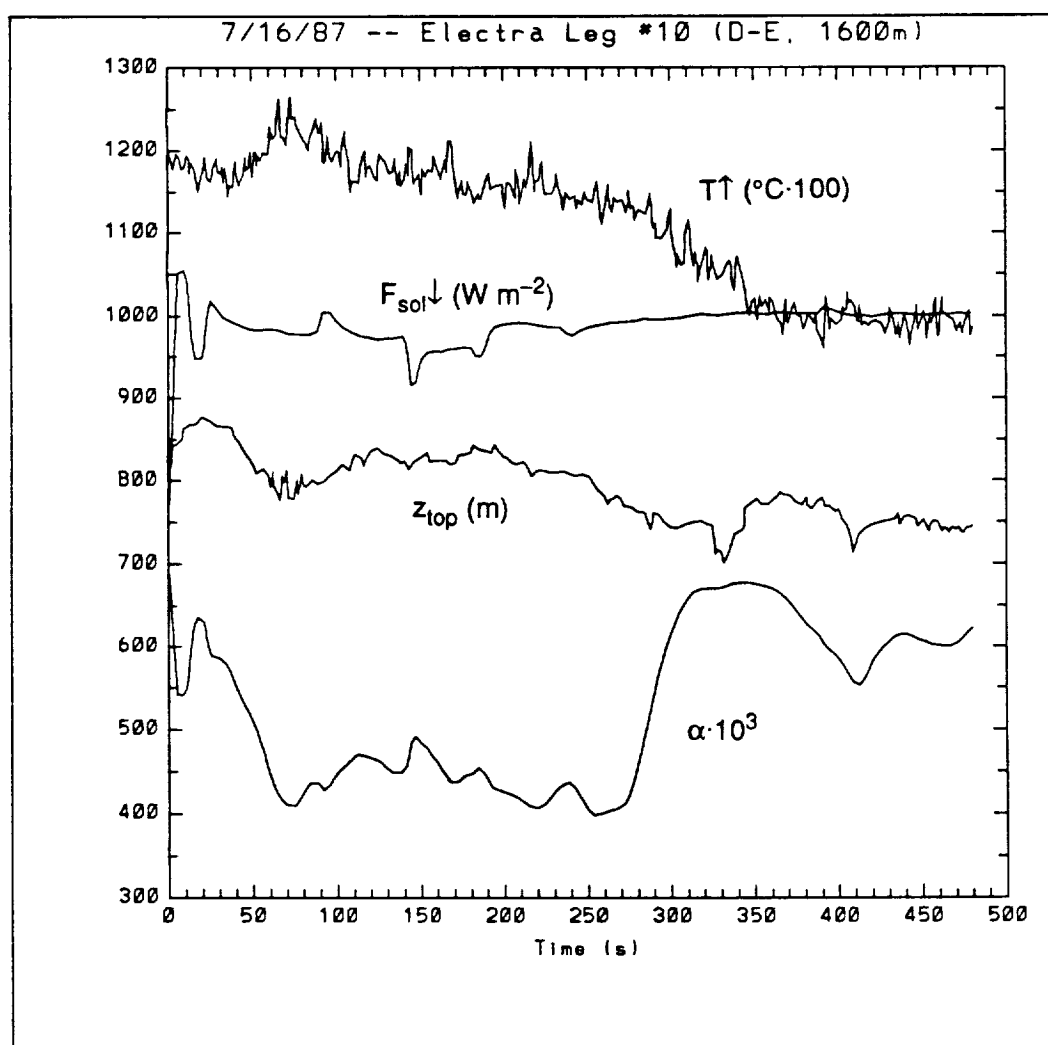


Fig. 2 Downward solar radiation $F_{\text{sol}\downarrow}$, cloud reflectance α , upwelling IR radiation (in terms of its temperature $T\uparrow$) and cloud-top height z_{top} , along the flight leg from D to E in Fig. 1.

in and out of the cloud top (as can be seen in the altitude data [solid] in Fig. 4).

Although the cloud was evolving during the mission, these maneuvers took only about an hour to complete, so that the data are nearly "synoptic" in terms of the time scale of the cloud. Because of this, several conclusions can be drawn from Fig. 3. First, it can be argued that the sub-cloud and cloud layers were decoupled. Consider the mixing line

between the surface air and that at cloud base. There is clearly a discontinuity from this line to the (two separate) in-cloud parcels. Also, the displacement of the 60-m air parcels from the subcloud mixing line can be accounted for by a radiative cooling rate of $\sim -0.5^\circ/\text{day}$, a very reasonable value.

If the layers were decoupled at the time of the measurements, then the surface moisture supply for the cloud was cut off, and entrainment of warmer air

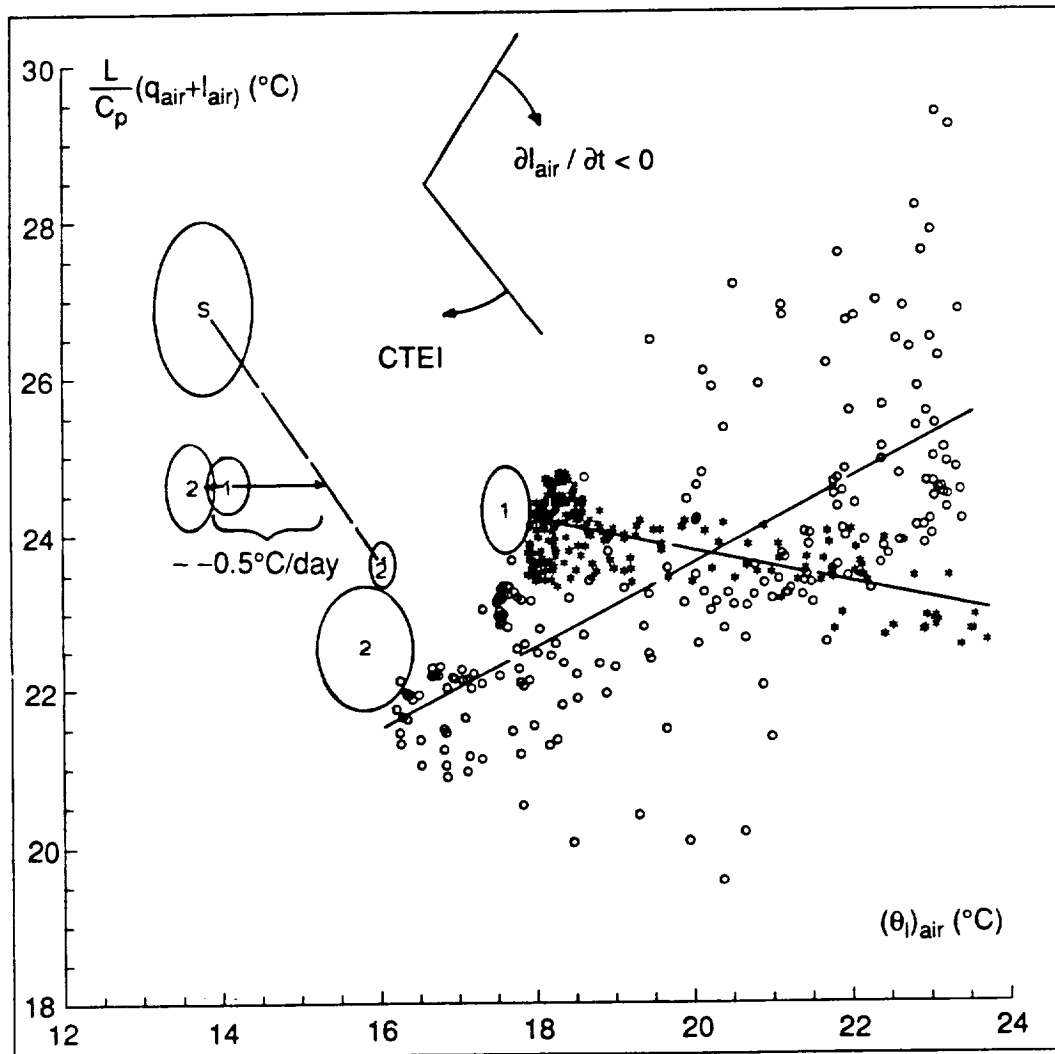


Fig. 3 Mixing diagram summarizing data between points D and E.

from above combined with solar heating (which probably lead to the decoupling in the first place) would tend to decrease the liquid water content of the cloud.

Note, however, the difference in the moisture content of the air above the inversion between segments 1 & 2. The dashed lines through the asterisks and circles in Fig. 3 are regression lines of these data points, and therefore are the best estimate of the mixing line for entrainment in the two segments. The

difference in the slope of these two mixing lines is highly significant.

At the top of Fig. 3, there are indicated two critical mixing lines. Cloud-top entrainment instability occurs for mixing lines having slopes less than (i.e., more negative than, or clockwise from) the line marked "CTEI". Clearly, that is not happening in the data. The other line is a mixing line for which entrainment would produce no change in cloud liquid water; mixing lines with smaller slopes

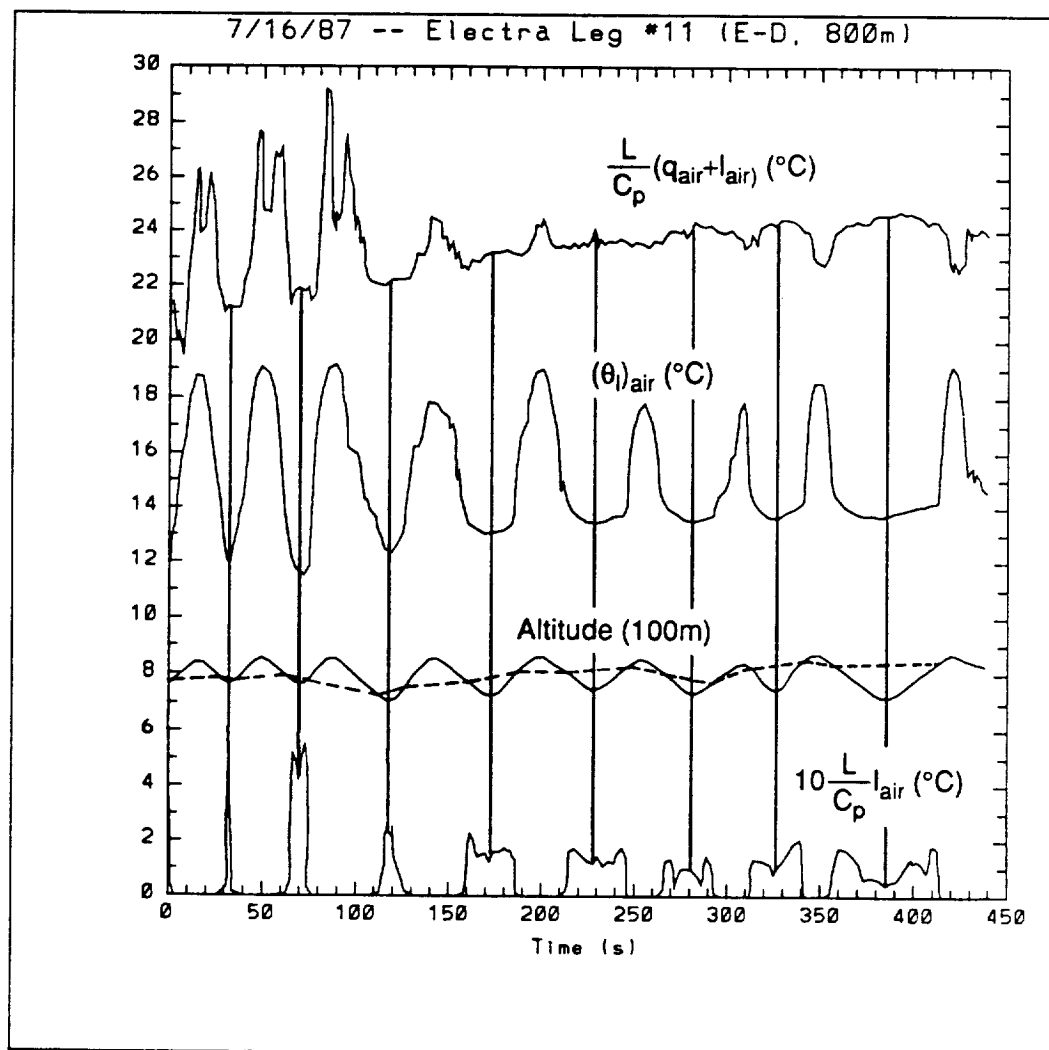


Fig. 4 Aircraft altitude, liquid (l_{air}) and total water ($q_{air} + l_{air}$) mixing ratios, and liquid potential temperature θ_l from cloud-top leg. Dashed line estimates cloud top from the liquid water data.

(in the same sense as previously) tend to decrease the cloud liquid water, and the rate of liquid water decrease is proportional to the difference in slope.

The difference in slope of the two regression lines is, in this context, highly significant. Although both imply mixing by entrainment that decreases the cloud liquid water, the segment 2 mixing (the circles) produces only about half the decrease of the segment 1 mixing. In fact, for segment 2, the *above-inversion air is acting as a moisture source for the cloud layer*.

3. Conclusion

The main point here is the importance of specifying correctly the upper

boundary condition in cloud models. This example shows that relatively small variations in the humidity of the air above the marine inversion can be lead to variations of cloud reflectance by as much as 50% (about 0.4 to 0.6, here). The relatively small scales of this phenomenon in this data set ($O[25 \text{ km}]$) are less important than the magnitude of the reflectance variability. Particularly in GCM's, calculating the humidity in the lower layers of the model is crucial for successful parameterization of marine stratocumulus clouds.

Acknowledgments: This research was supported by the Office of Naval Research and the National Aeronautics and Space Administration.

An Eight-Month Climatology of Marine Stratocumulus
Cloud Fraction, Albedo, and Integrated Liquid Water

C.W. Fairall and J.E. Hare
Department of Meteorology
Pennsylvania State University
University Park, PA 16802

J.B. Snider
NOAA/ERL/WPL
325 Broadway
Boulder, CO 80303

INTRODUCTION

As part of the FIRE/ETO program, extended time observations were made at San Nicolas Island (SNI) from March to October, 1987. A small ground station was installed at the NW tip of SNI, which is dominated by marine flow most of the time. Hourly averages of air temperature, relative humidity, wind speed and direction, solar irradiance, and downward longwave irradiance were recorded. The radiation sensors were standard Eppley pyranometers (shortwave) and pyrgeometers (longwave). San Nicolas Island also served as the focus of the first stratocumulus IFO during July, 1987.

The SNI data have been processed in several ways to deduce properties of the stratocumulus covered marine boundary layer (MBL). For example, from the temperature and humidity the lifting condensation level, which is an estimate of the height of the cloud bottom, can be computed. A combination of longwave irradiance statistics (mean and standard deviation) can be used to estimate fractional cloud cover. We will also describe an analysis technique used to estimate the integrated cloud liquid water content (W) and the cloud albedo from the measured solar irradiance. In this approach, the cloud transmittance is computed by dividing the irradiance measured at some time by a clear sky value obtained at the same hour on a cloudless day. From the transmittance and the zenith angle, values of cloud albedo and W are computed using the radiative transfer parameterizations of Stephens (1978). These analysis algorithms have been evaluated with 17 days of simultaneous and colocated mm-wave (20.6 and 31.65 GHz) radiometer measurements of W and lidar ceilometer measurements of cloud fraction and cloudbase height made during the FIRE IFO. The algorithms are then applied to the entire data set to produce a climatology of these cloud properties for the eight month period.

SHORTWAVE CLOUD/RADIATION PARAMETERIZATION

Solar radiative transfer through stratocumulus clouds can be computed with reasonable accuracy given a specification of the appropriate microphysical variables (optical thickness, single scattering albedo, asymmetry factor, and zenith angle). For our application, we wish to use measurements of a particular bulk cloud radiative transfer property (transmission coefficient) to deduce the integrated liquid water content and the albedo (solar reflection coefficient) of the overlying cloud. In order to streamline this process, we have chosen to use a radiative transfer parameterization (Stephens, 1978), rather than a full blown multiband radiative transfer code. From a measurement of cloud transmission coefficient and a specification of solar zenith angle, we obtain from the parameterization the optical thickness and the cloud albedo. A second parameterization relating optical thickness to integrated liquid water is used to compute W.

A detailed description of the algorithm and an evaluation using the FIRE/IFO data has been previously described (Fairall et al., 1988) so we will summarize here. Values of W estimated from the solar transmittance are on average 65% of the values derived from the microwave radiometer. A log-log linear regression yields a slope very near one with a correlation coefficient of 0.87. The rms scatter about the regression line represents about 35% variability in the value of W . In pondering the disagreement between the two measurements, we feel the best evidence suggests that the microwave radiometer values are quite accurate. It is possible that the actual cloud droplet concentrations were substantially less than the assumed value of $100/\text{cm}^3$. Also, Coakley and Snider (1989) have suggested that nonlinear effects could affect our result. Using a Taylor expansion of the transmission coefficient, we can relate the mean water content to the mean transmission coefficient by

$$\langle W \rangle = W(\langle \text{Tr} \rangle) [1 + S (\sigma_w / \langle W \rangle)^2] \quad (1)$$

The dimensionless nonlinear sensitivity coefficient, S , is given by

$$S = -(1/2) [\partial^2 \text{Tr} / \partial (\ln(W))^2] / [\partial \text{Tr} / \partial (\ln(W))] \quad (2)$$

We have used the Stephen's parameterization to evaluate (2) by numerically computing finite difference first and second derivatives at various values of zenith angle and mean integrated liquid water content. As defined here, S is positive over the range of values of W of interest here (it becomes negative at very small values of W), so small scale cloud variability tends to cause us to underestimate W from the mean transmission coefficient. We have used the high speed time series of W from the microwave radiometer to compute σ_w on a one hour time scale. A typical value for σ_w / W is on the order of 0.25. Larger values are observed for smaller W , but this is compensated by the decrease in S . Using a value of $S=1.2$ for $W \approx 50 \text{ g m}^{-2}$, we find that nonlinear effects have reduced the pyranometer estimates of W by about 3%. This appears to be almost negligible, but we admit that this result is very sensitive to the value of σ_w / W used.

LONGWAVE PARAMETERIZATION FOR CLOUD FRACTION

Cloud fraction is a very thorny issue that is just beginning to receive theoretical interest in cloud models. The definition of cloud fraction is often confused by the concepts of scale. A 24 hour period of broken clouds may yield the same average cloud cover as 12 hours of solid stratus followed by 12 hours of clear skies, but on a larger scale the stratus may be considered to be part of a broken cloud field. For our purposes, we will consider cloud fraction, f , to be the fraction of time in one hour that a narrow field of view instrument in a zenith pointing mode (i.e., a lidar ceilometer) detects the presence of a cloud overhead.

Since it is well known that the downward longwave radiative flux received at the surface is substantially greater (by roughly 100 W m^{-2}) in the presence of stratocumulus clouds versus clear skies, we decided to develop an algorithm to use the pyrgeometer time series to estimate f . We considered two approaches: (1) compute f by comparing the measured downward longwave, L_m , to anticipated values for clear, L_o , and stratocumulus conditions, L_s , and (2) compute f by comparing the standard deviation of downward longwave, σ_1 , to L_o and L_s . The values for L_o and L_s are obtained from standard bulk models of downward longwave irradiance. In the end we chose method (2) because it was significantly less sensitive to the details of our determination of L_o and L_s at the extremes (i.e., $f=0$ or 1.0).

If the formulae for L_o and L_s were accurate, we would postulate that a reasonable estimate of the cloud fraction would be given by $f = (L_m - L_o) / \Delta$ where $\Delta = L_s - L_o$. However, these simple models do not take in enough information to describe a large part of the variability of L_o and L_s (Siegel and Dickey, 1986). In an effort to obtain a more reasonable estimate, we decided to use the variance of the measured radiation, σ_1^2 . With a bit of mathematical manipulation, we can show that

$$\sigma_1^2 = \langle (L - \langle L \rangle)^2 \rangle = f(1-f)\Delta^2 \quad (3)$$

We can express the solution to (3) as

$$f = (1 \pm [1 - (m\sigma_1^2/\Delta^2)]^{1/2})/2 \quad (4)$$

where for the quadratic form of (4) we have $m=2$. We have left this exponent as an adjustable parameter because of the wide field of view of the pygeometer. A comparison with the lidar ceilometer showed (Fig. 1) that $m=1$ gives a better fit to the FIRE IFO data. Since (4) is double valued, we need a method to select which sign (+ or -) is appropriate. Here we use the measured mean irradiance; if $L_m < L_o + \Delta/2$, then we use the negative sign in (4). This implies that our algorithm will be most inaccurate when it yields $f=0.5$, where the result is critically dependent on the accuracy of the bulk formulae.

EIGHT MONTH STATISTICS

The system at SNI provided a continuous record of 30 minute averages of the data from Julian day 50 to 285. One period (day 142 to 154) was lost due to an extended power outage. The summer heavy stratocumulus season is apparent in the time series of weekly averaged mean cloud cover (Fig. 2) deduced from the longwave algorithm. A variety of statistics have been computed from this data base. Frequency distributions have been computed for albedo (Fig. 3a), integrated cloud liquid water (Fig. 3b), and cloud fraction (Fig. 3c). These data imply that the typical daytime stratocumulus at SNI has an integrated liquid water content of about 75 g m^{-2} and an albedo of 0.55.

An average diurnal cycle of cloud fraction for the three summer months (Fig. 4a) shows a substantial modulation of the clouds, presumably caused by the cloud absorption of solar energy. The resultant warming of the mixed layer raises the cloudbase and reduces W . Despite the limitations of the solar data we have computed average diurnal cycles for albedo (Fig. 4b). In order to broaden the part of the diurnal cycle covered, we have relaxed the restriction on solar zenith angle to permit computation for $\mu > 0.1$. The same analysis for W (not shown) indicates that the mean values of W appear to increase from very low values for the first three hours after sunup, which is considered to be evidence that our algorithm is not reliable if $\mu < 0.4$. Only the seven hours centered about local noon can be considered usable for liquid water. The albedo computation is probably reliable over the entire interval; the increased albedo at low incidence angle is expected.

It is also important to avoid overselling this approach. The algorithms developed here are considered to be most appropriate for marine stratocumulus. They have been verified against a single 17-day data set. The cloud fraction algorithm we have used is most effective as a cloud versus non-cloud indicator, and obviously will work best with very low cloudbase and solid clouds. The ceilometer is a more appropriate device for this purpose (it also yields more accurate cloudbase height than the lifting condensation level computation), but it costs an order of magnitude more than the pyrgeometer.

The pyranometer algorithm provides important information on cloud microphysical and radiative transfer properties, but only during the day. The microwave radiometer provides far superior performance for measuring W, but only a few systems exist in the world and their cost, compared to a pyranometer, is astronomical.

Acknowledgements This work is supported by NASA grant NAG 1-652. The authors wish to express special thanks to Richard Dixon and Carl Otten of PMTC for aiding and abetting the installation and maintenance of the ETO system at SNI, to Dick Thompson of the Department of Meteorology, PSU, who put the system together and kept the data flowing, and to Bruce Albrecht and Tom Ackerman for various overstimulating discussions.

References

- Coakley, J.A., Jr., and J.B. Snider, 1988: Observed reflectivities and liquid water content for marine stratocumulus. Extended Abstracts, Symposium on the Role of Clouds in Atmospheric Chemistry and Global Climate, American Meteorological Society, 175-177.
- Fairall, C.W., R. Rabadi, and J. Snider, 1988: Estimating integrated cloud liquid water from extended time observations of solar irradiance. Proceedings FIRE Symposium on Clouds, Climate, and Radiation, Vail, Colorado, 5pp.
- Siegel, D.A., and T.D. Dickey, 1986: Variability of net longwave radiation over the eastern north Pacific Ocean. J. Geophys. Res., **91**, 7657-7666.
- Stephens, G.L., 1978: Radiation profiles in extended water clouds. II: Parameterization schemes. J. Atmos. Sci., **35**, 2123-2132.

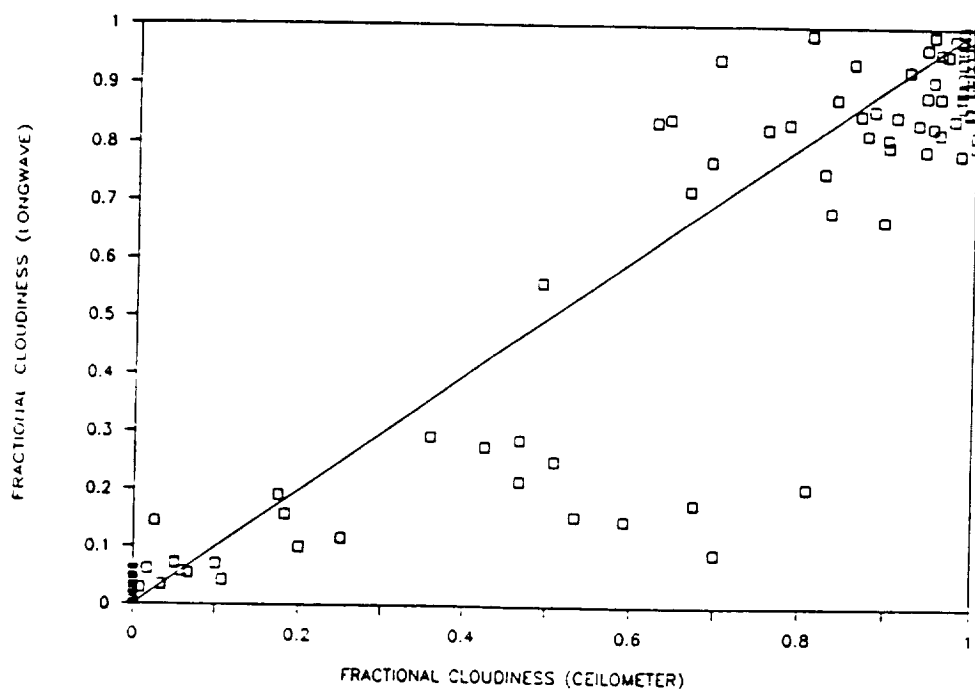


Fig. 1. Fractional cloudiness (f) estimated via (4) versus direct measurements by the lidar ceilometer during the FIRE IFO period.

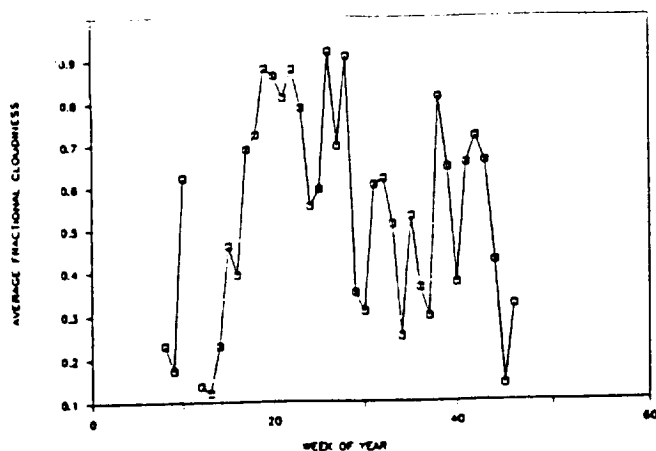


Fig. 2. Time series of weekly averaged fractional cloud cover, computed from the longwave irradiance, for the eight month data period. The stratocumulus season is evident as the high values of f in the April to September period.

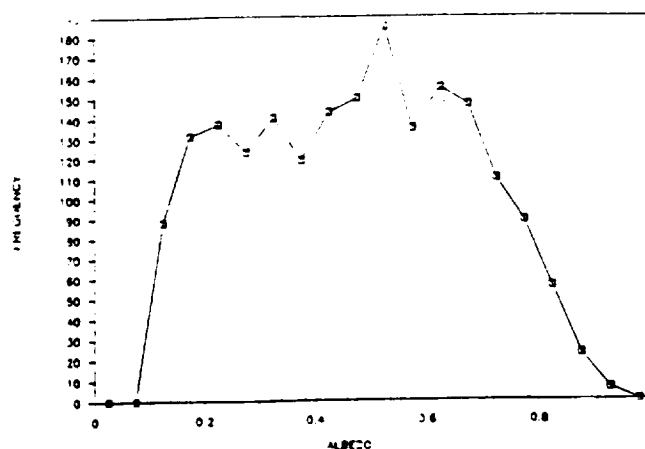


Fig. 3a. Frequency distributions of cloud albedo using the one-hour data, computed using the methods described in the text, for the eight month period.

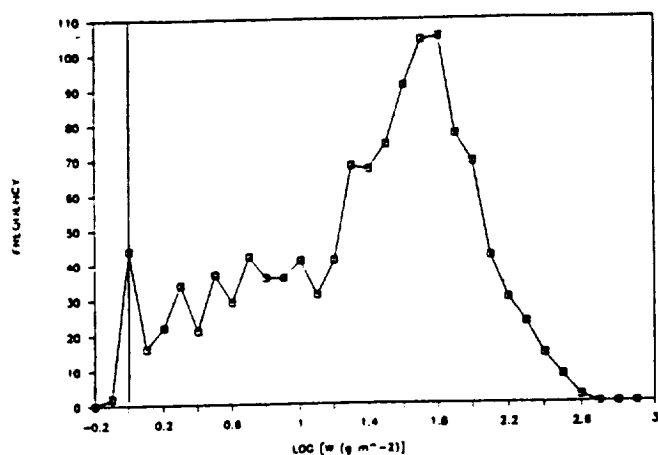


Fig. 3b. As in Fig. 3a but for integrated cloud liquid water content, W .

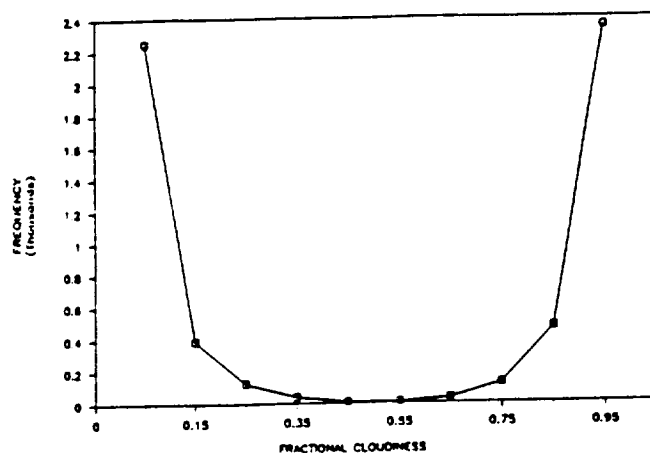


Fig. 3c. As in Fig. 3b but for cloud fraction, f .

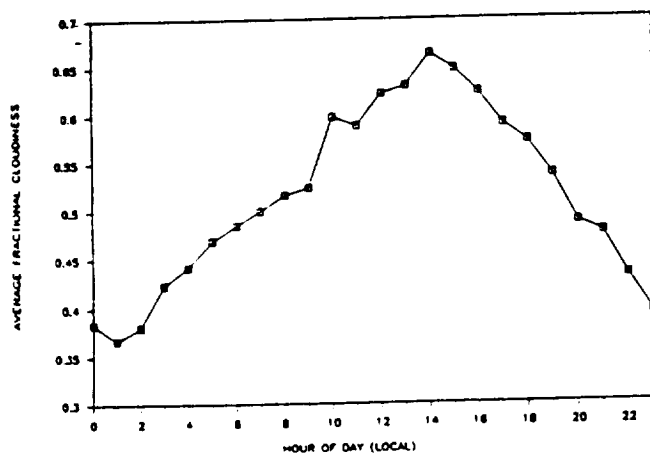


Fig. 4a. Average diurnal variation (using local time) for fractional cloudiness, derived from the longwave irradiance, during the three summer months.

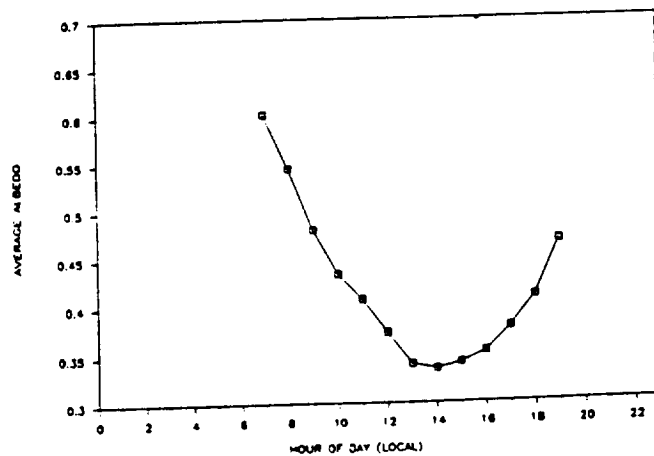


Fig. 4b. As in Fig. 4a but using shortwave irradiance derived values of cloud albedo.

Mesoscale Variability of Free Tropospheric Humidity
Near San Nicolas Island During FIRE

A.B. White, C.W. Fairall, and D.W. Thomson
Department of Meteorology
503 Walker Building
Pennsylvania State University
University Park, PA 16802

INTRODUCTION

Humidity variability at the top of the marine boundary layer (MBL) and in the free troposphere has been examined using a variety of measurements taken on and around San Nicolas Island (SNI) during the FIRE IFO in July, 1987. Doppler wind profiler reflectivity recorded at two minute time resolution has provided the most continuous record and detail of small scale humidity fluctuations. Rawinsonde data was available from both an island site and the research vessel Point Sur. The information extractable from these sources is somewhat limited due to the frequency of launches (3-4/day at SNI and 6/day on the Point Sur). Some additional data was available from instrumented aircraft although scheduling flights in the neighborhood of the island was difficult due to restrictions on the air space. Other relevant data was collected at SNI near the radar and rawinsonde launch sites. A continuous record of cloud base altitude was logged by a ceilometer. Doppler acoustic sounder (sodar) reflectivity data provided a good record of inversion height. The sodar also monitored turbulent temperature fluctuations in the MBL. A small ground station recorded hourly averages of solar irradiance and downward longwave irradiance.

This paper describes analysis in progress of the various data sets described above for two adjacent two day periods from 11 July to 14 July. The earlier period was chosen because the marine inversion was unusually high and there was increased frequency of rawinsonde launches at SNI. The later period was chosen because of the significant descent with time of an elevated inversion indicated by the radar data. Throughout the four day period, but especially in the first half, the turbulent humidity structure calculated from Doppler radar reflectivity shows excellent agreement with humidity profiles evaluated from rawinsonde data.

INTERPRETATION OF DOPPLER RADAR REFLECTIVITY

Penn State's Doppler wind profiler used at SNI operates at a frequency of 404.37 MHz. For FIRE, the pulse width was set at 1 μ s to provide the best possible range resolution while satisfying the receiver bandwidth constraint. The pulse repetition frequency was 10,000 Hz. Processing of radar reflectivity is accomplished in the following manner. The complex video of 288 consecutive pulses are coherently averaged (time domain integration). A set of 64 of these integrations is processed by a fast fourier transform (FFT) to produce one spectrum. Incoherent averaging is then performed on 8 of these variance spectra to produce the two minute averaged spectrum from which the signal/noise ratio (SNR) is extracted.

Since radar backscatter occurs in a volume (V_s) defined by the pulse and beam widths, volume reflectivity (η) replaces the more familiar backscatter cross-section (σ), where $\eta = \sigma / V_s$. The volume reflectivity is related to the SNR by the spectral radar equation (VanZandt et al., 1978)

$$\eta = \frac{9\pi c k B (\alpha T_c + T_{rx})}{2 \alpha^2 P_t F_r A_p \cos(\chi)} \left(\frac{R}{\Delta R}\right)^2 (SNR), \quad (1)$$

where c is the speed of light, k is Boltzmann's constant, B is the bandwidth of the integrating filter, α is the combined antenna/line efficiency, T_c and T_{rx} are noise temperatures for cosmic noise and the receiver, P_t is the transmitted power, F_r is the pulse repetition frequency, A_p is the antenna area, χ is the off vertical beam axis angle, R is the range, and ΔR is the range resolution. Based on comparison with a previously calibrated 50 MHz Doppler wind profiler located in central Pennsylvania, the overall antenna efficiency was chosen to be 0.18. Additional calibrations of the antenna using aircraft data are currently underway. At $\lambda=0.742$ m, $\alpha T_c \ll T_{rx}$ so to a first approximation cosmic noise interference may be neglected. With the appropriate values inserted, (1) becomes

$$\eta = 7.67 \times 10^{-28} R^2 SNR. \quad (2)$$

The backscatter intensity of the radar's signal depends on the mean refractive index gradient existing in the scattering volume. Therefore, the refractive index structure function parameter (C_n^2) can be written in terms of the radar's volume reflectivity (Ottersten, 1969)

$$C_n^2 = (\eta/0.38) \lambda^{(1/3)}. \quad (3)$$

Insertion of $\lambda=0.742$ m and (2) into (3) yields

$$C_n^2 = 1.83 \times 10^{-27} R^2 SNR. \quad (4)$$

Both temperature and humidity fluctuations may contribute to variations in the refractive index within the scattering volume. In radar studies of C_n^2 at low altitudes, the contribution due to temperature fluctuations is usually ignored (Wesley, 1976). Conversion from C_n^2 to C_q^2 is then (following Burk, 1980)

$$C_q^2 = C_n^2 (1667 T^2 / P)^2, \quad (5)$$

where T is the temperature and P is the pressure (in mb) within the scattering volume. Combining (5) and (4) yields the final form of the equation used to determine C_q^2 from Doppler radar reflectivity;

$$C_q^2 = 5.08 \times 10^{-21} R^2 SNR (T^2 / P)^2. \quad (6)$$

RAWINSONDE DATA

During the FIRE IFO, Colorado State University operated a cross-chain Loran atmospheric sounding system (CLASS) at SNI. Scientists from the Naval Postgraduate School launched VIZ Loran-type sondes from the Point Sur. For additional information on the CLASS system and details on processing of the SNI rawinsonde data, see Schubert, et al. (1987a). Water vapor mixing ratio (q) was computed in the standard way.

RESULTS

Fig. 1 shows a time-height cross-section of $\log(C_q^2)$ contours (g/kg) from (6) for July 11-12. In this and the following figures, time in hours is measured continuously starting at 0z on 11 July. Higher values of C_q^2 correspond to regions of increased scattering from turbulent humidity fluctuations. In regions of active turbulence, the structure function parameter (C_x^2) for a particular variable (x) is proportional to the square of the vertical gradient of x (Fairall et al, 1988)

$$C_x^2 = 1.6\gamma_x(C_u^2/N^2)(\partial x/\partial z)^2, \quad (7)$$

where x could be T, q, or n; C_u^2 , a measure of local turbulence, is the velocity structure function parameter, N is the Brunt-Vaisala frequency; and $\gamma_x \geq 0.3$ is a constant. Thus, C_q^2 should correlate well with vertical humidity gradients.

For comparison, Fig. 2 shows q contours (g/kg) derived from rawinsonde data for the same time period shown in Fig. 1. The swath of high $\partial q/\partial z$ across the middle of Fig. 2 is evidence of the MBL inversion height decreasing from about 1000 m at the beginning of 11 July to about 750 m at the end of 12 July. Note that the humidity gradients are well correlated with C_q^2 except for a period from 23z to 29z in which C_q^2 reaches a local minimum while $\partial q/\partial z$ approaches its maximum value.

This apparent disagreement with the relationship in (7) can be analyzed using additional data obtained from the remote sensors located at SNI. A record of cloud base measured by the ceilometer (Schubert et al., 1987b), is shown in Fig. 3. Clear sky is depicted by a point at 960 m. The period labeled 23z to 27z shows a sharp decrease in cloud base, suggesting a period of strong subsidence which eventually leads to clearing just after 27z. Wind speed contours from merged sodar/wind profiler data sets (Syrett, 1988) are shown in Fig. 4. Here, the period from 23z to 29z is characterized by light winds and negligible vertical wind shear. Thus for the period in question, one may conclude that although a strong humidity gradient exists, the mechanisms that would normally generate turbulence in the region of the gradient such as cloud top entrainment and vertical wind shear, are not present, resulting in lower values of C_q^2 .

REFERENCES

- Burk, S.D., 1980: Refractive index structure parameters: Time-dependent calculations using a numerical boundary-layer model. J. Appl. Meteor., 19, 562-576.
- Fairall, C.W., D.W. Thomson, and R. Markson, 1988: An aircraft and radar study of temperature and velocity microturbulence in the stably stratified free troposphere. Preprint Vol. Eighth Symposium on Turbulence and Diffusion, Amer. Meteor. Soc., Boston, MA, 61-65.
- Ottersten, H., 1969: Atmospheric structure and radar backscattering in clear air. Radio Sci., 4, 1179-1193.

- Schubert, W.H., P.E. Ciesielski, T.B. McKee, J.D. Kleist, S.K. Cox, C.M. Johnson-Pasqua, and W.L. Smith, Jr., 1987a: Analysis of boundary layer sounding data from the FIRE marine stratocumulus project. Colorado State University Atmospheric Science Paper No. 419, Fort Collins, CO 80523, 101 pp.
- Schubert, W.H., S.K. Cox, P.E. Ciesielski, and C.M. Johnson-Pasqua, 1987b: Operation of a ceilometer during the FIRE marine stratocumulus project. Colorado State University Atmospheric Science Paper No. 420, Fort Collins, CO 80523, 34 pp.
- Syrett, W.J., 1988: Hourly wind, potential temperature and Richardson number profiles at San Nicolas Island during project FIRE. FIRE Technical Report No. 2, Dept. of Meteor., Pennsylvania State University, University Park, PA 16802, 49 pp.
- VanZandt, T.E., J.L. Green, K.S. Gage, and W.L. Clark, 1978: Vertical profiles of refractivity turbulence structure constant: Comparison of observations by the Sunset Radar with a new theoretical model. Radio Sci., 13, 819-829.
- Wesely, M.L., 1976: The combined effect of temperature and humidity fluctuations on refractive index. J. Appl. Meteor., 15, 43-49.

Acknowledgements. This work is supported by ONR contract N00014-86-K-0688. The authors wish to express special thanks to Bob Peters, Dick Thompson, and Scott Williams of the Department of Meteorology, PSU, for their part in the development and installation of PSU instrumentation at SNI.

Fig. 1 Time-height cross-section of $\log(C_q^2)$ contours (g/kg) calculated from Doppler radar reflectivity.

Fig. 2 Time-height cross-section of specific humidity contours (g/kg) from rawinsondes launched at SNI. Data was compiled by Schubert et al., (1987a).

Fig. 3 Filtered cloud base versus time from ceilometer data collected at SNI during FIRE (after Schubert et al., 1987b). Clear sky is depicted by a point at 960 m.

Fig. 4 Time-height cross-section of wind speed contours (m/s) derived from merged sodar/wind profiler data sets (after Syrett, 1988).

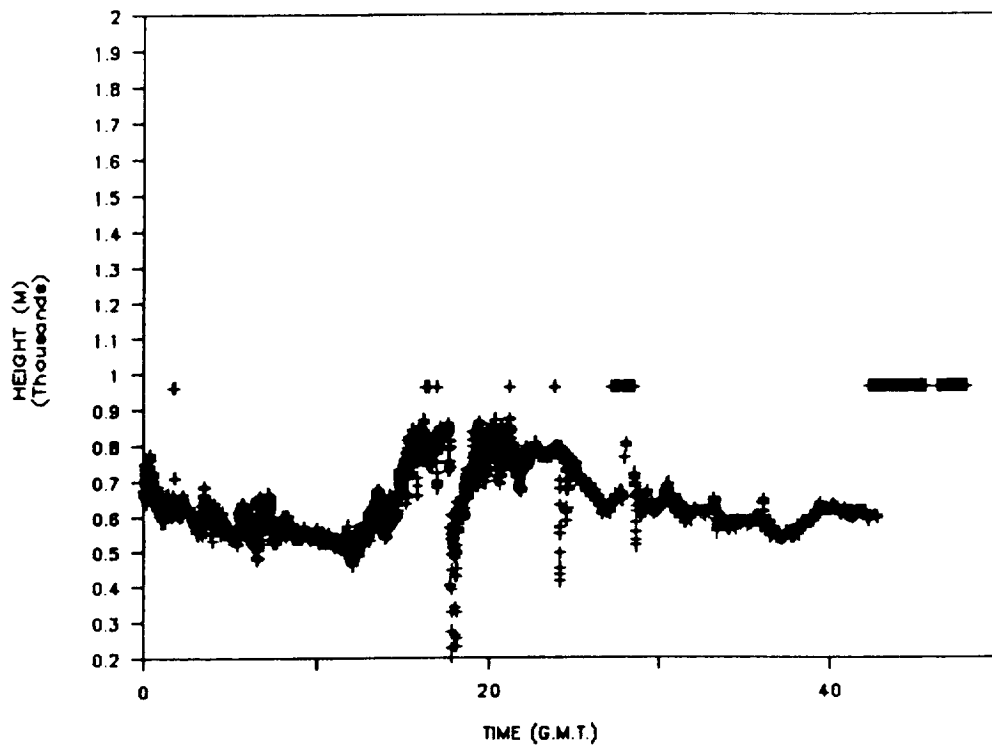


Fig. 3 Filtered cloud base versus time from ceilometer data collected at SNI during FIRE (after Schubert et al., 1987b). Clear sky is depicted by a point at 960 m.

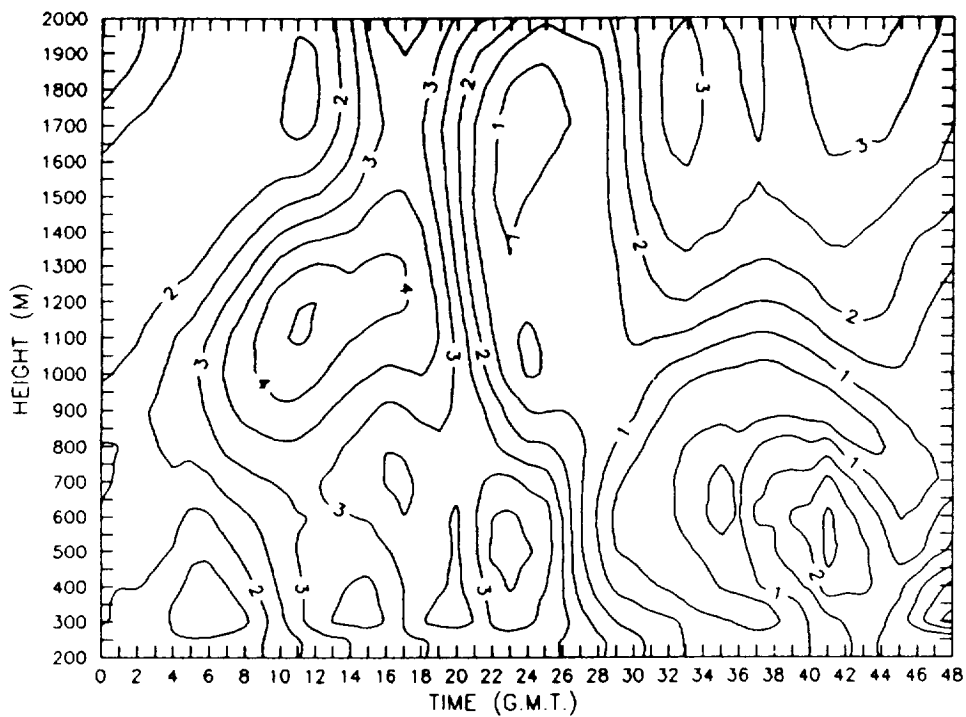


Fig. 4 Time-height cross-section of wind speed contours (m/s) derived from merged sodar/wind profiler data sets (after Syrett, 1988).

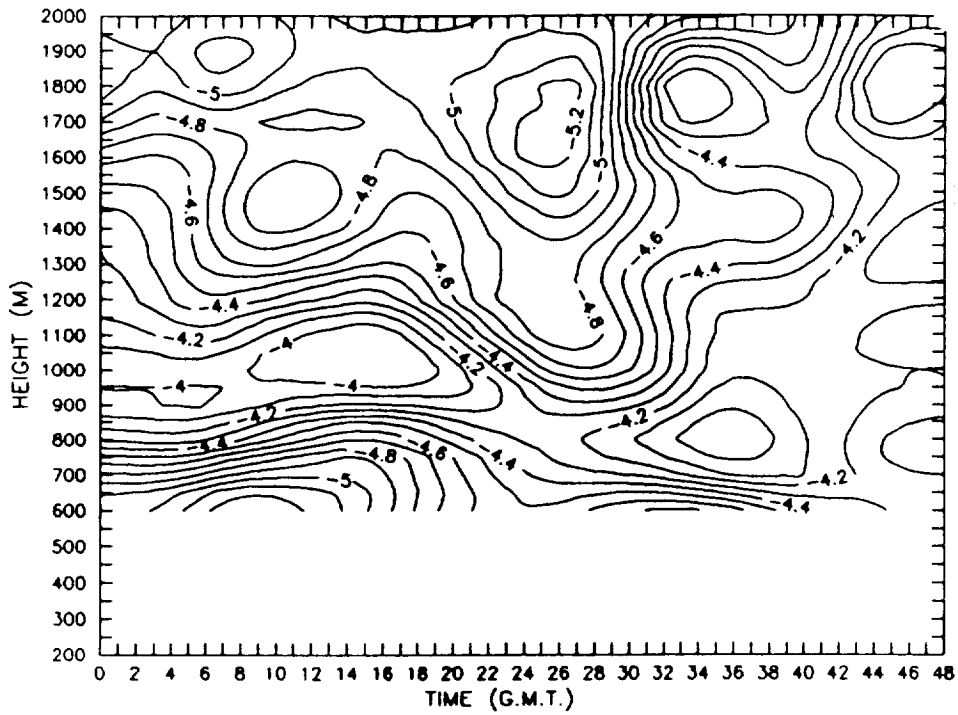


Fig. 1 Time-height cross-section of $\log(C^2/q)$ contours (g/kg) calculated from Doppler radar reflectivity.

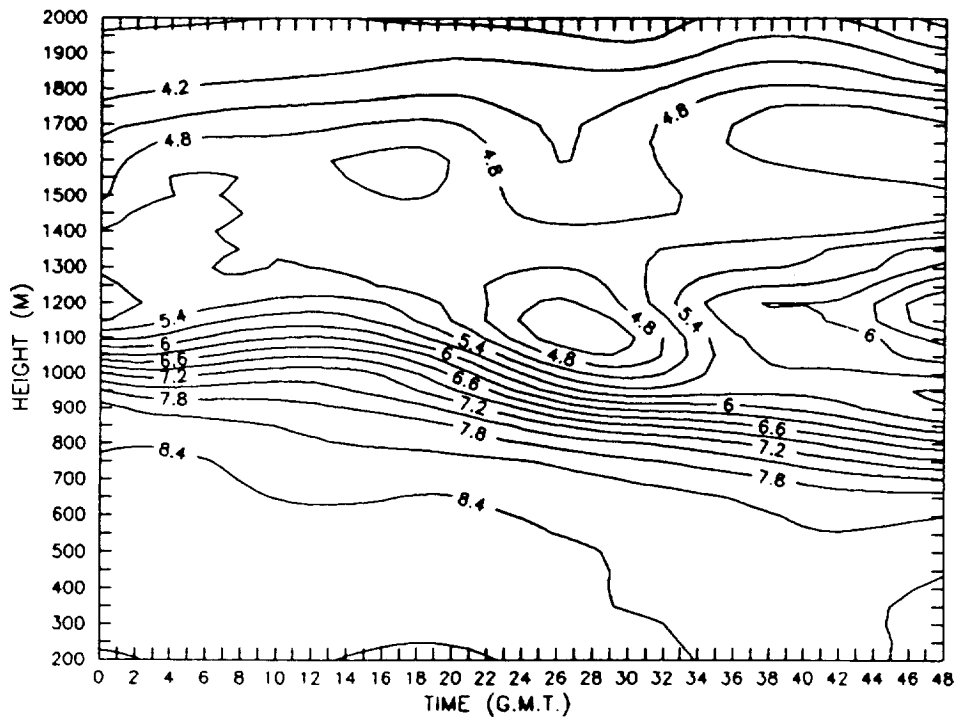


Fig. 2 Time-height cross-section of specific humidity contours (g/kg) from rawinsondes launched at SNI. Data was compiled by Schubert et al., (1987a).

THE ABOVE-INVERSION MOISTURE STRUCTURE OBSERVED DURING FIRE

Kevin A. Kloesel
Department of Meteorology
Penn State University
University Park, PA 16802

I Introduction

Analysis of thermodynamic parameters obtained over the FIRE region from the NCAR Electra aircraft during ascent and descent soundings through and above the subsidence inversion reveals the existence of alternating dry and moist layers in the free atmosphere just above the inversion. This dry/moist wedge structure has been observed before over both the tropical and subtropical oceans (Lilly, 1968; Miller and Ahrens, 1970; Riehl, 1979; and Kloesel and Albrecht, 1989). In this presentation, the structure of these layers, as well as a preliminary investigation of their source are examined.

II. Observed Moisture Structure

Three distinct types of above-inversion moisture structure were encountered during the experiment. On some flights, a single moist layer was observed above a dry free atmosphere/inversion interface (Figure 1A). On other flights, the structure was much more complex with multiple dry/moist layers (Figure 1B). Furthermore, observations on several flights show a free atmosphere above the inversion with mixing ratios higher than those observed in the boundary layer (Figure 1C).

Presently, radiosonde soundings from coastal stations from Alaska to Mexico, as well as CLASS soundings from San Nicolas Island (Schubert, et al, 1988) are being used in conjunction with the aircraft soundings to determine the regional extent of this layered structure above the inversion.

III. Determining the source of the above-inversion moisture structure

The main process that would allow moisture to be injected into the free atmosphere is penetrating convection that would occur in areas where the inversion is either weakened or non-existent. Analysis of the soundings

discussed above reveal that there is no significant breakdown of the subsidence inversion over the FIRE region until the very end of the experiment (July 18, 1987). Therefore, the source region for these layers is likely to be upstream of the region. Analysis of the u and v components of the wind, as well as comparisons of soundings taken several hours apart in the same location reveal that these layers may be advected in the horizontal and vertical by the sub-tropical high pressure system. Figure 2 illustrates two mixing ratio soundings taken two hours apart in approximately the same location on Electra Flight 4 (July 5, 1987). This comparison shows a subsiding moist layer.

This mechanism of advection and subsidence of layers in the free atmosphere is in agreement with a theory proposed by Riehl, 1979, when discussing motions in the trade wind regime. It appears that sinking motion in subsidence regions does not occur uniformly over a deep atmospheric layer, but is concentrated in thin isentropic sheets that slant downward along air trajectories.

To determine the source region of these layers, 5-day back isentropic trajectory analyses from NMC Global grids (provided by John Merrill, Univ. Rhode Island) were used.

While case studies of each Electra flight are still being compiled, and some problems exist with the trajectory analysis over a data sparse region such as the Pacific Ocean, some interesting patterns are emerging. For cases that have a layered moist/dry structure above the inversion such as Flight 5 (Fig.1A), the air appears to have two different points of origin, one moist and one dry. The trajectories for this case are shown in Figure 3A,B. For cases that do not have the layered structure, such as Flight 1, only one source region is suggested by the trajectory analysis (Figure 4A,B).

IV. Conclusions and further work

It appears that the alternating moist/dry layers above the subsidence inversion/free atmosphere interface originate upstream from the FIRE region and are advected along downward slanting isentropic surfaces around the semi-permanent sub-tropical high pressure system. It also appears that the layers are meso/synoptic scale in nature, and therefore their occurrence may be predictable by current modeling techniques. Ozone data is also being used to see if the dry wedges may have stratospheric origins.

The importance of these layers with respect to boundary layer modeling and the prospects of how these layers would effect the type of air (moist or dry) entrained into the boundary layer are still being developed. However, the existence of these layers may have implications in forecasting fractional cloudiness and stratocumulus break up.

V. References

- Kloesel, K.A. and B.A. Albrecht, 1989: Low-level inversions over the tropical Pacific-Thermodynamic structure of the boundary layer and the above-inversion moisture structure. *Mon. Wea. Rev.*, 117, 87-101.
- Lilly, D.K., 1968: Models of cloud-topped mixed layers under strong inversions. *Quart. J. Roy. Meteor. Soc.*, 94, 292-309.
- Miller, A., and D. Ahrens, 1970: Ozone within and below the west coast temperature inversion. *Tellus XXII*, 328-340.
- Riehl, H., 1979: The trade wind inversion. Climate and Weather in the Tropics, Academic Press, New York, NY, 10003, 202-249.
- Schubert, W.H., P.E.Ciesielski, T.B.McKee, J.D.Kleist, S.K.Cox, C.M.Johnson-Pasqua, and W.L.Smith, Jr. 1988: Analysis of boundary layer sounding data from the marine stratocumulus project. FIRE Volume 2. Atm. Sci. Paper 419, Colo. St. Univ. Dept. of Atm. Sci., Ft. Collins, CO 80523, 97pp.

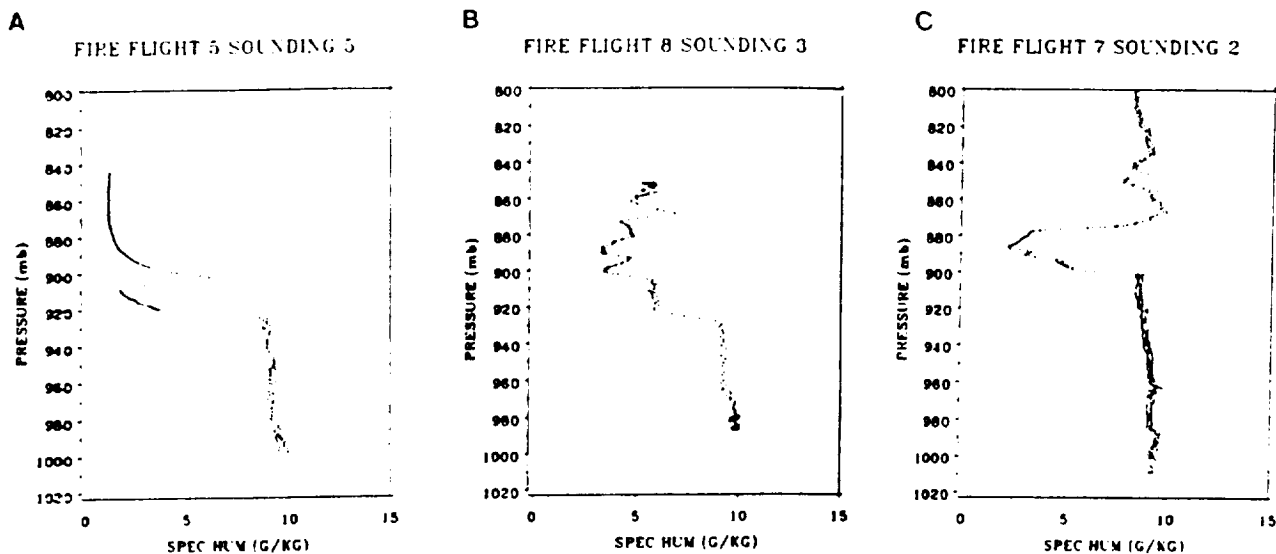


Figure 1. Vertical specific humidity (g/kg) profiles from (A) Electra flight 5, July 7, 1987, (B) Electra flight 8, July 14, 1987 and (C) Flight 7, July 11, 1987.

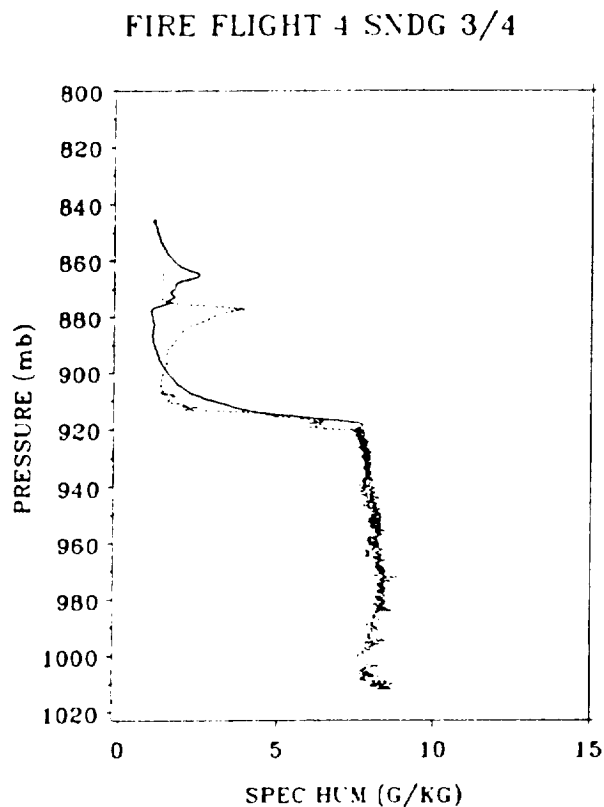


Figure 2. Vertical specific humidity (g/kg) profile from 32.5N 121.5W on Electra flight 4, July 5, 1987 at 1800UTC (solid) and 2000UTC (dashed).

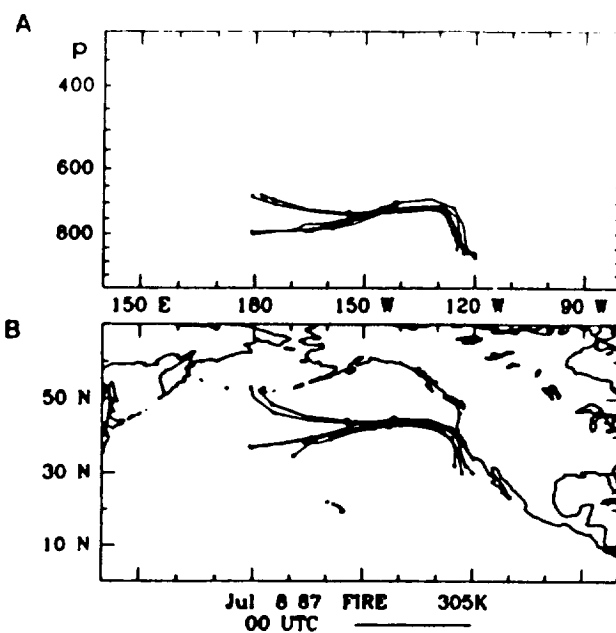


Figure 3. 305K Isentropic surface trajectories ending just above the inversion top at 0000UTC July 8, 1987 (Flight 5) in and around the FIRE region. Both the vertical (A) and horizontal (B) trajectories are provided. The distance between two dots on a specific trajectory represents the distance traveled in 24hours.

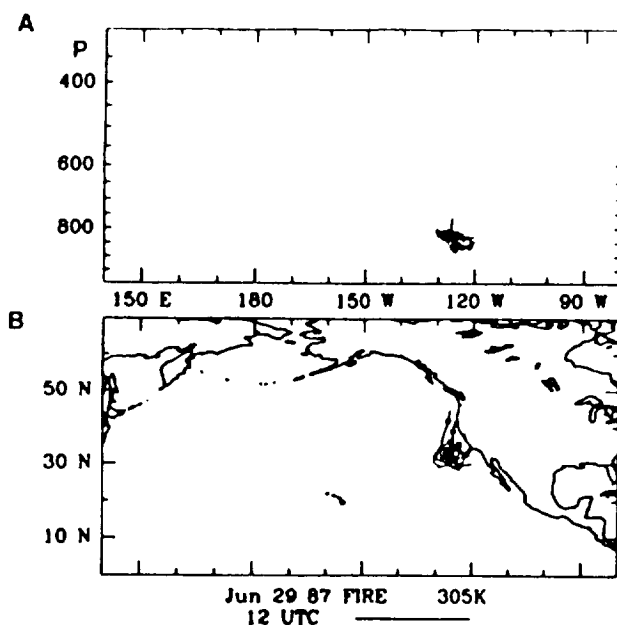


Figure 4. Same as Figure 3 but for 1200UTC June 29, 1987 (Flight 1).

	PAGE
M02.01 Reflectivities of Uniform and Broken Stratiform Clouds--An Update Coakley, Jr., J. A., and B. P. Briegleb	71
M02.02 Observed Cloud Reflectivities and Liquid Water Paths--An Update Coakley, Jr., J. A., and J. B. Snider	75
M02.03 Spectral Absorption of Marine Stratocumulus Clouds Derived from <i>In Situ</i> Cloud Radiation Measurements King, Michael D., Lawrence F. Radke, and Peter V. Hobbs	79
M02.04 Cloud Optical Parameters as Derived from the Multispectral Cloud Radiometer Nakajima, Teruyuki, and Michael D. King	85

Reflectivities of Uniform and Broken Stratiform Clouds--An Update

J.A. Coakley, Jr.
Department of Atmospheric Sciences
Oregon State University
Corvallis, OR 97331-2209

B.P. Briegleb
National Center for Atmospheric Research
Boulder, CO 80307-3000

We have compared the reflectivities of uniform and broken stratiform clouds obtained from the NOAA-9 and NOAA-10 overpasses collected during the FIRE Marine Stratocumulus IFO, and we have compared these reflectivities with those obtained through radiative transfer calculations performed for plane-parallel cloud models. Our objective was to determine the extent to which plane-parallel radiative transfer calculations could reproduce the reflectivities observed for uniform clouds and to determine the extent to which finite cloud effects cause broken clouds to reflect differently than uniform clouds. The latter study is to provide guidance in the parameterization of finite cloud effects in general circulation climate models as well as to assess the ability of plane-parallel theory, which is used by ISCCP to retrieve cloud properties, to treat the reflectivities of broken clouds.

Some results from this study were reported at the last FIRE Science Team meeting and some were reported elsewhere (Coakley and Briegleb, 1989). Improvements since the previous reports include 1) the analysis of additional satellite passes and 2) a modification to the analysis which helps to show the significance of the differences in reflectivities for uniform and broken clouds.

All NOAA-9 and NOAA-10 daytime passes for the FIRE IFO were processed using the spatial coherence method. For this study observations were collected for 60 km subframes which 1) contained a single layer of stratiform clouds, 2) of the 1 km fields of view, had greater than 10% that were overcast and 3) had a similar fraction that contained broken clouds. By restricting the observations to such subframes we are able to report on the properties of the reflectivities for uniform clouds, as deduced from the overcast fields of view, and the properties for the same clouds when they are broken, and thereby, are subject to finite cloud effects. For the broken clouds, we obtain the reflectivity by taking the mean reflectivity for the ensemble of fields of view containing broken clouds to be given by

$$r = (1 - A_c) r_s + A_c r_c \quad (1)$$

where A_c is the fractional cloud cover for the ensemble, r_s is the reflectivity for the cloud-free ocean background and r_c is the desired cloud reflectivity. r_s is obtained from observations when the region is cloud-free. A_c is obtained from the spatial coherence results using radiances at 11 μm .

For the calculated results we used an adding-doubling method for solving the radiative transfer equation and Mie calculations for

representative droplet size distributions to obtain the single scattering phase functions. These phase functions were fit to double Henyey-Greenstein phase functions to capture both forward and backward peaks of the scattering. Because the AVHRR is uncalibrated, we normalized the observations so that a suitable average of the observed radiances was made to match a similarly derived average of the calculated radiances.

Figure 1 shows comparisons of the calculated and observed anisotropy of the $0.63\ \mu\text{m}$ reflectivities for the NOAA-9 and NOAA-10 overpasses. The observed and calculated results match well within the uncertainties of the observations.

Figure 2 shows differences (uniform - broken) between the reflectivities of uniform clouds and their broken counterparts. Uniform clouds have significantly higher reflectivities for all satellite zenith angles. Nevertheless, at least for the stratiform clouds observed during FIRE, the anisotropy of the $0.63\ \mu\text{m}$ reflected radiation seems to be unaffected by finite cloud effects.

The reflectivity of broken stratiform clouds would appear to be amenable to plane-parallel theory albeit at reduced reflectivities. The reduction in reflectivity might be due to finite cloud effects, but the reduction is also consistent with lower liquid water paths for broken clouds. We have performed similar analyses for radiation reflected at $3.7\ \mu\text{m}$. The absorption of solar radiation at $3.7\ \mu\text{m}$ by water droplets substantially alters the findings.

Reference

Coakley, J.A., Jr. and B.P. Briegleb, 1989: Reflectivities of Uniform and Broken Marine Stratiform Clouds. Proceedings of IRS '88. (in press).

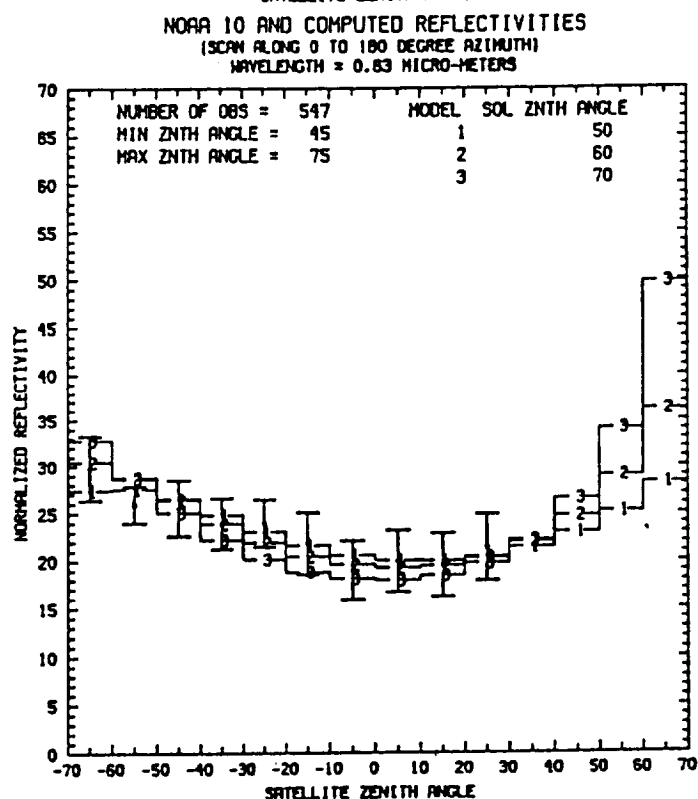
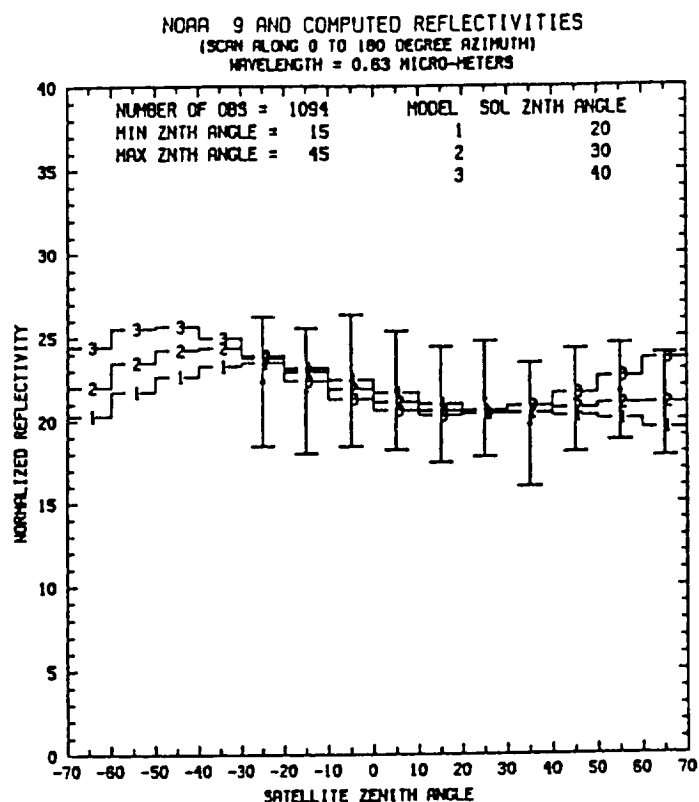


Figure 1. Observed and calculated normalized reflectivities for uniform stratocumulus. Negative satellite zenith angles indicate backscattered radiation; positive satellite zenith angles indicate forward scattering. The error bars indicate one standard deviation of the observed reflectivities.

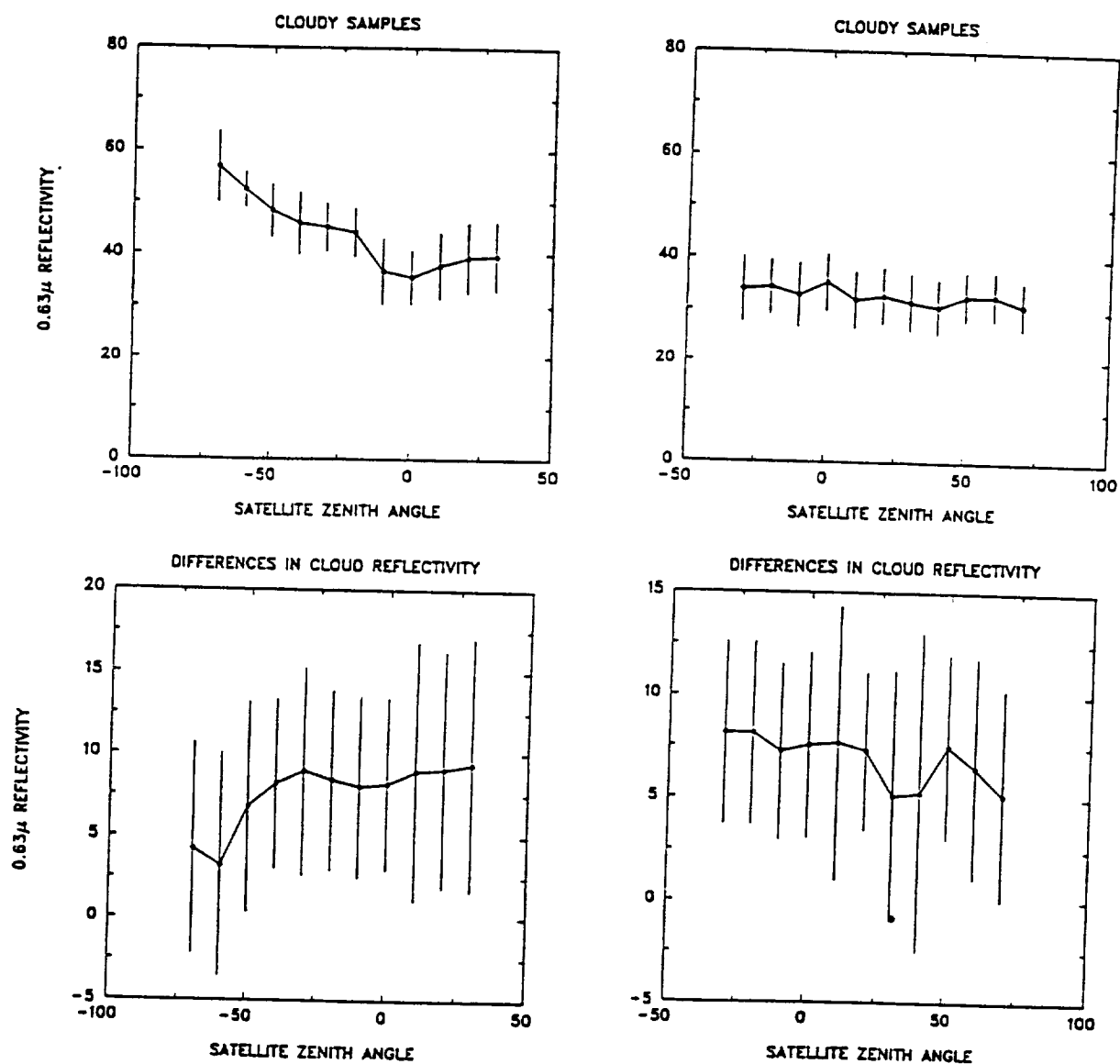


Figure 2. Observed reflectivities for uniform clouds and differences between reflectivities for uniform clouds and their broken cloud counterparts (uniform-broken). The error bars for the differences indicate one standard deviation for the difference.

Observed Cloud Reflectivities and Liquid Water Paths--An Update

J.A. Coakley, Jr.
Department of Atmospheric Sciences
Oregon State University
Corvallis, OR 97331-2209

J. B. Snider
NOAA/ERL Wave Propagation Laboratory
Boulder, CO 80303

We have used the FIRE microwave radiometer observations of liquid water path from San Nicolas Island and simultaneous NOAA AVHRR observations of cloud reflectivity to test a relationship between cloud liquid water path and cloud reflectivity that is often used in general circulation climate models (Stephens, 1978). Here we report on the results of attempts to improve the data analysis which was described at the previous FIRE Science Team Workshop and elsewhere (Coakley and Snider, 1989). The improvements included the analysis of additional satellite passes over San Nicolas and sensitivity studies to estimate the effects on the observed reflectivities due to 1) nonzero surface reflectivities beneath the clouds, 2) the anisotropy of the reflected radiances observed by the AVHRR, 3) small scale spatial structure in the liquid water path and 4) adjustments to the calibration of AVHRR.

NOAA-9 and NOAA-10 AVHRR data and San Nicolas Island microwave radiometer data were analyzed for all satellite passes for which San Nicolas Island and neighboring 60 km regions were overcast and there was no precipitation detected by the surface observers. The 1 minute liquid water path measurements obtained from the microwave radiometer were averaged for the hour containing the satellite overpass to obtain a value representative of overcast conditions. The average $0.63 \mu\text{m}$ reflectivity for 1 km AVHRR fields of view that were within 60 km of San Nicolas Island and which were identified as being overcast was taken to represent the reflectivity of overcast conditions. The standard deviation of the reflectivity for these fields of view was taken to represent the typical variability in the reflectivity.

Figure 1 shows the observed $0.63 \mu\text{m}$ reflectivities and the parameterized cloud albedo for the liquid water paths observed with the microwave radiometer. The parameterized albedo is that developed by Stephens (1978) for nonabsorbing clouds. To obtain the agreement shown, we multiplied the reflectivities observed with NOAA-9 by 1.25 and those observed with NOAA-10 by 1.35. These factors gave the best linear least-squares fit with zero offset between the observed reflectivity and parameterized cloud albedo. As discussed below, we take these factors to represent adjustments to the calibration of the AVHRR instruments.

Because the parameterization is for cloud albedo while the observations are of the bidirectional reflectivity for clouds over a reflecting surface, we considered making corrections to the observations to allow for the reflectivity of the underlying surface, the anisotropy of the reflected radiation

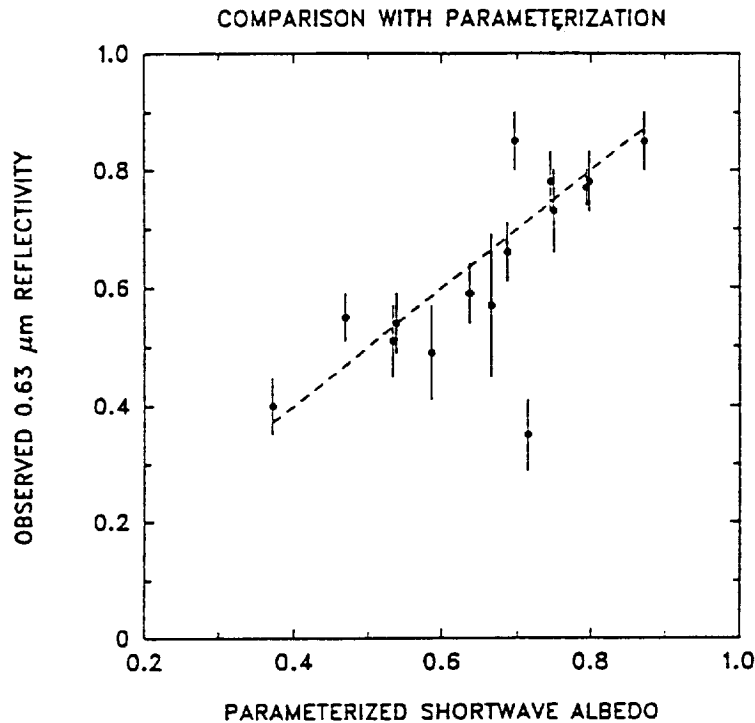


Figure 1. Observed 0.63 μm reflectivities and albedos calculated using the microwave liquid water paths in the parameterization developed by Stephens (1978). The line indicates perfect agreement. The observations for NOAA-9 were multiplied by a factor of 1.25 and the observations for NOAA-10 were multiplied by 1.35. The error bars indicate the typical variability in the reflectivities as deduced from the observations.

and the small scale spatial structure in the liquid water path which is not resolved by the AVHRR observations.

To first order in surface albedo, the reflectivity as observed by the AVHRR is given by

$$R' = R_c + \alpha_s (1 - R_c)^2 \quad (1)$$

where R_c is the cloud reflectivity and α_s is the surface reflectivity for the particular viewing geometry. α_s is deduced from reflectivities observed under cloud-free conditions. The desired quantity is the cloud reflectivity, R_c , which is deduced by solving (1). We find that for the current set of observations $R' - R_c$ is generally less than 0.02 and as a result is a fraction of the typical variability in R' which is 0.05.

Concerning the anisotropy of the reflected radiances, the observations for NOAA-9 indicate that the reflectivities are nearly isotropic (after effects due to surface reflectivities have been removed). Consequently, for the

NOAA-9 observations no adjustments are made (Coakley and Briegleb, 1989). For NOAA-10, the observations indicate that the reflected radiation is slightly anisotropic. We allow for the anisotropy by assuming that for the forward scattering direction the observations are representative of all azimuths $0 < \phi < \pi/2$ and for the backward scattering direction the observations are representative of all azimuths $\pi/2 < \phi < \pi$. These assumptions give rise to the definition of a bidirectional reflectivity which can be used to convert the observed reflectivities to albedos. Allowing for the anisotropy of the reflected radiances for NOAA-10, we find that the absolute difference between the cloud albedo and the cloud reflectivity, $|\alpha_c - r_c|$ is generally less than 0.04, which is comparable to the variability of the observed reflectivities.

Because the 1 km AVHRR data is unable to resolve the spatial structure which is evident in cloud reflectivities, and because the relationship between liquid water path and cloud reflectivity saturates for large values of the liquid water path, we suspect that the values of the reflectivities reported here fall below those that would be expected from the parameterized relationship using the mean of the liquid water path derived from the microwave radiometer observations. To estimate the degree to which the small scale variability in liquid water path affects the observed reflectivity, we assume that the parameterized relationship holds, and we evaluate the mean reflectivity which is taken to be given by

$$\langle r_c \rangle = \int r_c(L)P(L)dL \quad (2)$$

where $P(L)dL$ is the probability of the liquid water path lying between L and $L+dL$. We assume the probability distribution to be given by

$$P(L) = AL^N \exp(-\Gamma L) \quad (3)$$

with N and Γ are adjusted to give the mean and standard deviations in the liquid water paths observed with the microwave radiometer and A is a normalization constant.

We find that the effect of small scale variability on the reflectivity is small when $L/\sigma_L \ll 1$ where σ_L is the standard deviation of the liquid water path, i.e. when the variability is indeed small, when L is small so that the reflectivity becomes a linear function of L , and when L is sufficiently large that the reflectivity has, for practical purposes, reached saturation. Saturation appears to be reached for $L > .05$ mm. At most, the difference between the observed and expected values of cloud reflectivity are, $r_c(\langle L \rangle) - \langle r_c \rangle = 0.03$. Again the correction to the reflectivity is small compared to the variability in the observed reflectivities.

If the factors used to obtain the results in Figure 1 are due to calibration adjustments, then by far the largest corrections to the observed data will be corrections for calibration. Corrections for the factors considered above result in changes to the observations which are generally less than 5% and only in one instance do the corrections amount to 22%. For the case of the comparison for NOAA-9, we note that the correction, 1.25, is similar to that obtained from experiments performed to determine the calibration, 1.20

(Whitlock *et al* 1988). Similar calibration experiments have been performed for NOAA-10 but the results are as yet unavailable.

In conclusion, the results shown in Figure 1 indicate that at least the functional form of the parameterization developed by Stephens (1978) is correct. Furthermore, for the NOAA-9 observations, once corrections are made for the instrument's calibration, the parameterized albedo is typically within 5% of the observed reflectivities.

References

- Coakley, J.A., Jr. and B.P. Briegleb, 1989: Reflectivities of uniform and broken stratiform clouds--an update. Extended Abstracts, FIRE Science Team Workshop, 11-14 July, Monterey, (this volume).
- Coakley, J.A., Jr. and J.B. Snider, 1989: Observed Reflectivities and Liquid Water Content for Marine Stratocumulus. Extended Abstracts, AMS Symposium on the Role of Clouds in Atmospheric Chemistry and Global Climate, pp. 175-177.
- Stephens, G.L. 1978: Radiation profiles in extended water clouds. II: Parameterization schemes. *J. Atmos. Sci.*, **35**, 2123-2132.
- Whitlock C.H. W.F. Staylor, G. Smith, R. Levin, R. Frouin, C. Gautier, P.M. Teillet, P.N. Slater, Y.J. Kaufman, B.N. Holben and S.R. Lecroy, 1988: AVHRR and VISSR satellite instrument calibration results for both cirrus and marine stratocumulus IFO periods. Presentation, FIRE Science Team Workshop, July 11-15, Vail, Colorado.

Spectral Absorption of Marine Stratocumulus Clouds Derived from *In Situ* Cloud Radiation Measurements

MICHAEL D. KING

*Laboratory for Atmospheres, Goddard Space Flight Center, NASA,
Greenbelt, MD 20771, USA*

LAWRENCE F. RADKE AND PETER V. HOBBS

*Department of Atmospheric Sciences, University of Washington,
Seattle, WA 98195, USA*

1. Introduction

A multiwavelength scanning radiometer has been used to measure the angular distribution of scattered radiation deep within a cloud layer at discrete wavelengths between 0.5 and 2.3 μm . The relative angular distribution of the intensity field at each wavelength is used to determine the similarity parameter, and hence single scattering albedo, of the cloud at that wavelength using the diffusion domain method. In addition to the spectral similarity parameter, the analysis provides a good estimate of the optical thickness of the cloud *beneath* the aircraft. In addition to the radiation measurements, we obtained microphysical and thermodynamic measurements from which the expected similarity parameter spectrum was calculated using accepted values of the refractive index of liquid water and the transmission function of water vapor.

In this paper, we present an analysis of the results obtained for a 50 km section of clean marine stratocumulus clouds on 10 July 1987. These observations were obtained off the coast of California from the University of Washington Convair C-131A aircraft as part of the First ISCCP Regional Experiment (FIRE). We will present a comparison of the experimentally-derived similarity parameter spectrum with that expected theoretically from the cloud droplet size distribution measured simultaneously from the aircraft. The measurements and theory are in very close agreement for this case of clean maritime clouds.

2. Results from observations on 10 July 1987

On 10 July 1987 the C-131A flew a tightly coordinated mission with the ER-2 aircraft, consisting of continually flying legs of 145 km in length. The C-131A was primarily making cloud radiation and cloud microphysics measurements deep within the cloud layer, whereas the ER-2 was flying well above the clouds. Figure 1 illustrates the zenith and nadir intensities as a function of distance (time) for measurements obtained inside clouds near the central portion of one of these flight lines. These data, corresponding to ob-

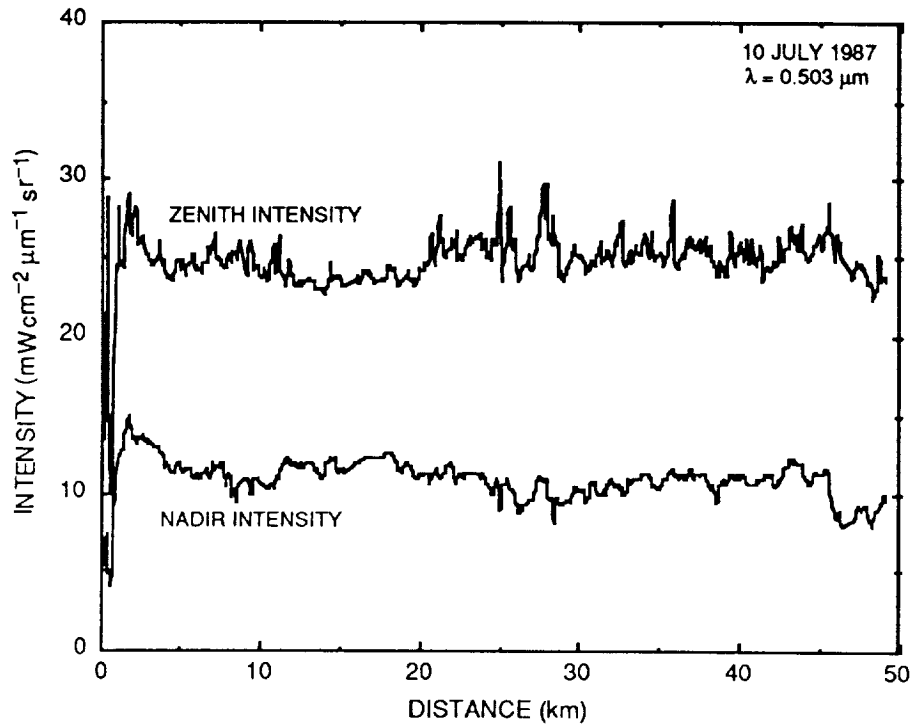


Fig. 1. Zenith and nadir intensities as a function of distance along the flight track for measurements obtained inside the clouds between 9:41 and 9:51 PDT. These measurements were obtained at a wavelength $\lambda = 0.503 \mu\text{m}$.

servations obtained with the cloud absorption radiometer (King et al. 1986) at $\lambda = 0.503 \mu\text{m}$, show that the zenith and nadir intensities were quite uniform within these clouds. A careful examination of Fig. 1 suggests that the data near the start of the flight line are too optically thin to have a diffusion domain, as evidenced by very low zenith and nadir intensity measurements. Furthermore, the measurements near 24.9 and 28.0 km, though probably in a cloud of sufficient optical thickness to have a diffusion domain, were obtained too near the cloud top, so the zenith measurements were contaminated by directly transmitted solar radiation.

The scaled optical thickness between the aircraft flight level and the base of the clouds was derived by applying the diffusion domain method to all scan lines of Fig. 1 that satisfied the diffusion domain criteria (see King et al. 1989 for details). Figure 2 illustrates the optical thickness $\tau_c - \tau$ as a function of distance, where we converted scaled optical thickness to optical thickness using the asymmetry factor $g = 0.8579$ applicable to this wavelength ($\lambda = 0.503 \mu\text{m}$) and derived for the measured cloud droplet size distribution. Of the 1000 scan lines presented in Fig. 1, 611 passed the restrictive selection criteria described in King et al. (1989). Among those measurements excluded from our analysis were the optically thin scans at the beginning of the time series and the measurements that were contaminated by the sun (at distances of 24.9 and 28.0 km). As expected, the measurements between 11.5 and 19.4 km that had a

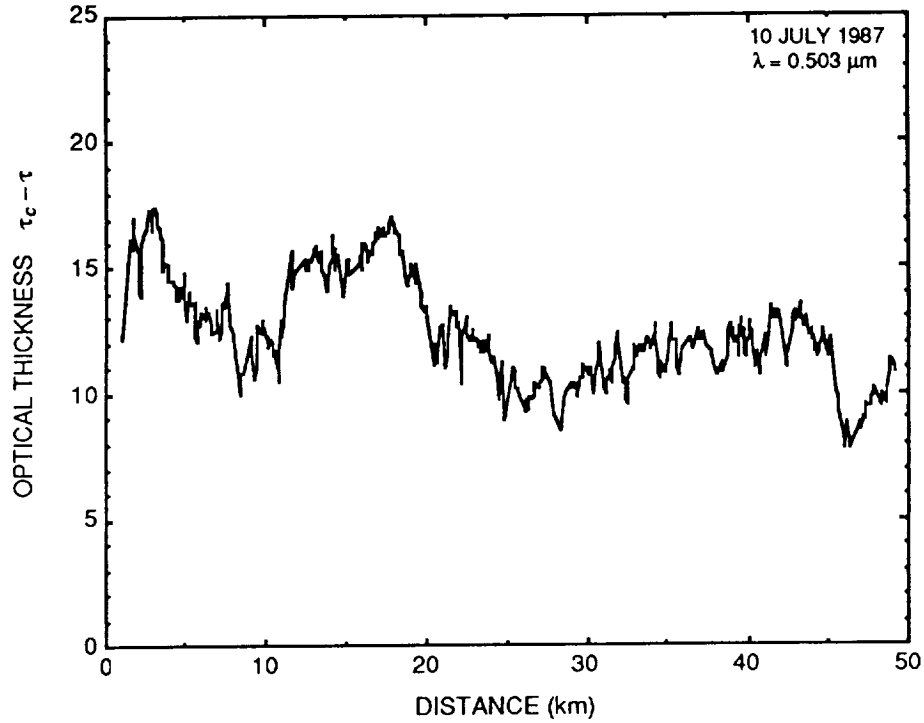


Fig. 2. Optical thickness beneath the aircraft for all measurements of Fig. 7 that satisfy the diffusion domain criteria.

relatively low zenith intensity and relatively high nadir intensity correspond to a region of large optical thickness beneath the aircraft.

Given the surface reflectivity and optical thickness (or scaled optical thickness) of an individual scan at a specified wavelength, the intensity ratio $I(\tau, -1)/I(\tau, 1)$ is reduced solely to a function of similarity parameter s . Utilizing formulas summarized in King et al. (1989), we were thus able to calculate the intensity ratio as a function of similarity parameter and match this functional relationship with the measured intensity ratio to derive a value of the similarity parameter for a given measurement and wavelength.

Figure 3 illustrates the similarity parameter as a function of distance for four wavelengths of the CAR determined in this manner. The similarity parameter s , defined as $s = [(1 - \omega_0)/(1 - \omega_0 g)]^{1/2}$, is a function of the asymmetry factor g and the single scattering albedo ω_0 . The tendency for the similarity parameter to decrease with increasing distance, especially noticeable at 1.64 and 2.20 μm , is due to a modest decrease in the effective radius of the cloud droplets over this distance and not to a decrease in the absorption content of the cloud droplets themselves. Due to the use of a filter wheel to measure the intensity field in channels 8-13, diffusion domain measurements were obtained in this time interval for between 71 and 87 scans, depending on filter position, in contrast to 611 for the first seven, simultaneously sampled, channels.

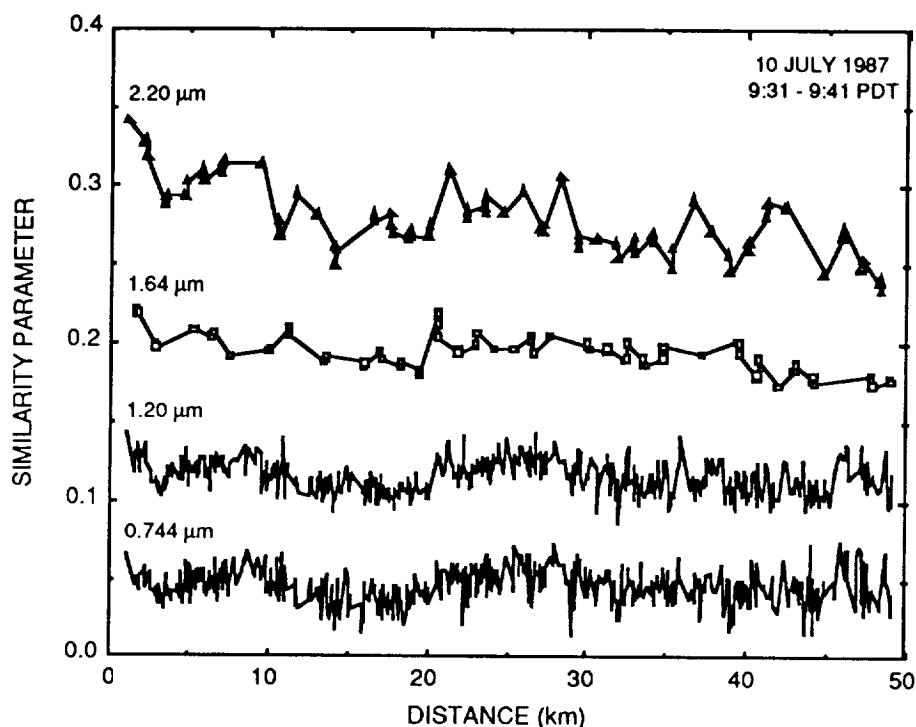


Fig. 3. Similarity parameter as a function of distance for four wavelengths of the cloud absorption radiometer.

Figure 4 illustrates the mean and standard deviation of the spectral similarity parameter for all thirteen channels of the CAR obtained from aircraft measurements on 10 July 1987. Although the conversion from s to ω_0 is not unique, due to the moderate spectral variation of g , we have provided a single scattering albedo scale in this figure as a matter of convenience. This scale, shown on the right-hand side of Fig. 4, is strictly applicable at $\lambda = 0.754 \mu\text{m}$. Based on profile ascents and descents following these measurements, the stratocumulus cloud layer was determined to be 440 m thick with a cloud base at 490 m.

In addition to the experimental results obtained using the CAR, Fig. 4 illustrates calculations of the similarity parameter as a function of wavelength for a cloud composed of water droplets only (solid curve) and droplets plus saturated vapor at 10.3°C (dashed curve). The water droplet computations were based on a combination of Mie theory and complex angular momentum theory (Nussenzweig and Wiscombe 1980) applied to the measured cloud droplet size distribution. The water vapor computations, on the other hand, were based on assuming the cloud to be composed of saturated vapor and applying the necessary pressure and temperature scaling to obtain an equivalent absorber amount ($w = 0.41 \text{ g cm}^{-2}$). The water vapor transmission functions were then computed for this cloud layer at a resolution of 20 cm^{-1} using LOWTRAN 5 (Kneizys et al. 1980). The absorption optical depths thus ob-

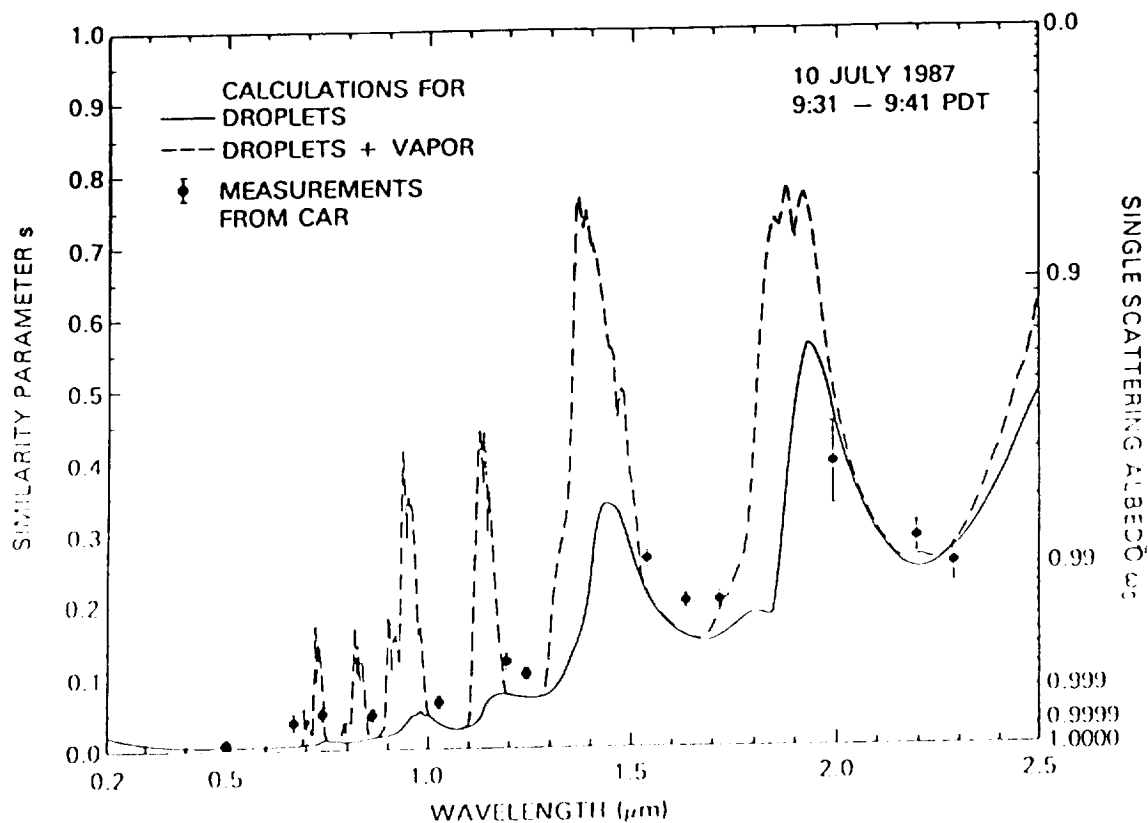


Fig. 4. Calculations of the similarity parameter as a function of wavelength for water droplets alone (solid line) and drops plus vapor (dashed line) for the cloud droplet size distribution and water vapor conditions of the marine stratocumulus cloud of 10 July 1987. The single scattering albedo scale is valid at $\lambda = 0.754 \mu\text{m}$, where the cloud asymmetry factor $g = 0.848$. The measurements derived from the cloud absorption radiometer (solid circles with error bars) are averages of the similarity parameter derived by applying the diffusion domain method to the 50 km section of this cloud.

tained were combined with the corresponding optical properties for cloud droplets, where we further assumed that the total cloud optical thickness $\tau_c = 16$ at a wavelength of $0.754 \mu\text{m}$.

The very close agreement between the measurements and theory shows that, *in this case*, the absorption of solar radiation by the clouds can be accounted for largely by the droplets and that the large drops (drizzle) did not produce significant "anomalous absorption." Based on these results we are forced to conclude that "anomalous absorption," as discussed by Twomey (1976), Davies et al. (1984) and Stephens and Tsay (1989), was not significant in the marine stratocumulus clouds that we sampled on 10 July 1987.

REFERENCES

- Davies, R., W. L. Ridgway and K. E. Kim, 1984: Spectral absorption of solar radiation in cloudy atmospheres: A 20 cm^{-1} model. *J. Atmos. Sci.*, **41**, 2126-2137.
- King, M. D., M. G. Strange, P. Leone and L. R. Blaine, 1986: Multiwavelength scanning radiometer for airborne measurements of scattered radiation within clouds. *J. Atmos. Oceanic Tech.*, **3**, 513-522.
- _____, L. F. Radke and P. V. Hobbs, 1989: Determination of the spectral absorption of solar radiation by marine stratocumulus clouds from airborne measurements within clouds. Submitted to *J. Atmos. Sci.*
- Kneizys, K. X., E. P. Shettle, W. O. Gallery, J. H. Chetwynd, Jr., L. W. Abreu, J. E. A. Selby, R. W. Fenn and R. A. McClatchey, 1980: Atmospheric transmittance/radiance: Computer code LOWTRAN 5. AFGL-TR-80-0067, Air Force Geophysics Laboratories, Hanscom AFB, 233 pp.
- Nussenzveig, H. M., and W. J. Wiscombe, 1980: Efficiency factors in Mie scattering. *Phys. Rev. Lett.*, **45**, 1490-1494.
- Stephens, G. L., and S. C. Tsay, 1989: On the cloud absorption anomaly. Submitted to *Quart. J. Roy. Meteor. Soc.*
- Twomey, S., 1976: Computations of the absorption of solar radiation by clouds. *J. Atmos. Sci.*, **33**, 1087-1091.

Cloud Optical Parameters as Derived from the Multispectral Cloud Radiometer

TERUYUKI NAKAJIMA[†] AND MICHAEL D. KING

*Laboratory for Atmospheres, Goddard Space Flight Center, NASA,
Greenbelt, MD 20771, USA*

1. Introduction

Simultaneous measurements of the liquid water content and particle size have assumed an important role in cloud physics as they help elucidate the mechanism of cloud particle formation and the mechanism of air mass-mixing in stratus clouds. Such measurements can reveal the modification of cloud air masses by anthropogenic aerosol particles (Coakley et al. 1987, Durkee 1989). Studies of the climatic impact of these modification processes on cloud microphysics seems to be urgent for understanding mechanisms of climate change. GCM simulations can be improved by introducing a parameterization of cloud optical properties in terms of integrated liquid water content (liquid water path) and particle size (Slingo 1989).

Motivated by the above mentioned circumstances, we have been developing remote sensing techniques for simultaneously retrieving the cloud optical thickness and effective particle radius, from which the liquid water path can be inferred. Nakajima and King (1989a) have shown a good agreement between the effective radius derived from *in situ* cloud microphysics observations and that derived from reflected solar radiation measurements, with a slight overestimation occurring in the remote sensing method. Also Durkee (1989) found a good correlation between the *in situ* value of the effective particle radius and the cloud reflectance at 3.7 μm .

In this paper we will present statistical features of the cloud optical thickness (or liquid water path) and effective particle size for marine stratocumulus clouds. These results have been obtained during four days (7, 10, 13 and 16 July 1987) of observations with the Multispectral Cloud Radiometer (ER-2) and Thematic Mapper (Landsat-5) during the First ISCCP Regional Experiment (FIRE).

2. Results

The optical thickness (τ_c) and effective particle radius (r_e) for 7, 10, 13 and 16 July 1987 have been retrieved by analyzing reflected solar radiation mea-

[†] Permanent affiliation: Upper Atmosphere and Space Research Laboratory, Faculty of Science, Tohoku University, Sendai 980, Japan.

measurements at the 0.754, 1.65 and 2.16 μm channels of the MCR onboard the NASA ER-2 aircraft. The algorithm used to derive these parameters has been described by Nakajima and King (1989b). We have also applied the same method to data obtained from band 2 (0.56 μm) and 7 (2.22 μm) of the Landsat-5 Thematic Mapper on July 7 and 16.

The areas used in the present analysis are approximately 30 km \times 100 km for the MCR data, and 150 km \times 150 km for the Thematic Mapper. *In situ* cloud liquid water content and effective radius were obtained from measurements obtained with the Johnson-Williams (JW) liquid water content meter and three different PMS cloud probes (FSSP, OAP-200X and OAP-200Y) on board the University of Washington C-131A aircraft.

Figure 1 shows comparisons between the remote sensing-derived values of the effective radius and the *in situ* values, where we have partitioned the results into three different cloud optical thickness ranges, *i. e.*, $5 \leq \tau_c < 10$, $10 \leq \tau_c < 15$ and $15 \leq \tau_c < 20$. The remote sensing values have been adjusted to the cloud center where the C-131A was flying (see Nakajima and King 1989b for details), and the data with $\tau < 5$ have been omitted because of the uncertainty in the retrieval for optically thin clouds. From the results presented in this figure we see that for thin clouds ($5 \leq \tau_c < 10$) the remote sensing values are in excellent agreement with the *in situ* values. As the cloud optical thickness increases, however, the remote sensing values become progressively larger than the *in situ* values for $r_e \leq 10 \mu\text{m}$, and vice versa for $r_e > 10 \mu\text{m}$. The former phenomenon is likely related to the so-called cloud absorption anomaly in the near infrared region (NIR), *i. e.*, the cloud looks darker than the theoretical expectation from *in situ* microphysical parameters (*e.g.*, Stephens and Platt, 1987). On the other hand, the latter phenomenon is caused by the drizzle mode particles which can be measured by the PMS-OAP cloud and precipitation probes. The remote sensing values have only a weak sensitivity to these drizzle mode particles which tend to exist relatively low in the clouds.

Figure 2 shows comparisons of the liquid water path (gm^{-2}) estimated from the remote sensing quantities as

$$W_{\text{remote}} = 2 r_{\text{center}} \tau_c / 3, \quad (1)$$

and by the *in situ* measurements as

$$W_{\text{in situ}} = w_m \Delta z, \quad (2)$$

where r_{center} is the effective radius derived from remote sensing after adjustment for vertical inhomogeneity (Nakajima and King 1989b), τ_c the remote sensing-derived cloud optical thickness, w_m the measured liquid water content from the JW liquid water content meter, and Δz the cloud geometrical

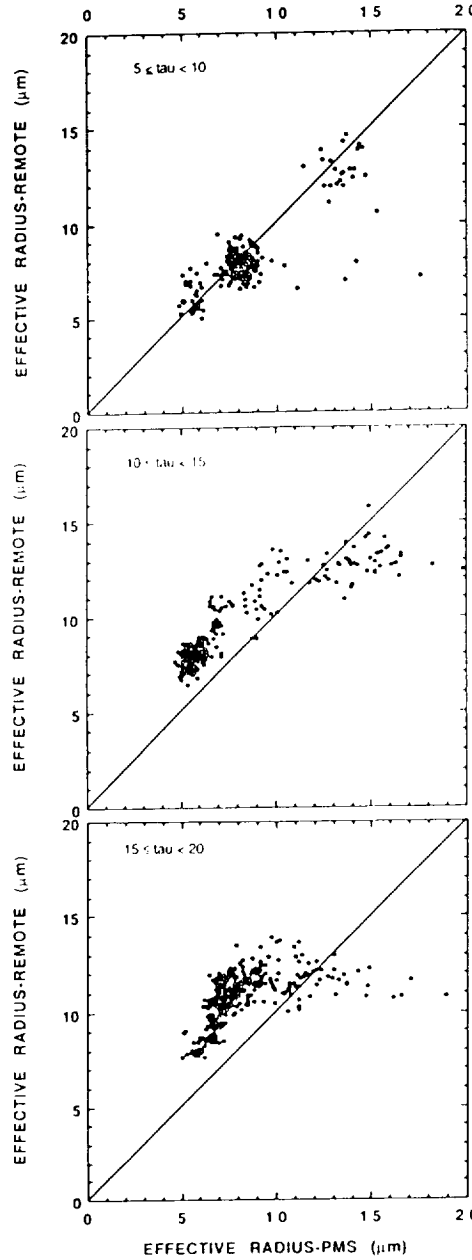


Fig. 1. Scatter diagrams comparing the *in situ* effective radius with the remote sensing effective radius. Three different optical thickness range cases (*i. e.*, $5 \leq \tau_c < 10$, $10 \leq \tau_c < 15$ and $15 \leq \tau_c < 20$) are shown in three separate panels.

thickness. The geometric thickness of the cloud has been estimated as an equivalent thickness which gives the liquid water path obtained by integrating vertical profiles of the liquid water content.

Although there is large uncertainty in the estimation of Δz , we observe a tendency to underestimate the liquid water path retrieved from our remote sensing method by 20% to 40%. From Eq. (1), together with Figs. 1 and 2, we conclude that the remote sensing optical thickness is somewhat *smaller* than

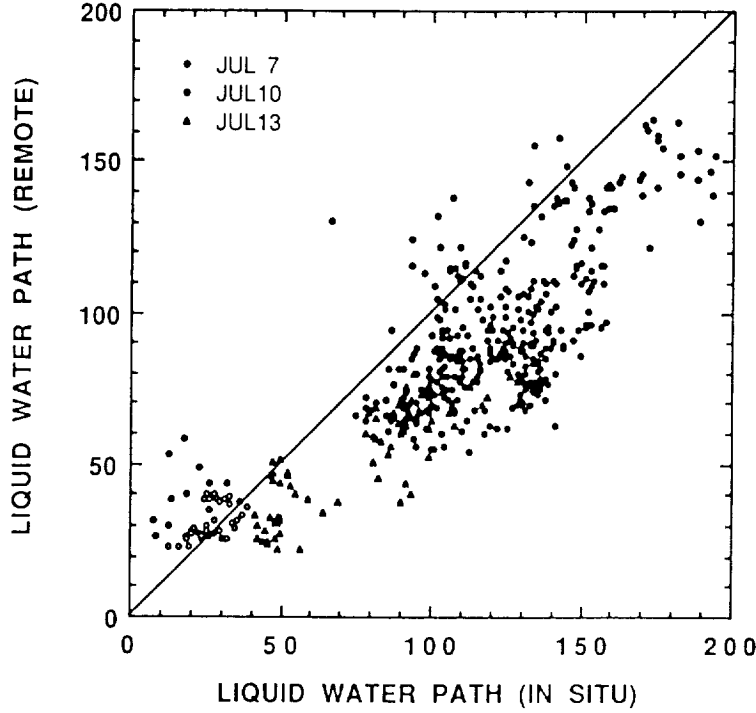


Fig. 2. Comparison of the liquid water paths derived from *in situ* measurements and estimated from remote sensing methods.

the expected value from *in situ* measurements by $\sim 50\%$ for thick clouds with $\tau \approx 20$ and $r_e \approx 8 \mu\text{m}$, roughly corresponding to the case for 10 July 1987. For such thick clouds the channel 1 ($\lambda = 0.754 \mu\text{m}$) intensity is mostly sensitive to the optical thickness, with little sensitivity to particle radius, and thus the intensity at $\lambda = 0.754 \mu\text{m}$ is significantly smaller than the expected value from *in situ* measurements.

Although there is some discrepancy between the *in situ* and remote sensing values of W and r_e , it is worthwhile to examine the correlation between these two quantities, especially given the recent interest in parameterizing the shortwave radiative properties of clouds in terms of these two parameters (Slingo 1989). Figure 3 shows two dimensional histograms of W and r_e for the four days of our observations. The five contour lines for each day show the 10, 30, 50, 70 and 90% occurrence levels. Other than 10 July, the contour lines are confined in a rather small area having the different peaks depending on days. The composite pattern of all contours with different days shows a weak positive correlation between W and r_e . The rough tendency may be expressed as

$$r_e \approx 0.333 W^{1/4}. \quad (3)$$

A similar comparison for *in situ* quantities is shown in Fig. 4. Since we have relatively large particles on 7 July and very large drizzle particles on 10 July,

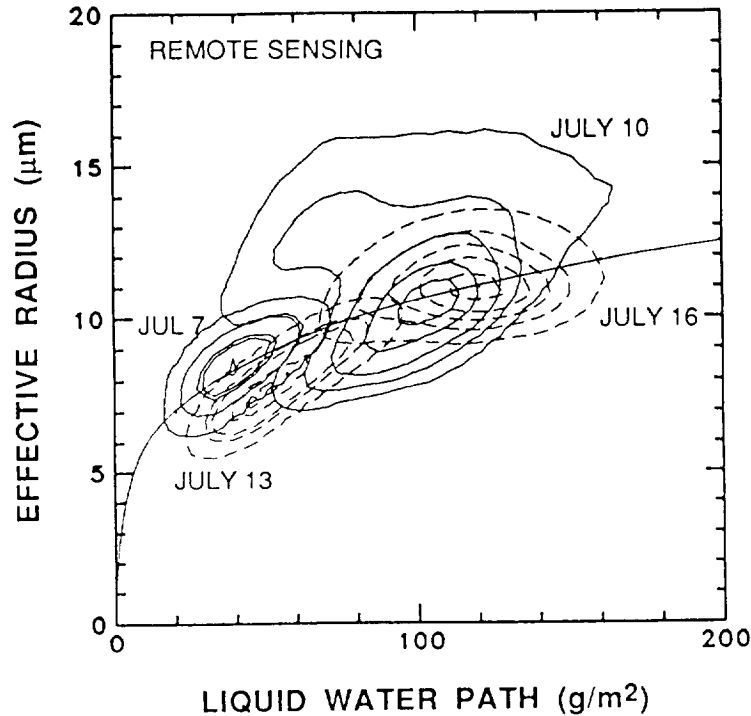


Fig. 3. Joint probability density function for the liquid water path and the effective radius derived from reflected solar radiation measurements. Five contour lines for each day shows 10, 30, 50, 70 and 90 % occurrence levels. The solid continuous line fits the rough tendency of the contours.

the overall pattern is more complicated than that presented in Fig. 3. If we disregard the drizzle particles, the effective radius is relatively insensitive to the liquid water path. The difference in the sensitive altitude within clouds between *in situ* and remote sensing is at least partly responsible for some of the difference in the tendency shown in Figs. 3 and 4.

3. Concluding remarks

As a result of our investigation, we have observed some interesting relationships between the liquid water path and the effective particle radius. We observed a systematic bias in the effective radius derived by our remote sensing method, with the tendency to overestimate the effective radius increasing as the cloud optical thickness increases. Since this can be a good guideline for solving the NIR cloud absorption anomaly problem, we need to compile more data in order to determine whether this is a general tendency for marine stratocumulus clouds. Although we also found some tendency of underestimating the cloud optical thickness from reflection function measurements, we need to be careful about drawing any conclusions because of the large uncertainty in estimating the liquid water path using Eq. (2).

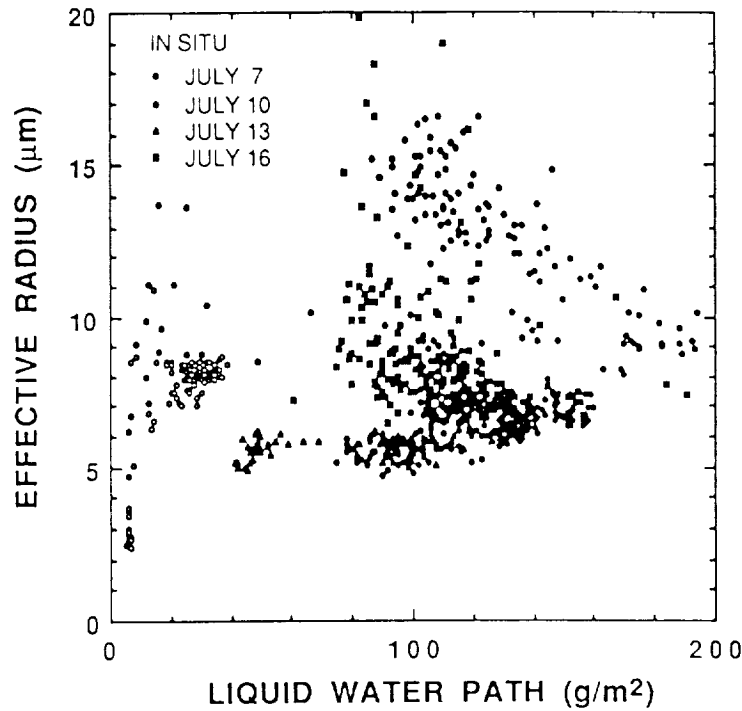


Fig. 4. Comparison of the liquid water path and the effective radius derived from *in situ* measurements.

As for the dependency of the effective radius on liquid water path, we conclude that the effective radius is relatively independent of the liquid water path with some weak positive correlation for clouds lacking significant drizzle development. For reflected solar radiation the existence of drizzle particle is not important, whereas the transmitted solar radiation is expected to have some dependence on drizzle mode particles. Consequently we need to use a vertically inhomogeneous cloud model with a two mode size distribution to produce a consistent cloud radiative model valid for both reflected and transmitted radiation.

Since the above results depend strongly on the calibration of the radiometers and *in situ* instruments, more ground (aircraft) truth will be required to further extend the results shown here.

Acknowledgements: Drs. L. F. Radke of the University of Washington and J. D. Spinhirne of Goddard Space Flight Center are gratefully acknowledged for valuable discussion and for providing their data.

REFERENCES

- Coakley, J. A., Jr., R. L. Bernstein and P. A. Durkee, 1987: Effect of ship-stack effluents on cloud reflectivity. *Science*, **237**, 1020–1022.
- Durkee, P. A., 1989: Observations of aerosol-cloud interactions in satellite-detected visible and near-infrared radiance. *Proceeding of Symposium on the role of clouds in atmospheric chemistry and global climate*. Anaheim, Calif., 157–160.
- Nakajima, T., and M. D. King, 1989a: Cloud optical parameters as derived from the multispectral cloud radiometer. *IRS '88: Current Problems in Atmospheric Radiation*, J. Lenoble and J. F. Geleyn, Eds., A. Deepak Publishing, 18-21.
- _____, and _____, 1989b: Simultaneous determination of the optical thickness and effective particle radius of clouds from reflected solar radiation measurements. Part I: Theory.. Submitted to *J. Atmos. Sci.*
- Slingo, A., 1989: A GCM parameterization for the shortwave radiative properties of water clouds. *J. Atmos. Sci.*, **46**, 1419–1427.
- Stephens, G. L., and C. M. R. Platt, 1987: Aircraft observations of the radiative and microphysical properties of stratocumulus and cumulus cloud fields. *J. Clim. Appl. Meteor.*, **26**, 1243–1269.

	PAGE
M03.01 Satellite-Derived Cloud and Radiation Fields Over the Marine Stratocumulus IFO Young, David F., Patrick Minnis, and Edwin F. Harrison	95
M03.02 Analysis of ER-2 Radiometer and Lidar Observations from the 1987 Marine Stratus Experiment Spinhirne, J. D., R. Boers, T. Nakajima, and W. D. Hart	101
M03.03 The Radiation Budget of Stratocumulus Clouds Measured by Tethered Balloon Instrumentation: Variability of Flux Measurements Duda, David P., Graeme L. Stephens, and Stephen K. Cox	103

SATELLITE-DERIVED CLOUD AND RADIATION FIELDS OVER THE MARINE STRATOCUMULUS IFO

David F. Young
Aerospace Technologies Division, Planning Research Corporation
Hampton, Virginia 23666

Patrick Minnis and Edwin F. Harrison
Atmospheric Sciences Division, NASA Langley Research Center
Hampton, Virginia 23665-5225

1. Introduction

The Geostationary Operational Environmental Satellite (GOES) is the only source for nearly continuous areal coverage of clouds within the California marine stratocumulus region. This paper presents a summary of the cloud parameters derived from GOES data during the First ISCCP Regional Experiment (FIRE) Marine Stratocumulus Intensive Field Observations (IFO).

2. Data and Methodology

Hourly, 1-km visible (VIS, $0.65\mu\text{m}$) and 4x8-km infrared (IR, $11.5\mu\text{m}$) data from GOES-West (135°W) were analyzed with the hybrid bispectral threshold method (HBTM) of Minnis et al. (1987) on a 0.5° latitude-longitude grid which includes the area between 36°N and 28°N and 115°W and 125°W . This grid encompasses the locations of most surface and aircraft operations during the IFO. Data were analyzed for the period July 1-19, 1987. Missing data occurred for entire 24-hour intervals during July 5, 10, and 16. Other sporadic data dropouts reduced the available data to 13 - 16 days for a given hour. Some navigation problems were also encountered, so these results are considered to be preliminary. The VIS data were converted to narrowband reflectance using the calibration of C. H. Whitlock (1988, personal communication). Vertically integrated liquid water content (LWC) was derived from the cloud albedos using the regression fit to microwave data derived by Minnis et al. (1989a). Cloud-top altitudes and surface temperatures for the GOES-West results were estimated from the cloud-top temperature and clear-sky temperatures in the manner described by Minnis et al. (1989b). GOES-East (75°W) 3-hourly, 8-km VIS and IR data were analyzed in the same fashion for July 2-19 except that a 2.5° grid was used. The grid overlays the area between 10°N and 40°N and 110°W and 145°W . Poor spatial and temporal sampling was encountered in the southwestern portion of the grid. High viewing zenith angles reduce the quality of the results in the northwestern corner of the area.

3. Results and Discussion

An overview of the mean cloud amounts is shown in Fig. 1 for (a) GOES East and (b) GOES-West. The average total cloudiness is nearly the same for both satellite views as seen in Fig. 2. Generally, the mean cloud amounts within the IFO area ranged from 60 to 90% with steep gradients near the coast. The diurnal variations of total cloudiness are also very similar for the two views as seen in Fig. 3 for a 2.5° region centered at 31.3°N , 118.7°W . Figure 4 gives the mean diurnal variations of total cloudiness for all 0.5° regions viewed from GOES-West. These "mini-plots" were derived from 3-hourly averages with missing data filled by linear interpolation.

Thus, the curves are smoother and the extrema have been diminished compared to the observed cloud amounts (e.g., Minnis et al., 1989a). The diurnal ranges are greatest along the coastal regions. Cloudiness is relatively constant south of San Nicolas Island (SNI) between the coast and 123°W. Further west, the diurnal range increases again. According to the GOES-East results (Young et al., 1989), this increase in the diurnal range continues to at least 145°W. Clear-sky and cloud-top temperatures are presented in Figs. 5a and 5b, respectively. The gradient in cloud-top temperature is primarily from west to east, while the ocean clear-sky temperature varies from north to south west of 120° and west to east eastward of 120°W. Mean cloud-top altitudes (Fig. 6) range from 450 m northwest of SNI to values greater than 750 m near the southwestern corner of the area. Average cloud-top altitude for the entire area is ~ 600 m. The mean cloud albedos given in Fig. 7 translate directly to LWC in Fig. 8. Maximum values of mean daytime LWC exceed 80 gm^{-2} in the vicinity of SNI. Liquid water contents decrease westward to a minimum of less than 30 gm^{-2} near 35°N.

The results presented here summarize a much more detailed hourly data set. Some of the parameters have been derived from relationships developed from combinations of other FIRE data. Others were verified using various FIRE data sets. Therefore, the derived parameters should be consistent with other IFO data sets. In general, the results are not greatly different than those found during previous years (Minnis et al., 1988). Thus, it appears that the IFO period is relatively typical of California marine stratocumulus during July. East-west gradients in cloud-top height, diurnal cloud variations, and LWC, however, suggest that the IFO region may not be typical of stratocumulus over the open ocean.

REFERENCES

- Minnis, P., E. F. Harrison, and G. G. Gibson, 1987: Cloud cover over the eastern equatorial Pacific derived from July 1983 ISCCP data using a hybrid bispectral threshold method. J. Geophys. Res., **92**, 4051- 4073.
- Minnis, P., E. F. Harrison, and D. F. Young, 1988: Extended time observations of California marine stratocumulus from GOES for July 1983-1987. FIRE Science Team Workshop, Vail, CO, July 11-15, 195-199.
- Minnis, P., C. W. Fairall, and D. F. Young, 1989a: Intercomparisons of GOES-derived cloud parameters and surface observations over San Nicolas Island. Presented at FIRE Annual Meeting/ASTEX Workshop, Monterey, CA, July 10-14.
- Minnis, P., D. F. Young, R. Davies, M. Blaskovic, and B. A. Albrecht, 1989b: Stratocumulus cloud height variations determined from surface and satellite measurements. Presented at FIRE Annual Meeting/ASTEX Workshop, Monterey, CA, July 10-14.
- Young, D. F., P. W. Heck, P. Minnis, and E. F. Harrison, 1989: Marine stratocumulus cloud parameters from GOES during the 1987 FIRE Intensive Field Observation period. Proc. AMS Symp., Role of Clouds in Atmospheric Chemistry and Global Climate, Anaheim, CA, Jan. 30-Feb. 3, 178-180.

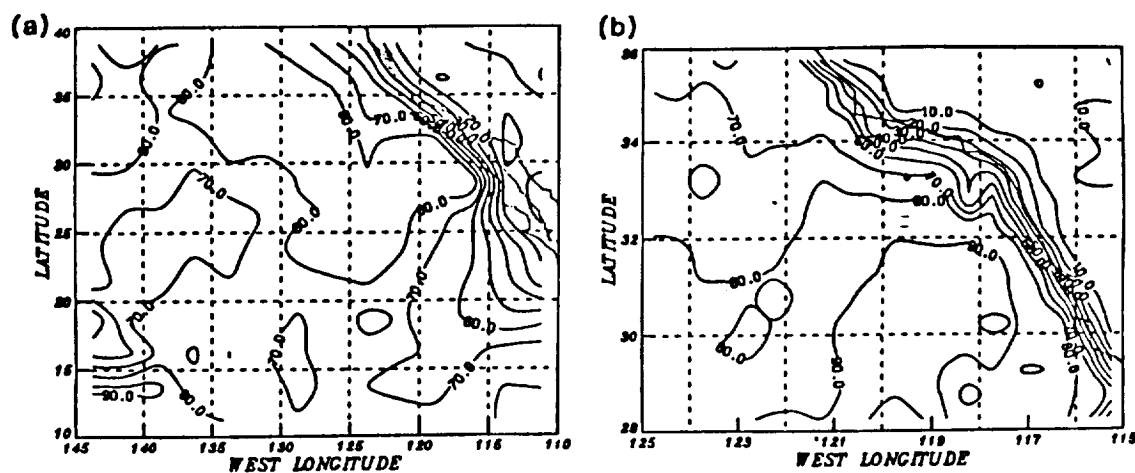


Fig. 1. Mean cloud amount (%) for July 2-19, 1987.

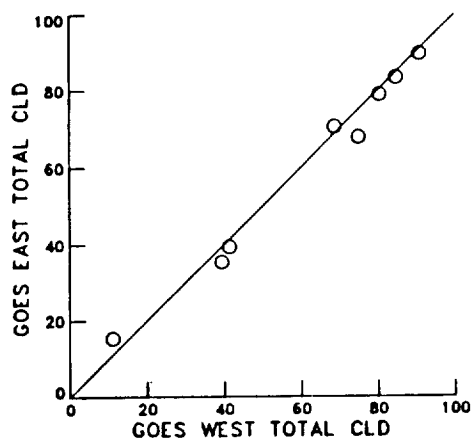


Fig. 2. Correlation of IFO mean cloud amounts for 2.5° regions.

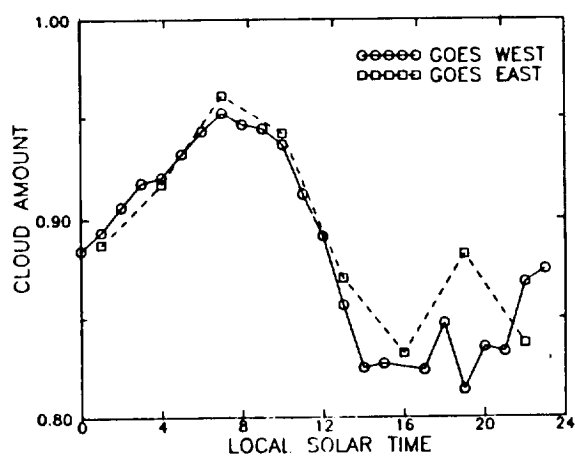


Fig. 3. Mean IFO cloud amounts for 2.5° region centered at 31.3°N , 118.7°W .

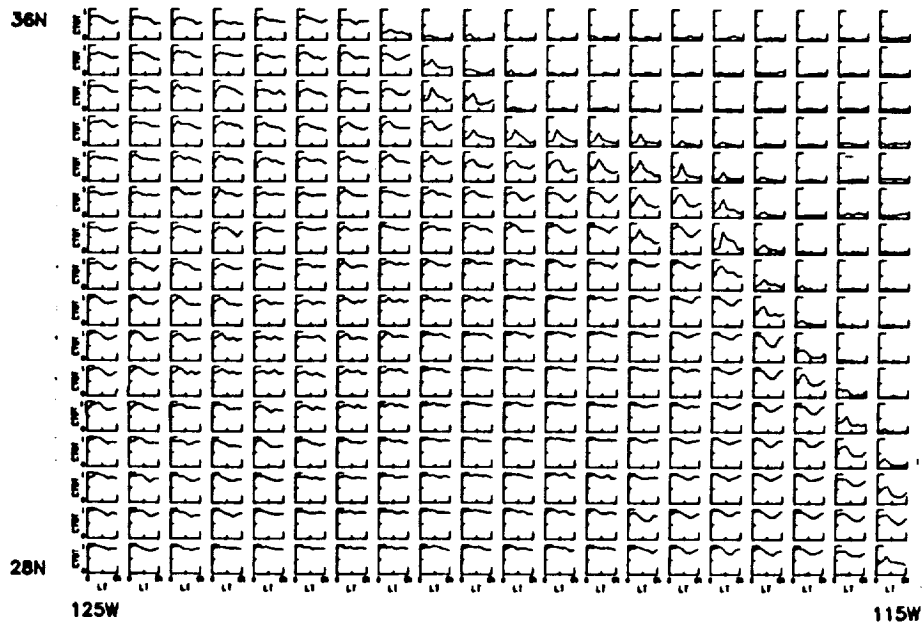


Fig. 4. Mean 3-hourly, GOES-West IFO cloud amounts for all 0.5° regions.

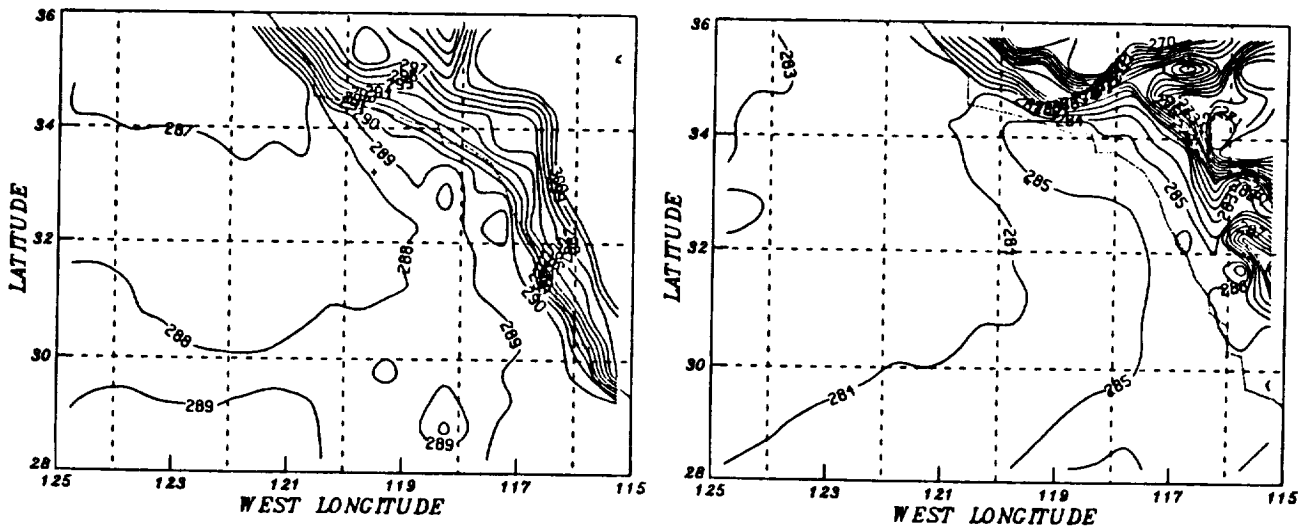


Fig. 5. GOES-West-derived equivalent blackbody temperatures (K) for IFO.

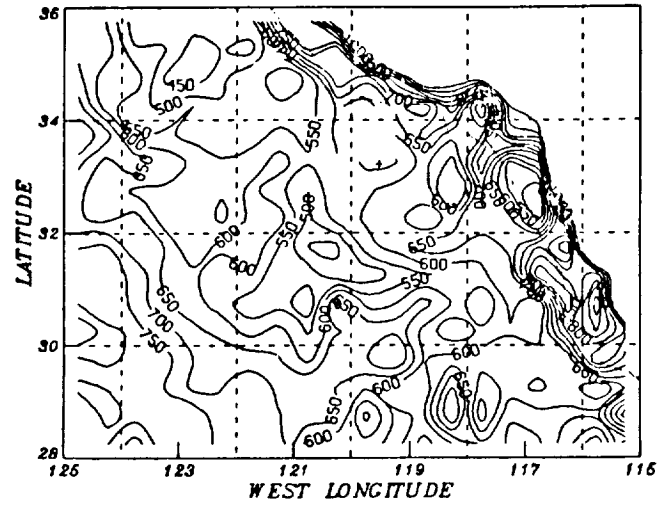


Fig. 6. Mean cloud-top altitudes (m) from GOES-West IFO data.

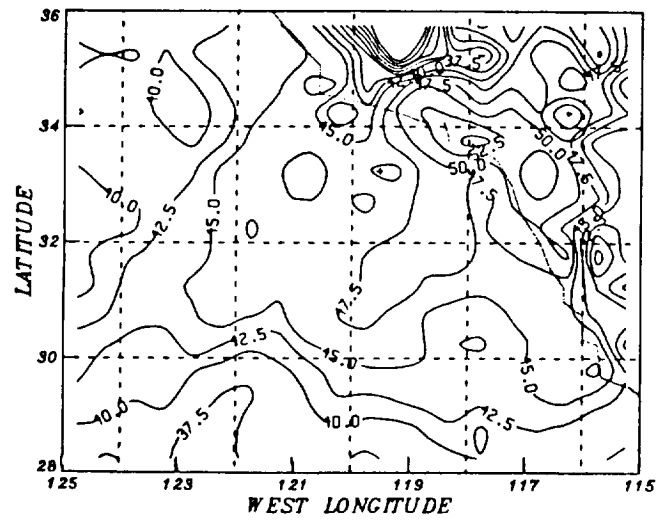


Fig. 7. Mean IFO visible cloud albedos (%).

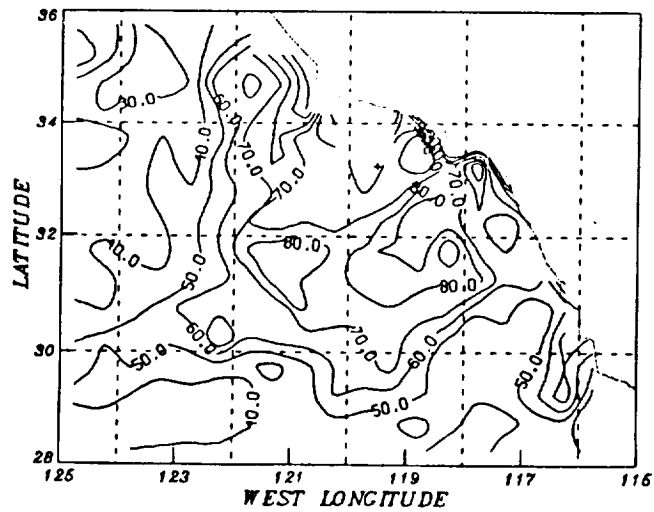


Fig. 8. Mean IFO daytime cloud liquid water content (gm^{-2})

Analysis of ER-2 Radiometer and Lidar Observations from the 1987 Marine Stratus Experiment

J. D. Spinhirne, R. Boers¹, T. Nakajima¹ and W. D. Hart²

Laboratory for Atmospheres
NASA Goddard Space Flight Center
Greenbelt, MD 20770

Extensive remote sensing observations of marine stratus clouds were acquired from the NASA ER-2 aircraft during the 1987 FIRE stratus field experiment. The observations included high spatial resolution imaging radiometry at eighteen wavelengths and active lidar cloud top profiling. Analysis of these data can provide results to both enhance and extend aircraft in situ cloud physics observations. Initial analysis results from the 1987 field experiment are to be reported.

For the spectral imaging radiometry observations of the marine stratus, a unique and potentially useful result was obtained. For near infrared wavelengths, a large number of the bidirectional reflectance observations included persistent and significant single scattering features. With few exceptions, the features were not correspondingly observed at visible wavelengths. Distinct variations of scattering angles for these near infrared glory measurements were observed which are thought to result from changes in the cloud top droplet size distribution. An initial comparison to direct cloud physics measurements gives a good agreement (Spinhirne and Nakajima, 1989). The initial results indicate that observation of the single scattering features of the bidirectional reflectance of water clouds should be a direct and accurate means to

remotely sense microphysical parameters of water clouds.

The analysis of lidar returns from marine stratus cloud tops have been shown to be potentially valuable for study of the microphysical and dynamic characteristics of the clouds (Boers et al., 1988, Spinhirne et al., 1989). Analysis involving cloud top water content and height spectra has been applied to some of the extensive lidar observations of the 1987 field experiment. Derivation of cloud top radiative parameters and comparison to in situ observations are planned. Initial results are to be presented.

References.

Boers, R., J. D. Spinhirne and W. D. Hart, 1988: Lidar observations of the fine-scale variability of marine stratocumulus clouds. *J. Appl. Meteor.*, 27, 797-810.

Spinhirne, J. D., R. Boers and W. D. Hart, 1989: Cloud top liquid water from lidar observations of marine stratocumulus. *J. Appl. Meteor.*, 28, 81-90.

Spinhirne, J. D. and T. Nakajima, 1989: Observation and analysis for the bidirectional reflectance of stratus clouds at near infrared wavelengths. Preprint volume of the Symposium on the Role of Clouds in Atmospheric Chemistry and Global Climate, American Meteorological Society, 296-299.

¹ University Space Research Association

² Science Systems Applications Inc.

The Radiation Budget of Stratocumulus Clouds Measured by Tethered Balloon Instrumentation: Variability of Flux Measurements

David P. Duda, Graeme L. Stephens and Stephen K. Cox
Department of Atmospheric Science
Colorado State University
Fort Collins, CO 80523

Measurements of longwave and shortwave radiation were made using an instrument package on the NASA tethered balloon during the FIRE Marine Stratocumulus experiment. Radiation data from two pairs of pyranometers were used to obtain vertical profiles of the near-infrared (.7 - 2.8 μm) and total solar (.3 - 2.8 μm) fluxes through the boundary layer, while a pair of pyrgeometers supplied measurements of the longwave fluxes in the cloud layer. The radiation observations were analyzed to determine heating rates and to measure the radiative energy budget inside the stratocumulus clouds during several tethered balloon flights. The radiation fields in the cloud layer were also simulated by a two-stream radiative transfer model, which used cloud optical properties derived from microphysical measurements and Mie scattering theory.

The vertical profiles of the observed longwave cooling rates were similar in structure and magnitude not only to previous measurements of marine stratocumulus (Stephens et al., 1978; Slingo et al., 1982), but also to the cooling rates computed by the two-stream radiative transfer model. However, the solar heating rates measured in the clouds were significantly larger than the rates calculated in the model and appeared more important to the radiative energy balance of the cloud than previously expected. An analysis of the variability of the radiative flux data is being made in order to determine the reliability of the heating rate measurements, and how the variability of the data affects the radiative energy balance measurements in the cloud.

Solar albedo measurements showed that the visible spectrum tended to be reflected by the clouds more than the near IR spectrum. This is similar to the results reported by Hignett (1987), although the discrepancies between the observed and calculated near

IR to visible albedo ratios were generally small and could be explained by the uncertainties in the albedo ratio measurements. The ratio of the reflected near IR to reflected visible light remain fairly uniform during each flight except for the case on July 10, 1987, which sampled a nonhomogeneous cloud. For this flight, the visible albedo decreased relative to the near IR albedo. This suggests that the effects of heterogeneities on the radiative transfer through the cloud may be more important in the visible than in the near IR.

The computed solar reflectivities and absorptivities of the clouds tended to be lower than the observed values, while the calculated transmissivities were much higher than those measured by the instrument package. Since these radiative properties are also sensitive to the variability in the flux measurements, further analysis will be done to examine the variability of these properties.

ACKNOWLEDGEMENTS: This research was supported by the Atmospheric Sciences Section of the National Science Foundation under Contract ATM-8415127 and Office of Naval Research under Contract N00014-87-K-0228.

	PAGE
M04.01 Structural Analysis of Stratocumulus Convection <u>Siems, S. T.</u> , M. B. Baker, and C. S. Bretherton	107
M04.02 On the Dynamic and Thermodynamic Structures of Marine Stratocumulus Lauferweiler, Mark J., and <u>Hampton N. Shirer</u>	113
M04.03 A Stratocumulus Thermodynamic Analysis: July 5 Case Study <u>Austin, Philip</u>	119
M04.04 Turbulence Spectra of the FIRE Stratocumulus-Topped Boundary Layers Young, G. S., J. J. Nucciarone, and B. A. Albrecht	125
M04.05 Turbulence Structure in Clear and Cloudy Regions of the 7 July 1987 Electra Mission Khalsa, Siri Jodha Singh	131
M04.06 Diurnal Variation in the Turbulent Structure of the Cloudy Marine Boundary Layer During FIRE 1987 <u>Hignett, Phillip</u>	137

Structural Analysis of Stratocumulus Convection

S.T. Siems*, M.B. Baker† and C.S. Bretherton*

*Applied Mathematics Department, †Geophysics Program
University of Washington, Seattle, WA 98195**I. Introduction**

In an earlier study (Siems et al, 1989) we found that *explosive* cloudtop entrainment instability (CTEI) is possible only when a parameter defined as D is of order unity, where

$$D = -\Delta\theta_v(\chi^*)/\Delta\theta_v. \quad (1)$$

Here χ^* is the fraction of environmental air in the exactly saturated mixture of cloudy and environmental air. $\Delta\theta_v(\chi^*)$ is the virtual potential temperature difference of this mixture relative to the unmixed cloud, while $\Delta\theta_v$ is the difference between the unmixed fluids.

Our examination of data from the FIRE project and other data sets leads us to conclude that the enhancement of D is unlikely to ever be sufficient to bring about explosive CTEI under stratocumulus conditions. It therefore appears that cloud breakup occurs via other processes, possibly related to decoupling of the cloud and subcloud layers. To better understand this latter possibility, we have investigated the nature of the turbulent elements and convective motions involved in transport of heat and moisture in cloudtopped boundary layers. We have sought in particular to test the simple conceptual picture of the turbulence which has emerged indirectly or by assumption in previous studies of radiatively driven Sc in which surface fluxes are weak. According to this picture, negatively buoyant thermal or plume like structures descend from the bottom of the radiatively cooled layer near cloudtop, merging to form downdrafts, presumably convective cell edges, within which heat and moisture are transported down. The return flow is broader and pushes up the cloud-clear inversion into hummocks, creating baroclinic torques and rebound momentum at the stratified interface. In the absence of overall shear, these processes should be responsible for entrainment, which is maximum in the intermittent valleys between hummocks. The descending streams are aided in their downward propagation until cloudbase by evaporative cooling, to the extent they remain saturated. Purely evaporatively cooled parcels, however, can proceed downward once they become unsaturated only at the expense of TKE within the layer. This conceptual model has been explored by Nicholls (1989). The situation in the case that shear and/or surface fluxes are important has been documented (Brost et al, 1982) but a similar conceptual picture is not available. Since both were important sources of TKE during the FIRE project, we have investigated the structure of the small scale variability in dynamic and thermodynamic properties in order to construct such a picture. At the time of writing this abstract we have not had time to compare our results to those of Nicholls (1989), but those comparisons will be presented at the FIRE workshop. The emphasis of the work at present has predominantly been on small scale features; however, larger scales are noted throughout.

In this abstract we focus on the following questions:

- 1) What processes are important in entrainment, where is it maximum and what scales are important? What is the nature of this mixing across the inversion?
- 2) To what extent are the local dynamics organised by large scale fluctuations in cloud properties? (where here large means greater than ten kilometers or so)
- 3) Which parcels form the roots of the upward moving plumes/thermals at the top of the lower surface layer, and which form the initial downdrafts at the base of the radiatively cooled layer at cloudtop? What are the roles of radiative cooling, evaporative cooling and surface fluxes relative to mechanical forcing in driving these parcels?
- 4) Is decoupling evident and to what extent does this affect the circulation?

II. Research Methods

We have examined 1 and 20 Hz data from the Electra flights made on July 5, 1987. The flight legs consisted of seven horizontal turbulent legs at the inversion, midcloud and below cloud, plus 4 soundings made within the same time period. The cloud deck was thin but solid, for the most part, with

three dimensional structure intermittently noted by the flight scientist. Cloudtop was flat, sloping upward to the south west. Cloudbase was quite ragged, with intermittent small cumulus clouds below.

We used the Rosemount temperature sensor and the average of the top and bottom dewpoint sensors, lagged by two seconds, for preliminary temperature and humidity measurements at 1 Hz. The FSSP was working poorly on this day. We therefore used the Johnson-Williams sensor for the 1 Hz liquid water readings. This data was interpolated to 20 Hz data creating a source of error in the liquid water content; however, this error this induces in the total water content and θ_v is quite small. The noted drift of the JW sensor is also on this order of magnitude. The Lyman-alpha hygrometer was calibrated following the method of Paluch (personal communication 1989) for 20 Hz and corresponding 1 Hz measurements. This gave satisfactory agreement with the dewpoint sensors in cloud, but the calibration is dependent on the relative humidity; extremely dry environmental parcels require special adjustment. Ozone measurements are useful when crossing the inversion but lose importance in the cloud layer as the noise exceeds possible shifts.

III. Results

a) Inversion Structure and Entrainment

A typical 20 Hz sounding near the inversion is shown in Figure 1. There is clear evidence of several individually well-mixed regions, of vertical extent $h = 50$ meters or less, through which Q_T and O_3 are quite constant and between which there are very sharp gradients over less than 1 mb. A study of the conserved variables shows that these layers (hereafter referred to as intermediate inversion layers or IILs) are not the product of direct mixing between the cloud and environment at this instant. Interestingly, the rather homogeneous nature of an individual IIL suggests that it did not arise from a uniform or gradient mixing process, but rather from a discrete process similar to that of Broadwell & Breidenthal (1982). Indeed even the transition between IILs is nonuniform. The IILs persist for hours during which they radiatively cool to equilibrium and are sorted by buoyancy. The layers are distinctly subsaturated, which could not arise from the removal of drops alone.

In examining the overall nature of this inversion region, we find that the velocity jump is approximately 8 m/s, $\Delta\theta_v$ about 8 K, and thus the Richardson's number, $Ri = g'h/\Delta U^2$, where $g' = g\Delta\theta_v/\theta_v$, is less than $1/4$ for h less than 60 m. These regions are thus probably Kelvin Helmholtz vortices forming near the tops of the cloudy hummocks. Note that from vertical soundings it is impossible to distinguish localised Kelvin Helmholtz vortices from horizontally extended layers.

We can roughly estimate the entrainment rate into this shear layer due to these vortices from laboratory and theoretical studies of turbulent mixing in free shear layers (Dimotakis, 1989). These results show that the entrainment into a shear layer of horizontal velocity difference ΔU is determined by two parameters, namely, $s = \rho_2/\rho_1$ and $r = U_2/U_1$, where the label 2 is associated with the more slowly moving fluid. (i.e., the upper air, in the July 5 case study). In the presence of density stratification one would expect the shear layer thickness to be fully developed near $h_{\max} = (\Delta U)^2/g'$. The fraction of fast moving air flowing into the shear layer, according to these studies, is

$$C = s^{1/2}(1 + .68(1-r)/(1+r)) \quad (2)$$

Thus for the free shear layer we can estimate an entrainment velocity

$$w_e \approx U_{ave} h_{\max} L^{-1}/(1+C) \quad (3)$$

where L is the distance it takes for the shear layer thickness to grow to saturation. This entrainment rate would be characteristic of those portions of newly created surface over which $h/h_{\max} < 1$; as the surface ages the shear layer thickness approaches h_{\max} and entrainment stops, creating intermittency in the entrainment. Using parameters characteristic of the inversion on July 5 we have $\Delta U = 8 \text{ m/s}$, $U_{ave} = 8 \text{ m/s}$, $g' = .2$, $s = .98$, $r = 0.33$, $C = 1.3$ (i.e., there is 30% more cloudy than noncloudy air in the shear layer). For the laboratory free shear layer the thickness of the molecularly mixed shear layer grows at a rate $h_{\max}/L = .075$ at $s = 1$. Thus we estimate an entrainment velocity of .3 m/s in regions of scale $L = 60/.075 = 800 \text{ m}$. This entrainment velocity would destroy the cloud rapidly, if prolonged; thus the problem is to determine what fraction of the surface is active at any given time and the rate of removal of the lowest IIL. This could occur through the lowest IIL cooling until this layer

alone becomes unstable to Kelvin-Helmholtz instability. Entrainment via shear is clearly much more efficient locally than the baroclinic torque mechanism (Breidenthal and Baker, 1985) or the rebound mechanism (Linden, 1973), both of which are proportional to the inverse Richardson's number for the layer, yielding entrainment velocities of several tenths of a centimeter per second.

b) Local Dynamics and Large Scale Forcing

Two flight legs were examined at the inversion, passing in and out of cloud turrets. A two-stream radiative transfer model estimates the cloud turrets on these legs are approximately 40 m deep if we assume uniform liquid water mixing ratio $.3 \text{ g/m}^3$. This depth is consistent with the lidar measurements. These variations are far greater than can be explained on the basis of turbulent velocities carrying cloudy air into the stratified interface, and must result from a larger scale forcing.

Another symptom of the local effects of larger scale forcing appears to be the presence of upper level fluid below cloudtop in mixed parcels of scales 100 m and more. According to the work of Dimotakis & Brown (1976), and Broadwell & Breidenthal (1982), molecular scale mixing of two fluids in a turbulent eddy occurs only after the two fluids have been in contact over a time comparable to an eddy revolution time. That is, the vortex Richardson's number for eddies responsible for molecular scale mixing must be of order unity. From the observed velocity spectrum it can be shown that for a parcel 100 m in scale to meet this criterion the maximum fraction of upper layer fluid it can contain is on the order of 8%. We have shown earlier that evaporative cooling does not substantially modify this picture. One possible mechanism by which the unbalanced mixing ratios might be created is that small bits of upper level air are drawn down by radiatively cooled cloud parcels, or by the cloud circulations on larger scales, around the edges of the cloud top undulations.

Cloudtop radiative cooling modifies the properties of the upper 50 meters or so of the cloud. If this dominates in driving local dynamics, we expect to see descending, negatively buoyant, liquid water rich parcels whose scales are determined by the requirement that they remain coherent long enough to be substantially cooled. However, the descending parcels are usually relatively dry and tend to be grouped in thinner liquid water regions, indicating significant entrainment is involved in the downdrafts. To understand this better, we note that for a longwave cooling rate,

$$d\theta/dt \approx (F/\rho c_p) \cdot l^{-1} \quad (4)$$

in a parcel of scale l , with F the net LW flux from the parcel. Assuming a persistence time $\tau \approx (l^2/\epsilon)^{1/3}$ (assuming an inertial subrange characterised by TKE dissipation rate ϵ), we find the cooling possible in a parcel of scale l is

$$\delta\theta/\theta = w_r/w(l) \quad (5)$$

where $w_r \approx F/\rho c_p \theta$ is a measure of the cooling rate and $w(l) = (l\epsilon)^{1/3}$. For typical values of the cloudtop parameters $F = 80 \text{ W/m}^2$, $\epsilon = 10^{-3} \text{ m}^2/\text{s}^3$ as estimated from the vertical velocity spectrum midcloud, we find that $w_r = 10^{-4} \text{ m/s}$, so only very small parcels can cool several tenths of a degree at cloudtop before losing their coherence. Thus the descending parcels which are several hundred meters or more in horizontal scale are not driven directly by their own radiative cooling, but are rather responding to larger scale forcing. This conclusion is supported by the fact that they are not always the coolest parcels, as will be shown below.

c) Convective Elements

There were two flights at midcloud levels; one flying upwind and the other flying cross wind. The downward solar flux ranged from 860 W/m^2 to 650 W/m^2 during this leg, which, by our simple radiation model, would imply that the plane was between about 100 and 200 m below cloudtop. This is roughly consistent with upward flux observations based on the soundings. The trend is consistent with the observation that cloudtop sloped upward moving out to sea.

We have conditionally sampled the data in the horizontal flight legs at the inversion, midcloud and below cloud, to determine the characteristics of the up- and downdrafts. Figures 2 and 3 show the 20 Hz histograms of θ_e and Q_T (a) for a 45 second subcloud section; (b) for the parcels for which w is in the upper 10% of the values measured, and c) for those parcels for which w was in the lowest 10% of the values measured. While this is not a sophisticated method to isolate up- and downdrafts, it is a

conservative first cut. We see that average values of θ_e and Q_T are found in all parcels, independent of w , whereas the uppermost values of Q_T and θ_e are found only in updrafts and lowest values of Q_T and θ_e are found only in the downdrafts. The distribution of values of these parameters is tighter in the updrafts than in the downdraft data in the midcloud segments. We have looked at similar information for all the flight legs, and find broadly similar patterns within and below cloud. We do not see organisation either in the spacing or location of the up- and downdrafts activity in the subcloud legs, whereas there is a suggestion of roughly 5 km spacing in the downdrafts in the midcloud legs, consistent with convective cell geometry. Moreover, the correlations of thermodynamic properties with extremes in vertical velocity are fairly weak suggesting that buoyancy is not dominating the structure. We find the cutoffs defining the up- and downdrafts change markedly on entering cloudbase; that is, the upper ten per cent of the positive velocity excursions are much higher below cloud than in cloud, while the lowest ten per cent of the velocities have small w below cloud and much larger in cloud. Thus buoyancy differences are probably not driving these parcels continuously up to the inversion. An interesting note is that the average velocity is positive in the subcloud layer, contrary to the classical picture of subsidence. Simple parcel calculations show the buoyancy differences existing in this situation are so small that minor excursions in initial vertical velocity (at top or bottom), due to initial forcing, can have substantial impact on velocities of parcels in the middle of the layer.

Horizontal wind variations are correlated with updrafts at low levels, in the sense that the air coming from below has less horizontal momentum than that from above. These correlations are lost above cloudbase suggesting that it should not be used as a horizontal tracer.

d) Decoupling of Cloud and Subcloud

As seen from above, it is not necessarily the warmest or the most buoyant parcels which rise the fastest from low levels to mix with the air above. In fact, the strong updraft regions do not even penetrate the cloud layer. This is seen in the Paluch diagrams (see Figure 4) which show two regions for a given sounding. The first is the from near ocean surface to approximately cloud base. We see a rather uniform mixing line. Note that moist, warm parcels correspond with the updrafts of the previous section. This mixing line can support the notion of mixing with the SST (Boers & Betts, 1988). We next examine the cloud region only. We see that the warm, moist parcels of this section do indeed mix with the air above the inversion but these updrafts do not correspond to the updrafts of the subcloud region. Thus we find that the sounding is decoupled. This height-dependent variation is far greater than has been observed in the course of longer level flights of the plane indicating that horizontal motion is not believed to be accountable for the evident decoupling.

IV. Discussion

Our data suggest that larger scale forcing, both by shear at cloudtop and by surface fluxes, determine the small scale motions within clouds on July 5. Direct correlation of buoyancy fluctuations and vertical motions on small (100 m to several kilometer) scales is weak. Analysis suggest that shear layer mixing across the inversion dominates the entrainment.

Acknowledgments

We are grateful to R. Breidenthal for very useful conversations. P. Austin has been a tremendous help throughout all the data difficulties. We also thank R. Pincus for his time and effort. This research was supported by NSF grant ATM-862-0165.

References

- Boers, R. and A.K. Betts (1988). *J.Atmos.Sci.* 45, 1156-1175.
- Breidenthal, R. and M. Baker (1985). *J.Geophys.Res.* 90, 13055-13062.
- Broadwell, J. and R. Breidenthal (1982) *J.Fluid Mech.* 125, 397-410.
- Brost,R., D.Lenschow and J. Wyngaard (1982). *J.Atmos.Sci.* 39, 800-817.
- Dimotakis, P. and G. Brown (1976). *J.Fluid Mech.* 93, 535-560.
- Dimotakis, P. (1989). *27th Aerospace Sciences Meeting*, Reno
- Nicholls, S. (1989). *Q.J.Roy.Met. Soc.* 115, 487-513.
- Siems, S., C. Bretherton, M. Baker, S. Shy and R. Breidenthal (1989). submitted to *Q.J.Roy.met.Soc.*

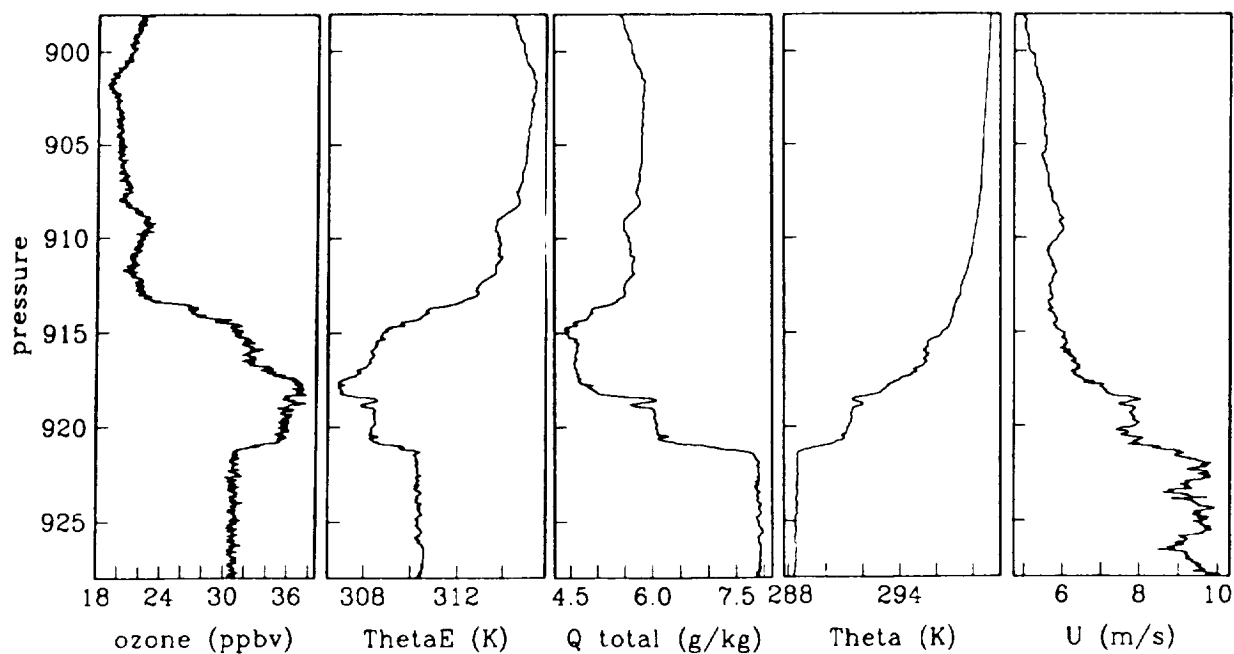


Figure 1. Sounding through cloudtop: 20:16:00-20:17:00.

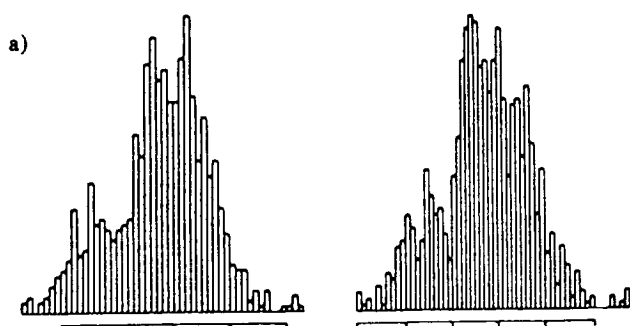
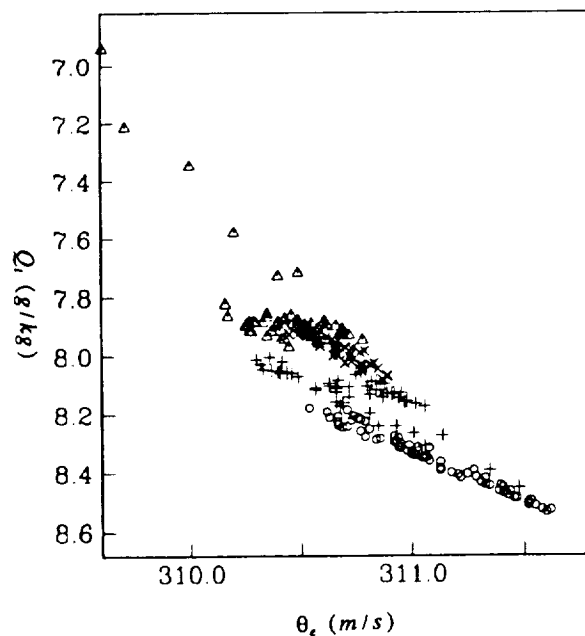
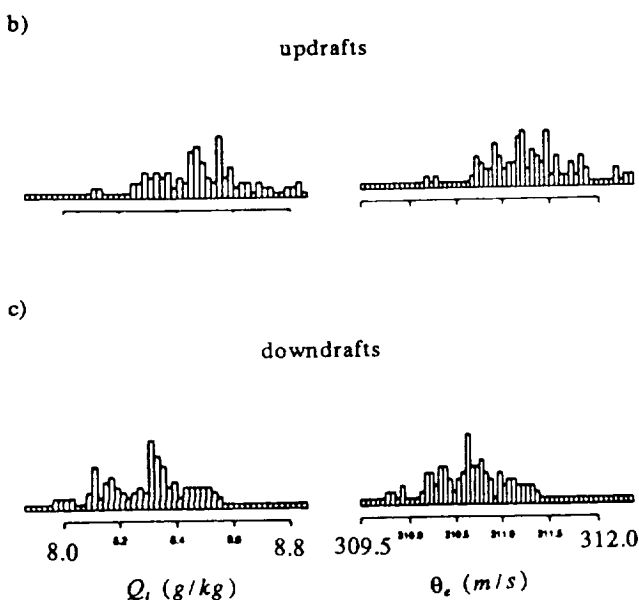


Figure 2. Histogram for θ_e and Q_t for (a) all parcels of a 45 second segment at 20 Hz, (b) in updraft parcels (c) and in downdraft parcels.

Figure 3. 20:14:30-20:18:30 sounding denoted by pressure to highlight decoupling. \circ - 1000-980 mb; $+$ - 980-960 mb; \times - 960-940 mb; ∇ 940-920 mb.



On the Dynamic and Thermodynamic Structures of Marine Stratocumulus

Mark J. Laufersweiler and Hampton N. ShirerDepartment of Meteorology
The Pennsylvania State University
University Park, PA 16802

Latent heating effects on stratocumulus circulations have been studied successfully with a nine-coefficient spectral model of two-dimensional shallow Boussinesq convection (Laufersweiler and Shirer, 1989: JAS, 1133-1153). Further, more realistic investigations are being performed currently with a larger, 18-coefficient spectral model, in which the effects of cloud top radiational cooling and in-cloud radiational heating are also being represented. Because assuming a rigid lid at the inversion base may have affected previous results significantly, we have raised the domain top to include the lower portion of the capping inversion. As in the previous model, a uniform cloud base is assumed and latent heating effects are included implicitly such that the motions in the sub- and above-cloud regions are dry adiabatic and the motions in the cloud region are moist adiabatic. The effects of forcing by radiational heating profiles that are tied to the cloud layer, such as the one used by Nicholls (1984: QJRMS, 783-820), will be investigated, as will profiles measured during the FIRE experiment.

One concern of using truncated spectral models is that the phenomena are so poorly represented that they can change dramatically as the number of spectral coefficients is increased. The efficacy of the nine-coefficient model results is checked by examining the steady state solutions of the 18-coefficient model for parameter values used by Laufersweiler and Shirer (1989), which corresponds to the case of a moderately deep cloud and no capping inversion (Fig. 1). Here, the horizontally asymmetric circulation patterns that have narrow downdraft areas and broad updraft areas are virtually the same as those found in the smaller spectral model (Fig. 1b). Also captured in the case of weaker heating is an elevated circulation centered at cloud base (Fig. 1a). Thus, the results of the smaller model are substantiated.

Since one of the goals of studying the new model is to represent a more realistic domain, the second test of the model is to investigate whether the steady solutions are suppressed in the case of an inversion with no cloud. The capping inversion should limit the convective circulations, but we do not force this to happen with the imposition of a rigid lid at the inversion base. Figure 2 shows the steady solutions for the case of a relatively strong inversion of $10^{\circ}\text{C}/\text{km}$ that begins at a height of $0.8z_t$, as indicated by the tic. For the case when the value of the Rayleigh number is near its critical value (Fig. 2a), the circulations are weak and located in the sub-inversion region of the domain. For a higher value of the Rayleigh number (Fig. 2b), the circulation has intensified but is still restricted to the sub-inversion region; importantly, the updrafts only penetrate into the inversion by a small amount. Thus, the model is correctly representing the effects of an inversion by properly suppressing the convection.

Figures 3 and 4 are the first investigations into the performance of the model when both the cloud and an inversion are represented. Figure 3 shows the steady solutions for a weak inversion having a value of $2^{\circ}\text{C}/\text{km}$ and Fig. 4 shows the steady solutions for a fairly strong inversion having a value of $10^{\circ}\text{C}/\text{km}$. The higher value of the inversion strength, although large, is still on the order of $1/2$ of the values of the inversion strength that were measured during FIRE, typically around 18 to $20^{\circ}\text{C}/\text{km}$. By comparing the figures, we observe that the intensity of the circulation patterns for the weaker inversion is stronger than that for the stronger inversion; however, we are concerned that for higher values of the Rayleigh number, the circulations penetrate too deeply into the inversion. This result may be due to the fact that the latent heating, as represented in this model, is warming the flow far more than that found in the actual boundary layer. Possibly, inclusion of radiative forcing will compensate for this effect.

The research for this work was supported in part by the National Science Foundation through Grant ATM-8619854 and by the Office of Naval Research through Contract N000014-86-K-06880.

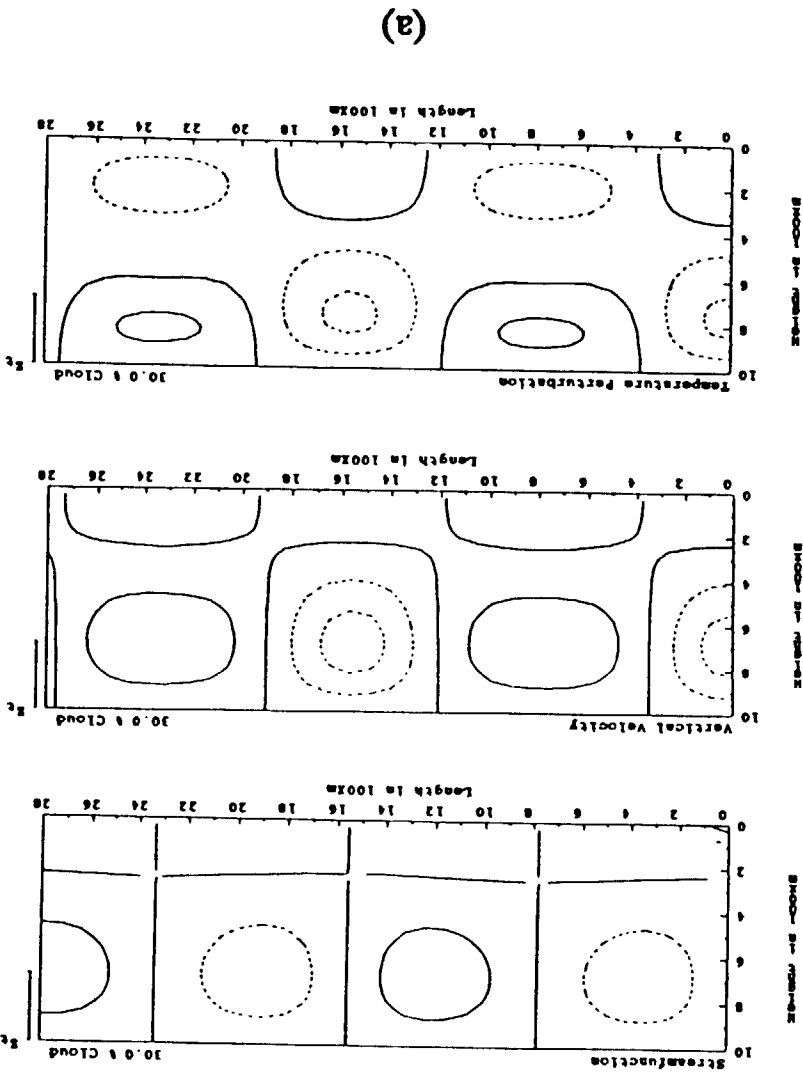
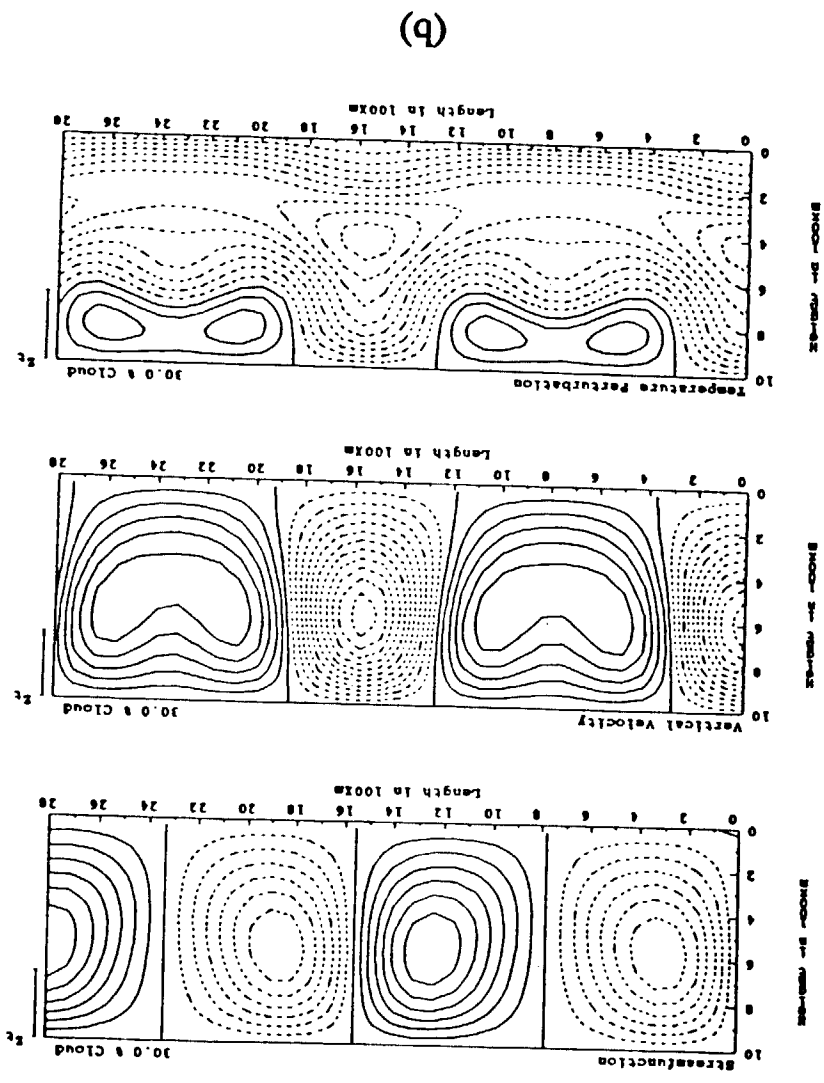
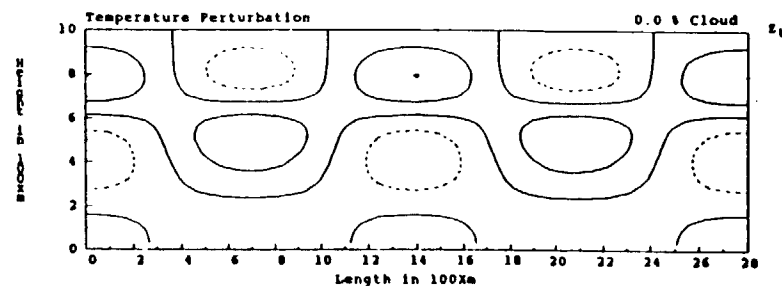
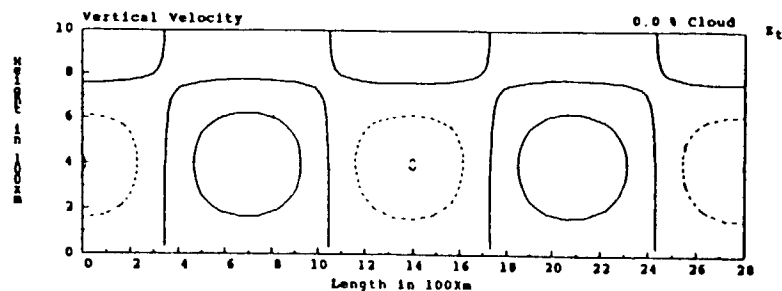
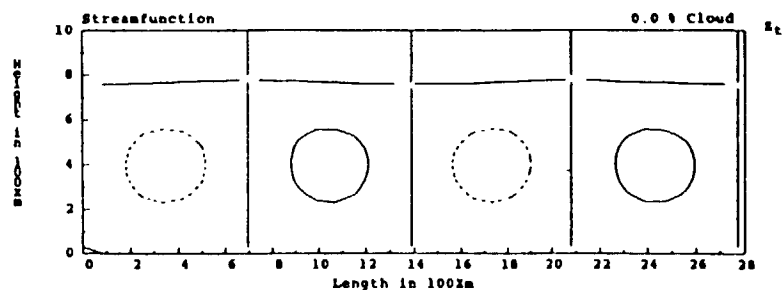


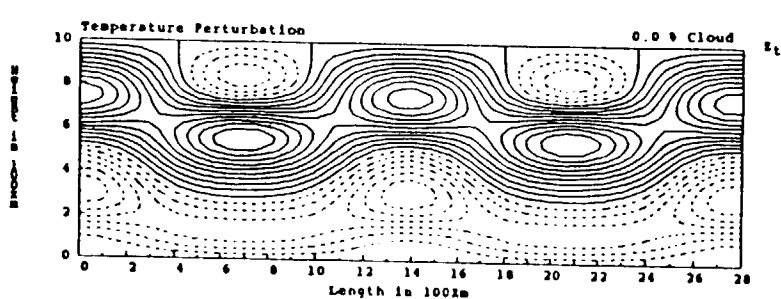
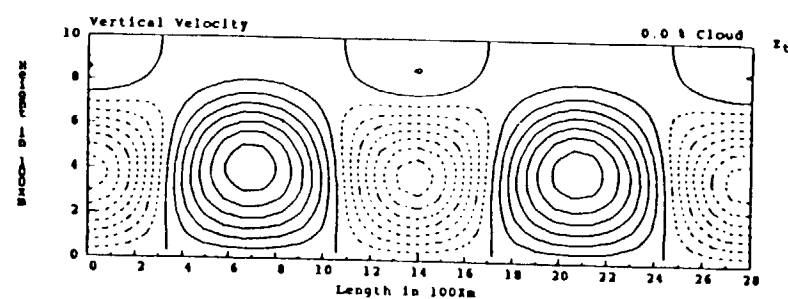
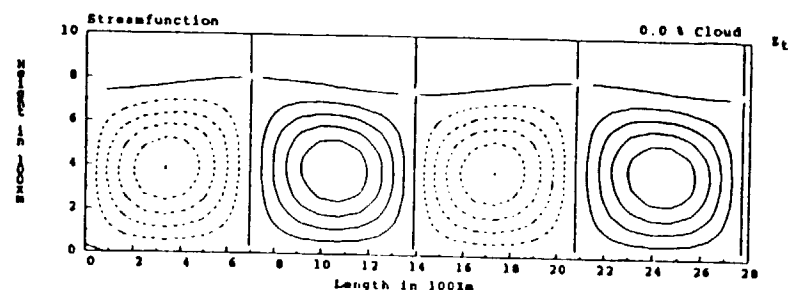
Figure 1. The steady state dimensionless streamfunction w^* , vertical velocity w and temperature perturbation T^* for a cloud covering 30% of the domain for $Ra - Ra_c = 4.9$ (a) and 84.9 (b) for a non-inversion case corresponding to the nine-coefficient model. Here the cloud region is indicated by the vertical line



to the right of each figure. The dashed lines represent negative values of the fields. The contour intervals are 1 for the streamfunction, 1 for the vertical velocity and 15 for the temperature perturbation.



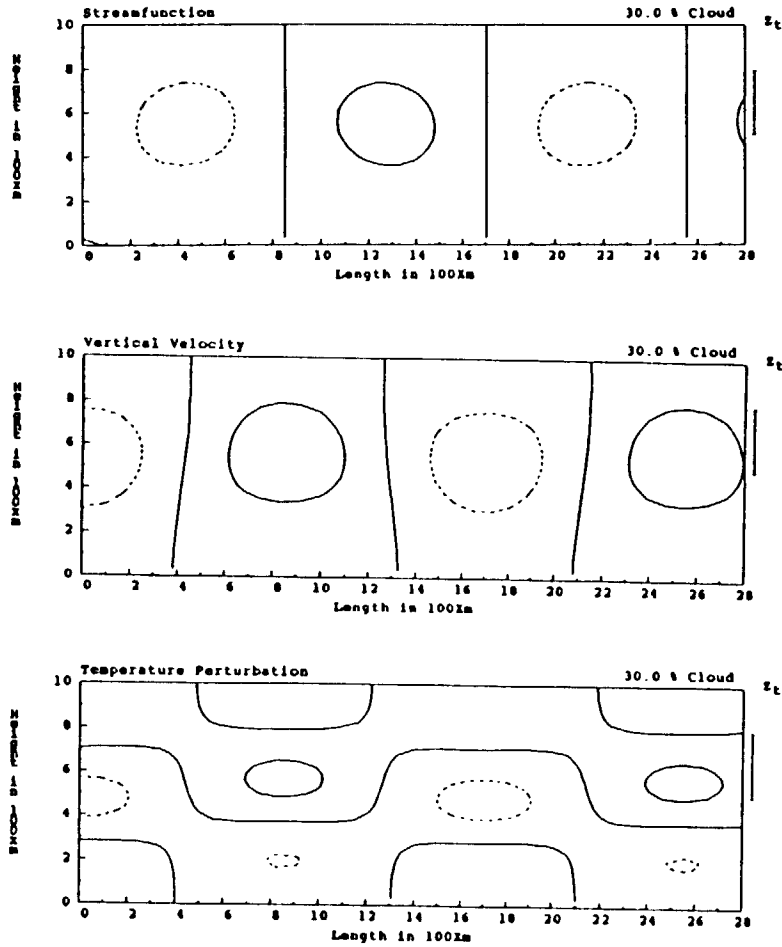
(a)



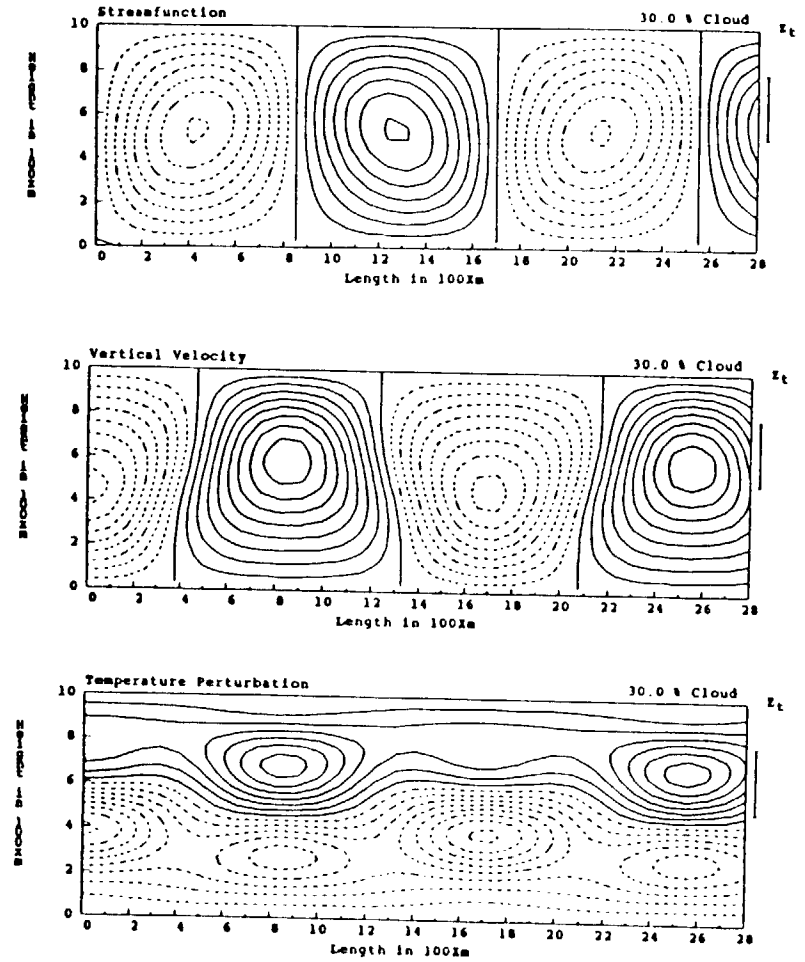
(b)

Figure 2. The steady state dimensionless streamfunction ψ^* , vertical velocity w^* and temperature perturbation T^* for a cloud-free case with an inversion based at $z = 0.7z_i$ and having the value 10°C/km for $Ra - Ra_c = 7.8$ (a) and

97.8 (b). On the right of each figure, the base of the inversion is shown by the tic. The dashed lines represent negative values of the fields. The contour intervals are the same as in Fig. 1.



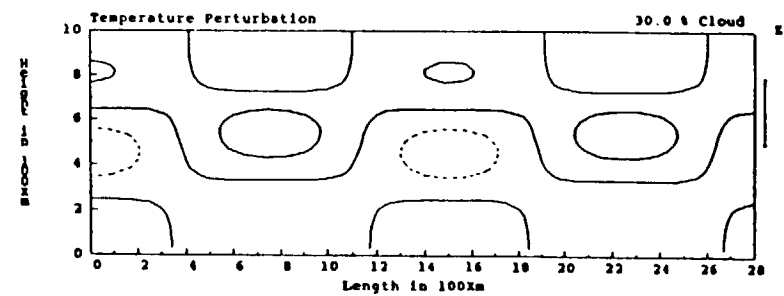
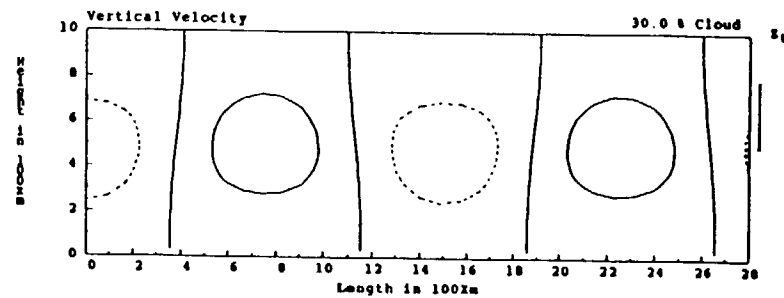
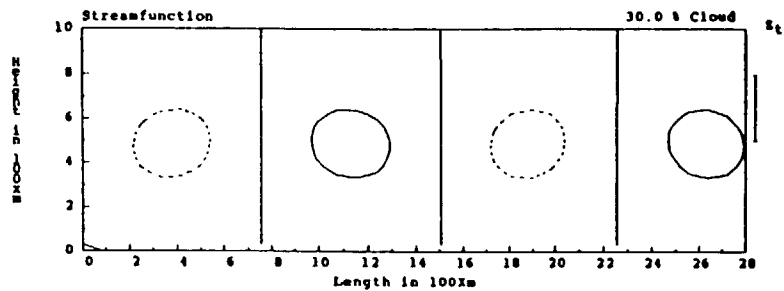
(a)



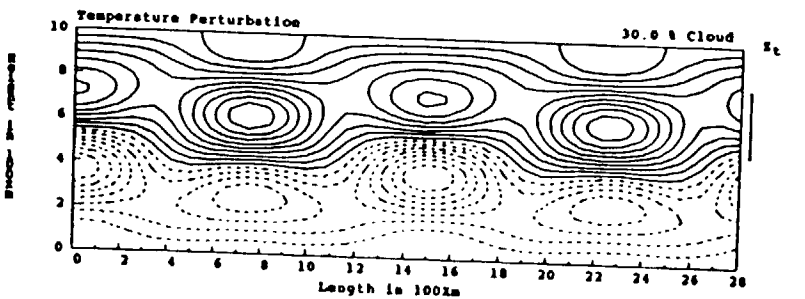
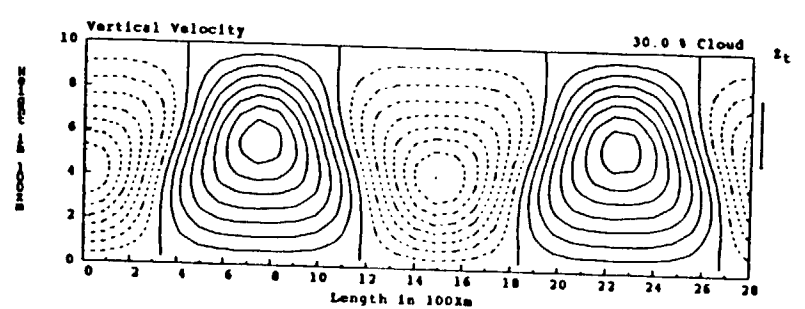
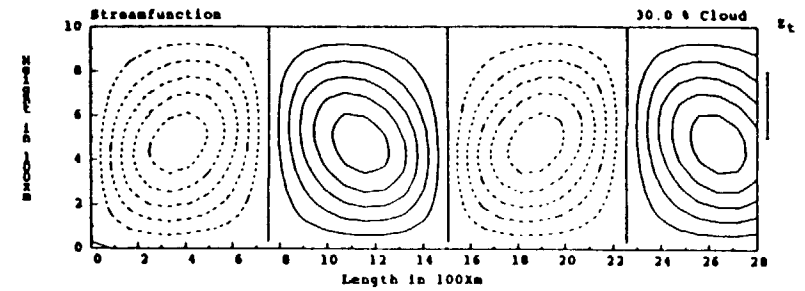
(b)

Figure 3. The steady state dimensionless streamfunction ψ^* , vertical velocity w^* and temperature perturbation T^* for a cloud covering 30% of the domain with an inversion based at $z = 0.8z_1$ having the value 2°C/km for

$Ra - Ra_c = 4.9$ (a) and 74.9 (b). On the right of each figure, the cloud region is indicated by the vertical line, with the inversion base at cloud top. The dashed lines represent negative values of the fields. The contour intervals are the same as in Fig. 1.



(a)



(b)

Figure 4. The steady state dimensionless streamfunction ψ^* , vertical velocity w^* and temperature perturbation T^* for a cloud covering 30% of the domain with an inversion based at $z = 0.8z_1$ having the value $10^\circ\text{C}/\text{km}$ for

$Ra - Ra_c = 13.7$ (a) and 56.3 (b). On the right of each figure, the cloud region is indicated by the vertical line, with the inversion base at cloud top. The dashed lines represent negative values of the fields. The contour intervals are the same as in Fig. 1.

A Stratocumulus Thermodynamic Analysis: July 5 Case Study

Philip Austin

*Programme in Atmospheric Science, #217 Geography, 1984 West Mall,
University of British Columbia, Vancouver, British Columbia V6J 1W5 Canada*

1. Introduction

On July 5 (NCAR Electra flight 4, Mission 186-G) the Electra flew a single aircraft mission which consisted of cross and along-wind legs at 6 different altitudes between 10:43 — 16:00 PDT (17:43 — 23:00 GMT). The leg length was kept short (8–10 minutes) to permit maximum vertical resolution, and there were 8 soundings. Observer notes report a thin, solid stratocumulus cloud deck which gradually became more broken in the afternoon. Winds were from the north at $10 - 13 \text{ ms}^{-1}$ throughout the flight.

This abstract presents sea surface temperature measurements and conservative variable analyses for several of the July 5 legs. These results are preliminary to a study of the thermodynamic budget on July 5; they indicate that:

1. The sea surface temperature dropped more than 1 K (from 17.3°C to 15.9°C) over the course of the flight (18:01 and at 21:51 GMT).
2. Mixing lines for each of the horizontal sub-cloud legs show the effect of a strong north-south gradient in SST. The source points for the observed mixtures have SSTs colder than those observed in the flight area.
3. There is a clear demarcation over a transition of 5–10 km between air to the south and cooler, ($\Delta T = -0.3^{\circ}\text{C}$) moister ($\Delta r_v = 1 \text{ g/kg}$) air to the north. The FSSP measurements indicate there are small clouds/scud 250 m below cloud base on the cold northern side of this transition. The transition is seen in the saturation point diagrams at 984 mb, 959 mb, and 946 mb. There is no corresponding change in the horizontal wind across the transition regions.

2. Observations

Figure 1 shows the height/latitude cross sections of the flight tracks. Also shown is the time at the mid-point of the track, the pressure level (in mb), and the aircraft direction of travel. The stars indicate the location of the transition between air masses mentioned above in item (3).

Two minute averages of sea surface temperature measurements from two of the surface legs are shown in Figure 2a (18:01 — 18:21) and 2b (21:56 — 22:08 GMT). The technique of Liu and Katsaros (1980) has been used to correct for emission from overlying clouds. The SST measurements show a strong north-south SST gradient late in the flight, and a 1 K cooling (or 1 K radiometer drift) over the 4 hours of the flight.

An independent check of the SST measurement is provided by the mixing diagrams in Figures 3a and 3b. We have used the saturation point notation of Betts (1982), with (θ_*, Q_*) denoting the potential temperature and total water mixing ratio of air taken to its lifting condensation level. These variables mix linearly and are conserved under adiabatic transformations, i.e. air that is a mixture from two sources will have values of (θ_*, Q_*) that fall on a line between the two source points. The saturation points of 3 representative SSTs are also shown; it appears from these mixing diagrams that the surface air was originally cooler than the (θ_*, Q_*) of the coldest 15.9°C observed sea surface temperature.

Also striking in both 3a and 3b is the separation of the saturation points into two distinct groups. The separation is observed in each of three sub-cloud legs. Figure 4 shows the temperature, mixing ratio, and droplet concentration measurements for the 984 mb penetration. The lower θ_* branch in Figure 3a is composed of points sampled over the last 2.5 minutes of the time series shown in Figure 4. The radiometric temperature measurement from the PRT6 is included. It indicates that the observed cooling is real, and not an artifact of thermometer wetting by the cloud droplets observed in the sub-cloud region.

References

- Betts, A.K., 1983: Thermodynamics of mixed stratocumulus layers: saturation point budgets. *J. Atmos. Sci.*, **40**, 2655–2670.
- Liu, W.T., and K.B. Katsaros, 1980. Preliminary analysis of the sea surface temperature variations during JASIN '78, *JASIN News*, 18, 3–4.

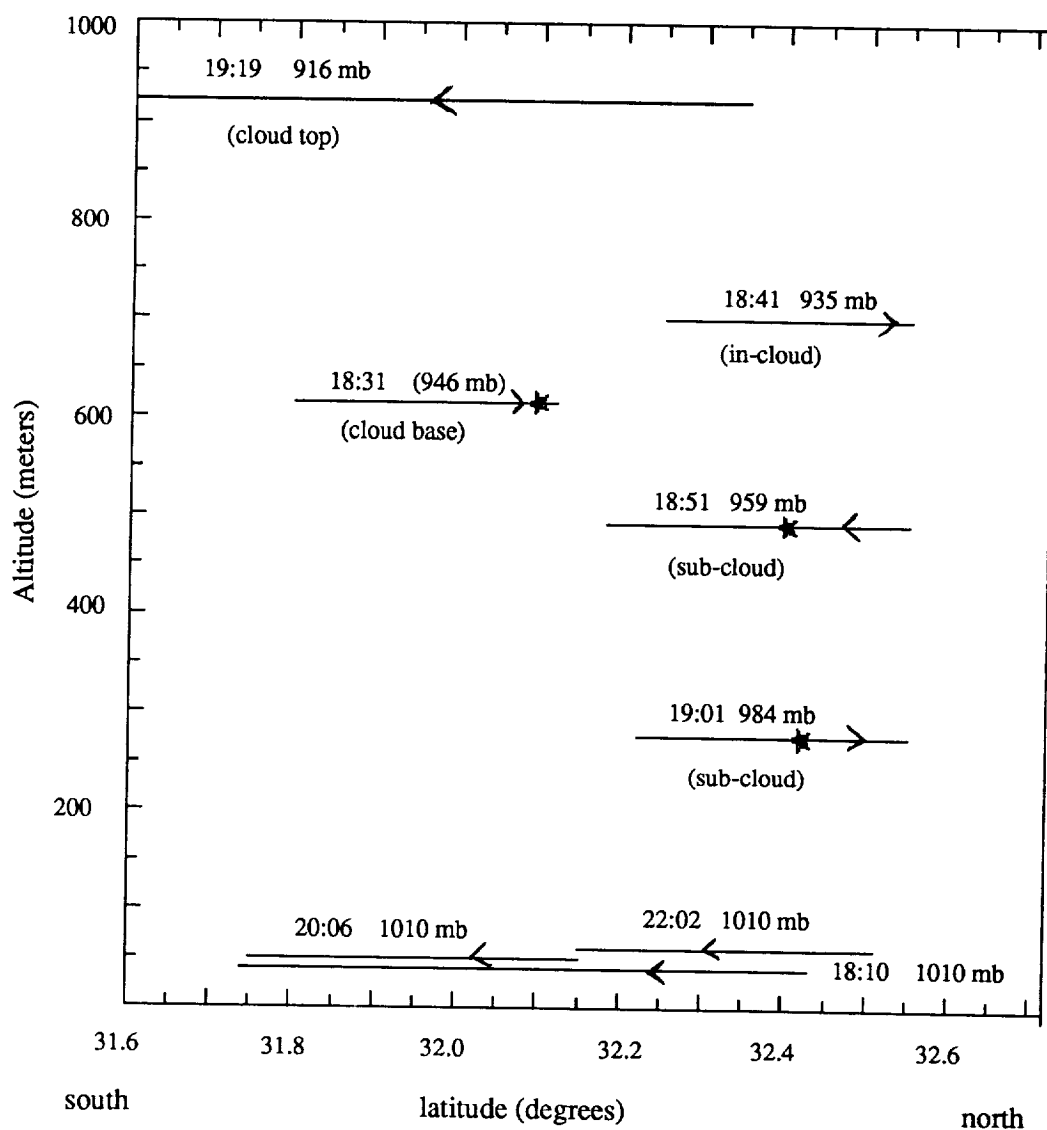


Figure 1 Height/latitude cross section of level Electra legs on July 5. Pressure at flight level, GMT time in the middle of the leg, direction of travel, and approximate location of cloud top and cloud base are noted. Stars indicated location of the transition from warm to cold region.

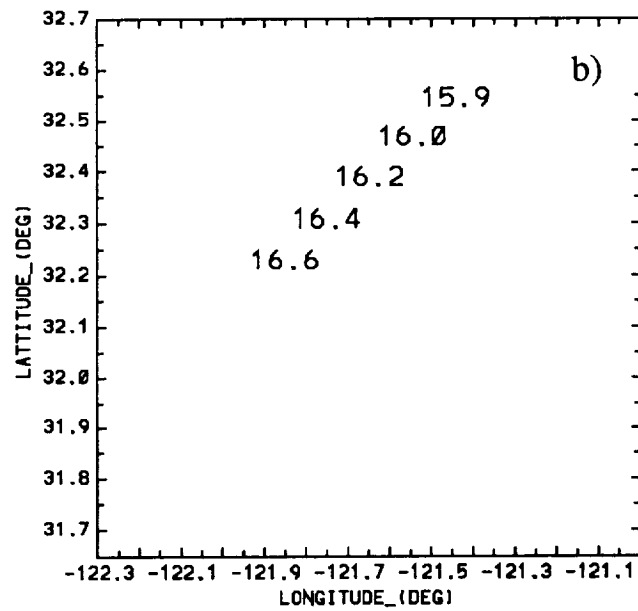
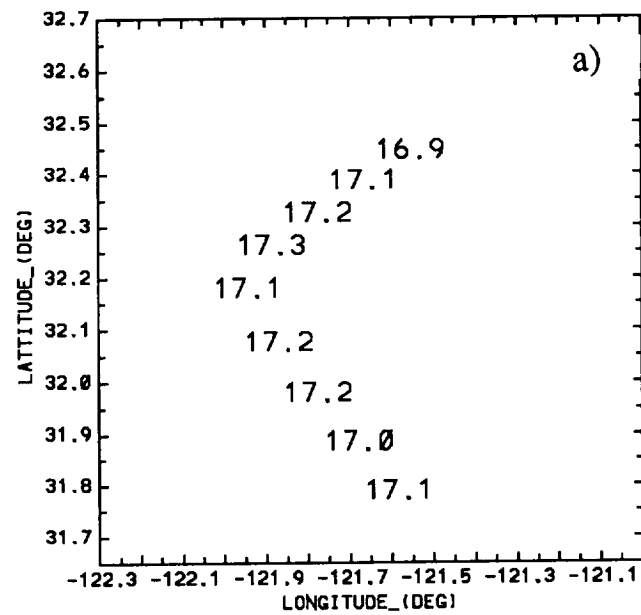


Figure 2 a). Two minute averages of SST (°C) from the 1010 mb leg 18:01 — 18:21 GMT. b) As in a), for 21:56 — 22:08 GMT

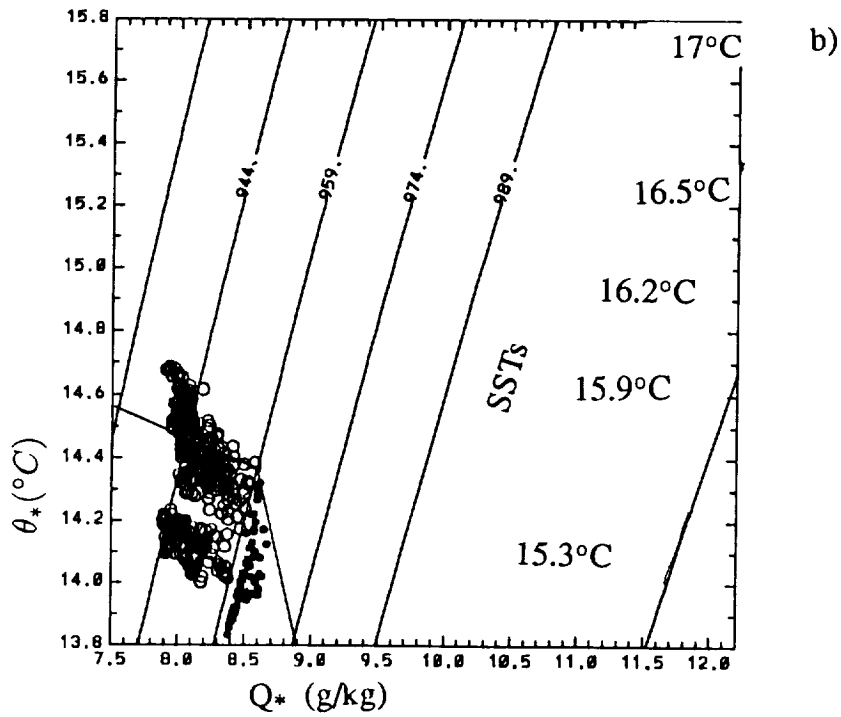
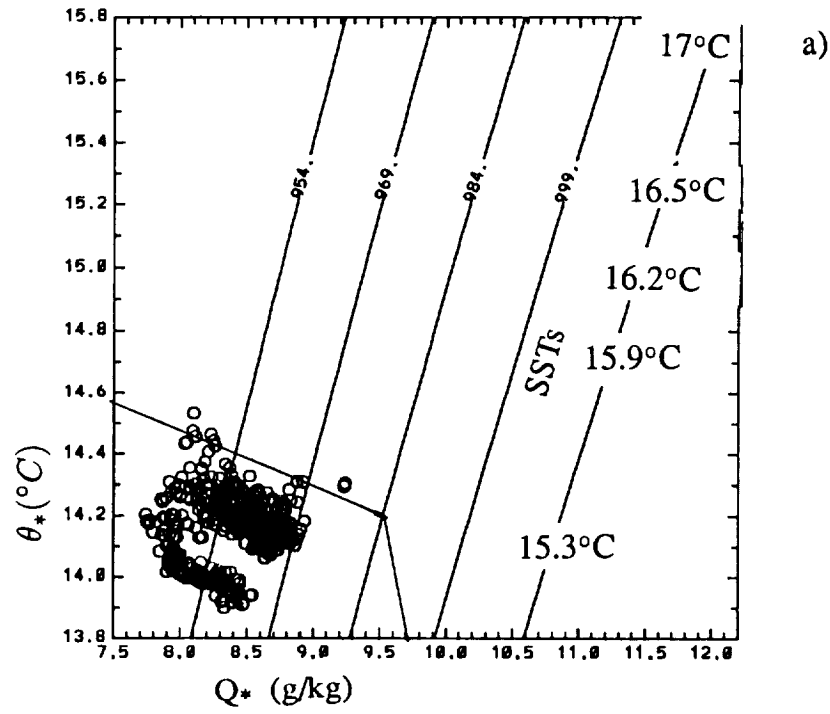


Figure 3 a) θ_* - Q_* diagram for the 984 mb leg (18:57-19:05 GMT). Saturation points for SSTs from Fig. 2 are also shown. The 289 K θ_v density isopleth is given for reference. b) As in a), but for the 959 mb (18:47 - 18:55 GMT) leg. Unsaturated points are denoted by open circles, saturated points by dots. θ_v isopleth is 289 K

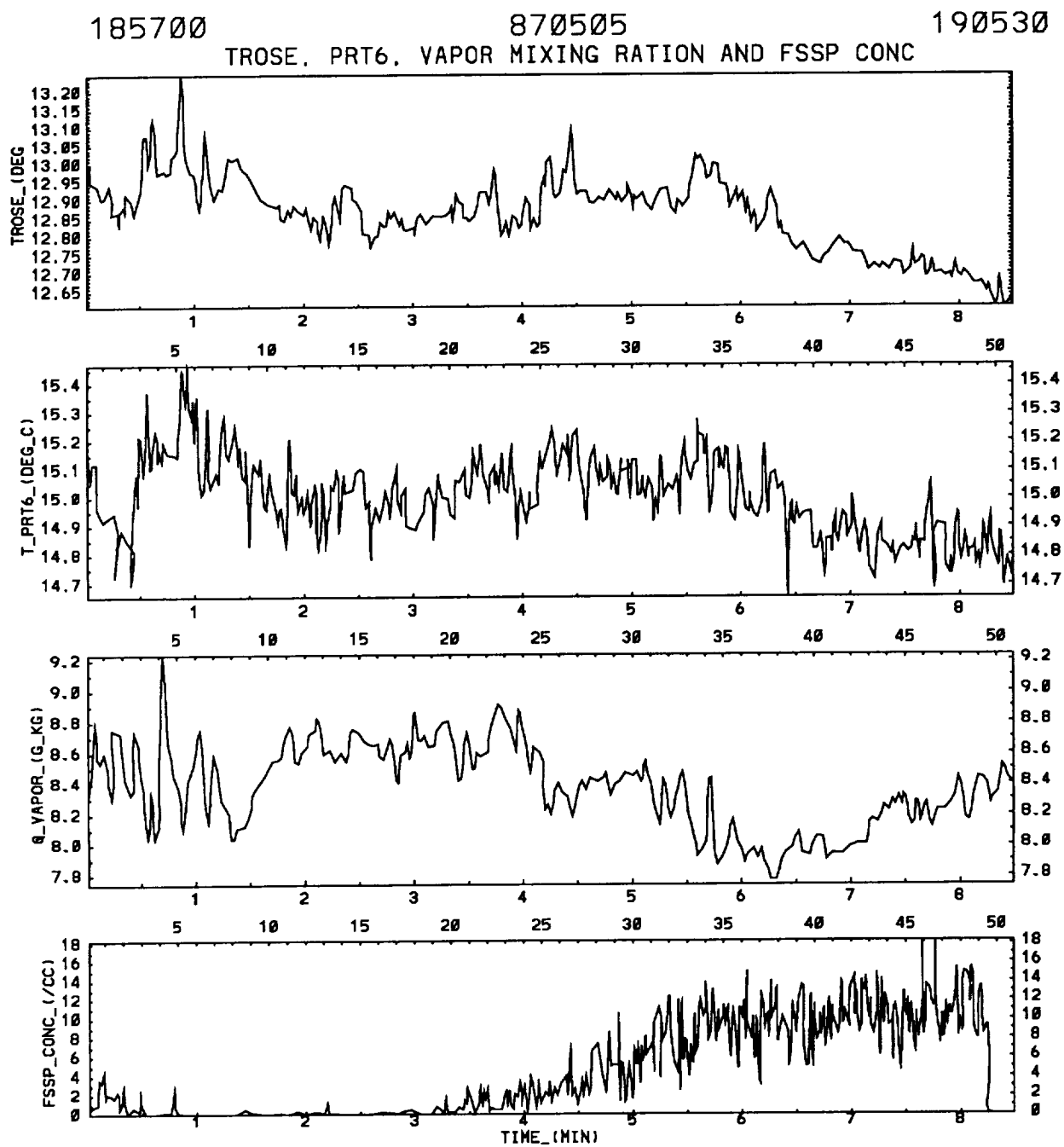


Figure 3 Time series of a) Rosemont temperature, b) PRT6 radiometric temperature, c) Vapor mixing ratio (from top Cambridge dewpoint thermometer) and d) FSSP droplet concentration for the 984 mb leg shown in 3a. Top abscissa label is distance (km).

Turbulence Spectra of the FIRE Stratocumulus-topped Boundary Layers

by

G. S. Young, J. J. Nucciarone and B. A. Albrecht

Abstract

There are at least four physical phenomena which contribute to the FIRE boundary layer turbulence spectra: boundary layer spanning eddies resulting from buoyant and mechanical production of turbulence kinetic energy (the microscale subrange); inertial subrange turbulence which cascades this energy to smaller scales; quasi-two-dimensional mesoscale variations; and gravity waves. The relative contributions of these four phenomena to the spectra depend on the altitude of observation and the variable involved (vertical velocity, temperature and moisture spectra are discussed). The physical origins of these variations in relative contribution will be discussed below. As expected from theory (Kaimal et. al., 1976), mixed layer scaling of the spectra (ie. nondimensionalizing wavelength by Z_i and spectral density by Z_i and the dissipation rates) is successful for the microscale subrange and inertial subrange but not for the mesoscale subrange.

The most striking feature of the normalized vertical velocity spectra shown in figure 1 is the lack of any significant mesoscale contribution. The spectral peak results from buoyant and mechanical production on scales similar to the boundary layer depth. The decrease in spectral density at larger scales results from the suppression of vertical velocity perturbations with large horizontal scales by the shallowness of the atmosphere. The spectral density also decreases towards smaller scales following the well known inertial subrange slope.

There is significant variation in the shape of the normalized spectra with height. However, the spectra assume similar forms within each of three height ranges: 0.1-0.4 Z_i , 0.4-0.9 Z_i , 0.9-1.0 Z_i . The mid mixed layer spectra, 0.4-0.9 Z_i , closely resemble those observed in the overland convective boundary layer (Young, 1987). The spectra for the lower mixed layer, 0.1-0.4 Z_i , are similar but have a lower spectral peak than those for the mid mixed layer or those for similar height ranges in the overland CBL. This difference in spectral form may be related to the greater contribution of mechanical production relative to buoyant production for this height range of the FIRE boundary layers. The FIRE turbulence kinetic energy dissipation profiles fall into two classes which support this hypothesis. Some of these dissipation profiles are nearly constant with height, suggesting that buoyant production is the dominant energy source while, others of them decrease linearly with height, suggesting that mechanical production resulting from surface stress is an important energy source. This form of mechanical production makes much less of a contribution to the turbulence spectra at higher levels in the FIRE boundary layers and is entirely absent in purely convective boundary layers. The peaks of the upper mixed layer spectra, 0.9-1.0 Z_i , are shifted to a significantly smaller scale than those at lower levels because of the eddy size limitation imposed by the adjacent capping inversion. This effect is physically similar to that observed in the surface layer. There is also a secondary peak in the upper mixed layer vertical velocity spectra at wavelengths much greater than Z_i which may be associated with gravity waves in the capping inversion. Thus, considerable insight into

ORIGINAL PAGE IS
OF POOR QUALITY

the dynamical processes at work in the boundary layer and capping inversion can be diagnosed from the observed variations of the FIRE vertical velocity spectra with height.

The temperature spectra shown in figure 2 have a somewhat different form than the vertical velocity spectra because they do exhibit a strong mesoscale contribution. The mesoscale subrange is separated from the microscale peak by a shallow spectral gap ranging up to a decade in width. The microscale peak and the inertial subrange are well normalized by mixed layer scaling while the mesoscale subrange is not. The temperature spectra in the mid and lower mixed layer are similar without any indication of the change in shape observed with the vertical velocity spectra. It is possible that because the stratification is weak the mechanical mixing does not affect the shape of the temperature spectra as much as it does the shape of the vertical velocity spectra. Any gravity wave contribution to the temperature spectra in the upper mixed layer is indistinguishable from the mesoscale contribution. The differences between the temperature and vertical velocity spectra highlight the relative importance of mesoscale and microscale contributions to the variance of these two quantities.

The moisture spectra shown in figure 3 are dominated by their mesoscale contribution to an even greater extent than are the temperature spectra. The mesoscale contribution to the moisture spectra is so strong that except in the lowest layer, 0.1-0.3 Z_1 , no microscale peak can be distinguished. In the mid and upper mixed layer the mesoscale spectra merges more or less smoothly into the inertial subrange spectra. In the lower mixed layer, on the other hand, there is a separate microscale peak separated from the mesoscale by a shallow spectral gap a decade wide. Further investigation involving dissipation rates for temperature and moisture variance will help explain the differences in relative contribution of mesoscale and microscale processes to the FIRE boundary layer. The relative contribution of these two scales may have a significant impact on other aspects of the marine atmospheric boundary layer including the cloud size distribution and the horizontal scales of variation in the radiative budget.

References

- Kaimal, J. C., J. C. Wyngaard, D. A. Haugen, O. R. Cote, Y. Izumi, S. J. Caughey and C. J. Readings, 1976: Turbulence structure of the convective boundary layer. J. Atmos. Sci., 33, 2152-2169.
- Young, G. S., 1987: Mixed layer spectra from aircraft measurements, J. Atmos. Sci., 44, 1251-1256.

Normalized W Spectra

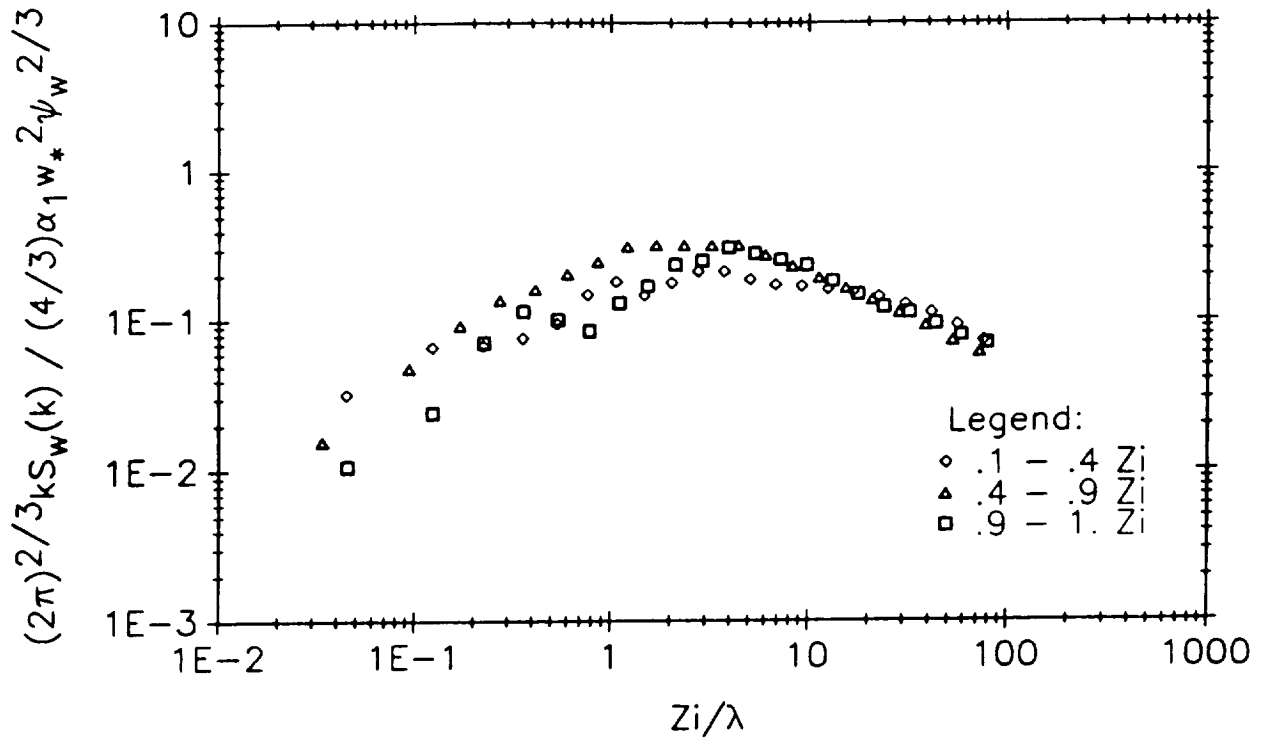


Fig. 1 Average vertical velocity spectra for the lower, middle and upper FIRE mixed layer. The spectra have been nondimensionalized using mixed layer scaling following Young (1987). Both axes are logarithmic.

Normalized Temperature Spectra

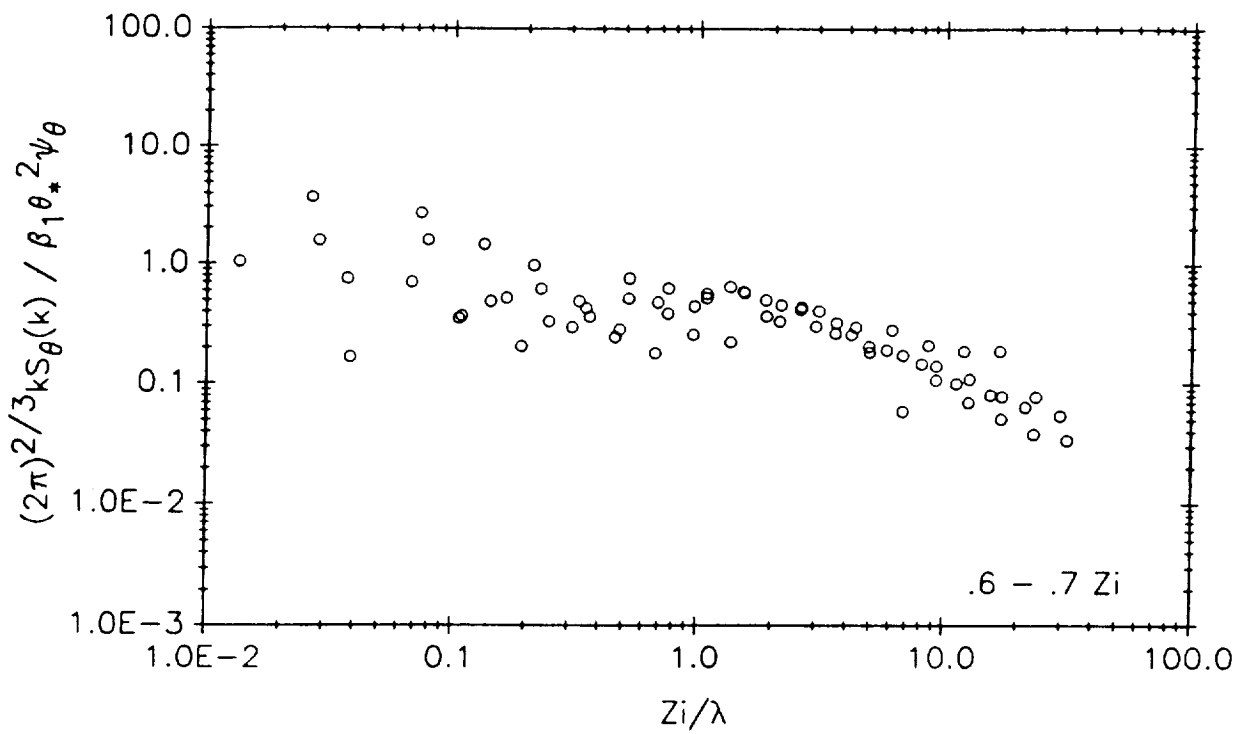


Fig. 2 Sample temperature spectra from FIRE flight legs in the mid mixed layer. The spectra have been nondimensionalized using mixed layer scaling following Young (1987). Both axes are logarithmic.

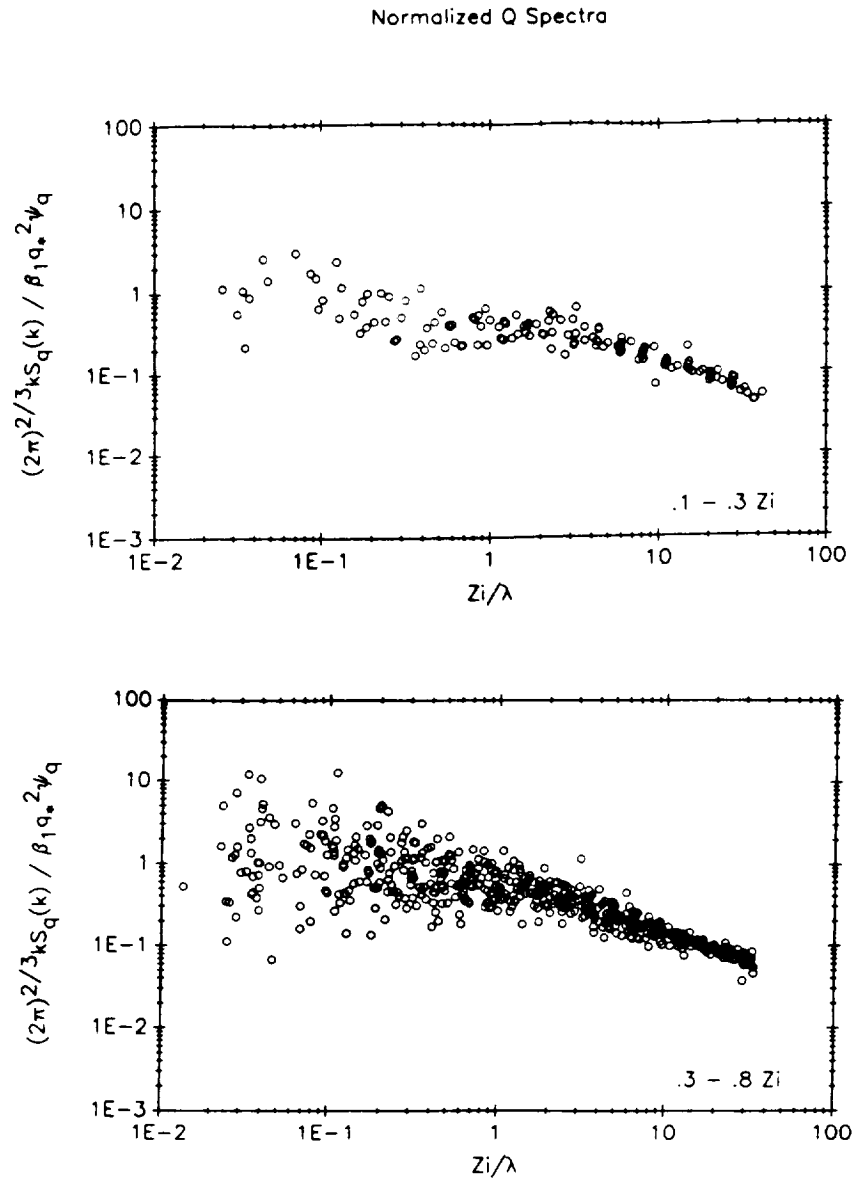


Fig. 3 Sample moisture spectra from FIRE flight legs in the lower and middle mixed layer. The spectra have been nondimensionalized using mixed layer scaling following Young (1987). Both axes are logarithmic.

Turbulence Structure in Clear and Cloudy Regions of the 7 July 1987 Electra Mission

Siri Jodha Singh Khalsa
Cooperative Institute for Research in Environmental Sciences
University of Colorado
Boulder, Colorado 80309-0216

I. Introduction

The 7 July mission of the 1987 FIRE marine stratocumulus intensive field observations has been chosen by several researchers for analysis because a well-defined transition from stratocumulus to clear conditions was sampled by the aircraft on this day. It is hoped that by studying this case we can learn something about the processes responsible for the maintenance and breakup of stratocumulus layers, a primary objective of FIRE.

The preliminary analysis reported on here is based on data from the Electra flight of this day. The properties of turbulence elements, i.e. updrafts and downdrafts, are examined to gain information on the nature of the turbulent exchanges through the boundary layer and across the inversion. Since such exchanges in large measure determine the stability and structure of cloud layers, a study of draft properties should be informative. These results will also be useful in the development of boundary layer models that are based on draft circulations (e.g. Randall, 1988; Hanson, 1988).

II. Methodology

The technique that we use is conditional sampling based on an indicator function. The indicator function is set to +1 or -1 when the vertical velocity exceeds predetermined positive or negative thresholds. Other variables are sampled based on this indicator function and conditional averages computed. Prior to computing the indicator function all variables are linearly detrended and a high pass filter is applied to remove fluctuations greater than about 8 km in length. As done in previous studies (e.g. Khalsa and Greenhut, 1985) the thresholds are based on the one-sided vertical velocity variances about zero. Also, no change of state that lasts less than 0.2 sec is allowed.

III. Conditions on 7 July 1987

Four turbulence measuring legs were flown on 7 July 1987 (Fig. 1). The first 50m leg was flown towards the west, followed by a 370m leg just below cloud base and a 580m leg just below cloud top. A leg at 50m was repeated approximately 2 1/2 hours after the first, but shifted to the east because of the movement of the cloud boundary.

The cloud boundary that was the focus of this mission was aligned approximately with the mean wind, making the cross-wind turbulence legs normal to it. The cloud boundary in the measurement region was found to move to the east at approximately 3 ms^{-1} . Each flight leg was divided into cloudy, transition and clear segments. The cloudy region to the east was generally solid stratocumulus, transition had approximately 50% cloud cover and "clear" had only widely scattered small cumulus.

The wind speed at 50m was from 330° and varied from 15 ms^{-1} in the east to 10 ms^{-1} in the west. Sea surface temperature was lower in the east by about 1°C . Momentum flux and sensible and latent heat fluxes at 50m were smaller in the cloudy region. The smaller stress in the east despite greater wind speed implies a smaller transfer coefficient, in accord with the greater stability

implied by cooler surface temperatures. The sensible and latent heat fluxes in all three regions were much smaller during the second 50m leg.

Another difference between the first and second 50m legs was in skewness which was a factor of two smaller during the second leg in both clear and cloudy regions. At 370m the second, third and fourth moments are all larger in the cloudy region compared to the clear region, probably a result of circulations originating in the cloud layer. In the cloudy region near cloud top the skewness is negative and the kurtosis is 3.6 compared to a positive variance and a kurtosis of 9.5 in the clear region. Negative skewness probably arises from strong sinking motions. The large kurtosis in the clear region is due to the fact that the latter part of the highest leg in the clear region actually penetrated the inversion towards the end of the run (the inversion sloped downward towards the west) resulting a high degree of intermittency in the time series.

IV. Conditional Sampling Results

Conditional sampling results from the four aircraft flight legs in the clear, transition and cloudy regions are shown in Fig. 2. Lines show the vertical variation of conditional averages for updrafts, downdrafts and the environment (i.e. everything that is not updraft or downdraft). The second 50m leg was slightly lower in altitude than the first.

The conditionally sampled vertical velocity (Fig. 2a) for updrafts and downdrafts ranges in magnitude from 0.5 to 1 ms^{-1} except for the 580m level in the clear region. Updrafts leave the surface layer with positive buoyancy but soon begin to decelerate as they entrain environmental air and do work against a slightly stable stratification.

The cloudy region has the smallest 50m magnitudes of w' , a consequence of the cooler surface temperatures and therefore weaker buoyant forcing. In contrast, this region has the largest magnitudes of w' at 370m and magnitudes near cloud top exceed those of the clear region by approximately a factor of two, with downdrafts having larger magnitudes than updrafts. This suggests that circulations in the upper half of the boundary layer are being driven by local processes and not surface forcing.

In the transition region the magnitudes of w' at 50m are similar to those in the clear region but w' does not decrease away from the surface. The magnitudes at cloud top are the largest of the three regions. It may be that the vertical motions in this region were driven by both surface and cloud layer processes.

Updraft temperature perturbations (Fig. 2b) are positive at 50m in the clear region and switch to negative above. Downdrafts have negative T' at 50m and slightly positive T' at 370m. A negative value of T' near the inversion in the clear region is somewhat unusual in that downdrafts are expected to contain warm air entrained from above the inversion. However, if entrainment is weak, the downdrafts that are measured will be dominated by cool updrafts that have turned over at the inversion. Further discussion of draft overturning is contained in the next section.

In the cloudy region updraft T' is near zero at all levels except near the inversion where it attains the largest value of any class in all 3 regions. Downdraft T' at this level has the largest negative value of any region. These magnitudes are approximately 50% of the standard deviation in T at this level. The signs of the perturbations indicate that the circulations in the cloud layer are thermally direct and are being driven by processes near the cloud top.

The transition region displays a mixture of properties found in the clear and cloudy regions. For example, updrafts in the first 50m leg have positive T' and a negative T' at 370m, as in the clear region but a negative T' again near the cloud top, as in the cloudy region.

Conditionally sampled absolute humidity perturbations are shown in Fig. 2c. All updrafts are moist and all downdrafts are dry, as expected. Downdraft ρ_v' is nearly constant with height in the cloudy and transition regions whereas it decreases with height in the clear region. As with the T' perturbation for downdrafts near the inversion in the clear region, this is contrary to what would be expected if downdrafts were mainly air entrained from above the inversion. The large ρ_v' perturbations for updrafts in the transition region are also puzzling. To explain these results we have to look in more detail at the nature of the drafts near the inversion.

V. Draft Characteristics Near the Inversion

A greater understanding of the nature of turbulent elements can be gained by further classifying updrafts and downdrafts by their mean temperature and moisture perturbations. In this way we can distinguish, for example, between downdrafts that originate as entrained inversion air and downdrafts that originate as overturning updrafts. In the first case the drafts will be dry and in the second moist. In Tables 1, 2, and 3 the following conditional sampling results from the 580m leg are given: number of events expressed as percentage of total events in each state (up, down or environment); mean draft length; horizontal wind perturbation in the direction of the mean wind; and virtual temperature perturbation. Only the dominant classes which together account for 80-90% of the drafts in each region are given.

In the clear region the significant classes are warm/dry and cool/moist. Entrained air will be warm and dry and will have a positive u' perturbation due to a positive shear across the inversion. Warm/dry events make up 49% of all downdrafts at this height in this region. The most common updraft class is cool/moist. These drafts carry a u' deficit. Both of these classes, warm/dry and cool/moist exist as both updrafts and downdrafts, indicating that drafts can overturn and still remain distinct. Note also that in the clear region the size of the overturned drafts is greater than the originating draft. The u' perturbation is not always preserved which may be a result of vertical momentum being converted to horizontal momentum in the process of overturning. The small mean q' for downdrafts (Fig. 2c) probably results from the compensating effects of dry entrained downdrafts and moist overturned updrafts in the average.

In the cloudy region cool/dry is by far the dominant downdraft class, accounting for nearly three-fourths of all downdrafts. This air has a positive momentum perturbation, indicating it has come from above the inversion, and is negatively buoyant. This entrained air is probably cooled by evaporation of cloud liquid water making the parcel negatively buoyant. Radiative cooling may also play a role. These downdrafts descend to below cloud base, as suggested by the substantial magnitudes of conditionally averaged vertical velocity at 370m. A fraction of the cool/dry downdrafts turn over and are sampled as cool/dry updrafts. These retain, in the mean, the positive u' and negative T_v' perturbations they had as downdrafts.

The dominant updraft class is warm/moist, which has negative u' and positive buoyancy perturbations. The downward flux of mass in sinking parcels produces compensating upward motion, but the conditionally averaged w' for warm/moist updrafts is nearly a factor of two greater than the threshold value used to define the updrafts making it unlikely that this is mere "compensating" motion. Moisture-driven updrafts from lower in the boundary layer may attain a positive temperature perturbation upon reaching the cloud layer as latent heat is released. Overturned warm/moist events are also seen as downdrafts. The portion of the time series not classified as updraft or downdraft, the environment, has equal numbers of the dominant updraft and downdraft classes.

Both clear and cloudy conditions are sampled in the transition region so some of each type of thermodynamic class is represented. Cool/dry is the most common downdraft class, characteristic of the cloudy region. The average negative buoyancy is half that for the cloudy region. Cool/moist events are also present but the sizable positive u' perturbation suggests that they are

not overturned surface-based updrafts. The large negative u' for warm/moist events suggests that these have come from below, as conjectured for the cloud region. Even in the environment state warm/moist events have a u' that is an order of magnitude greater than for the other classes. The warm/moist environment class is also distinguished by small mean size which more characteristic of draft states.

Warm/dry downdrafts are also present in the transition region, indicating entrained air that has not mixed with cloud layer air. Warm/dry air makes up over one third of the environment with event sizes over twice as large as for the other classes. This air probably occurs in the region between clouds.

VI. Conclusions and Future Work

A conditional sampling analysis has shown that the properties of updrafts and downdrafts reflect the nature of the forcing of convective motions in the clear and cloudy boundary layers of the 7 July 1987 flight. In the clear region, draft statistics are characteristic of a boundary layer in which convective motions are forced from the surface and entrainment is driven by impinging surface-based updrafts (and perhaps also horizontal wind shear). In the cloudy region, the strongest convective motions are driven by cloud layer processes, apparently evaporative cooling of entrained parcels. If this were strong enough it would lead to cloud breakup. In the transition region there is a combination of clear and cloudy layer processes. Cool/dry downdrafts, which we believe to be the "agents" of cloud-top entrainment instability (CTEI), are more prevalent and more negatively buoyant in the cloud layer than in the transition layer. Thus it is difficult to use CTEI to explain why the transition region was less cloudy than the region to the east. Apparently the cloud layer is maintained through the resupply of moisture from lower in the boundary layer evidenced by the greater number and larger vertical velocity of cool/moist updrafts at cloud base in the cloudy region compared to the transition region.

Further work needs to be done before we have a full understanding of the processes producing the cloud conditions observed on this day. We plan to include cloud liquid water, particle size and ozone in the conditional sampling analysis. A conserved parameter analysis of draft properties will be performed and results compared with the analysis of Betts and Boers (1989) who looked at mean conditions in each region. We will also examine draft statistics for evidence of differences in conditions above the inversion that may have been a factor in determining whether or not a cloud layer could be maintained.

V. References

- Betts, A.K. and R. Boers, 1989: A cloudiness transition in a marine boundary layer. *Proceedings of the FIRE Science Meeting*, Monterey, CA, July 1989.
- Hanson, H.P., 1988: Plume mechanics and stratocumulus convection. *Proceedings of the FIRE Science Team Workshop*, Vail, CO, July 1988.
- Khalsa, S. J. S., and G. K. Greenhut, 1985: Conditional sampling of updrafts and downdrafts in the marine atmospheric boundary layer. *J. Atmos. Sci.*, **42**, 2550-2562.
- Randall, D.A., 1988: Fractional cloudiness in shallow cumulus layers. *Proceedings of the FIRE Science Team Workshop*, Vail, CO, July 1988.

Acknowledgments

This work was supported by the Marine Meteorology Program of the Office of Naval Research.

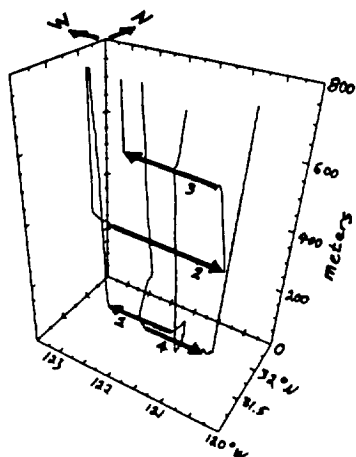


Figure 1. Turbulence flight legs of the NCAR Electra on 7 July 1987.

Significant Classes - CLEAR - 580m				
Table 1				
	%	(m)	u'	T_v'
warm/dry	49	68	0.18	0.06
cool/moist	38	100	0.00	-0.08
ENVR				
warm/dry	42	214	0.05	0.06
cool/moist	50	178	-0.06	-0.05
UP				
warm/dry	30	96	0.03	0.06
cool/moist	51	63	-0.18	-0.08
Significant Classes - CLOUDY				
Table 2				
	%	(m)	u'	T_v'
cool/dry	74	78	0.12	-0.06
warm/moist	20	45	-0.24	0.04
ENVR				
cool/dry	46	121	0.10	-0.05
warm/moist	46	124	-0.10	0.05
UP				
cool/dry	22	67	0.26	-0.05
warm/moist	65	79	-0.18	0.07
Classes - TRANSITION				
Table 3				
	%	(m)	u'	T_v'
cool/dry	38	72	0.10	-0.03
cool/moist	26	57	0.18	-0.07
warm/dry	25	78	0.00	0.06
warm/moist	11	39	-0.23	0.09
ENVR				
cool/dry	23	167	0.03	-0.02
cool/moist	34	172	0.04	-0.04
warm/dry	23	412	0.02	0.02
warm/moist	20	68	-0.30	0.06
UP				
cool/dry	24	49	0.49	-0.04
cool/moist	34	54	0.04	-0.07
warm/dry	6	26	-0.05	0.06
warm/moist	36	79	-0.46	0.11

Tables. Conditional sampling statistics for thermodynamically classified events in the clear (Table 1), cloudy (Table 2), and transition (Table 3) regions. Data is from the 580m leg. The variables given are: number of events expressed as a percentage of the total number of events in each state (updraft, downdraft, environment), the mean event length in meters, and the along-wind velocity perturbation in m/s, and the perturbation virtual temperature in °C.

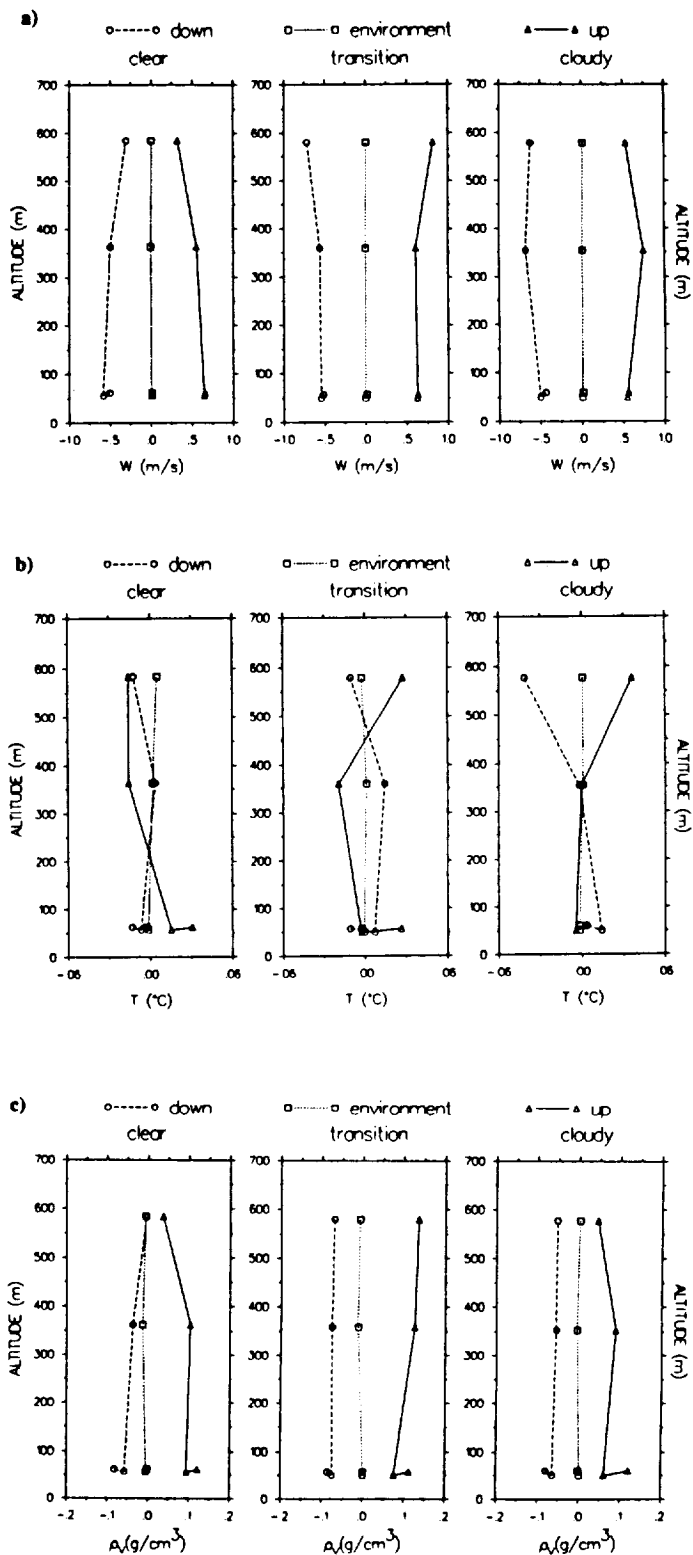


Figure 2. Vertical variation of conditionally sampled a) vertical velocity, b) temperature and c) absolute humidity from the four turbulence flight legs shown in Figure 1. Statistics were computed separately for the clear, transition and cloudy segments of each leg.

Diurnal Variation in the Turbulent Structure of the CloudyMarine Boundary Layer During FIRE 1987Phillip Hignett

Meteorological Office Research Unit
 RAF Cardington
 Bedfordshire MK42 0TH
 England

During the 1987 FIRE marine stratocumulus experiment the U.K. Meteorological Office operated a set of turbulence probes attached to the tether cable of a balloon based on San Nicolas Island. Typically six probes were used; each probe is fitted with Gill propeller anemometers, a platinum resistance thermometer and wet and dry thermistors, to permit measurements of the fluxes of momentum, heat and humidity. The orientation of each probe is determined from a pair of inclinometers and a three-axis magnetometer. Sufficient information is available to allow the measured wind velocities to be corrected for the motion of the balloon. A full description of this turbulence system can be found in Lapworth and Mason (1988).

On the 14th/15th July measurements were made over the period 1530-0200 UTC and again, after a short break for battery re-charging and topping-up the balloon, between 0400-0800 UTC. Data were therefore recorded from morning to early evening, and again for a period overnight. Six probes were available for the daytime measurements, five for the night. Data were recorded at 4 Hz for individual periods of a little over an hour. The intention was to keep a minimum of one probe at or just above cloud top; small changes in balloon height were necessary to accommodate changes in inversion height.

The most direct comparison, and contrast, can be drawn between the overnight period and that around local noon. In both cases the mean inversion height was very similar and the parameter $u_* / f z_i$ ($=R$) was equal to ~ 3.5 . This parameter, being proportional to the ratio of the height of a steady neutrally-stable boundary layer to that of the capping inversion, is useful in establishing the broad relationship between the current observations and those of other experiments. For example, Nicholls(1984) and Nicholls and Leighton(1986) present observations for which R varied mainly from 0.6 to 3, with a single strong wind case at $R \sim 7$. This latter case is similar to the observations of Brost et al(1982) for which $R \sim 10$. Hence we might expect the current observations to show most similarity to the buoyancy dominated flows of Nicholls and Nicholls and Leighton.

The ability of the balloon system to make simultaneous measurements at several levels allows the vertical structure of the boundary layer to be displayed without resort to composites. Figures 1 and 2 show the velocity vectors of the longitudinal and vertical

components over 30 second averages (giving a spatial resolution of ~ 170 metres), with the mean horizontal wind subtracted. The daytime data of Figure 1 are from 1908-1958 UTC (i.e. immediately before local noon) and correspond to an horizontal length scale of 18km, based on the mean wind. The upper 2 levels were above cloud, while the third was just below cloud top; the cloud base in this period varied from about 220 to 300 metres. The nocturnal data in Figure 2 were taken between 0645-0738 UTC, and again correspond to a length scale of 18km; the top level is just below cloud top and cloud base was approximately 140 metres.

There is a striking contrast in the degree of variability between the velocity fields in Figures 1 and 2. Both show regions of divergence and convergence near cloud top and organised up and down draughts; however, at night the magnitudes of these gust velocities are much higher and coherent structures occupy the whole depth of the boundary layer, rather than just the cloud layer.

Turbulent statistics were calculated from 2-hour periods, one straddling local noon and one at night. These were sub-divided into half-hour averaging intervals for the evaluation of variances and fluxes. The vertical velocity variances for the day (closed squares) and night (open triangles) are plotted on Figure 3; the heights have been normalised by the inversion height. The daytime profile characteristically shows very low values above cloud, a distinct maximum in the cloud layer and evidence of a second weak maximum below cloud. In contrast, the nocturnal data show a more turbulent layer well-mixed from inversion to surface in a manner analogous to that of a convective boundary layer heated from below (e.g. Lenschow et al, 1980).

These features are also reflected in the behaviour of the equivalent potential temperature flux, shown in Figure 4. During both day and night the flux maxima are located close to cloud top; however, whereas the nocturnal data give the appearance of a single mixed layer driven by a cloud-top buoyancy flux, the daytime profile shows a distinct minimum in the region of cloud base increasing again to a weak surface flux.

The daytime boundary layer, around local noon, therefore consists of a cloud mixed layer, driven by a cloud-top buoyancy flux, surmounting a weakly-driven layer of depth $\sim 0.2u_c/fz_i$, a value reminiscent of the results of the JASIN experiment (e.g. Slingo et al (1982), Nicholls(1985)). The top of this layer, however, and the base of the cloud mixed layer are not clearly associated with cloud base, as observed from the surface, which tended to be variable and ill-defined during this period. Mixed-layer similarity of the two datasets can be shown by normalising and replotting against $1-z/h$, where h is the mixed layer depth. The vertical velocity variances were normalised by w_c , the convective velocity scale, and the fluxes by the maximum value at cloud top. The results are displayed on Figures 5 and 6. A satisfactory collapse of the data is achieved except for w^2 as $1-z/h$ approaches unity; the lower boundary condition for the daytime mixed layer will be different from that at night when w^2 must go to zero at the surface.

The evidence presented strongly supports the notion that, for at least part of the daytime, the cloud layer becomes decoupled from the surface following the absorption of solar radiation at depth within the cloud layer. The surface fluxes on this occasion are weak and the growth of any surface Ekman layer is limited. Further evidence, derived from the TKE budget and turbulence length scales, for this argument will be presented.

References

Brost, R.A., Wyngaard, J.C. and Lenschow, D.H., 1982: Marine stratocumulus layers: Part II. Turbulence and entrainment. *J. Atmos. Sci.*, **39**, 818-836

Lapworth, A.J. and Mason, P.J., 1982: The new Cardington balloon-borne turbulence probe system. *J. Atmos. Ocean. Tech.*, **5**, 699-714

Lenschow, D.H., Wyngaard, J.C. and Pennell, W.T., 1980: Mean-field and second-moment budgets in a baroclinic convective boundary layer. *J. Atmos. Sci.*, **37**, 1313-1326

Nicholls, S., 1984: The dynamics of stratocumulus: aircraft observations and comparisons with a mixed-layer model. *Quart. J. R. Met. Soc.*, **110**, 783-820

-----, 1985: Aircraft observations of the Ekman layer made during JASIN. *ibid.*, **111**, 391-426

Nicholls, S. and Leighton, J., 1986: An observational study of the structure of stratiform cloud sheets: Part I. Structure. *ibid.*, **112**, 431-460

Slingo, A., Nicholls, S. and Schmetz, J., 1982: Aircraft observations of marine stratocumulus during JASIN. *ibid.*, **108**, 833-856

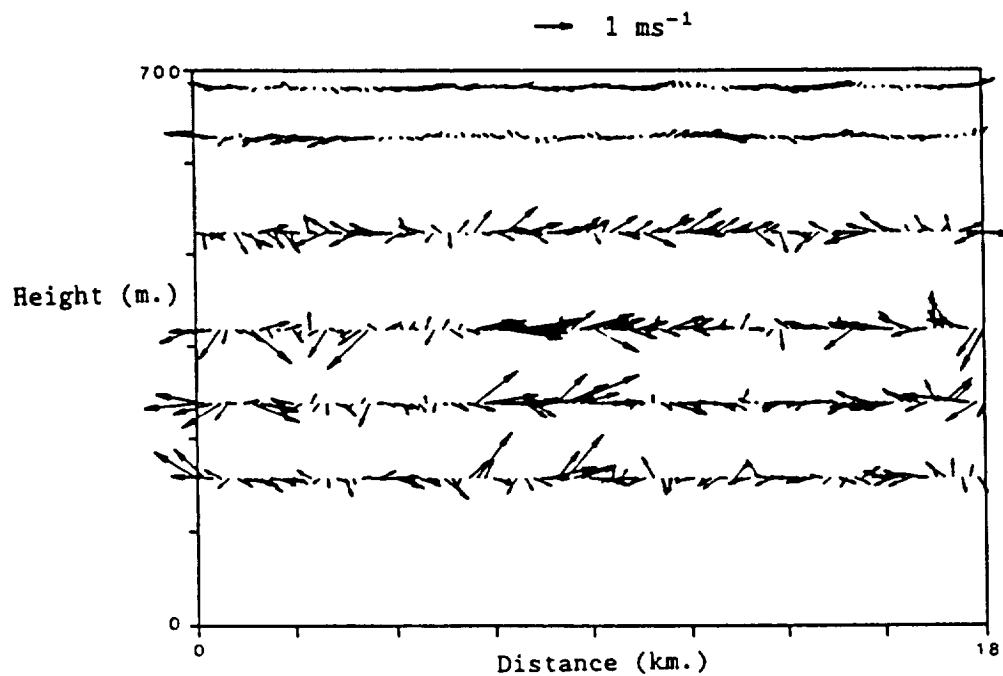


Figure 1: height-distance velocity cross-section for 1908-1958 UTC 14th July. Details in text.

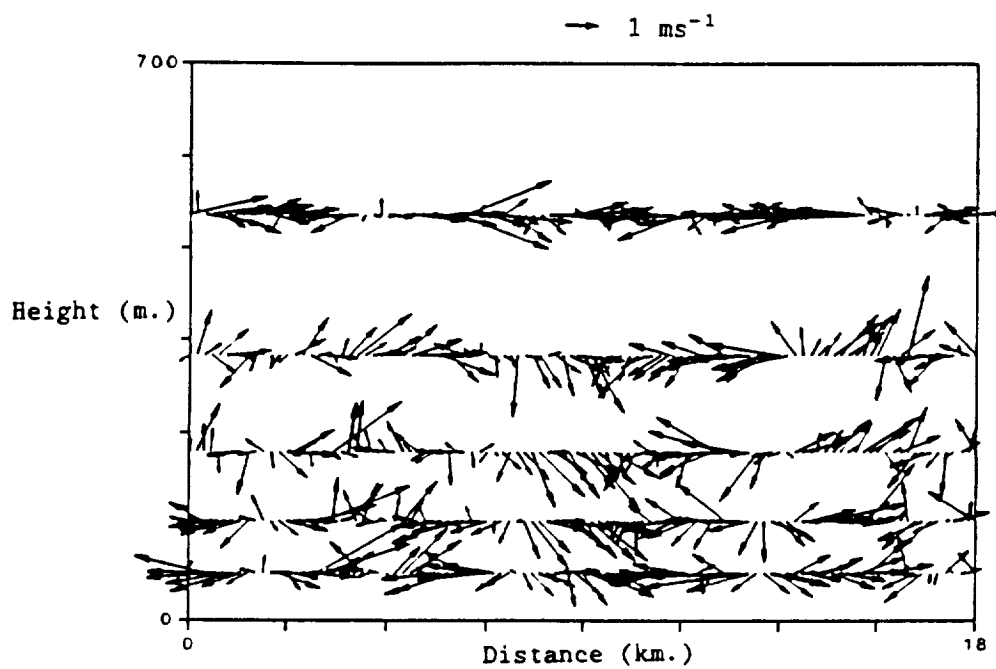


Figure 2: as Fig. 1 but for 0645-0738 UTC 15th July

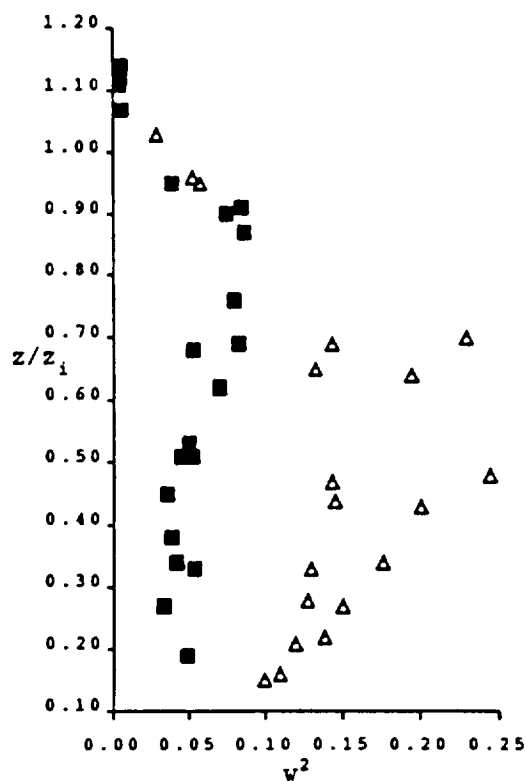


Figure 3: vertical velocity variance versus normalised height: day(squares), night(triangles)

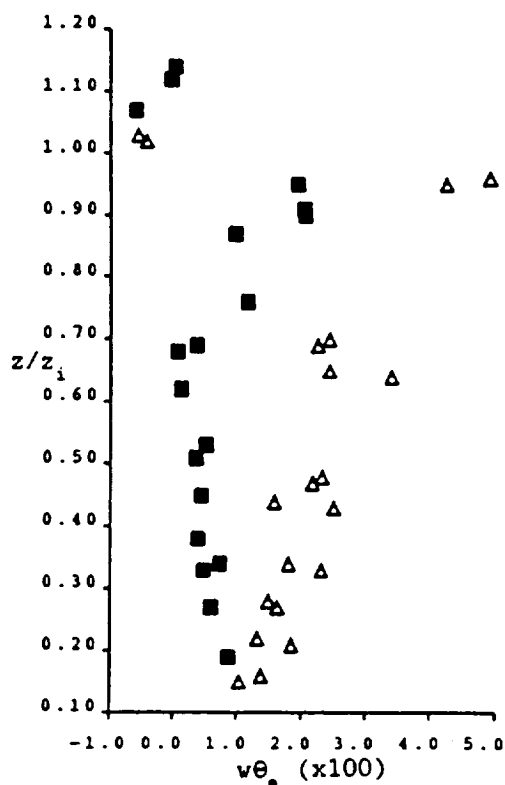


Figure 4: equivalent potential temperature flux versus normalised height.

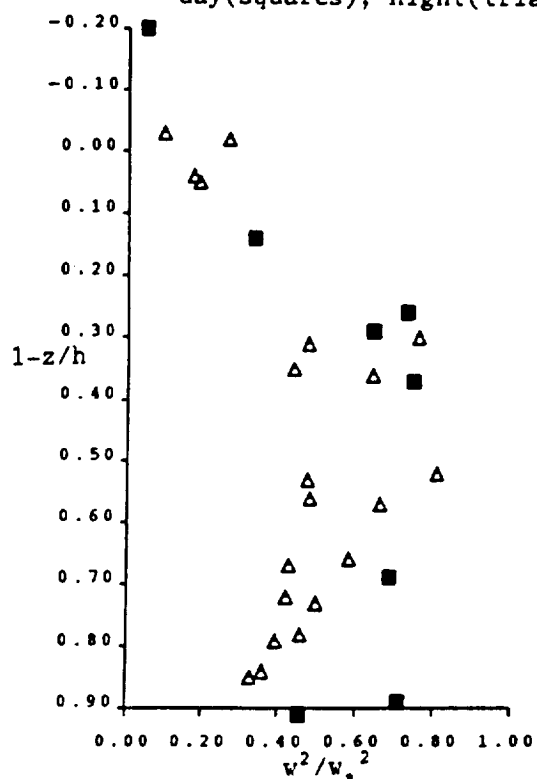


Figure 5: scaled vertical velocity variance

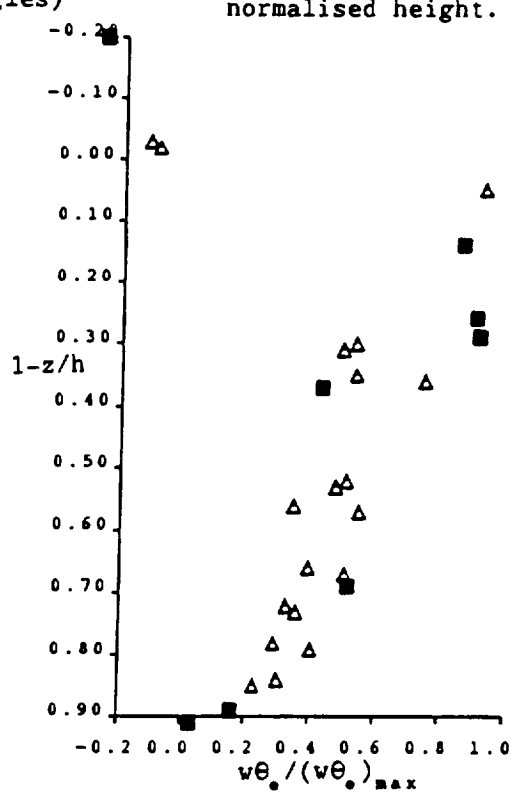


Figure 6: scaled equivalent potential temperature flux

	PAGE
M05.01 Supersaturation, Droplet Spectra, and Turbulent Mixing in Clouds <u>Gerber, H.</u>	145
M05.02 The Influence of Continental Sources of Aerosols on the Marine Stratocumulus During FIRE IFO-I Durkee, Philip A.	151
M05.03 Observations of Anthropogenic Cloud Condensation Nuclei Hudson, James G.	157
M05.04 Direct and Remote Sensing Observations of the Effects of Ships on Clouds Radke, Lawrence F., Peter V. Hobbs, James A. Coakley, Jr., and Michael D. King	163
M05.05 Optical Properties of Marine Stratocumulus Clouds Modified by Ship Track Effluents King, Michael D., and Teruyuki Nakajima	165

SUPERSATURATION, DROPLET SPECTRA, AND TURBULENT MIXING IN CLOUDS

H. Gerber

Naval Research Laboratory, Washington, DC 20375-5000

I. Introduction

Much effort has recently gone into explaining the observed broad precoalescence size distribution of droplets in clouds and fogs, because this differs from the results of condensational growth calculations which lead to much narrower distributions. The correct explanation of this difference is important, since the observed broadening has a strong influence on the optics of the clouds, as well as on their colloidal stability. Existing explanations, which have yet to be proved definitive, have generally dealt with the interaction of turbulence with the cloud, such as in entrainment and mixing (Telford et al., 1984; Jonas and Mason, 1982; Baker et al., 1980; Clark and Hall, 1979; and many others). Most have dealt with the "favored-droplet hypothesis", which states that due to the statistical nature of turbulence some "favored" droplets experience a lifetime in the clouds which is more conducive to condensational growth (or evaporation) than other droplets, and hence cause the broadening (e.g., Cooper, 1989).

A good example of droplet size-distribution broadening was observed on flight 17 (25 July) of the NRL tethered balloon during the 1987 FIRE San Nicolas Island IFO. On this date a stratocumulus cloud cover formed rapidly from clear sky conditions. The balloon was aloft at the time, and was able to penetrate the Sc clouds 7 min. after their formation. These virgin clouds, which could not include the complexity of upwind evolution, contained significant numbers of 32.5μ diameter droplets (the largest size bin of the CSASP particle spectrometer). Such large droplets cannot easily be explained by a standard updraft argument. Instead, observed RH and wind shear in the vicinity of these clouds suggested a formation mechanism which included Kelvin-Helmholtz induced mixing of a nearly saturated layer. These observations motivated us to take another look at the interaction between cloud microphysics and turbulent mixing. We used the findings of Broadwell and Breidenthal (1982) who conducted laboratory and theoretical studies of mixing in shear flow, and those of Baker et al. (1984) who applied the earlier work to mixing in cloud. Rather than looking at the 25 July case at SNI, we chose instead to look in detail at earlier fog observations made at SUNY (6 Oct., 1982) which also indicated that shear-induced mixing was taking place, and which had a better collection of microphysical measurements including more precise supersaturation measurements (see Gerber, 1980 for description of technique) and detailed vertical profiles of meteorological parameters; see Fig. 1.

In this study we address the following questions:

1. Does B-B (Broadwell-Breidenthal) mixing, or gradient diffusion control droplet evolution in shear situations involving nearly saturated air?
2. Can B-B mixing account for the observed large transient supersaturations which can last as long as tens of seconds?
3. Can B-B mixing account for strong droplet broadening and the appearance of the largest droplets?

II. Broadwell-Breidenthal Mixing

B-B mixing describes a mixing process different from the usual approach in which turbulent mixing occurs via gradient diffusion. The latter is only reasonably successful when the scale of the turbulence is small in comparison to

the distance across which the diffusing quantity is changing significantly. Broadwell and Breidenthal (1982) clearly demonstrated in laboratory measurements that gradient diffusion between two species in shear flow does not hold, but is instead governed by another mechanism consisting essentially of a two stage mixing process: For most of the lifetime of a decaying eddy containing two species, the identity of the species remains largely intact. Only as the Kolmogorov microscale is reached do the two species rapidly mix with each other by molecular diffusion.

We first apply B-B mixing to an eddy with properties estimated from the 6 Oct. fog case. The eddy had a characteristic dimension $L = 6.9\text{m}$, it consisted of two saturated parcels with a difference in temperature of 3°C (which is the maximum temperature difference observed over the height of the micromet tower), and it contained droplets with a size distribution given by curve 0715 in Fig. 1 and measured at about $\text{RH} = 100\%$. We derive an expression similar to the classical equation

$$S(t) = Q_1 \int dh - Q_2 \int dw \quad (1)$$

giving the time evolution of supersaturation $S(t)$ in terms of the mass balance of total water in an ascending cloud parcel (e.g., see Squires, 1952). Instead of the excess (supersaturated) vapor released by the change in height dh of the parcel, we include the release of excess vapor by the B-B mixing of the saturated parcels. Under isobaric conditions, and under the assumption that the rate of release of excess moisture is proportional to the rate of formation of interfacial area between the two saturated parcels in the eddy we find

$$S(t) = \left[\left(\frac{x}{x_s K} - 1 \right) \left(1 - \frac{t_k}{\tau_L} \right)^{3/2} \left(1 - \frac{t}{\tau_L} \right)^{-3/2} - \left[\frac{1}{\rho_a x_s K} \right] \int_r 4\pi r N(r) C \left(S(t) - \frac{A}{r} + \frac{B}{r^3} \right) dt \right] \quad (2)$$

$$K = \frac{L^2 M_0 \Delta w}{RT^2 C_p} + 1$$

where x = vapor mixing ratio of mixed eddy, x_s = saturation mixing ratio of mixed eddy, w = liquid water mixing ratio, $N(r)$ = particle density at radius r , C = rate constant, t_k = time to reach Kalmogorov turbulence scale, τ_L = time for complete homogenization, and other symbols have the usual meaning.

The predictions of (2) are illustrated in Fig. 2. The curve labeled 0715 shows a rapid release of excess moisture at around 35 sec of the calculation, with a maximum value of S near the maximum $S = 0.43\%$ that can be achieved by mixing two saturated parcels with a 3°C temperature difference, and with a decrease of S from the maximum corresponding to the takeup by growing droplets and lasting tens of seconds. Curve 0719 corresponds to the use of the distribution labeled 0719 in Fig. 1 as the initial condition (initial $\text{LWC} = 0.09 \text{ g/m}^3$); and the curve for X10 uses the 0719 distribution with 10 times the LWC value. We can conclude from Fig. 2 that (a) the B-B mixing mechanism causes the formation of transient supersaturations in the fog, (b) the release of excess vapor is faster than the time scale of droplet response, and (c) the time constant of the decay of the transient S is approximately proportional to the integral radius of the droplets as is evident from the second term of (2).

These conclusions are supported by the observations in the 6 Oct. fog. Mixing was clearly shear induced as indicated by the stable temperature profile, gradient diffusion could not have caused the observed supersaturation transients because of the magnitude of the temperature gradient, and the observed transients were of a magnitude consistent with the maximum temperature differences observed with height.

III. Broadening of Droplet Size Distribution

An important consequence of B-B mixing as illustrated in Fig. 2 is that the release of excess vapor appears to be essentially independent of the droplet content, and thus can be treated separately from the conversion of the vapor to liquid, which depends approximately on the integral radius. It is thus possible to use the droplet growth equation

$$r \frac{dr}{dt} = c \left(S - \frac{A}{r} + \frac{B}{r^3} \right) \quad (3)$$

with an average S parameterized in terms of the integral radius, if the maximum value of $S(t)$ is measured or estimated.

To fully exploit this possibility, the integral form of (3) was rewritten to give a set of analytical expressions

$$r \approx f \left(r_0, S, t, r_d \right) \quad \text{for} \quad \begin{cases} r_d > 10^{-6} \text{ cm} \\ r_0 > r_d \\ S > -1 \\ t > 0 \\ \text{particle type} \end{cases} \quad (4)$$

which give one-equation solutions to the time dependence of r , given S (r_0 = initial radius, r_d = dry nucleus radius). This approach greatly speeds up the calculations, because (3) is implicit in r and usually requires numerical integration, and is difficult to use for small droplets. Equation (4) is mathematically well behaved, and it gives the proper transitions between activated droplets and haze particles; see Fig. 4. Equation (4) should be useful in improving the coupling between microphysics and dynamic models.

A model was developed to evaluate the effects of B-B mixing on droplet broadening. The approach, as in Nichols (1987), was to combine the effects of stochastic turbulent diffusion with explicit microphysical calculations. However, in the present case only droplet growth by diffusion is considered. Furthermore, this model, rather than being driven by models of turbulent diffusion, is driven by the observed statistics of S and eddy size (see Fig. 3). Highlights of the model include: The Monte-Carlo approach is used to randomly mix eddies in a Lagrangian framework. The mixing process includes contributions from mixing eddies proportional to their volume, and conserves particle concentration, liquid water volume, and total nuclei volume. Calculations are done in $N(r)$ space using (4), and timescales are estimated from Eulerian observations of eddy frequency and the droplet integral radius.

Some initial runs of the model are shown in Figs. 5 and 6. Using the measured cumulative probability of S and L shown in Fig. 3 with the 0715 size distribution to initialize the model, results in the droplet spectrum for $t = 15$ min shown in Fig. 5. On the average droplets have evaporated to smaller sizes

in this case. This is consistent with the slightly subsaturated conditions reflected by the means in Fig. 3. The statistics in Fig. 3 were collected 1.5-m above a grassy surface in post sunrise fog where some warming of the surface was taking place. The second example in Fig. 6, which illustrates the flexibility of this model, shows a double-peaked distribution with significant broadening and maximum droplet sizes close to the ones observed in the 6 Oct. fog. For this case the S distribution in Fig. 3 was biased by $S = + .001$, the time scale of the excess S decay was set at a constant 20 s, and 80% of the final eddies making up the distribution in Fig. 6 correspond to $t = 3$ min while the rest is for $t = 15$ min. Other runs of the model (not shown), using S decay coupled to the integral radius as suggested by B-B mixing, gave significantly broadened size distributions, but none with peaks in the size distribution exceeding about 10 μm diameter even for $t = 60$ min.

IV. Conclusions

The observations in the 6 Oct. fog and the initial results of the stochastic condensational growth model suggest the following conclusions on the importance of Broadwell-Breidenthal mixing in fogs and clouds:

(a) B-B mixing of nearly saturated parcels at different temperature causes large transient supersaturations as observed in the 6 Oct. and other fogs.

(b) These transient supersaturations and turbulent mixing cause droplet spectral broadening governed by the "favored droplet hypothesis".

(c) The effect of B-B mixing on droplet broadening is approximately proportional to the temperature difference of nearly saturated mixing parcels and inversely proportional to the integral droplet radius, thus hazes and clouds of low LWC with strong temperature gradients will see the largest effects.

(d) B-B mixing could not explain the observation of 30- μm diameter droplets in the 6 Oct. fog. The rapid increase of droplet size observed 1.5-m above the surface is partially explained by the downward mixing of this fog which formed 20 min earlier aloft. It is proposed that B-B mixing contributes primarily to the mid-size peak (about 5 μm diameter) often found in these fogs, and that the large droplet peak is due to very large supersaturations generated by another mechanism found higher up in the fog.

Baker, M.B., R.G. Corbin and J. Latham, 1980: The influence of entrainment on the evolution of cloud droplet spectra: I. A model of inhomogeneous mixing. Quart. J. Roy. Met. Soc., 106, 581-598.

Baker, M.B., R.E. Breidenthal, T.W. Choularton and J. Latham, 1984: The effects of turbulent mixing in clouds. J. Atmos. Sci., 41, 299-304.

Broadwell, J.E., and R.E. Breidenthal, 1982: A simple model of mixing and chemical reaction in a turbulent shear layer. J. Fluid Mech., 125, 397-410.

Clark, T.L., and W.D. Hall, 1979: A numerical experiment on stochastic condensation theory. J. Atmos. Sci., 36, 470-483.

Cooper, W.A., 1989: Effects of variable droplet growth histories on droplet size distributions. Part I: Theory. J. Atmos. Sci., in print.

Gerber, H.E., 1980: A saturation hygrometer for the measurement of relative humidity between 95% and 105%. J. Appl. Meteor., 19, 1196-1208.

Jonas, P.R., and B.J. Mason, 1982: Entrainment and the droplet spectrum in cumulus clouds. Quart. J. Roy. Met. Soc., 108, 857-869.

Nicholls, S., 1987: A model of drizzle growth in warm, turbulent, stratiform clouds. Quart. J. Roy. Met. Soc., 113, 1141-1170.

Squires, P., 1952: The growth of cloud drops by condensation. Aust. J. Sci. Res. A, 5, 59-86.

Telford, J.W., T.S. Keck and S.K. Chai, 1984: Entrainment at cloud tops and the droplet spectra. J. Atmos. Sci., 41, 3170-3179.

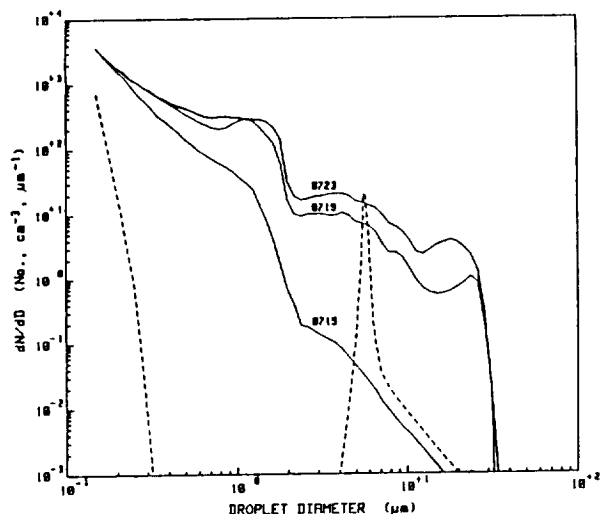


Fig. 1 - Size distribution dN/dD of droplets measured near the surface at indicated times in the fog on 6 Oct. Dashed curve results from classical condensational growth calculations with $S = 0.001$ for 5 min. with 0715 as the initial distribution.

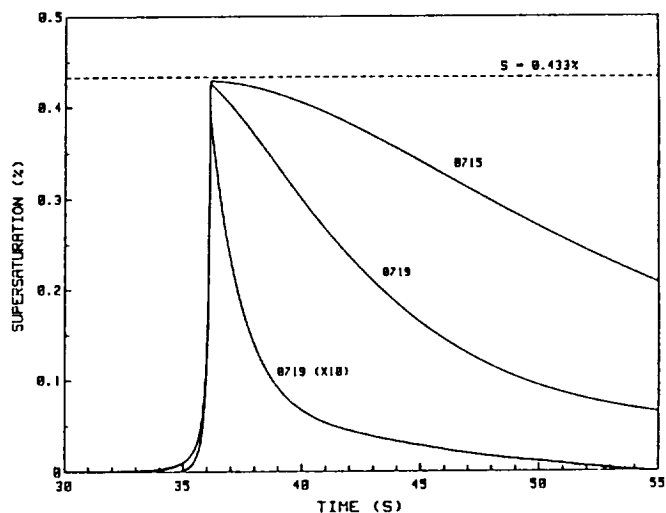


Fig. 2 - Time evolution of supersaturation for mixing of two saturated parcels with a temperature difference of 3 °C and different initial droplet size distributions, according to the Broadwell-Breidenthal mixing mechanism.

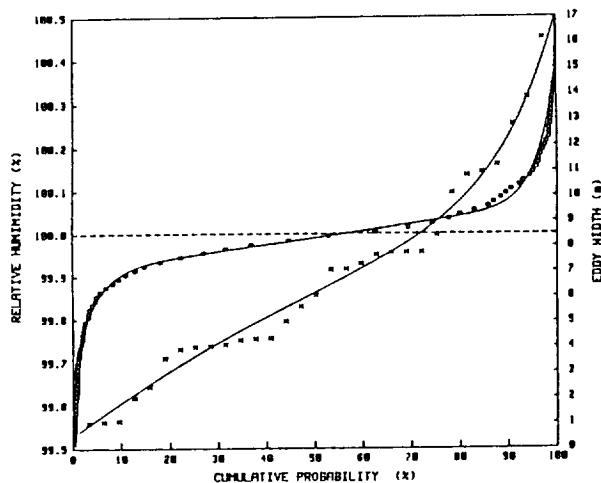


Fig. 3 - Cumulative probability distributions of supersaturation (o) and eddy width (x) measured near the surface during the 6 Oct. fog.

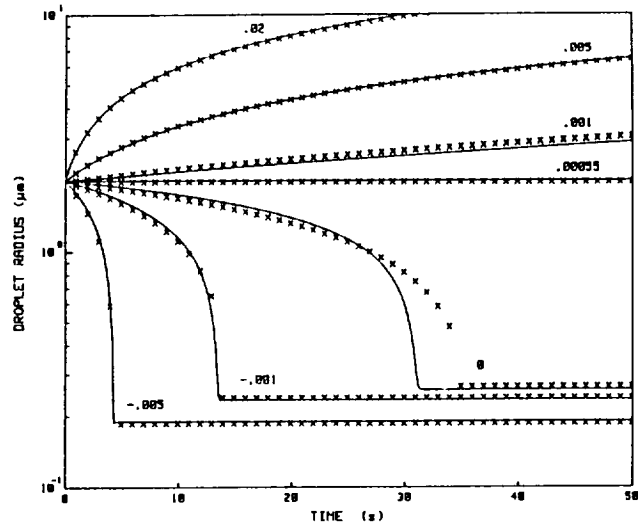


Fig. 4 - Comparison of the growth rate of a 2-μm droplet formed on an urban nucleus calculated with the exact growth equation (3) and with the approximate analytical expressions (4;x) as a function of the indicated supersaturations.

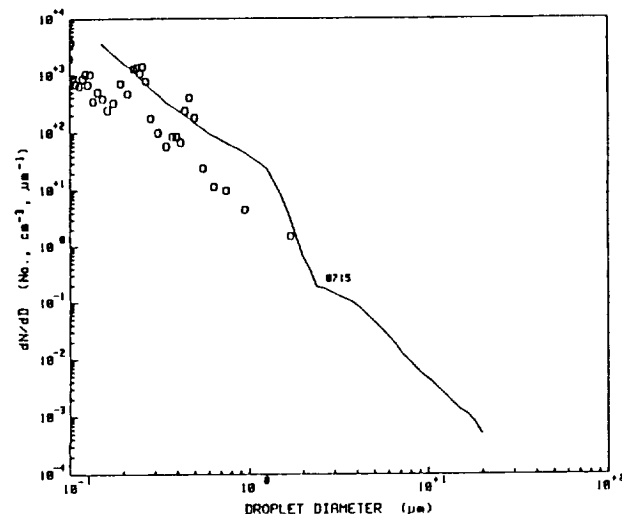


Fig. 5 - Predicted evolution of dN/dD after 15 min. according to the stochastic condensational growth model using the statistics in Fig. 3 and the 0715 distribution for initialization.

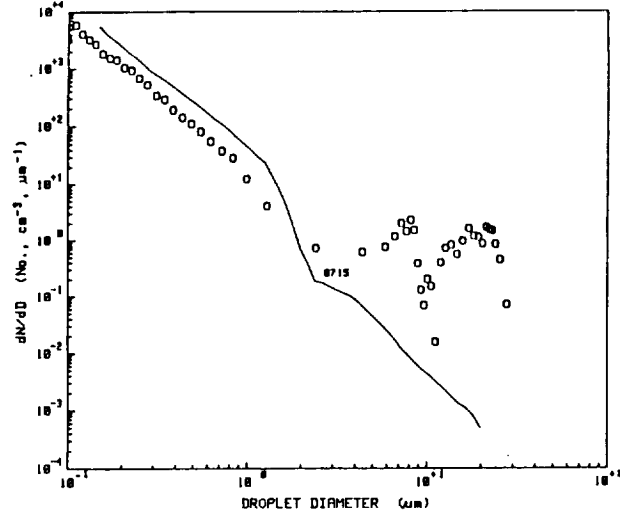


Fig. 6 - Same as Fig. 5, except that supersaturation statistics in Fig. 3 were biased by $S = + 0.001$, and parcels with different time histories were averaged.

The Influence of Continental Sources of Aerosols on the Marine Stratocumulus during FIRE IFO-I

PHILIP A. DURKEE

*Department of Meteorology, 63De
Naval Postgraduate School
Monterey, CA 92943*

INTRODUCTION

The effects of aerosols on the microphysical characteristics of marine stratocumulus clouds can have a significant impact on climate processes through modification of cloud radiative properties. The effect of aerosols on clouds and the impact on climate processes have recently been discussed by several authors (Twomey et al., 1984; Coakley et al., 1987; Charlson et al., 1987). Of particular concern in this presentation is the potential for observing variations of cloud characteristics that might be related to variations of available aerosols. The results of comparisons between aircraft-measured microphysical characteristics and satellite-detected radiative properties of marine stratocumulus clouds are presented here. These results are extracted from Mineart (1988) and Durkee and Mineart (1989) where the analysis procedures and a full discussion of the observations are presented. Due to the space available, only a brief description of the results will be presented.

The satellite data used here are from the National Oceanic and Atmospheric Administration (NOAA) Advanced Very High Resolution Radiometer (AVHRR) collected at the Scripps Satellite Oceanography Facility. The AVHRR channel 1 ($0.63 \mu\text{m}$), channel 2 ($0.86 \mu\text{m}$), channel 3 ($3.7 \mu\text{m}$), and channel 4 ($11 \mu\text{m}$) data were used in the analysis. Cloud microphysical data were obtained by instruments on the NCAR Electra during cloud-penetrating missions in support of the field operations from 29 June - 19 July 1988.

RESULTS

Mineart (1988) presents four case studies that show a consistent relationship between cloud microphysical characteristics and cloud radiative properties. The most dominant effect is observed in cloud reflectance at $3.7 \mu\text{m}$ wavelength (AVHRR channel 3). Fig. 1 shows the observed relationship between aircraft-measured cloud droplet size and satellite-measured cloud reflectance. At this wavelength, moderate absorption by the cloud droplets limits the dependence of cloud reflectance on cloud thickness and liquid water content (primary determinants of reflectance at visible wavelengths). Therefore the primary determinant of cloud brightness at $3.7 \mu\text{m}$ is the cloud droplet size distribution (reflectance increases with decreasing droplet size). The dashed lines in Fig. 1 are the theoretical relationships for three size distributions.

The effects of droplet size on cloud reflectance are also theoretically expected at shorter wavelengths although the effects of cloud thickness and LWC will become more important as absorption decreases. To assess the effects at $0.63 \mu\text{m}$ wavelength (AVHRR channel 1), reflectance values were normalized to a constant LWC (0.3 g m^{-3}) and thickness (200 m). The results of normalization are shown in Fig. 2. Although the relationship appears weak and there is significant scatter, a decrease in reflectance with increasing droplet size is suggested ($\approx 10\%$ decrease with droplet size increase from 5 to $12 \mu\text{m}$ radius).

The primary modifier of cloud brightness at $3.7\ \mu\text{m}$ wavelength shown in Fig. 1, is influence from continental air masses (Mineart, 1988). Presumably, continental air containing significantly more CCN than marine air, produces clouds with smaller droplets relative to clouds in typical marine air masses. These microphysical differences between marine and continental clouds can be observed in the satellite-detected radiative properties of the clouds. The connection between cloud brightness and continental air mass is made through analysis of air motion trajectory calculations. Cloud brightness is directly related to cloud droplet size distribution through analysis of particle measurements made on board the NCAR Electra aircraft. Analysis of CCN measurements on board the Electra still need to be performed.

Continental aerosol sources were observed during the FIRE IFO to interact with marine stratocumulus in three ways:

- 1) **During periods of large scale offshore flow and subsequent cloud development.** Most of these events occur to the north of the main stratus deck (coastal OR and northern CA during the FIRE IFO). The continentally influenced air-mass then moves southward under the influence of the subtropical high pressure system and is incorporated into the main stratus deck.
- 2) **By local scale offshore flow and entrainment into the cloud.** This off shore flow is usually confined to stable layers just above preexisting cloud. Hudson has reported large increases in CCN concentration above cloud during the FIRE IFO (reported in Albrecht, et al., 1988). These processes need further study.
- 3) **By direct injection into the cloud in coastal regions, especially from urban sources.** Durkee (1989) reports several cases of urban influence on aerosol and cloud processes. These effects are identified by the spatial and temporal relationships to urban centers.

Composites of satellite-measured radiative characteristics have been prepared to assess the large-scale effects of continental aerosol sources on cloud characteristics. Tettelbach (1987) presented the first monthly summary of the eastern North Pacific Ocean. Fig. 3 and 4 are the results of cloud reflectance composites for August 1986. These results illustrate a clear distinction between cloud reflectance at $3.7\ \mu\text{m}$ and $0.63\ \mu\text{m}$ wavelengths. As mentioned above, $0.63\ \mu\text{m}$ reflectance is primarily determined by cloud thickness and LWC. The brightest clouds in Fig. 1 (AVHRR channel 1) are associated with the large scale divergence pattern of the subtropical high and the region of coldest upwelled water along the northern CA and OR coast. Reflectance at $3.7\ \mu\text{m}$ is determined mostly by droplet size. Fig. 4 (AVHRR channel 3) shows bright clouds are associated with the coastal regions of CA, with the brightest clouds occurring immediately downwind of Los Angeles, CA. Summaries of the FIRE IFO time period and other months of 1987 are being processed and should be ready for presentation at the workshop.

CONCLUSIONS

Relationships between cloud reflectance and cloud characteristics have been illustrated by comparing AVHRR satellite data and aircraft measurements. A relationship of higher reflectances from smaller cloud droplet size spectra is confirmed for $3.7\ \mu\text{m}$ wavelength (AVHRR channel 3) and is suggested for $0.63\ \mu\text{m}$ wavelength (AVHRR channel 1). A primary source of droplet size variations is related to continental/marine air mass differences. Continental air masses are generally have higher concentrations of aerosols, higher concentrations of cloud droplets, and therefore smaller mean cloud droplet radius, than marine air masses. The strong dependence of $3.7\ \mu\text{m}$ reflectance on cloud droplet size distribution allows inference of cloud composition characteristics from satellite observations. Further, satellite-detected cloud reflectance can be used to investigate the influence of continental air masses on marine cloud formation and subsequent effects on the cloud radiative properties.

ACKNOWLEDGEMENTS

The Scripps Satellite Oceanography Facility is acknowledged for real-time analysis support during the FIRE operations and for data collection support. Craig Motell and Rick Kohrs helped with the data analysis. This research is supported by the Office of Naval Research and the Naval Postgraduate School.

REFERENCES

- Albrecht, B. A., D. A. Randall and S. Nicholls, 1988: Observations of marine stratocumulus clouds during FIRE. *Bull. Amer. Meteor. Soc.*, **69**, 618-626.
- Charlson, R. J., J. E. Lovelock, M. O. Andreae, and S. G. Warren, 1987: Oceanic phytoplankton, atmospheric sulphur, cloud albedo and climate. *Nature*, **326**, 655-661.
- Coakley, J. A., Jr., R. L. Bernstein and P. A. Durkee, 1987: Effect of ship-stack effluents on cloud reflectivity. *Science*, **237**, 953-1084.
- Durkee, P. A., and G. M. Mineart, 1989: Multispectral satellite analysis of marine stratocumulus cloud microphysics. In preparation for submission to *J. Geophys. Res.*
- Mineart, G. M., 1988: Multispectral satellite analysis of marine stratocumulus cloud microphysics. Masters Thesis, Naval Postgraduate School, Monterey, California, 138 pp.
- Tettelbach, F. M., 1987: Stratocumulus and cloud-free reflectance from multispectral satellite measurements. M.S. Thesis, Naval Postgraduate School, Monterey, California, 68 pp.
- Twomey, S., M. Piegrass and T. L. Wolfe, 1984: An assessment of the impact of pollution on global cloud albedo. *Tellus*, **36B**, 356-366.

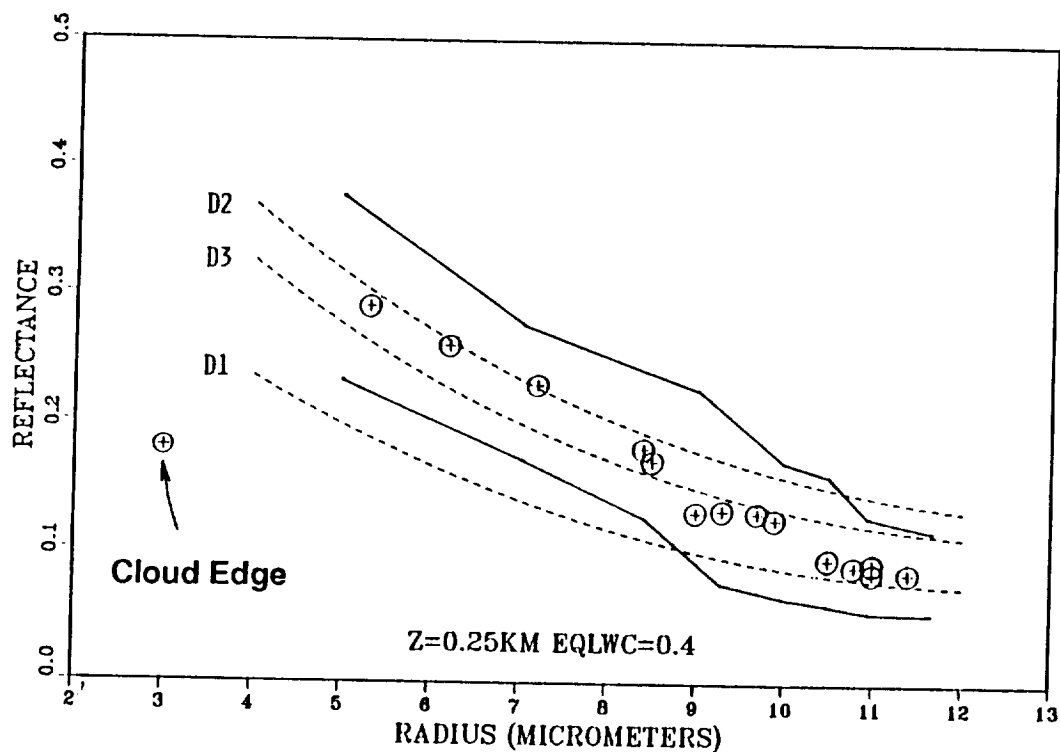


Fig. 1. Satellite-measured $3.7 \mu\text{m}$ reflectance vs aircraft-measured droplet size. Dashed lines indicate model reflectance for distributions of different widths (D2-narrow, D1-wide, D3-moderate). Solid lines indicate the 95% confidence interval for the data points.

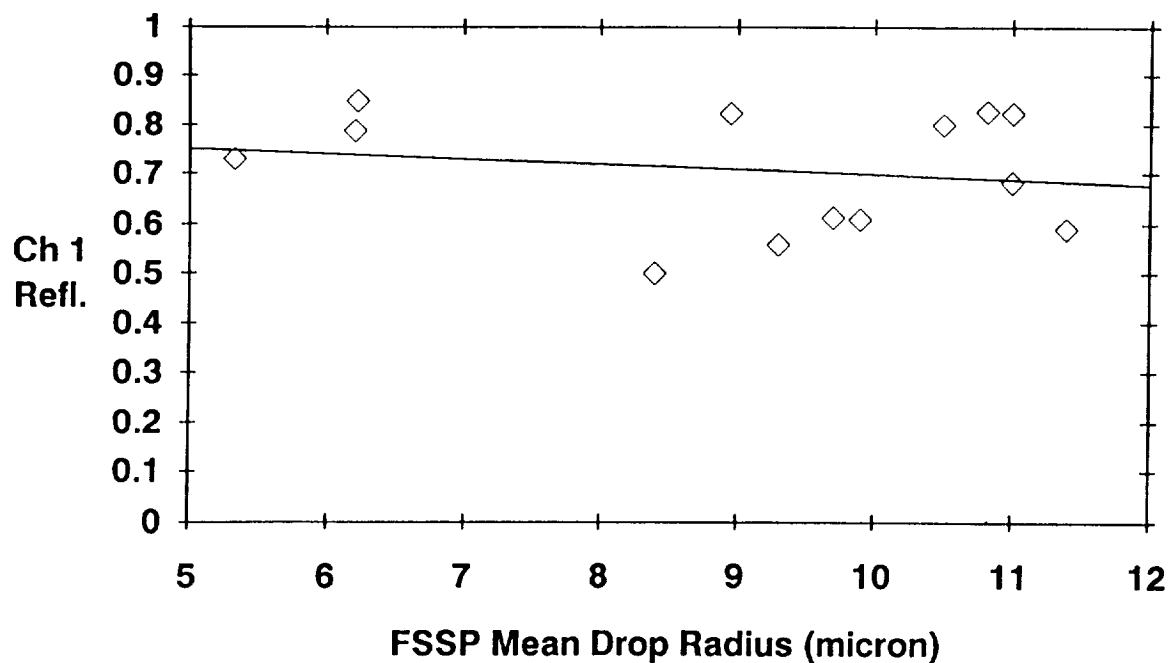


Fig. 2. Same as Fig. 1 but for $0.63 \mu\text{m}$ reflectance and normalized to thickness = 200 m and $\text{LWC} = 0.30 \text{ gm m}^{-3}$.

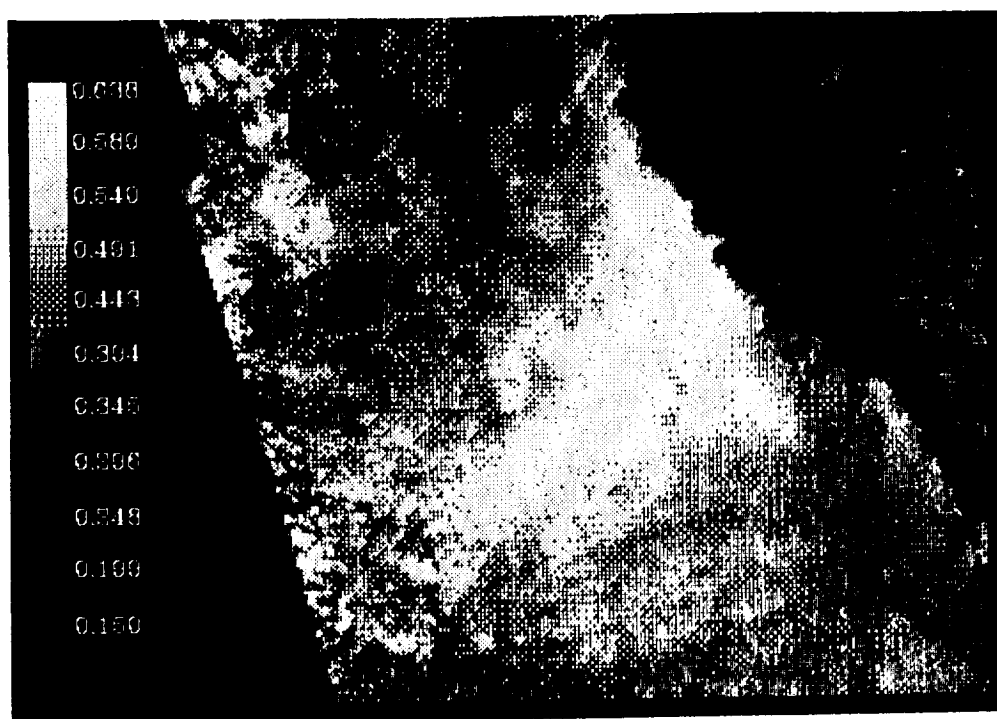


Fig. 3. Cloud reflectance from composited AVHRR Channel 1 ($0.63 \mu\text{m}$ wavelength) data for August 1986.

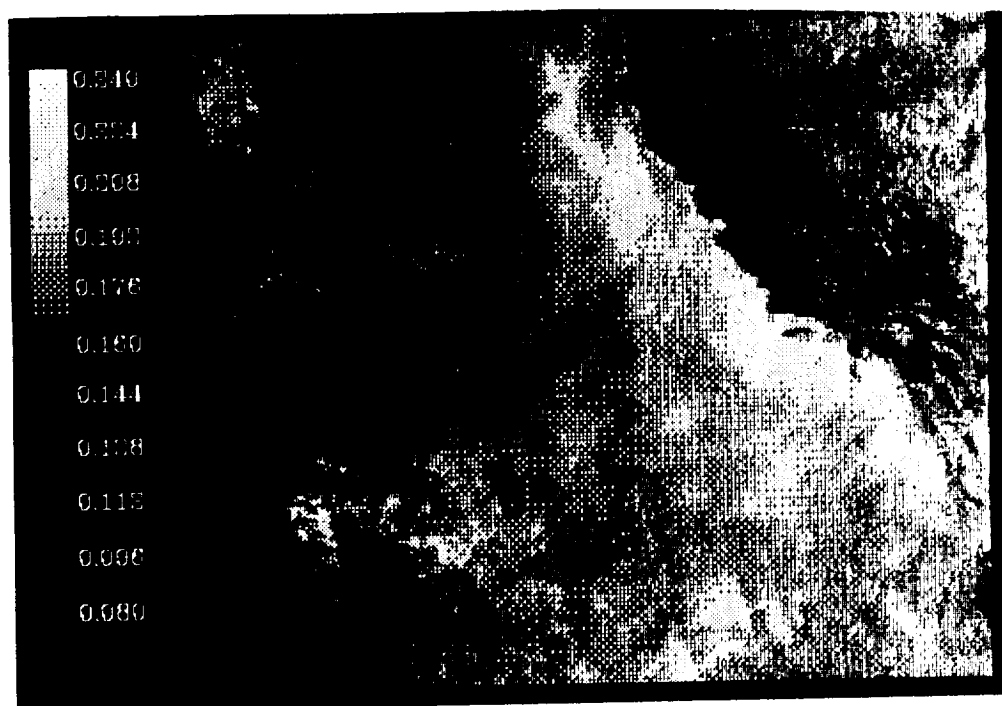


Fig. 4. Same as Fig. 3 but for AVHRR Channel 3 ($3.7 \mu\text{m}$ wavelength) data.

ORIGINAL PAGE IS
OF POOR QUALITY

Observations of Anthropogenic Cloud Condensation Nuclei

by James G. Hudson
Desert Research Institute
University of Nevada System
P.O. Box 60220
Reno, Nevada 89507

CCN concentrations and spectral measurements obtained with the DRI instantaneous CCN spectrometer (Hudson, 1989) over the last few years are presented. Recent articles by Wigley (1989), Schwartz (1988), Charleson et al (1987), Coakley et al (1987), and others have pointed out the climatic importance of cloud microphysics. The particles which affect cloud microphysics are cloud condensation nuclei (CCN). The commonly-observed order of magnitude difference in cloud droplet concentrations between maritime and continental air masses (i.e. Squires, 1958) was determined to be caused by systematic differences in the concentrations of CCN between continental and maritime air masses (e.g. Twomey and Wojciechowski, 1969).

Twomey (1977) first pointed out that cloud microphysics also affects the radiative properties of clouds. Thus continental and anthropogenic CCN could affect global temperature. Resolution of this "Twomey effect" requires answers to two questions 1) whether anthropogenic CCN are a significant contribution to atmospheric CCN and 2) whether they are actually affecting cloud microphysics to an extent which is of climatic importance. The reasons for the contrast between continental and maritime CCN concentrations are not understood. Ayers et al. (1982) measured the anthropogenic CN (total particle) production rate for Australia to be $1.4 \times 10^4 \text{ cm}^{-2} \text{ s}^{-1}$ over the entire continent. Thus even in this most sparsely populated continent the anthropogenic production of CN seemed to completely dominate natural CN production. The issue is far from resolved and the anthropogenic rate is at least a significant fraction of the natural rate.

The work presented here addresses the question of the relative importance of anthropogenic CCN. These observations should shed light on this complex question although further research is being conducted in order to produce more quantitative answers. Accompanying CN measurements made with a TSI 3020 condensation nucleus (CN) counter are also presented.

The first part of fig. 1 shows extremely low CCN concentrations obtained with light onshore winds along the California coast. This figure also shows a typical example of the immediate change to much higher CCN concentrations in urban areas. This seems to indicate that there is direct production of CCN with no intermediate coagulation processes needed in order to explain the existence of the CCN as the air would have spent only a few minutes over land. The higher concentrations shown in the second part of this figure were obtained throughout the city of Santa Cruz on untravelled residential streets as well as main highways. Fig. 2 shows a nearly simultaneous measurement obtained 10 km inland from the coast with only unpopulated and undeveloped land between. These results indicate that natural processes were not causing a change in the CCN concentration as

the air moved in from the coast over a period of about an hour. This again demonstrates the weakness of the natural source of CCN.

Fig. 3 shows one specific particle formation process which was observed on numerous occasions at various locations. The order of magnitude increase in CCN concentration was associated with the passage of a diesel powered vehicle. Fig. 4 shows another example of CCN production from a diesel or fuel oil engine; in this case a plume from a ship offshore from San Diego. This shows that ships indeed are a source of CCN as suggested by Conover (1966) and Coakley et al (1987).

Fig. 5 was obtained under conditions of offshore flow over the southern California area. In the rural areas of California throughout the Owens Valley and on into the Los Angeles basin the concentration of CCN was very low as shown in the early part of this figure. This is a concentration level which is more characteristic of maritime rather than continental air. However these low concentrations were measured over a very wide area and the air must have spent considerable time over the continent in this type of weather situation. As the vehicle moved into the Los Angeles basin through the Cajon pass much higher concentrations were encountered. From that point and to the west and south the CCN concentration was uniformly higher. Consistently high concentrations were detected with the 12 second data collection times which were used. Even though there was a continuous offshore flow of air (Santa Ana condition) the concentration within the basin was continuously maintained at high levels by the production of particles. This result seems to indicate that the concentration of CCN here is dominated by anthropogenic processes.

The aircraft measurement shown in fig. 6 shows an abrupt transition from maritime to continental air over the state of Washington. This order of magnitude change occurs over a horizontal distance of about 30 km at an altitude of about 3,300 m above sea level. This abrupt change which was observed several times is indicative of a rather strong continental source. This is more consistent with the anthropogenic sources which were observed at the surface rather than natural sources which were at best very weak. These higher concentrations were consistently measured over the North American continent except at low altitudes. A weak continental source ought to result in a more gradual transition to higher concentrations over the continent.

Fig. 7 shows an example where the CCN concentration seems to be proportional to the population within an air basin. These measurements were obtained from the vehicle as it was driven on U.S. highway 395 through Reno, Carson City, Minden, Gardnerville, and Topaz Lake on the California border. These measurements were obtained under stagnant weather conditions which held the air stationary for more than a day. This allowed particle concentrations to build up within each air basin. The highest concentrations were obtained in Reno which has the highest population and population density. The concentration showed an abrupt decrease upon entering the Carson City basin which is much less populated. The lowest concentrations are seen

in the least populated Topaz Lake basin. This certainly shows that the CCN concentration in these continental air basins is dominated by local anthropogenic processes.

The most important result of these measurements is that the production of CCN by anthropogenic processes is quite apparent but the natural continental source of CCN has still not been measured. If the increased CCN concentrations of continental air are due to anthropogenic processes then this could constitute a significant element of climatic change. Even if this were true for only the continental air and not at all for maritime air then this would constitute a significant climatic change even through the Twomey effect alone. However the continental aerosol may also influence maritime clouds. Prospero and Savoie (1989) show that much of the nitrate aerosol in the mid Pacific is of continental origin while a portion of the sulfate is also of continental origin (Savoie and Prospero, 1989). These results indicate that much of this continental component of CCN is probably of manmade origin. However further research is continuing to quantify this source.

- Ayers, G.P., E.K. Bigg, D.E. Turvey, and M.J. Manton, 1982: Urban influence on condensation nuclei over a continent. Atmos. Environ., 16, 951-954.
- Charlson, R.J., J.E. Lovelock, M.O. Andreae, and S.G. Warren, 1987: Oceanic phytoplankton, atmospheric sulphur, cloud albedo and climate, Nature, 326, 655-661.
- Coakley, J.A., Jr., R.L. Bernstein and P.A. Durkee, 1987: Effect of shipstack effluents on cloud reflectivity. Science, 237, 1020-1022.
- Conover, J.H., 1966: Anomalous cloud lines. J. Atmos. Sci., 23, 778-785.
- Hudson, J.G., 1989: An instantaneous CCN spectrometer. J. Atmos. & Ocean. Tech. Accepted for publication June 22, 1989.
- Prospero, J.M. and D.L. Savoie, 1989: Effect of continental sources on nitrate concentrations over the Pacific Ocean, Nature, 339, 687-689.
- Savoie, D.L. and J.M. Prospero, 1989: Comparison of oceanic sources of non-sea-salt sulphate over the Pacific Ocean, Nature, 339, 685-687.
- Schwartz, S.E., 1988: Are global cloud albedo and climate controlled by marine phytoplankton? Nature, 336, 441-445.
- Squires, P., 1958: The microstructure and colloidal stability of warm clouds, Part II - The causes of the variations in microstructure, Tellus, 10, 262-271.
- Squires, P., 1966: An estimate of the anthropogenic production of cloud nuclei, J. Rech. Atmos., 2, 297-307.
- Twomey, S., 1977: The influence of pollution on the shortwave albedo of clouds. J. Atmos. Sci., 34, 1149-1152.
- Twomey, S. and T.A. Wojciechowski, 1969: Observations of the geographical variations of cloud nuclei. J. Atmos. Sci., 26, 684-688.
- Wigley, T.M.L., 1989: Possible climate change due to SO₂-derived cloud condensation nuclei. Nature, 339, 365-367.

albedo of clouds. J. Atmos. Sci., 34, 1149-1152.

Twomey, S. and T.A. Wojciechowski, 1969: Observations of the geographical variations of cloud nuclei. J. Atmos. Sci., 26, 684-688.

Wigley, T.M.L., 1989: Possible climate change due to SO₂-derived cloud condensation nuclei. Nature, 339, 365-367.

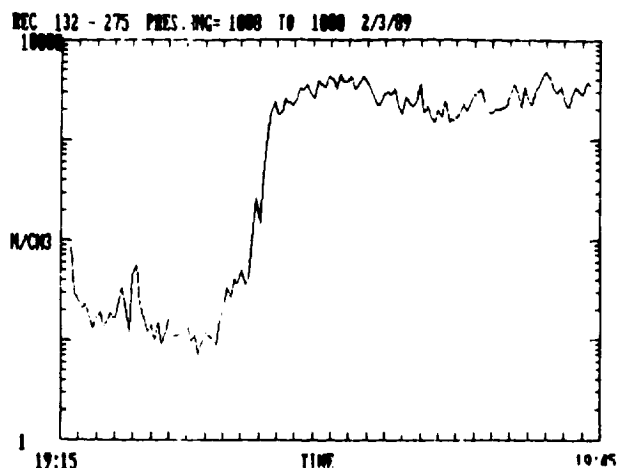


Fig. 1. CCN concentrations obtained while travelling on highway 1 near Santa Cruz, California.

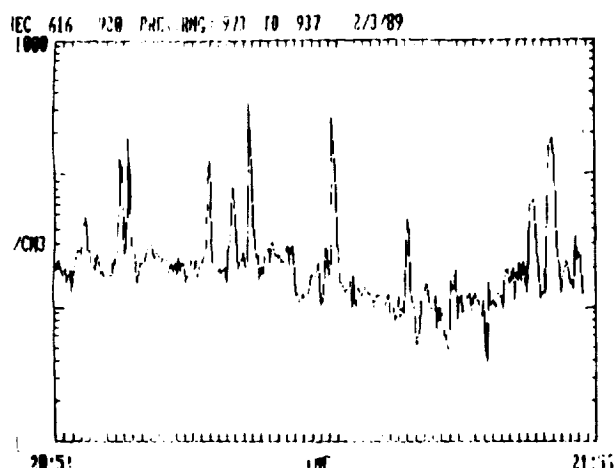


Fig. 2. CCN concentration obtained while driving through the Big Basin Redwood state park 10 miles inland from the coast north of Santa Cruz, California.

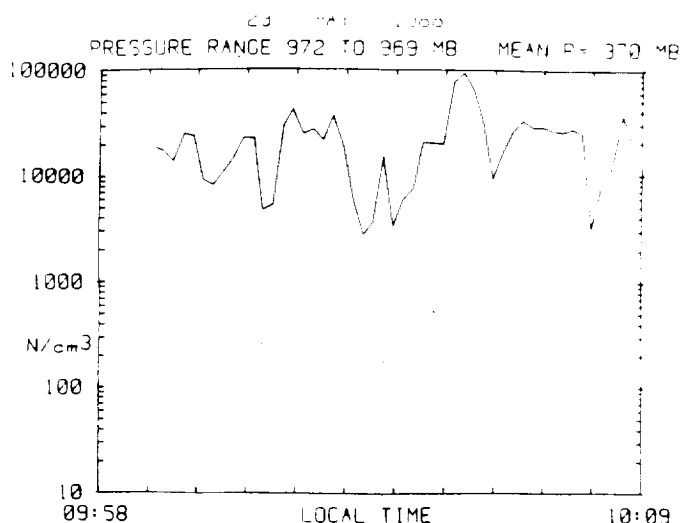


Fig. 3. CN (solid line) and CCN (dotted line) concentration on I-5 in Oregon. A diesel truck was encountered at 10:03.

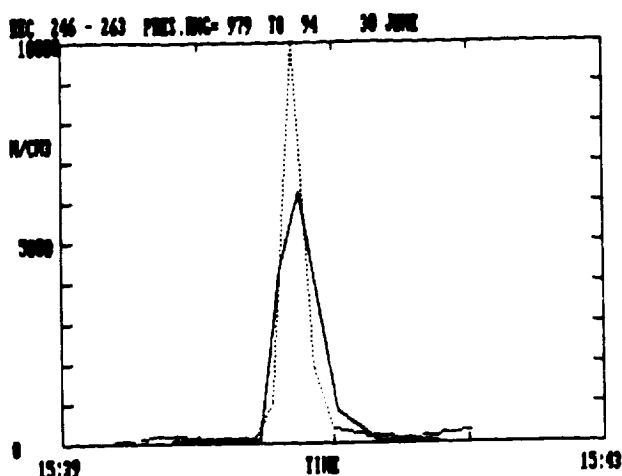


Fig. 4. CN (dotted line) and CCN (solid line) concentrations obtained while flying through a ship plume off the southern California coast.

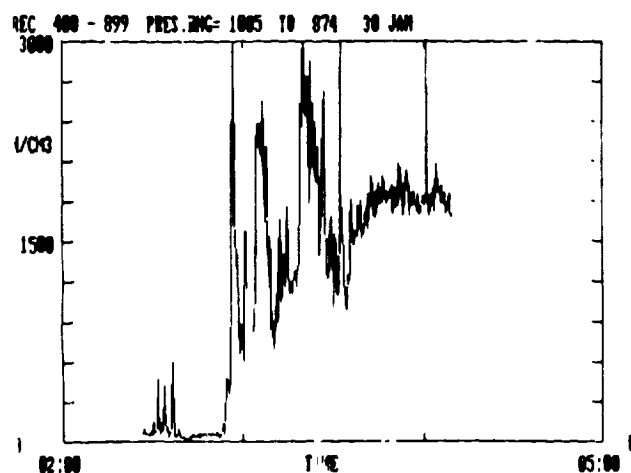


Fig. 5. Surface CCN concentration while driving into the Los Angeles basin. Most of these measurements were obtained while travelling on I-15. Passage through the Cajon Pass into Los Angeles occurred shortly before 0300. The final measurements were obtained in Anaheim, California. These measurements were obtained under Santa Ana wind conditions (offshore flow).

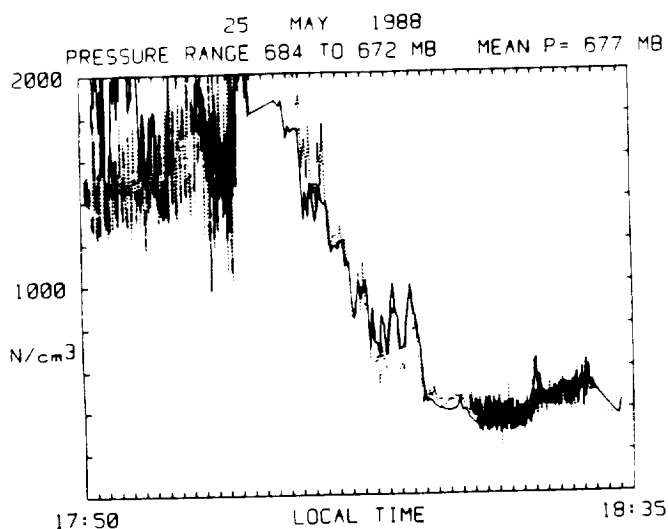


Fig. 6. CN (solid line) and CCN (dotted line) plotted against time during a flight over the state of Washington. This was a flight from Boise, Idaho which shows the transition from continental to maritime aerosol in the flight toward the west.

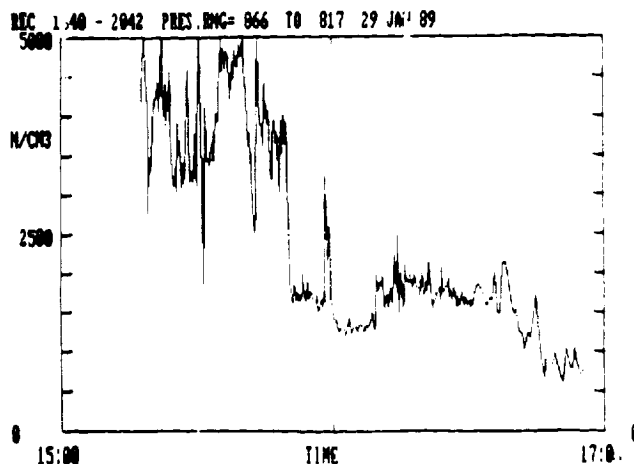


Fig. 7. CCN concentration obtained while travelling on U.S. 395 through western Nevada.

**DIRECT AND REMOTE SENSING OBSERVATIONS OF THE EFFECTS OF
SHIPS ON CLOUDS**

LAWRENCE F. RADKE AND PETER V. HOBBS

Department of Atmospheric Sciences, University of Washington, Seattle, WA 98195

JAMES A. COAKLEY JR.

Department of Atmospheric Sciences, Oregon State University, Corvallis, OR 97331

and

MICHAEL D. KING

Laboratory for Atmospheres, Goddard Space Flight Center, NASA, Greenbelt, MD 20771

Under certain conditions ships can affect the structure of shallow overlying layer clouds. It has been suggested that this is due to particles emitted from the ships, which increase the concentration of cloud condensation nuclei in the air, which, in turn, increases the concentrations of cloud droplets and reduces the average size of the droplets. Two ship track signatures in stratus clouds were observed simultaneously from a satellite and from an aircraft. The airborne measurements showed that in the "ship tracks" the droplet sizes and concentrations, as well as the total concentrations of particles, were substantially different from those in adjacent clouds. Furthermore, in situ solar radiation measurements showed a significant enhancement in the upwelling radiance within the ship tracks at visible wavelengths and a significant reduction in radiance at 2.2 micrometers. Remote sensing measurements from the NOAA-10 satellite showed the effects of these differences in cloud structure as an enhancement in cloud reflectivity at 0.63 and 3.7 micrometers. These observations support the contention that ship track signatures in clouds are produced primarily by particles generated by ships.

Optical Properties of Marine Stratocumulus Clouds Modified by Ship Track Effluents

MICHAEL D. KING AND TERUYUKI NAKAJIMA[†]

*Laboratory for Atmospheres, Goddard Space Flight Center, NASA,
Greenbelt, MD 20771, USA*

1. Introduction

The angular distribution of scattered radiation deep within a cloud layer was measured in marine stratocumulus clouds modified by the emissions from ships. These observations, obtained at thirteen discrete wavelengths between 0.5 and 2.3 μm , were obtained as the University of Washington Convair C-131A aircraft flew through a pair of roughly parallel ship tracks off the coast of southern California on 10 July 1987.

In the first of these ship tracks, the cloud droplet concentration increased from 40 cm^{-3} to 107 cm^{-3} (125 cm^{-3} in the second ship track). Simultaneous to this spectacular change, the aircraft measured interstitial aerosol (Aitken nucleus) concentration that increased from 400 cm^{-3} to 1000 cm^{-3} and cloud liquid water content that increased from 0.30 g m^{-3} to 0.75 g m^{-3} . Broadband pyranometer measurements showed that the upwelling flux density increased from 150 W m^{-2} to 280 W m^{-2} . These *in situ* microphysics and broadband pyranometer results, together with AVHRR satellite images obtained with the NOAA-10 satellite, are described in detail by Radke et al. (1989).

In this paper, we present internal scattered radiation measurements at selected wavelengths obtained with the cloud absorption radiometer (King et al. 1986) for a 100 km section of marine stratocumulus clouds containing these two ship track features.

2. Results from observations on 10 July 1987

On 10 July 1987 the C-131A was flying within a marine stratocumulus cloud layer enroute to a planned mission with the ER-2 aircraft when it encountered two regions approximately 17 km in width that were apparently modified by the effluents from ships. The C-131A was primarily making cloud radiation and cloud microphysics measurements deep within the cloud layer, which was located ~300 km from the airfield on Coronado Island, San Diego.

[†] Permanent affiliation: Upper Atmosphere and Space Research Laboratory, Faculty of Science, Tohoku University, Sendai 980, Japan.

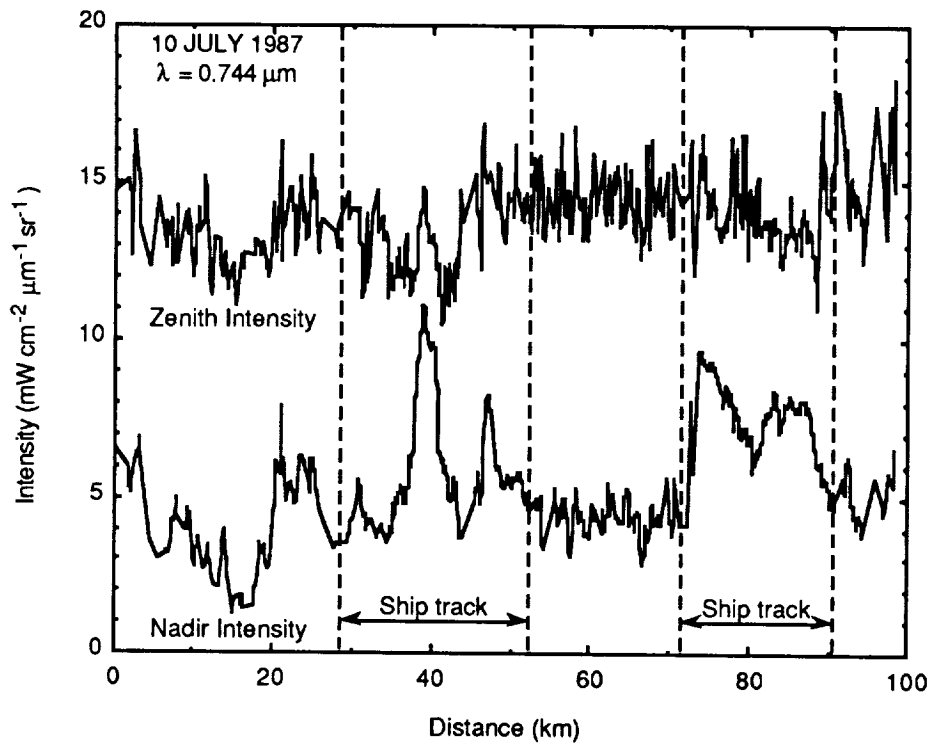


Fig. 1. Zenith and nadir intensities as a function of distance for measurements obtained inside the clouds between 8:49 and 9:10 PDT. These measurements were obtained at a wavelength $\lambda = 0.744 \mu\text{m}$.

Figures 1 and 2 illustrate the zenith and nadir intensities as a function of distance (time) for measurements obtained inside clouds for a 100 km section of this cloud. These data, corresponding to observations obtained with the cloud absorption radiometer at 0.744 and 2.20 μm , respectively, show that the zenith and nadir intensities were substantially modified by the effluents from the ships. At $\lambda = 0.744 \mu\text{m}$ (Fig. 1), the upwelling (nadir) intensity increased from approximately 4 to 11 $\text{mW cm}^{-2} \mu\text{m}^{-1} \text{sr}^{-1}$ in the first ship track, with a somewhat less dramatic, though more uniform, increase in the second ship track. The downwelling (zenith) intensity, on the other hand, showed a modest decrease in both ship tracks. These changes are consistent with the fact that the total optical thickness of the cloud layer increased, and are a direct consequence of the observation that the total concentration and concentration of small droplets increased, while the mean droplet radius decreased. In fact, Radke et al. (1989) estimate, based on these microphysical changes, that the total optical thickness of the cloud layer increased by a factor of ~ 2.6 in the first ship track (2.1 in the second ship track).

At $\lambda = 2.20 \mu\text{m}$ (Fig. 2), both the upwelling (nadir) and downwelling (zenith) intensities decreased within the ship tracks. Again, the change is the most dramatic and the least uniform in the first ship track. The explanation for these changes can be understood as follows. As the optical thickness in-

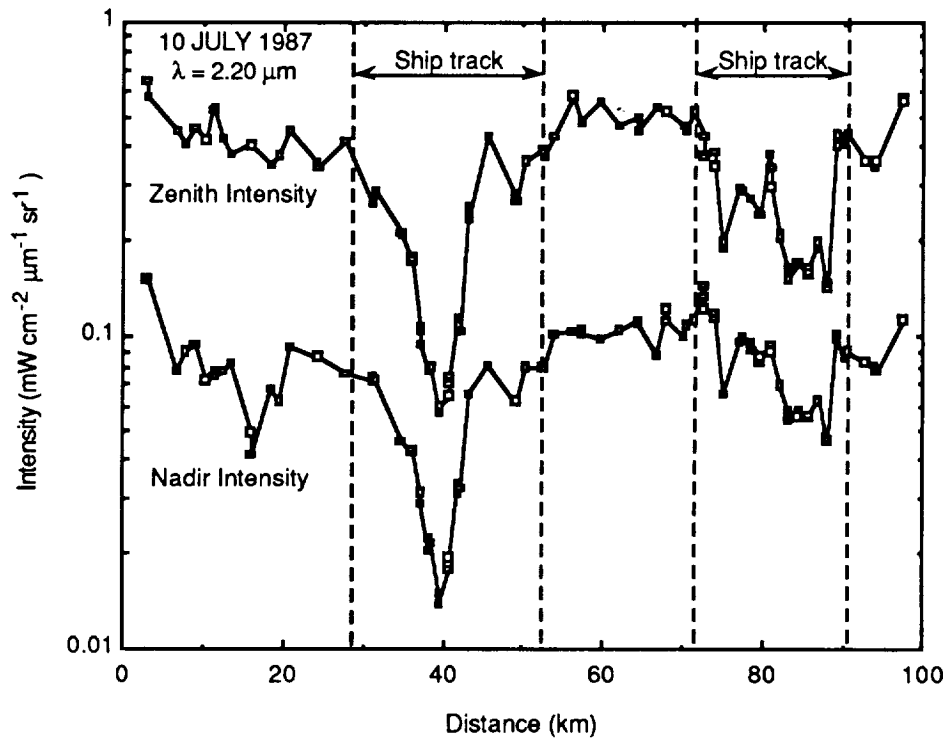


Fig. 2. As in Fig. 1 except for $\lambda = 2.20 \mu\text{m}$.

creases, the additional scattering leads to increased attenuation of solar radiation at this absorbing wavelength. The intensity distribution is thus reduced in all directions within the cloud. This is not the case for reflected solar radiation, on the other hand, since increasing the optical thickness will always lead to increasing the reflection function at all wavelengths.

Figures 1 and 2 represent dramatically different similarity parameters, and hence single scattering albedos, within the cloud (cf. King et al. 1989). At $\lambda = 0.744 \mu\text{m}$ the single scattering albedo $\omega_0 \sim 1.0$, whereas at $\lambda = 2.20 \mu\text{m}$ $\omega_0 \sim 0.99$. In order to examine the transition of the zenith and nadir intensities as the single scattering albedo, and hence wavelength, varies, we have examined the nadir intensity (Fig. 3) and zenith intensity (Fig. 4) as a function of distance for selected wavelengths between 0.744 and $2.20 \mu\text{m}$. The curves for 0.744 and $2.20 \mu\text{m}$ are the same as those presented in Figs. 1 and 2. For the zenith intensity (Fig. 3), the transition from an enhanced intensity at $0.744 \mu\text{m}$ to a reduced intensity at $2.20 \mu\text{m}$ is striking. At some wavelength between 1.20 and $1.64 \mu\text{m}$, these results suggest that the changes in the optical properties of the cloud resulting from ship track effluents would be imperceptible. The broadband pyranometer measurements, which integrate over all angles and the entire solar spectrum, follow very closely the changes at $0.744 \mu\text{m}$ (cf. Radke et al. 1989).

For the zenith (downwelling) intensity, illustrated in Fig. 4, the intensity decreases at all wavelengths, though the reduction at $0.744 \mu\text{m}$ is extremely

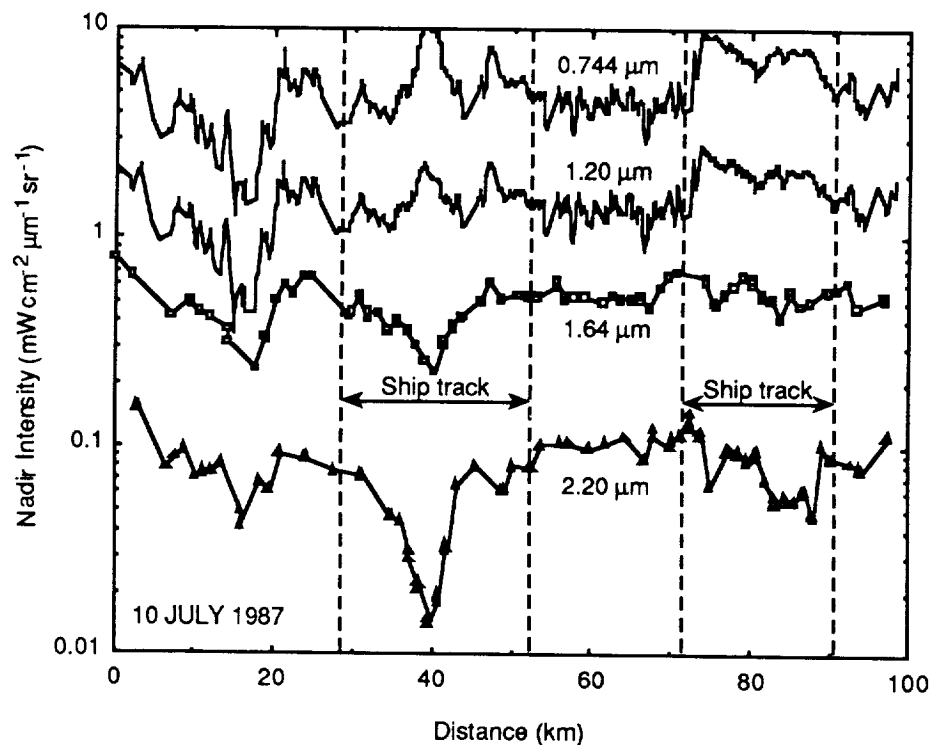


Fig. 3. Nadir (upwelling) intensities as a function of distance for measurements obtained inside the clouds between 8:49 and 9:10 PDT. These measurements were obtained at selected wavelengths between 0.744 and 2.20 μm .

small, as noted above (cf. Fig. 1). The effects of increasing absorption (wavelength) are quite apparent in this figure. The broadband pyranometer, which again reflects primarily the measurement at nonabsorbing wavelengths near 0.744 μm , showed that the zenith (downwelling) flux density is virtually unchanged in the ship tracks, as expected from an examination of Fig. 4.

Though the major changes in the internal scattered radiation field within the ship track events of these marine stratocumulus clouds can be explained by changes in cloud optical thickness, both above and below the aircraft, it is conceivable that soot particulates from the ship exhaust could also affect the spectral intensity field within the clouds. In fact, one would expect that, in addition to increasing optical thickness by the emission of cloud condensation nuclei, the ship exhaust might lead to increased absorption by the cloud droplets. Two competing effects are possible: 1) increasing absorption from aerosols, either as a result of dirty water or interstitial aerosol; or 2) decreasing absorption because the cloud droplets are smaller. Our initial analysis, based on the diffusion domain method of King et al. (1989), shows that the latter effect dominates. In the first ship track the effective radius computed from the in situ cloud droplet size distribution decreases from 12.5 to 10.5 μm , and in the second ship track from 11.2 to 7.5 μm (Radke et al. 1989).

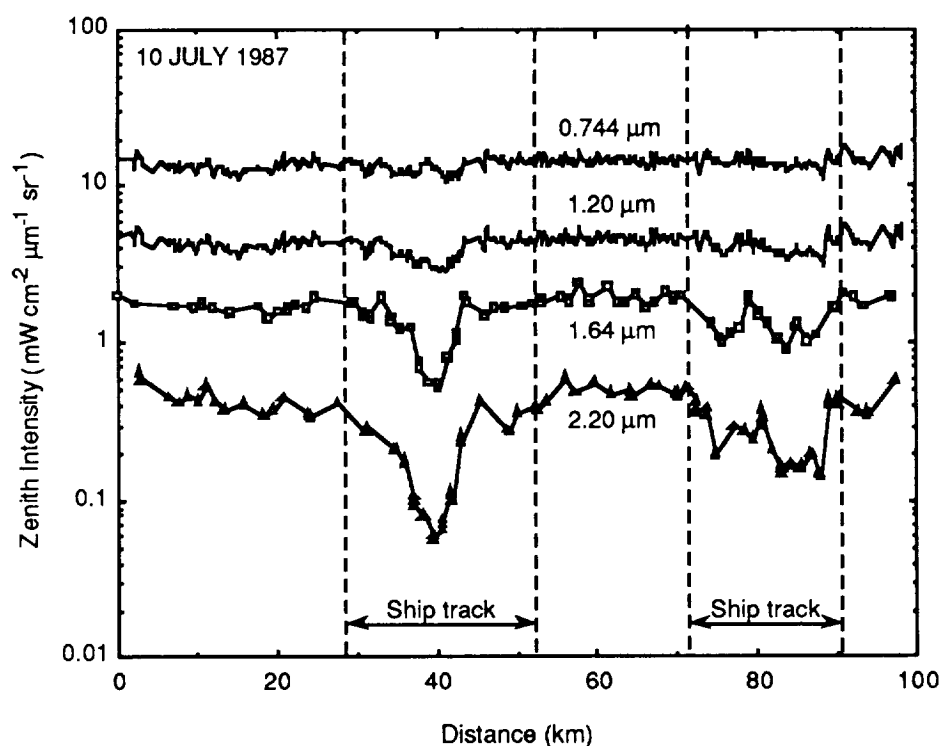


Fig. 4. As in Fig. 3 except for zenith (downwelling) intensities.

REFERENCES

- King, M. D., M. G. Strange, P. Leone and L. R. Blaine, 1986: Multiwavelength scanning radiometer for airborne measurements of scattered radiation within clouds. *J. Atmos. Oceanic Tech.*, **3**, 513-522.
- _____, L. F. Radke and P. V. Hobbs, 1989: Determination of the spectral absorption of solar radiation by marine stratocumulus clouds from airborne measurements within clouds. Submitted to *J. Atmos. Sci.*
- Radke, L. F., J. A. Coakley, Jr. and M. D. King, 1989: Direct and remote sensing observations of the effects of ships on clouds. Submitted to *Science*.

	PAGE
M06.01 A Unified View of Convective Transports by Stratocumulus Clouds, Shallow Cumulus Clouds, and Deep Convection Randall, David A.	173
M06.02 STRATUS: An Interactive Steady State Mixed Layer Model for Personal Computers Guinn, Thomas A., and Wayne H. Schubert	179
M06.03 A Case Study of Cumulus Formation Beneath a Stratocumulus Sheet: Its Structure and Effect on Boundary Layer Budgets <u>Barlow, R. W.</u> , and S. Nicholls (deceased)	185
M06.04 Verification of the Naval Oceanic Vertical Aerosol Model During FIRE Davidson, K. L., <u>G. de Leeuw</u> , S. G. Gathman, and D. R. Jensen	191
M06.05 Modification of the Background Flow by Roll Vortices <u>Shirer, Hampton N.</u> , and Tracy Haack	197
M06.06 A Cloudiness Transition in a Marine Boundary Layer Betts, Alan K., and Reinout Boers	203
M06.07 Analysis of Marine Stratocumulus Clearing Events During FIRE Kloesel, Kevin A.	211
M06.08 FIRE Aircraft Observations of Horizontal and Vertical Transport in Marine Stratocumulus Paluch, Ilga R., and <u>Donald H. Lenschow</u>	213
M06.09 Vertical-Velocity Skewness in the Marine Stratus-Topped Boundary Layer <u>Moeng, Chin-Hoh</u> , Richard Rotunno, and Ilga Paluch	219
M06.10 Laboratory Experiments on Stability and Entrainment of Oceanic Stratocumulus-- Part I: Instability Experiment Shy, Shenqyang S.	225

*Paper to be presented in the
Marine Stratocumulus Large-Scale Environment and Modeling Session*

A UNIFIED VIEW OF CONVECTIVE TRANSPORTS BY STRATOCUMULUS CLOUDS, SHALLOW CUMULUS CLOUDS, AND DEEP CONVECTION

David A. Randall

Department of Atmospheric Science
Colorado State University
Fort Collins, Colorado 80523

1. Introduction

We have developed a bulk PBL model with a simple internal vertical structure and a simple second-order closure, designed for use as a PBL parameterization in a large-scale model. The model allows the mean fields to vary with height within the PBL, and so must address the vertical profiles of the turbulent fluxes, going beyond the usual "mixed-layer" assumption that the fluxes of conservative variables are linear with height. This is accomplished using the same convective mass flux approach that has also been used in cumulus parameterizations. The purpose of this brief paper is to show that such a mass flux model can include, in a single framework, the "compensating subsidence" concept, downgradient mixing, and well-mixed layers.

2. Generalized mass flux model

The "convective mass flux" concept introduced by Arakawa has been used in a variety of modeling and observational studies, most directed either at deep cumulus convection or at stratocumulus convection; the connections between the two applications have not been made previously.

For an ascending region with fractional area σ , the conservation equations for mass and an arbitrary scalar ψ can be written as

$$\frac{\partial}{\partial t}(\rho\sigma) = -\sigma\nabla \cdot (\rho\bar{\mathbf{V}}) + \rho(\mu - \nu) - \rho \frac{\partial}{\partial p}(\omega_u\sigma), \quad (2.1)$$

$$\begin{aligned} \frac{\partial}{\partial t}(\rho\sigma\psi_u) = & -\sigma\left\{\nabla \cdot (\rho\bar{\mathbf{V}}\psi) + \nabla \cdot [\rho\bar{\mathbf{V}}(\psi_u - \bar{\psi})]\right\} + \rho(\mu\psi_u - \nu\psi_u) \\ & - \rho \frac{\partial}{\partial p}(\omega_u\sigma\psi_u) - \rho\tau_{ds}^{-1}\sigma(\psi_u - \bar{\psi}) + \rho\sigma\left[g\frac{\partial f_{v,u}}{\partial p} + S_{v,u}\right], \end{aligned}$$

(2.2)
for the ascending parcels. Similar equations can be written for the descending regions. Here the generic variable ψ represents an intensive thermodynamic variable such as the potential temperature or the mixing ratio of water. Other notation is as follows: ρ is the density; \mathbf{V} is the horizontal velocity vector; $\omega = -\rho g w$, where w is the vertical velocity, and g is the acceleration of gravity; and p is pressure. The air entering rising parcels has been assumed to have the average properties of the sinking parcels, and vice versa. Area averages satisfy

$$\overline{(\quad)} = (\quad)_u \sigma + (\quad)_d (1 - \sigma), \quad (2.3)$$

where an overbar denotes an area average (over a grid box, say); this notation will be used only where necessary to avoid confusion. Subscripts u and d denote upward and downward moving parcels, respectively. We can interpret μ^{-1} and ν^{-1} as time scales for mass flow from downdrafts into updrafts, and from updrafts into downdrafts, respectively. The vertical turbulent flux of ψ due to small eddies is denoted by f_ψ . The small-eddy fluxes are logically necessary near the top and bottom of the PBL, where the organized vertical motions associated with the convective circulations must vanish. The time scale for destruction of the convective circulations by lateral mixing due to smaller-scale turbulence is τ_{dis} . The source of ψ per unit mass per unit time is denoted by S_ψ . This could represent, for example, the effects of radiation.

From (2.1) and (2.2) and the corresponding "downdraft" equations, and using (2.3), we can recover the area-averaged conservation equations for mass and ψ :

$$\frac{\partial}{\partial t} \rho = -\nabla \cdot (\rho \bar{\mathbf{V}}) - \rho \frac{\partial \bar{\omega}}{\partial p}, \quad (2.4)$$

$$\frac{\partial}{\partial t} (\rho \bar{\psi}) = -\nabla \cdot (\rho \bar{\mathbf{V}} \bar{\psi}) - \rho \frac{\partial}{\partial p} [\bar{\omega} \bar{\psi} - g(F_\psi + f_\psi)] + \rho \bar{S}_\psi. \quad (2.5)$$

Naturally, all terms involving μ , ν , and τ_{dis} have dropped out of (2.4-5). In (2.5), the turbulent fluxes associated with the convective circulations are represented by

$$\begin{aligned} g \mathcal{F}_\psi &= -\overline{\omega \psi'} = -[(\omega_u - \bar{\omega})(\psi_u - \bar{\psi})\sigma + (\omega_d - \bar{\omega})(\psi_d - \bar{\psi})(1 - \sigma)] \\ &= -\omega_* (\psi_u - \psi_d), \end{aligned} \quad (2.6)$$

where

$$\omega_* \equiv \sigma(1 - \sigma)(\omega_u - \omega_d) \quad (2.7)$$

is a convective mass flux, which has been defined in such a way that it is less than or equal to zero. The total turbulent flux of ψ is $F_\psi = \mathcal{F}_\psi + f_\psi$.

From the "updraft" mass conservation equation (2.1) and the corresponding "downdraft" equation, we can derive an expression for $\partial\sigma/\partial t$

$$\frac{\partial\sigma}{\partial t} + \bar{\omega} \frac{\partial}{\partial p} \sigma + \frac{\partial}{\partial p} \omega_* = \mu - \nu. \quad (2.8)$$

By neglecting the local time rate of change and large-scale advection terms, we can simplify (2.8) to a more recognizable form:

$$\partial\omega_*/\partial p = \mu - \nu. \quad (2.9)$$

According to (2.9), the vertical distribution of ω_* is closely related to the profiles of μ and ν .

We can also derive the conservation equation for the *variance of ψ* that is associated with the convective circulations:

$$\begin{aligned} \frac{\partial}{\partial p} [\omega_*(1-2\sigma)(\psi_u - \psi_d)] = & 2g\mathcal{F}_\psi \frac{\partial \bar{\psi}}{\partial p} - [(\mu + \nu) - 2A\omega_*/\delta p_M](\psi_u - \psi_d)^2 \\ & + 2(\psi_u - \psi_d)Z_\psi, \end{aligned} \quad (2.10)$$

where

$$Z_\psi = \sigma(1-\sigma) \left[g \frac{\partial}{\partial p} (f_{\psi,u} - f_{\psi,d}) + (S_{\psi,u} - S_{\psi,d}) \right]. \quad (2.11)$$

In (2.10), we have neglected the local time-rate-of-change and large-scale advection terms, although we use them in our numerical model. According to (2.12), transport balances the combined effects of dissipation and production. Using conventional Reynolds averaging, we find corresponding to (2.10) that

$$\frac{\partial}{\partial p} (\overline{\omega'\psi'^2}) = 2 \left[-\overline{\mathbf{V}'\psi'} \cdot \nabla \bar{\psi} + gF_\psi \frac{\partial \bar{\psi}}{\partial p} - \epsilon_\psi + \overline{\psi'S'_\psi} \right] \quad (2.12)$$

Here ϵ_ψ is the molecular dissipation rate. Comparison of (2.10) with (2.12) reveals a term-by-term correspondence. Note that, in (2.10), the sign of the triple correlation is determined by the value of σ . Variance is transported upward for $\sigma < 1/2$, and downward for $\sigma > 1/2$.

The damping factor $\sigma(1-\sigma) \tau_{\text{dis}}^{-1}$, which appears in (2.10), can be simplified by noting that small eddies will be most effective at reducing the differences between the ascending and descending branches of the plumes when one of the two branches is much narrower than the other, and least effective when the two branches have the same width. On this basis, we assume that $T_{\text{dis}}^{-1} \equiv \sigma(1-\sigma) \tau_{\text{dis}}^{-1}$ is independent of σ . We also adopt the definition $(T_{\text{dis}})^{-1} \equiv -A \omega_*/\delta p_M$, where A is positive and nondimensional. This is motivated by the idea that the capacity of small eddies to dissipate the convective circulations by lateral diffusion increases as ω_* increases, and as the PBL depth decreases, so that A should be less variable than T_{dis} .

Assuming that the inflow and outflow layers do not overlap, we can eliminate μ and v in (2.12), to obtain

$$\mathcal{F}_v X - (1 - 2\sigma) \frac{\partial \mathcal{F}_v}{\partial p} = -g^{-1} \left(\omega_* \frac{\partial \bar{\psi}}{\partial p} + Z_v \right), \quad (2.13)$$

where

$$X \equiv \frac{\partial \sigma}{\partial p} + (1 - \sigma - \delta) \omega_*^{-1} \frac{\partial \omega_*}{\partial p} + \frac{A}{\delta p_M}. \quad (2.14)$$

$$\delta = \begin{cases} 1, & \text{for } \frac{\partial \omega_*}{\partial p} > 0 \quad (\text{inflow}) \\ 0, & \text{for } \frac{\partial \omega_*}{\partial p} \leq 0 \quad (\text{outflow}). \end{cases} \quad (2.15)$$

The ω_* term of (2.14) is never negative, so it contributes to X in the same sense as the positive A term. It follows that $X \geq 0$ unless σ increases strongly upward. The ω_* and A terms of (2.14) both arise from dissipative processes. The $\partial \sigma / \partial p$ term of (2.14) arises from the transport term of (2.10).

3. Discussion

Several conclusions can be drawn from (2.13-14), by considering the case $S_v = 0$, so that $Z_v = 0$.

First, if $(1 - 2\sigma)/X$ is small (σ near $1/2$ and strong dissipation), we get

$$\mathcal{F}_v \equiv -\frac{\omega_*}{gX} \frac{\partial \bar{\psi}}{\partial p}. \quad (3.1)$$

This is a downgradient diffusion formula, with diffusion coefficient $-\omega_*/(gX)$.

Next, consider a layer that is well-mixed in several conservative variables ψ_1, ψ_2 , etc. In order to satisfy (2.13) simultaneously for all of the variables we must take

$$X = 0, \quad (3.2)$$

$$\sigma = 1/2. \quad (3.3)$$

Since, according to (3.3), σ is a constant, (2.14) implies that X is the sum of two non-negative terms. Then (3.2) implies that each term must be zero, so that

$$\omega_* = \text{constant}, \quad (3.4)$$

$$A = 0. \quad (3.5)$$

Referring back to (2.10), we find a trivial balance in which gradient production, transport, and dissipation are all zero. (When $\sigma = 1/2$, the variance transport by triple correlations vanishes.)

Finally, suppose that X is small (weak dissipation), and that σ is small. Then (2.14) reduces to

$$\frac{\partial \mathcal{J}_\psi}{\partial p} \equiv \frac{\omega_*}{g} \frac{\partial \bar{\psi}}{\partial p}. \quad (3.6)$$

This balance is characteristic of the temperature and moisture budgets of tropical cumulus layers, in which "compensating subsidence" produces the convective effects on the mean profiles. Arakawa (1969) derived (3.6); it has also been discussed by Ooyama, among others. [The "detrainment" term included in cumulus parameterization theories is also present in (2.13-14); it arises from the gradient of ω_* in (2.14).]

For the cumulus regime, the conservation equation for $\bar{\psi}$ can often be approximated by a balance between vertical advection and convective transport, i.e.

$$\frac{\partial \mathcal{J}_\psi}{\partial p} \equiv \frac{\bar{\omega}}{g} \frac{\partial \bar{\psi}}{\partial p}. \quad (3.7)$$

Comparing (3.6) and (3.7), we find that

$$\sigma = (1 - \omega_*/\bar{\omega})/2. \quad (3.8)$$

For tropical cumulus layers with large-scale rising motion, $\omega_* \equiv \bar{\omega}$, so that (3.8) is consistent with observations that show $\sigma \ll 1$. For the case of large-scale sinking motion, (3.8) predicts larger values of σ , again in qualitative agreement with observations.

These results show that (2.14-15) are consistent with a variety of observed balances in convective layers. They provide a dynamical interpolation between the "compensating subsidence" and "mixing length" regimes.

ACKNOWLEDGEMENTS

References have been made informally to save space. Support for this research was provided by NASA's Climate Program under Grant NAG-1-893, and by the Office of Naval Research under Contract N00014-89-J-1364.

STRATUS: AN INTERACTIVE STEADY STATE MIXED LAYER MODEL FOR PERSONAL COMPUTERS

Thomas A. Guinn and Wayne H. Schubert

Department of Atmospheric Science, Colorado State University, Fort Collins, CO 80523

1. INTRODUCTION

We present here a steady-state, horizontally homogeneous, cloud-topped marine boundary layer model based primarily on the work of Lilly (1968) and Schubert et al. (1979). The conservative thermodynamic variables are equivalent potential temperature θ_e and total water mixing ratio $q + \ell$. Some of the differences between this and Lilly's (1968) model are: (1) radiation is allowed to penetrate into the boundary layer; (2) cloud top values of longwave radiation, equivalent potential temperature, and water vapor mixing ratio are linear functions of height derived from climatological data at California coastal stations; (3) the closure assumption assumes a weighted average of Lilly's (1968) maximum and minimum entrainment theories. This model has been programmed in FORTRAN and will run interactively on an IBM-compatible personal computer. The program allows the user to specify the geographical location, the wind speed, the sea-surface temperature, the large scale horizontal divergence, and the initial guess for cloud top height. Output includes the steady state values of cloud top and cloud base height, mixed layer equivalent potential temperature and total water mixing ratio, and the associated convective and radiative fluxes. The notation used throughout this abstract is that of Lilly with the exception that the subscript U replaces UH .

2. RADIATION PARAMETERIZATION

Since longwave cooling off cloud top is the important driving mechanism in the cloud-topped marine boundary layer, the radiation parameterization warrants a detailed description. We follow the philosophy that, consistent with the limitation of the vertical thermodynamic structure to two degrees of freedom, the vertical resolution of the radiative cooling should also be limited to two degrees of freedom. This means radiation can appear at most in the mixed layer thermal budget equation, and the cloud top jump condition. This is slightly more general than Lilly's restriction of the radiative cooling to the cloud top jump condition. Thus, we write the equations for the changes in radiative fluxes across cloud top and across the mixed layer as

$$F_U - F_H = (\rho c_p)^{-1} \left\{ (1 - \mu)(\sigma T_H^4 - \mathcal{L}_U^\downarrow) - (1 - \mu')\mathcal{S} \right\}, \quad (1)$$

and

$$F_H - F_S = (\rho c_p)^{-1} \left\{ \mu(\sigma T_H^4 - \mathcal{L}_U^\downarrow) - \mu'\mathcal{S} \right\}, \quad (2)$$

where ρ is the constant air density, σ is the Stefan-Boltzmann constant, T_H is the cloud top temperature in Kelvin, \mathcal{L}_U^\downarrow is the downward longwave radiative flux attributed to that portion of the atmosphere which lies above the mixed layer, \mathcal{S} is the absorbed broadband

shortwave radiative flux, and μ and μ' are the longwave and shortwave radiation partitions respectively. These partitions can take on values from zero to one. If both are set to zero, the radiation parameterization reduces to Lilly's case. Here and in the following sections the subscript U will refer to those properties of the upper air just above cloud top, the subscript H will refer to those properties just below cloud top, the subscript S will refer to those properties at the surface, and the subscript 0 will refer to those properties at some small height above the surface (typically taken to be 10 m). For this model, the downward longwave radiative flux term in (1) and (2) is expressed as a linear function of cloud top height. The function was derived based on the July average sounding data for the five years 1976–1980 as extracted from the *U.S. Dept. of Commerce Climatological Data, National Summary*. Two California locations were used, San Diego and Oakland. The sounding data combined with the midlatitude ozone profile as taken from the *U.S. Standard Atmosphere Table, 1976* and a uniform carbon dioxide profile of 0.501 g kg^{-1} was input into a broadband longwave radiation model written by Cox (1973). The model output was used to calculate the required linear relationships for the two locations. The resulting equations are given by

$$\mathcal{L}_U^\downarrow = \begin{cases} 314.0 + 0.03077H & \text{for Oakland,} \\ 333.1 + 0.32360H & \text{for San Diego,} \end{cases} \quad (3)$$

where the units for \mathcal{L}_U^\downarrow and H are Wm^{-2} and m respectively. The value of the absorbed solar radiation is that suggested by Lilly (1968), i.e. $S = 22.3 \text{ Wm}^{-2}$.

To calculate T_H , we start with the equation for potential temperature at cloud top (θ_H). The potential temperature at cloud top is equal to the potential temperature at cloud base (θ_h) plus the change that occurs when following a moist adiabat from cloud base to cloud top, i.e.

$$\theta_H = \theta_h + \frac{b}{a} \left(\frac{\alpha}{1 + \alpha} \right) (H - h). \quad (4)$$

In addition, θ_h can be calculated from our conservative thermodynamic variables by use of the definition of θ_e , i.e.

$$\theta_h = \theta_e - \frac{L}{c_p}(q + \ell). \quad (5)$$

To obtain the expression for the temperature at cloud top (T_H), we use both Poisson's equation and the integrated hydrostatic equation in potential temperature form. The resulting expression is

$$T_H = \left[\theta_h + \frac{b}{a} \left(\frac{\alpha}{1 + \alpha} \right) (H - h) \right] \left(\frac{p_H}{p_0} \right)^\kappa, \quad (6)$$

where p_H is determined hydrostatically from H .

3. THE COMBINED CONVECTIVE-RADIATIVE MODEL

With the discussion of the radiation parameterization completed, we can now write the combined convective-radiative model. The model equations, which are listed below, consist of two surface flux equations, the cloud base equation, the cloud top jump definitions, the cloud top temperature equation, the radiation equations, the consistency relation, the entrainment assumption, the mixed layer equivalent potential temperature and total water budget equations, and the cloud top jump condition on equivalent potential temperature.

These thirteen equations form a closed set in the thirteen unknowns H , h , θ_e , $(q + \ell)$, $\Delta\theta_e$, $\Delta(q + \ell)$, T_H , $(F_U - F_H)$, $(F_H - F_S)$, $(\overline{w'\theta'_e})_0$, $\overline{w'(q' + \ell')}_0$, $(\overline{w'\theta'_e})_H$, and $\overline{w'(q' + \ell')}_H$.

$$(\overline{w'\theta'_e})_0 = C_T V (\theta_{eS} - \theta_e) \quad (7)$$

$$\overline{w'(q' + \ell')}_0 = C_T V [q_S - (q + \ell)] \quad (8)$$

$$h = \frac{(1 + \alpha)(q_S - q_0) - a(\theta_{eS} - \theta_e)}{b} \quad (9)$$

$$\Delta\theta_e = \theta_{eU} - \theta_e \quad (10)$$

$$\Delta(q + \ell) = q_U - (q + \ell) \quad (11)$$

$$T_H = \left[\theta_h + \frac{b}{a} \left(\frac{\alpha}{1 + \alpha} \right) (H - h) \right] \left(\frac{p_H}{p_0} \right)^\kappa, \quad (12)$$

$$F_U - F_H = (\rho c_p)^{-1} \left\{ (1 - \mu)(\sigma T_H^4 - \mathcal{L}_U^\downarrow) - (1 - \mu')\mathcal{S} \right\}, \quad (13)$$

$$F_H - F_S = (\rho c_p)^{-1} \left\{ \mu(\sigma T_H^4 - \mathcal{L}_U^\downarrow) - \mu'\mathcal{S} \right\}, \quad (14)$$

$$\begin{bmatrix} a_{11} & a_{12} \\ a_{21} & a_{22} \end{bmatrix} \begin{bmatrix} \frac{(\overline{w'\theta'_e})_H}{\theta} \\ \frac{\overline{w'(q' + \ell')}_H}{\theta} \end{bmatrix} = \begin{bmatrix} b_1 \\ b_2 \end{bmatrix} \quad (15, 16)$$

$$\frac{\partial\theta_e}{\partial t} = \frac{(\overline{w'\theta'_e})_0 - (\overline{w'\theta'_e})_H - (F_H - F_S)}{H} \quad (17)$$

$$\frac{\partial(q + \ell)}{\partial t} = \frac{(\overline{w'q'})_0 - \overline{w'(q' + \ell')}_H}{H} \quad (18)$$

$$\frac{\partial H}{\partial t} = \frac{F_U - F_H - (\overline{w'\theta'_e})_H}{\Delta\theta'_e} - DH. \quad (19)$$

Equations (15) and (16) are simply a shorthand matrix notation for the consistency relation and the closure assumption. In the following section we discuss the steady-state solutions to the above model.

4. THE STEADY-STATE SOLUTIONS

In the steady-state case all derivatives with respect to time are set to zero, which results in a system of nonlinear algebraic equations. The method we have chosen to use in solving for the steady-state solutions is to reduce our system of equations to one equation in H . We can then use a simple secant method algorithm to iteratively find its zero. Before describing the steady-state model equations, it should be mentioned that the total water flux $\overline{w'(q' + \ell')}$ becomes constant with height. This can be seen directly from (18). For this reason, the subscripts on this variable are deleted.

The first step is to derive expressions for the surface fluxes of equivalent potential temperature and total water. The former is accomplished by eliminating the dependent variables θ_e and $(\overline{w'\theta'_e})_H$ between the steady-state forms of (7), (17) and (19). The resulting expression is

$$(\overline{w'\theta'_e})_0 = \frac{(F_U - F_H) + (F_H - F_S) + DH(\theta_{eS} - \theta_{eU})}{\left(1 + \frac{DH}{C_T V}\right)}. \quad (20)$$

The latter expression is derived similarly, resulting in

$$\overline{w'(q' + \ell')} = \frac{DH(q_S - q_U)}{\left(1 + \frac{DH}{C_{TV}}\right)}. \quad (21)$$

It should be noted that the cloud top values of equivalent potential temperature and water vapor mixing ratio (θ_{eU} and q_U respectively) are linear functions of height derived from the same climatological data as used in the radiation parameterization.

We can also eliminate θ_e from our cloud base equation. This is accomplished by substituting (7) and (8) into (9). The resulting expression is

$$h = \frac{(1 + \alpha)\overline{w'(q' + \ell')} - a(\overline{w'\theta'_e})_0}{bC_{TV}}. \quad (22)$$

To derive an expression for $(\overline{w'\theta'_e})_H$, we eliminate θ_e from (19) by using (7), which results in

$$(\overline{w'\theta'_e})_H = (F_U - F_H) - \frac{DH}{C_{TV}}(\overline{w'\theta'_e})_0 + DH(\theta_{eS} - \theta_{eU}). \quad (23)$$

Finally, we need to derive the steady-state closure equation. Before this can be done, however, it is necessary to provide expressions for the virtual potential temperature flux at the surface, just below cloud base, just above cloud base, and at cloud top, respectively. These expressions can be shown to take the form

$$(\overline{w'\theta'_v})_0 = (\overline{w'\theta'_e})_0 - \left(\frac{L}{c_p} - \bar{\theta}\delta\right)\overline{w'(q' + \ell')}, \quad (24)$$

$$(\overline{w'\theta'_v})_{h-} = (\overline{w'\theta'_e})_h - \left(\frac{L}{c_p} - \bar{\theta}\delta\right)\overline{w'(q' + \ell')}, \quad (25)$$

$$(\overline{w'\theta'_v})_{h+} = \left(\frac{1 + a\bar{\theta}(1 + \delta)}{1 + \alpha}\right)(\overline{w'\theta'_e})_h - \bar{\theta}\overline{w'(q' + \ell')}, \quad (26)$$

$$(\overline{w'\theta'_v})_H = \left(\frac{1 + a\bar{\theta}(1 + \delta)}{1 + \alpha}\right)(\overline{w'\theta'_e})_H - \bar{\theta}\overline{w'(q' + \ell')}, \quad (27)$$

where $(\overline{w'\theta'_e})_h$ is given by

$$(\overline{w'\theta'_e})_h = \left(1 - \frac{h}{H}\right)(\overline{w'\theta'_e})_0 + \frac{h}{H}(\overline{w'\theta'_e})_H. \quad (28)$$

With the above variables defined, we can now derive our closure equation. We use a weighted average of Lilly's (1968) maximum and minimum entrainment case to close our system equations. This closure equation takes the form

$$\frac{k}{H} \int_0^H \overline{w'\theta'_v} dz + (1 - k)(\overline{w'\theta'_v})_{\text{minimum}} = 0, \quad (29)$$

where k is a weighting parameter which can take on values in the range $0 \leq k \leq 1$. If we assume the daily averaged solar radiation is never strong enough to overcome the longwave

cooling and thus produce a net warming affect, the minimum virtual potential temperature flux must always be just below cloud base. This can be seen from (17). With this in mind, (29) can be integrated to give

$$\frac{2(1-k)}{k}(\overline{w'\theta'_v})_{h-} + (\overline{w'\theta'_v})_H + (\overline{w'\theta'_v})_{h+} + \frac{h}{H}[(\overline{w'\theta'_v})_S + (\overline{w'\theta'_v})_{h-} - (\overline{w'\theta'_v})_H - (\overline{w'\theta'_v})_{h+}] = 0. \quad (30)$$

We now have a closed set of equations (12)–(14), (20)–(28), and (30) in the unknowns H , h , T_H , $(F_U - F_H)$, $(F_H - F_S)$, $(\overline{w'\theta'_e})_H$, $(\overline{w'\theta'_e})_h$, $(\overline{w'\theta'_e})_0$, $w'(q' + \ell')$, $(\overline{w'\theta'_v})_H$, $(\overline{w'\theta'_v})_{h+}$, $(\overline{w'\theta'_v})_{h-}$, and $(\overline{w'\theta'_v})_0$. The method we have chosen to solve this system of equations can be explained in the following four step iteration sequence.

- (1) Make an initial guess of the cloud top height H and the cloud top jump in radiative flux $(F_U - F_H)$.
- (2) Using the current estimates of H and $(F_U - F_H)$, calculate in order $(\overline{w'\theta'_e})_0$, $w'(q' + \ell')$, h , $(\overline{w'\theta'_e})_H$ and the four virtual potential temperature fluxes using (20)–(27).
- (3) Again using the current estimate of H , calculate the new radiation variables T_H , $(F_U - F_H)$, and $(F_H - F_S)$. This newly calculated value of $(F_U - F_H)$ will be used in the next iteration if another iteration is required.
- (4) Using the above fluxes, check to see if (30) is satisfied to within some tolerable limit. If it is not, use the secant method to produce a new estimate of H and repeat steps (2)–(3) until (30) is satisfied.

5. RUNNING THE PROGRAM

The FORTRAN source code for the above model is stored on the attached floppy disk in the file STRATUS.FOR and the executable code in the file STRATUS.EXE. To run the program, simply enter STRATUS. You will be prompted to enter the sea-surface temperature, the large scale horizontal divergence, the wind velocity, and the initial guess for cloud top height. The output consists of cloud top and cloud base height, mixed layer equivalent potential temperature and total water mixing ratio, values of the convective and radiative fluxes and the cloud top temperature.

6. REFERENCES

- Cox, S.K., 1973: Infrared heating calculations with a water vapor pressure broadened continuum. *Quart. J.R. Meteor. Soc.*, **99**, 669–679.
- Lilly, D.K., 1968: Models of cloud-topped mixed layers under a strong inversion. *Quart. J.R. Meteor. Soc.*, **94**, 292–309.
- Schubert, W.H., J.S. Wakefield, E.J. Steiner, S.K. Cox, 1979: Marine stratocumulus convection. Part I: Governing equations and horizontally homogeneous solutions. *J. Atmos. Sci.*, **36**, 1286–1307.
- U.S. Dept. of Commerce, Environmental Science Services Administration, Environmental Data Service, 1976–1980: *Climatological Data, National Summary*. Govt. Printing Office, Washington, DC.

A Case Study Of Cumulus Formation Beneath A Stratocumulus Sheet:
Its Structure And Effect On Boundary Layer Budgets.

R.W.Barlow & S.Nicholls (deceased)

Met.O.15,
The Meteorological Office,
Bracknell, Berkshire,
RG12 2SZ
ENGLAND.

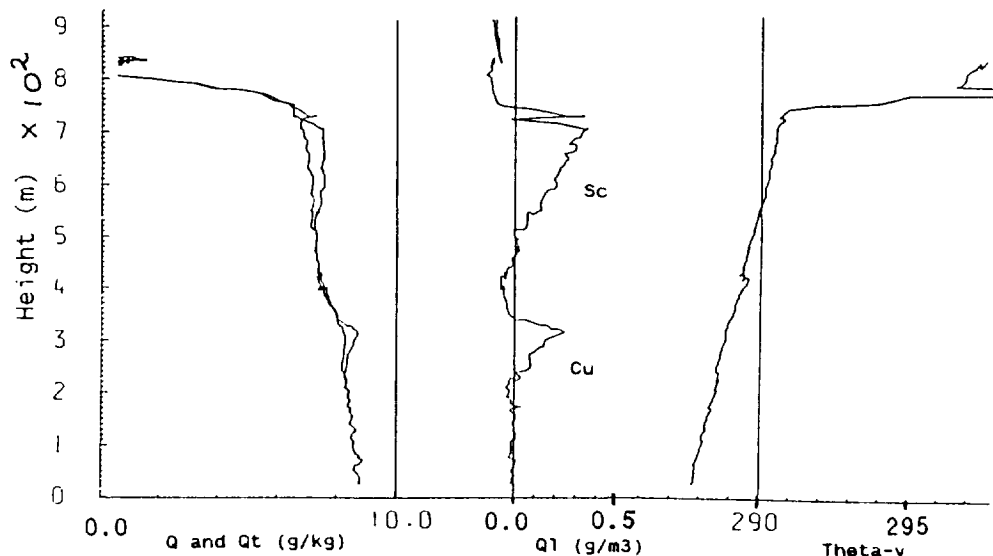
Introduction:

On several occasions during the FIRE Marine Stratocumulus IOP off the Californian coast, small cumulus were observed to form during the morning beneath the main stratocumulus deck. This occurs in the type of situation described by Turton & Nicholls (1987) in which there is insufficient generation of TKE from the cloudtop or the surface to sustain mixing throughout the layer, and a separation of the surface and cloud layers occurs. The build up of humidity in the surface layer allows cumuli to form, and the more energetic of these may penetrate back into the Sc deck, reconnecting the layers. The results presented in this abstract were collected by the UKMO C-130 aircraft flying in a region where these small cumulus had grown to the extent that they had penetrated into the main Sc deck above. In the following paragraphs we will examine the structure of these penetrative cumulus and discuss their implications on the layer flux and radiation budgets.

Aircraft Observations :

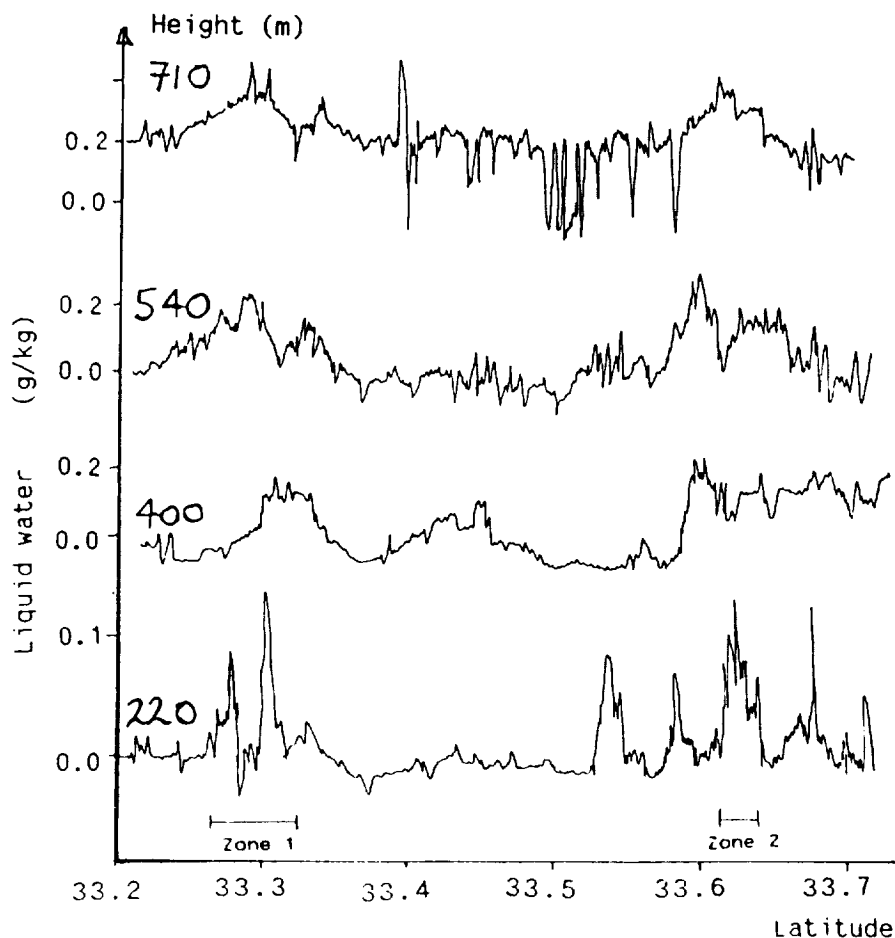
An aircraft profile through the boundary layer on the 16th July is shown in fig.1, and illustrates the main features of the case very well. The local time was about midday, and the weak mixing is evident from the slope of the theta-v line. The separation of the layers can be seen as a discontinuity in the Q_t profile, although no density interface is visible in theta-v.

Fig.1 : Profiles through boundary layer.



The C-130 flew 60km legs along a north/south line at various levels. Due to the extremely light winds (less than 1.5 m/s mean) the aircraft ground position corresponds to its air position for the section of the flight we will examine. Thus we are justified in overlaying data from different times. Fig.2 represents a cross-section along the flight line for the Johnson-Williams derived liquid water content. Each JW trace has been plotted with its origin position representing the height of the run. The JW values are not absolute. The lower two runs are below the main Sc base, and the upper two are at the Sc base and top. Several areas of small cumulus can be seen in the lower runs, but there are two zones (marked in fig.2) where the enhanced LWCs in the upper runs show that they have penetrated right up to the inversion at the top of the main deck, spreading as they rise. For each run shown the times when the aircraft was well within the cumulus or penetration regions were determined. We can characterise the zones by calculating mean quantities for them separately, and comparing them with the whole-run quantities. (Because the duration flying in the zones is much smaller than the whole run, the whole-run means approximately represent the stratocumulus layer).

Fig.2 : Liquid water cross-section along flight track



Thermodynamics and microphysics:

Taking the surface layer air as representative for the source air of the cumuli, it is found that thermodynamically there is very little difference from the Sc layer air. Mean Theta-e is indistinguishable, but Qt is 8.7 g/kg for the upper layer and 9.1 g/kg for the surface layer air. These agree with the observed cloud bases from the Q1 profiles shown in fig.3(a). The dots are whole-runs and the means from the two zones are numbered accordingly. The best fit line for the zones uses both sets of data. The whole-run profile has a ratio of Q1 to the adiabatic value of 0.76, while the zones values is lower at 0.56 due to the ascending Cu entraining air of lower total water content from the surrounding Sc as it rises.

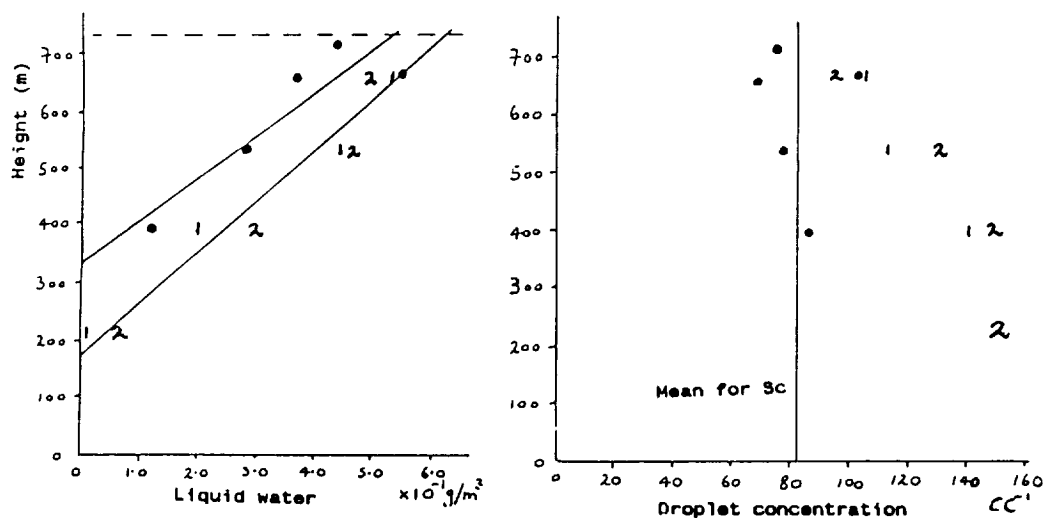


Fig. 3 : (a) Mean Q1 profiles. (b) Mean conc. profiles.

This mixing process is well illustrated by the profile of FSSP derived droplet concentrations in fig.3(b). Within stratocumulus droplet concentration is usually found to be constant with height (Nicholls & Leighton, 1986), and so we can use it as a roughly conservative variable. When we look at the microphysics of the zones as opposed to the whole run, we find that the air they are bringing up from the surface layer has a far higher droplet concentration. The whole-run values are constant at about 80 cc^{-1} , whereas the zone values at the Cu cloudbase are close to 150 cc^{-1} . As the Cu plumes rise they spread out and mix with the surrounding Sc layer air, and we see the mean concentration in the zones linearly decreasing until it almost equals the whole-run value by the time the inversion is reached. The profiles of mean volume radius are almost identical for the two situations.

Fluxes:

Both heat and moisture fluxes for the whole-run averages tend to be about half an order of magnitude smaller than typical values from other FIRE flights. Due to their size, the scatter is relatively large and so no pattern can easily be seen. This is consistent with the picture of a poorly mixed layer. It would seem reasonable to expect the fluxes in the zones to be higher, as the Cu carry heat and moisture up through the layer, but here we find a measurement problem. Because of the very

short sampling distance in the zones (3 to 4 km) the error variance is large (upto 80% using the method of Lenschow & Stankov, 1986). Thus we cannot determine a representative flux measurement for the zones.

More structure is apparent if we consider the TKE flux (fig.4(a)). The whole-run values are small, but the zone values show a clear maximum at the Cu base, decreasing towards the cloud top (as TKE is used to entrain more quiescent surrounding air) to equal the Sc value. Scatter is still fairly large due to the short sampling period.

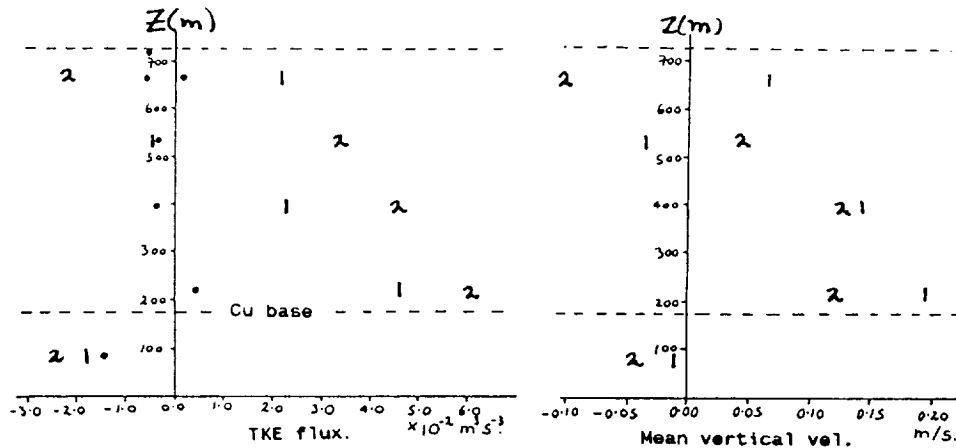


Fig.4 : (a) TKE flux. (b) Mean vertical velocity (in zones)

The mean vertical velocity also shows the structure of the Cu in the zones, following the same trend as the TKE flux. The updraft values are small compared to normal Cu values, but an inspection of a vertical velocity timeseries shows that there are several sharp updrafts within the zones, and that we are averaging across some quiescent areas between them.

Radiation:

Because of the non-linear relationship between cloud water and radiation, it is likely that the radiative properties of the mean cloud will not be the same as the mean radiative properties. So to assess the impact of the presence of the zones on the radiation budget, radiation models using whole-run conditions and zone conditions were compared. The models used were those of Slingo & Schrecker (1982) for the longwave and Roach & Slingo (1976) in the shortwave, with nine levels below the inversion and a subtropical standard atmosphere above it (As Turton & Nicholls, 1987). Comparing the radiative properties of the zones with those derived from whole-run thermodynamics we find that (i) the albedo increases, reflecting more shortwave back into space, and letting less through into the boundary layer and (ii) the absorptance of the cloud increases so that a smaller proportion of the cloudtop flux reaches the ground. The longwave fluxes are virtually unchanged between the two cases. Quantitatively, this means that:

- (1) The cloud layer receives 12 Wm⁻² more, almost doubling its previous budget of 13 Wm⁻².
- (2) The surface receives 139 Wm⁻² less, a reduction of 37%.
- (3) about 130 Wm⁻² more are being reflected back into space. This has been verified using the upward and downward facing radiometer data for the two regions. However it is apparent from this data that the regions corresponding to the radiative properties of the Cu are much wider than

the vertical velocities or LWC's would suggest, occupying more than half of the run.

Landsat thematic mapper band-4 reflectivity data taken at the time the C-130 was operating shows bright spots corresponding exactly to the positions of the zones. The Landsat picture shows that regions of penetrative convection lie in streets, and that the C-130 track has cut across about 3 perpendicularly. Hence we know that the cross-section sampled by the C-130 is representative of the whole region. Because band-4 is sensitive to total liquid water column, it also detects small Cu beneath the Sc that have not yet penetrated it, and so there is no sharp change in intensity at the edges of the zones. Thus we cannot use this kind of image *a priori* to diagnose the existence of Cu penetration.

Summary:

Small cumulus were observed to form beneath and penetrate into a stratocumulus sheet. No discontinuity in $\theta-v$ could be found between the surface and detached mixed layers, but there was a clear jump of 0.4 g/kg in q_t . FSSP data showed that the surface layer air produced a far higher droplet concentration in the Cu than the Sc layer air above. The decrease of the concentration with height in the Cu shows that the plumes penetrated right up to the inversion, but spread out and entrained lower total water content air as they rose.

Heat and moisture fluxes within the Sc were small, but values could not be determined for the Cu areas due to the short sampling times. In the Cu areas TKE flux and mean vertical velocity both showed a maximum near Cu cloudbase, decreasing as the plumes rose into the Sc.

Using typical values for the Sc layer and the penetrative Cu (regarded as a cloud-layer from Cu base to the inversion) radiative properties were modelled for the two cases. Under the Cu areas the surface budget decreases by 37%, and 130 Wm⁻² more are reflected back into space from cloud-top, relative to areas just containing Sc.

Radiometer data showed that the radiation conditions predicted for the Cu occupy more area than suggested by q_l or vertical velocities. Hence any calculation of mean radiative properties based on mean thermodynamic properties will not be valid when penetrative convection is present.

References:

- Nicholls, S, and J.Leighton, 1986: An observational study of the structure of stratiform cloud sheets. Part I: Structure. Quart. J. Roy. Met. Soc., 112, 431-460.
- Roach, W.T. and A.Slingo, 1976: A high resolution infra-red radiative transfer scheme to study the interaction of radiation with cloud. Quart. J. Roy. Met. Soc., 105, 603-614.
- Slingo, A. and H.M.Schrecker, 1982: On the shortwave properties of stratiform water clouds. Quart. J. Roy. Met. Soc., 108, 407-426.
- Lenschow, D.H. and B.B.Stankov, 1986: Length scale in the convective boundary layer. J. Atmos. Sci., 43, 1198-1209.
- Turton, J.D. and S.Nicholls, 1987: A study of the diurnal variation of stratocumulus using a mixed layer model. Quart. J. Roy. Met. Soc., 113, 969-1009.

VERIFICATION OF THE NAVAL OCEANIC VERTICAL AEROSOL MODEL DURING FIRE

K.L. Davidson¹, G. de Leeuw,^{1,2} S.G. Gathman³ and D.R. Jensen⁴1. Naval Postgraduate School, Department of Meteorology, Code 63
Monterey, California 93943-5000, U.S.A.2. Physics and Electronics Laboratory TNO
P.O. Box 96864, 2509 JG The Hague, The Netherlands3. Naval Research Laboratory, Code 4117
Washington D.C., 20375, U.S.A.4. Naval Ocean Systems Center, Code 543
San Diego, California 92152-5000, U.S.A.

1. INTRODUCTION

The Naval Oceanic Vertical Aerosol Model (NOVAM) has been formulated to estimate the vertical structure of the optical and infrared extinction coefficients in the marine atmospheric boundary layer (MABL), for wavelengths between 0.2 and 40 μm ¹. NOVAM was designed to predict, utilizing a set of routinely available meteorological data, the non-uniform and non-logarithmic extinction profiles which are often observed. NOVAM is based on a combination of empirical and physical models for the processes that determine the aerosol dynamical behaviour. The extinction properties are calculated from the aerosol profiles using Mie theory.

NOVAM is restricted to the marine atmosphere. The differences between NOVAM and land-based models are the marine type of scaling used for the turbulent controlled processes near the sea surface, and the determination of the surface concentrations with the Navy Aerosol Model (NAM).² NAM has been extensively updated from the original. It produces a particle size distribution at a height of 10 m above the surface from the input data of wind speed, visibility and relative humidity. This NAM-generated surface-layer particle size distribution is mixed throughout the MABL by turbulent-controlled processes, further modified by relative-humidity effects. Various models describing these processes are included in NOVAM, such as a simple mixed-layer model³ and a shallow convection case.⁴ Provision has been made to include other models such as for deep convection. The selection of the model is based on the vertical stratification, cloud cover, cloud type, wind speed, and the requested wavelength for the extinction calculation. If the information on the vertical structure is not available a default relative humidity profile, based on the surface observations, is generated.⁵ This default profile is also used when the required input parameters do not satisfy the presently supported models. For the calculation of extinction for wavelengths between 1 and 11 μm below marine stratus clouds an empirical model⁶ is used. This stratus model applies only to wind speeds less than 5 m/s.

For the initial evaluation of NOVAM, data from the July 1987 FIRE experiment was used. Aerosol particle size distributions, aerosol scattering and required meteorological parameters throughout the MABL were obtained from both airborne and surface based platforms. The aerosol-derived extinction properties throughout the MABL are compared with the NOVAM estimates.

2. THE FIRE/EOMET EXPERIMENTS

The Navy's EOMET (Electro-Optics METeorology program) participation in FIRE was both to be supportive of FIRE and to build a quality data base from which NOVAM could be evaluated. Measurements were made from an aircraft, a balloon and a ship. An overview of the measurements made by the EOMET group is presented in table 1.

The R/V Point Sur, operated for the National Science Foundation by the California State University System for the Naval Postgraduate School (NPS), made continuous (24 hour/day) measurements for the period 7-16 July, 1987. The R/V Point Sur was generally located 30-40 km upwind (Northwest) of San Nicolas Island (SNI).

The Naval Ocean Systems Center (NOSC) airborne platform was utilized to characterize the low level structure of the marine boundary layer. Flights were made on 15, 19, 23 and 24 July, 1987. The prescribed flight pattern for the NOSC aircraft consisted of spiral profiles taken near the Naval Research Laboratories (NRL) ground facility at SNI and upwind of SNI near the R/V Point Sur. Each flight was scheduled to occur simultaneously with the NOAA-9 satellite overpass.

The NRL balloon facility⁷ was located at the northwest tip of SNI approximately 17 m above sea level. The NRL aerostat system consisted of a 538 m³ balloon, with a lifting capacity of 227 kg and a flat bed trailer which serves as a "mobile" mooring system. The instrument package hangs 35 meters below the balloon and the power source to eliminate exhaust contamination near the sensitive aerosol sensing devices. The platform is aligned with the wind by an aerodynamic mechanism. During FIRE, 13 aerosol profiles were measured on 16, 18, 19, 20, 22, 23, 24 and 25 July, 1987.

Extinction profiles were obtained in three independent ways:
-NOVAM calculations utilizing measured meteorological parameters,
-Mie calculations utilizing aerosol size distributions,
-Direct measurements of extinction (molecular and aerosol) at one wavelength by means of a spherical nephelometer.

3. SYNOPTIC SITUATION AND SURFACE MEASUREMENTS ON THE R/V POINT SUR, 14-16 JULY

The meteorological synoptic scale situation during the 14-16 July period was controlled by two pressure systems. A stationary 1032-1036 mb closed surface high pressure system was located west of Washington State and British Columbia, Canada. A well-defined thermal low was located over Southern California. These two systems caused west to northwest winds in the vicinity of SNI due to the outflow from the high located to the northwest.

The time series of surface-layer parameters obtained from the R/V Point Sur for 14-16 July are presented in Figure 1. Features of interest are the steadily decreasing wind speeds and the diurnal variation of both the wind speed and direction. The steady decrease in wind speed was associated with the thermal low which was moving northeast (more inland) from the Baja of California on 14 July to the California-Nevada border on 16 July. The eastern Pacific surface high pressure systems remained nearly stationary during this period. Steadily decreasing wind speeds are important to the production of marine aerosols.

TABLE 1. Meteorological Measurements by the EOMET Group during FIRE.

Measurement	Instrument	Frequency
I. NPS: R/V Point Sur		
<u>Mean Surface Layer:</u>		
Radiation(short,total)	radiometers	continuous
Vector wind	propeller/vane	continuous
Temperatures:		
Air	resistance therm.	continuous
Dew point	cooled mirror	continuous
Sea surface	floating thermistor	continuous
Waves	bridge observation	1 per hour
Turbulence		
Wind	hot-film anemometer	continuous
Humidity	Lyman-alpha Sensor	continuous
Aerosol and Radon		
.08 to 1.5 μm radius	PMS ASASP	continuous
0.5 to 12 μm radius	PMS CSASP	continuous
Radon concentration	HV filter	1 per hour
<u>Mixed Layer and above:</u>		
Vector wind	rawinsonde	6 per day
Temperature	rawinsonde	6 per day
Humidity	rawinsonde	6 per day
Inversion height and strength	rawinsonde/sodar	6 per day/continuous
Turbulence	sodar	continuous
II. NRL Aerostat, SNI		
Air temperature	dry bulb thermometer	5 Hz
Relative humidity	dry/wet bulb psychrometer	5 Hz
	saturation hygrometer	5 Hz
Liq. water conc.	forward scatt. meter	5 Hz
Wind vector	bivane anemometer/ inclinometers/compasses	5 Hz
Visual scattering	nephelometer	1 Hz
Altitude	altimeter	1 Hz
Aerosol, 0.5-16 μm radius	PMS CSASP	1 Hz
Videorecordings	video recorder	continuous
III. NOSC AIRBORNE PLATFORM		
Temperatures:		
Air	Rosemont	continuous
Dew point	EG&G cooled mirror	continuous
Sea surface	Barnes IR	continuous
Cloud top	Barnes IR	continuous
Aerosol, 0.25-15 μm radius	PMS ASSP	continuous
15-150 μm radius	PMS OAP	continuous
Altitude	Rosemont	continuous

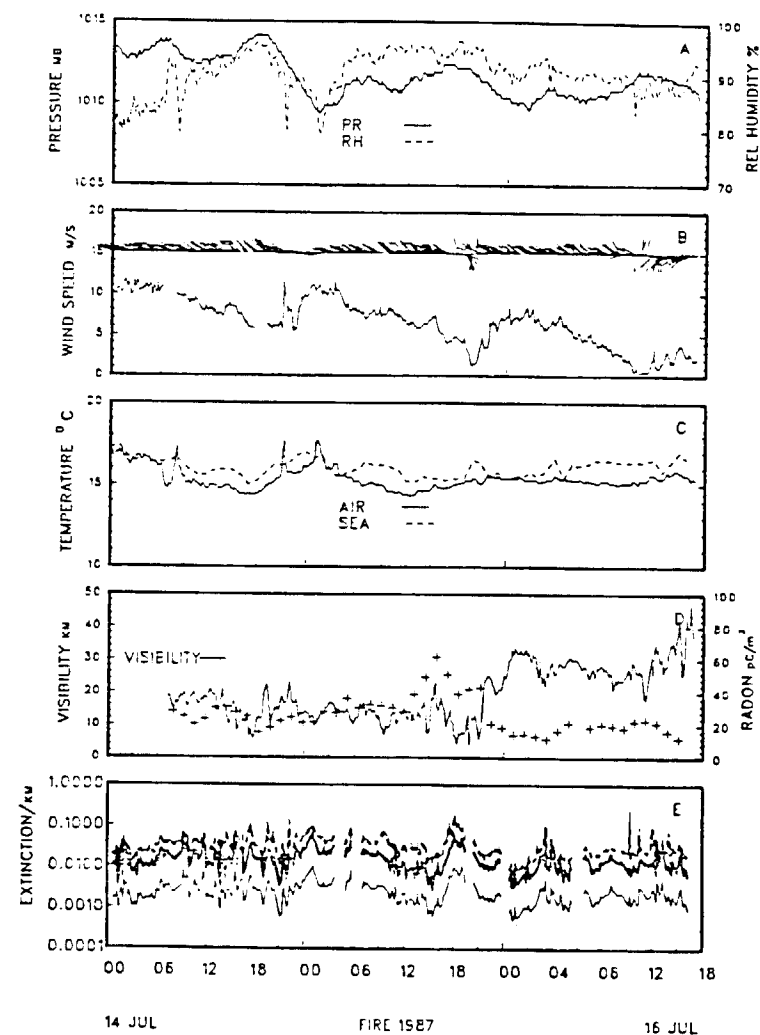


Figure 1. Time series of R/V Point Sur surface observations, July 14-16, 1987:

- atmospheric pressure and relative humidity
- wind speed and wind direction
- air temperature and sea surface temperature
- visibility and Radon concentrations (+)
- extinction coefficients calculated from the aerosol particle size distributions for wavelengths of 0.55, 0.63, 0.69, 1.06 and 10.6 μm (top to bottom traces).

Note that the time is UT, i.e. 7 hours ahead of local time (PDT).

The diurnal variations in wind speed and direction, during the 24-hour periods, were concluded to be due to the intensification of the thermal low, east of the area, during the local afternoon. This could imply a local circulation influenced by the land-sea proximity.

Evidence that there was a land-sea influence associated with the diurnal variation appears in the diurnal variation of the Radon concentration. Whether the Radon was advected horizontally or arrived in the mixed layer due to entrainment is unknown. The increase in temperature and decrease in humidity on the diurnal scale could be associated with entrainment of warm dry air from above the inversion. The entrainment of overlying air with continental aerosol is as important to NOVAM's performance as the horizontal advection of continental air.

The continental influence is obvious in the afternoon of 15 July, when the Radon concentrations peaked to 60 pCi/m^3 . The increased Radon concentrations, a clear indication of continental influences, are followed by an increase in the extinction coefficients. The increase in the extinction coefficients is observed at all wavelengths from the visible to the far IR.

4. SIMULTANEOUS AIRCRAFT AND BALLOON FLIGHTS DURING THE STRATUS CASE OF 15 JULY 1987

Evaluation of the NOVAM stratus model utilized the aircraft- and balloon-derived meteorological profiles and surface-based observations for the stratus conditions of 15 July 1987, 1500-1700 (PDT). A uniform stratus layer (100% cover) existed at and upwind of SNI with a base around 400 m and tops at 700 m. Winds were northwesterly at 5 m/s. Cloud base at SNI was determined at 320 m from the balloon liquid-water measurements. Drizzle was observed at the ground. Extinction coefficients fluctuated from 80 km^{-1} in the cloud, to low values (0.01 km^{-1}) above the cloud layer. The balloon RH instrument was pegged at 100% throughout the whole boundary layer. Upwind, however, the relative humidity below the clouds varied in the vertical between 95% and 100%, as determined from the aircraft data. The surface relative humidity at the R/V Point Sur, approximately 30 NM upwind from SNI, was 92% (Figure 1). This is a classic case of a stratus deck in which warm dry conditions existed above the moist marine stratus layer.

Extinction profiles for this situation are shown in Figure 2. Figure 2a shows the AMP sensitivity of NOVAM for the visible wavelengths. Note that NOVAM selected the mixed-layer model for these calculations because the sub-stratus model does not apply to wavelengths smaller than $1 \mu\text{m}$. The fluctuations in the extinction coefficients determined from all sources are generally contained within the AMP limits. In the regions around 120 m and those above 320 m, where the extinction coefficients are outside the NOVAM bounds, the aircraft-observed relative humidities approached 100% - a region where NOVAM is not applicable. The problem here is that the hygroscopic aerosol (like sea salt droplets in the MABL) can be activated when relative humidities go slightly over 100%. The activated aerosols grow in size very fast and behave as cloud droplets⁸ and cannot be described by equations that apply to subsaturated aerosol. This puts them into the arena of fog or cloud physics, and outside of the realm of aerosol modeling - including the capabilities of NOVAM. Figure 2d shows the liquid water concentration profile and Figure 2e the measured size distributions associated with this supersaturation phenomenon.

Figures 2b and 2c show the $1.06 \mu\text{m}$ and $10.6 \mu\text{m}$ extinction profiles. The sub-stratus model is not as sensitive to the AMP as the mixed-layer model.

Differences between the measured extinction coefficients and NOVAM estimates are in the high-humidity regions just described. The peak in the size distributions shown in Figure 2e affects the far IR more than the near IR.

5. CONCLUDING REMARKS

We have illustrated the value of NOVAM for estimating the non-uniform and non-logarithmic extinction profiles, based on a severe test involving conditions close to and beyond the limits of applicability of NOVAM. A more comprehensive evaluation of NOVAM from the FIRE data is presented in ref. 9, which includes a clear-air case. For further evaluation more data are required on the vertical structure of the extinction in the MABL, preferably for different meteorological conditions and in different geographic areas (e.g. ASTEX).

6. ACKNOWLEDGEMENTS

NOVAM is developed in the EOMET applied research program managed by Dr. Juergen Richter (NOSC). Special thanks go to Mike H. Smith and Ian E. Consterdine of UMIST for making excellent aerosol measurements on the NRL Aerostat. R.E. Larsen (NRL) made the Radon measurements, Peter Guest, Keith Jones (NPS) and Jeff James (NRL) assisted in data collection on the R/V Point Sur. Pat Boyle and Tamar Neta (NPS) assisted in the analysis. GdL participated in this program while he held a National Research Council Research Associateship at the Naval Postgraduate School.

REFERENCES

1. G. de Leeuw, K.L. Davidson, S.G. Gathman and R.V. Noonkester, "Physical models for aerosol in the marine mixed-layer," Proc. AGARD electromagnetic wave propagation panel specialists' meeting on "Operational decision aids for exploiting or mitigating electromagnetic propagation effects", San Diego, CA, USA, 15-19 May, 1989, pp. 40-1 to 40-8.
2. S.G. Gathman, "Optical properties of the marine aerosol as predicted by the Navy aerosol model," Opt. Eng. 22 (1983) pp. 57-62.
3. C.W. Fairall and K.L. Davidson, "Dynamics and modeling of aerosols in the marine atmospheric boundary layer," in: E.C. Monahan and G. Mac Niocaill, eds., Oceanic Whitecaps, Dordrecht, D. Reidel (1986) pp. 195-208.
4. K.L. Davidson and C.W. Fairall, "Optical properties of the marine atmospheric boundary layer: aerosol profiles," in: Ocean Optics VIII, Proc. SPIE, Vol. 637 (1986) pp. 18-24.
5. S.G. Gathman, "Model for estimating meteorological profiles from shipboard observations," 1978, NRL Report 8279, Washington D.C.
6. V.R. Noonkester, "Profiles of optical extinction coefficients calculated from droplet spectra observed in marine stratus cloud layers" J. Atmos. Sci. 42 (1985) pp. 1161-1171.
7. J.E. James, H. Gerber, S.G. Gathman, M. Smith and I. Consterdine, "Navy tethered balloon measurements made during the "FIRE" marine stratocumulus IFO July 1987," 1989, NRL Memorandum Report 6445, Washington D.C.
8. N.H. Fletcher, "The physics of rain clouds," Cambridge at the Univ. press, 1962.

9. S.G. Gathman, G. de Leeuw, K.L. Davidson and D.R. Jensen, "The Naval Oceanic Vertical Aerosol Model: Progress Report," Proc. AGARD Fall 1989 Symp. on Atmospheric Propagation in the UV, Visible, IR and MM-Wave Region and Related Systems Aspects." Copenhagen, 9-13 October, 1989.

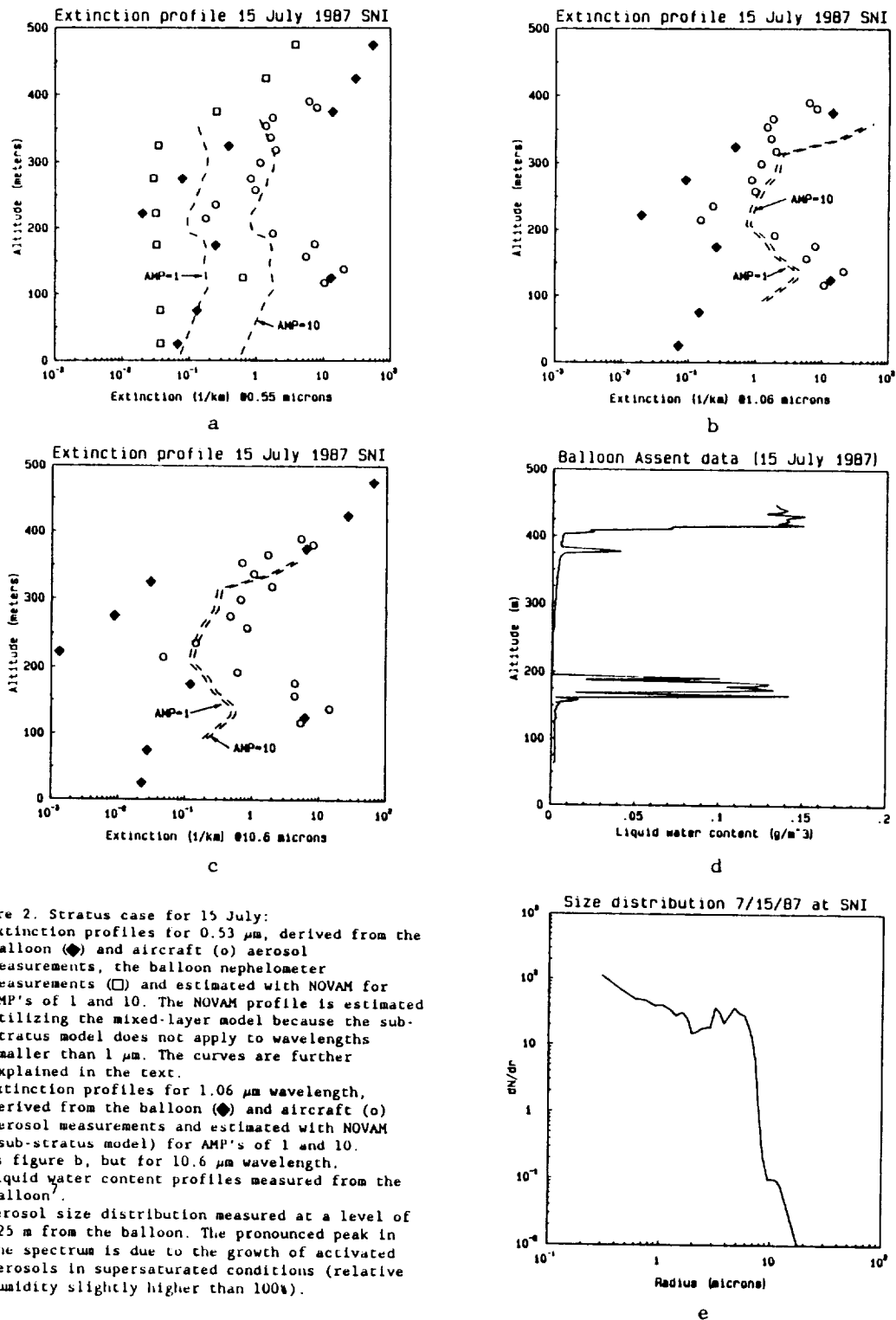


Figure 2. Stratus case for 15 July:

- extinction profiles for 0.53 μm , derived from the balloon (\blacklozenge) and aircraft (o) aerosol measurements, the balloon nephelometer measurements (\square) and estimated with NOVAM for AMP's of 1 and 10. The NOVAM profile is estimated utilizing the mixed-layer model because the sub-stratus model does not apply to wavelengths smaller than 1 μm . The curves are further explained in the text.
- extinction profiles for 1.06 μm wavelength, derived from the balloon (\blacklozenge) and aircraft (o) aerosol measurements and estimated with NOVAM (sub-stratus model) for AMP's of 1 and 10.
- as figure b, but for 10.6 μm wavelength.
- liquid water content profiles measured from the balloon.
- aerosol size distribution measured at a level of 125 m from the balloon. The pronounced peak in the spectrum is due to the growth of activated aerosols in supersaturated conditions (relative humidity slightly higher than 100%).

MODIFICATION OF THE BACKGROUND FLOW BY ROLL VORTICES

Hampton N. Shirer and Tracy Haack
 Department of Meteorology
 The Pennsylvania State University
 University Park, PA 16802

Use of observed wind profiles, such as those obtained from ascent or descent aircraft soundings, for the identification of the expected roll modes is hindered by the fact that these modes are able to modify the wind profiles. When such modified wind profiles are utilized to estimate the critical values of the dynamic and thermodynamic forcing rates, large errors in the preferred orientation angles and aspect ratios of the rolls may result. Nonlinear analysis of a 14-coefficient spectral model of roll circulations shows that the primary modification of the background wind is the addition of a linear component. When the linear profile having the correct amount of shear is subtracted from the observed cross-roll winds, then the pre-roll wind profile can be estimated. In this paper, a preliminary test of this hypothesis is given for a case in which cloud streets were observed during FIRE.

The amount of error in the expected orientation angle that is introduced by using the roll-modified winds as the basic state can be illustrated using the Ekman wind profile. A typical Ekman cross-roll profile U_p is given in Fig. 1a. The geostrophic wind is from the west and the Ekman wind direction is also from the west when $z = \pi D$, where $D = 115$ m is the Ekman depth; because the model contains a right-handed coordinate system in which the roll axis is parallel to the y-direction, southerly winds have negative values. An inflection point mode may develop from this wind profile. It has a preferred orientation angle of 5° to the right of the geostrophic wind, or 275° , while the preferred aspect ratio $a = 2z_T/L$ is 0.7; here $z_T = 600$ m is the domain height, so the expected roll spacing L is approximately 1700 m. The 14-coefficient model is integrated for these values of orientation angle and aspect ratio and for a set of supercritical values of the dynamic forcing rates, given by a Reynolds number $Re = |\underline{V}(z_T)z_T/(\pi\nu)$, and the thermodynamic forcing rates, given by the Rayleigh number $Ra = gz_T^3\Delta_zT/(\nu\kappa T_{00}\pi^4)$; here $|\underline{V}(z_T)|$ is the wind at the domain top, ν and κ are the eddy viscosity and thermometric conductivity respectively, and Δ_zT is a combined measure of the sea surface/air temperature difference and the environmental lapse rate of potential temperature. For this example, the critical values are $Re_c = 91$ and $Ra_c = 0$, and the forcing rates $Re = 100$ and $Ra = 100$ are used in the integration. The linear cross-wind profile U_L created in this case is shown in Fig. 1b. After this linear profile is added to the original Ekman one, the low-level wind speed increases, as does the shear near the inflection point (Fig. 1c). Use of this modified profile U_M in the stability analysis produces an orientation angle for the inflection point mode that is 15° further to the right of the geostrophic wind than the angle produced by the original Ekman profile. However, the preferred aspect ratio does not vary considerably. For this example, therefore, the primary consequences of using the wrong basic wind profile are a large error in the expected orientation angle of the rolls and an overestimate of the cross-roll shear in the basic state winds.

Cloud streets in relatively clear air were observed in the western half of the Landsat scene on July 7, 1987. A descent sounding measured on Flight 5 of the Electra between 2136 and 2137:30 UTC was used to provide the observed wind and temperature profiles for the analysis (Figs. 2a, 3b). Moisture measurements, lidar data, and flight video tapes were used to provide an estimate of the domain height $z_T = 450$ m, and the layer mean wind direction of 340°

gave an estimate of the observed roll orientation; this orientation agrees well with that found on the Landsat image provided us by Dr. Robert F. Cahalan. When the observed wind profile is used in the stability analysis, an orientation 35° to the right of the mean wind direction, or 15° (slightly east of north), is obtained for the thermal mode. This is the only likely mode since the cross-roll profile does not have an inflection point (Fig. 2a), and, as calculated by Dr. Bruce A. Albrecht, the sea surface temperature exceeded the surface air temperature by approximately 0.5°C . Clearly 35° is an unacceptably large error in the orientation angle. Thus the next task is to find the linear cross-roll wind profile U_L that must be removed from the one in Fig. 2a in

order that the resulting profile produces the correct orientation angle $\beta = 0^\circ$. A range of slopes is considered, and the effects on the preferred orientation angle β_p given by the stability analysis are shown in Fig. 2b. Because the orientation angle varies monotonically with changes in the slope m of the removed profile, the hypothesized roll contribution is easy to identify. The linear cross-roll profile whose removal gives 0° as the preferred roll orientation is displayed in Fig. 2c. A total wind speed variation of 1.6 m/s is estimated to have been produced by the rolls. The estimated pre-roll basic wind profile U_p that gives the correct orientation angle is shown in Fig. 2d; note its quadratic form that is often associated with thermally forced roll circulations.

The above method for estimating the roll contribution to the background wind profile is acceptable only if integration of the model for reasonable values of the parameters produces the necessary wind modification U_L . The results of this test are given in Fig. 3. In Fig. 3a the transition curves are shown, together with an estimate of the forcing values characterizing the atmosphere. The dashed line shows the transition curve for the thermal mode when the observed profile U_M in Fig. 2a is used, while the solid line shows the curve when the estimated pre-roll profile U_p in Fig. 2d is used. A few of the preferred orientation angles β_p and aspect ratios a_p are given for both curves; note that when the assumed roll modification is removed from the observed wind profile, the orientation angle is much improved and the aspect ratio is increased, implying that the expected roll spacing is decreased. The quadrilateral encloses the parameter region corresponding to that for the atmosphere. A sea surface/air temperature difference ranging between 0.2°C and 0.8°C , a lapse rate of 9.5°C/km characterizing the lower portion of the temperature profile in Fig. 3b, and eddy viscosity and thermometric conductivity variations between $10\text{ m}^2/\text{s}$ and $50\text{ m}^2/\text{s}$ were used to produce the vertices of the quadrilateral; these vertices are $(Ra, Re) = (0, 45); (10, 45); (0, 190); (125, 190)$. It is reassuring that the transition curves pass through the left side of the quadrilateral, implying that rolls supporting the cloud streets were generated by the thermal mode. The star in Fig. 3a shows the values of Ra and Re used to integrate the model. Because this point is well beyond the critical values given by the solid curve, a range of aspect ratios may be used in the integration; if too large an aspect ratio is chosen, then a temporally complicated roll solution results. However, when an aspect ratio of 0.9 is picked, which implies that the atmosphere evolved along a path roughly paralleling the right edge of the quadrilateral, then a nonlinear solution representing a propagating roll having a steady amplitude results. This solution is shown in Fig. 3c, and it produces the cross-roll wind profile modification shown in Fig. 3d. Clearly, this roll produces the necessary modification that is given in Fig. 2c, indicating that the amount of shear removed to estimate the pre-roll profile in Fig. 2d is plausible. This roll mode propagates from right to left at the rate 0.3 m/s , as might be expected in these coordinates because the pre-roll winds are mostly negative and of this magnitude in Fig. 2d. Moreover, the maximum speeds in the updraft are 0.8 m/s . Finally, the roll spacing of approximately 1 km is also reasonable, as indicated by inspection of the Landsat image. Thus by removing the contribution of the roll circulations to the measured wind profile, a pre-roll basic state wind profile is found that gives a reasonable roll mode. Further tests of this approach are planned with other wind profiles measured during FIRE.

Acknowledgments. Mark Laufersweiler helped us read the FIRE data tapes using a program written by Jeff Nucciarone. Dr. Robert Cahalan provided us a Landsat image and Dr. Bruce Albrecht gave us the appropriate sea surface temperature values. This research has been partially supported by the National Science Foundation through Grant ATM-8619854 and by the Office of Naval Research through Contract N000014-86-K-06880.

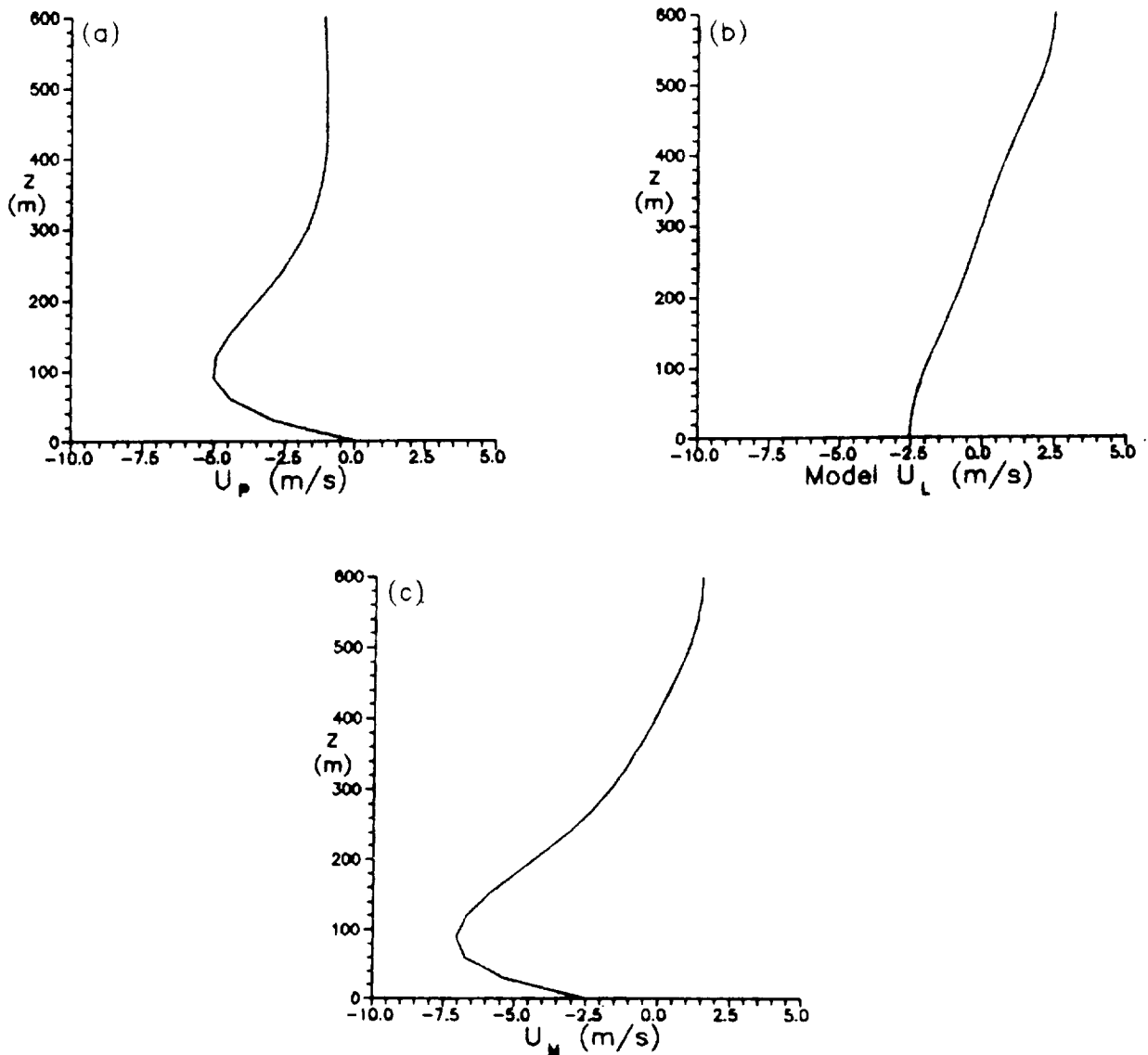


Figure 1. Ekman profile with a westerly geostrophic wind that is used to illustrate how much the orientation angle β may change when a roll-modified wind profile is used in the stability analysis. Here $\nu = \kappa = 25 \text{ m}^2/\text{s}$ and $z_T = 600 \text{ m}$. In (a) the original cross-roll profile U_P is given for an Ekman depth $D = 115 \text{ m}$ and a roll, or y -axis, orientation of 275° ; the negative values correspond therefore to southerly winds. In (b) the linear modification U_L of the cross-roll winds by the rolls is shown when $Re = 100$, or $Re - Re_c = 9$, and $Ra = 100$, or $Ra - Ra_c = 100$. In (c) the total modified cross-roll profile U_M is given.

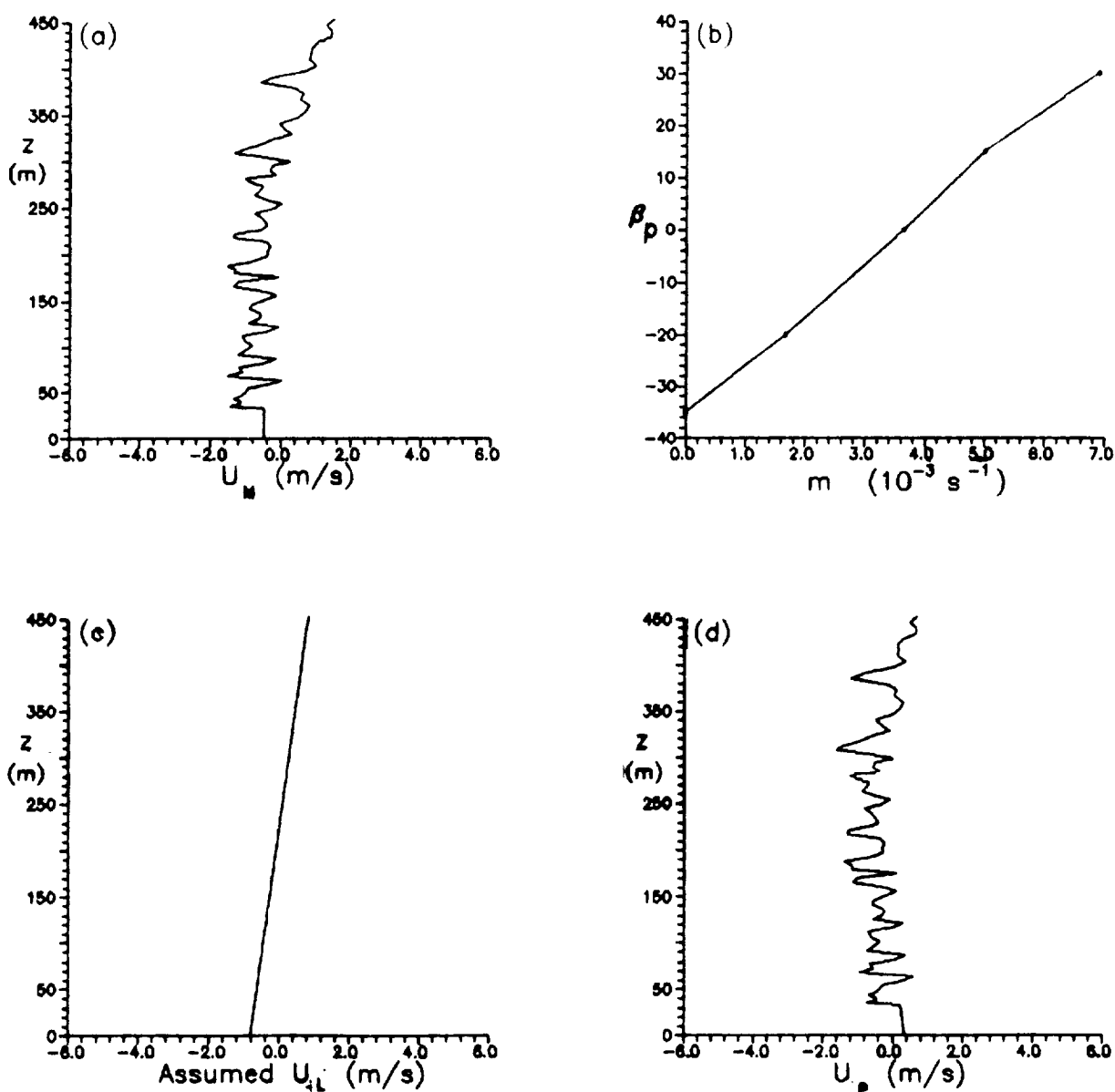


Figure 2. Cross-roll wind profiles for the descent sounding measured by the NCAR Electra in the predominantly clear air on July 7, 1987 (Flight 5) between 2136 and 2137:30 UTC; the cross-roll, or x-, direction is 70° (-ENE), so that negative values correspond to winds having directions less than 340° . In (a) the measured profile U_M is given, with the wind speed from the lowest level extrapolated to the surface. In (b) is shown the preferred orientation angle β_p relative to the mean wind direction (positive values to the left, negative values to the right) that is given by the stability analysis, as a function of the slope m in the cross-roll linear wind profile $U_L = mz + b$ that is removed from the one in (a). In (c) the optimal linear profile U_L is shown that gives an orientation angle $\beta_p = 0^\circ$. In (d) the estimated pre-roll profile U_p is given that is found by subtracting the profile in (c) from the one in (a).

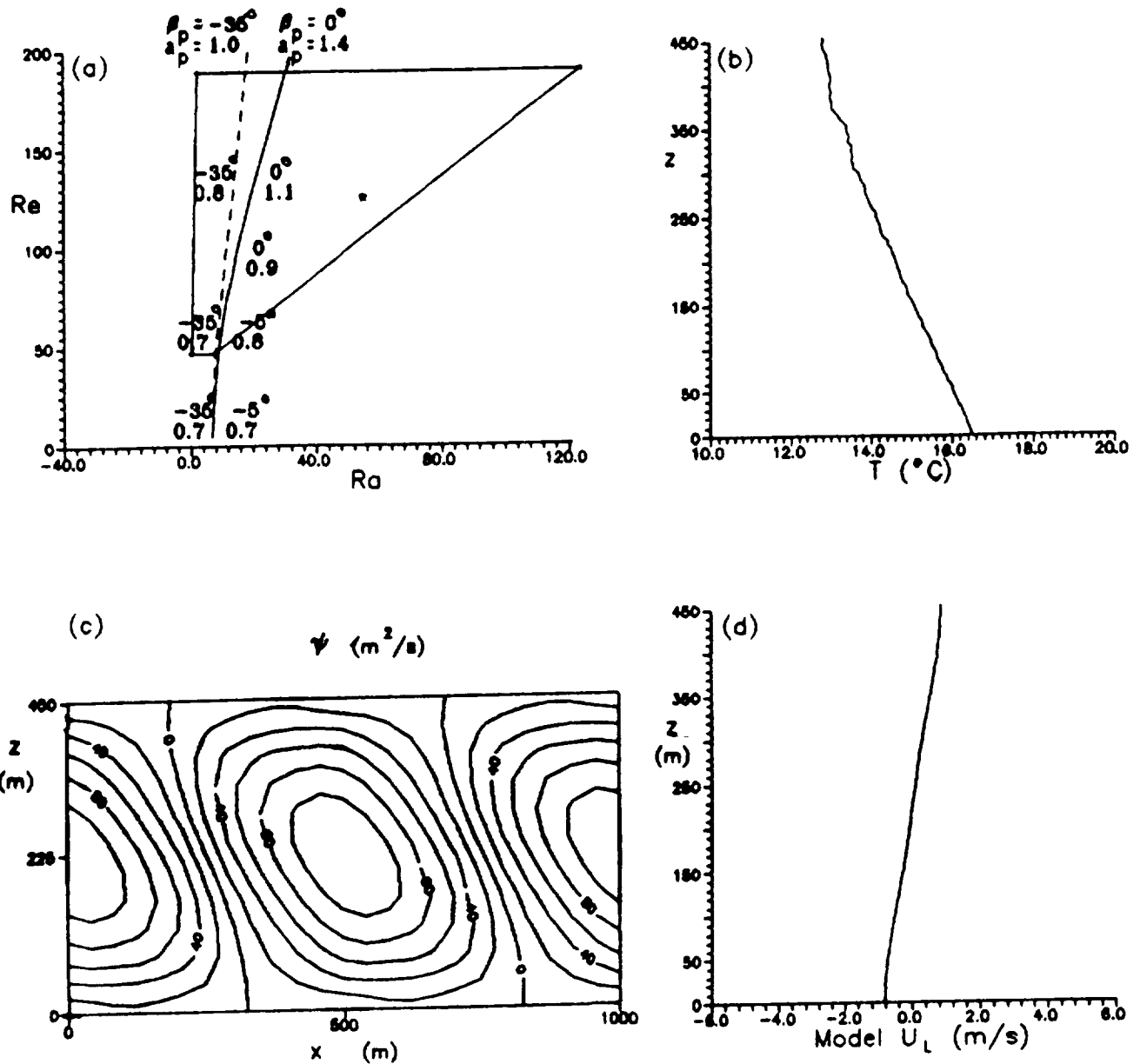


Figure 3. Results from the 14-coefficient spectral model. In (a) the dashed line denotes the transition curve obtained when the measured wind profile in Fig. 2a is used, the solid line denotes the transition curve obtained when the estimated pre-roll wind profile in Fig. 2d is used, the numbers next to the curves denote the preferred orientation angle β_p and aspect ratio a_p , the quadrilateral encloses the parameter values for the atmosphere, and the star denotes the parameter values used in the model integration. In (b) the observed temperature profile from the descent sounding of Fig. 2a is shown; the lapse rate in the lower part of the sounding is combined with an estimate of the sea surface/air temperature difference to calculate values of Ra for the quadrilateral in (a). In (c) and (d) the nonlinear solution to the 14-coefficient model is shown for $Ra = 55$, $Re = 125$, $\beta = 0^\circ$, $a = 0.9$ and the estimated pre-roll wind profile given in Fig. 2d; in (c) the roll circulation, which propagates at a steady rate of 0.3 m/s from right to left, is shown and in (d) the calculated roll-produced modification U_L of the wind profile is shown.

A CLOUDINESS TRANSITION IN A MARINE BOUNDARY LAYER

Alan K. Betts
RD2, Box 3300
Middlebury, VT 05753
and

Reinout Boers
Code 617, NASA/Goddard Space Flight Center
Greenbelt, MD 20771
June 1989

1) Introduction:

Boundary layer cloudiness plays several important roles in the energy budget of the earth. Low level stratocumulus are highly reflective clouds which reduce the net incoming short-wave radiation at the earth's surface. Climatically, the transition to a small area fraction of scattered cumulus clouds occurs as the air flows over warmer water. Although these clouds reflect less sunlight, they still play an important role in the boundary layer equilibrium by transporting water vapor upwards, and enhancing the surface evaporation (Betts, 1986; Betts and Ridgway, 1989). The First ISCCP (International Satellite Cloud Climatology Project) Regional Experiment (FIRE) included a marine stratocumulus experiment off the southern California coast from June 29 to July 19, 1987 (Randall et al, 1984; Albrecht et al, 1988). Among the objectives of this experiment were to study the controls on fractional cloudiness, and to assess the role of cloud-top entrainment instability, CTEI, (Randall, 1980; Deardorff, 1980) and mesoscale structure in determining cloud type.

The focus of this paper is one research day, July 7, 1987, when coordinated aircraft missions were flown by four research aircraft, centered on a Landsat scene at 1830 UTC. The remarkable feature of this Landsat scene (see other papers for photo) is the transition from a clear sky in the west though broken cumulus to solid stratocumulus in the east. In this paper, we analyze the dynamic and thermodynamic structure of this transition in cloudiness using data from the NCAR Electra. By averaging the aircraft data, we shall document the internal structure of the different cloud regimes, and show that the transition between broken cumulus and stratocumulus is associated with a change in structure with respect to the CTEI condition. However, this results not from sea surface temperature changes, but mostly from a transition in the air above the inversion, and the breakup appears to be at a structure on the unstable side of the wet virtual adiabat.

2) Data Collection and Processing

The flight plan for the Electra (Kloessel et al (1988)), and the data processing is discussed in the extended paper.

a) Averaging of Data into Cloudiness Regimes

The boundary between the cumulus and stratocumulus regimes was moving slowly eastward throughout the time of the Electra

flight. We used observer's notes and the lidar on the aircraft to give an estimate of the mean velocity of the boundary of 3ms^{-1} . Four regions were identified according to the observed cloudiness which we will refer to as Clear, Cumulus, Broken and Stratocumulus. Clear refers to the far western area where no clouds were present. Only a small fraction of the flight time was spent in this area. Cumulus refers to the region where small puffs of cumulus clouds were visible, but before the clouds developed into larger cells. Broken refers to the transition region between the Cumulus and Stratocumulus where the fractional cloudiness varied between 30% and 75%. Stratocumulus refers to the region towards the west where few holes appeared between clouds and the boundary layer was almost overcast. Approximately equal flight time was spent in the last three regions.

We computed the saturation level quantities of equivalent potential temperature, liquid water potential temperature, and total water mixing ratio and averaged the data of the main east-west flight legs and profile runs in pressure interval bins of 5 hPa for the four cloudiness regimes.

b) Determination of sea surface pressure and temperature

We attempted to compute the sea surface pressure by averaging the sea surface pressure values on the NCAR-Electra aircraft tapes. Inconsistent results were found when different flight legs and levels were compared, with variations of as much as 3 hPa between flight legs means. However horizontal pressure gradients showed consistently an approximately 1.2 hPa decrease in pressure from east to west over a 1 degree longitude interval. We also extrapolated the pressure versus radar altitude plot to the surface, but this surface pressure extrapolation suffers from an uncertainty of 1-2 hPa. We decided to retain the gradients in average sea surface pressure, and use a mean sea surface pressure of 1016 hPa consistent with surface synoptic charts.

For the sea surface temperature we used the radiometric temperature from the downward looking radiometer corrected for sea surface emission of sky radiation. A necessary estimate of the sky radiation was available from the upward looking radiometer.

3) Results

a) Horizontal gradients and fluxes near the surface

Fig. 1 shows the west-east cross-section of θ for the sea surface and the average of the two runs at 1010mb. This average was generated by binning the data in 0.05 longitude intervals. To the west in the cumulus and clear regions there is a positive sea-air θ difference, while under the stratocumulus there is a reversal because of the large drop of SST. We computed the surface sensible and latent heat fluxes using the bulk aerodynamic method. Wind-speeds are much higher on the stratocumulus side. We used a constant transfer coefficient of 1.10^{-1} , estimated from Stage and Businger (1981). We compared these bulk fluxes with those measured with the gust-probe system on the Electra (Albrecht, 1989, personal

communication), and found good agreement, considering the number of independent measurements being combined, the residual uncertainties in the sea surface pressure, and our corrections to the Electra temperature and dewpoint observations. The surface latent heat flux decreases across the cumulus-stratocumulus transition, and the surface sensible heat flux falls to near zero or becomes negative.

b) Thermodynamic Profiles

Fig. 2 has four panels showing the average vertical profiles of potential temperature and dewpoint (as a potential temperature) through the BL. Several features can be seen clearly. With the transition from cloud free to stratocumulus regimes (panels (a) to (d)). The BL deepens and, as would be expected, becomes moister until it is saturated. The inversion lifts but becomes stronger. The thermodynamic structure above the inversion shows dramatic differences. There is a tongue of very dry air immediately above the clear region, and this is capped by a moist layer above. The dry tongue disappears with the transition to stratocumulus, and so does the moist layer.

c) Conserved Variable Diagrams

Fig. 3 shows the four thermodynamic profiles on a conserved variable plot of saturation potential temperature, θ^* against total water q^* (Boers and Betts, 1988). Below cloud-base one can see a mixing line profile (Betts, 1982) nearly parallel to the dry virtual adiabat as found by Betts and Albrecht (1987). Above cloud-base and through the inversion, a linear mixing profile with a characteristic slope can be seen. The wet virtual adiabat $\theta_{v,w}^* = 310K$ is shown. We see that because of the relatively cool and dry tongue of air above the cloud-free and cumulus CBL's, the mixing line profile through the CBL is very unstable to the wet virtual adiabat in Figs. 3a, 3b. However, the profile through the stratocumulus, and overlying inversion is close to neutral with respect to a wet virtual adiabat. The wet virtual adiabat represents the stability criteria (Betts, 1983) for cloud-top entrainment instability (CTEI), which was suggested as one mechanism for the breakup of stratocumulus by the unstable downward mixing of inversion level air (Randall, 1980; Deardorff, 1980). There has been considerable discussion as to whether CTEI is a sufficient condition for the breakup of stratocumulus (Hanson, 1984; Albrecht et al, 1985; Randall, 1984; Rogers and Telford, 1986; Kuo and Schubert, 1988; Siems et al, 1989 and others). Fig. 3 suggests that CTEI is an important reference process associated with the transition between cumulus and stratocumulus boundary layers, because the mixing line profile through the cumulus layer is very unstable to CTEI whereas through the stratocumulus, it is nearly neutral (albeit slightly unstable). At this time near local noon the stratocumulus does appear to be thinning through the rise of cloud base as it is strongly destabilized by radiative cooling at cloud-top and warming at cloud-base. In this case the highly unstable thermodynamic structure on the cumulus side arises from

the relatively cool layer above the inversion, not from the modest increase in SST, or a large change in mixing ratio above the inversion.

4. Discussion and Conclusions

The transition in structure associated with this transition in cloudiness from a clear sky through tiny cumulus, broken stratocumulus to a solid stratocumulus deck appears to be associated with a large change in the slope of the mixing line. Above the cumulus, the inversion is lower but much weaker in strength and the air above still quite dry, so that the mixing line through the cloud layer is very unstable to the wet virtual adiabat: the criterion for CTEI. Above the stratocumulus, the much stronger inversion gives rise to a mixing line which is only marginally unstable to the CTEI criterion, apparently not enough to break up the solid cloud layer in the face of mixing driven by radiative destabilization and shear generation at the surface. The figures show a clear progression from the clear air, where the mixing down of very dry air ($\approx 2\text{gKg}^{-1}$) appears to be sufficient to prevent any cumulus from forming, to the cumulus regime. Likewise the transition region shows an intermediate thermodynamic structure between cumulus and stratocumulus. From the thermodynamic structure of the broken stratocumulus we can make an estimate (if we ignore all advective effects and assume local equilibrium) of the critical mixing line slope for the formation or breakup of the stratocumulus. Expressed in terms of the slope of the wet adiabat, we obtain

$$(\partial\theta/\partial p)_{\text{CTEI}} \approx 0.7 \text{ } \Gamma_w$$

This is more unstable than the wet virtual adiabat which has a slope of $0.9 \text{ } \Gamma_v$. There is also some indication in this data that the stratocumulus layer partly uncouples near local noon as has been suggested by Nicholls (1984), and seen in the FIRE data (eg. Betts (1989). The stratocumulus cloud-base as determined by lidar rises 10mb during the flight pattern (2.5 hrs), while the LCL of the low level air descends about 10mb during the same time.

ACKNOWLEDGEMENTS:

AKB has been supported by the NSF under Grant ATM-8705403 and the NASA GSFC under Contract NAS5-30524: RB by the National Office of Climate Research under Dr. Schiffer. We are grateful to B.A. Albrecht and K. Kloessel for data and synoptic advice.

REFERENCES:

- Albrecht, B. A., R. Penc, and V. Schubert, 1985: An observational study of cloud-topped mixed layers. *J. Atmos. Sci.*, **42**, 800-822.
- Albrecht B.A., D.A. Randall and S. Nicholls; 1988: Observations of marine stratocumulus during FIRE. *Bull. Amer. Meteor. Soc.* **69**, 618-626.
- Betts, A. K., 1982: Saturation Point Analysis of Moist Convective Overturning. *J. Atmos. Sci.*, **39**, 1484-1505.
- Betts, A.K., 1983: Thermodynamics of mixed stratocumulus layers: saturation point budgets. *J. Atmos. Sci.*, **40**, 2655-2670.
- Betts, A. K., 1986: A new convective adjustment scheme. Part I: Observational and theoretical basis. *Quart. J. Roy. Meteor. Soc.*, **112**, 677-692.
- Betts, A.K. 1989: Diurnal variation of California coastal stratocumulus from two days of boundary layer soundings.

- Tellus, 41A, (in press).
- Betts, A. K., and B. A. Albrecht, 1987: Conserved variable analysis of boundary layer thermodynamic structure over the tropical oceans. J. Atmos. Sci., 44, 83-99.
- Betts, A.K. and W. L. Ridgway, 1989: Climatic equilibrium of the atmospheric convective boundary layer over a tropical ocean. J. Atmos. Sci., 46, (Aug)
- Boers, R., and A. K. Betts, 1988: Saturation point structure of marine stratocumulus clouds. J. Atmos. Sci., 45, 1157-1175.
- Deardorff, J.W., 1980: Cloud-top entrainment instability. J. Atmos. Sci., 37, 131-147.
- Hanson, H. 1984: On mixed layer modelling of the stratocumulus topped marine boundary layer. J. Atmos. Sci., 41, 1226-1236.
- Kloessel, K.A., B.A. Albrecht, and D.P. Wylie, 1988: FIRE Marine stratocumulus observations Summary of operations and synoptic conditions. FIRE Tech. Report No.1. Dept. of Meteor., Penn State Univ., Univ. Park, PA 16802. 191 pp.
- Kuo, H-C, and W.H. Schubert, 1988: Stability of cloud-topped boundary layers. Quart. J. Meteor. Soc., 114, 887-916.
- Lilly, D. K., 1968: Models of cloud-topped mixed layers under a strong inversion. Quart. J. Roy. Meteor. Soc., 94, 292-309.
- Nicholls, S. 1984: The dynamics of stratocumulus: Aircraft observations and comparisons with a mixed layer model. Quart. J. Roy. Meteor. Soc., 110, 783-820.
- Randall, D.A., 1980: Conditional instability of the first kind upside-down. J. Atmos. Sci., 37, 125-130.
- Randall, D. A., 1984: Stratocumulus cloud deepening through entrainment. Tellus, 36A, 446-457.
- Randall, D.A., J.A. Coakley, C.W. Fairall, R.A. Kropflin and D.H. Lenschow, 1984: Outlook for research on subtropical marine stratiform clouds. Bull. Amer. Meteor. Soc., 65, 1290-1301.
- Rogers, D., and J.W. Telford, 1986: Metastable stratostops. Quart. J. Roy. Meteor. Soc., 112, 481-500.
- Schubert, W.H., J. S. Wakefield, E. J. Steiner, and S. K. Cox, 1979: Marine stratocumulus convection. Part I: Governing equations and horizontally homogeneous solutions. J. Atmos. Sci., 36, 1286-1307.
- Stage, S. A. and J. A. Businger, 1981: A model for entrainment into a cloud-topped boundary layer. Part I: Model description and application to a cold air outbreak. J. Atmos. Sci., 38, 2213-2229.
- Siems, S.T., C.S. Bretherton, M.B. Baker, S. Shy, and H.T. Breidenthal, 1989: Buoyancy reversal and cloud-top entrainment instability. Submitted to Quart. J. Roy. Meteor. Soc.

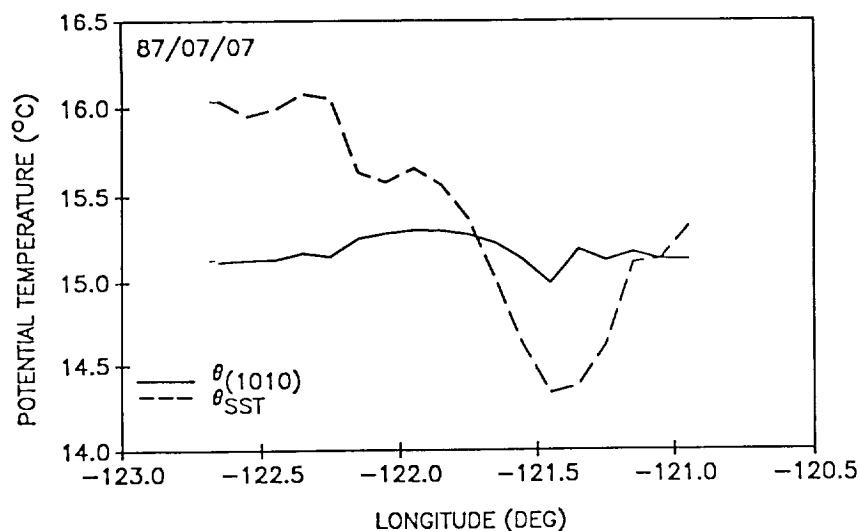


Fig. 1 Cross-section of θ for sea surface and 1010mb.

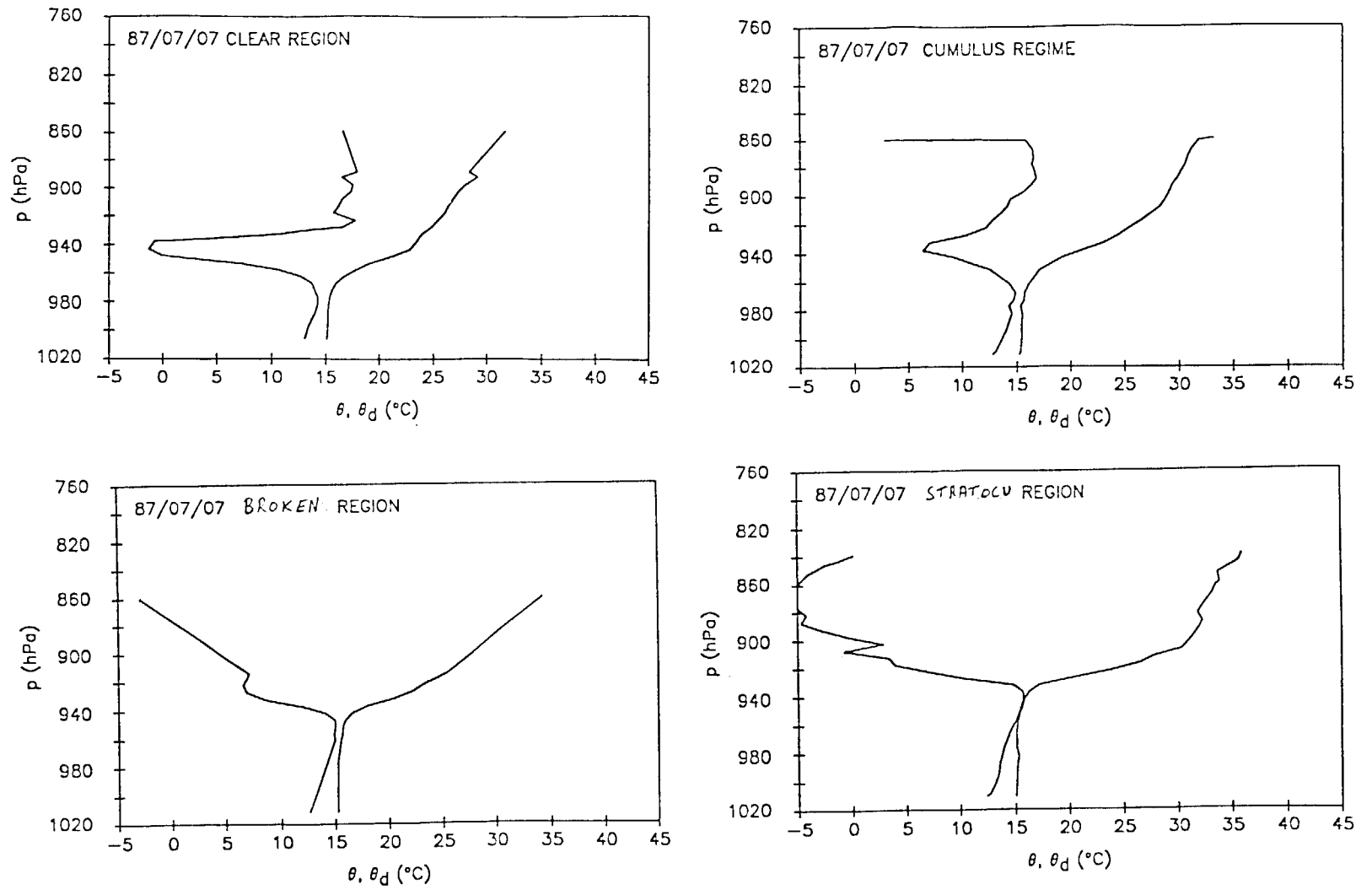


Fig. 2 Mean thermodynamic profiles for four regimes: clear, cumulus, broken, stratocumulus.

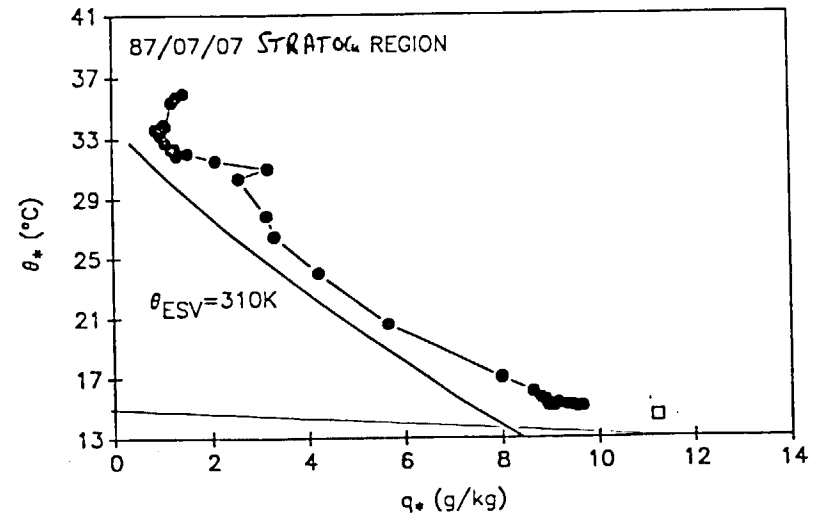
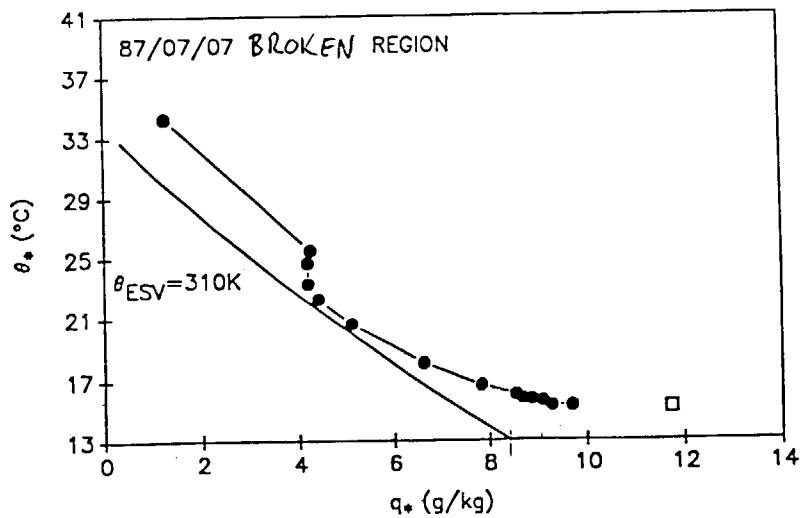
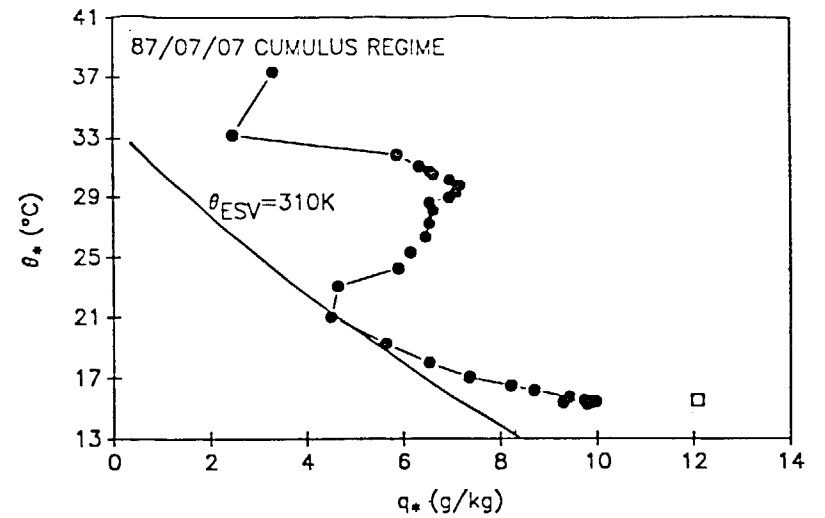
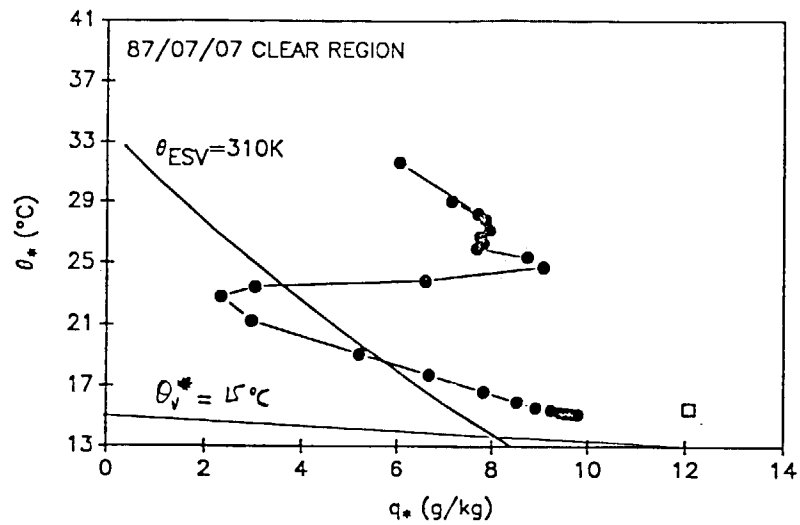


Fig. 3 Conserved variable plots (θ^* , q^*) showing profiles for four regimes.

ANALYSIS OF MARINE STRATOCUMULUS CLEARING EVENTS DURING FIRE

(POSTER SESSION)

Kevin A. Kloesel
Department of Meteorology
Penn State University
University Park, PA 16802

I Introduction

During FIRE, three major stratocumulus clearing events took place over the project region. The purpose of this poster session is to analyze these clearing events using synoptic variables to determine if these clearing events can be predicted by current modeling techniques. A preliminary statistical evaluation of the correlation between satellite cloud brightness parameters and NMC global model parameters is available in Wylie, et al, 1989.

II. Analysis of clearing events

The three major clearing events over the project area occurred July 3-4, July 6-7, and July 17-18. A fourth major clearing event occurred July 13-15 just to the north of the project area and will be included in this analysis.

Two synoptic scenarios appear to govern the clearing events. The first is the occurrence of a ridging of the surface Pacific sub-tropical high into the Pacific Northwest. This ridging enhances the offshore flow at the surface along the Oregon and northern California coastlines resulting in a dryer boundary layer than if the fetch was over water. This occurred as a prelude to the clearing events July 3-4, July 6-7, and July 13-15. This synoptic scenario also occurred, however, when no substantial clearing took place. Therefore, other processes must be evaluated. The second scenario is the existence of strong cold air advection (as determined by 1000-500mb thickness patterns) in association with the northwesterly flow on the back side of synoptic disturbances. An especially strong low pressure disturbance with strong cold air advection was responsible for the widespread clearing at the end of the experiment (July 17-18).

III. References

- Wylie, D., B.B.Hinton, and K.A.Kloesel, 1989: The relationship of marine stratus clouds to wind and temperature advection. *Mon Wea Rev* (accepted for publication).

FIRE Aircraft Observations of Horizontal and Vertical Transport
in Marine Stratocumulus

Ilga R. Paluch and Donald H. Lenschow
National Center for Atmospheric Research*
Boulder, Colorado 80307

INTRODUCTION

A major goal of research on marine stratocumulus is to try to understand the processes that generate and dissipate them. One approach to studying this problem is to investigate the boundary layer structure in the vicinity of a transition from a cloudy to a cloud-free region to document the differences in structure on each side of the transition. Since stratiform clouds have a major impact on the radiation divergence in the boundary layer, the transition from a cloudy to a clear boundary layer is a region of large horizontal inhomogeneity in air temperature and turbulence intensity. This leads to a considerable difference in horizontal and vertical transports between the cloudy and cloud-free regions.

We use measurements from the NCAR Electra aircraft during Flights 5 (7 July 1987) and 10 (18 July 1987) of FIRE for this purpose. Flight 5 coincided with a Landsat overflight, and was designed to investigate the transition across a well-defined N-S cloud boundary, since the Landsat image can document the cloud cover in considerable detail. Turbulence legs were flown about 60 km on both sides of the cloud boundary. Flight 10 was flown at night in an area of scattered small cumuli and broken cloud patches.

DISCUSSION OF OBSERVATIONS

Figure 1 shows data from two soundings, about 200 km apart, from Flight 5. The sounding on the left was taken in an area covered with a stratiform deck; the sounding on the right was in a cloud-free region. Profiles of liquid water content, potential temperature, and total water mixing ratio are shown. As can be seen in the stratiform sounding, there are sharp changes in potential temperature and total water mixing ratio at the inversion, whereas in the clear-air sounding the changes are gradual. These differences are a common feature of the cloudy and cloud-free soundings observed during both the Dynamics and Chemistry of Marine Stratocumulus (DYCOMS) experiment and FIRE.

* The National Center for Atmospheric Research is sponsored by the National Science Foundation.

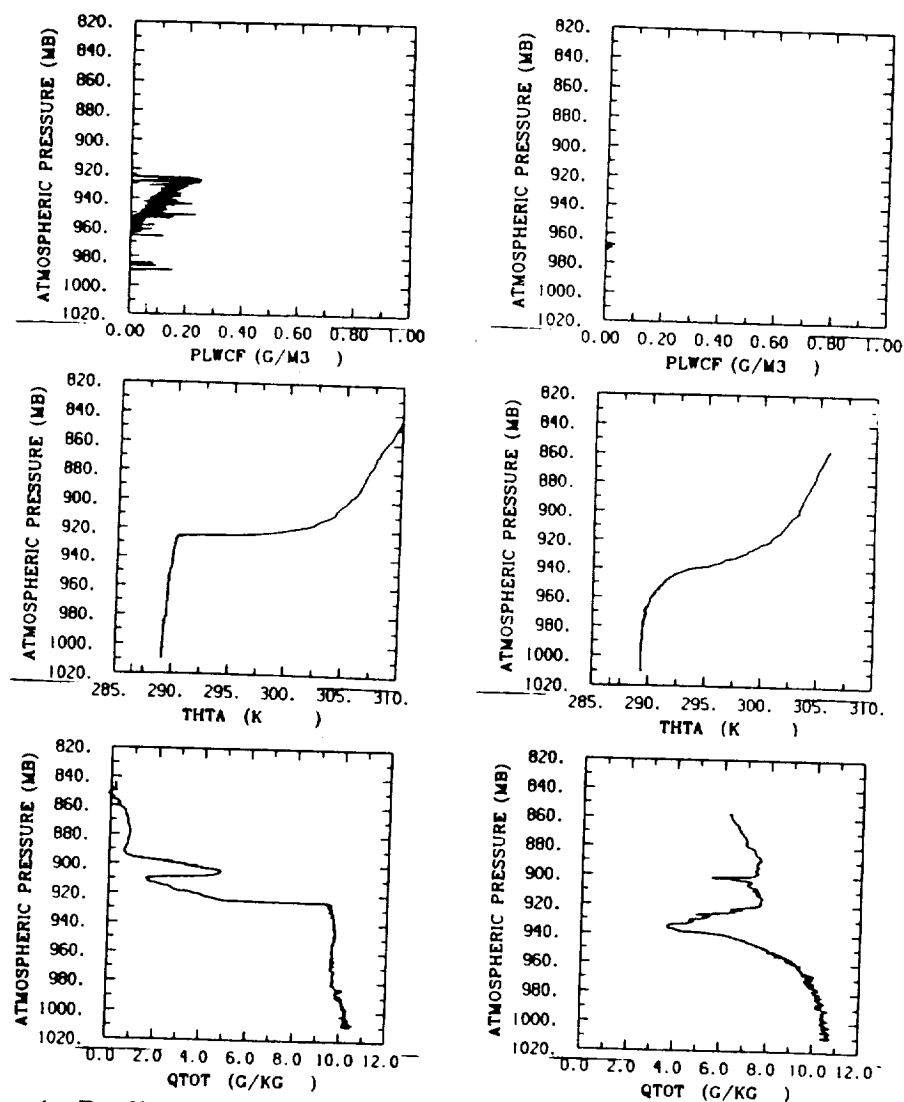


Figure 1. Profiles of liquid water content (PLWCF) from a Particle Measuring Systems FSSP, potential temperature Θ (THTA), and total water (vapor and liquid) mixing ratio (QTOT). From flight 5; 7 July, 1987.

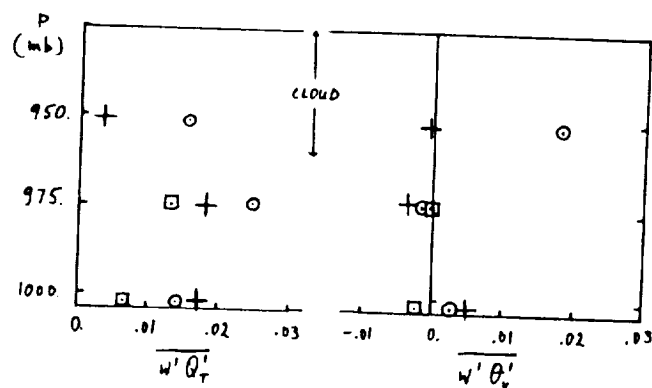


Figure 2. Total water and buoyancy fluxes measured by the Electra on flight 5, 7 July 1987. The circles and squares represent fluxes from stratiform regions, the crosses data from cloud-free regions. For further explanation see text.

Figure 2 shows vertical moisture and buoyancy fluxes¹ measured during constant altitude flight legs on this day. The circles and squares represent data from stratiform regions, the crosses are data from clear air regions. At the two lowest levels (at 1010 and 975 mb), the squares represent portions of the flight leg where the sea surface temperature, measured by a surface temperature radiometer, was in the 15.0-15.8 C range; the circles and crosses correspond to a sea surface temperature in the 15.7-16.5 C range. As expected, the fluxes show some dependence on the sea surface temperature at the two lower flight levels. The buoyancy flux at 975 mb, however, is very small compared to that in cloud, which indicates that the surface buoyancy flux is likely to be relatively unimportant in the turbulence energy budget of this boundary layer. The upper level (950 mb) flight passed through the stratiform deck, and there the sea surface temperature could not be measured. In cloud, the buoyancy flux rises because of radiational cooling near cloud-top, which enhances mixing and entrainment at cloud top; consequently the moisture flux in cloud is also enhanced. By comparison, in the cloud-free region the moisture and buoyancy fluxes are negligible at 950 mb. As a result, there is little mixing and the temperature stratification is more stable (Fig. 1).

It is possible that at least some of the differences between the cloudy and cloud-free soundings in Fig. 1 are due to differences in horizontal advection. That is, the air in the cloudy region may have a different origin and have different thermodynamic properties than that in the cloud-free region. To minimize the effect of advection we examine several short soundings from Flight 10, where adjacent cloudy and clear areas were traversed in several up and down passes, as sketched in Fig. 3.

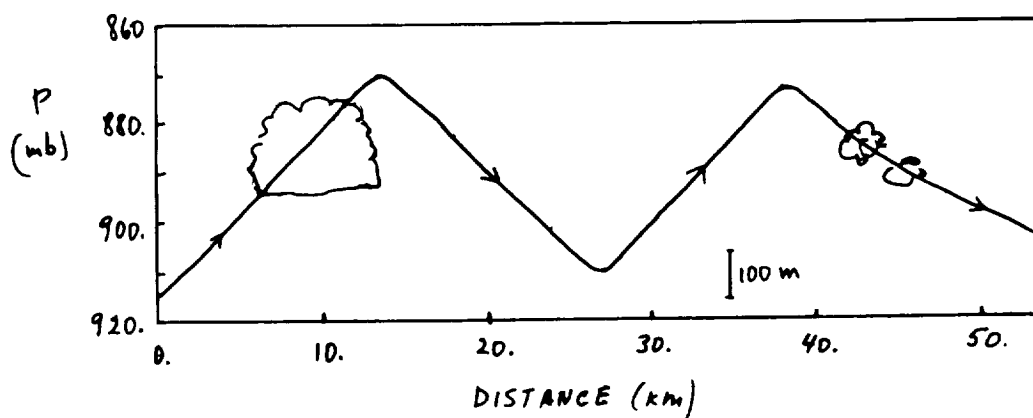


Figure 3. Sketch of the flight pattern used in Fig. 4.

Soundings from the above passes are shown in Fig. 4. The plots show liquid water content, potential temperature, total water mixing ratio, vertical velocity, east velocity component, and north velocity component. As in the sounding in Fig. 1, here too

¹ i. e. $\overline{w'q'}$ and $\overline{w'\theta'_v}$, where w is vertical velocity, q the total water mixing ratio, θ_v the virtual potential temperature, the prime indicates departures from a least squares linear fit to the time series, and the overbar an average over a horizontal flight segment.

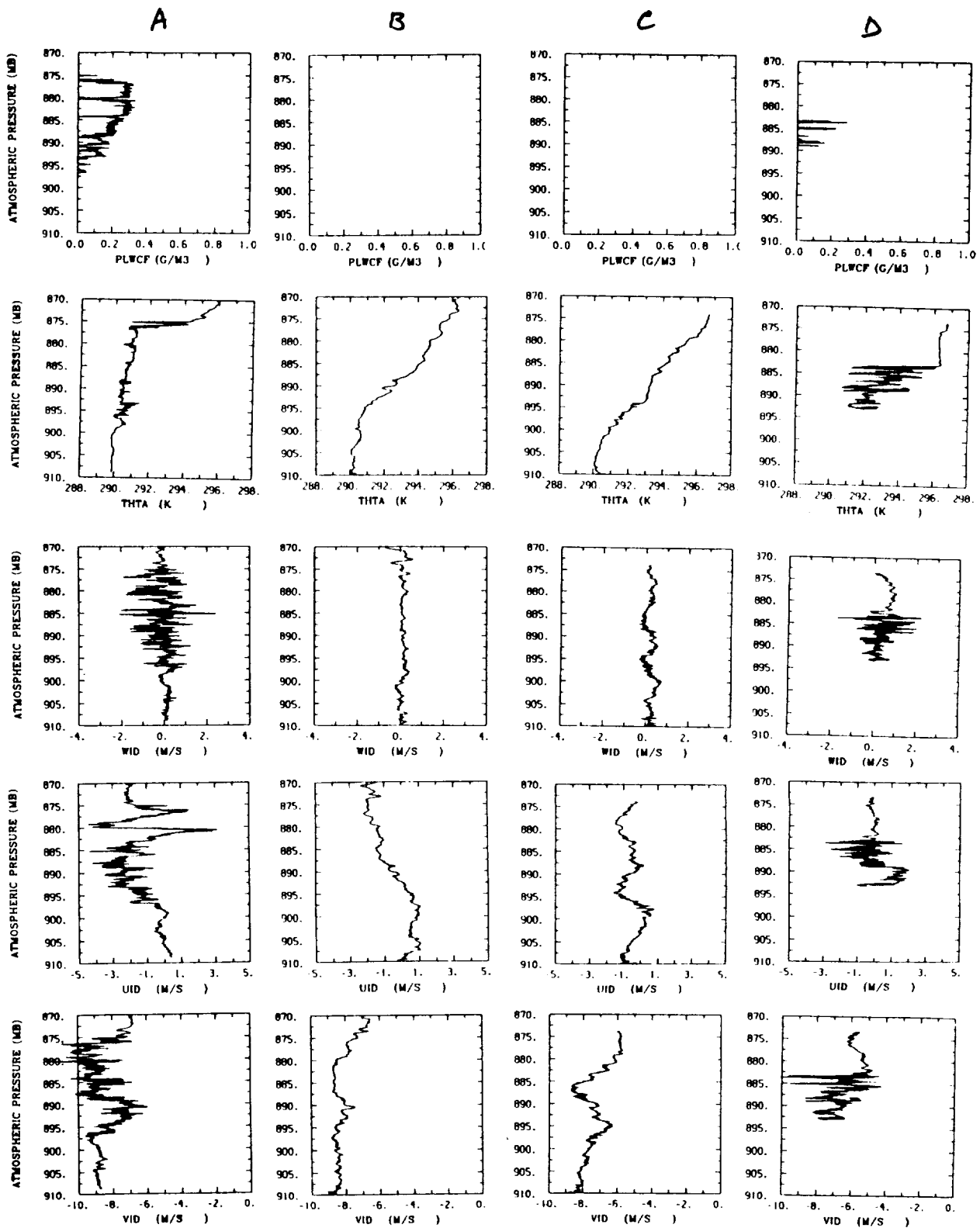


Figure 4. Profiles of liquid water content (PLWCF), potential temperature (THTA), vertical velocity (WID), east velocity component (UID), and north velocity component (VID) from Flight 10, 18 July 1987.

the clear-air temperature and moisture profiles change gradually with height (B and C), whereas in the presence of cloud or cloud patches there are abrupt changes in temperature and moisture at the inversion (A and D).

Comparing the first two soundings we note that the temperature in the cloudy air is significantly colder than in the adjacent clear air. The maximum difference in temperature reaches 4 K just below the inversion, at 875 mb, where the horizontal separation between the two soundings was only about 4 km. Clearly, such a temperature difference can be expected to lead to a circulation that would tend to reduce the difference. This instability can be viewed in terms of a simple situation, described by Margulis (1906) and often discussed in textbooks (for example, Hess, 1958), where two airmasses of different temperatures are side-by-side. Seeking a stable configuration, the airmasses then rearrange themselves so that the colder air rests below the warmer air. It can be shown from energy balance that the velocity of such a circulation is of the order of

$$V = \frac{1}{2}gh \frac{\Delta\theta_v}{\theta_v}$$

where g is the gravitational acceleration, and $\Delta\theta_v$ is the virtual potential temperature difference between the two airmasses, initially extending over a height h . For the present case $\Delta\theta \sim 3\text{K}$ and $h \sim 200\text{m}$, so that the mean velocity $V \sim 2\text{m s}^{-1}$, which is well within the range of the present observations. Thus we expect that motions due to instabilities at the cloud and clear-air interfaces contribute to the velocity fluctuations. Since they tend to move cloudy air downward and under the adjacent cloud-free air, they likely erode the cloud edges and may lead to dissipation of the cloud.

In the last sounding the aircraft encountered a few turbulent cloud patches below an inversion located about 8 mb lower than the inversion in the first sounding. Below the inversion there are large fluctuations in temperature but, unlike the first sounding, the temperature fluctuations are positive as well as negative with respect to the nearby clear-air temperature profile. Thus, while there are large temperature instabilities locally, the region as a whole is more stable with respect to the nearby clear-air temperature profile than the cloud region encountered in the first sounding. It is likely that this sounding represents the dissipating stages of a cloud region which earlier may have been similar to that encountered in the first sounding.

REFERENCES

- Hess, S., 1958: Introduction to theoretical meteorology. Holt, Rinehart and Winston, New York; pp. 297-302.
- Margulis, M., 1906: Zur Sturmtheorie, Met. Zeit., 23, pp. 481-497.

VERTICAL-VELOCITY SKEWNESS IN THE MARINE STRATUS-TOPPED BOUNDARY LAYER

Chin-Hoh Moeng, Richard Rotunno, and Ilga Paluch
National Center for Atmospheric Research*
P.O. Box 3000, Boulder, Colorado

1. Motivations

Vertical-velocity skewness, $S_w \equiv \overline{w^3}/(\overline{w^2})^{3/2}$, in a turbulent flow is important in several regards. S_w is indicative of the structure of the motion—when it is positive, updrafts are narrower and stronger than surrounding downdrafts, and vice versa. The quantity $\overline{w^3}$ represents the vertical flux of the vertical component of turbulence energy, which dominates the turbulent energy transport in buoyancy-driven turbulence. Therefore, $\overline{w^3}$ may be an important quantity that determines the entrainment rate in the buoyancy-driven boundary layer.

Aircraft measurements often suggest cool, narrow downdrafts at some distance below the stratus cloud top, indicating a negative S_w (Nicholls and Leighton, 1986). This seems natural as the turbulence within the stratus-topped boundary layer (CTBL) is driven mainly by the radiative cooling at the cloud top (although sometimes surface heating can also play a major role.) One expects intuitively (e.g., Nicholls, 1984) that, in the situations where cloud-top cooling and surface heating coexist, the turbulence statistics in the upper part of the CTBL are influenced more by the cloud-top cooling, while those in the lower part, more by the surface heating. Thus one expects negative S_w in the upper part, and positive in the lower part, in this case. In contradistinction, large-eddy simulations (LES) of the CTBL show just the opposite: The S_w is *positive* in the upper part and *negative* in the lower part of the layer. Figure 1 shows the vertical distribution of $\overline{w^3}$ and S_w from a $(40)^3$ large-eddy simulation (Moeng, 1986) of the CTBL with both cloud-top cooling and surface heating.

To understand the nature of vertical-velocity skewness, we study the simplest type of buoyancy-driven turbulence—turbulent Rayleigh-Benard convection—through direct numerical simulations. The following is an abstract version of the paper by Moeng and Rotunno (1989).

2. Turbulent Rayleigh-Benard convections

Consider a shallow, incompressible fluid between two infinite horizontal plates with the bottom one maintained at a higher temperature than the top. When the Rayleigh number, $R_a \equiv g\beta\Delta TD^3/(\mu\kappa)$, is larger than a critical number, the fluid is unstable and if large enough becomes turbulent. Here, D is the distance between the upper and lower plates,

* The National Center for Atmospheric Research is sponsored by the National Science Foundation.

ΔT is the temperature difference between the plates, g is the acceleration of gravity, β is the coefficient of volume expansion, and μ and κ are the coefficients of molecular viscosity and conductivity.

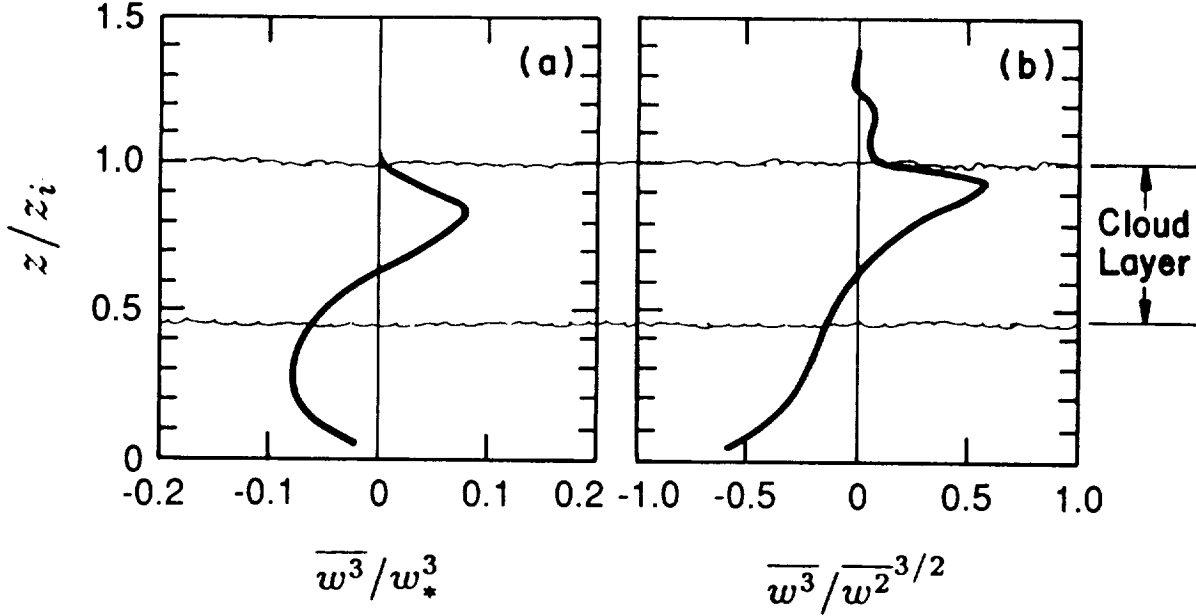


Figure 1 Profiles of (a) flux of vertical-velocity variance, and (b) vertical-velocity skewness in the stratus-topped boundary layer obtained in a $(40)^3$ large-eddy simulation (after Moeng 1986.) The convective scaling velocity, $w_* \equiv [\beta g z_i B_c]^{1/3}$, where B_c is the layer-averaged buoyancy flux in the cloud layer.

Direct numerical simulations solve the Navier-Stokes equations exactly with no uncertain parameters, thus the simulations are in a sense exact except for possible numerical errors. We carry out two experiments in the fully turbulent regime (at R_a on the order of 10^5): Experiment HC (for ‘Heating and Cooling’) includes both bottom heating and top cooling. Experiment H (for ‘Heating’) has only bottom heating. Although we do not actually carry out an Experiment C (for ‘Cooling’), we will refer to it as such with the understanding that it is a symmetry of Experiment H with obvious sign changes on the w and T fluctuations.

Figure 2 shows S_w -distributions for Experiments H, C, and HC. Bottom-heating-only generates positive vertical-velocity skewness throughout and S_w increases with height away from the source. Similarly, top-cooling-only generates negative vertical-velocity skewness throughout and its negative magnitude increases downward away from the source. When bottom heating and top cooling coexist, S_w is positive in the upper layer and negative in the lower layer. Adding S_w -distribution from Experiment H to that from Experiment C, we obtain a profile similar to that from Experiment HC.

Therefore, understanding the nature of the S_w -distribution for the bottom-heating-

only (or the top-cooling-only) is necessary first step toward understanding why there is negative S_w in the lower half and positive S_w in the upper half in the case with both top-cooling and bottom-heating.

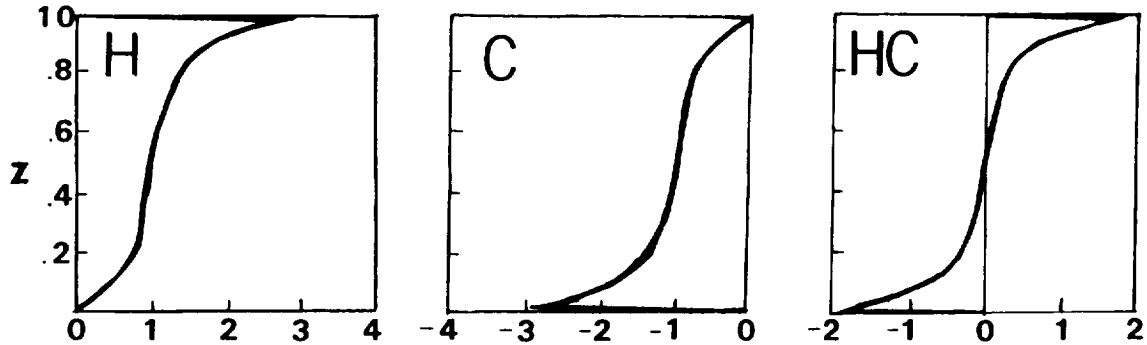


Figure 2 Profiles of vertical-velocity skewness from Experiments H, C, and HC.

3. Physical mechanism responsible for w -skewness

The mechanism responsible for the increase of S_w with height in the bottom-heating case can be easily understood by examining the structure of the turbulent eddies. The planform structure shown in Fig. 3 indicates an irregular cellular pattern in the lower levels, and more isolated and discrete updrafts in the upper levels. The total area covered by updrafts decreases with height. Since the skewness is related to the ratio of the total area covered by updrafts to the area covered by downdrafts, Fig. 3 indicates an increase of S_w with height.

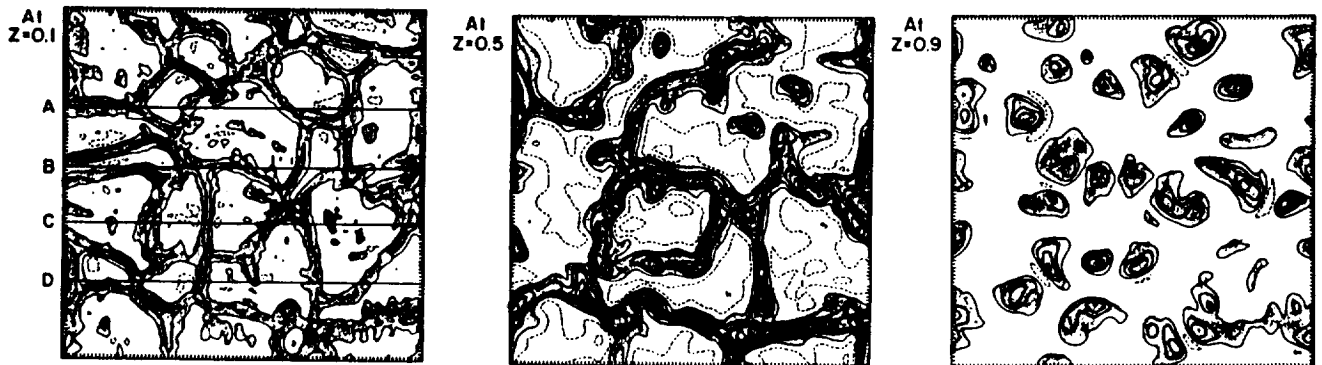


Figure 3 Horizontal cross sections of w from Experiment H. The shaded areas indicate positive values. The solid and dashed contour lines (contour interval, 0.1) represent positive and negative values, respectively. Vertical cross sections through the locations marked A,B,C and D are shown in Fig. 4.

To get a better view of the eddy structure, we show in Fig. 4 the vertical cross sections along four y-locations marked in the left panel of Fig. 3. Here we see a few big eddies penetrate into the top, while others never make it to the top, which is typical for a fully developed turbulent flow. The area covered by individual updrafts remains relative constant with height, while the number of updrafts decreases. Therefore, the net area covered by updrafts decreases with height, and S_w increases with height.

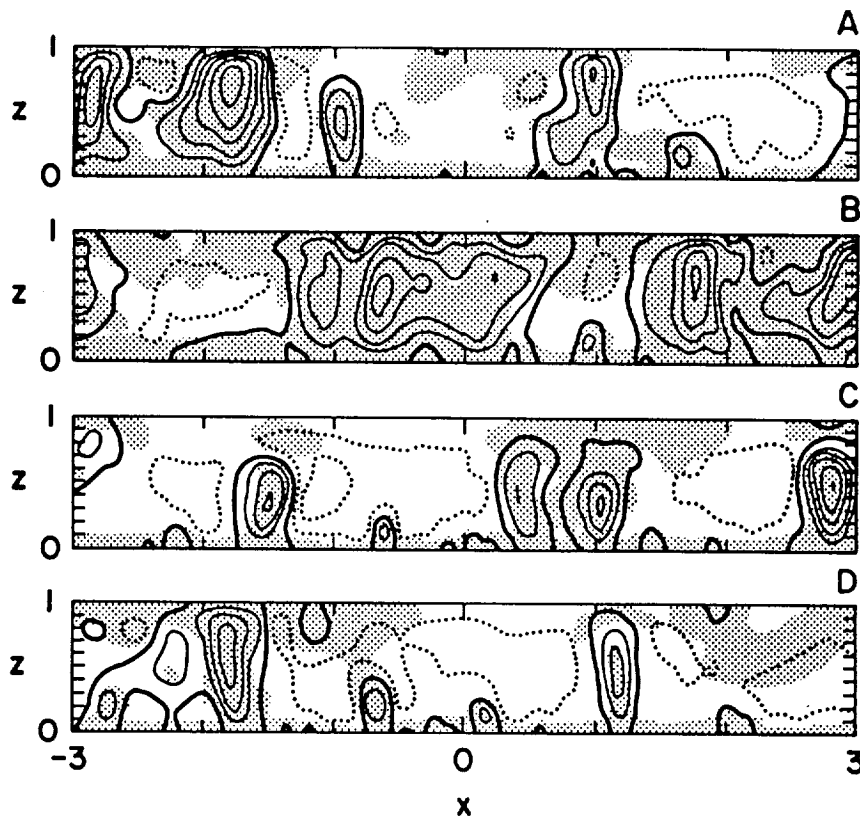


Figure 4 Vertical (x-z) cross sections through the locations marked in Fig. 3. The shaded area represents regions where $T - \bar{T} > 0.3$. Areas of $w > 0$ are enclosed by the thick solid line; the solid and dotted contour lines (contour interval, 0.1) indicate positive and negative values of w , respectively.

4. Stratus-topped PBL

When a stratus cloud layer exists in the upper part of the PBL, there is always longwave radiative cooling at the cloud top. For the case of no surface buoyancy flux, the CTBL resembles Experiment C, and for the case with a positive surface flux, it resembles Experiment HC, except for the difference of existing entrainment process in the CTBL.

In the case with a positive surface flux, the LES results show negative S_w in the lower

half and positive S_w in the upper half of the CTBL, in agreement with Experiment HC. Nicholls and Leighton (1986)'s aircraft data show negative S_w within some distance below cloud top (their Fig. 12). With only one exception, the cases they analyze have zero surface fluxes. Therefore S_w should be negative throughout the CTBL, as indicated by Experiment C, and it is so observed.

We have analyzed the FIRE data for S_w . We will present our results in the meeting.

REFERENCES

- Moeng, C.-H., 1986: Large-eddy simulation of a stratus-topped boundary layer. part I: Structure and budgets. *J. Atmos. Sci.*, **43**, 2886–2900.
- Moeng, C.-H. and R. Rotunno, 1989: Vertical-velocity skewness in the buoyancy-driven boundary layer. Submitted to *J. Atmos. Sci.*
- Nicholls, S., 1984: The dynamics of stratocumulus: aircraft observations and comparisons with a mixed-layer model. *Quart. J. Roy. Meteorol. Soc.*, **110**, 783–820.
- Nicholls, S. and J. Leighton, 1986: An observational study of the structure of stratiform cloud sheets: Part I. Structure. *Quart. J. Roy. Meteorol. Soc.*, **112**, 431–460.

LABORATORY EXPERIMENTS ON STABILITY AND ENTRAINMENT OF OCEANIC STRATOCUMULUS -- Part I: Instability Experiment

SHENQYANG S. SHY

Department of Aeronautics and Astronautics, FS-10
University of Washington, Seattle, WA 98195

1. INTRODUCTION

The existence and persistence of marine stratocumulus play a significant role in the overall energy budget of the earth. Their stability and entrainment process are important in global climate studies, as well as for local weather forecasting.

Lilly(1968) and Randall(1980) recognized that the evaporative cooling of unsaturated air which had been entrained into a cloud can under some conditions cause the entrained air to sink unstably as a convective downdraft. They called it conditional instability of the first kind upside-down (CIFKU). It was suggested (Randall, 1980; Deardorff, 1980) that the CIFKU was responsible for the breakup of subtropical stratocumulus layers as long as such nonlinear buoyancy reversal occurred. Contrary to the expectations of Randall and Deardorff, Turner and Yang (1963) in their laboratory simulation on entrainment at the top of stratocumulus clouds suggested that the entrainment was slightly reduced by nonlinearity and the change would be negligible in practice. Caughey et al. (1985) and Nicholls and Turtin (1986) suggested that evaporative cooling enhances entrainment over that expected in the linearly mixing case from observations in stratocumulus. However, Hanson (1984) and Albrecht et al. (1985) observed that clouds do not necessarily thin or breakup due to evaporative cooling, as had been suggested by Randall and Deardorff.

These apparent contradictions may arise from three reasons; namely, (1) the Richardson number effect, (2) the mixing model, or (3) the Reynolds number effect. First, cloud top entrainment instability (CTEI) is an interfacial instability. It requires that the dry unsaturated air entrains into the cloud and then the two fluids mix together to release additional kinetic energy from mixing-induced buoyancy reversal, thereafter leading to a runaway entrainment. The questions then arise: What is the entrainment mechanism in order that the two fluids can be mixed together across an inversion? What are the key parameters that dominate the process of entrainment? What is the physical mechanism that determines instability? As Miles (1986) noted, the Richardson number is seminal for our understanding of atmospheric dynamics and is the dominant parameter in any rational discussion of stratified flow. It indicates the response of the interface to the turbulence. Neither the experimental approaches nor the numerical simulations have investigated the effect of the Richardson number on the buoyancy reversal case. Therefore, that may explain why so little is known about the impact of buoyancy reversal on entrainment rate. The physics of the breakup process remains poorly understood and unsolved. Second, in many numerical simulations of cloudtop turbulent entrainment and instabilities the equations of motion are two dimensional and laminar, neglecting the density perturbation everywhere except in the gravitational term (Boussinesq approximation) with the consequence that the convective motions due to perturbation from buoyancy reversal may be sustained much longer than it should be. The highly dissipative behavior which necessarily accompanies the turbulent mixing is missing in the simplified equations. Third, neither the experiments nor the numerical simulations have studied turbulent flows at large Reynolds number. The Reynolds number based on the eddy's characteristic length scale at the interface estimated from Turner and Yang (1963) and Townsend (1964) papers to be below 50. It follows that their results may not correspond to fully turbulent mixing flow.

The purposes of our experimental simulations are to study this process and to address these paradox. In this paper we investigate the effects of buoyancy reversal, followed by two types of experiments. (1) An instability experiment involves the behavior of a fully turbulent wake near the inversion generated by a sliding plate. Due to buoyancy reversal, the heavy, mixed fluid starts to sink, turning the potential energy created by the mixing process into kinetic energy, thereby increasing the entrainment rate. (2) An entrainment experiment, using a vertically oscillating grid driven by a controllable speed motor, produces many eddy-induced entrainment at a surface region on scales much less than the depth of the layer.

2. EXPERIMENTAL METHODS

2-1 Density as a Function of Mixture Ratio

Evaporative cooling in atmospheric clouds produces mixtures whose density can be greater than either parent parcel. In clouds, the density relationship is composed of two essentially straight lines (Fig.1a). In the laboratory, an imperfect approximation to this has been realized. Density is plotted as a function of the mixture fraction of the upper fluid for water-alcohol mixtures in figure 1b, using the same fluid system as Turner (1966).

Glycol is added to the alcohol in order to raise the density nearer to that of water. The density is a maximum at a mixture fraction $p=p^*$. For these experiments, p^* is in the range of about 0.3 to 0.7. The range can be extended from 0.1 to 0.7 by adding appropriate amounts of potassium iodide and glycerine into the two fluids. A dimensionless buoyancy reversal parameter is defined as follows:

$$D \equiv \frac{\rho(p^*) - \rho(p)}{\rho(p) - \rho(0)} \quad \text{for } p < p^*,$$

which indicates the ratio of the maximum density change at p^* to the density difference between two layers fluid. $\rho(p)$ is the density of mixed fluid consisting of p parts of pure fluid and $(1-p)$ parts of pure lower fluid; $\rho(1)$ is the density of pure upper fluid (the simulated dry, unsaturated layer). $\rho(0)$ is the density of pure lower fluid (the simulated cloud). Before a run ($p=0$), the initial value of D , D_i , was selected from a value between 0 to 15 for these experiments.

2-2 The Apparatus

The apparatus is sketched in figure 2. Two lucite mixing boxes with different geometries were used, a vertical circular cylinder of 15 cm inside diameter and 30 cm height which we call 'small box' and one 28x28x60 cm height, the 'large box'. Both boxes were separated into two compartments by a thin, horizontal sliding stainless steel plate of 0.07 cm thickness. Before a run, the compartment below the plate was filled with water and that above the plate with a mixture of alcohol and glycol.

2-3 Flow Visualization Technique

By adding a pH indicator, phenolphthalein in one fluid and appropriate base in the two-layer fluids, the initially colorless fluids became dark red when they mixed. The volume mixing ratio of lower to upper fluid at which this occurs is the equivalence ratio ϕ , which can be chosen to be about 20. This means that 100 c.c. of pure lower fluid needs only to mix with 5 c.c. of pure upper fluid to turn red. The chemistry is fast.

3. RESULTS FOR INSTABILITY EXPERIMENT

3.1 Large Disturbance

It is important that the initial perturbation be sufficiently large at the interface to insure that the flow is above the mixing transition (Breidenthal, 1981) so that the results correspond to the high Reynolds number atmosphere case. The plate was withdrawn quickly enough to create a fully turbulent wake at the interface, where the Richardson number ($Ri = \Delta\rho g\delta/\rho\omega^2$) based on the thickness (δ) of the wake, its maximum density difference ($\Delta\rho$) with the underlying fluid, and the average speed of the withdrawing plate (ω) was small ($Ri < 6$). Then the behavior of the interface depended on the initial $D=D_i$.

(A) Flow Structure

The results of several runs are described for several values of the initial buoyancy reversal parameter D_i .

(1) Linear case, $D_i=0$

The initial disturbance decayed quickly. The mixture was intermediate in density between that of the two initial fluids, and therefore it accumulated at the inversion. The evolution of the experiment at different stages is shown in figure 3a.

(2) Nonlinear case, $D_i>0$

a) $0 < D_i < 1.0$ Figure 3b shows the evolution of the system at different times for relatively weak nonlinearity ($D_i=0.2$). For $D_i < 1$, the interface tilted gently and then promptly returned back to horizontal after the heavy mixed parcel descended. Note that the interface remained almost flat. After the turbulence decayed, samples of the fluid at the bottom of each tank and just below the interface were taken to determine their composition and the current value of D . These measurements were repeated at five and ten minutes. Neither the composition of the bottom fluid nor D changed significantly during this time.

b) $D_i > 1.0$ Figure 3c shows the evolution of the flow at different times for a case of stronger buoyancy reversal ($D_i=2.0$). For $D_i > 1$, again the heavy, mixed fluid produced by the initial perturbation descended into the lower layer. However, a distinct difference was observed in the interface for this case: It became strongly tilted. The heavy, descending parcel formed a vortex structure which tilted the interface, which in turn fed the structure fresh fluid from above, thereby maintaining the structure as it grew. An 'entrained tongue' of upper fluid was pulled into the lower fluid. Sustained vigorous entrainment and mixing occurred. Soon, however, the walls constrained the flow as the structure filled the lower region and consumed all the lower fluid. Then the effective value of D across the inversion was reduced, and the Richardson number was increased. The system became stable again. Figure 3d shows

the evolution of the flows at four times for $D_i=5.0$. The interface tilt is even more pronounced. The system was unstable in the sense that an 'entrained tongue' was formed, leading to a plume like runaway entrainment.

(B) Instability Condition for Large Disturbance

The results for the large box are qualitatively the same as those for the small box, except for a time lag. Figure 4 shows D at 40 sec in the small box and at 100 sec in the large box as a function of its initial value. We saw above that for D_i greater than 1.3, the interface became strongly tilted to form a tongue of upper fluid which descended below the level of the undisturbed inversion. This tongue was engulfed into the descending parcel. Runaway entrainment proceeded until a large enough fraction of upper fluid was mixed into the lower fluid to change the composition to where D was reduced to be about 1.

3.2 Small Disturbance

If the plate was pulled out slowly such that the Richardson number was large ($R_i \gg 6$) and Reynolds number based on the thickness of the wake at the interface was small ($Re < 100$), the sustained vigorous mixing was absent for even D_i up to 10. The mixtures due to this small disturbance started to descend and result in slowly convective motion in the lower layer fluid especially near the interface that slowly drained the layer fluid above. The observation showed that many convective cells on the inversion trapped and produced the mixtures which sank and dripped many streamers from the interface, and thus generated further agitation and mixing, but at a relatively slow rate as long as $D > 0$. This slowly convective motion continued until D went to zero, in which the mixtures were no longer heavier than the lower fluid (environment saturated). Although this phenomenon may be important in nature, the present experiments are to study the case where the disturbances are driven from some turbulent source other than a laminar molecular diffusion process.

4. DISCUSSION AND MODEL

The central surprise of these results is that the system is stable to strong perturbation unless the buoyancy reversal parameter D is greater than 1. The original concept of the instability predicts a critical value of D near zero, so that any heavy, mixed parcels produced would, upon falling, energize the turbulence in the lower fluid enough to precipitate enough additional mixing to generate runaway entrainment. Apparently, the mere production of heavy mixed fluid is neither a sufficient condition nor a necessary condition for instability.

Here we present a simple physical model based on the experimental observations. Consider a sizable vortex δ of large enough circulation Γ in which the vortex has an excess of kinetic energy (small R_i), it engulfs fluid from above and below the inversion, mixing them together to form a heavy vortex core of density ρ^* as sketched in figure 5a. The experimental data indicate that $R_i = g'\delta/\omega^2 < 6$ for the occurrence of such phenomenon (Shy, 1989), where the velocity of the vortex ω is proportional to Γ/δ and $g' = (\rho^* - \rho_0)g/\rho_0$. At point A in the figure, the heavy vortex induces an overturning force per unit volume $F_o = (\rho^* - \rho_0)g$. At the same time, baroclinic torques generate vorticity at the tilted interface (tongue) near A which tends to restore the interface to horizontal. In other words, the rebounding vorticity at the interface corresponds to a restoring force per unit volume $F_r = (\rho_0 - \rho_1)g$ at A. Stability depends on the ratio F_o/F_r . Therefore,

$$\frac{\text{Overturning Force}}{\text{Restoring Force}} = \frac{\rho^* - \rho_0}{\rho_0 - \rho_1} = D_i.$$

It is important to note that the initial perturbation be sufficiently large at the interface ($R_i \sim 1$) to ensure that the vortex reaches approximately its maximum density of ρ^* , followed that the instability may depend on the initial value of D , D_i . The interface is stable to strong perturbation if $F_o < F_r$ ($D_i < 1$), the mixing is largely confined to that of the initial heavy vortex without much additional engulfment of upper fluid (dry dir). The vortex can not pull down the tongue due to its relatively weak buoyancy reversal. Indeed, the tilted interface (tongue) will recoil back to horizontal because of its lighter density (ρ_1). This mixing structure is termed 'thermal-like mode' as shown in figure 5b, implying that the heavy parcel would sink like a downward movement of thermal convection due to gravitation, thereafter detaching from the interface and re-distributing itself into the lower layer fluid (clouds). For $F_o > F_r$ ($D_i > 1$), the vortex has strong buoyancy reversal to pull the tongue down further to trigger sufficiently additional entrainment from above. The interface is unstable and the vortex will continue to engulf fluid. Such a structure is then termed 'plume-like mode' as shown on figure 5c, suggesting that the heavy, descending parcel could tilt the interface to form an entrained tongue, leading to a plume-like runaway entrainment or penetrative downdraft. The transition from stable to unstable behavior is sharp because the criterion for instability depends on the amount of mixing due to the depressed tongue. Until the tongue can be drawn down further by strong buoyancy reversal ($D_i > 1$), the amount of mixing is modest. Indeed, other experimental results, to be reported in Part II, indicate that the entrainment rate under continual forcing is a weak function of D below the instability transition.

ACKNOWLEDGEMENTS

The author is indebted to Professor Robert Breidenthal for his guidances and advices in this course. Deep appreciations go to Professor Marcia Baker for introducing the problem to us and for many stimulating discussions about stratocumulus clouds. The author also appreciated and benefited from interaction and discussions with Professor Chris Bretherton and Mr. Steve Siems. This research was supported by NSF Grant ATM-8611225A02.

REFERENCES

- Breidenthal, R.E. 1981: Structure of turbulent mixing layers and wakes using a chemical reaction. *J. Fluid Mech.*, **109**, 1-24.
- Caughey, S., B. Crease and W. Roach 1982: Afield study of nocturnal stratocumulus II, Turbulence structure and entrainment. *Quart J. Roy. Meteor. Soc.*, **109**, 124-144.
- Deardorff, J.W. 1980: Cloudtop entrainment instability. *J. Atmos. Scie.*, **37**, 131-147.
- Hanson, H.P. 1984: On mixed-layer modelling of the stratocumulus topped marine boundary layer. *J. Atmos. Scie.*, **41**, 1226-1234.
- Lilly, D.K. 1968: Models of cloud-topped mixed layers under a strong inversion. *Quart J. Roy. Meteor. Soc.*, **94**, 292-309.
- Miles, J. 1987: Richardson's number revisited. The 3rd International Symp. on Stratified Flows, California Institute of Technology Preprints, Vol 1, 1-7.
- Nicholls, S. and J. Turton 1986: An observational study of the structure of stratiform cloud sheets, part II: Entrainment. *Quart J. Roy. Meteor. Soc.*, **112**, 461-480.
- Randall, D.S. 1980: Conditional instability of the first kind upside down. *J. Atmos. Scie.*, **37**, 125-130.
- Shy, S.S. and R.E. Breidenthal, 1989: Laboratory experiments on the cloudtop entrainment instability. To appear in *J. Fluid Mech.*
- Shy, S.S. 1989: On instability and entrainment of an inversion from mixing-induced buoyancy reversal. Submitted to *J. Fluid Mech.*
- Siems, S.T., C.S. Bretherton, M.B. Baker, S.S. Shy and R.E. Breidenthal 1989: Buoyancy reversal and cloudtop entrainment instability. Submitted to *Quart J. Roy. Meteor. Soc.*
- Townsend, A.A. 1964: Natural convection in water over an ice surface. *Quart J. Roy. Meteor. Soc.*, **90**, 248-259.
- Turner, J.S. 1966: Jets and plumes with negative or reversing buoyancy. *J. Fluid Mech.*, **26**, 778-792.
- Turner, J.S. and I.K. Yang 1963: Turbulent mixing at the top of stratocumulus clouds. *J. Fluid Mech.*, **17**, 212-224.

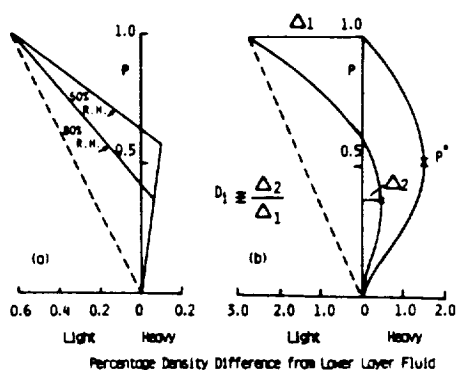


Figure 1: Mixing density as a function of mixture fraction p of upper fluid. (a) Cloud at 20°C and 700 mb, containing 1g/kg of liquid water mixing with an environment 20°C cooler having various relative humidities (R.H.) (Turner, 1966) (b) The experimental two-layer fluids, consisting of alcohol and glycol mixtures in various proportions, mixing with water, using the same fluid system as Turner (1966). The dash line represents the linearly mixing case (environment saturated).

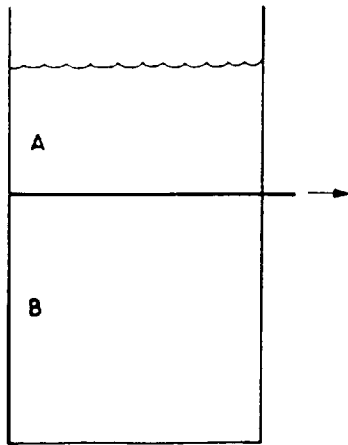


Figure 2: Sketch of the apparatus. A - mixtures of alcohol and glycol. B - water.

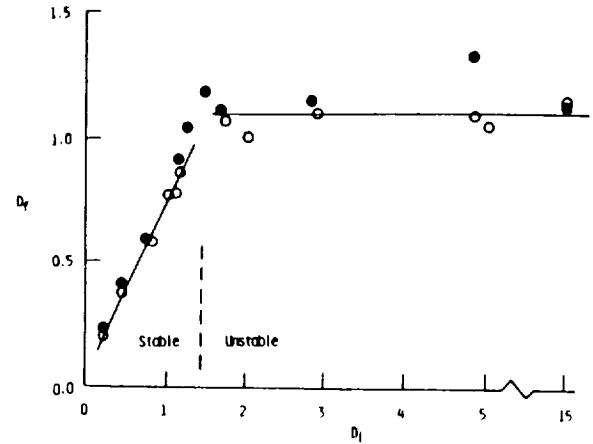


Figure 4: The final value of D , as a function of its initial value D_i . White circles, large box; Dark circles, small box. For $D_i < 1.0$, the system is stable; for $D_i > 1.3$, the system is unstable, under strong perturbation.

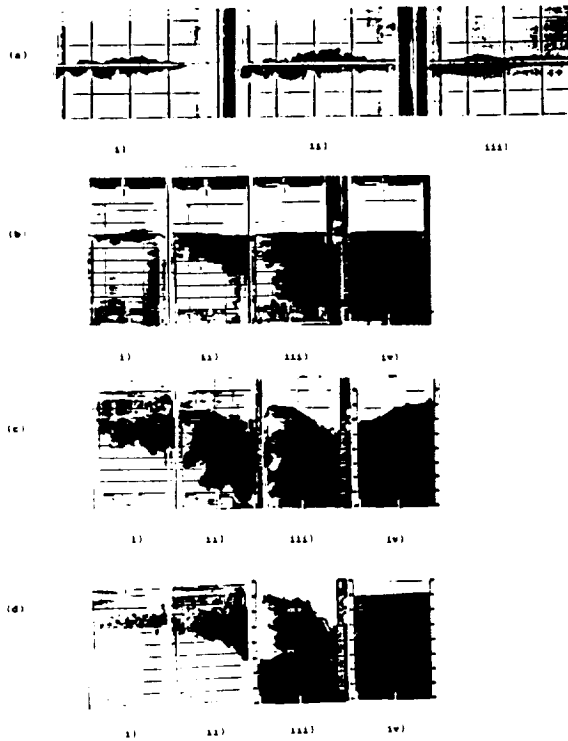
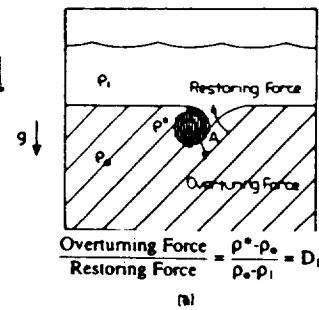


Figure 3: The evolution of the flows.
 (a) $D_i = 0.0$ i) 1.0sec ii) 2.5sec iii) 45.4sec.
 (b) $D_i = 0.2$ i) 0.9sec ii) 5.7sec iii) 13.8sec iv) 44.7sec.
 (c) $D_i = 2.0$ i) 3.7sec ii) 7.4sec iii) 9.9sec iv) 27.4sec.
 (d) $D_i = 5.0$ i) 1.0sec ii) 3.5sec iii) 9.9sec iv) 97.2sec.

Model



Small Ri

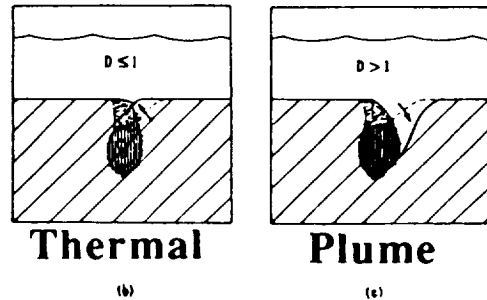


Figure 5: Model of the entrainment process and the instability.

	PAGE
M07.01 Overview	***
Randall, David A.	
M07.02 Objectives	***
Randall, David A.	
M07.03 Management Plan	***
McDougal, David S.	
M07.04 FIRE Central Archive	***
Olsen, Lola M.	
M07.05 General Discussion	***
Cox, Stephen K.	

	PAGE
M08.01 On the Dynamic and Thermodynamic Structures of Marine Stratocumulus Laufersweiler, M. J., and Hampton N. Shirer	***
M08.02 Analysis of Marine Stratocumulus Clearing Events During FIRE Kloesel, Kevin A.	***
M08.03 Cloud Top Distributions and Cloud Top Entrainment Instability Boers, Reinout, and James D. Spinhirne	***
M08.04 Comparative Climatology of Four Stratocumulus Regimes Hanson, Howard P.	***
M08.05 Laboratory Experiments on Stability and Entrainment of Oceanic Stratocumulus-- Part II: Entrainment Experiment Shy, Shenqyang S.	235
M08.06 High Resolution Infrared Measurements Kessler, B., and Robert Cawley	241
M08.07 On Estimating Scale Invariance of Stratocumulus Cloud Fields Seze, Genevieve, and L. A. Smith	***
M08.08 Spectral Absorption of Marine Stratocumulus Clouds Derived from In Situ Cloud Radiation Measurements King, Michael D., Lawrence F. Radke, and Peter V. Hobbs	***
M08.09 Turbulent Statistics in the Vicinity of an SST Front: A North Wind Case, FASINEX February 16, 1986 Stage, Stephen A., and Chris Herbster	247

LABORATORY EXPERIMENTS ON STABILITY AND ENTRAINMENT OF OCEANIC STRATOCUMULUS -- Part II: Entrainment Experiment

SHENQYANG S. SHY

Department of Aeronautics and Astronautics, FS-10
University of Washington, Seattle, WA 98195

1. INTRODUCTION

In the classic stable layer case in which density is a linear tracer of the mixture composition between two layers of fluid, turbulent entrainment destroys the available turbulent kinetic energy or it re-stratifies the flow during the decay of a turbulent event. This is because the stratification inhibits the vertical motions of the interface which marks the edge of the turbulence. In contrast to the classic case, the evaporation of the cloud droplets for which unsaturated air is entrained into a cloud causes cooling, and hence an increase in density, such that this additional downward movement due to buoyancy reversal may affect the dynamics of entrainment and instabilities of cloudtop.

The primary interest in this study is to investigate the effect of buoyancy reversal and Richardson number on the simulation of turbulent entrainment into marine stratocumulus clouds or the Weddell Sea. The key question to be addressed in this note is: What is the effect of buoyancy reversal (evaporative cooling) on entrainment rate?

The oscillating grid-turbulence experiments, in which the turbulent kinetic energy is mechanically produced at a surface region on scales much less than the depth of the layer, have been used to investigate the entrainment mechanisms across an inversion for a couple of decades. For instance, many experiments have been made at observing and parameterizing the entrainment across a density stratification after the basic laboratory grid-oscillation experiment of Rouse and Dodu (1955). Turner (1968) showed that the turbulent motions producing the entrainment were directed toward the interface and the entrainment rate was a function of Richardson number in linearly stably stratified fluid. Oscillating grid-turbulence measurements (Thompson & Turner, 1975; McDougall, 1979; Long & Fernando, 1983; E & Hopfinger, 1986) indicated a spacial decay of the horizontal root mean square (r.m.s.) turbulent velocity w near the interface of the form $w \propto z^{-1}$, where z was measured from a virtual origin.

In order to make the comparison of entrainment rate with and without buoyancy reversal, a series of grid-oscillation experiments with linear density change of the mixtures (water - salt water system) was first completed using the same flow visualization techniques as before (Part I). In this note we organize our results using three parameters, namely, buoyancy reversal parameter (D), Richardson number (Ri) and Reynolds number (Re). Only one variable can be changed at a time. Conditions may be controlled. Most importantly, runs may be repeated.

2. EXPERIMENTAL METHODS

2-1 The Apparatus

The apparatus is sketched in figure 1. A transparent tank of 28x28x60 cm height is separated into two compartments by a thin horizontal sliding stainless plate of 0.07cm thickness. Before a run, the compartment below the plate was filled with water and that above the plate with a mixture of alcohol and ethylene glycol for nonlinear case, using the same fluid system (Part I: Fig.1). It consists of a grid of 1.12 cm square bars, aligned in a square array of mesh size $M=5.60$ cm. The grid, placed horizontally in the tank, can be oscillated vertically with varied frequencies from 1 to 10 Hz by a speed-controlled motor. The stroke was fixed at $S=2$ cm for all experiments. The grid was mounted on a 0.64cm diameter connecting rod which was supported by a 7.62cm long linear bearing and connected with the motor by two ball bearings on a cam. Compared to the earlier non-buoyancy-reversing experiments in which the density of mixtures is a linear function of the concentration, the improvements here are the following. First, there is no interference between the connected rod and the interface during the grid-oscillation, because the rod does not penetrate the interface. Second, the sliding plate sealed by o-rings is provided across the center so that the tank can be filled conveniently while maintaining the purity of the two layers before the run. Without this feature, the nonlinear density changes can cause considerable mixing during the filling even before the mechanical stirring is begun. Therefore, a thin removable partition between two layers is necessary for the buoyancy reversal case. An electrical timer recorded the elapsed time for these experiments.

2-2 The Characteristics of Oscillating Grid Turbulence

According to E & Hopfinger (1986), the empirical relations for calculating the r.m.s. horizontal component of turbulent velocity w and the integral length scale d of the turbulence near the interface are

$$\omega = C_1 S^{3/2} M^{1/2} f_z^{-1} \quad \text{and} \quad \delta = C_2 z \quad (1)$$

where $C_1 \approx 0.3$ and $C_2 \approx 0.1$, using the same constants as Mory & Hopfinger (1985); M , S and f are the mesh size, stroke and frequency of the oscillating grid respectively. To reduce the wall effect, the grid was designed by assuming the walls were planes of symmetry as suggested by E & Hopfinger (1986). Also, the maximum frequency used in this study was 6 Hz to avoid the unwanted circulating motions at high frequencies (McDougall, 1979).

(A) Experiments for linearly mixing case

Figure 2 is the schematic diagram of the experiments in the linear case. Choosing the Z^* axis as positive-upward (figure 2a), the density $\rho(Z^*)$ is given by

$$\rho = \begin{cases} \rho_1 & (Z^* > z) \\ \bar{\rho} & (-H_0 < Z^* < z - h) \end{cases} \quad (2)$$

where h is the interface thickness, which is generally much less than z . Here

$$\bar{\rho} = \rho_1 \frac{z - Z_0}{z - H_0} + \rho_0 \frac{Z_0 - H_0}{z - H_0}$$

and

$$\Delta\rho = \bar{\rho} - \rho_1 = (\rho_0 - \rho_1) \cdot \frac{Z_0 + H_0}{z + H_0} \quad (3)$$

where Z_0 is the initial position of the interface measured from the mid-plane of the oscillating grid and ρ_1 and ρ_0 are the initial densities of the upper and lower layers respectively.

For these linearly stratified experiments, the initial normalized density difference between two layers $((\rho_0 - \rho_1)/\rho_0)$ was typically set around 0.5% to 3%. The Reynolds number based on the grid's mesh size and frequency can be up to 10^4 and the typical Reynolds number $w d / \nu$ near the interface was ≈ 120 , which may be large enough for viscous effects to be negligible. The mixed-layer depth z , as shown in figure 3a, is a function of time. The evolution of growing interface was recorded to establish a depth-time relation. The entrainment rate and Richardson number are then denoted as follows:

$$E = \frac{w_e}{\alpha} \quad \text{and} \quad R_i = \frac{g \Delta \rho d}{\rho \alpha^2} \quad (4)$$

where $w_e = dz/dt$ and w , d , $\bar{\rho}$ and $\Delta\rho$ are given in Eq. (1) and (3). It is important to note that the scales used to define R_i are the r.m.s. horizontal component of turbulent velocity w and the integral length scale d of the turbulence near the interface instead of the velocity of oscillating grid and layer depth, using the same empirical relations found by E & Hopfinger (1986).

(B) Experiments for nonlinearly mixing case

Figure 3 shows the schematic diagram of the experiments in nonlinear case. Three different grid locations with respect to the interface were used: above (A), below (B) and center (C) on the interface. For these experiments, the stroke was set at 2 cm with a frequency of 1 - 6 Hz. The density $\rho(Z^*)$ as showing in figure 3b is given by

$$\rho(Z^*) = \begin{cases} \rho_1 & Z^* > z \\ \bar{\rho} & -H' < Z^* < z \end{cases} \quad (5)$$

where H' is the actual mixing region indicated by color. H' is equal to H_0 after the full lower layer has turned dark red. The density jump across the inversion is then approximately given by

$$\Delta\rho = \bar{\rho} - \rho_1 = \begin{cases} (\rho_0 - \rho_1) + \frac{\rho^* - \rho_0}{\rho^*} \cdot \frac{z - Z_0}{z + H'} & \text{before saturation} \\ \frac{\rho^* - \rho_1}{1 - \rho^*} \cdot \frac{Z_0 + H_0}{z + H_0} & \text{after saturation,} \end{cases} \quad (6)$$

where ρ^* is the maximum density at mixing fraction p^* on the buoyancy reversal curve as shown in figure 1b (Part I). The buoyancy reversal parameter D is then denoted by

$$D = \begin{cases} \frac{\rho^* - \bar{\rho}}{\bar{\rho} - \rho_1} & \text{before saturation} \\ 0 & \text{after saturation} \end{cases} \quad (7)$$

We used the same empirical equation (Eq. 1) to determine the characteristic turbulent velocity and length scales near the inversion for the nonlinear case because the same grid-turbulence was used as that of the linear case. From Eq. (4) and (6), the entrainment rate and the Richardson number were then calculated. A pH sensitive dye identified regions of mixing was used to detect optically how 'buoyancy reversal' created by mixing process disrupted the inversion leading to plume-like runaway entrainment.

3. RESULTS FOR ENTRAINMENT EXPERIMENT

3-1 Stably Stratified Flow Without Buoyancy Reversal

Figure 4 shows the evolution of the flow which developed in experiment (A) at different times. At time = 7 sec after the motor started (Fig.4(a)), the stratification flattens the eddies generated from the oscillating grid. The eddies recoiled back, entrained and mixed fluid, turning it dark red into the turbulent flow, where Ri is about 47. As time increases, the mixed-layer deepens and the Ri near the interface increases, corresponding to a low value of entrainment rate. The experimental data for the mixed-layer depth v.s. time can be best fitted by a power law relation of the form $z = at^b$, with a being a constant for a given oscillating frequency and $b = 0.18$ for these experiments. Both constants are determined by a small least square program. Compared to the earlier linear experiments, the exponential constant b is close to $b \approx 1/5$ (E & Hopfinger, 1986) and $b \approx 2/11$ (Fernando & Long, 1983). Figure 5 shows the logarithmic plots of the entrainment rate E as a function of local Richardson number Ri . For the different grid positions, these experimental data approximately obey

$$E = C Ri^{-3/2}, \quad \text{for } Ri > 6, \quad (8)$$

where $C \approx 2.0$. For comparison, E & Hopfinger's data are included in Fig.5, where $C \approx 3.8$ (E & Hopfinger, 1986), and $C \approx 2.5$ (Turner, 1973) with the same slope for $Ri > 7$. It is important to note that the entrainment rate tends to depend less strongly on Ri and flatten to a somewhat constant level at small value of $Ri (< 6)$. The transition of $Ri \approx 6$ is close to the value of maximum internal wave generation (Carruthers & Hunt, 1986) and the E & Hopfinger's data. For $Ri \sim 1$, the vortex or eddy has the excess kinetic energy such that it engulfs fluid into itself as it rotates. As Ri increases ($Ri > 6$), the buoyancy becomes important, so that the entrainment is dominated by an eddy-rebounding process (Linden, 1973).

3-2 Stratified Flow with Buoyancy Reversal

(A) Experiment A

(1) $Di=1.0$

Figure 6 shows the evolution of the nonlinear experiment A for $Di=1.0$ at four different times. The mixtures are either trapped by the interaction among these eddies or created by internal wave breaking as interface tilted, where upon they descend and detach slowly from the inversion, while the turbulent layer remains pure and unmixed (colorless). At time ≈ 5 sec after the grid started, the heavy mixtures descended, while the interface remained flat where $Ri \approx 97$ and $D \approx 0.9$. As time increases, more entrained fluid sinks into the non-turbulent layer, bringing the interface even closer to the oscillating grid, where the Ri and D are reduced. The changes in interface's structure with varying Richardson number are also shown in figure 6. At about 20 minutes after starting grid the upper turbulent layer starts to turn red because of entraining fluid from below, where the growing interface is about 5 cm away from the middle plane of oscillating grid and $Ri \approx 6$. Some mixtures still continue to descend into non-turbulent layers due to buoyancy reversal. The key point regarding the interfacial instability is that the system is stable in the sense of no runaway entrainment occurs in this case. For $Di < 1.0$, we saw that the turbulent kinetic energy of the mixed parcel created by the mixing-induced buoyancy reversal was not large enough to ruin the interface leading to positive feedback entrainment. Indeed, the heavy mixture only re-distributes itself into the lower layer (the simulated clouds) without much perturbation of the interface. The entrainment was modest during a run.

(2) $Di=2.5$

Figure 7 shows the evolution of experiment A for $Di=2.5$ at five subsequent times. At $t \approx 14$ sec after starting the grid motion, the interface remained stable even at $D \approx 1.9$, when $Ri \approx 15$. At $t \approx 33$ sec, there was more dilution of the lower fluid layer by the upper fluid, reducing both the Ri and D . At $t \approx 45$ sec, the interface became more convoluted such that runaway entrainment was incipient, while the upper layer (grid-turbulence side) still remained pure and unmixed, when $Ri \approx 6$ and $D \approx 1.3$ as shown in figure 7c. A strikingly vigorous entrainment then occurred that disrupted the interface. Very quickly, the two layers were mixed together. The instability is apparently parameterized by the Richardson number as well as the buoyancy reversal parameter.

(B) Experiment B ($Di=2.0$, $f=4\text{Hz}$)

Figure 8 shows the evolution of the flow which developed in experiment B for an initial value of $D=2.0$ at four different times. At $t = 5$ sec, the interface became strongly convoluted. The associated rapid entrainment occurred. This rapid entrainment was sustained only a couple seconds. The heavy mixtures, upon descending, were quickly homogenized by grid turbulence which in turn restrained the vertical motions of the interface because of the strong stratification. At $t \approx 13$ sec, the heavy mixed fluid reached the bottom of the tank, while the interface relaxed back to horizontal, associated with a low entrainment rate. At the turning point in which rapid entrainment relaxed to slow entrainment, the measured Ri was again about 6 and $D > 1$. As time passed, there was more dilution of the lower fluid layer (the simulated clouds) by the upper fluid (the simulated dry air), decreasing D and increasing Ri . The variations in the structure of the interface are shown in figure 8(a-d), which are photographs taken at $Ri \approx 5.0$ (a), 8.8(b), 16.1(c) and 30.3(d).

3-3 Instability Condition

In figure 9 we have plotted the buoyancy reversal parameter D as a function of local Ri for two series of experiments A and B. These experiments reveal three main points. First, it is surprising that the system is stable for

strong perturbations if buoyancy reversal is comparable to or less than the initial stratification ($D \leq 1.0$) as shown in figure 9. Second, the interface can be stable for $D > 1.0$, if Ri is much larger than 6. Third, the system is unstable in the sense of the inversion becoming largely convoluted associating a rapid positive feedback entrainment, if $D > 1$ and $Ri < 6$.

3-4 Entrainment rate as a function of Ri and D

For simplicity, in figure 10 we only include two runs of experiment (B) with two different initial values of D , which indicates the nonlinear entrainment rate as a function of Ri and D . It shows that the entrainment rate in the nonlinear case only increases about twice that of the linear case due to buoyancy reversal at $D \approx 0.5$ and $Ri \approx 10$. As Ri increases, the stronger stratification inhibits the vertical motion of the interface, followed by inhibiting the effect of buoyancy reversal. The current experimental data suggested that the effect of buoyancy reversal on the entrainment rate can be negligible, if Ri is large ($Ri > 50$) and D is small ($D < 0.5$).

4. DISCUSSION AND CONCLUSION

A stratified interface is stable to the buoyancy reversal instability for surprisingly large values of D . A new instability mechanism is proposed, which considers the mixing process at the interface. For the type of density curves studied here, under strong perturbations, the mixed parcel must have a buoyancy reversal comparable to the initial stratification before the interface is unstable. This is in accord with a simple model of the interface mixing process, as well as aircraft observations of long-live marine stratocumulus clouds. These clouds' remarkable longevity in the face of finite D indicates that they can be stable (Hanson, 1984; Albrecht et al., 1985; Siems et al., 1989). The present work suggests that buoyancy reversal as well as the disturbance must be large for Cloudtop Entrainment Instability. The effect of buoyancy reversal (evaporative cooling) does not always enhance the entrainment rate over that in the inert case, but it may be negligible if Ri is large ($Ri > 50$) and D is small ($D < 0.5$). This work may shed some light on the fundamental mechanism of the breakup process of the subtropical stratocumulus clouds into tradewind cumulus. These results may also be related to the instability in the Weddell Sea off of Antarctica.

Acknowledgements

This research was supported by NSF Grant ATM-8611225A02.

References

Shy, S.S. 1989: On instability and entrainment of an inversion from mixing-induced buoyancy reversal. Submitted to *J. Fluid Mech.*

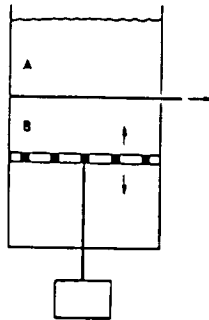


Figure 1: Sketch of the apparatus. A: Mixtures of alcohol and ethylene glycol. B: water. It consists of a square array grid, driven by a speed-controlled motor.

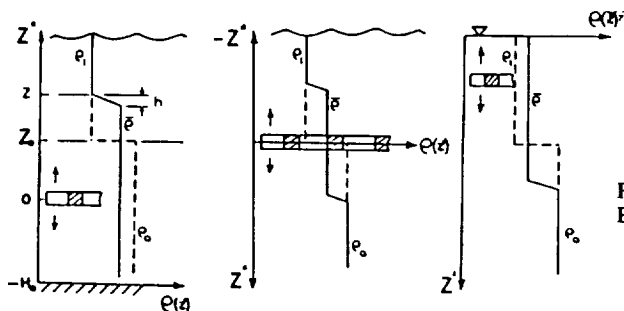


Figure 2: Schematic diagram of the experiments in linear case. Three different grid positions with respect to the interface were used: (a) Below (B); (b) Center (C); (c) Above (A) the interface.

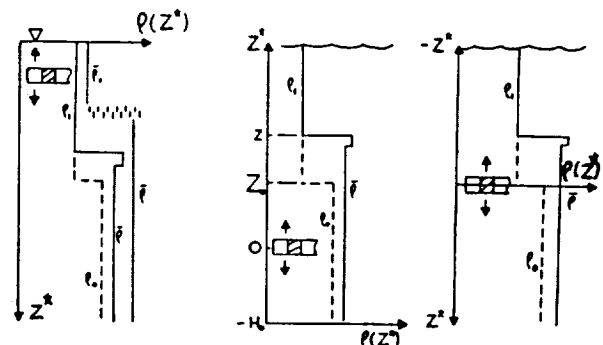


Figure 3: Schematic diagram of the experiments in nonlinear case: (a) Experiment (A); (b) Experiment (B); (c) Experiment (C).

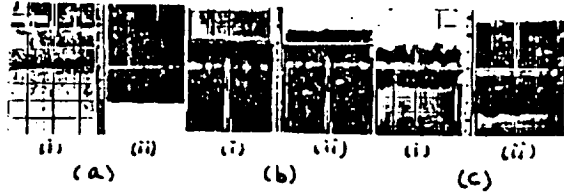


Figure 4: The evolution of the experiments for linearly mixing case. (a) Experiment A : $Z_0 = 10\text{cm}$, $S = 2\text{cm}$ and $f = 3\text{Hz}$, (i) $t = 11.1\text{sec}$, $R_i \approx 47$ (ii) $t = 1,840\text{sec}$, $R_i \approx 120$; (b) Experiment B : $Z_0 = 6\text{cm}$, $S = 2\text{cm}$ and $f = 3\text{Hz}$, (i) $t = 8.5\text{sec}$, $R_i \approx 15$ (ii) $t = 900.3\text{sec}$, $R_i \approx 35$; (c) Experiment C : $Z_0 = 0\text{cm}$, $S = 2\text{cm}$ and $f = 4\text{Hz}$ (i) $t = 3.1\text{sec}$, $R_i \approx 1$ (ii) $t = 220.4\text{sec}$, $R_i \approx 34$.

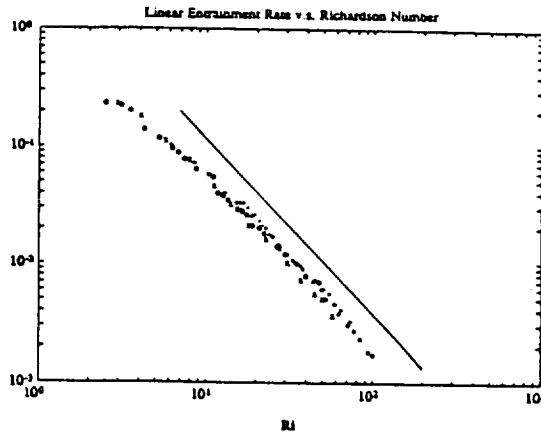


Figure 5: Log plot of linear entrainment rate $E = w_e/w$ as a function of Richardson number $R_i = g\Delta\rho\delta/\rho\omega^2$. Grid locations and oscillating frequency: interface, $f = 4\text{Hz}$ (o); 10cm above interface, $f = 4\text{Hz}$ (Δ); 5 cm below interface, $f = 4\text{Hz}$ (+) and $f = 6\text{Hz}$ (x). For comparison, E & Hopfinger's (1986) data (solid line) with the slope of -1.5 are included.

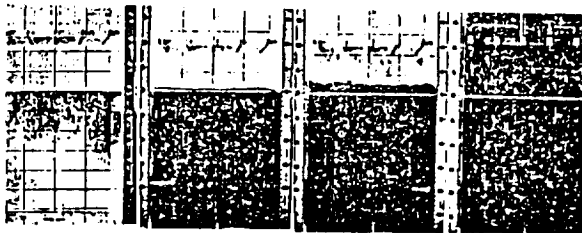


Figure 6: The evolution of experiment A for $D_i = 1.0$. The grid was positioned 11 cm above the initial interface and oscillated at 3Hz with 2 cm stroke: (a) $t = 4.8\text{sec}$, $R_i = 96.6$; (b) $t = 493.1\text{sec}$, $R_i = 38.5$, $D = 0.83$; (c) $t = 1053.4\text{sec}$, $R_i = 22.1$, $D = 0.59$; (d) $t = 1295.2\text{sec}$.

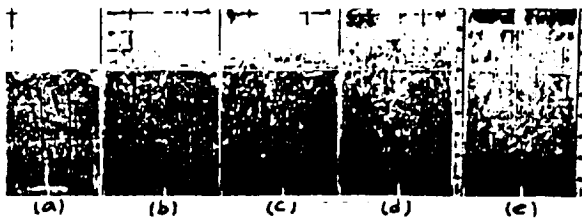


Figure 7: The evolution of experiment A for $D_i = 2.5$. Where $Z_0 = 10\text{cm}$, $f = 4\text{Hz}$ and $S = 2\text{cm}$: (a) $t = 14.1\text{sec}$, $R_i = 15.2$, $D = 1.9$ (b) $t = 33.6\text{sec}$, $R_i = 10.3$, $D = 1.7$ (c) $t = 45.4\text{sec}$, $R_i = 6.3$, $D = 1.3$ (d) $t = 50.8\text{sec}$ (e) $t = 55.6\text{sec}$.

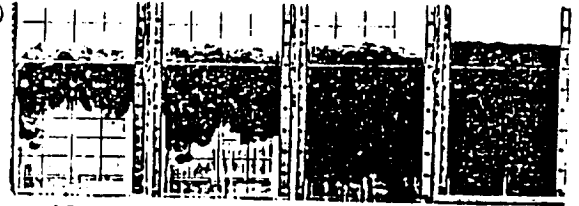


Figure 8: The evolution of experiment B for $D_i = 2.0$. The grid was positioned 5 cm below the interface and oscillated at $f = 4\text{Hz}$ with 2 cm stroke: (a) $t = 5.2\text{sec}$, $R_i \approx 5.0$, $D \approx 1.80$ (b) $t = 8.1\text{sec}$, $R_i \approx 8.8$, $D \approx 1.00$ (c) $t = 13.2\text{sec}$, $R_i \approx 16.1$, $D \approx 0.78$ (d) $t = 91.9\text{sec}$, $R_i \approx 30.3$, $D \approx 0.54$.

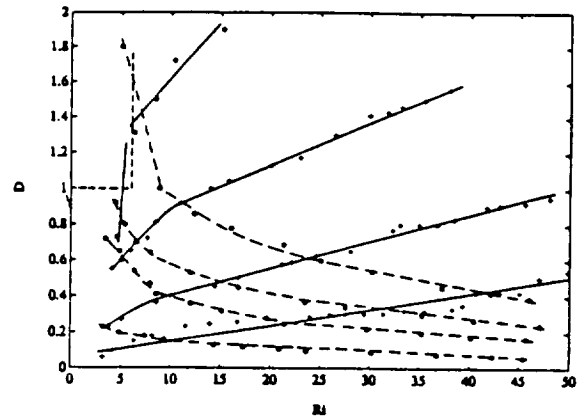


Figure 9: Buoyancy reversal parameter as a function of Richardson number: (a) Experiment A : +, $Z_0 = 11\text{cm}$, $f = 3\text{Hz}$, $S = 2\text{cm}$ for $D_i = 0.7$, 1.0 and 1.7; o, $Z_0 = 10\text{cm}$, $f = 4\text{Hz}$, $D_i = 2.5$. (b) Experiment B : o, $Z_0 = 5\text{cm}$, $f = 4\text{Hz}$, $S = 2\text{cm}$ for $D_i = 0.3$, 0.8, 1.0 and 2.0.

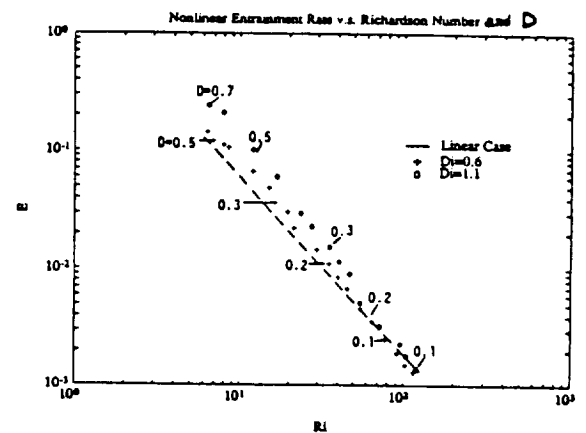


Figure 10: Log plot of nonlinear entrainment rate E as a function of Richardson number and buoyancy reversal parameter D . Where $Z_0 = 5\text{cm}$, $f = 4\text{Hz}$ and $S = 2\text{cm}$ for both runs with two different initial values of D . Dash line is E v.s. R_i for linear case.

HIGH RESOLUTION INFRARED MEASUREMENTS

B. Kessler* and Robert Cawley
 Naval Surface Warfare Center
 White Oak, Silver Spring, MD 20903-5000

Sample ground-based cloud radiance data from a high resolution infrared Sensor are shown and the Sensor characteristics are presented in detail. The Sensor was funded by NSWC and is dedicated to the Navy's Infrared Analysis Measurement and Modeling Program (IRAMMP) sponsored by ONT. The purpose of IRAMMP is to establish a deterministic radiometric data base of cloud, sea and littoral terrain clutter to be used to advance the design and development of Infrared Search and Track (IRST) systems as well as other infrared devices. The Sensor is a dual band radiometric Sensor and its description, together with that of the Data Acquisition System (DAS), are given in Tables I and II. The Data Acquisition System was designed by NRL and built by Telenetics of Seabrook, Maryland under NRL direction. Its characteristics are described in Table III.

A schematic diagram of the Sensor optics is shown in Figure 1. The optics are a three mirror all reflective system; off-axis, nonspherical surfaces are used to provide good area coverage in the focal plane. The scan mirror is external to the optics assembly which is sealed off from the outside environment by a ZnSe plate. The sealed off optics section is kept at a slight overpressure by exhausting the used dry nitrogen gas used for the J-T cryogenics for the Dewar/detector assemblies. The only other transmissive optical component is a dichroic beamsplitter to separate the 3-5 μm and 8-12 μm radiation. Athermal optics is achieved by using an all aluminum structure for the optical bench and the mirrors.

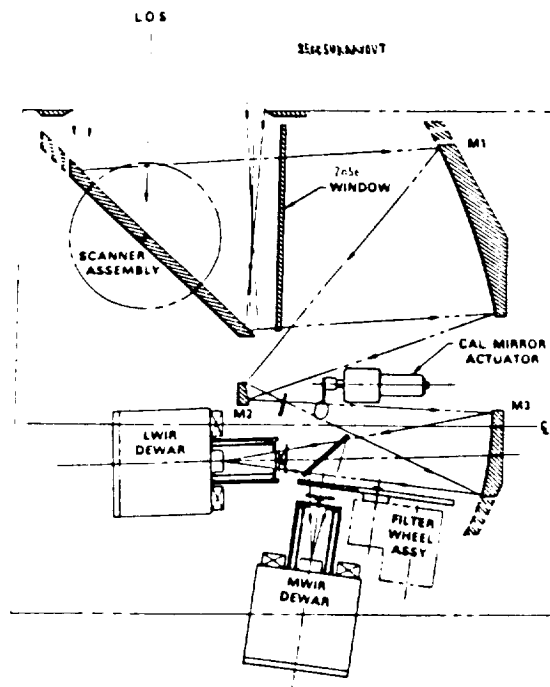


Figure 1

ORIGINAL PAGE IS
 OF POOR QUALITY

* Dept. of Physics, Catholic University of America, Washington, D.C. 20064

Table I
Sensor Description

<u>Feature</u>	<u>Description</u>
Dual Window IR operation	nominal 2-5 μm (MWIR) and 8-12 μm (LWIR)
Telescope Aperture	4.2"
f/#	f/3.2
IFOV (AZ.xEL.:mrad)	0.22 x 0.23
Dwell Time	370 μsec
TFOV	
narrow TFOV (AZ)	5 5/8°
wide TFOV (AZ)	22.5°
narrow TFOV (EL)	1.6°
wide TFOV (EL)	3.2°
Detector crosstalk between channels	<-27db
AZ Scan Rate	33.4°/sec or 17.4°/sec
Revisit Time	
(5 5/8°AZ x 1.6°EL. at 33.4°/sec scan)	3.5/sec
Sensor Head Weight	80 lbs.
Focal Plane Array Compatibility	Modular Dewars
Detectors	
No. detectors/waveband	120
Detector Size	3 mils x 3 mils
1/f noise shoulder	
MWIR (HZ)	0.4
LWIR (HZ)	300
NEAT at 33.4°/sec scan speed	
MWIR	0.047C°
LWIR	0.032C°
NEI (W/cm ²)	
MWIR	$2.7 \times 10^{-14} \pm 10\%$
LWIR	$2.7 \times 10^{-13} \pm 10\%$
Detector and Electronics	
Dynamic Range	84db
Pixel Registration	
Single Color	<0.3 x IFOV
Color-to-Color	<0.3 x IFOV
Detector Array	120 detectors, staggered, contiguous
D* Detectivity	MWIR $\approx 8 \times 10^{10}$ LWIR $\approx 3.2 \times 10^{10}$
6 Selectable Spectral filters in MWIR	YES
Samples/dwell	3.25
Azimuth Shaft Encoder	18 bits; incremental
Scan Linearity	1/8 IFOV per 4° of AZ. Scan
Scan Mirror Drive	Digital serve control system
Radiometric Absolute	better than 5%
Repeatability	better than 3%
Temperature Range to be measured	
3-5 μm	270°K to 450°K
8-12 μm	220°K to 700°K

Table I -- Continued
Sensor Description

<u>Feature</u>	<u>Description</u>
<u>Electronics</u>	
Dynamic Range	84db
Video bandpass (3db)	
MWIR	0.0 to 2500 HZ
LWIR	0.4 to 2500 HZ
<u>Cold Shielding</u>	
Geometric Re-imaging cold shielding	>95% effective

Figure 2 is a photograph of the Sensor head.



Figure 2

Table II
MWIR Spectral Bandpass Filters

<u>Filter No</u>	<u>Cut-On (microns)</u>	<u>Cut-Off (microns)</u>	<u>% T</u>
1	1.96	6.15	80
2	2.21	2.45	77
3	2.98	5.05	87
4	3.45	4.18	79
5	3.79	4.87	92

Table III
DAS(NRL)

<u>Sensor Inputs</u>	<u>DAS Action</u>
analog: -10v to +10v(LW) 0v to +10v(MW) rms noise \approx 0.0007v	Digitized to 15 bits Digitized to 14 bits 1 bit = 0.00061v Digitization rate is 8800 128-word samples/sec
digital: scan mirror shaft position	15 bits recorded, 1 bit = 47.937 μ r (average) of optical scan angle recorded in header words (see attached sheet)
housekeeping	Digital time (to 0.1ms) obtained from time code generator Synchronization words put in header for recognition at playback 8800 HZ.
Sample clock	0.0664 mr/sample
Angular spacing of sample	
Samples per detector for 5.6° picture = 1480	
Total data for each 5.625° picture	380 kB
Data rate	4.5 MB/sec
One HDDR tape	30 minutes of real time data 60 standard 9-track tapes (6250 ips)
Bit error rate (BER)	10^{-8} to 10^{-9}
NRL "Quick-Look"	To examine data base in the field (VAX 11725)
Data Base Management System (DBMS)	Questech Incorporated

The point response function for the Sensor is shown in Figure 3. The sampling resolution is 0.0664 mr. It can be seen that the half power full width is approximately 3.6 samples in LWIR and 3.9 in MWIR. Since there are 3.25 samples/dwell the resolution is $3.6/3.25 = 1.1$ IFOV for LWIR and $3.9/3.25 = 1.2$ IFOV in MWIR. This translates into $1.1 \times 0.22\text{mr} = 0.24\text{mr}$ LWIR and $1.2 \times 0.22\text{mr} = 0.26\text{mr}$ MWIR.

Figure 4 shows a sample "carpet plot" of cloud radiance against azimuth using the new IRAMMP Sensor. Results of a fractal characterization analysis of similar data, taken by a similar, progenitor Sensor under the older, Navy Background Measurement and Analysis Program (BMAP) are given elsewhere at this meeting.¹

¹ Patricia H. Carter and Robert Cawley, "Fractal characterization of infrared cloud radiance", ASTEX Workshop, Monterey, 12 July, 1989.

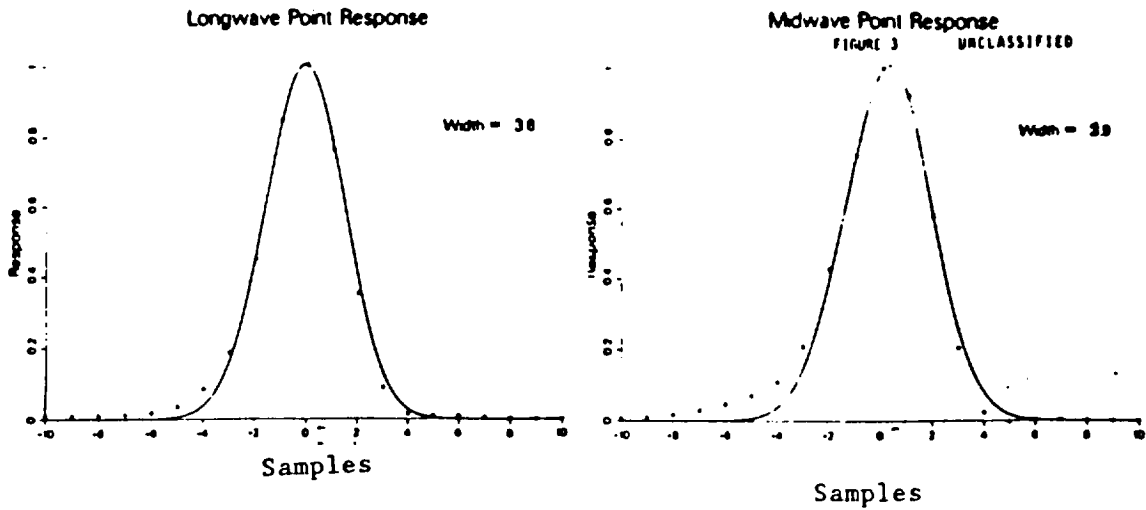
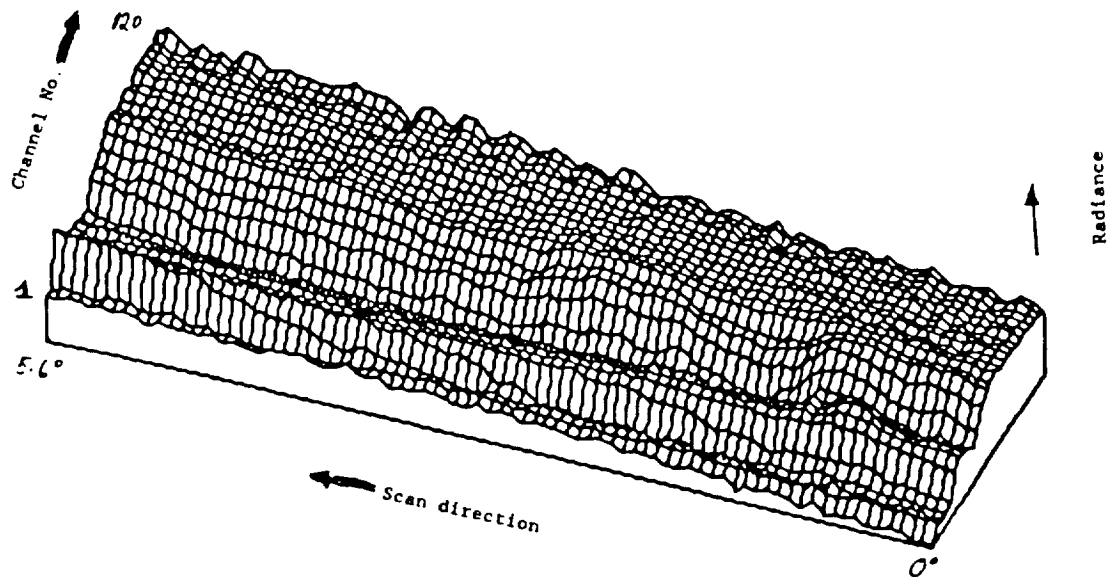


Figure 3

ORIGINAL PAGE IS
OF POOR QUALITY



Carpet Plot of Cloud; MWIR (New IRAMMP Sensor)

Figure 4



A poster presented at the FIRE/ASTEX Workshop, Monterey, CA, July 10-14, 1989.

Turbulent Statistics in the Vicinity of an SST Front: A North Wind Case, FASINEX¹ February 16, 1986.

Steven A. Stage & Chris Herbster
Department of Meteorology
Florida State University
Tallahassee, Florida

1. This is FASINEX contribution number 76.

Turbulent Statistics in the Vicinity of an SST Front: A North Wind Case, FASINEX February 16, 1986.¹

Steven A. Stage & Chris Herbster
Department of Meteorology
Florida State University
Tallahassee, Florida 32306-3034

1. This is FASINEX contribution number 76.

Summary

The technique of boxcar variances and covariances is used to examine NCAR Electra data from FASINEX. This technique has been developed to examine changes in turbulent fluxes near an SST front. The results demonstrate the influence of the SST front on the MABL. Data shown here are for February 16, 1986, when the winds blew from over cold water to warm. The front directly produced horizontal variability in the turbulence. The front also induced a secondary circulation which further modified the turbulence.

1

References

Gennaro H. Crescenti: Turbulent Variances and Covariance in a Non-Homogeneous Marine Atmospheric Boundary Layer. M. S. Thesis, Florida State University, Tallahassee, FL, April, 1988.

Stage, S.A., and R.A. Weller, 1985: The Frontal Air-Sea Interaction Experiment (FASINEX); Part I: Background and Scientific Objectives. Bull Amer. Meteor. Soc., **66**, 1511-1520.

Stage, S.A., and R.A. Weller, 1986: The Frontal Air-Sea Interaction Experiment (FASINEX); Part II: Experimental Plan. Bull Amer. Meteor. Soc., **67**, 16-20.

2

Boxcar Covariances

The technique follows Crescenti (1988). Let the boxcar average of any measured variable $S(t)$ be defined by

$$\langle S \rangle(t) = (1/T) \int_{-T/2}^{T/2} S(t+t') dt' \quad (1)$$

where T is the length of the boxcar. Then we can define the boxcar covariance of S and R by

$$\text{COV.}(S,R) = (1/T) \int_{-T/2}^{T/2} [S(t+t') - \langle S \rangle(t)] [R(t+t') - \langle R \rangle(t)] dt'. \quad (2)$$

3

Note that the arguments of $\langle S \rangle$ and $\langle R \rangle$ are functions of t and therefore that the covariance is just the covariance which would be obtained by breaking the data into blocks of length T . This is *not* the value obtained by finding S' and R' using a high pass running mean filter and then taking the boxcar average of their product. That covariance would have $t+t'$ as the argument for $\langle S \rangle$ and $\langle R \rangle$ above. Further let the correlation between S and R be given by

$$\text{COR}_{\mu}(S,R) = \frac{\text{COV}_{\mu}(S,R)}{[\text{COV}_{\mu}(S,S) \text{COV}_{\mu}(R,R)]^{.5}} \quad (3)$$

We are then able to define the detrended covariance of S and R as

4

$$\text{COV}(S,R) = \text{COV}_{\mu}(S,R) [1 - \text{COR}_{\mu}(S,t) \text{COR}_{\mu}(R,t) / \text{COR}_{\mu}(S,R)] \quad (4)$$

The above is the same value obtained by taking a block of data centered at time t and computing the covariance between linearly detrended S and R . A detrended correlation can also be defined from COV . All of the figures shown here use detrended covariances and correlations.

Further let R_{μ} denote the Hilbert transform of R and define the boxcar coherence as

$$\text{COH}(S,R) = [\text{COV}(S,R)^2 + \text{COV}(S,R_{\mu})^2]^{.5} \quad (5)$$

Finally let the boxcar phase angle be

$$\text{Phase}(S,R) = \text{Tan}^{-1} [\text{COV}(S,R) / \text{COV}(S,R_{\mu})] \quad (6)$$

5

Results

The Data: All data shown are from the Frontal Air-Sea Interaction Experiment (FASINEX, see Stage and Weller, 1985, 1986). These data were obtained by the NCAR Electra flying at 35 m elevation on February 16, 1986.

On the flight leg shown the mean winds were 7.8 m/s from 31 deg--nearly perpendicular to the SST front from over cold to warm water (right to left in these plots). Other flight legs on this same day show similar features.

Following Crescenti (1988), all boxcars shown here use 60 s (6 km) averages. Horizontal wind components have been rotated so that U is along the mean wind for the leg.

6

Regions in the flow: The SST front was very sharp and was located between 60 and 64 km. The total magnitude of the front was 2.5°C. Based on examination of all the statistics, the flow can be divided into 5 regions as follows:

R1: Over the cold water upwind (north) of the front.

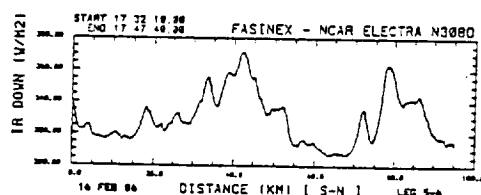
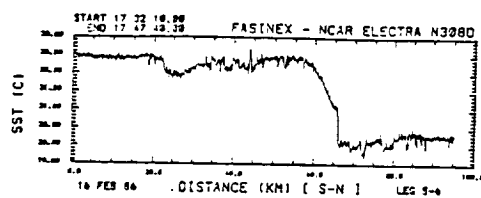
R2: A dry downdraft region ~20 km wide over and just upwind of the front.

R3: A ~30 km wide region of enhanced convection just downwind (south) of the front believed to represent a secondary circulation cell.

R4: A narrow (~10 km wide) region at the downwind edge of R3 believed to be the boundary of the secondary circulation cell.

R5: Flow over warm water farther downwind.

7



8

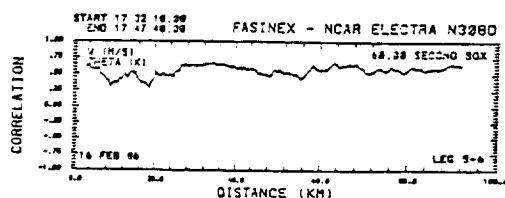
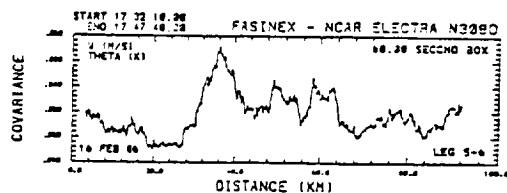
Heat and Vapor

The heat flux, $COV(W, \Theta)$, was upward and produced increasing Θ throughout the leg. $COV(W, \Theta)$ decreased from R1 to R2 then sharply increased at the front and remained high in R3. It decreased in R4 and R5, but remained higher than in R1. COR, COH and Phase were all relatively flat indicating that changes in the heat flux were caused by changes in the variances of W and Θ .

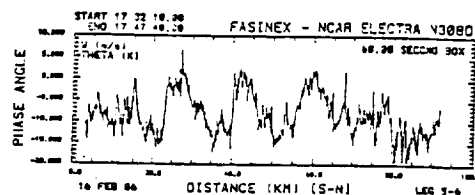
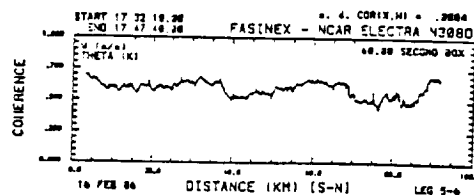
R2 is seen in Q , W and P_{35m} as a dry, high pressure downdraft.

Q was high in R1, was suppressed by the downdrafts in R2, and then gradually increased in R3 before decreasing in R4. Vapor flux (not shown on poster) was upwards and showed little change during the leg.

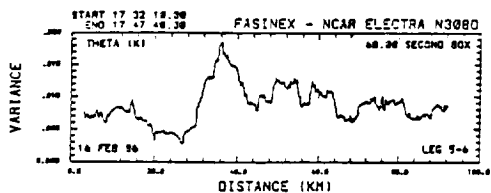
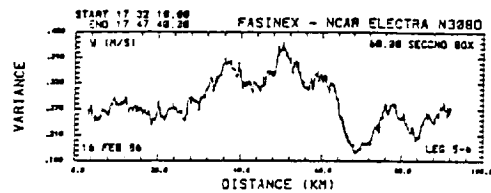
9



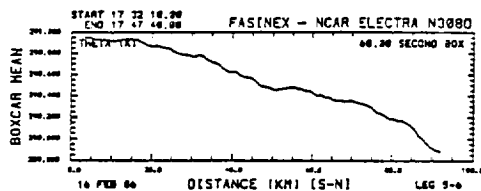
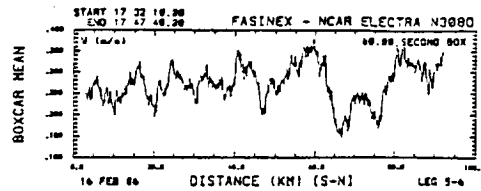
10



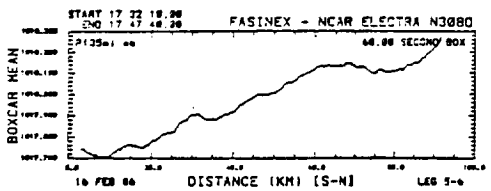
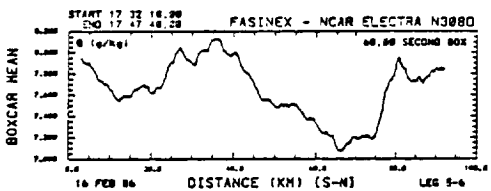
11



12



13



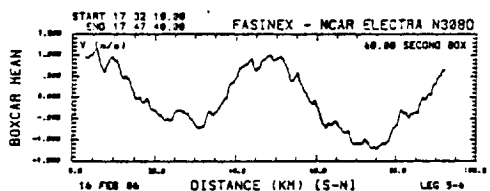
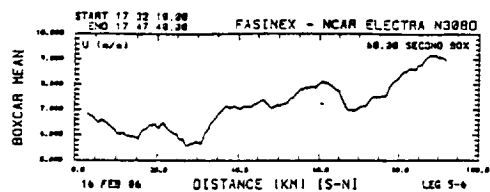
14

Momentum

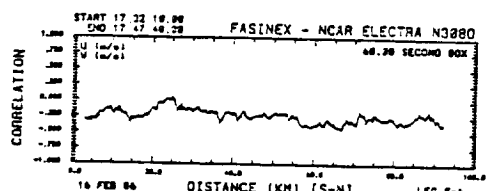
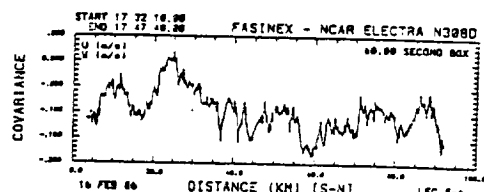
U shows locally lower wind in R2 and R4 and higher in R3. V is remarkably sinusoidal suggesting possible wave motion. Winds are more westerly in R2 and R4 and more easterly in R1, R3, and R5. Stress ($-\text{COV}(U, W)$) is largest in R2. This enhanced stress near the front is the result of a change in the phase angle between U and W, not COR or COH. Stress is surprisingly similar in R1 and R3.

Stress, COR, and COH are near zero in R4. It is this feature which led us to identify R4 as a distinct region rather than simply the boundary between R3 and R5. Both U and W have high variances in R4. We do not yet understand the mechanism producing low stress in R4, but believe that it is associated with the boundary of the secondary cell in R3.

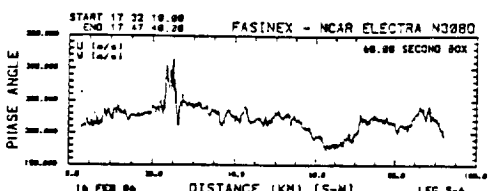
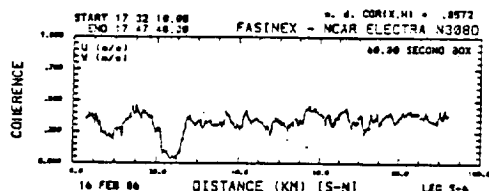
15



16



17

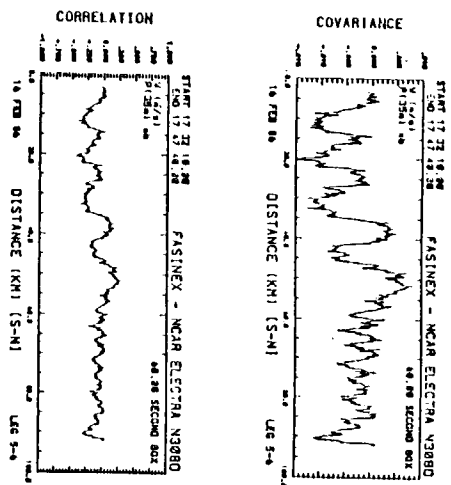


18

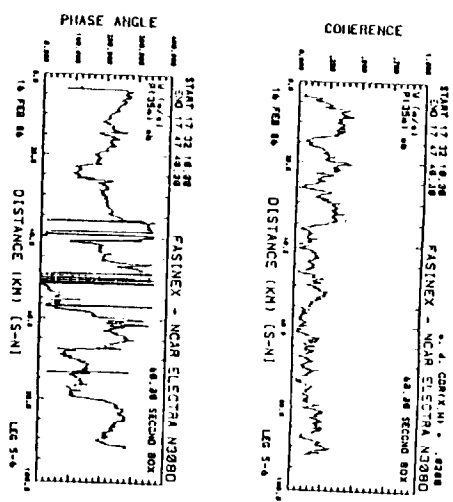
W and P_{35m}

These plots are shown because of their intriguing, wave-like character. The wavelength of these fluctuations is ~4 km over the cold water and ~8 km over the warm. The amplitude of fluctuations is also much larger over warm water. We speculate that these fluctuations may be a modulation of the turbulence by horizontal roll vortices. One puzzling aspect of these plots is that COR changes wavelength and magnitude around 56 km, but that COH changes around 36 km.

19



20



21

ORIGINAL PAGE IS
OF POOR QUALITY

EXTENDED TIME
SESSION E01: Satellite Studies
CHAIRMAN: James A. Coakley

Wednesday, July 12, 1989

	PAGE
E01.01 A Comparison of ISCCP and FIRE Satellite Cloud Parameters Gibson, Gary G., Patrick W. Heck, David F. Young, Patrick Minnis, and Edwin F. Harrison	257
E01.02 Comparison of Satellite Based Cloud Retrieval Methods for Cirrus and Stratocumulus Parker, Lindsay, and Bruce A. Wielicki	263
E01.03 Retrievals, Validation, and Analysis of Cloud Properties from AVHRR Data Arking, Albert, et al	***

A COMPARISON OF ISCCP AND FIRE SATELLITE CLOUD PARAMETERS

Gary G. Gibson, Patrick W. Heck, David. F. Young
Aerospace Technologies Division, Planning Research Corporation
Hampton, Virginia 23666

Patrick Minnis and Edwin F. Harrison
Atmospheric Sciences Division, NASA Langley Research Center
Hampton, Virginia 23665-5225

1. Introduction

One of the goals of the First ISCCP Regional Experiment (FIRE) is the quantification of the uncertainties in the cloud parameter products derived by the International Satellite Cloud Climatology Project (ISCCP). This validation effort has many facets including sensitivity analyses (Rossow et al., 1989) and comparisons to similar data or theoretical results with known accuracies. The FIRE provides cloud-truth data at particular points or along particular lines from surface and aircraft measurement systems. Relating these data to the larger, area-averaged ISCCP results requires intermediate steps using higher resolution satellite data analyses. Errors in the cloud products derived with a particular method can be determined by performing analyses of high-resolution satellite data over the area surrounding the point or line measurement. This same analysis technique may then be used to derive cloud parameters over a larger area containing similar cloud fields. It is assumed that the uncertainties found for the small-scale analyses are the same for the large scale so that the method has been "calibrated" for the particular cloud type; i.e., its accuracy is known. Differences between the large-scale results using the ISCCP technique and the "calibrated" method can be computed and used to determine if any significant biases or rms errors occur in the ISCCP results. In this paper, selected ISCCP results are compared to cloud parameters derived using the hybrid bispectral threshold method HBTM (Minnis et al., 1987) over the FIRE IFO and extended observation areas.

2. Stratocumulus

GOES-West ISCCP B3 data taken every 3 hours during July 17-31, 1983 analyzed with the HBTM on a 2.5° latitude-longitude grid between 40°N and 10°N and 145°W and 110°W (Minnis et al., 1988) are compared to the corresponding C1 (Rossow et al., 1988) results. The cloud data have been stratified as total, low, midlevel, and high clouds. The ISCCP low, middle, and high clouds are those with cloud-top pressures $p > 800$ mb, $800 \text{ mb} \geq p > 440$ mb, and $p \leq 440$ mb, respectively. HBTM low, middle, and high clouds are those with cloud-top altitudes, $z < 2$ km, $2 \text{ km} \leq z < 6$ km, and $z \geq 6$ km. There are two primary types of ISCCP cloud cover, VIR, determined with visible and infrared data, and IR, determined with infrared-data alone. The two cloud amounts are the same at night. As noted by Minnis et al. (1988), the cloud amounts, diurnal cloud variations, and cloud-top heights do not vary dramatically on an interannual basis over this area. Also, the cloud properties derived from the satellite near the coast are very much like those determined over the open ocean within this grid. Thus, the large-scale average properties derived for this region are similar to those determined over smaller areas. Initial validations of the HBTM are

described elsewhere (e.g., Minnis and Harrison, 1984; Minnis and Wielicki, 1988; and Minnis et al. (1989a,b).

Figure 1 shows the mean HBTM-derived total, low, and sum of middle and high cloud amounts. Total and low cloud amounts increase from the California coast to a maximum of 91% near 20°N, 130°W with a relative maximum in low cloudiness within the IFO region. This extensive cover of low clouds is referred to as the main stratocumulus region. Significant amounts of upper-level clouds occur in the southeastern quadrant of the grid. Differences between the HBTM and VIR results are shown in Fig. 2, while the HBTM-IR differences are plotted in Fig. 3. Neglecting the land areas, the mean VIR total cloud amounts (Fig. 2a) are $2 \pm 6\%$ greater than the HBTM values. Most of the ISCCP clouds, however, are placed in the middle layer as seen in the differences in Figs. 2b and 2c. More clouds are found with the HBTM over the main stratocumulus region than with the IR results. The IR underestimates total cloudiness by $7 \pm 11\%$.

The differences in the 3-hourly means are examined in Fig. 4 for two large regions outlined in heavy lines in Fig. 1c. The western box is designated the PAC region, while the other is the IFO region. Over the PAC region (Fig. 4a), there is generally good agreement between the results for all three analysis techniques. The HBTM cloudiness is very close to the IR results during the day but greater at night. Addition of the visible data increases the ISCCP cloud amounts so the VIR cloud cover exceeds the HBTM amounts during the day. On average, the HBTM and IR cloud amounts are the same, while the VIR cloudiness is greater than the HBTM's. This tendency for slight daytime overestimation by the VIR technique (relative to the HBTM) and underestimation with the IR method is accentuated near the coast over the IFO region (Fig. 4b). There, the IR diurnal range is much smaller than the HBTM's with a 20% underestimate in total cloudiness at night and more than 10% during the day. The VIR data only underestimate the cloud cover during the night leading to an overall cloud amount deficit of 10%.

The overestimation of ISCCP cloud-top heights over the stratocumulus region is probably due to the use of low-resolution NMC soundings over areas with strong boundary-layer inversions (Minnis et al., 1989b). The VIR cloud amounts agree quite well with the HBTM results primarily because of the effects of underestimation at night and overestimation during the day. This result is consistent with the Landsat analyses of Parker and Wielicki (1989). The differences between the results over the PAC and FIRE regions are attributable to the variations in contrast between the clear-sky and cloudy temperatures. Near the coast, the clouds are lower than those further west so fewer pixels are cold enough to pass the 3-K threshold. Diurnal variations in cloud amount determined with either the VIR or IR techniques should be used carefully. While both techniques appear to give the correct times for maximum and minimum cloudiness, there may be significant discrepancies in the diurnal ranges and the variations in cloudiness between the extrema.

3. Cirrus

Another method for validating an algorithm is to apply it directly to a high-resolution satellite data set corresponding to a cloud-truth set. The complete ISCCP algorithm was not available for this study so an attempt is made here to simulate its relevant characteristics. The adjustment of cloud-top temperature to account for the infrared semi-transparency relies on a

relationship between the visible and infrared optical depths, τ_v and τ_e , respectively. In the ISCCP algorithm, $\tau_v = 2\tau_e$ (Rossow et al., 1988). The value of τ_v is determined from the observed reflectance by first isolating the cloud reflectance by accounting for the surface and atmospheric contributions to the reflectance. The cloud reflectance is related to τ_v using the results of a radiative transfer model of clouds based on a scattering phase function determined from Mie theory using a droplet size distribution with an equivalent radius of 10 μm . Once the value of τ_v is determined, the observed cloud temperature for a given pixel is adjusted in the same manner used by Heck et al. (1989). The corrected temperature is then compared to the tropopause temperature and, if lower, set to the tropopause value. The temperatures or corresponding pressures for each pixel are then averaged for the area of interest to obtain an average cloud-top temperature or altitude.

The approach of Heck et al. (1989) is used here with some modifications to simulate the ISCCP cloud-height adjustment scheme. Instead of an empirical cloud bidirectional reflectance model, a τ_v -dependent model is used here which was constructed from the results of an adding-doubling model of radiative transfer (Takano and Liou, 1989) using a Mie-scattering phase function determined for a droplet distribution with an effective radius of 10 μm . The temperature of each cloudy pixel is adjusted individually using $\tau_v = 2\tau_e$. Averages are constructed from the adjusted pixel temperatures. Otherwise, all other steps are the same as those used by Heck et al. (1989). This simulated ISCCP algorithm was then applied to the lidar-satellite data used by Heck et al. (1989). The lidar-derived cloud-top heights are used as a reference set in the same manner used by Heck et al. (1989) to determine uncertainties in the results from the empirical method.

Comparisons of the simulated ISCCP cloud-top heights and the lidar cloud-center and cloud-top altitudes are shown as crosses in Figs. 5a and 5b, respectively. On average, the simulated ISCCP cloud-top heights are 2.8 km lower than the lidar cloud-center heights and 4.7 km lower than the lidar cloud-top altitudes. The range of differences leads to a large rms error of 3.4 km in the cloud-center height comparison. Average cloud heights for the 2.5° region bounded by 42.5°N and 45°N and 87.5°W and 90°W are also shown in Fig. 5 as circles. The ISCCP adjusted cloud-top heights are taken from the GOES C1 data for October 27 and 28, 1986. Averages from the 0.5° regional results of Heck et al. (1989) are used as the reference heights. The two lower cloud heights were observed on the 27th. The other three cases fall within the envelope of simulated data. Without the two low-level clouds, the observed ISCCP cloud-top heights are 1.7 km lower than the reference cloud-center heights and 2.5 km lower than the cloud-top heights.

The results shown in Fig. 5 demonstrate some consistency between the simulated and actual ISCCP cloud-top height results for semitransparent cirrus. Other cirrus IFO studies have indicated that the Mie scattering phase function is not a good representation of scattering in cirrus clouds. These preliminary findings support those conclusions.

REFERENCES

- Heck, P. W., G. G. Gibson, P. Minnis, and E. F. Harrison, 1989: Satellite derived cloud fields during the FIRE IFO case study. Presented at FIRE Annual Meeting/ASTEX Workshop, Monterey, CA, July 10-14.
- Minnis, P., and E. F. Harrison, 1984: Diurnal variability of regional cloud and clear-sky radiative parameters derived from GOES data, Part I: Analysis method. J. Clim. Appl. Meteor., **23**, 993-1011.
- Minnis, P., E. F. Harrison, and G. G. Gibson, 1987: Cloud cover over the eastern equatorial Pacific derived from July 1983 ISCCP data using a hybrid bispectral threshold method. J. Geophys. Res., **92**, 4051- 4073.
- Minnis, P., and B. A. Wielicki, 1988: Comparison of cloud amounts derived using GOES and Landsat data. J. Geophys. Res., **93**, 9385-9403.
- Minnis, P., E. F. Harrison, and D. F. Young, 1988: Extended time observations of California marine stratocumulus from GOES for July 1983-1987. FIRE Science Team Workshop, Vail, CO, July 11-15, 195-199.
- Minnis, P., C. W. Fairall, and D. F. Young, 1989a: Intercomparisons of GOES-derived cloud parameters and surface observations over San Nicolas Island. Presented at FIRE Annual Meeting/ASTEX Workshop, Monterey, CA, July 10-14.
- Minnis, P., D. F. Young, R. Davies, M. Blaskovic, and B. A. Albrecht, 1989b: Stratocumulus cloud height variations determined from surface and satellite measurements. Presented at FIRE Annual Meeting/ASTEX Workshop, Monterey, CA, July 10-14.
- Parker, L., and B. A. Wielicki, 1989: Comparison of satellite based cloud retrieval methods. Presented at FIRE Annual Meeting/ASTEX Workshop, Monterey, CA, July 10-14.
- Rossow, W. B., L. C. Garder, P. Lu, and A. Walker, 1988: International Satellite Cloud Climatology Project (ISCCP), Documentation of cloud data. WCRP Report, August, 78 pp.
- Rossow, W. B., L. C. Garder, and A. A. Lacis, 1989: Global, seasonal cloud variations from satellite radiance measurements. Part I: Sensitivity of analysis. J. Clim., **2**, 419-418.
- Takano, Y. and K. N. Liou, 1989: Radiative transfer in cirrus clouds: I. Single scattering and optical properties of oriented hexagonal ice crystals. J. Atmos. Sci., **46**, 3-20.

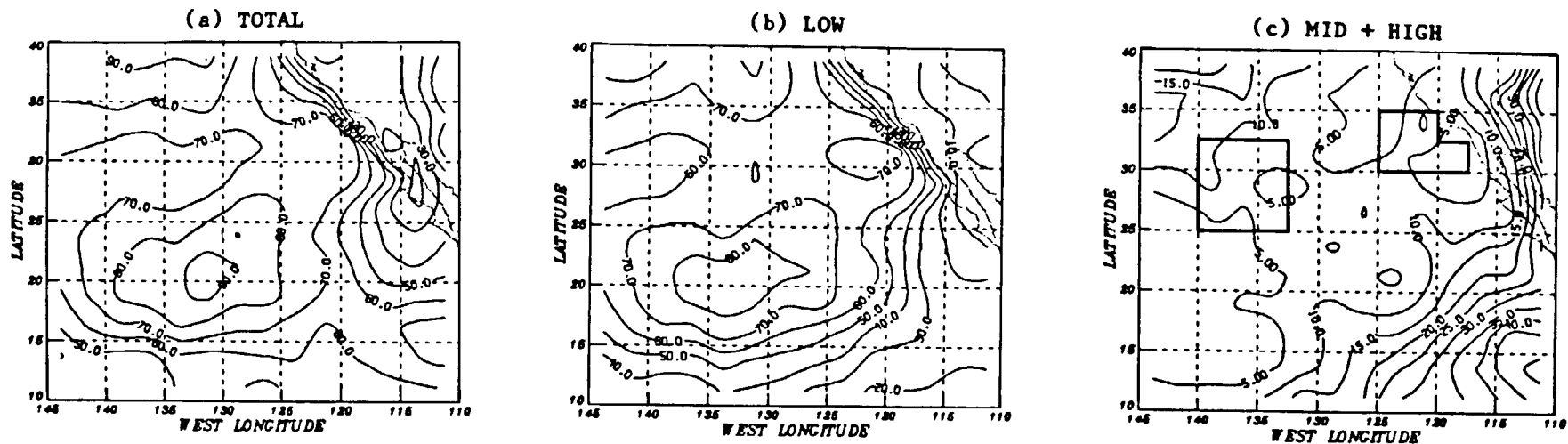


Fig. 1. Cloud amounts (%) derived with HBTM for July 17-31, 1983.

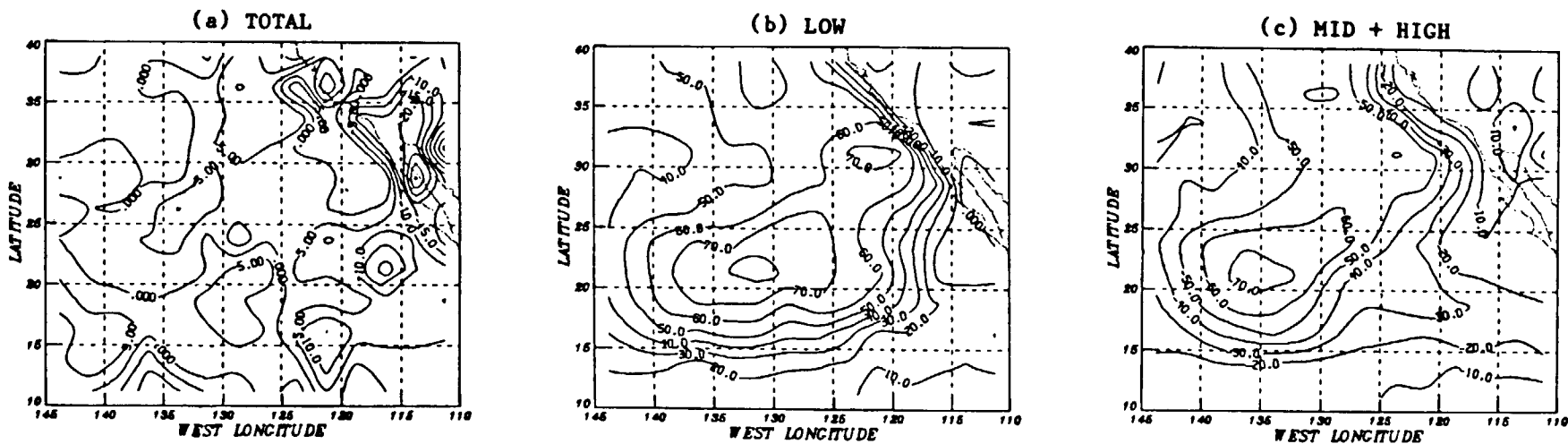


Fig. 2. Differences between HBTM and VIR cloud amounts (%) for July 17-31, 1983.

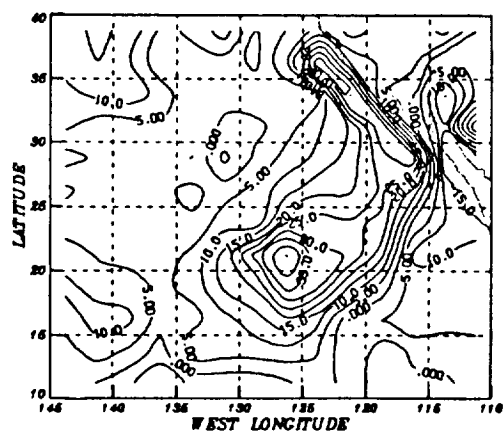


Fig. 3. Same as Fig. 2 except for HBTM and IR total cloud amounts.

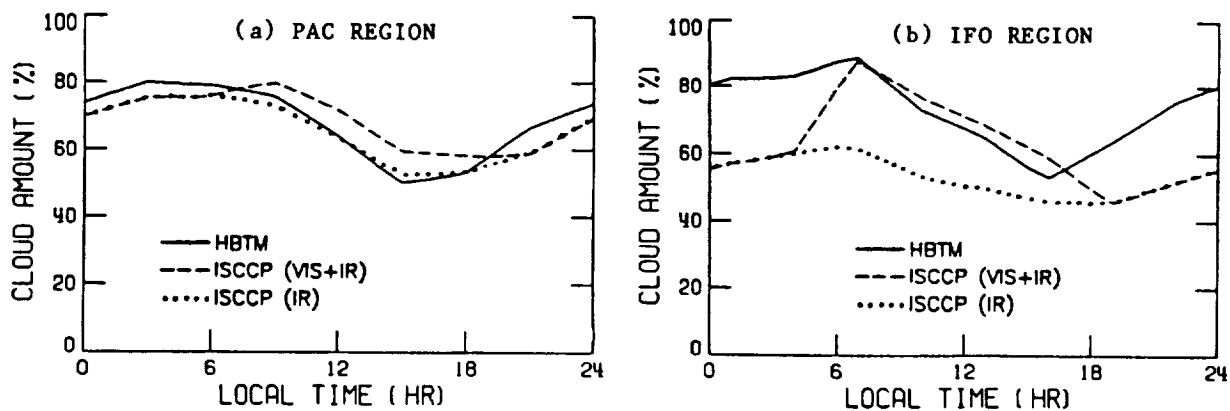


Fig. 4. Diurnal variations in mean total cloudiness for July 17-31, 1986.

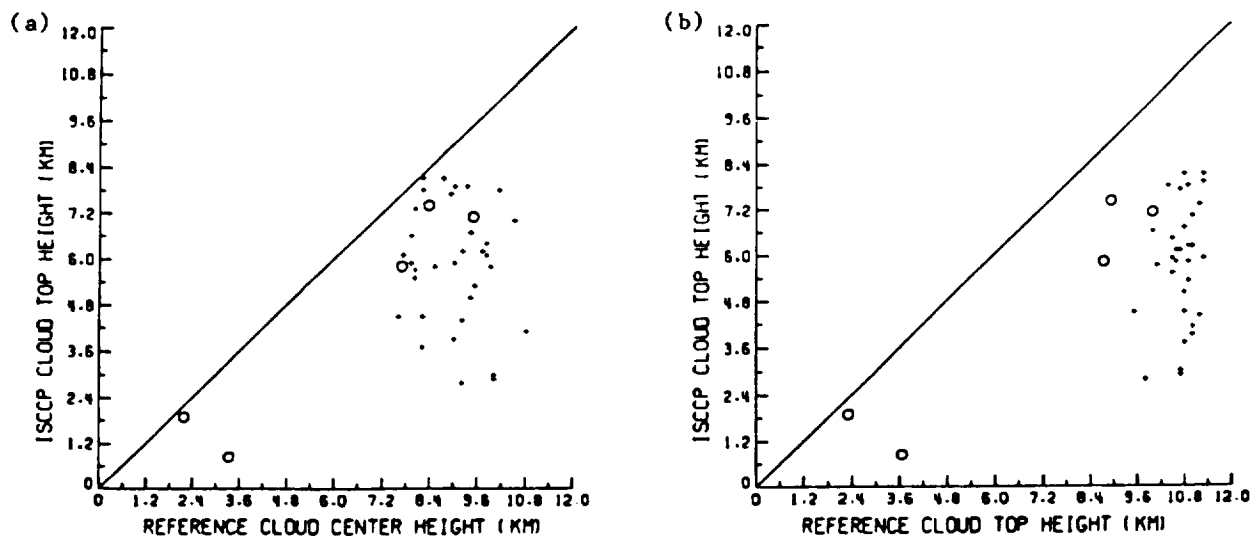


Fig. 5. Comparison of simulated and actual ISCCP cloud heights to reference data.

COMPARISON OF SATELLITE BASED CLOUD RETRIEVAL METHODS FOR CIRRUS AND STRATOCUMULUS

Lindsay Parker
Aerospace Technologies Division, Planning Research Corporation
Hampton, VA. 23666

Bruce A. Wielicki
Atmospheric Sciences Division, NASA Langley Research Center
Hampton, VA. 23665-5225

1. INTRODUCTION

One difficulty in using satellite remote sensing data is the spatial variability of cloud properties on scales smaller than most meteorological satellite fields of view (approximately 4 to 8 km). The present study examines the variation of satellite derived cloud cover as a function of the satellite sensor spatial resolution for seven cloud cover retrieval methods:

- | | |
|------------------------------------|---|
| 1. Reflectance Threshold: | Threshold = clear-sky reflectance $R_{clr} + 3\%$ |
| 2. Temperature Threshold: | Threshold = clear-sky temperature $T_{clr} - 3K$ |
| 3. ISCCP: | Bispectral threshold ($R_{clr} + 3\%$, $T_{clr} - 3K$) |
| 4. HBTM: | Hybrid Bispectral Threshold Method (Minnis et al., 1987) |
| 5. NCLE: | Bispectral method (Stowe et al., 1988) |
| 6. Spatial Coherence: | Coakley and Bretherton (1982) |
| 7. Functional Box Counting: | Lovejoy et al. (1987) |

The first two methods are simple mono-spectral thresholds which specify a satellite pixel as cloud filled if the measured reflectance is greater than the threshold, or if the measured equivalent blackbody temperature is less than the threshold.

The next three methods are bispectral, using one visible wavelength window channel and one thermal infrared wavelength window channel. For ISCCP, the pixel is classified as cloud filled if the measurement exceeds either one of the single spectral channel thresholds. The HBTM has a more complicated strategy explained in Minnis and Harrison (1984) and Minnis et al (1987). One of the critical features of the HBTM is a series of checks of retrieved cloud albedo against climatological values. The NCLE yields a weighted cloud cover from two independent estimates of total cloud cover (one from an infrared channel at $11.5\mu m$ and one from a UV channel at $0.38\mu m$). The philosophy of the NCLE is to use the TOMS reflectance channel for boundary layer clouds (i.e. low thermal contrast) and to use the THIR $11.5\mu m$ channel for middle and high level clouds (i.e. strong thermal contrast) as detailed in Stowe et al(1988).

The final two algorithms rely on the spatial variability within the cloud field to determine cloud cover. Spatial coherence assumes only that the cloud field occurs in a single layer and that the clouds are optically thick in the infrared window. Functional box counting uses the variation in reflectance threshold cloud cover over spatial scales observed by the satellite (here assumed to be 1 to 8 km for meteorological satellites) to predict the cloud cover for scales smaller than those observed (less than 1 km). This method relies on spatial scale invariance of the radiance fields to account for the resolution dependence of cloud cover. The study of Lovejoy et al (1986) used radar and GOES satellite data to indicate that this scale invariance held to scales in the atmosphere as small as 1 km.

Landsat Thematic Mapper (TM) data is used to test the spatial resolution dependence of the cloud algorithms. The TM radiometer has a near visible channel at $0.83\mu m$ and a thermal infrared window channel at $11.5\mu m$. The spatial resolution of the visible channel is 28.5 meters and the infrared channel is 114 meters. The full resolution data for these two spectral bands is then averaged in steps of two to provide spatial resolutions of 28.5m, 57m, 114m, 228m, 456m,

912m, 1824m, 3648m, and 7296m. These spatial resolutions are referred to in the following discussions as nominally 1/32, 1/16, 1/8, 1/4, 1/2, 1, 2, 4, and 8 km resolution data.

The ISCCP bispectral threshold applied to the full resolution data is used as the reference or "truth" cloud cover, after which the retrieval methods are applied to each of the spatial resolutions. For most of the scenes, sufficient clear regions are present in the full resolution Landsat data to use the peak of the bispectral histogram to define Rclr and Tclr. In the remaining scenes, the cloud field images were examined to select radiances in clear regions between cloud cells (at least 0.5 km from the nearest cloud cell). The same Rclr and Tclr are used at all spatial resolutions, for all retrieval methods, with the exception of the spatial coherence method which calculates its own clear and cloudy radiances. Note that reflectance is defined by $R = 100 \pi L / (S(t) \cos \theta_s)$ where L is spectral radiance derived using the calibration coefficients of Markham and Barker^S(1986), S(t) is the spectral solar constant for the date of the observation and θ_s is the solar zenith angle. Brightness temperature calibration for the thermal channel is also taken from Markham and Barker (1986). The Landsat viewing angles are within 5 degrees of nadir.

Studies of the fraction of pixels in the scene at cloud edge, and of the profile of reflectance and temperature near cloud edges indicate an uncertainty in the reference cloud fraction of 1 to 5% (Minnis and Wielicki, 1988).

2. RESULTS

The 24 cloud regions are 58.4 km by 58.4 km and are grouped and analyzed by cloud type (cirrus, cumulus, etc). Table 1 gives the location, date, reference cloud fraction, clear-sky brightness temperature (Tclr), clear-sky reflectance (Rclr), average cloudy pixel temperature (Tcld), average cloudy pixel reflectance (Rcld), and a description of the cloud types present. The descriptions are based on examination of the full resolution visible and infrared cloud images, and the bispectral histograms of the cloud fields. The cloud top temperatures given in the description are taken from the optically thick portions of the cloud fields as identified in the bispectral histograms (i.e. nadir reflectance greater than 40%). Where two distinct cloud levels occurred, both cloud tops are given. Time of observation for the Landsat sun-synchronous orbit is approximately 9:45 a.m. local time.

TABLE 1. CLOUD FIELD LOCATIONS, TIMES, AND PROPERTIES

Scene	Lat/Lon	Date Da/Mo/Yr	Cloud Cover	Rclr (%)	Rcld (%)	Tclr (K)	Tcld (K)	Description (Cld top temp)
A	19.7S/ 75.3W	7/13/87	0.671	2.5	19.5	289.7	287.5	Stratocumulus (285K)
B	20.7S/ 75.1W	7/13/87	0.915	2.5	28.2	289.7	286.5	Stratocumulus (284K)
C	33.7N/129.9W	7/10/87	0.521	3.3	21.4	288.8	285.6	Stratocumulus (283K)
D	26.4N/ 79.4W	1/14/83	0.708	4.0	44.6	298.0	280.5	Stratocumulus (272K)
E	25.7N/ 78.3W	1/14/83	0.390	3.5	52.4	296.3	277.4	Stratocumulus (270K)
F	31.8N/122.2W	7/07/87	0.662	3.8	33.3	289.7	284.8	Stratocumulus (283K)
G	31.8N/120.7W	6/30/87	0.889	2.7	38.7	288.8	282.9	Stratocumulus (282K)
H	28.3N/ 90.0W	1/06/83	0.718	3.2	11.8	305.4	279.2	Cirrus (\approx 220K)
I	44.6N/ 86.9W	10/28/86	0.950	4.3	13.8	280.5	266.5	Cirrus (\approx 243K, \approx 220K)
J	43.0N/ 87.5W	10/28/86	0.646	3.6	9.1	283.5	273.9	Cirrus (\approx 238K)
K	40.3N/ 71.8W	4/19/85	0.568	4.1	6.2	276.9	269.1	Cirrus (\approx 264K, \approx 254K)
L	40.3N/ 70.3W	5/30/85	0.839	5.3	8.6	278.5	270.5	Cirrus (\approx 262K)
M	28.9N/ 87.6W	3/15/84	0.625	3.5	14.9	287.8	273.1	Cirrus (\approx 254K)

a. Stratocumulus Cloud Fields

Results for stratocumulus are given in Fig. 1 (Scenes A-G, Table 1). The Reflectance, ISCCP and HBTM methods are within 0.05 of cloud "truth" for spatial resolutions less than 1/2 kilometer. These methods show a strong dependence on spatial resolution for pixel sizes beyond 1/2 kilometer. The Reflectance and ISCCP methods overestimate cloud fraction by 0.16 and the

HBTM by 0.09 for 8 kilometer data. The overestimation of cloud fraction is caused by partially filled pixels being considered as cloud filled pixels.

The Temperature threshold method underestimates cloud cover by about 0.20 at all spatial resolutions. Comparing the ISCCP bispectral result to the Reflectance and Temperature threshold results, we conclude that the solar reflectance channel dominates the bispectral cloud retrieval for stratocumulus. While this result is qualitatively expected, the magnitude of the difference in cloud cover (0.35) between the mono-spectral threshold methods is surprising. Examining Table 1, three of the stratocumulus cloud fields have $T_{clr} - T_{cld}$ of 2.2 to 3.2K. These same three cases also have the lowest cloud reflectances, ranging from 19.5 to 28.2%. The low reflectances indicate that substantial portions of the cloud field have $11.5\mu m$ emittances less than 1.0. In this case, substantial portions of the cloud field are missed by the $T_{clr} - 3K$ threshold. These optically thin portions of the cloud fields are also the cause of the underestimate of cloud cover by 0.12 for the Spatial Coherence results in Fig. 1. The Spatial Coherence method derives an effective cloud cover which is cloud fraction times cloud emittance.

For low clouds the NCLE algorithm gives strongest weighting to the cloud cover derived using the reflectance of the TOMS $0.38\mu m$ channel. Therefore, we would expect good results for the stratocumulus clouds. Fig. 1, however, indicates that the NCLE underestimates the cloud fraction by about 0.20. The NCLE algorithm determines its TOMS-based cloud cover as a linear function of reflectance between the clear reflectance and an assumed overcast cloud albedo of 50%. In the present analysis, Landsat nadir reflectance is substituted for albedo using the Earth Radiation Budget Experiment (ERBE) anisotropic models for overcast cloud (Suttles et al, 1988) to convert albedo to an equivalent nadir reflectance. This gives an overcast nadir reflectance of 51%, 48%, and 45% for solar zenith angles of 32° , 41° , and 49° respectively. The average stratocumulus nadir reflectance in Table 1, however, is only 34.0%. As a result, the NCLE algorithm underestimates the cloud fraction for these cloud cases. The NCLE albedo for overcast low cloud was derived by averaging the $0.38\mu m$ reflectance of TOMS fields of view (45 km at nadir) judged to be cloud filled (L. Stowe, personal communication). An examination of the Landsat spatially degraded data showed that the albedo of cloud filled pixels is a systematic function of pixel size. The average reflectance of $1/32$ km pixels is 34.0%, $1/8$ km is 37.0%, $1/2$ km is 42.3%, and 2 km is 47.0%. For 8 km pixels, only cloud fields D-G have overcast pixels, with an average reflectance of 58.1%. We conclude that the larger the spatial extent of the contiguous cloud cover, the larger the cloud optical depth. This brings into question the NCLE assumption of cloud cover linear in cloud reflectance. A caveat on this result, however, is the use of the Landsat $0.83\mu m$ Landsat channel to mimic the $0.38\mu m$ TOMS channel.

Finally, Fig. 1 shows that the Functional Box counting method underestimates cloud fraction for spatial resolution less than 1 kilometer. This method assumes the slope of the change in cloud cover from 1 to 8 km can be extended to scales less than 1 km. Fig. 1 demonstrates this method is incorrect. Cahalan (1988) and Welch et al (1989) found a break in the scale invariance between 0.5 and 1.0 km, consistent with the present results.

Fig. 2 gives a scatter plot of the estimated versus reference cloud fraction for each retrieval method. This figure demonstrates that the mean errors examined in Fig. 1 vary greatly from cloud field to cloud field.

Fig. 3 gives the Temperature, Reflectance, and ISCCP Bispectral thresholds which would result in unbiased cloud cover estimates for the seven stratocumulus cloud fields. As spatial resolution degrades, the reflectance and ISCCP thresholds must be further removed from the clear-sky background to avoid the biasing effect of partially cloudy pixels. ISCCP and the Reflectance threshold would require a threshold of 9.5% for stratocumulus clouds using 8km spatial resolution data. The Temperature threshold would require a threshold of $T_{clr} - 1.5K$ colder than the clear-sky temperature. Unfortunately, use of temperature thresholds much less than $T_{clr} - 3K$ would cause false detection of cloud given typical variations in ocean surface temperature and atmospheric water vapor.

b. *Cirrus Cloud Fields*

Results for cirrus are given in Fig. 4 (Scenes H-M Table 1). The results for cirrus are very different from the stratocumulus results. The cirrus results show little dependence on the sensor spatial resolution, indicating that the cirrus are not dominated by the small scale cellular features prevalent in the stratocumulus fields. The effect of spatial resolution on derived cloud cover is less than 0.02 for spatial scales less than 2 km, reaching 0.07 for the ISCCP algorithm using 8 km resolution data.

The agreement between the Temperature threshold and ISCCP bi-spectral results indicates the dominance of the $11.5\mu\text{m}$ channel for cloud detection of cirrus. Consistent with this view, the Reflectance threshold underestimates cirrus cloud cover by 0.18 to 0.25, depending on the spatial resolution. The cirrus clouds are optically thin with an average R_{cld} of 10.6%. As a result, the Reflectance threshold misses a substantial portion of the cloud field with reflectances less than 3% above the clear reflectance. The HBTM results are intermediate between the Reflectance and Temperature threshold results, underestimating cirrus cloud cover by 0.10 for 8 km resolution data.

The cloud cover underestimate by the Spatial Coherence method is larger than that found for stratocumulus because the cirrus emittance is lower. The Box Counting method underestimates cirrus cloud cover for two reasons. First, the reflectance threshold causes an underestimate as discussed above. Second, the scale invariance is again a poor approximation for spatial scales less than 1 km. For these cirrus clouds, the scale invariance appears to be a poor approximation even for scales of 1 to 8 km, in contrast to the result for stratocumulus cloud fields.

Finally, the NCLE result underestimates cirrus cloud cover by 0.38 to 0.42. This result appears to be caused by two factors. First, the NCLE uses a $T_{\text{clr}} - 6\text{K}$ threshold at $11.5\mu\text{m}$, thereby missing some of the cirrus detected by the ISCCP method using a $T_{\text{clr}} - 3\text{K}$ threshold. This was especially important for cloud fields K and L for which the average T_{cld} was only 7 to 8 K colder than T_{clr} . A second difficulty is that the TOMS reflectance channel cloud cover estimate is still being given significant weight by the NCLE algorithm. This is because much of the cirrus cloud field is warmer than the approximately $T_{\text{clr}} - 9\text{K}$ temperature used to separate low level from middle and high level clouds. These "warm" portions of the cloud field are treated as if they were low cloud, thereby using the TOMS channel cloud estimate. Since the cirrus reflectance is much less than 50%, the TOMS channel greatly underestimates the cirrus cloud cover.

Figure 5 gives the estimated versus reference cloud cover results for each individual cloud field. As for stratocumulus, the errors are not a simple constant bias. Figure 6 gives the threshold levels which if applied to the 6 cirrus fields would have resulted in an unbiased cloud cover. The thresholds show less dependence on spatial resolution than was found for the stratocumulus cloud cases.

3. SUMMARY

1. For the threshold methods, stratocumulus cloud cover is strongly dependent on satellite sensor spatial resolution. Cirrus cloud cover is weakly dependent on satellite sensor spatial resolution.
2. Differences between current cloud retrieval algorithms are large, especially between the ISCCP and NCLE algorithms.
3. Varying treatment of cloud optical thickness (i.e. shortwave reflectance or thermal emittance) appears to account for many of the differences in the cloud retrieval algorithms.
4. Functional Box Counting incorrectly estimates cloud fraction below 1 km due to breaks in the scale invariant power law between 0.5 and 1 km for stratocumulus and 2-4 km for cirrus.
5. For the threshold cloud retrieval methods, the solar reflectance channel dominates cloud cover retrieval for stratocumulus, while the thermal channel dominates for cirrus.

REFERENCES

- Cahalan, R. F., 1988: in Scaling, Fractals, and Nonlinear Variability in Geophysics, Ed. S. Lovejoy and D. Schertzer.
- Coakley, J. A. and F. P. Bretherton, 1982: JGR, **87**, 4917-4932.
- Lovejoy, S. et al, 1987: Science, **235**, 1036-1038.
- Markham, B. L. and J. L. Barker, 1986, Landsat Technical Notes, Aug. 1986.
- Minnis, P., E. F. Harrison, and G. G. Gibson, 1987: J. Geophys. Res., **92**, 4051-4073.
- Minnis P. and B. A. Wielicki, 1988: JGR, **93**, 9385-9403.
- Platt, C. M R. et al, 1980: MWR, **108**, 195-204.
- Stowe, L. L. et al., 1988: J. Clim., **1**, 445-470.
- Welch, R. M. et al., 1988: JAM, **27**, 341-362.

Fig. 1

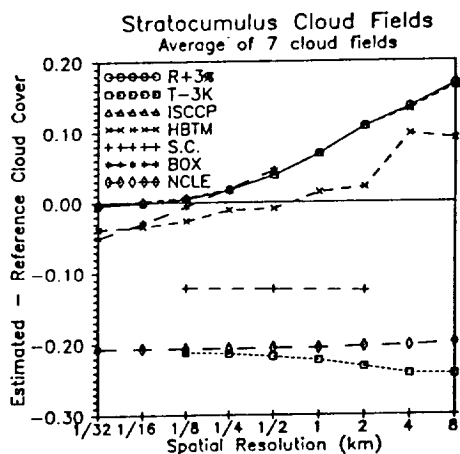


Fig. 2

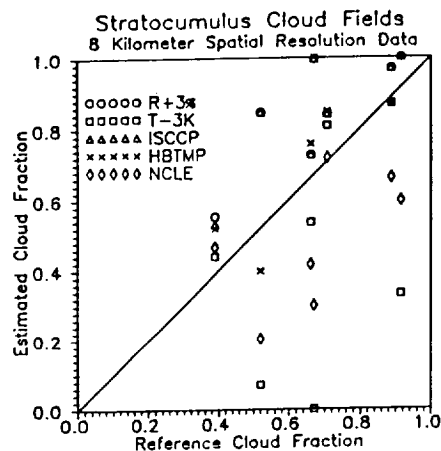


Fig. 3

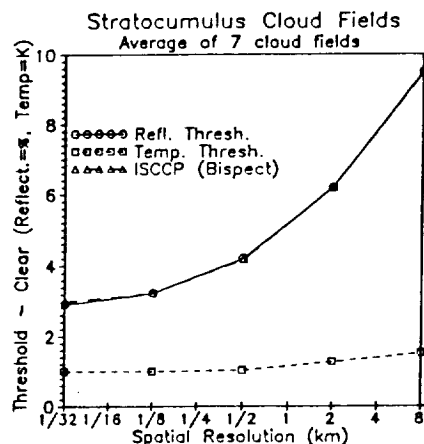


Fig. 4

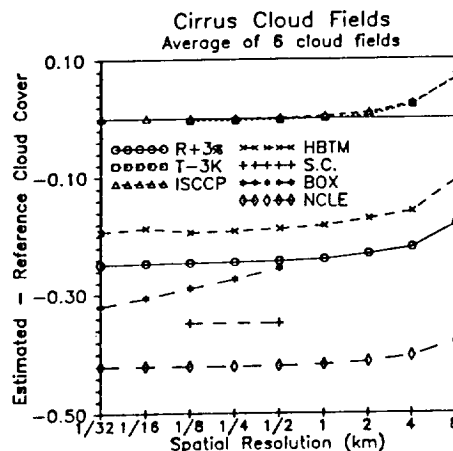


Fig. 5

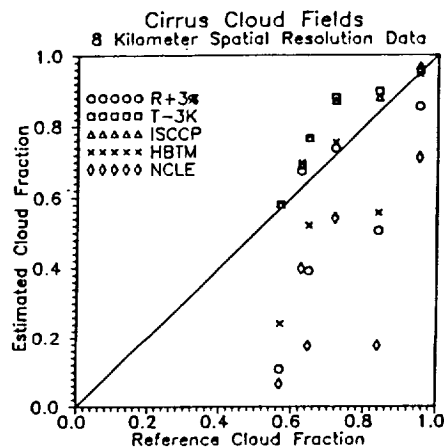
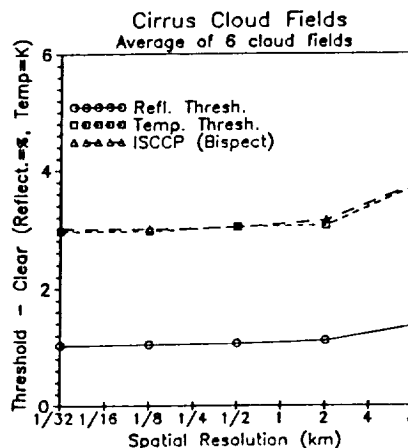


Fig. 6



EXTENDED TIME
SESSION E02: Surface-Based Studies
CHAIRMAN: James A. Coakley

Wednesday, July 12, 1989

	PAGE
E02.01 ETO Lidar Studies of Cirrostratus Altocumulogenitus: Another Role for Super-Cooled Liquid Water in Cirrus Cloud Formation <u>Sassen, Kenneth</u>	271
E02.02 Impact of Cirrus on the Surface Radiative Environment at the FIRE ETLA Palisades, NY Site Robinson, David A., <u>George Kukla</u> , and Allan Frei	275

ETO Lidar Studies of Cirrostratus Altocumulogenitus:
 Another Role for Supercooled Liquid Water
 In Cirrus Cloud Formation

Kenneth Sassen

Department of Meteorology
 University of Utah
 Salt Lake City, Utah 84112

ABSTRACT

Cirrus clouds have traditionally been viewed as cold, wispy or stratiform ice clouds, typically displaying optical phenomena such as haloes. A composition entirely of hexagonal ice crystals, of one habit or another, seems implicit in the definition of cirrus. Supercooled cloud droplets could only have a transitory existence in cirrus, since the concentrations of ice nuclei (IN) measured by various techniques (at the surface or in the lower troposphere) indicate an enormous number of IN that should be active at cirrus cloud temperatures. Reports of aircraft icing at cirrus cloud altitudes (itself a poorly defined criterion) were generally not well documented in the literature (for recent surveys see Rangno and Hobbs 1986 and Sassen et al. 1989a), and in view of the accepted -35° to -40°C threshold for "instantaneous" homogeneous nucleation, such reports do not appear to have altered the prevailing convention of viewing cirrus as exclusively ice clouds.

In light of recent instrumented aircraft and polarization lidar studies of cirrus clouds, however, it is clear that highly supercooled cloud droplets can sometimes be a component of cirrus clouds. The question of the prevalence of supercooled liquid water (SLW) in cirrus has implications for climate research, for it has been shown theoretically that thin SLW layers at the base of elevated cirrus clouds can have a relatively significant impact on radiation transfer through the cloudy atmosphere (Sassen et al. 1985). It remains to be determined if SLW is present abundantly enough in cirrus to play a significant role in the planet's radiation balance, or is merely a curious, infrequent occurrence.

To help evaluate this issue, the University of Utah polarization lidar FIRE Extended Time Observations (ETO) of cirrus clouds are being utilized to compile, among other parameters, a climatological record of SLW clouds associated with and within cirrus. Although our program is ongoing, and a proper assessment of the growing data base is in the future, on the basis of the observations collected so far it is appropriate to define the various modes of occurrence of SLW in cirrus clouds. (Note that the "definition" of cirrus clouds could seemingly exclude SLW-containing clouds as cirrus, but, as a former National Weather Service meteorological technician, my classification of cloud types is based on the "standard" visual appearance of clouds, with supporting all-sky photography.)

Figure 1 illustrates four distinct modes of the occurrence of SLW connected with cirrus cloud development identified from polarization lidar observations. Before discussing this figure, however, it is important to note that SLW (as used here) refers to the supermicron-sized cloud droplets measurable by in situ aircraft probes, which are shown by the stippled areas in Fig. 1. Thus ice nucleation at temperatures less than about -35° to -40°C likely involving the homogeneous freezing of haze particles (shown as dots in Fig. 1) is not considered here (see the companion paper by Sassen, Dodd and Starr). The existence of SLW clouds associated with cirrus can potentially impact radiative transfer to a much more significant extent than haze particle effects, and clearly affect attempts to evaluate satellite-viewed scenes containing high clouds (see, e.g., Wielicki et al. 1989).

Three of the modes have been described previously--the incorporation of supercooled altocumulus (and associated virga) into deepening cirrostratus (Sassen et al. 1989b), and the formation of SLW layers at the base of deep convective cirrostratus and orographic cirrus wave clouds (Sassen et al. 1989a). The cirrus cloud generation mechanism shown at the top of Fig. 1 involves the glaciation of a supercooled altocumulus cloud layer (essentially without ice particle "seeding" from higher cirrus), which can produce a fairly extensive cirrostratus cloud with cloud tops at or near the previously water-saturated layer. The resulting cloud is termed cirrostratus altocumulogenitus in recognition of the generation mechanism. The initial altocumulus glaciation may result from cloud top penetration into temperatures cold enough to promote homogeneous cloud droplet freezing, or according to the entrainment/drop evaporation mechanism proposed by Hobbs and Rangno (1985), for example. It is uncertain at this time whether significant additional ice nucleation occurs after altocumulus glaciation, or whether the cirrostratus ice particles are capable of persisting for long periods until complete sedimentation occurs and the altocumulus may again form to repeat the sequence. It is important to note that the precipitating ice crystals frequently, if not typically, display laser backscattering properties indicating horizontally oriented planar ice crystals, which minimizes the ice crystal fall speeds. Horizontally oriented plate crystals with diameters up to about 0.5 mm display terminal velocities in the $10\text{--}20\text{ cm s}^{-1}$ range (see Sassen 1980), such that periods of $\sim 2\text{ h}$ are required for crystals to sediment through a 1.0-km depth, even without considering the large-scale ascent rate. Cirrostratus altocumulogenitus clouds typically appear to have cloud thicknesses on the order of a few kilometers.

Acknowledgments. The FIRE Extended Time Observations based at our Facility for Atmospheric Remote Sensing (FARS) are currently being supported by NSF Grant ATM-85 13975 and NASA Grant NAG1-868. FARS has been jointly developed with funding from the National Science Foundation and the University of Utah.

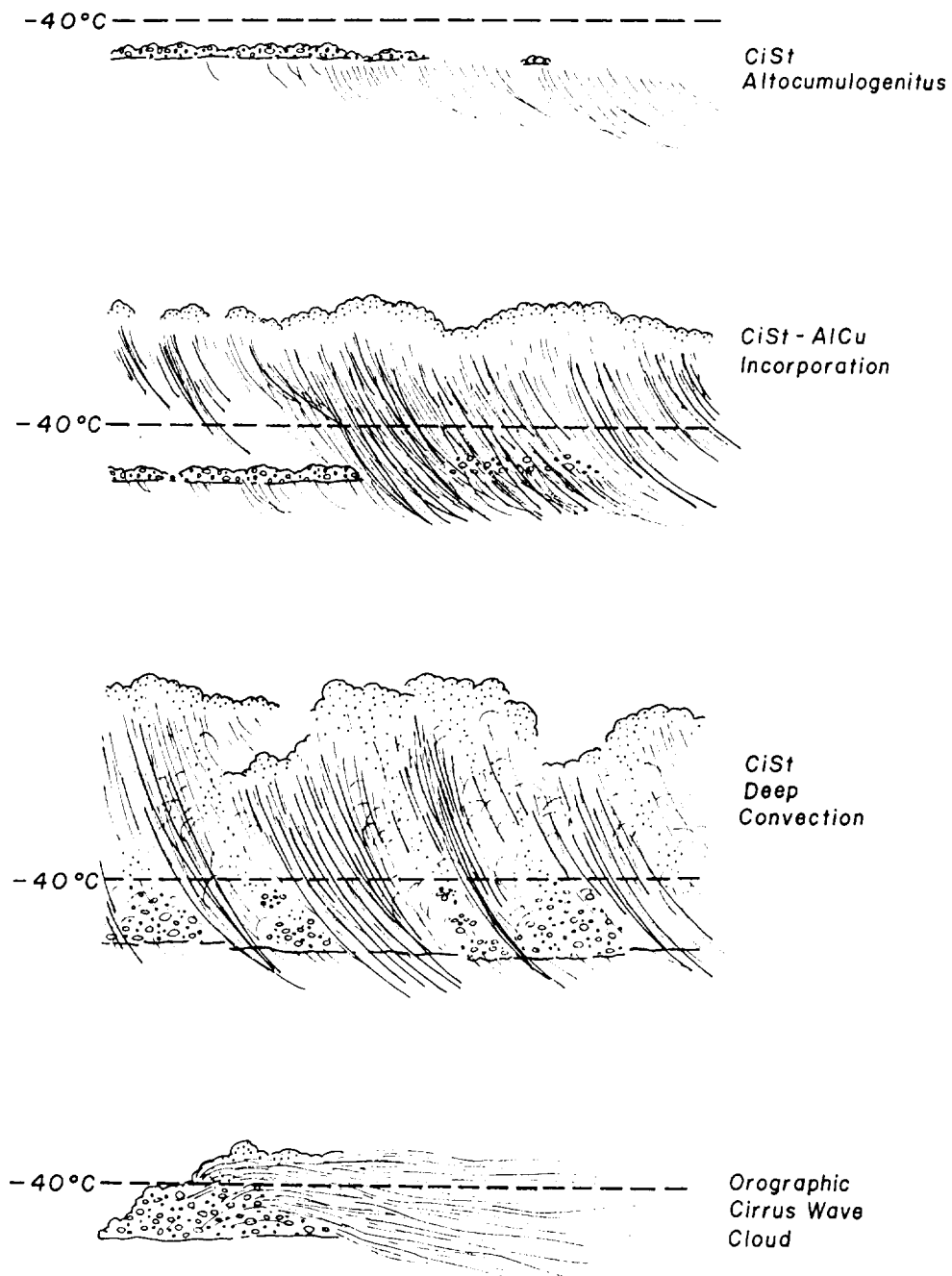


Fig. 1 Schematic view of four modes of occurrence of supercooled cloud droplets (stippling using open circles) connected with the development of various cirrus types. Horizontal scales can vary from tens to hundreds of kilometers: typical vertical scales are a few kilometers for the top and bottom types, and up to several kilometers for the middle two cases.

References

- Hobbs, P. V., and A. L. Rangno, 1985: Ice particle concentrations in clouds. *J. Atmos. Sci.*, **42**, 2523-2549.
- Rangno, A. L., and P. V. Hobbs, 1986: Deficits in ice particle concentrations in stratiform ice clouds with top temperatures $\leq -30^{\circ}\text{C}$? Preprints, 23rd Conf. on Radar Meteorology and the Conf. on Cloud Physics, Snowmass, CO, Amer. Meteor. Soc., 20-23.
- Sassen, K., 1980: Remote sensing of planar ice crystal fall attitudes. *J. Meteor. Soc. Japan*, **58**, 422-429.
- Sassen, K., K. N. Liou, S. Kinne and M. Griffin, 1985: Highly supercooled cirrus cloud water: Confirmation and climatic implications. *Science*, **227**, 411-413.
- Sassen, K., D. O'C. Starr and T. Uttal, 1989a: Mesoscale and microscale structure of cirrus clouds: Three case studies. *J. Atmos. Sci.*, **46**, 371-396.
- Sassen, K., C. J. Grund, J. Spinhirne, M. Hardesty and J. M. Alvarez, 1989b: The 27-28 October 1986 FIRE IFO cirrus case study: A five lidar overview of cloud structure and evolution. *Mon. Wea. Rev.*, **117** (in press).
- Wielicki, B. A., J. T. Suttles, A. J. Heymsfield, R. M. Welch, J. D. Spinhirne, M.-L. C. Wu, S. K. Cox, D. O'C. Starr, L. Parker and R. F. Arduini, 1989: The 27-28 October 1986 FIRE IFO cirrus case study: Comparison of radiative transfer theory with observations by satellite and aircraft. *Mon. Wea. Rev.*, **117** (in press).

in: Proceedings of the FIRE Science Meeting, Monterey, CA, 227-231 (1989)

IMPACT OF CIRRUS ON THE SURFACE RADIATIVE ENVIRONMENT AT THE FIRE ETLA PALISADES, NY SITE*

David A. Robinson
Department of Geography
Rutgers University
New Brunswick, NJ 08903

George Kukla and Allan Frei
Lamont-Doherty Geological Observatory of Columbia University
Palisades, NY 10964

1. INTRODUCTION

FIRE Extended Time Limited Area (ETLA) observations provide year-round information critical to gaining a better understanding of cloud/climate interactions. The Lamont/Rutgers team has participated in the ETLA program through the collection and analysis of shortwave and longwave downwelling irradiances at Palisades, NY. These data are providing useful information on surface radiative fluxes with respect to sky condition, solar zenith angle and season. Their utility extends to the calibration and validation of cloud/radiative models and satellite cloud and radiative retrievals. Here, the impact cirrus clouds have on the surface radiative environment is examined using Palisades ETLA information on atmospheric transmissivities and downwelling longwave fluxes for winter and summer cirrus and clear sky episodes in 1987.

2. MEASUREMENT PROGRAM

Downwelling hemispheric shortwave (SW: 0.28-2.8 μ m) and longwave (LW: 4.0-50.0 μ m) irradiances have been measured at Palisades, NY since December 1986. Observations are made with an Eppley Precision Spectral Pyranometer and an Eppley Pyrgeometer which were calibrated with Colorado State University instruments during the Cirrus IFO in October 1986, and have since been periodically recalibrated by the Eppley Laboratory. Pyrgeometer output contains an adjustment for body temperature but not for dome temperature. Data are transmitted to a Campbell CR-21 Digital Recorder, where one minute averages of ten second samples are stored and subsequently dumped to a cassette recorder. Using a Campbell C-20 Cassette Interface, these data are transferred to an Apple Macintosh computer for analysis and archiving. In addition to the full shortwave and longwave irradiances, hemispheric near infrared irradiance (NIR: 0.7-2.8 μ m) and diffuse components of the SW and NIR fluxes have also been measured for all or part of the past two and one half years.

Among the variables generated from the measured data is shortwave atmospheric transmissivity, which is simply the ratio of downwelling SW at the surface to incoming SW at the top of the atmosphere. Between 0.28-2.8 μ m, the latter is equal to 0.971 times the solar constant of 1366.97 W/m².

Palisades, NY (41°00' N, 74°55' W) is situated approximately 10 km north of the northern limits of New York City. The radiometers are mounted on the roof of a two story building approximately 130 meters above sea level. A daily log of sky conditions is maintained and fisheye (180°) sky photos are taken periodically coincident with overpassing NOAA 9 and Landsat satellites.

* This work is supported by NASA grant NAG-1-653.

3. EXPERIMENT DESIGN

The success of a comparative analysis such as this strongly depends on the selection of appropriate regional cirrus and clear episodes. In the present study, this involved interrogating detailed meteorological observations from NOAA first-order observation sites at Newark and LaGuardia Airports along with the more qualitative Palisades sky log. Palisades is situated 25 km north-northwest of LaGuardia and 40 km north-northeast of Newark. Airport observations of cloud type, percent total and percent opaque cloud cover, altitude of visible cloud bases and horizontal visibility were available digitally at three-hour intervals. Data were obtained from the National Climatic Data Center.

An interactive data management system was developed to extract intervals of cirrus and clear skies meeting specified criteria from the airport data files. To insure a regional nature to any interval selected, the criteria had to simultaneously be met at LaGuardia and Newark and be in agreement with the Palisades sky observations. Cirrus criteria included: 1) solar zenith angle (SZA) less than 80° (data quality diminishes greatly at higher SZAs due to pyranometer design and the presence of groves of trees near the horizon), 2) a full, broken or scattered cloud cover with bases of 6100 m (20000 ft) or higher, 3) no other clouds present, 4) horizontal visibility greater than 16 km (10 miles). Clear criteria included: 1) SZA less than 80° , 2) no clouds present and 3) visibility greater than 16 km. The visibility specification was made to reduce the influence of water vapor or dust in the lower troposphere on downwelling irradiance, thus, as much as possible, isolating the impact cirrus have on surface fluxes. Cirrus and clear episodes of at least three hours duration (eg. including at least two consecutive airport observations) from the winter (Jan., Feb., Dec.) and summer (Jun., Jul., Aug.) of 1987 were analyzed.

The study region sky is rarely reported to be completely covered with cirrus with no other clouds present. When cirrus are alone their coverage is normally observed to be broken (.6-.9) or scattered (.1-.5). For instance, in all of 1987 only 18 of the four daytime three hourly reports at Newark and 5 at LaGuardia noted overcast (1.0) cirrus with no other clouds present when visibility exceeded 16 km. This is partly due to the physical nature of cirrus clouds, but also appears to result from the subjective task of defining just when or where a cirrus cloud begins or ends; no doubt observers often miss subresolution cirrus. As the goal is to better understand cirrus impacts on the surface radiative environment, it is important to investigate these natural cirrus episodes, rather than the few cases when an easily observed cirrus overcast is present.

4. RESULTS

In 1987, some 46 winter hours met the cirrus criteria and 75 hours met clear specifications (fig. 1). The criteria were met less frequently in the summer of 1987, with 25 hours of cirrus and 36 hours of clear skies observed. The summer minimum was partly due to the limitations imposed by the visibility criterion

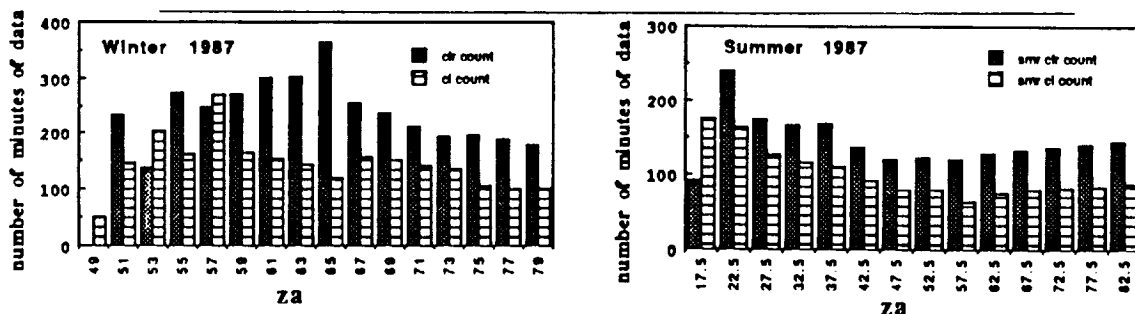


Figure 1. Number of minutes meeting prescribed cirrus (ci count) and clear (clr count) criteria in the winter (left) and summer (right) of 1987. Information is segregated by solar zenith angle (za) in 2° (winter) or 5° (summer) increments.

a) Shortwave transmissivity

Transmissivities for cirrus and clear episodes in winter and summer and seasonal values within each sky category were compared. All results were segregated according to zenith angle due to the impact SZA has on surface fluxes. For instance, in both seasons clear and cirrus transmissivities increased approximately 0.18 as the SZA decreased from 80° to 50° . This increase continued in summer as mid-day SZAs fell to 18° , however the rate from 50° to 18° was about half that found at higher SZAs. These curves roughly parallel atmospheric path lengths which vary from 5.8 at 80° to 1.6 at 50° to 1.1 at 20° .

Transmissivities during winter cirrus episodes were approximately 0.03 lower than clear-sky values (fig. 2). Cirrus values had a range of 0.05-0.10 within ± 1 standard deviation (SD) of the mean as compared with a 0.02-0.04 range with clear skies. The $+1$ SD transmissivities were similar for both cirrus and clear episodes. This is probably due to the presence of relatively clear skies between discontinuous cirrus.

Summer transmissivities during cirrus episodes ran some 0.01 to 0.08 lower than clear-sky values at zenith angles between 15° and 80° (fig. 2). On average, it appears that the difference is close to the 0.03 seen in winter, with the range in means primarily a function of the small cirrus sample.

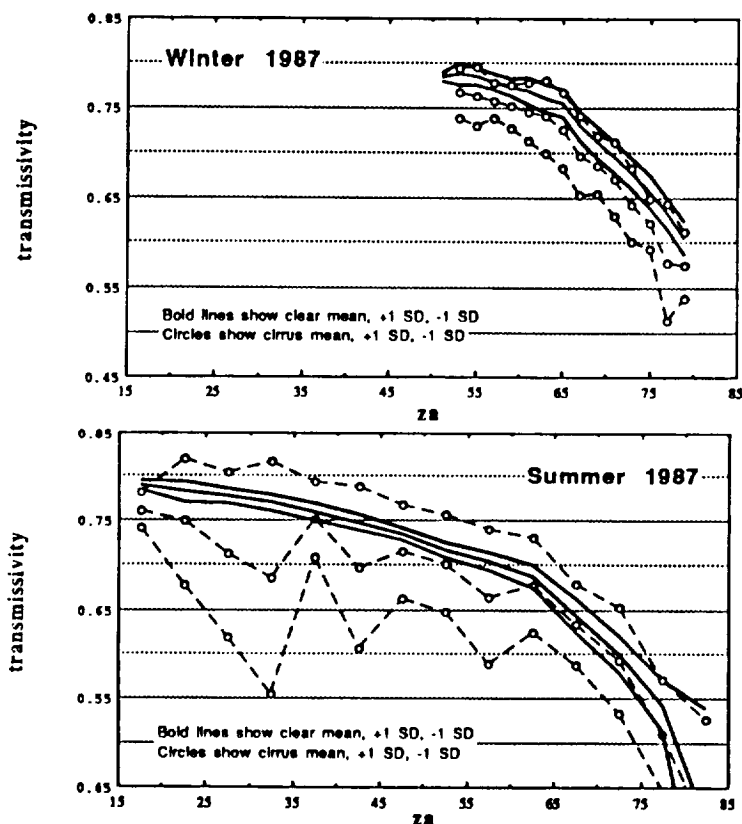


Figure 2. Transmissivities with cirrus and clear skies present in winter (top) and summer (bottom). Data are plotted by solar zenith angle (za).

During cirrus episodes, winter transmissivities at a given zenith angle were approximately 0.06-0.07 larger than summer values (fig. 3). Differences approached 0.10 when skies were clear (fig. 3). Seasonal differences may be a function of the several times greater amount of water vapor found in the summer atmosphere. Increased atmospheric dust and pollutants in a generally more stable atmosphere may also contribute to lower summer transmissivities. Again, it is worth emphasizing that this study minimized the effects of lower tropospheric moisture and turbidity by only considering episodes where horizontal visibility at the surface exceeded 16 km.

Coincidentally, winter and summer mid-day transmissivities under cirrus (0.76) and clear (0.79) skies were almost identical, despite roughly a 30° difference in SZA. This is at least partly a result of the seasonal differences in atmospheric composition.

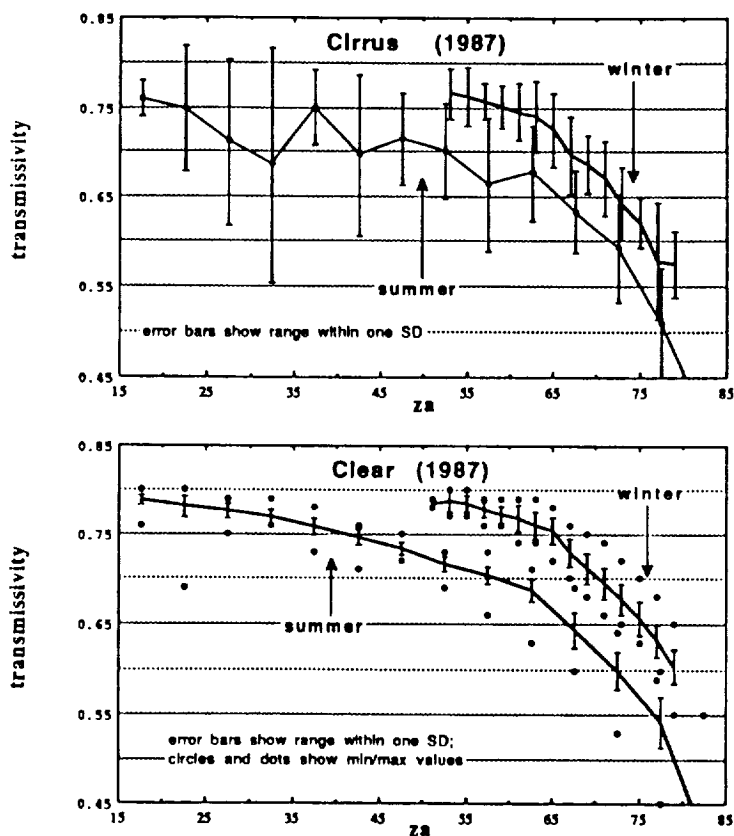


Figure 3. Summer versus winter transmissivities with cirrus (top) or clear (bottom) skies present. Data are plotted by solar zenith angle (za).

b) Downwelling longwave irradiance

Winter longwave irradiance with cirrus present was approximately 210 W/m^2 (fig. 4). This was some 30 W/m^2 higher than clear-sky values. In fact the -1 SD value for cirrus skies consistently exceeded the clear mean. Cirrus/clear differences of only about 15 W/m^2 were noted in summer (fig. 4). The clear mean and +1 SD values often fell between the cirrus mean and -1 SD cirrus values.

Longwave irradiance exhibited zenith angle dependence in the summer, increasing from 315 to 380 W/m^2 between SZAs of 80° and 20° in cirrus cases and 305-350 W/m^2 when skies were clear. Dome heating may have been responsible for a portion of the diurnal trend. The remainder may have been due to atmospheric temperature fluctuations. Evidence for the latter includes: 1) morning irradiances were consistently below afternoon readings at similar zenith angles, 2) cirrus irradiances increased more with decreasing SZA than clear values and 3) little SZA dependence was noted in the winter.

Interseasonal longwave values for cirrus and clear skies illustrate the warmer summer atmosphere. Irradiances were approximately 120 W/m^2 higher in summer than in winter during cirrus episodes and about 140 W/m^2 higher for clear skies.

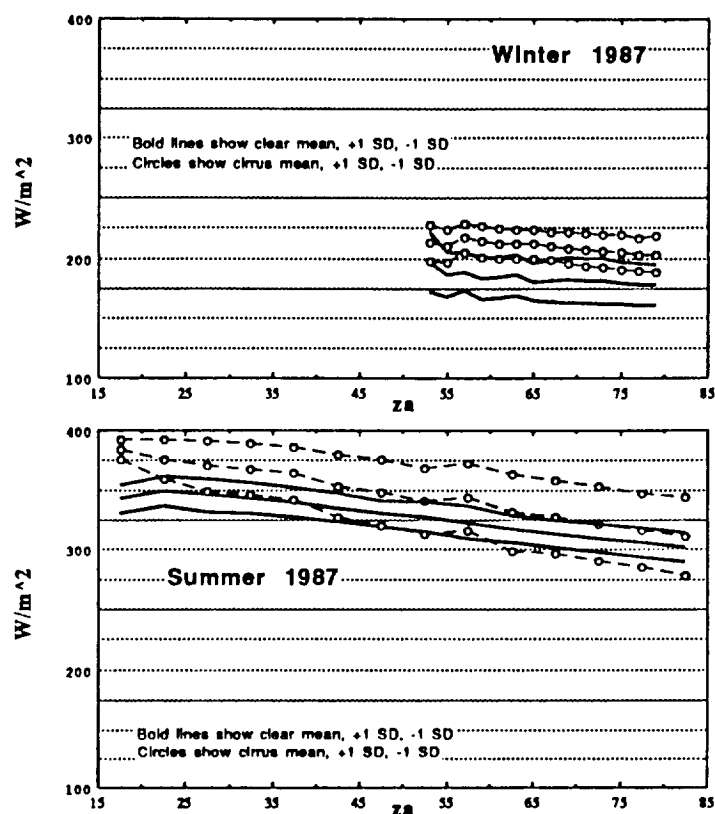


Figure 4. Downwelling longwave irradiance with cirrus and clear skies in winter (top) and summer (bottom). Data from 1987 daylight hours are plotted by solar zenith angle.

5. CONCLUSION

A limited data set gathered in 1987 at the Palisades, NY FIRE ETLA site suggests that cirrus have a larger impact on the surface radiative environment in winter than in summer. The presence of cirrus clouds in both seasons resulted in a decrease in atmospheric transmissivity of approximately 0.03 over clear skies. Downwelling longwave irradiances were about 30 W/m^2 higher for winter cirrus episodes and 15 W/m^2 higher in summer cases compared with clear-sky episodes. Data continue to be gathered at Palisades to refine these analyses and to expand the study by incorporating data on spectral and directional components of incoming shortwave fluxes and on the net radiation balance.

EXTENDED TIME
SESSION E03: Large-Scale Environment and Modeling
CHAIRMAN: James A. Coakley

Wednesday, July 12, 1989

	PAGE
E03.01 The Effects of Clouds on CO ₂ Forcing Randall, David A.	283
E03.02 Seasonal and Interannual Changes in Cirrus Wylie, Donald	289
E03.03 Relationship Between the Longwave Cloud Radiative Forcing at the Surface and the Top of the Atmosphere <u>Harshvardhan</u>	295
E03.04 Comparison of 30 Day Integrations With and Without Interactive Clouds Gordon, C. T.	301

Paper prepared for the FIRE Science Team Meeting, Monterey, California
July 1989

THE EFFECTS OF CLOUDS ON CO₂ FORCING

David A. Randall

Department of Atmospheric Science
Colorado State University
Fort Collins, Colorado 80523

The cloud radiative forcing (CRF) is the difference between the radiative flux (at the top of the atmosphere, say) which actually occurs in the presence of clouds, and that which would occur if the clouds were removed but the atmospheric state were otherwise unchanged. We also use the term CRF to denote warming or cooling tendencies due to cloud-radiation interactions. Cloud feedback is the change in CRF that accompanies a climate change.

The CO₂ forcing is defined, in analogy with the cloud forcing, as the difference in fluxes and/or infrared heating rates obtained by instantaneously changing the CO₂ concentration (doubling it, say) without changing anything else, i.e. without allowing any feedback. An increased CO₂ concentration leads to a reduced net upward longwave flux at the Earth's surface. This reduced net upward flux is due to an increased downward emission by the CO₂ in the atmosphere above. The negative increment to the net upward flux becomes more intense at higher levels in the troposphere, reaching a peak intensity roughly at the tropopause. It then weakens with height in the stratosphere. This profile implies a warming of the troposphere and cooling of the stratosphere.

The CO₂ forcing has been evaluated in the past using highly simplified models (e.g., Ramanathan *et al.*, 1979), but it is nevertheless highly desirable to evaluate it using GCMs, for two reasons: First, the GCMs take into account many more geographical and temporal variations, so that they can be expected to give more accurate and realistic results; and second, the CO₂ forcing should be determined using the same computational tool that is used to predict the response to the forcing, i.e. the GCM itself.

The CSU GCM has recently been used to make some preliminary CO₂ forcing calculations, for a single simulated, for July conditions. We called the longwave radiation routine twice, to determine the radiative fluxes and heating rates for both 2 x CO₂ and 1 x CO₂. As diagnostics, we have saved the two-dimensional distributions of the longwave fluxes at the surface and the top of the atmosphere, as well as the three-dimensional distribution of the longwave cooling in the interior. In addition, we have saved the pressure (near the tropopause) where the difference in the longwave flux due to CO₂ doubling has its largest magnitude. For convenience, we refer to this level as the "CO₂ tropopause". We have also saved the actual difference in the flux at that level. Finally, we have duplicated all of these fields for the hypothetical case of no cloudiness (clear sky), so that we can isolate the effects of the clouds.

Fig. 1 shows the zonally averaged net upward longwave flux difference due to a doubling of CO₂, at three levels: the Earth's surface, the CO₂ tropopause, and the top of the atmosphere (where $p = 0$). All of the numerical values are negative, since doubling CO₂ reduces the net upward flux at every level. At the Earth's surface, the CO₂ forcing reduces the net upward flux by about 2 W m⁻² in high latitudes, where there is little water vapor, but by only about 0.5 W m⁻² near the equator, where the lower troposphere is very humid and therefore relatively opaque in the infrared. The flux reductions at the CO₂ tropopause and the top of the atmosphere are not very

different from each other; this means that the flux difference across the stratosphere is relatively small (on the order of 0.5 W m^{-2}), but since the stratosphere contains much less mass than the troposphere, the stratospheric cooling and tropospheric warming can be of comparable magnitude, as we will see below. The flux reduction at the top of the atmosphere reaches about 5 W m^{-2} in the tropics, where the lower boundary is relatively warm, and is near 4 W m^{-2} at the summer pole, and near 2 W m^{-2} at the winter pole. It has a dip near the equator, which is due to the presence of extensive upper tropospheric cloudiness in the intertropical convergence zone (ITCZ). The clouds block the upwelling tropospheric radiation anyway, so that increasing the CO_2 concentration has relatively little effect. These cloud effects are discussed further later.

Fig. 2 shows the changes in the longwave heating of the troposphere and the longwave cooling of the stratosphere (both plotted as positive values, for convenience), in units of hundredths of a degree per day. The tropospheric warming peaks at more than 0.05 K day^{-1} in the tropics, where the downwelling infrared flux due to emission by warm CO_2 converges almost entirely within the humid atmosphere, so that very little reaches the surface (refer back to Fig. 1). The tropospheric warming is relatively weak in high latitudes, where the atmosphere is relatively dry. The stratospheric cooling is between 1.0 and 1.5 K day^{-1} , almost independent of latitude.

Fig. 3 shows the effects of clouds on the CO_2 forcing, in terms of the reduction in the net upward infrared flux at the surface, the CO_2 tropopause, and the top of the atmosphere. For the Earth's surface (solid line), a positive value on this plot indicates that the clouds act to reduce the CO_2 forcing of the surface. The largest positive values occur in high latitudes, where there are extensive low clouds that block the downward radiation due to CO_2 emission from the atmosphere. The tropical atmosphere contains so much water vapor that the clouds have relatively little effect; at any rate, the tropical clouds tend to have their bases in the middle troposphere, further away from the surface. The effects of the clouds on the CO_2 forcing at the CO_2 tropopause and the top of the atmosphere are practically the same, since the stratosphere is essentially cloudless. Again, positive values for the dashed and dotted curves indicate that the clouds tend to mitigate the reduction in the net upward longwave flux due to doubling CO_2 . Where the solid curve lies above the dashed/dotted curves, the clouds increase the CO_2 forcing of the troposphere. This occurs in high latitudes, where the clouds are found at low levels. Where the solid curve lies below the dashed/dotted curves, the clouds reduce the CO_2 warming of the troposphere. This occurs in the tropics and the middle latitudes of the summer hemisphere, where high clouds block the upwelling longwave radiation anyway.

Fig. 4 shows the latitude-height distribution of the CO_2 forcing, in hundredths of a degree per day. The tropospheric warming is most intense near the surface in the tropics, reaching about 0.16 K day^{-1} . There is actually a weak cooling at low levels in high latitudes, where temperature inversions occur near the surface. Recall that the CO_2 tropopause is defined as the level where the CO_2 -induced reduction in the net upward longwave flux is most intense; it separates tropospheric warming from stratospheric cooling. Fig. 4 shows that the height of the CO_2 tropopause is about 12 km , at all latitudes. There is a minor excursion to higher altitudes just north of the equator, due to the upper tropospheric cloudiness associated with deep convection in the ITCZ. Finally, Fig. 5 shows the effects of clouds in Fig. 4. The clouds tend to reduce the warming in the tropical and summer-hemisphere troposphere, and to increase it in the middle and high-latitude troposphere. They tend to increase the warming near the tropical tropopause, and to reduce the stratospheric cooling slightly.

Two strong caveats are needed here. First, these results are for a single day. They do not show how the CO_2 forcing varies diurnally or seasonally; we plan to investigate such diurnal and seasonal changes in the future. Second, these results tell nothing about how the climate system

will respond to the CO₂ forcing, since that response depends strongly on feedbacks within the system.

ACKNOWLEDGEMENTS

Support for this research was provided by NASA's Climate Program under Grant NAG-1-893.

REFERENCES

Ramanathan, V., M. S. Lian, and R. D. Cess, 1979: Increased atmospheric CO₂: Zonal and seasonal estimates of the effect on the radiation energy balance and surface temperature. *J. Geophys. Res.*, **84**, 4949-4958.

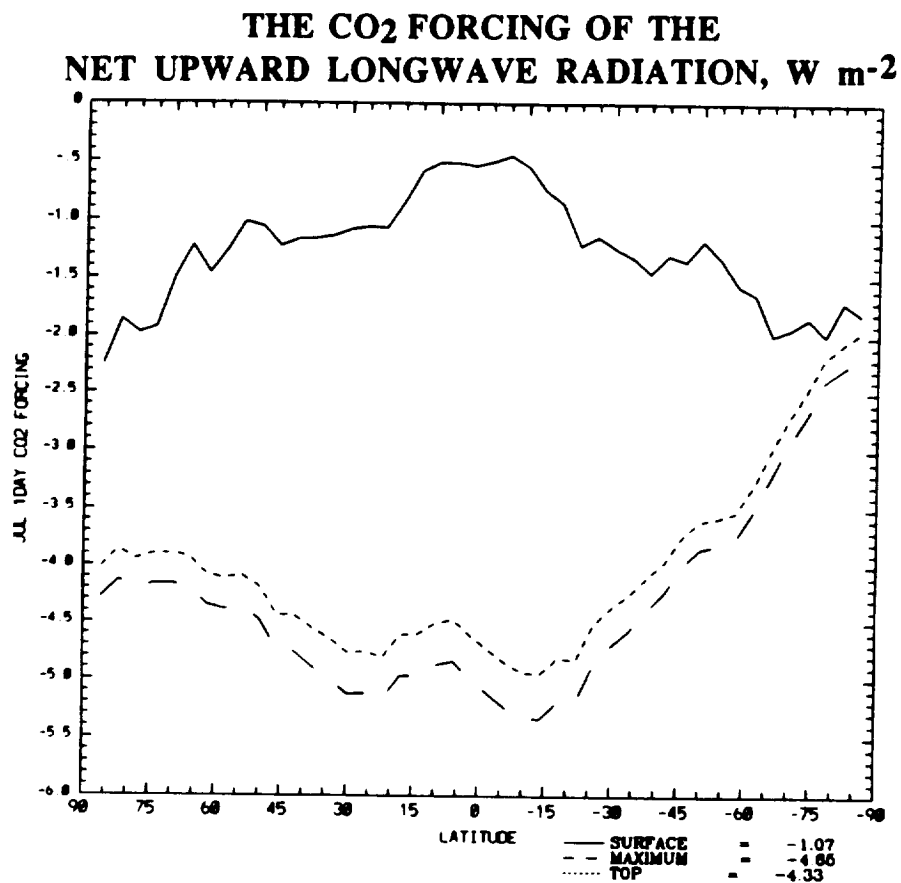


Figure 1

**THE EFFECTS OF CO₂
ON THE TROPOSPHERIC WARMING
AND STRATOSPHERIC COOLING, 0.01 K day⁻¹**

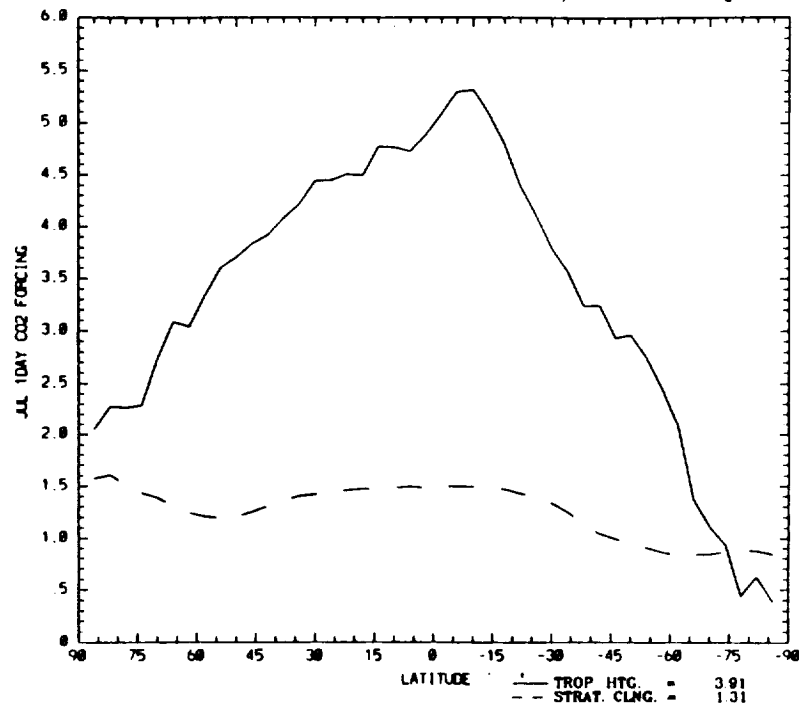


Figure 2

**THE EFFECTS OF CLOUDS ON THE CO₂ FORCING OF THE
NET UPWARD LONGWAVE RADIATION, W m⁻²**

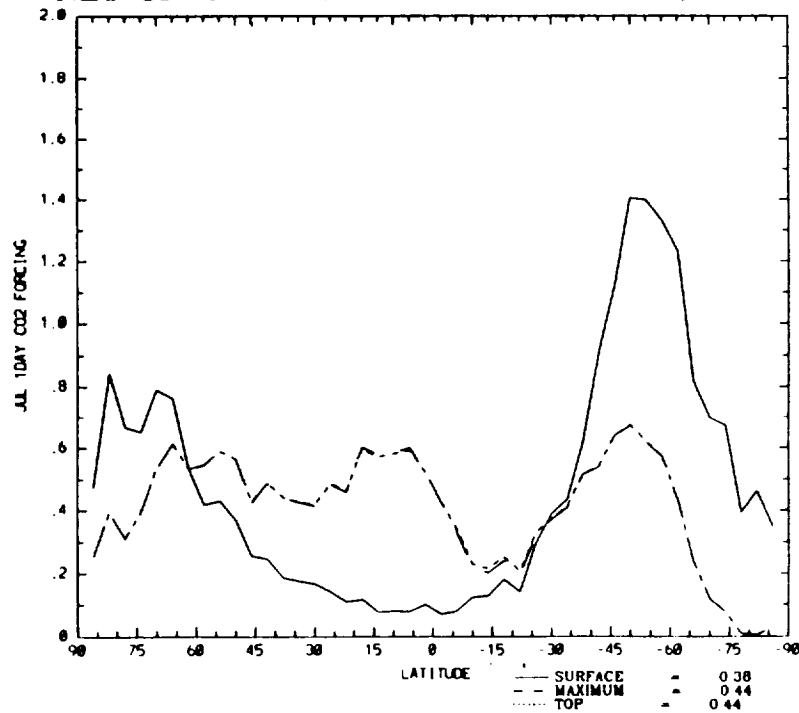


Figure 3

THE CO₂ FORCING, 0.01 K day⁻¹

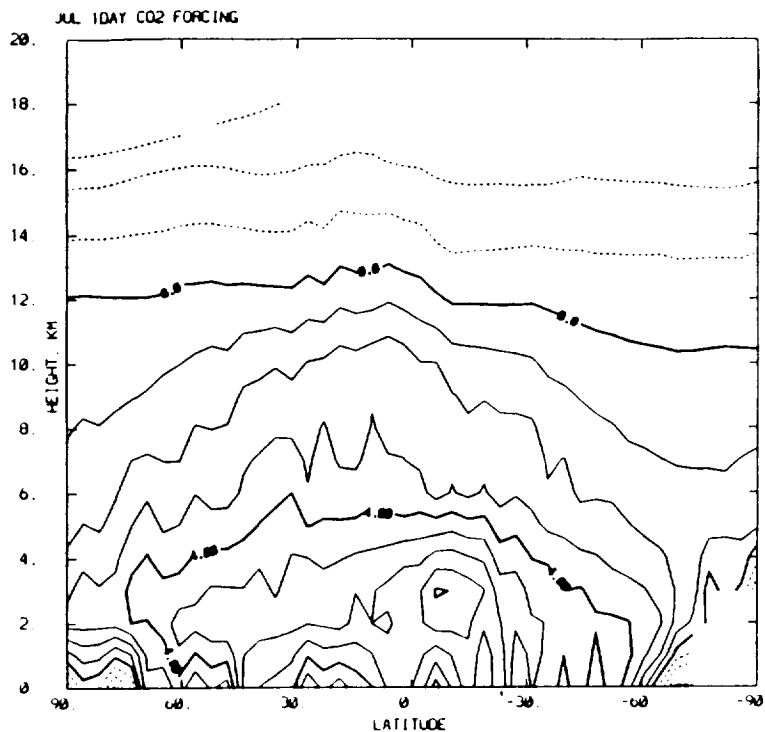


Figure 4

THE EFFECTS OF CLOUDS ON THE CO₂ FORCING, 0.01 K day⁻¹

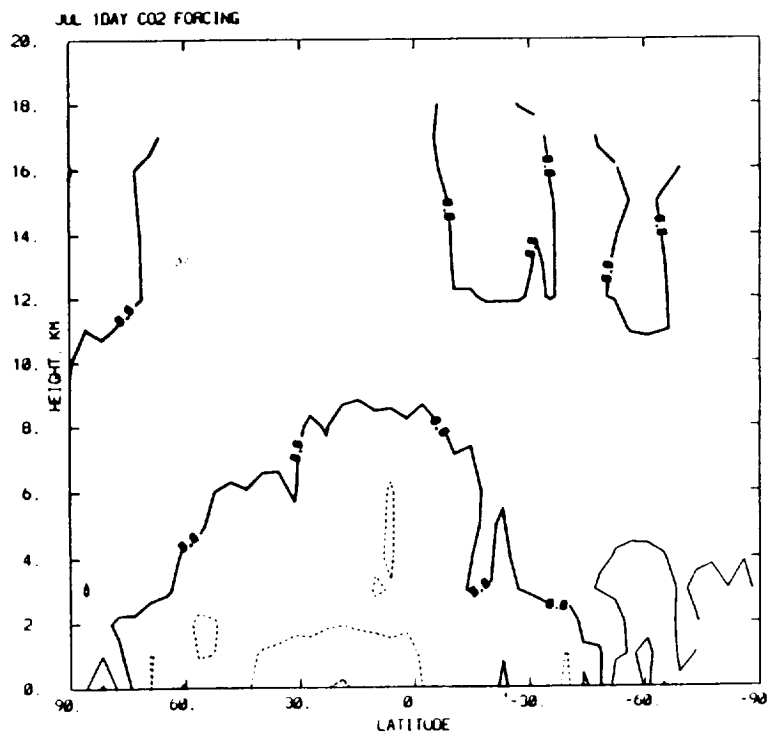


Figure 5

FIGURE CAPTIONS

- Figure 1: The meridional structure of the zonally averaged net upward longwave flux difference due to a doubling of CO₂, at the Earth's surface (solid line), the CO₂ tropopause (long dashes), and the top of the atmosphere (short dashes).
- Figure 2: The meridional structure of the CO₂-induced changes in the zonally averaged longwave heating of the troposphere (solid line) and the zonally averaged longwave cooling of the stratosphere (dashed line), both plotted as positive values, for convenience, in units of hundredths of a degree per day.
- Figure 3: The effects of clouds on the CO₂ forcing, in terms of the reduction in the net upward infrared flux at the surface (solid line), the CO₂ tropopause (long dashes), and the top of the atmosphere (short dashes). The units are W m⁻².
- Figure 4: The latitude-height distribution of the CO₂ forcing, in hundredths of a degree per day.
- Figure 5: The effects of clouds on the latitude-height distribution of the CO₂ forcing, in hundredths of a degree per day.

SEASONAL AND INTERANNUAL CHANGES IN CIRRUS

Donald Wylie
Space Science and Engineering Center
University of Wisconsin-Madison

1. Introduction

Statistics on cirrus clouds using the multispectral data from the GOES/VAS satellite have been collected since 1985. The method used to diagnose cirrus clouds and a summary of the first two years of data was given in Wylie and Menzel (1989) and at the 1988 FIRE Meeting in Vail, CO. This study has been expanded to three years of data which allows a more detailed discussion of the geographical and seasonal changes in cloud cover. Interannual changes in cloud cover also have been studied.

GOES/VAS cloud retrievals also have been compared to atmospheric dynamic parameters and to radiative attenuation data taken by a lidar. This abstract will discuss some of the highlights of these studies.

2. Geographical Distributions

Fig. 1 summarizes the geographical distribution of cloud cover over three year. This summary is very similar to the two year graphic in Wylie and Menzel (1989) except for some small regional features which appear because finer contour intervals were used (10% probability rather than the 20% previously used). This was possible because the increase in cloud observations from the extra year of data.

Similar winter to summer seasonal changes in the locations of cloud cover minima (top panels) and clear sky maxima (bottom panels) can be found in the three year summary as in the previously published summary. The same migration of the "sun belt" from Arizona and New Mexico in the winter (upper left panel) to southern California and southern Nevada in the summer (upper right) is apparent. The Probability of Clear Sky (lower panels) show the same general trends as the Probability of Opaque Cloud (upper panels) between the seasons.

Other seasonal changes include the increase of cloud cover off the California coast (top panel) as the marine stratus clouds become predominant in summer. A minimum in cloud cover along the East Coast appears in winter (upper left panel) and disappears in summer. A local maximum in opaque cloud cover occurred along the Appalachian mountains in the summer (upper right). Other cloud cover maxima were found in Washington and Oregon corresponding to the Coastal mountains.

Differences with the previous results can be found in western Missouri over part of the Ozark mountains in summer and over Lake Michigan in winter where small opaque cloud maxima are now apparent. The Northern Rocky mountains in Idaho and Montana show more local detail in both seasons. All of these features were in the previously published data but hidden by the choice of a large contour interval.

In the summer of 1988, an opaque cloud minima was found in central Montana extending down into Wyoming (upper right) which was part of the extreme drought.

Cirrus clouds (middle panels) exhibited very small geographical and seasonal variances over the continental U.S as previously published. They were found 20-40% of the time with a slight drop in the summer over the continent and a large drop over the Eastern Pacific ocean.

3. Interannual Variances

The variances in cloud cover between 1988 and 1987 were examined because the extreme drought and heat in the summer of 1988. The largest deficit in rainfall occurred in south and Ohio Valley in June, the states of Indiana, Ohio, Kentucky, Tennessee, Mississippi, Alabama, and Georgia according to Ropelewski (1988) see Fig. 2. Other rainfall deficiencies were found in the Midwest and northern plains states. The drought areas are indicated with shading in Fig. 2. But in June 1987, the drought areas received nearly normal precipitation (Arkin, 1988).

Cloud analyses from the two Junes were compared in the area of largest drought, from 30-42°N and 82-90°W (the box in Fig. 2). The GOES/VAS cloud analysis showed a decrease in high clouds, <400 mb, which was mainly cirrus (Table 1, 24% in June 87 compared to 20% in 88) and also a decrease in mid level clouds, 400-699 mb, (13% in 87 vs. 7% in 88). While low cloud reports increase from 24% in 87 to 33% in 88. The number of clear sky reports was nearly constant between the two years. These data indicate a change in the type of clouds found in this area between the two years. An large increase in low cloud occurred which were non-precipitating at the expense of deeper middle and high clouds.

Table 1: A comparison of GOES/VAS cloud analyses in the area, 30-42° N, 82-90°W, (box in Fig. 2) for June of 87 and 88.

Cloud Type		June 1987			June 1988		
		<u>Cirrus</u>	<u>Opaque</u>	<u>All</u>	<u>Cirrus</u>	<u>Opaque</u>	<u>All</u>
High	<400 mb	24%	4%	28%	20%	4%	24%
Middle	400-700mb	4	9	13	3	4	7
Low	>700 mb		24	24		33	33
Total		28%	37%	65%	23%	41%	64%
Clear				35%			36%

4. Comparison to Atmospheric Dynamic Features

Cirrus cloud observations from the GOES/VAS system were inspected to see what fraction were found inside dynamic features commonly thought to produce clouds and what fraction occurred outside of these dynamic features or in areas where dissipation of clouds was expected. This is an extension of the statistics presented at the 1988 FIRE meeting. More analyses have been added in more seasons.

The conclusions remain the same as last year. In summer, roughly one half of the cirrus observations were found near radar echoes while the other half was not. In winter this dropped to only 22% of the cirrus obs. being near radar echoes. No new data were added for this part of the comparison. Jet streams of $>35 \text{ ms}^{-1}$ in winter and $>25 \text{ ms}^{-1}$ in other seasons, contained 40 to 60% of the cirrus. However, in months when upper level winds were light, cirrus observations were found with nearly the same frequency as when winds were strong. Inside the jet stream most cirrus, 13 to 33%, were found accelerating into the entrance to the south of the jet axis (right rear quadrant). While the least cirrus were found, 4 to 10%, north of the axis in the entrance region (left rear quadrant). Approximately 20 to 23% of the cirrus were found in the exit of the jet core, the deceleration region (from left and right quadrants). Warm temperature advection was found with 44 to 71% of the cirrus in months where winds were high enough to define jet streams and temperature advection. Positive vorticity advection was found with 24 to 52% of the cirrus. However, a substantial amount of cirrus, from 19 to 35%, also occurred in negative vorticity advection.

These statistics show that large scale dynamics can explain up to one half of the cirrus over the U.S. Most of the other cirrus occurs in areas where the dynamic variables are weak or in a

transition from a positive to negative sign. The great complexity of the structure of cirrus and the thermodynamic conditions in which they were found is discussed in Starr and Wylie (1989). Greater detail in the analysis of atmospheric dynamic and thermodynamic features is needed to explain a large portion of the cirrus.

5. Comparison of Satellite with Lidar Radiative Properties

The GOES/VAS cloud analysis system estimates both the height of the cloud top and the emissivity of the cloud. This is defined as;

$$N\epsilon = \frac{I - I_{cl}}{B[T(P_c)] - I_{cl}} \quad (1)$$

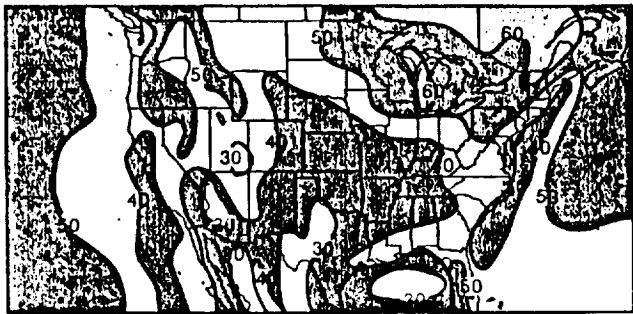
I is the radiance of the cloud measured by the satellite in the 11.1μ window channel. I_{cl} is the clear radiance of the window channel estimated for the location from surrounding clear fields of view N and $B[T(P_c)]$ is the radiance for the altitude temperature of the cloud. $N\epsilon$ is thus an effective emissivity that is the product of the clouds fractional coverage of the satellite field of view (N) and the emissivity (ϵ) of the cloud.

The infrared emissivity of cirrus clouds is related to the visible optical depth in that the lower the emittance of the cloud, the smaller its optical depth and reflectivity. There have been several models of this relationship. For this study the model of Hansen (1971) was used. Optical depths were measured by the HSRL lidar at UW on 28 October 1986. The mean altitude of the cirrus cloud was also taken from the lidar backscatter vertical profile while the infrared radiance of the cloud (I) and clear sky (I_{cl}) was measured by the GOES satellite. The radiance for the altitude of the cloud ($B(T(p))$), was derived from the mean cirrus cloud altitude and the temperature for that level given by a local sounding.

The results of the visible optical depth and infrared emissivity comparison are shown in Fig. 4. The model prediction of Hansen (1971) also is shown as a solid line. These data have a lot of scatter, however, they are distributed around the model results of Hansen. A comparison of similar visible and infrared data to model predictions is given in Minnis *et al.* (1989).

6. References

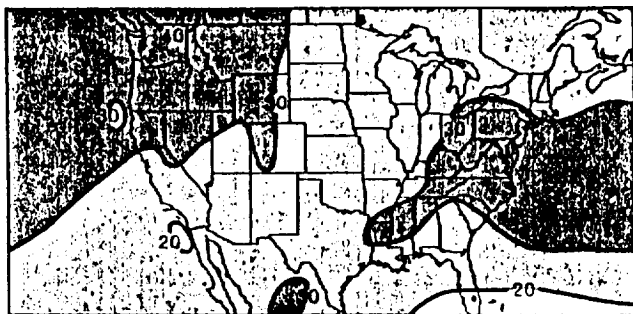
- Arkin, P.A., 1988: The global climate for June-August 1987: Mature phase of an ENSO warm episode persists., *J. Climate*, **1**, 306-324.
- Hansen, J.E., 1971: Multiple scattering of polarized light in planetary atmospheres. Part I: The doubling method., *J. Atmos. Sci.*, 120-125.
- Minnis, P.A., D.F. Young, K. Sassen, J. M. Alvarez, and C. Grund, 1989: The 27-28 October 1986 FIRE IFO cirrus case study: Cirrus parameter relationships derived from satellite and lidar data., Submitted to *Mon. Wea. Rev.*
- Ropelewski, C.F., 1988: The global climate for June-August 1988: A swing to the positive phase of the southern oscillation, drought in the United States, and abundant rain in monsoon areas., *J. Climate*, **1**, 1153-1174.
- Wylie, D.P., and W.P. Menzel, 1989: Two years of cloud cover statistics using VAS., *J. Climate*, **2**, 380-392.



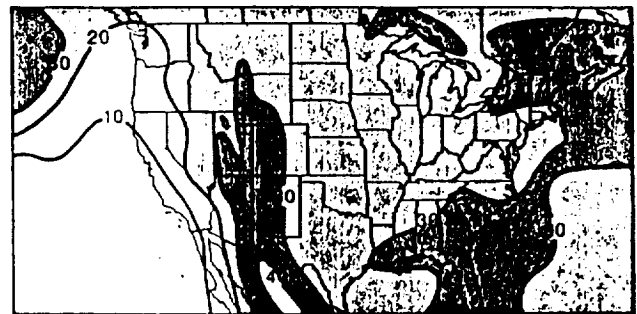
PROBABILITY OF OPAQUE CLOUD IN WINTER



PROBABILITY OF OPAQUE CLOUD IN SUMMER



PROBABILITY OF CIRRUS IN WINTER



PROBABILITY OF CIRRUS IN SUMMER



PROBABILITY OF CLEAR SKY IN WINTER



PROBABILITY OF CLEAR SKY IN SUMMER

THREE YEAR SUMMARY

WYLIE/MENZEL UNIV OF WISCONSIN-MADISON



Figure 1: The probability of opaque cloud, transmissive cirrus cloud, or clear sky from the GOES/VAS multispectral infrared data from 1985 to 1988.

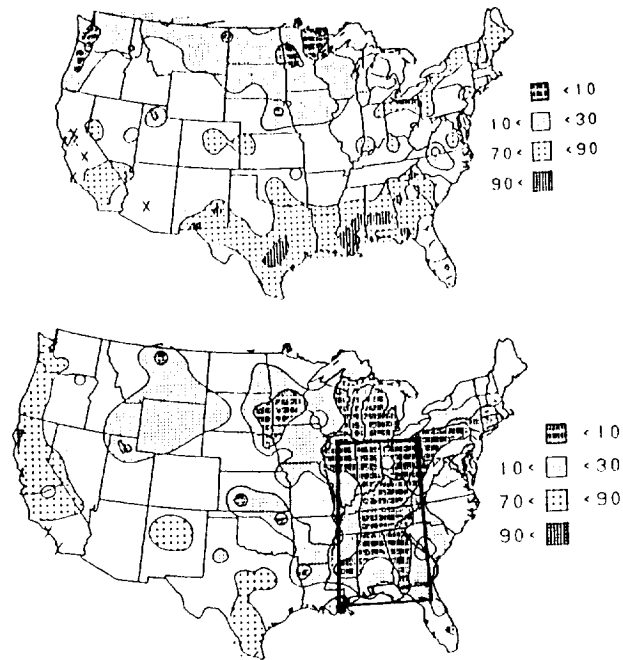


Figure 2: The June 1987 precipitation expressed as percentiles of the normal (Gaussian) distribution from Arkin (1987), upper panel, and June 1988 from Ropelewski (1988), lower panel.

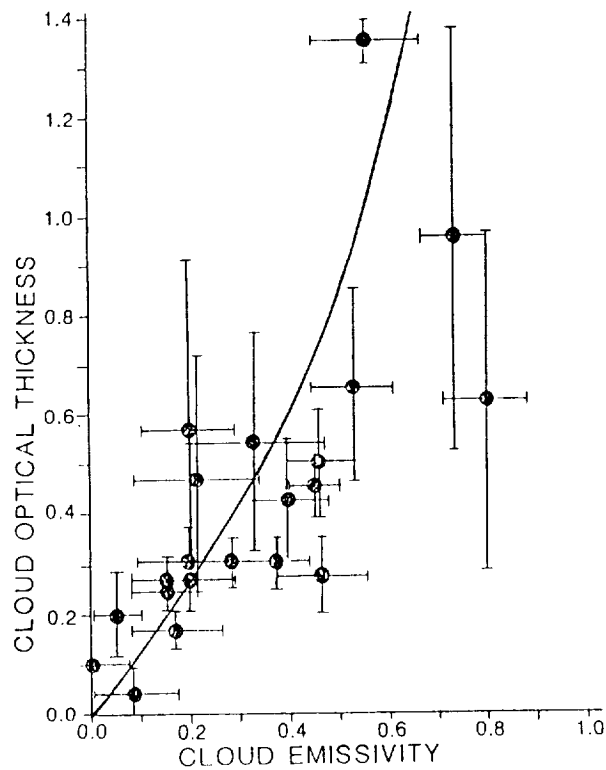


Figure 3: Cloud optical thickness measured by the HSRL lidar vs. Infrared emissivity measured from GOES/VAS satellite imagery.

RELATIONSHIP BETWEEN THE LONGWAVE CLOUD RADIATIVE FORCING AT THE SURFACE AND THE TOP OF THE ATMOSPHERE

Harshvardhan

Department of Earth and Atmospheric Sciences
Purdue University, West Lafayette, IN 47907

In order to achieve global coverage, any surface radiation climatology has to be based on satellite observations. In the last decade several schemes have been devised to obtain the surface solar insolation from top of the atmosphere reflected solar radiation (Tarpley, 1979; Gautier et al., 1980). More recently, attempts have been made to infer the components of longwave radiation at the surface from satellite sounder data using a radiative transfer model (Schmetz et al., 1986; Frouin et al., 1988; Gupta, 1989). In addition to the radiative transfer scheme, these methods require assumptions about the effective emitting temperature of cloud tops and bases. The one common theme in these methods is an assumption regarding the vertical extent of the cloudiness detected in the upwelling radiation. Once the top is placed using a coincident sounding, the position of the base is estimated by various methods, the simplest being an assumption of constant cloud depth. During the day, the reflected solar radiation has also been used to estimate the geometric depth of the cloud layer (Frouin et al., 1988), a complex procedure that involves assumptions regarding cloud microphysics and morphology.

Modeling studies have shown that although there are strong correlations between the solar upwelling radiative flux and surface flux, this is not true of the longwave (Ramanathan, 1986). However, if the clear sky component is considered separately such that the cloud longwave forcing at the top and at the surface are compared, a slightly different picture emerges. Figure 1 shows the monthly mean simulated longwave radiation at the top of the atmosphere and at the surface from a general circulation model (Harshvardhan et al., 1989). Each point represents a 4° latitude x 5° longitude grid. During the simulation, in addition to the hourly radiative fields generated as part of the model integration, a clear sky computation was also made every hour. The difference, which is the cloud forcing, was thus obtained at the top of the atmosphere and the surface. Figure 2 shows the longwave cloud radiative forcing at these levels for all the grid points in the model. This figure contains information on the relationship between emission from the cloud tops and bases in the model. For example, a subset of the simulated data for two latitude bands is shown in Figures 3 and 4. Figure 3 is for a region of high convective clouds and the cloud radiative forcing at the top is very large when cloudiness occurs where as the surface longwave fluxes are not affected much. Figure 4 is for a region of low clouds such that the cloud top emission is not too different from the surface emission but the downward longwave radiation is altered quite drastically in the presence of clouds.

During the FIRE Cirrus IFO, surface radiation measurements were made at several sites and co-incident satellite overpass data was also collected (LeCroy et al., 1989). It may be possible to extract the longwave cloud radiative forcing at the top and the surface from these data. If relationships, such as shown in Figures 3 and 4 are verifiable by observations, this information can be useful for the extraction of the surface longwave radiation from satellite data. The radiative transfer schemes used to convert upwelling spectral radiances into a downwelling longwave radiation can provide the clear sky component. The cloud radiative forcing at the top of the atmosphere can then modify the surface fluxes according to relationships shown in Figures 3 and 4. It should be noted that this procedure may be considered only for temporal averages and not for instantaneous deductions of surface fluxes. This would be most useful in compiling monthly mean regional climatologies of the surface longwave fluxes.

References

- Frouin, R., C. Gautier and J.-J. Morcrette, 1988: Downward longwave irradiance at the ocean surface from satellite data. *J. Geophys. Res.*, **93**, 597-619.
- Gautier, C., G. Diak and S. Masse, 1980: A simple physical model to estimate incident solar radiation at the surface from GOES satellite data. *J. Appl. Meteor.*, **19**, 1005-1012.
- Gupta, S.K., 1989: A parameterization for longwave surface radiation from sun-synchronous satellite data. *J. Climate*, **2**, 305-320.
- Harshvardhan, D.A. Randall, T.G. Corsetti and D.A. Dazlich, 1989: Earth radiation budget and cloudiness simulations with a general circulation model. *J. Atmos. Sci.*, **46**, (in press).
- LeCroy, S.R., C.H. Whitlock, L.R. Poole, J.M. Alvarez, D.A. Robinson, D.O'C. Starr and S.K. Cox, 1989: Surface radiation observations of cirrus cloud properties during the Wisconsin FIRE/SRB experiment. Proceedings of IRS 1988, A. Deepak Publishing, Hampton, VA.
- Ramanathan, V., 1986: Scientific uses of surface radiation budget data for climate studies. NASA RP 1169, 59-86.
- Schmetz, P., J. Schmetz and E. Raschke, 1986: Estimation of daytime downward longwave radiation at the surface from satellite and grid point data. *Theor. Appl. Climatol.*, **37**, 136-149.
- Tarpley, J.D., 1979: Estimating incident solar radiation at the surface from geostationary satellite data. *J. Appl. Meteor.*, **18**, 1172-1181.

JULY DATA (BETWEEN 86S AND 86N)

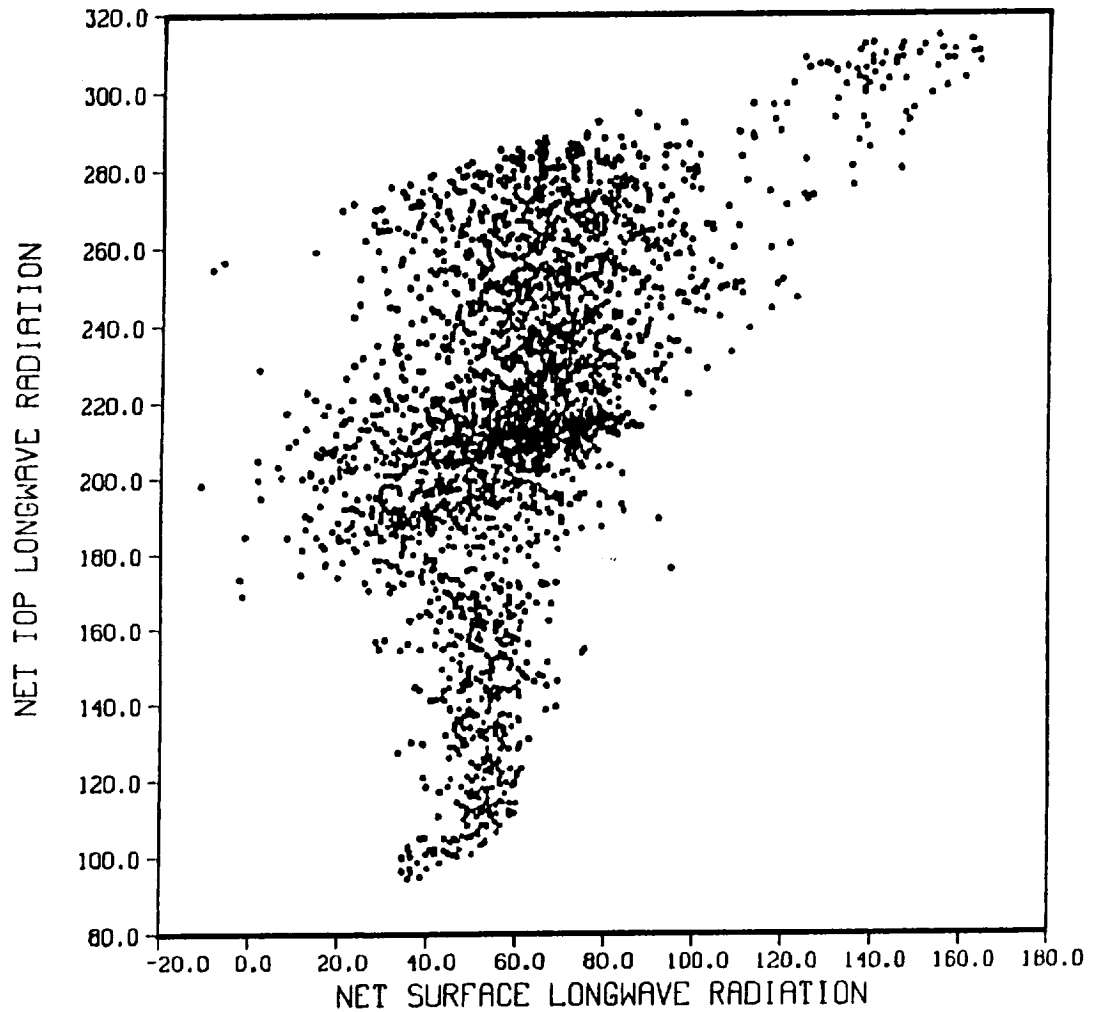


Figure 1. Monthly mean (July) outgoing longwave radiation at the top of the atmosphere plotted versus the net surface longwave radiation for each 4° lat x 5° long grid point of a general circulation model.

JULY DATA(FROM 86N TO 86S)

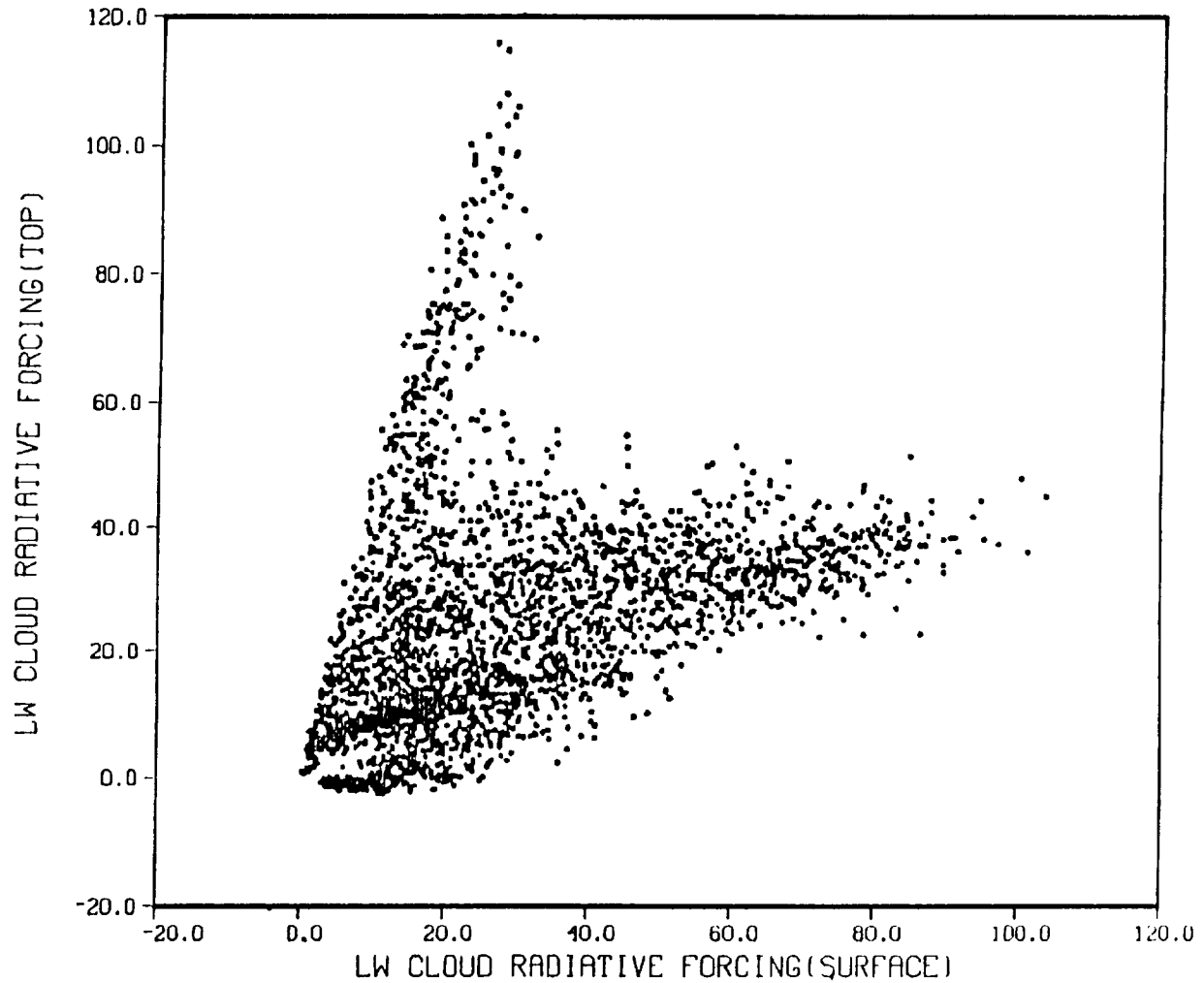


Figure 2. As in Figure 1 but for the longwave cloud radiative forcing at the top of the atmosphere plotted versus the forcing at the surface.

JULY DATA (BETWEEN 10N AND 14N)

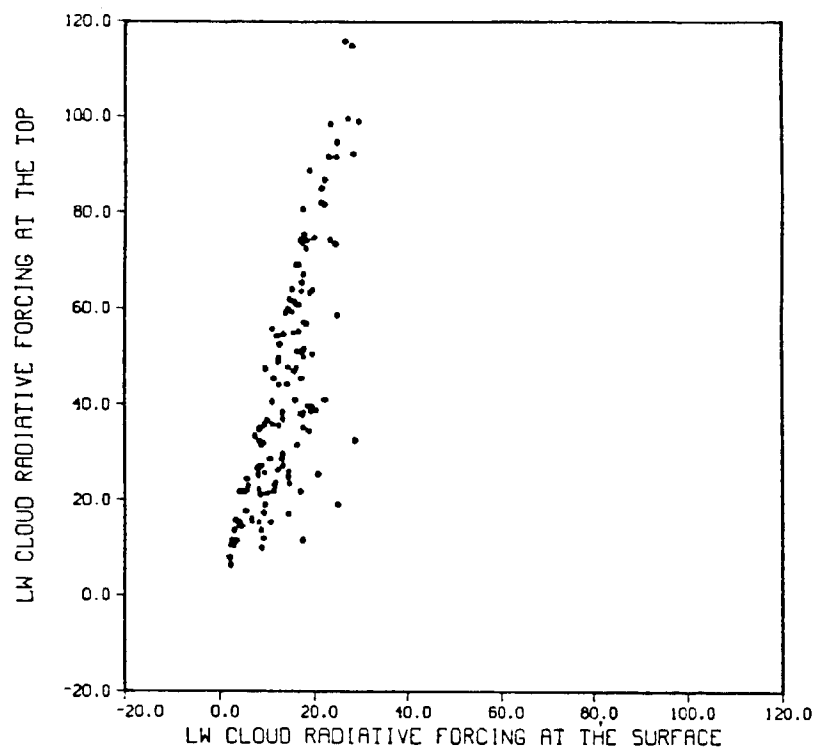


Figure 3. As in Figure 2 but for the grid points in a latitude band from 10N to 14N.

JULY DATA (BETWEEN 58S AND 62S)

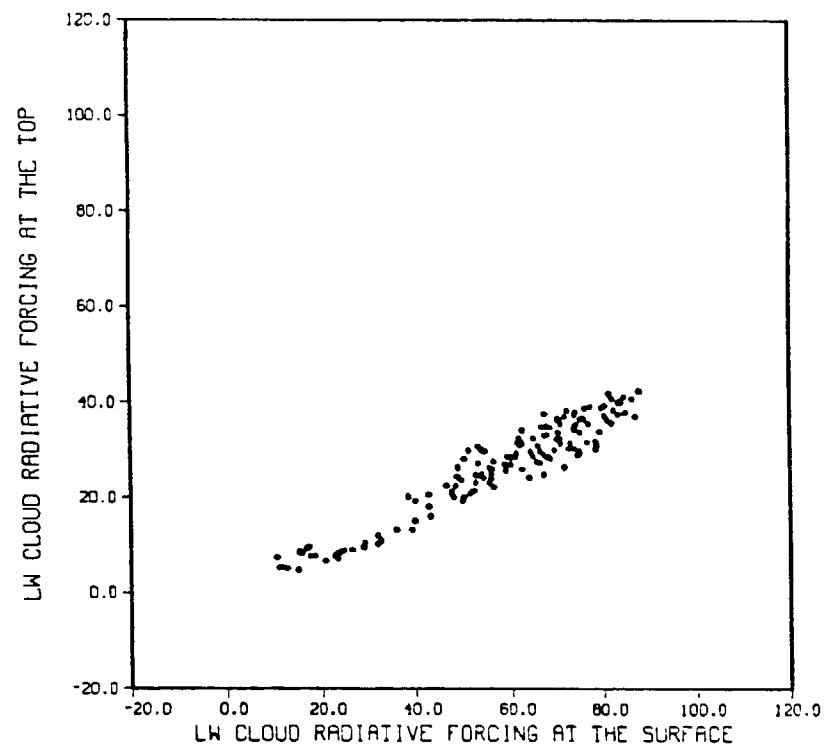


Figure 4. As in Figure 2 but for the grid points in a latitude band from 58S to 62S.

Comparison of 30 Day Integrations with and without Interactive Clouds

C.T. Gordon

Geophysical Fluid Dynamics Laboratory/NOAA
 Princeton University, P.O. Box 308
 Princeton, NJ 08542

A cloud-radiation interaction parameterization package has recently been incorporated into a global spectral GCM used for extended range prediction studies at GFDL. The elements of this package are summarized. Analysis of the time mean radiative and dynamical responses suggests that cloud-radiation interaction has a favorable impact, overall, on systematic errors. The possible relevance of this sensitivity study to FIRE is mentioned.

Fractional cloud amount is predicted empirically in a manner similar to J. Slingo (1987), although the humidity threshold is reduced to 70%, the relationship between cloud fraction and relative humidity is linear, and a shallow convective cloud type is predicted for radiative purposes. The optical depth of sub-freezing, cold clouds varies quadratically with temperature following Platt and Harshvardhan (1988). Otherwise, distinct constant values are specified for high, middle and low clouds. The long- and shortwave cloud optical properties are linked to the cloud optical depth, employing an algorithm of V. Ramaswamy (1987, personal communication).

The GCM's sensitivity to interactive clouds is investigated for the extended forecast range, by performing two sets of 30 day integrations for 3 winter and 3 summer cases (referred to by the respective dates of the initial conditions): (i) CLDRADI employs the above package of parameterizations; (ii) LONDON utilizes the GCM's standard specification of zonal mean cloud amount, absorptivity, reflectivity and **blackbody** emissivity. The CLDRADI and LONDON GCM's are identical in all other respects. The model resolution is R21L18, denoting rhomboidal spectral truncation at wave number 21 and 18 sigma levels in the vertical. The usual physical parameterizations are retained - Mellor-Yamada turbulence closure, Monin-Obukhov surface boundary layer, water bucket hydrology, Fels-Schwarzkopf radiation, moist convective adjustment and orography; and linear mountain gravity wave drag is incorporated. A few auxilliary integrations are performed for a single case to help clarify the results. For example, parameterized shallow convection in the spirit of Tiedke et al. (1988) is added in KSHLCNV; and the Platt-Harshvardhan temperature dependence of cloud optical depths is suppressed in WARM τ .

The 30 day mean CLDRADI total cloud amount for one winter and one summer case are shown in Fig. 1, and the CLDRADI, LONDON and observed OLR (winter case only) in Fig. 2. The GCM-predicted cloud amount fields and corresponding OLR fields are plausible in many respects, especially in the tropics, where they exhibit ITCZ-like and SPCZ-like features. In contrast, the OLR fields from the control integrations do not. The CLDRADI OLR fields agree better, overall, than LONDON with NIMBUS 7 earth radiation budget data. The tropical OLR minima are nonetheless too weak, especially over the Amazon. Some stratus may be noted off the west coasts of South America and Africa in January. Moving on to longwave radiative heating/cooling rates (not shown), the CLDRADI cirrus level

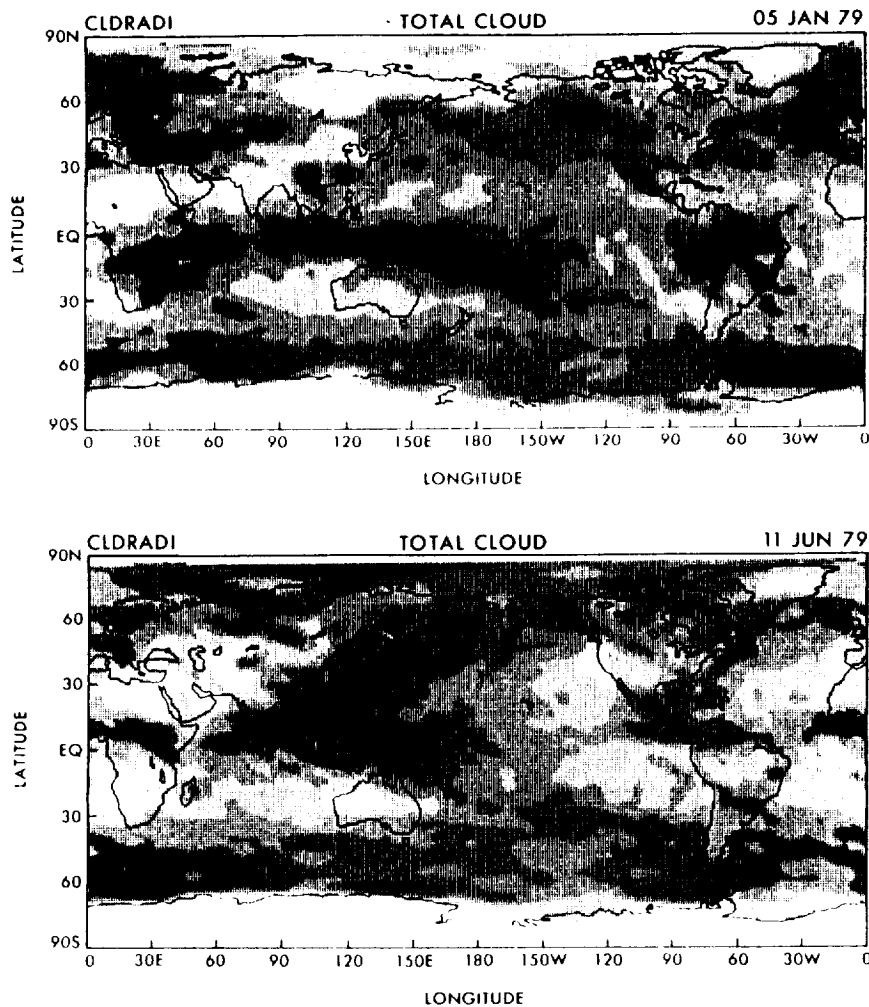


Fig. 1 Day 0-30 30 day mean CLDRADI total cloud amount for 05 Jan 1979 (top) and 11 June 1979 (bottom) cases. Blank = 0-20%; progressively darker shades of stippling for 20-100% in intervals of 20%.

heating is moderately stronger in amplitude, is much more zonally asymmetric, and occurs ~ 75 hPa higher in the atmosphere, compared to LONDON. Meanwhile, at low cloud top level (e.g., at ~ 700 hPa in the tropics), the longwave cooling is dramatically reduced in CLDRADI, accompanied by weaker latent heating and adiabatic cooling. The response is considerably enhanced, because the longwave cooling for clouds more than 1 layer thick is not smoothed. LONDON low clouds are particularly sensitive to this adjustment, being always 2 layers thick and zonally symmetric.

The zonal mean OLR tropical bias is positive and surprisingly similar (~ 7 or 8 Wm^{-2}) for both CLDRADI and LONDON. The higher tops of LONDON vs. CLDRADI low clouds apparently tend to compensate for the higher tops of CLDRADI high clouds. But the CLDRADI tropical bias can be almost eliminated, by suppressing the temperature-dependent Platt-Harshvardhan parameterization of cloud optical depth (not shown). Conversely, we were able to increase the OLR 5 to 6 Wm^{-2} by incorporating shallow convection and another 2 to 4 Wm^{-2} by confining the shallow convective cloud tops beneath 800 hPa instead of 750 hPa.

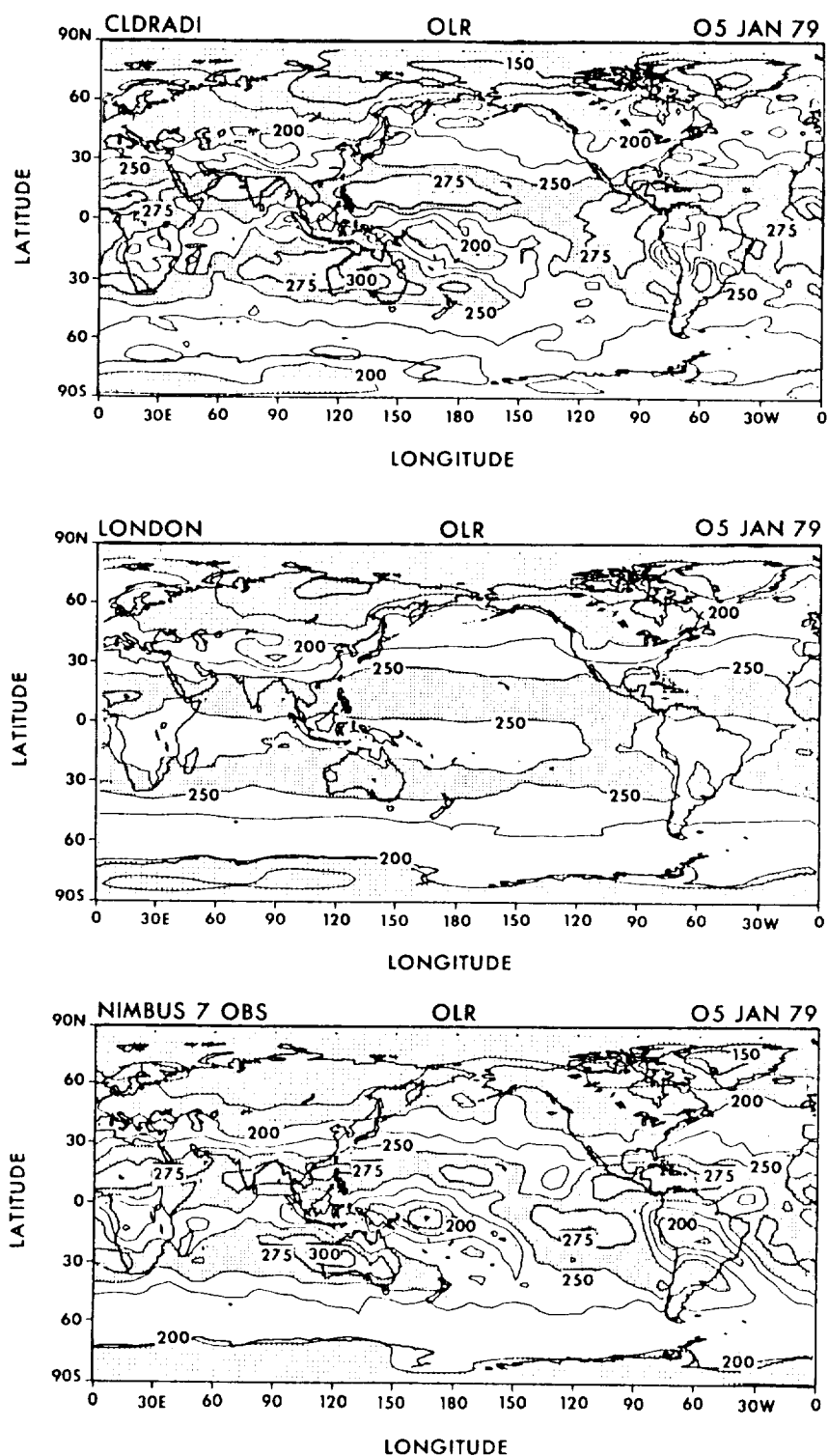


Fig. 2 Day 0-30 30 day mean outgoing longwave radiation. CLDRADI (top) and LONDON (middle) for case of 05 Jan 1979; NIMBUS 7 NFOV Obs (bottom). Contour int. = 25 Wm^{-2} .

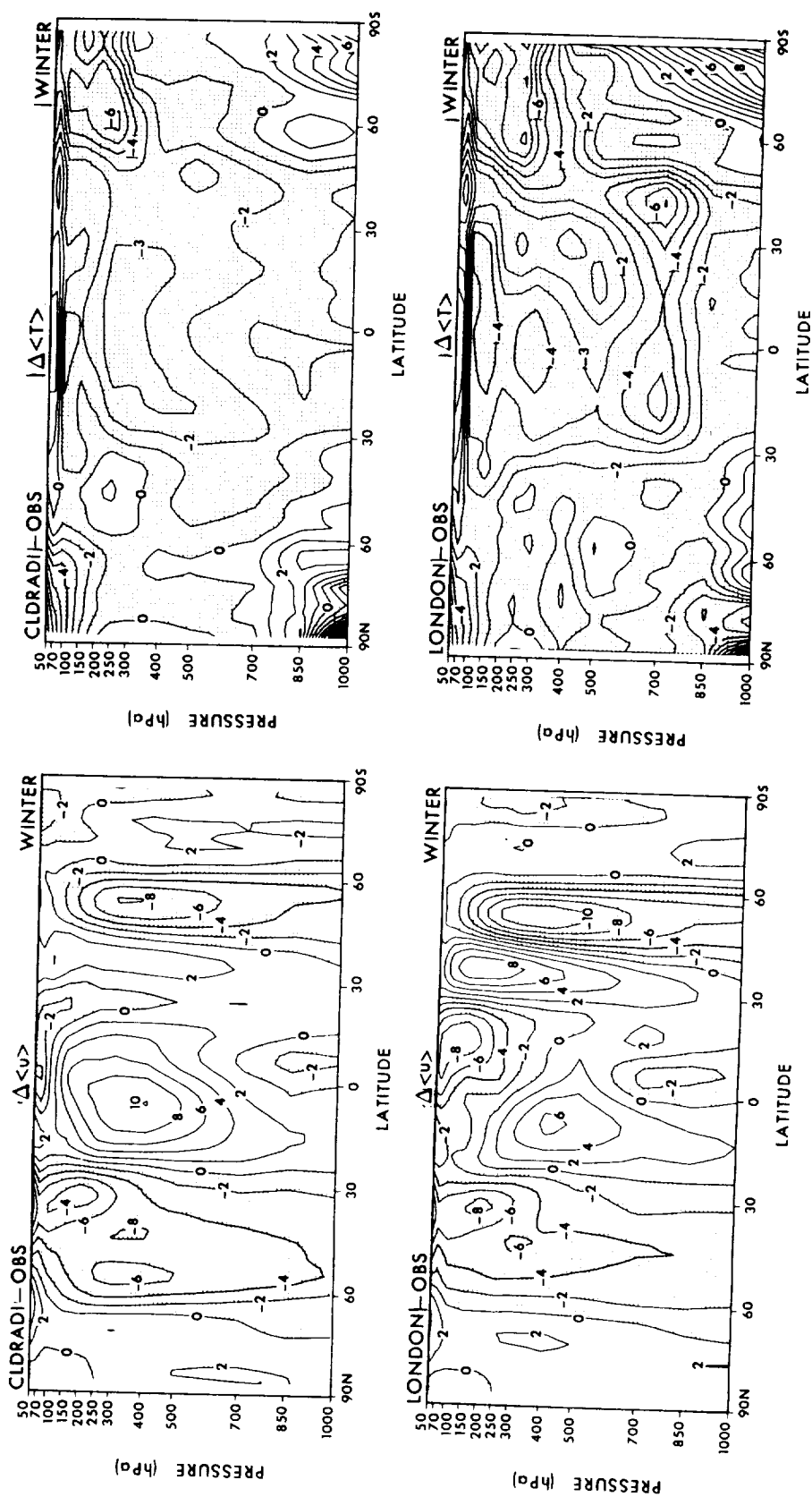


Fig. 3a Day 10-30 20 day winter ensemble mean, zonal mean zonal wind error in the latitude-pressure plane. CLDRADI (top), LONDON (bottom). Contour int. = 2 m s⁻¹.

Fig. 3b As in Fig. 3a, for zonal mean temperature error. Contour int. = 1°K.

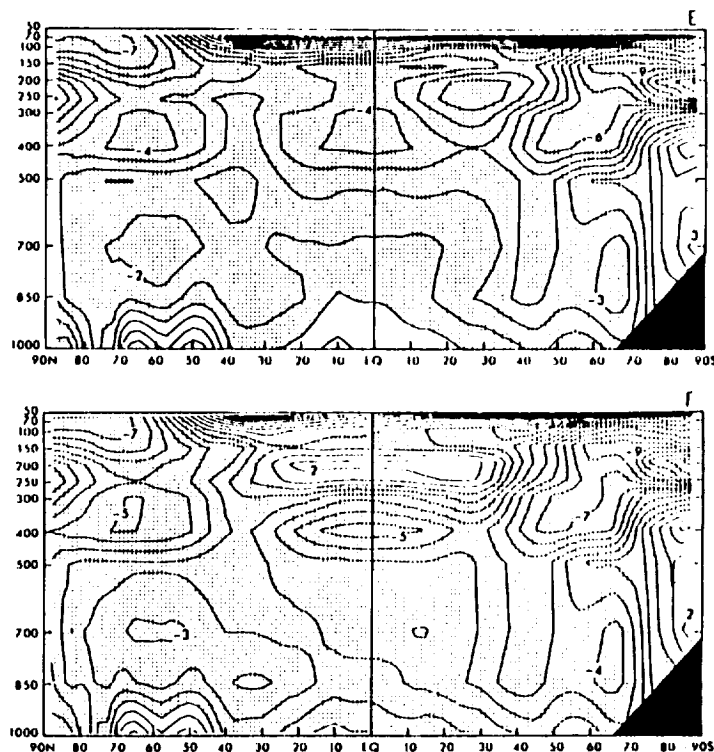


Fig. 4 30 day, 8 case ensemble mean, zonal mean temperature error in the latitude-pressure plane for N48L9 GCM with moist conv. adj. (top) and Arakawa-Schubert (bottom) parameterizations. Contour int. = 1°k. After Sirutis and Miyakoda.

Since contributions to OLR come from various vertical levels, it would be useful to have observations of cloud top and cloud base pressure in the subtropics and tropics as well as the observed vertical profiles of radiative flux and water vapor.

To assess the GCM's dynamical response to cloud-radiation interaction, we shall focus on systematic errors (with respect to NMC observation) and CLDRADI-LONDON differences of the zonal mean temperature and wind fields, because the CLDRADI-LONDON differences (not shown) tend to be statistically significant. The 3-case winter ensemble mean, zonal mean zonal wind and temperature errors are illustrated in Figs. 3a and 3b. The following features of the CLDRADI distributions compare more favorably with observation: a weaker cold bias, i.e., ~2k warmer, centered near the tropical tropopause, and weaker easterlies in the tropical lower stratosphere; weaker SH mid-latitude westerly jet and slightly stronger westerlies poleward of the jet during SH summer; a weaker cold bias in the tropical middle troposphere, and tropical and mid-latitude lower troposphere. In particular, the cold bias near the 700 hPa level in the 30°N-30°S latitude belt is ~4k. Near the South Pole, the lower troposphere is considerably warmer during SH winter and colder during SH summer, in closer agreement with observation, when cloud-radiation interaction is incorporated. The latter responses are essentially radiatively driven by a relative reduction in cloud cover. During NH winter, the CLDRADI zonal mean wind in the tropical upper troposphere is westerly, like observation, but too

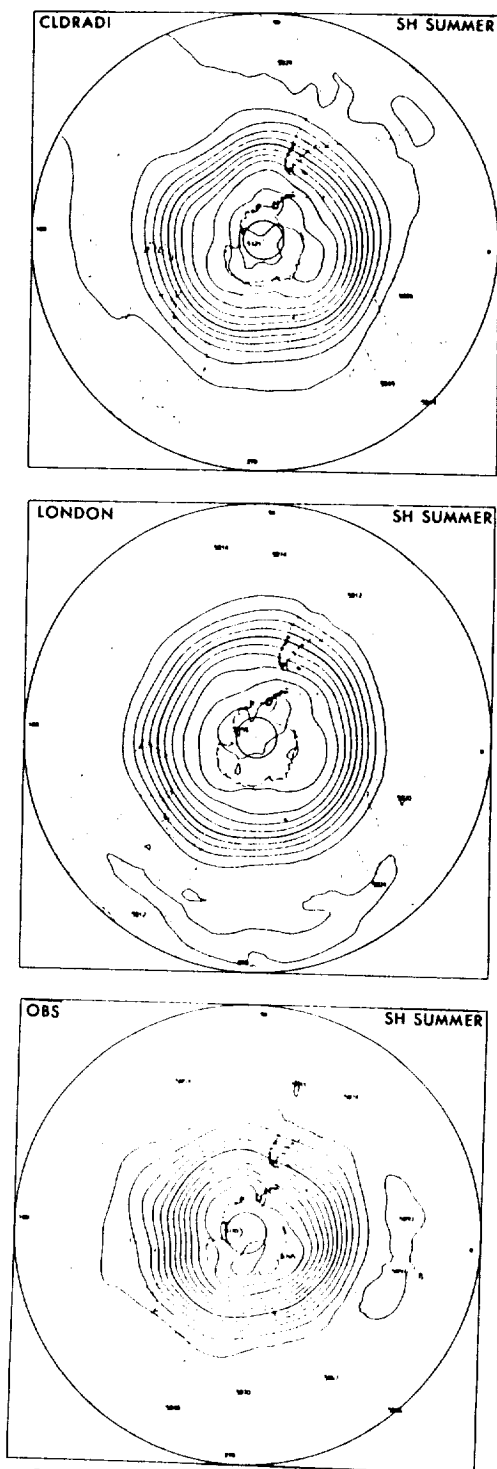


Fig. 5 Day 10-30 20 day ensemble mean 500 hPa geopotential height, for SH summer. CLDRADI (top), LONDON (middle) and NMC observation (bottom). Contour int. = 60 m.

strong, while the corresponding LONDON winds are easterly. Fig. 3b indicates that these westerly and easterly wind errors are of comparable magnitude.

The sensitivity of the systematic temperature error of a 30 day mean forecast by a 2° resolution 9 level GCM to the parameterization of cumulus parameterization is illustrated in Fig. 4. The results are based on an 8 case study by Sirutis and Miyakoda (1989). Note the dipole error structure associated with the Arakawa-Schubert (AS) parameterization in the tropical upper troposphere and the sign reversal near tropopause level when moist convective adjustment is replaced by AS. While the result may not surprise anyone, it illustrates that the systematic temperature error may not be a good indicator of the performance of a cloud-radiation parameterization. Clearly, some pairs of cumulus + cloud-radiation parameterizations are more effective than others at minimizing the systematic temperature error in the upper troposphere. Our present cloud prediction scheme tends to compensate for the apparent cold bias of the moist convective adjustment scheme. Similarly, the anvil cirrus parameterization of Randall et al. (1988), which promotes radiative cooling at tropopause level and warming at ~ 400 hPa, would tend to oppose the dipole structure of AS in Fig. 4. Conversely, the combination of Randall et al. + moist convective adjustment would probably increase the cold bias in our GCM. Under these circumstances, observed vertical profiles of radiation fluxes in the tropics or subtropics would be a useful verification tool.

The phase and amplitude prediction of geopotential height troughs and ridges at 500 hPa in SH summer is discernably improved when cloud-radiation interaction is incorporated into the model (Fig. 5). Also note the amplification of wavenumber 3. It may be primarily forced by stronger (radiative) diabatic heating in the SH tropics near the tropopause in the presence of more favorable zonal winds. In particular, the CLDRADI upper

tropospheric zonal mean westerlies may favor wave propagation to the SH extratropics, whereas the LONDON easterlies may inhibit it. In addition, radiatively induced warming in the tropics, and hence, a strengthening of the equator-to-pole temperature gradient could play a complimentary role, in analogy to Meehl and Albrecht (1988). Their GCM predicted a stronger circumpolar trough in SH summer, in response to enhanced tropical diabatic heating associated with a new parameterization of cumulus convection. Meanwhile, in the NH, where there is more background asymmetric forcing, the 500 hPa ridges tend to be stronger and troughs weaker; and there is no visible evidence of improved phase prediction, at least at R21 resolution.

The relevance of a global GCM sensitivity study to FIRE is not immediately obvious. But perhaps, the favorable impact of cloud-radiation interaction on systematic forecast error in our GCM is at least reassuring. More importantly, awareness gained of the limitations of OLR and temperature data for validating cloud prediction schemes, from the perspective of a GCMer poses a challenge to FIRE II or ASTEX. Namely, can their future observational programs measure vertical profiles of radiative cooling rates, cloud-related variables, water vapor and temperature over the entire troposphere for a region the size of a GCM grid box 250 km square? Horizontal means, computed from these measurements for a range of horizontal scales, could prove valuable for the development and validation of meso-scale and GCM scale cloud parameterizations.

References

- Meehl, G.A., and B.A. Albrecht, 1988: Tropospheric temperatures and southern hemisphere correlation. Mon. Wea. Rev., 116, 953-960.
- Platt, C.M.R., and Harshvardhan, 1988: Temperature dependence of cirrus extinction: Implications for climate feedback. J. Geophys. Res., 93, No. D9, 11051-11058.
- Randall, D.A., Harshvardhan, D.A. Dazlich, and T.G. Corsetti, 1988: Interactions among radiation, convection, and large-scale dynamics in a general circulation model. Submitted to J. Atmos. Sci.
- Sirutis, J., and K. Miyakoda, 1989: Subgrid-scale physics in one-month forecasts. Part I: Experiment with four parameterization packages. Manuscript now in process of internal review at GFDL.
- Slingo, J., 1987: The development and verification of a cloud prediction scheme for the ECMWF model. Q.J.R.M.S., 113, 899-927.
- Tiedke, M., W.A. Heckley, and J. Slingo, 1988: Tropical Forecasting at ECMWF: The influence of physical parameterization on the mean structure of forecasts and analyses. Q.J.R.M.S., 114, 639-664.

	PAGE
C01.01 Spatial Scales of Cirrus Cloud Properties Hein, Paul F., and Stephen K. Cox	311
C01.02 Interpretation of Cirrus Cloud Properties Using Coincident Satellite and Lidar Data During the FIRE Cirrus IFO Minnis, Patrick, Joseph M. Alvarez, David F. Young, Kenneth Sassen, and Christian J. Grund	317
C01.03 Properties of Cirrus from Multispectral AVHRR Imagery Data Coakley, Jr., J. A.	323
C01.04 Summary of Results and Conclusions Based on Analysis of Volume Imaging and High Spectral Resolution Lidar Data Acquired During FIRE Phase I: Part I Grund, C. J., and <u>E. W. Eloranta</u>	327
C01.05 Moisture and Heat Budgets of a Cirrus Cloud from Aircraft Measurements During FIRE <u>Gultepe, Ismail</u> , and Andrew Heymsfield	333

Spatial Scales of Cirrus Cloud Properties

Paul F. Hein and Stephen K. Cox

Colorado State University
Department of Atmospheric Sciences
Fort Collins, Colorado 80523

June 1989

1. Background

Through recent observational programs, such as FIRE, the structure of the cirrus cloud layer has recently been determined to be quite complex. Work of Sassen, *et al.* (1989) with lidar, aircraft and radar found a wide range of spatial scales from generating cells of about 1 km in size to mesoscale complexes of these cells on the order of 10's km, which are imbedded in the larger cirrus cloud. Smith, *et al.* (1989) with aircraft and Grund and Eloranta (1988) with lidar also found much spatial variability in the cirrus cloud parameters.

This research in studying the spatial scales of the cirrus, used data collected during the flight legs of the NCAR Sabreliner aircraft on four days during the FIRE Cirrus IFO to study the spatial scales of the cirrus, and will concentrate on the scales of the horizontal wind. The days examined are 22, 24, 28, and 31 October 1986. A variety of conditions existed on those days. On the 22nd and the 24th, a cirrostratus deck with convective cells was sampled in the vicinity of the exit region ridge of a closed low pressure system. Starr and Wylie (1988) classified the cirrus as "closed low cirrus". The cirrus of the 28th was classified as "warm front cirrus" (Starr and Wylie, 1988) because the cirrus was found ahead of the upper level short wave trough, capping the short wave ridge. The cirrus was optically thin and tenuous. The cirrus of the 31st was classified as "cold front cirrus" (Starr and Wylie, 1988) or "jet stream cirrus" (Conover, 1960) and was found on the eastern side of a short wave trough. A jet with wind speeds of about 50 m/s was measured in the cirrus top.

2. Data Analysis

The spatial scales of the cloud features can be described by power spectra (or spectral density graphs) and cumulative variance graphs. The cumulative variance graphs were created by first using a Fast

Fourier Transform (FFT) to create variance spectra. The variances were then summed in a cumulative fashion from the largest scalelengths (wavelengths) to the smallest. No detrending was done to the original data, and no smoothing or averaging was done to the spectral points. All the spectral points were included. This means that the values of the first five to ten spectral points of the large scalelengths should only be considered to be qualitatively correct. The cumulative variance at smaller scalelengths should be correct because a more accurate representation of the variance at the larger scalelengths should only redistribute the energy amongst the larger scalelengths. Note that each scalelength (or wavelength) contains both a "peak" and a "valley". The following graphs of cumulative variance may be interpreted as showing the percentage of variance explained by scalelengths larger than the given scalelength.

The power spectra likewise were created using an FFT and differ from the variance spectra by only a constant factor. However, the data for the power spectra were detrended and the first five spectral points were not used. The power spectra were smoothed with a six point average.

The optical properties of a cirrus cloud resulting from the downwelling shortwave and infrared radiation can be expressed by the infrared downward effective emittance ($\epsilon^* \downarrow$) and the shortwave effective extinction (ζ), which are defined by the following equations.

$$\epsilon^* \downarrow = \frac{H_B^{IR} \downarrow - \overline{H_T^{IR}} \downarrow}{\sigma \overline{T^4} - \overline{H_T^{IR}} \downarrow}$$

$$\zeta = \frac{\overline{H_T^{SW}} \downarrow - H_B^{SW} \downarrow}{\overline{H_T^{SW}} \downarrow}$$

where \overline{T} is the mean cloud temperature, $\overline{H_T^{SW}} \downarrow$ is the mean cloud top incident shortwave irradiance, and $\overline{H_T^{IR}} \downarrow$ is the mean cloud top downwelling infrared

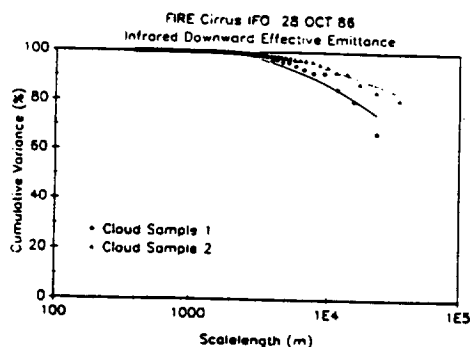


Figure 1: Cumulative variance graph of infrared downward effective emittance.

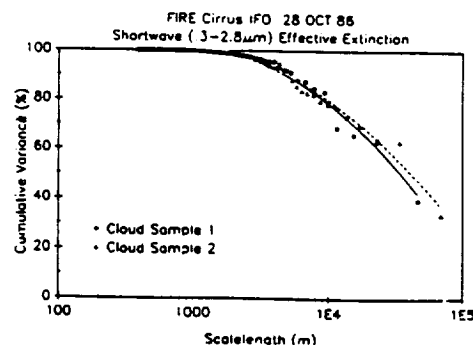


Figure 2: Cumulative variance graph of shortwave effective extinction.

irradiance. This makes $\epsilon^* \downarrow$ and ζ dependent only on the downwelling irradiance values ($H_B^{SW} \downarrow, H_B^{IR} \downarrow$) at cloud base. Note that there may be a significant reflected component of upwelling irradiance inherent in $\epsilon^* \downarrow$ and ζ .

3. Results

The spatial scales of infrared downward effective emittance and the shortwave effective extinction are described by the cumulative variance graphs of Figures 1 and 2 for the 28th. Most of the variance is found at the large scalelengths. For the infrared downward effective emittance, 90% of the variance is explained by scalelengths larger than 10 km; and for shortwave effective extinction, 90% of the variance is explained by scalelengths larger than 5 km. Thus, most of the variability of these clouds, as seen by the Sabreliner radiometric instrumentation, is determined by the larger features. Also, the similarity between the shortwave effective extinction curves shows that the clouds have the same spatial scales even though Cloud Sample 2 is less optically thick than Cloud Sample 1. A higher percentage of the variance is found at the larger scalelengths in the infrared downward effective emittance than in the shortwave effective extinction. This is because the shortwave radiation, being highly anisotropic, is not smoothed as much by the hemispheric view of the radiometric instrumentation as is the infrared. The scales are then better represented in the shortwave effective extinction graph. The cumulative variance graphs of the 28th show this dominance of the larger scales in providing the majority of the variance, and are representative of the other days.

Representative power spectra of the alongwind and crosswind components of the horizontal wind are seen in Figures 3 to 6, and of the corresponding downwelling shortwave and infrared irradiances in Figures

7 to 10. The power spectra show a range of slopes from $k^{-5/3}$ to k^{-3} . The wind power spectrum of the 22nd shows a $k^{-5/3}$ slope, while the wind spectrum of the 28th shows a k^{-3} slope. The power spectra of the wind for the 24th and the 31st have a range of slopes in between the $k^{-5/3}$ and k^{-3} slopes. The power spectra of the irradiances also have slopes constrained by the $k^{-5/3}$ slope and the k^{-3} slope, though the slopes are not always the same as the corresponding wind spectra. It is probable that the downwelling irradiances, modulated by the cloud elements, have their scales determined by eddies of the wind.

4. Discussion

The slope of the power spectra of the horizontal wind can be used to determine the energy transfer between the scales. Three dimensional turbulence has a $k^{-5/3}$ slope in the power spectra showing an energy cascade to smaller scales or larger wavenumber (k). The power spectra of effectively two dimensional turbulence displays a k^{-3} slope and a $k^{-5/3}$ slope in different wavenumber regions. The k^{-3} slope is a result of the transfer of eddy enstrophy (mean-squared vorticity) or the transfer of the square of quasi-geostrophic potential vorticity toward smaller scales. The $k^{-5/3}$ slope is a result of an energy cascade to larger scales. These cascades have been described by Gifford (1988), Charney (1971) and Kraichnan (1967). Gifford (1988) suggests that in the atmosphere the net energy cascade of the two dimensional $k^{-5/3}$ slope is to smaller scales. An alternate theory offered by VanZandt (1982) suggests the slope can be explained by internal gravity wave dynamics. However, Gage and Nastrom (1986) did not find the wave model to be completely supported by the observations. They suggested that observations of the background vertical velocity spectrum supports the wave model while the turbulence model is supported by the horizontal wind spectrum. It needs to

be noted that the two dimensional turbulence also known as geostrophic turbulence is normally applied at the synoptic scale and mesoscale motions. In this case the scales are smaller, having measured small mesoscale and large microscale motions (γ mesoscale and α microscale as characterized by Orlanski, 1975).

The scales are likely too small for Charney's geostrophic turbulence, however, the close proximity of the tropopause and the strong temperature inversion is likely constraining the eddies with a k^{-3} slope into an effectively two dimensional flow with an enstrophy cascade. The stabilities of the layers as described in Table 1 further support this hypothesis. Table 1 contains the vertical temperature gradient for the layer, the wind shear for the layer, and the Richardson number of the layer. The Richardson number is defined as

$$Ri = \frac{g}{\theta} \frac{\frac{\partial \theta}{\partial z}}{(\frac{\partial u}{\partial z})^2}$$

where θ is potential temperature, z is height, u is the wind speed, and g is the gravitational constant. The layer measured of the 22nd with the $k^{-5/3}$ slope is the most unstable of case, while that of the 28th with the k^{-3} slope is the most stable, supporting the hypothesis that strong stability restricts the eddies to an approximate two dimensional flow.

To summarize, the majority of the variance of the cirrus cloud properties is found at the larger scales. The radiative properties of the cloud appear to have their scales determined by the surrounding eddies, which modulate the cloud elements. The amount of variance or energy contained at each scale appears to be determined by the stability of the layer, which determines whether there is a two dimensional or a three dimensional turbulent cascade.

Table 1. Stability parameters for the cirrus layer.

Day	$\frac{\partial \theta}{\partial z}$ $^{\circ}K/m \times 10^{-3}$	$ \frac{\partial u}{\partial z} $ $s^{-1} \times 10^{-3}$	Ri
22	1.9	3.3	5.1
24	2.5	3.7	5.3
28	2.9	2.1	19.2
31	3.1	4.0-4.6	4.3-5.8

5. Acknowledgements

This research has been supported by National Aeronautics and Space Administration under grant NAG 1-554.

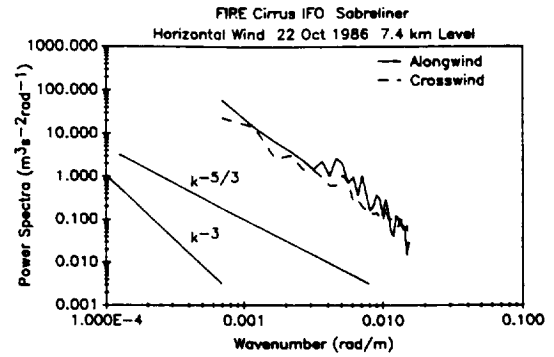


Figure 3: Power spectra of the alongwind and crosswind components of the horizontal wind: 22 Oct 1986.

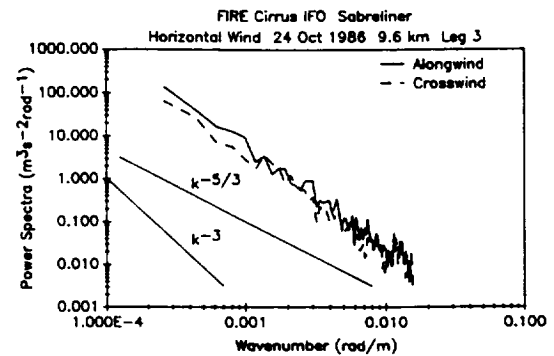


Figure 4: Power spectra of the alongwind and crosswind components of the horizontal wind: 24 Oct 1986.

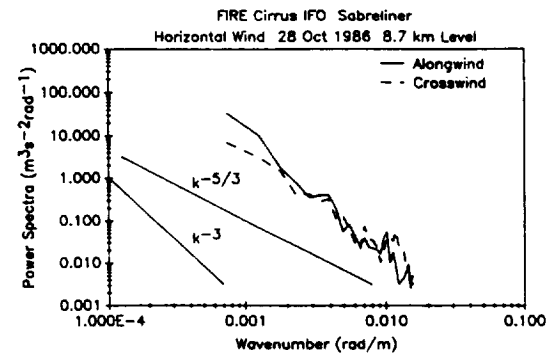


Figure 5: Power spectra of the alongwind and crosswind components of the horizontal wind: 28 Oct 1986.

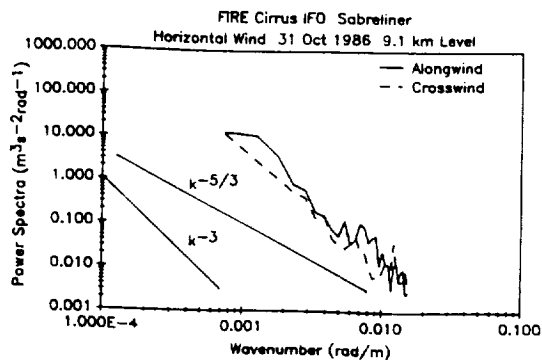


Figure 6: Power spectra of the alongwind and crosswind components of the horizontal wind: 31 Oct 1986.

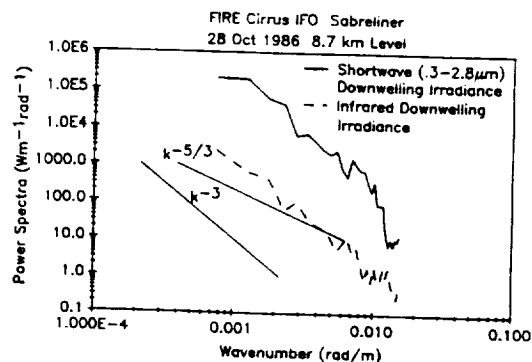


Figure 9: Power spectra of the downwelling shortwave and infrared irradiances: 28 Oct 1986.

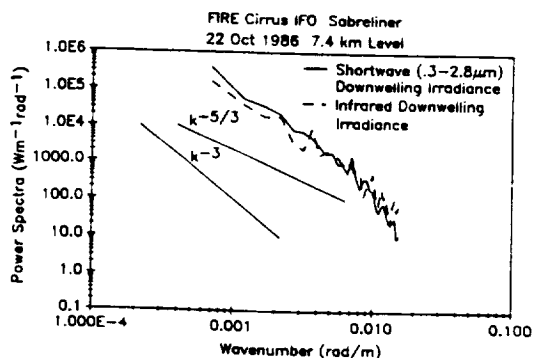


Figure 7: Power spectra of the downwelling shortwave and infrared irradiances: 22 Oct 1986.

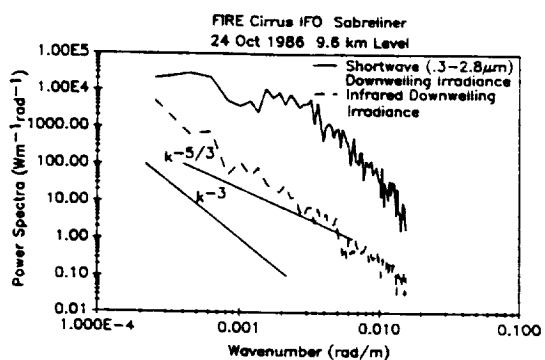


Figure 8: Power spectra of the downwelling shortwave and infrared irradiances: 24 Oct 1986.

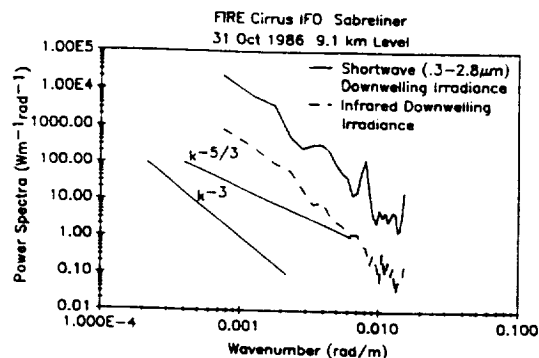


Figure 10: Power spectra of the downwelling shortwave and infrared irradiances: 31 Oct 1986.

6. References

- Charney, J., 1971: Geostrophic turbulence. *J. Atmos. Sci.*, **28**, 1087-1095.
- Conover, J., 1960: Cirrus patterns and related air motions near the jet stream as derived by photography. *J. Meteor.*, **17**, 532-546.
- Gage, K. S., and G. D. Nastrom, 1986: Theoretical interpretation of atmospheric wavenumber spectra of wind and temperature observed by commercial aircraft during GASP. *J. Atmos. Sci.*, **43**, 729-739.
- Gifford, F. A., 1988: A similarity theory of tropospheric turbulence energy spectrum. *J. Atmos. Sci.*, **45**, 1370-1379.
- Grund, C. J., and E. W. Eloranta, 1988: Optical and morphological properties of cirrus clouds determined by the high spectral resolution lidar during FIRE. *1988 Fire Science Team Workshop*, 52-56.
- Kraichnan, R. H., 1967: Inertial ranges in two-dimensional turbulence. *Phys. Fluids*, **10**, 1417-1423.
- Orlanski, I., 1975: A rational subdivision of scales for atmospheric processes. *Bull. Amer. Meteor. Soc.*, **56**, 527-530.
- Sassen K., D. O. Starr, and T. Uttal, 1989: Mesoscale and microscale structure of cirrus clouds: Three case studies. *J. Atmos. Sci.*, **46**, 371-396.
- Smith, W. L., Jr., P. F. Hein, and S. K. Cox, 1989: The 27-28 October 1986 FIRE IFO cirrus case study: In situ observations of radiation and dynamic properties of a cirrus cloud layer. *Mon. Wea. Rev.*, [in press].
- Starr D. O., and D. P. Wylie, 1988: Synoptic conditions producing cirrus during FIRE Cirrus IFO. *1988 Fire Science Team Workshop*, 5-12.
- VanZandt, T. E., 1982: A universal spectrum of buoyancy waves in the atmosphere. *Geophys. Res. Lett.*, **9**, 575-578.

**INTERPRETATION OF CIRRUS CLOUD PROPERTIES USING COINCIDENT
SATELLITE AND LIDAR DATA DURING THE FIRE CIRRUS IFO**

Patrick Minnis and Joseph M. Alvarez
Atmospheric Sciences Division, NASA Langley Research Center
Hampton, Virginia 23665-5225

David F. Young
Aerospace Technologies Division, Planning Research Corporation
Hampton, Virginia 23666

Kenneth Sassen
Department of Meteorology, University of Utah
Salt Lake City, Utah 84112

Christian J. Grund
Department of Meteorology, University of Wisconsin
Madison, Wisconsin 53702

1. Introduction

The First ISCCP Regional Experiment (FIRE) Cirrus Intensive Field Observations (IFO) provide a unique opportunity to examine the relationships between the satellite-observed radiances and various parameters which describe the bulk properties of clouds, such as cloud amount and cloud-top height. In this paper, lidar-derived cloud altitude data, radiosonde data, and satellite-observed radiances are used to examine the relationships between visible reflectance, infrared emittance, and cloud-top temperatures for cirrus clouds.

2. Data

Lidar backscatter data taken over Ft. McCoy (FMC), Wausau, and Madison, Wisconsin during the FIRE Cirrus IFO (October 19 - November 2, 1986) were used to define the cloud base, cloud-top altitude z_t , cloud thickness h , and effective cloud center altitude z_c . The last parameter is based on the distribution of backscatter intensity. Sassen et al. (1989) discuss the instrumentation and measurements in more detail. Soundings from Green Bay, Wisconsin, were used to determine the temperature-height relationships for all of the data. Cloud-top temperature T_t corresponds to z_t on the soundings. Mean cloud-center temperature T_c is found from z_c . Surface temperatures were used to supplement the clear-sky temperatures T_{cs} derived from the satellite data. Half-hourly VIS ($0.65\mu\text{m}$) and IR ($11.5\mu\text{m}$), 4-km data from the Geostationary Operational Environmental Satellite (GOES) were extracted along the wind vector at z_c for areas 4-pixels wide and ~ 16-pixels long. The VIS data were converted to reflectance ρ using the calibration of C. H. Whitlock (1988, personal communication). Clear-sky temperature is derived for each data strip whenever some clear pixels are observed in the VIS data. Otherwise, alternate methods are used to compute

T_{cs} . For all pixels (denoted as cloudy pixels) having an equivalent blackbody temperature, $T < T_{cs} - 3K$, the effective cloud beam emittance is

$$\epsilon = \{ [B(T) - B(T_{cs})] / [B(T_z) - B(T_{cs})] \}, \quad (1)$$

where T_z refers to the temperature at altitude z . The emittance is calculated twice for each satellite data strip using T_c and T_t in place of T_z . It is also assumed that

$$\epsilon = 1 - \exp(-\tau_e / \mu), \quad (2)$$

where the cloud IR optical depth is τ_e and μ is cosine of the viewing zenith angle. The cloud reflectance, ρ_c , is assumed to be related to the observed reflectance in the following manner.

$$\rho = T_a \rho_c + \rho_s T_c T_u + \alpha_{sd}(1 - \alpha_d)(1 - T_c - \alpha_c), \quad (3)$$

where T_a is the transmittance of the atmosphere above the cloud; T_c and T_u are the transmittances of the cloud to downward and upward direct radiation, respectively; ρ_s and α_{sd} are the clear-sky bidirectional reflectance and diffuse albedos, respectively; and α_d and α_c are the albedos of the cloud to diffuse and total radiation, respectively. Thus, $\alpha_d = \alpha_d(\tau_v)$; $\alpha_c = \alpha_c(\tau_v, \mu_0)$; and $\rho_c = \chi_c \alpha_c$. The cosine of the solar zenith angle is μ_0 . It is assumed that the anisotropic reflectance correction factor χ_c is independent of the VIS optical depth τ_v . Values for χ_c are taken from the empirical model of Minnis and Harrison (1984). The relationship between τ_v and cloud albedo is based on the results of Takano and Liou (1989) for a cloud containing randomly oriented hexagonal ice columns 125 μm long and 50 μm wide. Cloud transmittance also depends on the VIS optical depth. Mean values of T were computed for each discrete reflectance value.

In the ISCCP methodology, the scattering ratio, r , is used to relate the VIS optical depth to τ_e in order to correct for the semitransparency of the cloud. This quantity is equivalent to τ_v / τ_e . It is calculated here as

$$r = \frac{\sum_{i=1}^N (\tau_v / \tau_e)_i}{N},$$

where N is the number of cloudy pixels for each data strip. Details concerning the data and methodology are given by Minnis et al. (1989).

3. Results and Discussion

Figure 1 shows an example of the observed values of ϵ , ρ , and α_c for cirrus clouds over FMC at 15 UTC, October 28, 1986. Averaging the temperatures minimizes some of the noise introduced by cloud structure variations. Mean values of r computed at each half hour for the cirrus days during the IFO (October 22, 27, 28, and 30; November 1 and 2) are summarized in Table 1. It is expected that r is constant for a given cirrus cloud. Thus, the systematic variation of r with scattering angle θ indicates that the values of χ_c used here are inadequate. The mean value of $r = 2.1$, however, is very close to the value of 2.0 expected for large-particle clouds (e.g., Hansen and Travis, 1974). Assuming that the computed mean value of r is correct, it is possible to compute more realistic values of χ_c by forcing the results to yield $r = 2.1$ for each data strip. The average values of χ_c resulting from this process are shown as the dashed lines in Fig. 2. Obviously, the cirrus clouds scatter radiation more anisotropically than the average cloud. Optically thin clouds tend to mimic the single-scattering phase function. Optically thick clouds tend to reduce anisotropy through multiple scattering. Scattering ratios from Table 1 averaged according to T_c are shown in Fig. 3. The average values of r are 2.5 ± 0.2 for $T_c < 235$ K and 1.9 ± 0.2 for $T_c > 235$ K. The larger values of r are significantly different from 2.0 suggesting that the colder clouds contain a substantial number of small particles. The temperature dependency of r is similar to that found by Platt and Dilley (1981). The variation of cloud emittance (corrected for μ) with T_c given in Fig. 4 for the case study (October 27-28) is much like that determined by Platt et al. (1987) from ground observations. The data for the entire period, however, show greater increases of ϵ with temperature than found by Platt et al. (1987). Cloud thickness (Fig. 5) during the case study is also similar to the Platt et al. (1987) results. Ratios of $\epsilon(T_t) / \epsilon(T_c)$ are plotted against T_c in Fig. 6. The nearly linear dependency of these ratios on T_c indicates that the actual cloud-top temperature can be determined if T_c is found first. Other results from these analyses (Minnis et al., 1989) indicate that cloud shadows have a significant effect on the retrieved cloud albedos. This shadowing can result in "dark" pixels which are colder than T_{cs} and darker than ρ_s . Their effects must be considered in the retrieval of cirrus properties from VIS and IR data.

4. Concluding Remarks

The analysis of IFO data shows consistency with earlier cirrus studies suggesting that some simple parameterizations of cirrus cloud properties can be effectively utilized. Other results indicate that additional parameters may be derived from the satellite data. More cases taken over other areas will be needed to confirm the results presented here.

REFERENCES

- Hansen, J. E. and L. D. Travis, 1974: Light scattering in planetary atmospheres. Space Sci. Rev., 16, 527-610.
- Minnis, P., and E. F. Harrison, 1984: Diurnal variability of regional cloud and clear-sky radiative parameters derived from GOES data, Part III: November 1978 radiation parameters. J. Clim. Appl. Meteor., 23, 1032-1051.
- Minnis, P., D. F. Young, K. Sassen, J. M. Alvarez, and C. J. Grund, 1989: The 27-28 October 1986 FIRE Cirrus IFO case study: Cirrus parameter relationships derived from satellite and lidar data. Submitted to Mon. Wea. Rev.
- Platt, C. M. R., and A. C. Dilley, 1981: Remote sounding of high clouds: IV. Observed temperature variations in cirrus optical properties. J. Atmos. Sci., 38, 1069-1082.
- Platt, C. M. R., J. C. Scott, and A. C. Dilley, 1987: Remote sounding of high clouds, VI. Optical properties of midlatitude and tropical cirrus. J. Atmos. Sci., 44, 729-747.
- Sassen, K., C. J. Grund, J. Spinhirne, M. Hardesty, and J. M. Alvarez, 1989: The 27-28 October 1986 FIRE IFO cirrus case study: A five lidar view of cirrus cloud structure and evaluation. Submitted to Mon. Wea. Rev.
- Takano, Y. and K. N. Liou, 1989a: Radiative transfer in cirrus clouds: II. Theory and computation of multiple scattering in an anisotropic medium. J. Atmos. Sci., 46, 21-38.

UTC	Cases (IFO)	● (-)	All Data (IFO)		Case Study	
			τ_v	r	τ_v	r
1330	4	109	0.97	1.08	0.15	0.85
1400	3	117	1.84	1.42	0.17	1.19
1430	2	124	0.90	1.76	0.31	1.68
1500	3	131	1.46	2.01	1.46	2.01
1600	5	146	2.31	2.22	1.72	1.98
1630	2	153	2.44	1.74	---	---
1700	6	160	1.78	2.99	1.39	2.94
1800	6	173	2.20	3.49	1.94	5.65
1830	1	175	3.52	1.98	---	---
1900	7	168	2.50	2.81	0.63	3.13
1930	4	162	1.52	2.73	0.74	2.76
2000	8	154	1.93	2.68	1.28	3.06
2030	5	147	1.40	2.47	1.63	2.34
2100	6	140	1.06	1.99	0.97	2.46
2130	4	132	1.15	1.30	0.53	1.20
2200	5	125	0.67	0.83	0.28	0.68
Totals and means		71	1.69	2.08	1.04	2.07

Table 1. Reflectance parameters computed for all data.

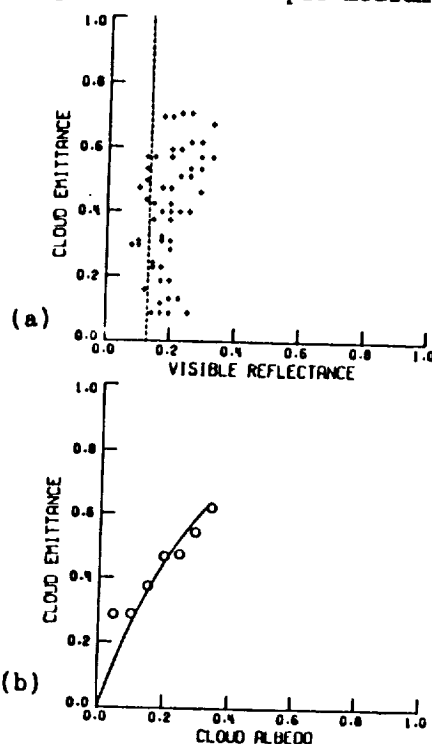


Fig. 1. Cloud emittances and observed (a) reflectances and (b) cloud albedos for cirrus clouds over FMC at 1500 UTC, October 28, 1986.

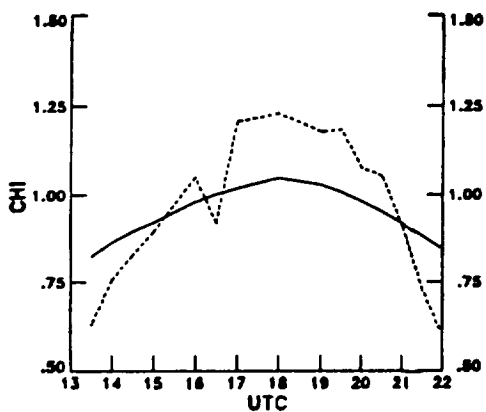


Fig. 2. Mean anisotropic reflectance correction factors for the IFO. The solid line is the nominal model; the dashed line represents the values derived for $r = 2.1$.

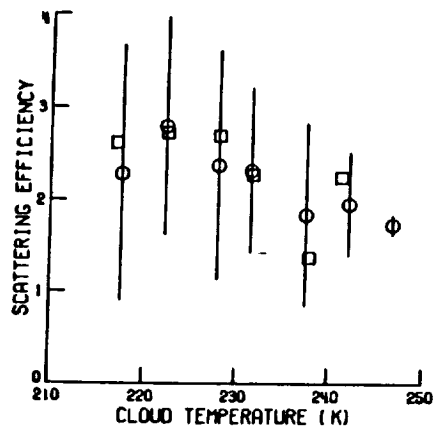


Fig. 3. Variation of mean scattering ratio with cloud-center temperature.

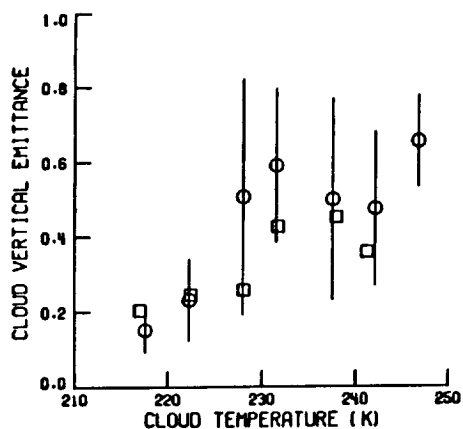


Fig. 4. Variation of cloud vertical beam emittance with cloud-center temperature.

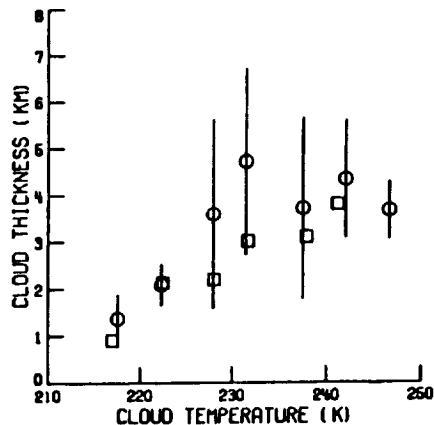


Fig. 5. Dependence of cloud thickness on cloud-center temperature.

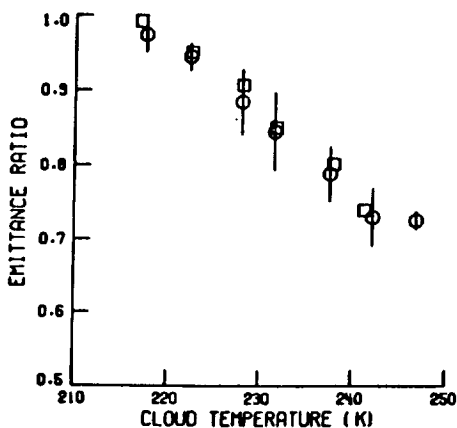


Fig. 6. Variation of emittance ratio with cloud-center temperature.

Properties of Cirrus from Multispectral AVHRR Imagery Data

J.A. Coakley, Jr.
 Department of Atmospheric Sciences
 Oregon State University
 Corvallis, OR 97331-2209

The discovery that the 11 μm and 12 μm window channels of AVHRR could be used to detect and even characterize the properties of cirrus (Inoue, 1985 and others) stimulated the present study which re-examines the general multispectral approach for retrieving cirrus cloud top temperature and emissivity. The approach is based primarily on work done for METEOSAT by Szejwach (1982) and draws on a wealth of previous investigations of multispectral approaches (Coakley, 1983; Platt, 1983; Arking and Childs, 1985). The generalized multispectral approach described here compliments the "CO₂ slicing method" used by Wylie (1988) and the bispectral threshold method used by Minnis *et al* (1988).

The approach is based on the recognition that for a cloud system that is semitransparent in the infrared, the emission for channel i which senses radiation with wavelength λ_i is given by

$$I_i = I_{si} + \epsilon_{ci} A_c (I_{ci} - I_{si}) \quad (1)$$

where I_{si} is the emission from the cloud-free region of the field of view and A_c is the fractional cloud cover within the field of view. ϵ_{ci} in (1) is an "effective mean" emissivity for the clouds within the field of view. Effects due to reflection of thermal radiation by the clouds are ignored in (1). I_{ci} is the emission that the clouds would have were they blackbodies. Determining I_{ci} is equivalent to determining the cloud top temperature.

Consider now the behavior of observations at independent infrared wavelengths λ_i and λ_j under three conditions: 1) single-layered, opaque clouds, 2) single-layered, semitransparent clouds (cirrus) and 3) multi-level opaque clouds. In general, a cloud system will exhibit any combination of these three cases. Here, wavelengths that are independent are taken to be those that exhibit different sensitivities of the emission to temperature, i.e. are at substantially different wavelengths, or they exhibit different sensitivities to the dependencies of the optical properties to hydrometeor concentrations or both.

For single-layered, opaque clouds, i.e. clouds that possess a single cloud top temperature, I_s and I_{ci} are constants at all wavelengths for the region containing the system. Likewise, because the clouds are opaque the emissivities, ϵ_c , are also constants and equal to the maximum values that the clouds can obtain. As a result, I_i is linearly proportional to I_j . This linear relationship is shown in Figure 1 for the 11 μm and 12 μm radiances obtained from NOAA-9 on the afternoon of October 28, 1986 during the case study period. The data is for a 250 km region containing the array of lidars that participated in the case study (Sassen *et al*, 1989). The linear relationship that is shown in the figure indicates that the upper-level clouds were opaque at 11 and 12 μm at the time of the satellite overpass. On the basis of the 11

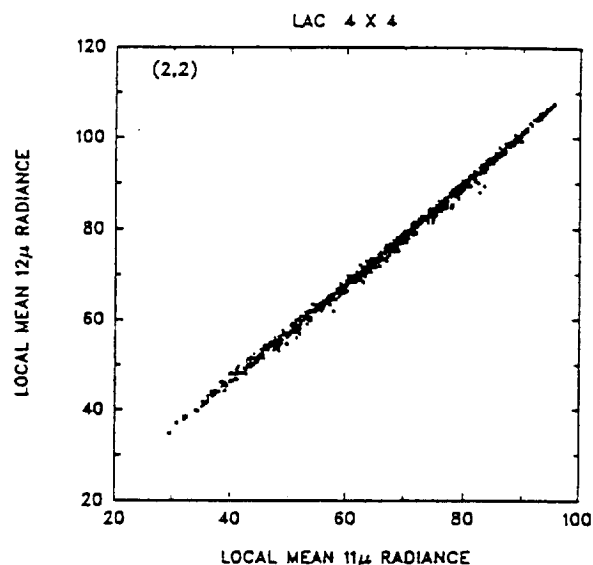


Figure 1. 11 μm and 12 μm AVHRR radiances for the afternoon NOAA-9 pass on October 28, 1986. The data is for a 250 km region containing the array of lidars that participated in the Cirrus IFO case study. Each point in the figure represents a 4 km portion of the 250 km region. The linear relationship between the radiances indicates that from the view of the satellite, the clouds are opaque at 11 and 12 μm . The variability in the 11 and 12 μm radiances indicate that the clouds are broken.

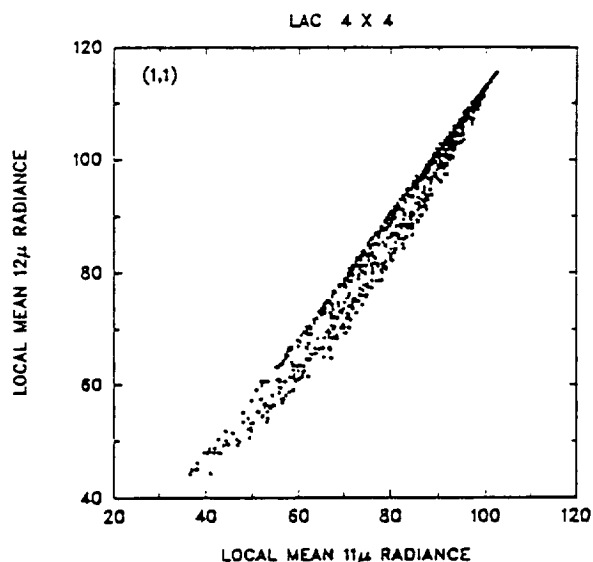


Figure 2. Same as Fig. 1 but for the 250 km region to the southwest of the lidar array. The curvature of the lower envelope of points indicates that the upper level clouds are semitransparent at some locations within the region. The intersections of the linear and nonlinear envelopes gives the cloud-free radiances, I_s and the radiance associated with opaque clouds, I_c . The cloud top temperature could be estimated from I_c .

and 12 μm radiances, these clouds would not be interpreted as cirrus with emissivities less than unity. While effects due to the reflection of thermal radiation have been ignored in this discussion, it is recognized that the maximum values of the emissivities attained by the clouds may be less than unity. The differential between unity and the maximum emissivity will affect the estimate of the cloud top temperature.

For a single-layered, semitransparent cloud system I_s and I_{ci} are constant for the region containing the clouds. The emissivities, however, can vary according to their dependence on hydrometeor concentrations. In general ϵ_{ci} is a nonlinear function of the hydrometeor concentration, and as a result ϵ_{ci} is a nonlinear function of ϵ_{cj} . Consequently, I_i will also be a nonlinear function of I_j . This nonlinear relationship is exhibited in Figure 2 which shows 11 μm and 12 μm radiances from the October 28 NOAA-9 pass for the 250 km region southwest of the lidar array. The curvature exhibited by the envelope of points is due to the semitransparency of the upper level clouds. The linear relationship exhibited by the other envelope indicates that within this 250 km region, the upper-level clouds also become opaque at some locations.

For clouds that are opaque but distributed in altitude, I_c will no longer be constant for the region containing the clouds. The emissivities, ϵ_c , will however be constant and near unity. As a result, the relationship between I_i and I_j will closely follow the dependence of the Planck function on temperature. That is, the relationship between I_i and I_j will again be nonlinear. In this case, however, the curvature will be opposite to that shown in Figure 2.

One notes that taking the three cases together, one obtains a linear relationship between I_i and I_j for opaque, single-layered clouds, a nonlinear relationship between I_i and I_j for semitransparent, single-layered clouds and another nonlinear relationship for opaque, multi-layered clouds which follows the relationship given by the Planck function. The latter relationship may be calculated *a priori*. All three curves, however, intersect at I_s and I_c where I_c is that of the upper-level system which is semitransparent. So, in principle, one should be able to extract estimates for the cloud top temperature from the intersection. Having the cloud top temperature, one then estimates the distribution of $\epsilon_c A_c$ in (1) from the distribution of observed intensities.

While the results shown here were for 11 and 12 μm radiances, better definition of the cloud top temperature is probably obtainable using 3.7 μm radiances in combination with the 11 and 12 μm radiances. During the day, however, at least for the cases shown in Figs. 1 and 2, reflection of solar radiation at 3.7 μm by low-level water clouds makes the analysis untenable. At night, at least with the NOAA-9 AVHRR, instrument noise in the 3.7 μm channel also makes the analysis untenable. The identification of semitransparent systems using 3.7 μm radiances has, however, been noted elsewhere (Molnar and Coakley, 1985).

References

- Arking A. and J.D. Childs, 1985: Retrieval of cloud cover parameters from multispectral satellite images. *J. Climate Appl. Meteor.*, **24**, 322-333.

- Coakley, J.A., Jr., 1983: Properties of multi-layered cloud systems from satellite imagery. *J. Geophys. Res.*, **88**, 10818-10828.
- Inoue, T., 1985: On the temperature and effective emissivity determination of semitransparent cirrus clouds by bi-spectral measurements in the 10- μ m window region, *J. Meteor. Soc. Jpn.*, **63**, 88-99.
- Minnis, P., J. Alvarez, D.F. Young, P.W. Heck and K. Sassen, 1988: Cirrus cloud properties derived from coincident GOES and lidar during the 1986 FIRE Cirrus IFO. FIRE Science Team Workshop, July 11-15, Vail, 145-149.
- Molnar, G., and J.A. Coakley, Jr., 1985: The retrieval of cloud cover from satellite imagery data: A statistical approach. *J. Geophys. Res.*, **90**, 12960--12970.
- Platt, C.M.R., 1983: On the bispectral method for cloud parameter determination from satellite VISSR data: Separating broken cloud and semitransparent cloud. *J. Climate Appl. Meteor.*, **22**, 429-439.
- Sassen, K., C.J. Grund, J. Spinhirne, M. Hardesty and J. Alvarez, 1989: The 27-28 October 1986 FIRE IFO cirrus case study: A five lidar overview of cloud structure and evolution. (preprint)
- Szejwach G., 1982: Determination of semi-transparent cirrus cloud temperature from infrared radiances: Application to METEOSAT. *J. Appl. Meteor.*, **21**, 384-393.
- Wylie, D., 1988: Where are cirrus clouds and why are they there? FIRE Science Team Workshop, July 11-15, Vail, 13-18.

Summary of Results and Conclusions Based on Analysis of Volume Imaging and High Spectral Resolution Lidar Data Acquired During FIRE Phase I: Part I

C. J. Grund and E. W. Floranta

University of Wisconsin
Department of Meteorology
1225 West Dayton St.
Madison, WI 53706

I. Introduction

The collection of long term global statistics on cloud cover, a major goal of ISCCP, may (potentially) be most easily accomplished with satellite based observations; however, measurements derived from passive satellite retrieval methods must be calibrated and verified by insitu or ground based remote sensor observations. Verification is not straight forward, however, because the highly variable nature of cloud altitude, morphology, and optical characteristics complicates the scaling of point measurements to satellite footprint sized areas. This is particularly evident for cirrus clouds which may be organized on horizontal scales of 10's of meters to 100's of kilometers, may exhibit physical depths of 10's of meters to 8 km or more, and have optical depths ranging from less than .003 to greater than 3. Cirrus clouds can strongly influence earths' radiative balance, but, because they are often transmissive, cirrus clouds are difficult to detect and characterize from satellite measurements.

Because of its precise ranging capabilities, spatial resolution and sensitivity, lidar observations have played an important role in the detection, depiction, and characterization of cirrus clouds. This paper summarizes some of the characteristics of cirrus clouds observed by the University of Wisconsin High Spectral Resolution (HSRL) and Volume Imaging Lidars (VIL) during the phase I IFO and ETO periods. Because of the volume of material, we have split our presentation into two parts: an overview oral summary and a more detailed poster presentation. Since the VIL data are most easily summarized in a visual format unsuitable for reproduction here, we have primarily reported HSRL measurement contributions in this 2 part abstract. Both poster and oral presentations will include this additional material, as well as examples of new VIL and HSRL instrument capabilities.

II. U.W. Lidar Instrumentation

The University of Wisconsin lidar group operates two unique lidar systems: the High Spectral Resolution Lidar (HSRL) and the Volume Imaging Lidar (VIL).

The HSRL is optimized to produce calibrated measurements of optical depth, extinction corrected cloud morphology, and backscatter phase function¹ (determined by particle size, composition, and shape). The HSRL spectrally separates Doppler broadened molecular backscatter from unbroadened (primarily elastic) cloud particle and aerosol backscatter. Using the known distribution of molecular scattering cross section to provide a calibration reference at every range, extinction is unambiguously determined from the observed molecular backscatter intensity. HSRL measurements of cirrus cloud optical properties were first acquired during the FIRE cirrus IFO in 1986. Since then, the HSRL has routinely operated to collect statistics on cirrus optical properties and in support of VAS cloud height verification studies².

The VIL, is optimized for rapid scanning of large atmospheric volumes. A high repetition rate laser (30 Hz) coupled with fast scanning mirrors (25° / sec) and a high speed data logging system (~.5 gigabyte/hr) writing to optical disk (2.6 gigabyte capacity) allow this system to produce 3-D reconstructions of cirrus cloud backscatter by assembling successive 2-D cross wind scans on a

graphics display terminal. Movie loops of successive wide angle scans taken along the mean wind direction reveal a mesoscale time history of cirrus evolution. From a single ground based location, the VIL can scan a 60 km wide segment of cirrus with 100 m resolution in 20 seconds. Cirrus data have been acquired with this system since the summer of 1987 in conjunction with specific field experiments.

III. Observed cirrus properties

a. *Optically thin cirrus*

Extensive fields of optically thin clouds are important for a number of reasons: background noise generated by thermal emissions from the cloud and ambient light scattered by the cloud can interfere with IR remote measurements, and, attenuation along shallow view angles, as in limb scanning, can become significant. If present globally, they may also have a significant impact on earth's radiative balance while going largely undetected by space-borne passive remote sensing techniques.

Plotted in fig.'s 1 and (2) are two of our best examples of this type of cloud. The data on these clouds were acquired during the FIRE IFO case study day³ October 28, 1986. Solid lines represent backscatter cross section contours in 10^{-7} (10^{-8}) $\text{m}^{-1} \text{sr}^{-1}$. The dashed lines indicate optical mid-cloud altitude (half the cloud optical thickness is accumulated to either side of this line), and dotted lines are wind speeds in m/s. Because the HSRL cannot distinguish between backscatter from aerosols and that from cloud particles, we cannot be certain that these tenuous veils of enhanced backscatter are cirrus; however, since denser cirrus were observed at these altitudes both before and after this time period, these features at least appear to be associated with cirrus. Average layer optical thickness in the vertical was $\sim .01$ ($\sim .003$). Wind-drift estimates suggest these layers extend for at least 266 km (180 km).

Isotachs plotted in fig. 1 from the special FIRE three-hourly radiosonde data show a general correlation between wind speed maxima and backscatter cross section contours (note the 26 m/s and 29 m/s patterns). Fig. 2 also suggests a correlation between wind shear and backscatter cross section (note the region between 9.5 and 10.5 km at 1000 UTC). These apparent pattern correlations have been observed in several cases, though a consistent set of correlation characteristics has not been established. It is not certain if the shear is part of the cirrus generation mechanism, or if cirrus formation and winds are both responding to the same environmental forcing.

b. *Mesoscale uncinus complex (MUC)*

Fig. 3 shows a contour map of a MUC⁵ observed on October 28, 1986 from 0500 - 0900 UTC. GOES IR images of this phenomena, combined with radiosonde winds, suggest that the MUC is a south-eastward propagating cirrus generation region embedded in a less intense, generally eastward moving, wind-driven cloud band. The NW-SE oriented cloud band was part of a more extensive cloud shield covering northern Wisconsin. The GOES IR images show the MUC passed directly over Madison, with the radiance minima occurring ~ 0700 (interpreted as the densest cloud region, not necessarily the highest cloud top, as for opaque clouds).

A series of uncinus generating cells are evident between 9.5 and 11 km, particularly between 0530 and 0700. Each of these cells is about 150 m thick. Cloud translation with the 10 km wind ($20 \text{ ms}^{-1} \pm 10 \text{ ms}^{-1}$) would suggest the cells are $\sim 4 - 12$ km across; thus, they have a height to width aspect ratio in the range $\sim 1:54 - 1:180$. The maximum $\beta_{\text{at}}/4\pi$ (normalized backscatter cross section) for this MUC was determined to be $.024 \text{ km}^{-1} \text{sr}^{-1}$ at 0722 near 8.7 km altitude, preceding the passage of a wind jet maximum of $\sim 34 \text{ ms}^{-1}$. Both the Ft. McCoy and Platteville soundings at 0300 and 0900 (0600 was not acquired) indicate the regions above 7.4 km were consistently moist ($>70\%$ RH with respect to ice) and occasionally reached supersaturation as high as $\sim 108\%$ with respect to ice. The radiosonde profiles also show an abrupt decrease in relative humidity below 7.4 km

suggesting the steep contour gradient at 0700 at 7.2 km altitude is related to rapid ice crystal evaporation in the dry environment beneath the complex. Profiles averaged from 0600-0750 indicate this system had a mean optical thickness of $.58 \pm 0.05$ which varied from 0.09 ± 0.03 at 0750 to 1.1 ± 0.3 at 0718. The bulk backscatter phase function averaged over the same time period was $0.042 \pm 0.015 \text{ sr}^{-1}$.

Isotachs, interpreted from the 0300 and 0900 Ft. McCoy radiosonde data, show an apparent relationship between wind speeds and the MUC backscatter cross section distribution. Note the close proximity in time and altitude between the wind speed maximum and the backscatter cross section maximum. Cloud bottom seems to occur where the time height cross section indicates relatively steady winds. The decrease in cloud top altitude seems to be related to the development of a wind minimum at 10.5 km. The jet and the wind minimum are of smaller scale than the FIRE IFO radiosonde network. They appear strongly only in the Ft. McCoy soundings, and are just discernible in the Platteville sounding data; thus, no attempt has been made to interpolate the radiosonde data to Madison observation times. Future observations of this type would benefit from a more dense temporal and spatial net of wind observations.

The MUC observations also demonstrate the limitations inherent in interpreting cirrus cloud morphology strictly from zenith time height cross section measurements. If the wind shear is deduced from the apparent slope of the virga trails, the wind maximum would be expected near the upper cloud level at ~10 km. In fact, the wind contours indicate the maximum of ~35 m/s near 8.5 km, decreasing to ~18 m/s at 10 km. Clearly, the time height cross section of this complex does not represent a stationary phenomena translating with the ambient winds but that the clouds are undergoing significant evolution. Cloud genesis is probably related to circulations about the mesoscale jet, and the apparent shape of virga may be partially governed by the local distribution of moisture.

c. *Alto-cumulus vs. cirrus*

From 1200 - 1500 UTC on 10/28, a two level cirrus / alto-cumulus formation was observed. Fig. 4 highlights the dissimilarity in lidar backscatter between these cloud types. The lower layer cloud appears to be formed from a series of relatively dense alto-cumulus cells with a .5-1 km long ice crystal fallout tail (identification as ACu is inferred from an all-sky photograph taken at Wausau and the fact that similar cloud structure was observed at Ft. McCoy and Wausau lidar data around this time period⁴). Ice virga is inferred from the environmental temperature (-25° to -30° C) and from higher resolution images of lidar backscatter. Wind-drift estimates indicate the ACu were about 20 km across, yet they were ~200 m thick, producing a height to width ratio of only 1:100. As the ACu developed, fig. 5 shows an increase in both the total cloud optical thickness and the backscatter phase function while the optical mid-cloud altitude decreased from ~11 km to ~7.5 km. The average cloud backscatter phase function peaks with the passage of each ACu cell. Because similar cloud features were also observed to produce little depolarization at Wausau and Ft. McCoy, we can infer, with some confidence, that the backscatter phase function peaks suggest these clouds are composed of super-cooled spherical water droplets⁴.

The ACu bands at ~7.6 km produce significantly greater backscatter than either the 9-12 km cirrus or the lower level virga between 6.4 and 7.1 km. The $\beta_{\text{av}}/4\pi$ maximum reached at 1419 exceeded $0.15 \text{ km}^{-1} \text{ sr}^{-1}$. One reason for this is that ACu are primarily composed of super-cooled liquid water droplets; because of optical surface wave phenomena, such droplets are more efficient at backscattering than non-spherical ice crystals. A second reason is that super-cooled water droplets are necessarily quite small, whereas, once glaciation begins, cloud particles accumulate mass rapidly because of the reduction of saturation vapor pressure with respect to ice; hence, ice particle fall speeds rapidly exceed vertical atmospheric motion, and particle mass distributes over an extended column, decreasing the local backscatter intensity. Since particle mass increases as the cube of the radius while the scattering cross section approximately follows the radius squared, the backscatter

cross section will also diminish as growth processes redistribute water mass from many small particles to fewer but larger ice crystals with substantial fall speeds.

The ACu dominate the optical thickness profile. Clearly, the occurrence of ACu can have significant impact on the radiative properties of the cloud independent of cloud top altitude and bottom altitudes.

d. *Cirrostratus*

Cirrus frequently form continuous layers with vertically developed cells of enhanced backscatter appearing near both cloud top and cloud bottom. Fig. 6 illustrates this type of formation observed on 10/28/86. The vertical elongation of backscatter cross section contours suggests an upward and/or downward redistribution of cloud particles. The top and bottom cellular morphology of this layer is most evident ~1610 where an apparent generating region near cloud top produces a virga trail which extends to, and perhaps seeds, a second region of strong backscatter near ~7.5 km. The lower regions (at 1610 and 1640) also appear to be precipitating as evidenced by the vertical elongation of the cloud bottom backscatter cross section contours. Note that the mid-cloud altitude follows regions of enhanced backscatter very closely and that there is no obvious relationship between the appearance of these regions and either cloud top or cloud bottom altitudes. Thus, the structures which dominate cloud optical properties are not necessarily indicated by either the cloud boundaries or the physical mid-cloud altitude.

With the exception of two periods, near 1540 and 1915, the cirrus optical thickness exceeded 0.1 forming an apparent cirrostratus layer (see fig. 7). The gap in cloud cover at ~1900 corresponds to the passage of a clear arc identified from satellite imagery⁵. Peaks in backscatter phase function ($\sim .038 \text{ sr}^{-1}$) tend to coincide with the occurrence of the regions of enhanced backscatter cross section independent of total optical thickness, while the regions between the cells usually produce the minima in the backscatter phase function of $\sim .02 - .026 \text{ sr}^{-1}$. This suggests differences in the microphysical properties for the particles associated with the cells compared with those of the surrounding cloud. One explanation may be that the regions of enhanced backscatter are areas of cloud particle generation which may contain an abundance of small supercooled water droplets (temperature at 7.5 km: $\sim -30^\circ \text{C}$, at 9.5: $\sim -45^\circ \text{C}$). An abundance of particles approaching molecular diameters could also produce the observed backscatter phase function and depolarization ratio effects. Unfortunately, the issue cannot be settled by insitu probe data because current instruments are incapable of resolving such small particles. In regions between the cells, it may be that sufficient time has elapsed so that the number density of droplets has been substantially diminished by differential vapor pressure effects between ice and water. The modulation of the bulk backscatter phase function also suggests that some of the apparent structure observed in the backscatter cross section plots is generated by microphysical changes and is not simply related to the cloud extinction cross section. This effect should be considered when deducing cloud morphological and optical characteristics from simple plots of lidar backscatter.

The backscatter contours in fig. 6 indicate a large scale pattern of intensification with a period of about 45 minutes; however, an examination of the higher time resolution pictures of the raw laser returns reveals the clouds contain a finer scale (~5 minute) structure imbedded in the larger scale organization. Wind drift estimates would suggest that these features have a horizontal scale of about 9-11 km. Thus, the height to width aspect ratio of the elementary structures is ~1:5 while the larger scale field of enhanced backscatter exhibits an aspect ratio of ~1:25.

Fig. 8 presents the backscatter cross sections observed for the cirrostratus, pre-warm frontal cloud system observed on Jan. 29-30, 1988. The maximum backscatter cross section of $4.3 \cdot 10^{-5} \text{ m}^{-1} \text{ sr}^{-1}$ was observed near 1:30 GMT. Twenty minute averaged optical thickness varied between .081 and 2.27, while the backscatter phase function varied from $.031 - .057 \text{ sr}^{-1}$.

Note the pattern of repeated, overlapping tilted cells evident in the first half of this data set. Optically thick cirrus frequently exhibit similar morphology. Using the mean cloud level wind to translate the temporal coordinate into the spatial domain suggests the cells are inclined at $\sim 7^\circ$ from the horizontal. A cloud of this type may appear homogeneous to a nadir viewing satellite sensor, but would not exhibit an optical thickness dependent only on the secant of the view angle. Wind-drift estimates indicate the cells were ~ 30 - 50 km wide producing height to width aspect ratios of $\sim 1:10$. Patterned departures from inverse-cosine-law behavior can have implications for radiative heat balance calculations and for the calibration of wide beam radiometers.

e. Particle microphysics

Cirrus sometimes form plate-like crystals which fall flat-face-down because of aerodynamics. In scanning through the zenith, the VIL has observed specular backscatter enhancements by a factor of at least 13, and larger enhancements seem possible. The e^{-1} full width of the forward scatter diffraction peak in one of these observations was $\sim 1.5^\circ$ (at $1.06 \mu\text{m}$) suggesting a minimum crystal diameter of $\sim 50 \mu\text{m}$. Some VIL cross sections have revealed thin (<200 m) layers exhibiting specular reflection immediately adjacent to similar layers which do not show specular backscatter enhancements. This suggests the microphysical properties of cirrus are quite heterogeneous. Because of the three dimensional heterogeneity of cirrus, the scientific yield from future experiments could be enhanced by a real time mapping of extended volumes around insitu microphysical measurements. Such mapping might even be used as an element in the selection and execution of flight plans.

Because of this potential for specular backscatter, the HSRL has been operated $3^\circ - 5^\circ$ from zenith, minimizing the impact of this effect on the measurements of backscatter phase function and backscatter cross section.

NOTE: Summary, References and Figures 3 - 8 may be found in:
part II of Grund and Eloranta ... see poster presentation section.

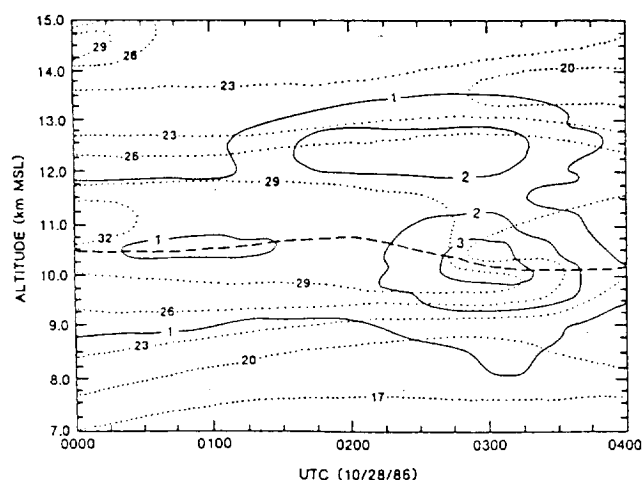


Fig. 1 Background veils of enhanced backscatter have been observed at cirrus altitudes even when cirrus are not present. This layer had an average optical thickness of ~ 0.1 . Backscatter cross section (—) in $10^{-7} \text{ m}^{-1} \text{ sr}^{-1}$, optical mid-cloud altitude (---), wind speed (···) in m/s. Note pattern correlations between wind speeds and backscatter cross section.

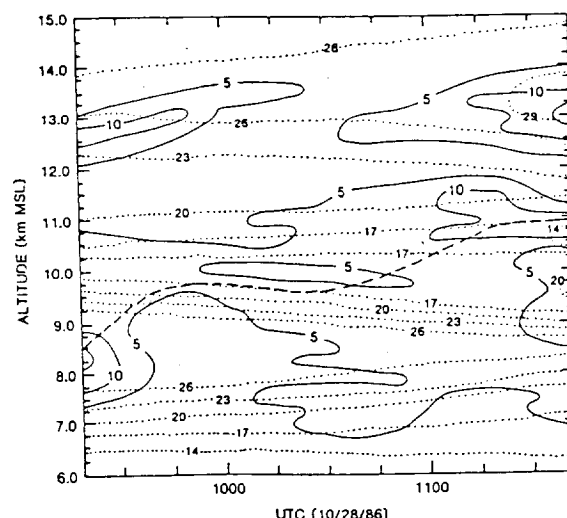


Fig. 2 A 2-layer region of enhanced backscatter. Average optical thickness was ~ 0.03 . Backscatter cross section (—) in $10^{-8} \text{ m}^{-1} \text{ sr}^{-1}$, optical mid-cloud altitude (---), wind speed (···) in m/s. Although wind profiles differ from fig. 1, correlations between wind and backscatter are still evident.

MOISTURE AND HEAT BUDGETS OF A CIRRUS CLOUD FROM AIRCRAFT MEASUREMENTS DURING FIRE

Ismail GULTEPE and Andrew HEYMSFIELD
National Center For Atmospheric Research¹
P.O. Box 3000
Boulder, Colorado 80307

1. INTRODUCTION

Increasing knowledge of cirrus cloud properties can contribute to general circulation model development and ultimately to a better understanding of climate. The objective of this study is to gain a better understanding of cirrus cloud characteristics. Observations from different sensors during the FIRE (First ISCCP (International Satellite Cloud Climatology Program) Regional Experiment) which took place in Wisconsin over Oshkosh (Starr, 1987) together with pertinent calculations will be used to understand the dynamical, microphysical, and radiative characteristics of these clouds.

2. SYNOPTIC CONDITIONS

Cirrus clouds on 31 October over Wisconsin formed in a thermally stable atmosphere. A cold front moved over the Wisconsin region at 0600 UTC. The winds were averaging 50

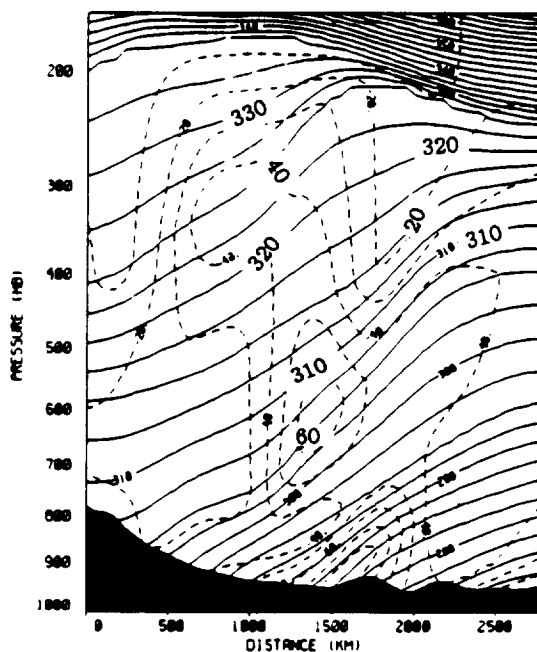


Figure 1. A cross section parallel to the jet stream at 12:00 UTC on 31 October 1986. Wisconsin region is between 1500 and 2000 km. The solid lines are for isentropic surfaces and the dashed lines are for relative humidity with respect to water.

¹ The National Center for Atmospheric Research is sponsored by the National Science Foundation.

m s^{-1} at 300 mb at 1200 UTC over Wisconsin. There was a weak upper level trough which deepened at 0000 UTC on 1 November. The cirrus cloud was situated between 400 and 300 mb over Wisconsin approximately between 1400 UTC and 1830 UTC on 31 October. Moisture advection from the southwest probably played an important role in the cirrus formation (see Figure 1) over Wisconsin.

3. MEASUREMENTS

The data for this research were taken by the NCAR King Air and rawinsondes on 31 October 1986 over Oshkosh. The primary measurements from the NCAR King Air were ice crystal concentration, size, habit, temperature, pressure, dew point, horizontal and vertical wind speed and direction, and infrared and solar radiances. The raw measurements were available for calculations at a rate of 1 Hz.

Two different flight patterns are used in this study: the first is the step-up maneuver and the second is the Lagrangian descent maneuver. The length of each constant altitude penetration was about 30 km and the separation in the vertical between two penetrations was about 300 m. The second maneuver called the Lagrangian spiral descent covered a time period of about 20 minutes (1616–1633 UTC for spiral I and 1657–1720 UTC for spiral II) for an entire cloud sounding on 31 October 1986. During these spirals, the aircraft descent rate was about 1.5 m s^{-1} .

4. METHODS OF ANALYSIS

In this section, the moisture and heat budget equations including internal sources (e.g., ice crystal growth) and external sources (e.g., radiative flux divergence) are given. The most important parameter in the budget equations is vertical velocity w . Therefore, first we explain its calculation in the following subsection. Then, different terms (e.g., advection and turbulent flux divergence) in the budget equations are discussed.

a. Vertical velocity calculation from hydrometeor data

Vertical velocity w used in the budget equations is calculated from the particle size spectra measurements. The simultaneous solution technique (Heymsfield, 1977) is used to obtain w . This technique requires the following terms derived from the PMS 2D-C probe measurements: ice water content (IWC), precipitation rate (PR), and terminal velocity (V_t) which are all dependent on habit. This technique does not need dew point temperature measurements.

b. Moisture budget calculation

The moisture budget for a cirrus cloud is calculated from the continuity equation of the water vapor mixing ratio. To the equations used by Wilfried (1984), we add two more terms: the vertical turbulent flux of the moisture and the ice crystal growth rate, and write the equation as:

$$\frac{\partial q}{\partial t} + \bar{U} \frac{\partial q}{\partial s} + \bar{w} \frac{\partial q}{\partial z} + \frac{\partial \overline{w'q'}}{\partial z} + \frac{\partial w_i}{\partial t} \frac{1}{\rho_a} = 0, \quad (1)$$

where t is the time, q the vapor mixing ratio, s the length along the aircraft longitudinal axis, z altitude. In Equation (1), the first term is the local change of the vapor mixing ratio, the second the horizontal advection, the third the vertical advection, the fourth the divergence of the turbulent moisture flux, and the last term the loss of moisture because

of the growth of ice crystals ($\frac{\partial w_i}{\partial t}$). The first term is calculated from two Lagrangian spiral descents which are separated from each other by approximately 43 minutes. The second term is obtained from the product of the longitudinal wind \bar{U} with respect to cloud and the change of the mixing ratio over the constant flight leg. The \bar{w} in the third term is average vertical velocity. Perturbations (*e.g.*, w') are obtained from the measured (w) by subtracting the average (*e.g.*, \bar{w}). The $\frac{\partial q}{\partial z}$ is obtained from q at two constant altitudes (from the step-up maneuver). The fourth term is calculated from the vertical variation of the turbulent flux at two constant altitudes. The depletion of vapor from the environment because of ice crystal growth is determined from equations given by Heymsfield (1975). The ρ_a in the last term is air density.

c. Heat budget calculation

The calculation of the heat budget of a cirrus cloud is also obtained from the continuity equations used by Telford and Warner (1964) with four additional terms as follows:

$$\frac{\partial \theta}{\partial t} + \bar{U} \frac{\partial \theta}{\partial s} + \bar{w} \frac{\partial \theta}{\partial z} + \frac{\partial \overline{w'\theta'}}{\partial z} + \left(\frac{\partial \theta}{\partial t} \right)_{IR} + \left(\frac{\partial \theta}{\partial t} \right)_{SW} + \frac{\partial w_i}{\partial t} \frac{L_s}{\rho_a C_p} = 0, \quad (2)$$

where the first term is the local change of potential temperature θ , the second the horizontal temperature advection, the third the vertical temperature advection, the fourth the vertical divergence of temperature flux. The fifth and sixth respectively are the local change of temperature due to the IR and SW radiative fluxes and the last term the latent heat release because of the ice crystal growth. In this term, L_s is the latent heat of sublimation and C_p the specific heat at constant pressure. The first term is obtained from the Lagrangian spiral descent profiles as discussed previously for the moisture budget. The over bar in (2) signifies the constant altitude flight leg (30 km) averages of the various parameters. The radiative cooling rate due to the IR and SW radiative flux divergences is calculated from the IR and SW upward and downward looking radiometers. The radiative cooling rate is obtained from the following equation (Welch *et al.*, 1980):

$$\left(\frac{\partial \theta}{\partial t} \right)_{IR,SW} = - \frac{(\frac{\partial F}{\partial z})_{IR,SW}}{C_p \rho_a}, \quad (3)$$

where F is measured irradiance.

5. RESULTS AND CONCLUSIONS

a. Relative importance of the moisture budget terms

The moisture budget of the cirrus on 31 October is calculated from (1). The terms used in (1) are the local change, horizontal and vertical advections, turbulent flux divergence, and ice crystal growth terms.

The values of the terms in the moisture budget equations are shown in Table 1. The layers from I to V in this table are between 7.9 and 9.4 km altitude with a vertical separation approximately 300 m. The negative (positive) sign indicates the moisture convergence (divergence) due to the advection. Moisture convergence is seen at low levels. At the upper levels, moisture divergence is more important. The sum of the terms in the layers,

excluding the local change term, gives a divergence of $0.031 \text{ mg kg}^{-1} \text{ s}^{-1}$ which is very close to the local change term. Moisture convergence is seen at layers II, III, and IV. The sum of the vertical moisture advection values results in a convergence of about $-0.095 \text{ mg kg}^{-1} \text{ s}^{-1}$. Turbulent flux divergence is one order of magnitude lower than other terms in the moisture budget equation. Turbulent flux divergence values add to about $0.003 \text{ mg kg}^{-1} \text{ s}^{-1}$. As a negative source (moisture divergence), ice crystal growth plays relatively an important role on the expenditure of vapor from the environment at mid-layers. The small residual value of about $0.002 \text{ mg kg}^{-1} \text{ s}^{-1}$ is probably due to errors in the wind component and the dew point measurements.

b. Relative importance of the heat budget terms

The heat budget of the cirrus cloud on 31 October is calculated from (2). The terms in the heat budget equation (see Table 2) are the local change, horizontal and vertical advection, turbulent flux divergence, ice crystal growth rate, and IR and SW flux divergence. A layer number in this table has the same meaning for those used in Table 1.

Negative values of the terms used in this section will represent cooling in the cirrus layers. Cold air advection in the lowest layer is about $8^{\circ}\text{C day}^{-1}$. Warm air advection is seen in layers III and V. The net warming due to the horizontal advection term through the layer is found to be about $0.5^{\circ}\text{C day}^{-1}$. The vertical heat advection is the most important term in the heat budget equation. Values of the turbulent flux divergence and ice crystal growth terms are about the same, but they are much smaller than the other terms in (2). The magnitude of the growth term for the entire cirrus is greater than that of the absolute radiative flux divergence terms in (2). The IR cooling rate shows that the cirrus cloud is warming at cloud base with cooling in the upper levels. The maximum cooling rate is found to be about $14^{\circ}\text{C day}^{-1}$ in layers III and IV, and warming about $7^{\circ}\text{C day}^{-1}$ in layer I. The IR cooling rate for the entire cirrus cloud is about $5^{\circ}\text{C day}^{-1}$. The SW cooling rate shows that the cirrus is cooling at cloud top and base. At mid-levels, a warming of about $8^{\circ}\text{C day}^{-1}$ and a similar cooling occurs in the adjacent layers. The sum of the IR and SW cooling rates for the entire cirrus cloud shows that the net cooling is about $1.1^{\circ}\text{C day}^{-1}$. Error in IR and SW irradiance measurements can be as much as 15% and 50%, respectively. The residual of about $7.0 \times 10^{-4}^{\circ}\text{C s}^{-1}$ between the local cooling rate and the sum of the other terms in (2) can be attributed to errors in the aircraft measurements.

Overall, it appears that the dynamic characteristics of the environment play a crucial role in the structure of the cirrus cloud. The IR cooling rate and release of latent heat are important in the upper layers, indicating higher ice crystal growth rates.

REFERENCES

- Heymsfield, A.J., 1975: Cirrus uncinus generating cells and the evolution of cirriform clouds. Part I: Aircraft measurements of the growth of the ice phase. *J. Atmos. Sci.*, 32, 789–808.
- , 1977: Precipitation development in stratiform ice clouds: A microphysical and dynamical study. *J. Atmos. Sci.*, 34, 367–381.
- Kahn, P.M., and H.K. Weickmann, 1969: High altitude radiometric measurements of cirrus. *J. Appl. Meteor.*, 147–154.
- Starr, D. O'C., 1987: A cirrus cloud experiment: Intensive field observations planned for FIRE. *Bull. Amer. Meteor. Soc.*, 68, 119–124.

Telford, J.W., and J. Warner, 1964: Fluxes of heat and vapor in the lower atmosphere derived from aircraft observations. *J. Atmos. Sci.*, 21, 539-548.

Welch, R.M, S.K. Cox, and W.G. Zdunkowski, 1980: Calculations of the variability of ice cloud radiative properties at selected solar wavelengths. *Appl. Opt.*, 19, 3057-3066.

Wilfried, B., 1984: *Evaporation Into the Atmosphere*. Published by D. Reidel Publishing Company, P.O. Box 17, 3300 AA Dordrecht Holland, 293 pp.

Table 1. The terms used in the moisture budget equation except the local cooling rate (see text for detailed discussion).

LAYER	$U \frac{\Delta q}{\Delta z}$ [mg kg ⁻¹ sec ⁻¹]	$\bar{w} \frac{\Delta \bar{q}}{\Delta z}$ [mg kg ⁻¹ sec ⁻¹]	$\frac{1}{\rho_a} \frac{\Delta w_i}{\Delta t}$ [mg kg ⁻¹ sec ⁻¹]	$\frac{\Delta(\bar{w}'q')}{\Delta z}$ [mg kg ⁻¹ sec ⁻¹]
I	-0.04	0.003	0.0062	-0.0098
II	-0.018	-0.041	0.0073	0.0057
III	0.05	-0.028	0.0056	0.0047
IV	0.031	-0.049	0.0053	-0.0023
V	0.008	0.020	0.0034	0.0054
TOTAL	0.031	-0.095	0.0284	0.003

Table 2. The terms used in the heat budget equation except the local cooling rate (see text for detailed discussion).

LAYER	$\bar{U} \frac{\Delta \theta}{\Delta z} \times 10^{-4}$ [°C sec ⁻¹]	$\bar{w} \frac{\Delta \bar{\theta}}{\Delta z} \times 10^{-4}$ [°C sec ⁻¹]	$\frac{\Delta \bar{w}'\theta'}{\Delta z} \times 10^{-4}$ [°C sec ⁻¹]	$\frac{L_i \Delta \bar{w}_i}{C_p \rho_a} \times 10^{-4}$ [°C sec ⁻¹]	$(\frac{\Delta \theta}{\Delta t})_{IR} \times 10^{-4}$ [°C sec ⁻¹]	$(\frac{\Delta \theta}{\Delta t})_{SW} \times 10^{-4}$ [°C sec ⁻¹]
I	-0.94	-1.31	0.20	0.18	0.80	-0.19
II	-0.1	-3.10	0.04	0.21	-1.39	1.05
III	0.29	-4.40	-0.07	0.16	1.50	-0.98
IV	0.05	-6.09	0.14	0.17	-1.45	0.97
V	0.85	-2.59	0.01	0.10	-0.06	-0.38
TOTAL	0.05	-17.50	0.32	0.82	-0.60	0.47

	PAGE
C02.01 The 27-28 October 1986 FIRE Cirrus Case Study: Meteorology and Clouds Starr, David O'C., and Donald P. Wylie	341
C02.02 Satellite-Derived Cloud Fields During the FIRE Cirrus IFO Case Study Heck, Patrick W., Gary G. Gibson, Patrick Minnis, and Edwin F. Harrison	345
C02.03 Comparison of Surface-Derived and ISCCP Cloud Optical Properties <u>Whitlock, C. H.</u> , L. R. Poole, S. R. LeCroy, W. B. Rossow, K. L. Bell, D. A. Robinson, and C. Grund	351
C02.04 The October 27-28, 1986, FIRE Cirrus Case Study: Cloud Microstructure Miller, Karen M., Andrew J. Heymsfield, and James D. Spinhirne	357
C02.05 Cirrus Microphysics and Radiative Transfer: Cloud Field Study on October 28th, 1986 Kinne, Stefan, Thomas P. Ackerman, Andrew J. Heymsfield, Francisco P. J. Valero, Kenneth Sassen, and James D. Spinhirne	363
C02.06 The 27-28 October 1986 FIRE IFO Cirrus Case Study: Comparison of Satellite and Aircraft Derived Particle Size Wielicki, Bruce A., J. T. Suttles, Andrew J. Heymsfield, Ronald M. Welch, James D. Spinhirne, Man-Li C. Wu, David O'C. Starr, Lindsay Parker, and Robert F. Arduini	369
C02.07 Cirrus Radiative Characteristics and the Radiative Impact of Small Particles <u>Stackhouse, Jr. Paul W.</u> , Graeme L. Stephens, and S. K. Cox	375
C02.08 Regional Conditions During the 25 October 1986 FIRE Cirrus/Alto cumulus Case Study Starr, David O'C., and Kenneth Sassen	381

The 27-28 October 1986 FIRE Cirrus Case Study: Meteorology and Clouds

David O'C. Starr
NASA Goddard Space Flight Center
Greenbelt, MD

and

Donald P. Wylie
Space Science and Engineering Center
University of Wisconsin
Madison, WI

Submitted to *Monthly Weather Review*
March, 1989.

ABSTRACT

Detailed descriptions of the rawinsonde-resolved meteorological conditions (3-hourly soundings) associated with a succession of five distinct mesoscale cirrus cloud regimes, that were intensively observed over a 36-hour period, are given. The synoptic scale systems in which these features were embedded are described and a brief overview of the experiment is given. Regional analyses of the static stability structure and vertical motion are presented and interpreted with respect to the characteristics of the corresponding cloud fields as deduced from satellite and lidar observations. The cloud fields exhibited a high degree of persistent mesoscale organization on scales of 20-500 km reflecting corresponding scales of dynamic and thermodynamic structure/variability as on the synoptic scale. Cloud generation was usually confined to layers less than 1 km deep (typically 0.5-km in depth) and cellular organization was evident in most cases irrespective of the thermal stratification. Multilayered development was prevalent (2-3 layers) and was associated with vertical structure of the temperature and moisture fields resulting primarily from vertical gradients in horizontal advection. One convective generation layer was usually present. Destabilization resulted primarily from advective processes that also led to the formation of a transient stable layer above and/or below the convective layer. Though resembling elevated frontal surfaces, the stable layers were not extensions of surface features. Cloud processes, primarily ice particle fall-out and evaporation but also including cloud top detrainment, contributed to generating the multilayered structure. Two cases of clouds spawned from an overlying cloud deck were seen where one involved natural seeding of an ice-saturated and conditionally unstable layer in which vigorous convective development was subsequently observed. Subvisual cirrus in the lower stratosphere were found to be associated with prior tropopause features (upwind) where denser cirrus existed. Inferences are drawn with respect to the parameterization of cirrus in large-scale models. In particular, vertical resolution on the order of 0.5 km will probably be required to adequately resolve the forcing required for implementation of a physically-based parameterization. Greater understanding of the nature and causes of the observed mesoscale structure is also needed.

SUMMARY AND CONCLUSIONS

The cirrus clouds observed on 27-28 October 1986 during the FIRE Cirrus Intensive Field Observation campaign were organized on a wide range of spatial scales. Three synoptic scale systems were identified: the "ridge-crest" cloud, the "ridge-axis" cloud band and the "baroclinic leaf" cloud. Each of these interconnected and long-lived cloud features had a length scale of 1000 km or more. Relative to the position of a weak low level cyclone, the ridge-crest cloud occurred to the northeast of the cyclone center and surface warm front, the ridge-axis cloud overlay a persistent weak trough in the surface pressure field and the baroclinic leaf cirrus shield was associated with the pre-cold frontal region. However, these extensive cloud systems resulted from upper level processes. Ageostrophic flow (slightly cross-isobaric) within a region extending from just upwind of the large-scale ridge axis (and over the ridge-crest) back toward the following trough axis was responsible for weak ascent and the resultant moisture supply to the large-scale cloud systems. The approximate coincidence of surface features and upper level cloud features reflects their common causes and mutual development rather than indicating a simple cause-effect relationship.

A high degree of persistent mesoscale organization was evident within each of the larger scale cirrus features. At least five distinct mesoscale regimes were intensively observed during the two-day period. Mesoscale uncinus complexes (after Sassen *et al.*, 1989a) in the form of longitudinal bands (20 km in width) along the ambient wind direction but propagating in the transverse direction in correspondence with the movement of the large-scale upper air pattern were observed during the early afternoon of the 27th. They were associated with the entrance region of a strong jet stream core and constituted the leading edge of the ridge-crest cloud that passed mostly to the north of the experiment area. Individual bands were maintained for up to nearly six hours. Later, patches of dissipating cirrus were observed that had formed near the juncture of the three large-scale cirrus systems. During the night, another banded and well-developed mesoscale uncinus complex was observed (Grund and Eloranta, 1989). On the 28th, a large mesoscale cloud system dominated (500 km across). Observations were made of the pre-disturbance cirrus and thin altocumulus and of the denser cirrus and cirriform altocumulus within the disturbance. The large wedge-shaped mesoscale cloud feature was embedded within the synoptic scale baroclinic leaf system and was evident for more than 12 hours. Later, irregular mesoscale patches (50 km across) of significantly enhanced cirrus were observed within the trailing portion of the baroclinic leaf cirrus shield. Other distinct mesoscale cirrus features were also evident as they propagated along the upwind edge of the baroclinic leaf region and had the typical "comma" shape often associated with extensive cirrus shields on the synoptic scale.

The high degree of mesoscale organization in the observed cirrus cloud fields was a manifestation of significant mesoscale structure in the dynamics and thermodynamics of the upper troposphere as shown by our analysis of the available rawinsonde data. Large-scale processes created a favorable environment for the realization of cloud features in association with this structure. The dominance of mesoscale processes, found here and in other recent studies (Sassen *et al.*, 1989a), has significant implications with respect to the parametric representation of cirrus clouds in large-scale atmospheric models. For example, even using three-hourly rawinsonde observations, analyses of the conditions associated with the 500-km disturbance observed on the 28th were unable to quantitatively diagnose the corresponding forcing (upward vertical motion) although there was strong evidence for ascent based on single station analyses. A judiciously placed special rawinsonde site would probably have allowed us to resolve this forcing. The diagnosed vertical motions for the two regimes observed on the 27th and the last regime on the 28th were quite reasonable and likely reflect the smaller amplitude of mesoscale variations of vertical velocity during these events.

Greater understanding of the origin and nature of the mesoscale cloud systems and the responsible dynamic processes is needed. If strong mesoscale organization is an important global

characteristic of cirrus, this must be taken into account in parametric treatments of cirrus for large-scale atmospheric models. We recommend that studies on this topic be initiated.

Another significant conclusion with respect to the structure of the cirrus cloud systems is that cloud generation typically occurred at multiple levels. This tendency for multilayered cloudiness conflicts with the assumption of a single cloud layer that is often invoked in the design of cloud retrieval algorithms for application to satellite observations. Furthermore, the depth of individual generating layers ranged from less than 0.5 km to about 1 km. If the tendency for multilayered structure and shallow cloud generation layers is widely prevalent, there are important ramifications for modeling cirrus. We suggest that the vertical resolution in mesoscale "cloud process" models (e.g., Starr and Cox, 1985a) should be on the order of 50 m to adequately capture the true character of the cloud generation and maintenance processes. It is also clear that the vertical resolution of large-scale atmospheric models must also be compatible with the observed scales in order that diagnosis of cirrus generation proceed from physical principles (Starr, 1987a). Otherwise, the parametric treatment must also account for the important effects of unresolved vertical structure of essentially large-scale model parameters in determining cloud response. Based on this case study, a vertical resolution of about 0.5 km is needed. Substantial improvements in the resolution of jet streams and interactions between the upper and lower troposphere would also very likely result.

Very detailed analyses of the rawinsonde soundings have been presented and compared to qualitative physical descriptions of cloud structure derived from the extensive cloud lidar observations reported in Sassen *et al.* (1989b). In essence, we have attempted to understand why the clouds occurred and what determined their character. This task was greatly complicated by the lack of horizontal resolution of the sonde data. This was compounded by the rather poor vertical resolution of standard rawinsonde data at middle and upper tropospheric levels that made it difficult to unambiguously identify similar features at different locations and times. The enhanced temporal resolution (3-hourly soundings) was crucial and somewhat compensated for the deficiencies in spatial resolution. We also benefited greatly from the availability of high vertical resolution data routinely obtained at a special supplemental rawinsonde site. Despite the inherent uncertainties and the lack of moisture data at high levels, good correspondence between observed thermodynamic and dynamic structure and the cloud observations was found.

The lidar observations reported in Sassen *et al.* (1989b) revealed that small scale cellular structures (0.5 to 2 km in width) were prevalent in most of the observed cirrus strata. In some cases, we were able to identify a corresponding layer of nearly neutral thermal stratification. When free convection was indicated, it was common to find some cells penetrating significantly into overlying stably stratified layers. A thin cirrostratus layer usually occurred at about the height of the highest cell tops. The underlying layer was often conditionally unstable though generally dry. Evaporation of falling ice crystals (precipitation streamers) may have contributed significantly to its destabilization. However, cellular structures were also found when there was no evidence of convective instability. Maintenance of these structures, likely initiated by shear-induced small scale waves, may have resulted from the effects of latent and radiative heating patterns as shown by Starr and Cox (1985b). Alternatively, local pulsations in microphysical processes (crystal nucleation, growth and fallout) in a sheared environment might be responsible, as shown in Sassen and Dodd (1989). Nonetheless, it is important to note that cellular convective-appearing structure does not always indicate the presence of free convection although it often does. Furthermore, layers of conditional instability are more likely to be associated with the precipitation zone than with the cloud generation layer itself. More-detailed considerations of the nature and origin of observed cellular structure are possible based upon the aircraft observations as in Heymsfield *et al.* (1989) and Smith *et al.* (1989).

Differential (in the vertical) temperature advection appears to have been an important factor in producing the static stability structures that were found to be highly related to cloud generation

and character. In this respect, the effects of vertical shear of the horizontal wind speed associated with embedded jet flows were paramount on the 27th while temperature gradients associated with a pool of relatively warm air were important on the 28th. Vertical structure in diabatic heating (and cooling) associated with cloud processes was also significant in this respect. In some instances, the region of cloud formation could be characterized as strongly resembling a frontal overrunning situation, i.e., ascent and destabilization over a sloped elevated layer of substantial static stability. However, the underlying stable layer was transient and not an extension of a surface front. Rather, it appeared to form somewhat in place through a frontogenetic process driven by vertical gradients in horizontal temperature advection.

Evidence was found for cloud-spawned multilayered development resembling the subcloud moistening and destabilization mechanism hypothesized by Starr and Cox (1985b). Late on the 28th, an initial non-convective cirrus layer appeared to spawn a highly convective cirrus layer below. Natural cloud seeding may have played an important role in the development of the 2-km deep cirriform altocumulus within the mesoscale disturbance on the 28th. Glaciation and growth of large crystals in a stably stratified thin altocumulus layer (pre-disturbance) likely led to natural cloud seeding of an underlying ice-saturated and conditionally unstable layer resulting in cloud formation and vigorous convection extending upward through the initial cloud layer. In each case, generation of the lower cloud layer may be partly attributed to the ice fallout process associated with the presence of relatively large particles in the spawning cloud layer.

Another interesting aspect of this case study is that subvisual cirrus were observed on the 27th in a stably stratified layer in the lower stratosphere. These "clouds" were a residual (mostly evaporated) of subtropopause cirrus formed upwind in association with a higher tropopause and had advected over the lower tropopause that was forming. The temperature lapse rate in the upwind source region was more tropospheric. The juxtaposition of tropopauses in the vicinity of the subvisual cirrus and the rapidly changing stratification in the intervening layer coincided with the presence of a strong jet core at the lower pause and a secondary wind maximum above.

We acknowledge that uncertainties exist in our analyses and interpretations. Nonetheless, the information and insights represent important and unique inputs for model-based efforts to understanding of cirrus. For example, suitably initialized cloud process models may be used to investigate relationships between atmospheric structure and local cloud response for the variety of situations comprising this case. Results of such simulations can be compared to the observed cloud properties to provide a basis for model improvement and validation. Efforts in this area are planned. The available data base will be even greater after additional case studies of the 1986 FIRE Cirrus IFO observations are completed.

- Heymsfield, A.J., K.M. Miller and J.D. Spinhirne, 1989: The 27-28 October 1986 FIRE Cirrus Case Study: Cloud microstructure. (submitted to *Mon. Wea. Rev.*)
- Grund, C. J., and E.W. Eloranta, 1989: The 27-28 October 1986 FIRE Cirrus Case Study: Cloud optical properties determined by high spectral resolution lidar. (submitted to *Mon. Wea. Rev.*)
- Sassen, K., D.O.C. Starr and T. Uttal, 1989a: Mesoscale and microscale structure of cirrus clouds: Three case studies. *J. Atmos. Sci.*, **46**, 371-396.
- Sassen, K., C.J. Grund, J.D. Spinhirne, M. Hardesty and J.M. Alvarez, 1989b: The 27-28 October 1986 FIRE Cirrus Case Study: A five lidar overview of cloud structure and evolution. (submitted to *Mon. Wea. Rev.*)
- Sassen, K., and G.C. Dodd, 1989: Haze particle nucleation simulations in cirrus clouds, and applications for numerical modeling and lidar studies. (submitted to *J. Atmos. Sci.*)
- Smith, W.L., P. Hein and S.K. Cox, 1989: The 27-28 October 1986 FIRE Cirrus Case Study: In situ observations of radiation and dynamic properties of a cirrus cloud layer. (submitted to *Mon. Wea. Rev.*)
- Starr, D.O.C., and S.K. Cox, 1985a: Cirrus clouds, Part I: A cirrus cloud model. *J. Atmos. Sci.*, **42**, 2663-2681.
- Starr, D.O.C., and S.K. Cox, 1985b: Cirrus clouds, Part II: Numerical experiments on the formation and maintenance of cirrus. *J. Atmos. Sci.*, **42**, 2682-2694.
- Starr, D.O.C., 1987a: A cirrus cloud experiment: Intensive field observations planned for FIRE. *Bull. Amer. Meteor. Soc.*, **67**, 119-124.

SATELLITE-DERIVED CLOUD FIELDS DURING THE FIRE CIRRUS IFO CASE STUDY

Patrick W. Heck and Gary G. Gibson
Aerospace Technology Division, Planning Research Corporation
Hampton, Virginia 23666

Patrick Minnis and Edwin F. Harrison
Atmospheric Sciences Division, NASA Langley Research Center
Hampton, Virginia 23665-5229

1. Introduction

The First ISCCP Regional Experiment (FIRE) Cirrus Intensive Field Observation (IFO) program measured cirrus cloud properties with a variety of instruments from the surface, aircraft, and satellites. Surface and aircraft observations provide small-scale point and line measurements of different micro- and macrophysical properties of advecting and evolving cloud systems. Satellite radiance data may be used to measure the areal variations of the bulk cloud characteristics over meso- and large-scales. Ideally, the detailed cloud properties derived from the small-scale measurements should be tied to the bulk cloud properties typically derived from the satellite data. Full linkage of these data sets for a comprehensive description of a given cloud field, one of the goals of FIRE, should lead to significant progress in understanding, measuring, and modeling cirrus cloud systems. In this paper, the relationships derived from intercomparisons of lidar and satellite data by Minnis et al. (1989a) are exploited in a mesoscale analysis of the satellite data taken over Wisconsin during the Cirrus IFO Case Study.

2. Data and Methodology

Daytime half-hourly, 1-km visible (VIS, 0.65 μm) and 4x8-km infrared (IR, 11.5 μm) GOES data were used to construct bispectral histograms on a 0.5° latitude-longitude grid between 42°N and 47°N and 87°W and 92°W during 27-28 October 1986. The VIS data are stored as counts between 0 and 63 which were converted to radiance and reflectance, ρ . The IR data are stored as counts between 0 and 255 which are converted to equivalent blackbody temperature, T . Soundings taken every 6 hours over Green Bay, Wisconsin were used to determine the vertical variation of temperature. Linear interpolation between the soundings was used to estimate the temperatures at each half hour.

The parameters of interest here are cloud amount, C ; cloud-top temperature, T_t ; cloud-center temperature, T_c ; cloud-top height, z_t ; cloud-center height, z_c ; cloud thickness, h ; cloud emittance, ϵ ; VIS optical depth, τ_v , and clear-sky temperature, T_{cs} . The relationships between these parameters during the IFO were explored by Minnis et al. (1989a,b) using combined satellite-lidar data. A simple physical model is used here to relate the observed reflectance to cloud optical depth:

$$\rho = T_a \chi_c \alpha_c + T_c T_u \rho_s + a_{sd}(1 - \alpha_d)(1 - T_c - \alpha_c). \quad (1)$$

Cloud albedo is $\alpha_c = \alpha_c(\tau_v, \mu_0)$; the diffuse cloud albedo is $\alpha_d = \alpha_d(\tau_v)$; and the cloud anisotropic reflectance factor is χ_c . The values for the albedos are determined in the same manner as Minnis et al. (1989b) using the results of Takano and Liou (1989). Values for χ_c are taken from the results of Minnis et al. (1989a). Ozone transmittance above the cloud is T_a ; T_c and T_u are the transmittances of the cloud to direct downward and upward VIS radiation, respectively; ρ_s is the clear-sky reflectance; α_{sd} is the diffuse clear-sky albedo; and μ_0 is the cosine of the solar zenith angle. The infrared optical depth is $\tau_e = 2.17\tau_v$. The effective infrared beam emittance is $\epsilon = 1 - \exp(-\tau_e / \mu)$, where μ is the cosine of the viewing zenith angle. Assuming a pixel is completely cloud-filled,

$$T_c = B^{-1}\{[B(T) - (1 - \epsilon)B(T_{cs})] / \epsilon\}. \quad (2)$$

Details for computing T_t , z_c , z_t , and h are given in Minnis et al. (1989b).

The basic approach to deriving these parameters from a histogram is outlined below.

- 1) Consider all pixels with $T < T_{cs} - 3K$ as cloudy.
 - 2) Assign pixel to altitude level: low, middle, or high (Fig. 1).
 - 3) Compute average reflectance for each temperature in a layer.
 - 4) Compute τ_v for each observed temperature within the layer.
 - 5) Compute T_c , T_t , and ϵ for each observed T in the layer.
 - 6) Compute average T_c , T_t , τ_v , and ϵ for each layer.
 - 7) Compute z_c , z_t , and h for each layer from results of (6).
 - 8) Compute mean values for each variable by combining layer results.
- The functions P_m and P_h describe the VIS-IR thresholds between low and middle and between middle and high cloud, respectively.

3. Results and Discussion

This approach was applied to the lidar-satellite data of Minnis et al. (1989a) to determine the errors in the resulting cloud parameters. A comparison of selected parameters for total cloudiness is shown in Fig. 2 for Fort McCoy data. Figure 3 shows the comparison of the lidar cloud-top heights and the satellite-derived high cloud-top altitudes. The comparison results are summarized in Table 1. The satellite-derived total cloud-center heights agree well with the lidar, on average, while the corresponding cloud-top altitudes are underestimated by 0.5 km. If only high clouds (as detected by the satellite) are considered, the satellite results agree with the lidar values of z_t , but underestimate the values of z_c . These differences may be attributed to several effects. Some midlevel cloudiness may have been within the satellite field of view and still not have advected over the lidar sites. Partially cloud-filled pixels may have decreased the altitudes of some pixels or the values of χ_c may have been inadequate at some hours.

Examples of the derived values of high and midlevel cloud fraction, z_c , and ϵ are shown in Figs. 4 - 7 for 15, 18, and 21 UTC during October 28, 1986. At 15 UTC, most of the clouds are above 6 km (Fig. 4). Midlevel cloudiness is confined to the southern portion of the region (Fig. 5). Average values of z_c range between 7 and 9 km (Fig. 6). The thicker clouds, as determined by the emittances, are primarily in the northern half of the IFO box (Fig. 7). By midday (18 UTC), an area of clearing has moved into central Wisconsin. Cloud-center heights have increased to 11 km in the east while some scattered high and midlevel clouds follow the clearing line. At 21 UTC, the average cloud heights vary from 7 to 9 km again with significant midlevel cloudiness in the northern half of the box. Some mesoscale structure is evident in the emittance fields.

4. Concluding Remarks

The cloud parameters derived with the empirical technique described represent the most accurate, detailed areal cloud properties available for the Case Study. Additional research using other IFO results with theoretical calculations is needed to generalize the technique used here.

REFERENCES

- Minnis, P., J. M. Alvarez, D. F. Young, K. Sassen, and C. J. Grund, 1989a: Interpretation of cirrus cloud properties using coincident satellite and lidar data during the FIRE IFO. Presented at FIRE Annual Meeting/ASTEX Workshop, Monterrey, CA, July 10-14.
- Minnis, P., P. W. Heck, and E. F. Harrison, 1989b: The 27-28 October 1986 FIRE Cirrus IFO case study: Cloud parameter fields derived from satellite data. Submitted to Mon. Wea. Rev.
- Takano, Y. and K. N. Liou, 1989b: Radiative transfer in cirrus clouds: II. Theory and computation of multiple scattering in an anisotropic medium. J. Atmos. Sci., **46**, 21-38.

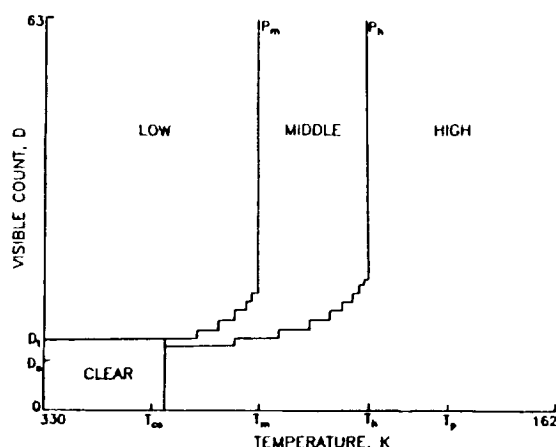


Fig. 1. Schematic diagram of histogram analysis.

Difference (Lidar - Satellite)	bias	rms
Total cloud		
z_c (km)	-0.08	0.94
z_t (km)	0.53	0.90
h (km)	0.29	1.00
ϵ	0.00	0.05
r_v	-0.03	0.13
High clouds only		
z_c (km)	-0.41	1.13
z_t (km)	-0.09	0.63

Table 1. Differences between cloud parameter values derived with lidar-satellite data set and satellite data only.

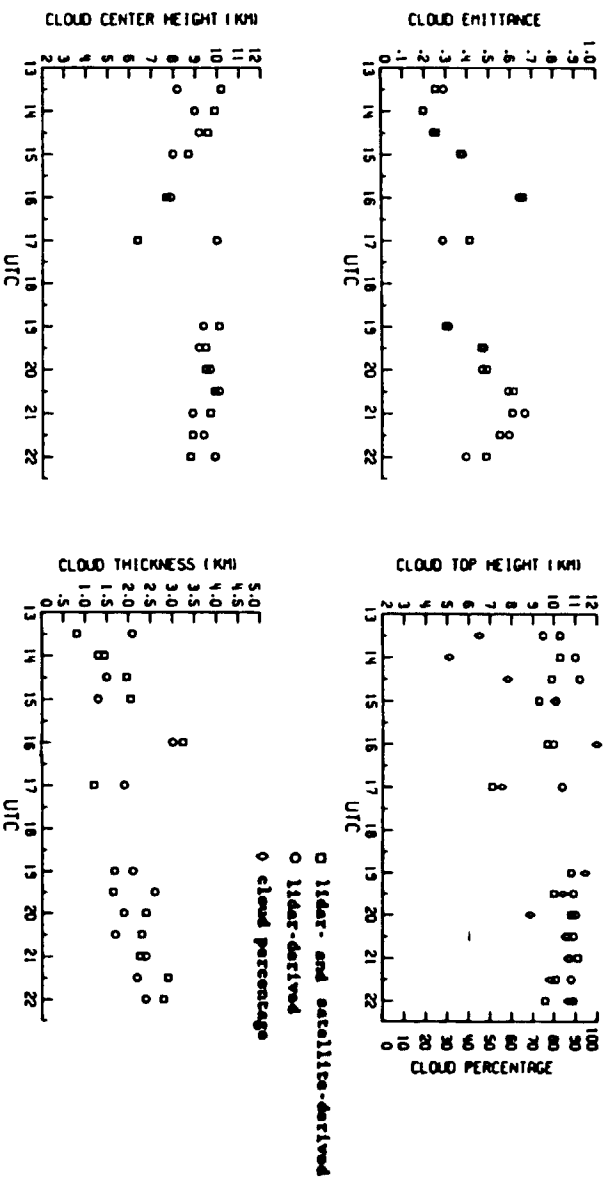


Fig. 2. Comparison of lidar and satellite-derived cloud parameters over Ft. McCoy, WI during October 28, 1986.

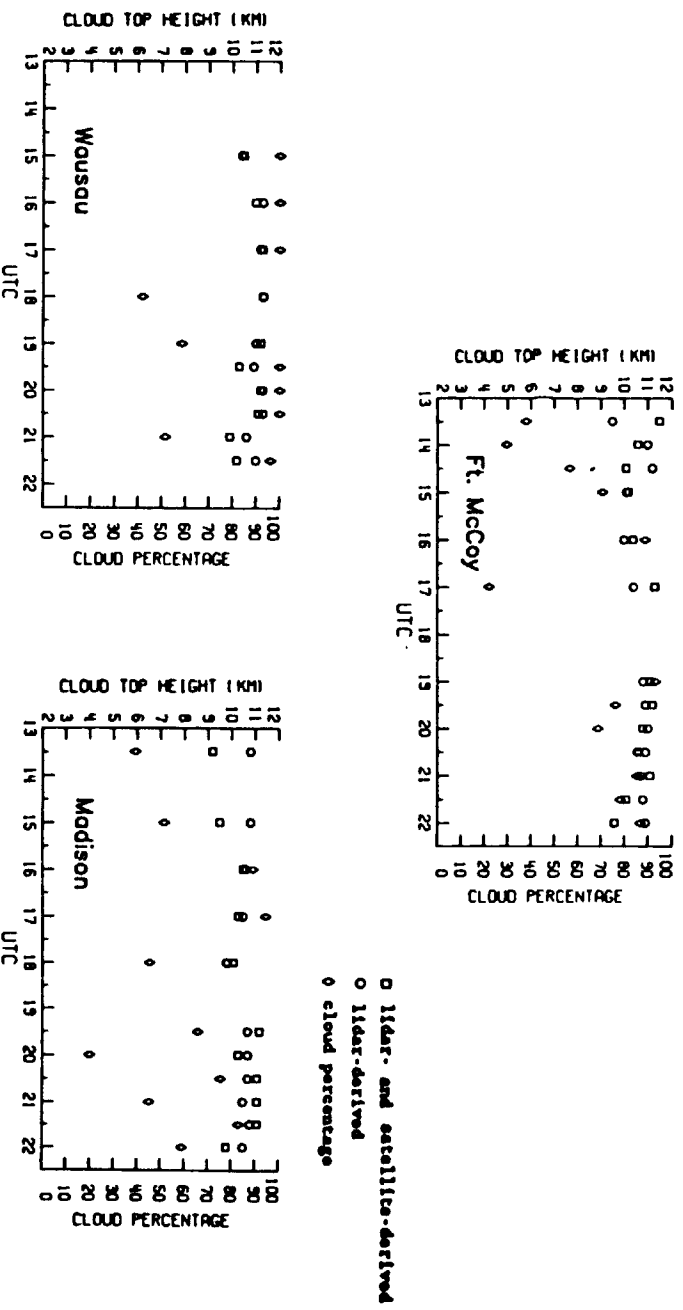


Fig. 3. Comparison of satellite-derived high cloud-top heights with lidar data for October 27-28, 1986.

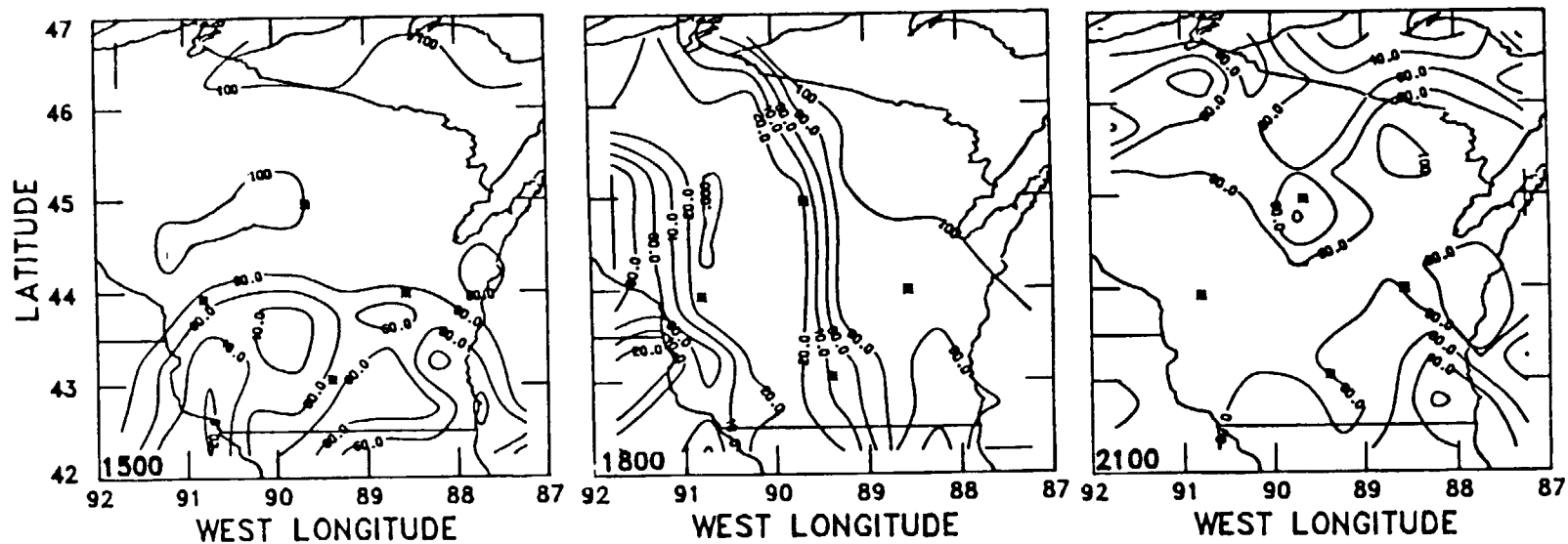


Fig. 4. GOES-derived high cloud amounts (%) for October 28, 1986.

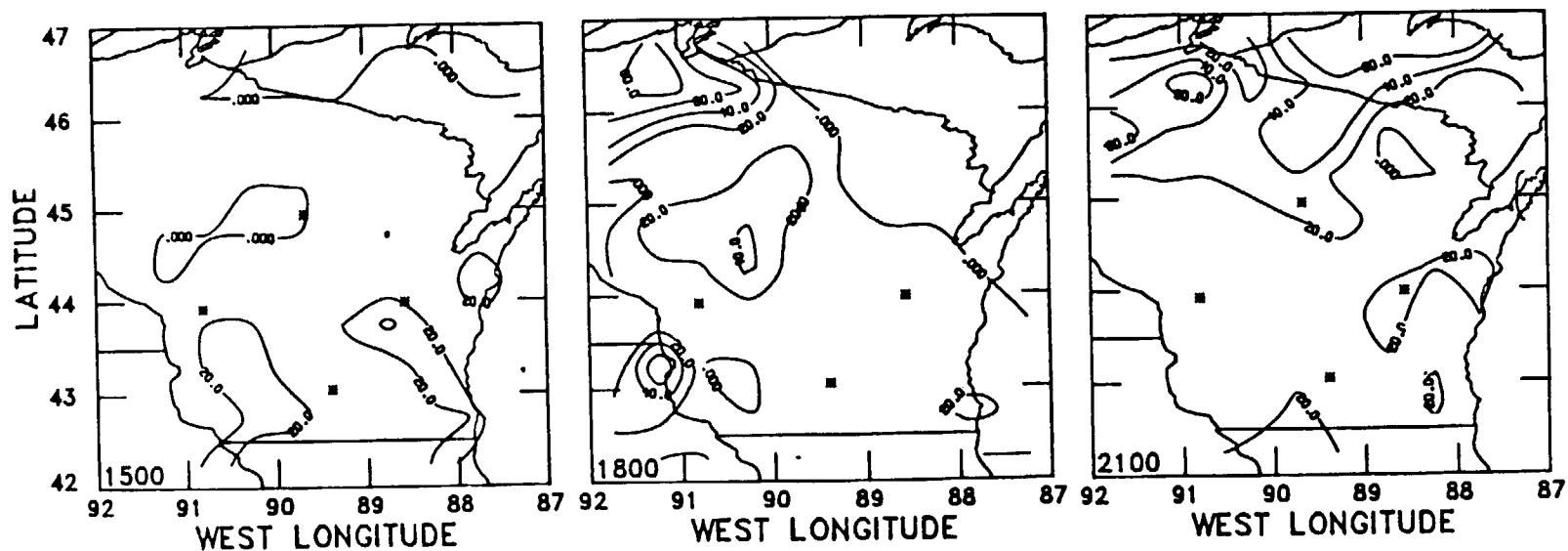


Fig. 5. GOES-derived midlevel cloud amounts (%) for October 28, 1986.

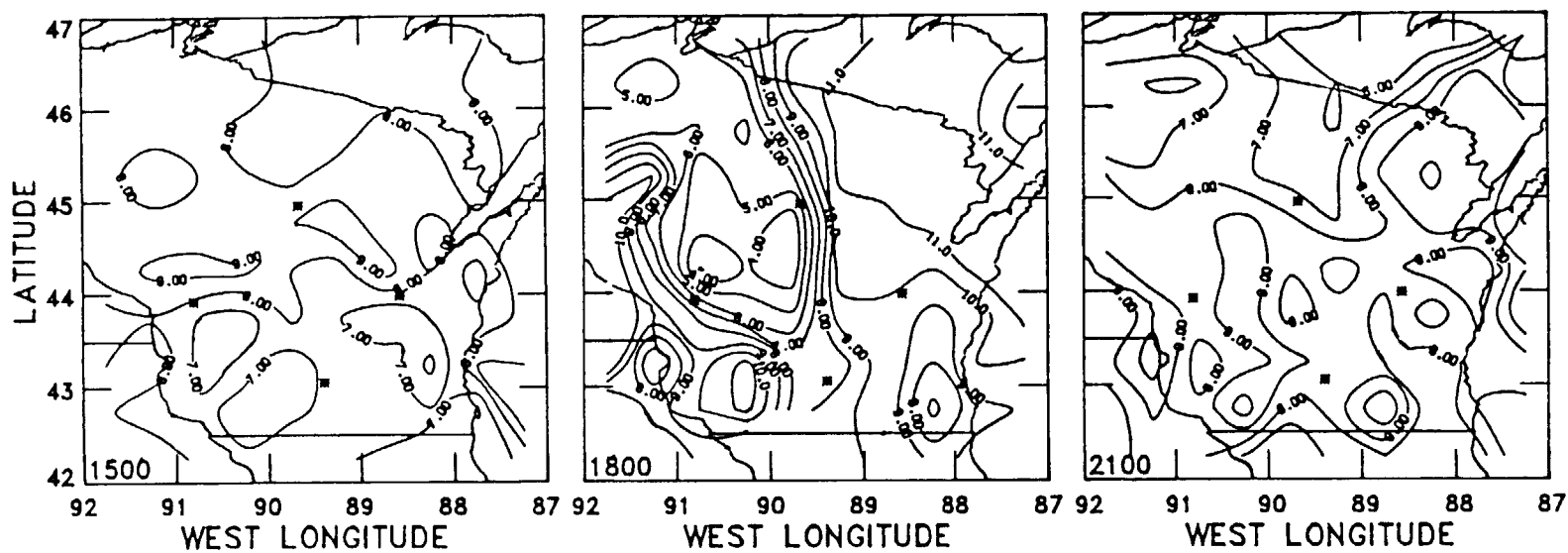


Fig. 6. GOES-derived cloud-center heights (km) for October 28, 1986.

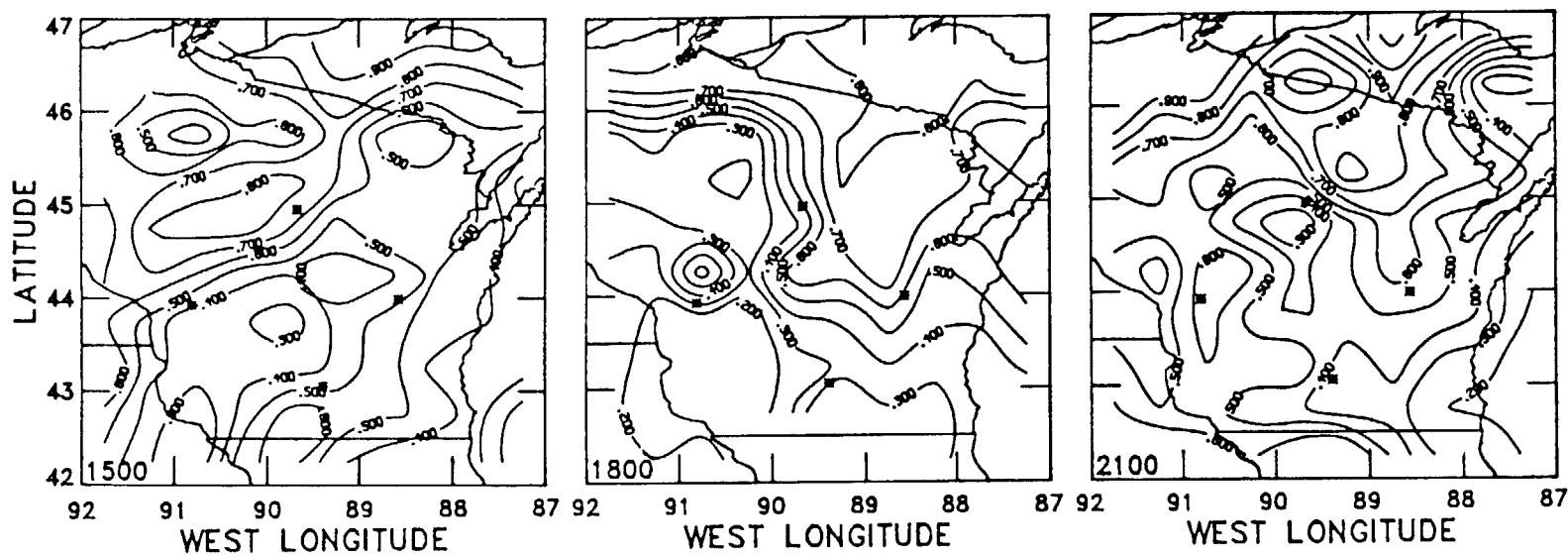


Fig. 7. GOES-derived cloud emittances for October 28, 1986.

COMPARISON OF SURFACE-DERIVED AND ISCCP CLOUD OPTICAL PROPERTIES

C. H. Whitlock and L. R. Poole
Atmospheric Sciences Division
NASA Langley Research Center
Hampton, Virginia 23665-5225

S. R. LeCroy
Planning Research Corporation
Hampton, Virginia 23666

W. B. Rossow and K. L. Bell
NASA Goddard Institute for Space Sciences
New York, New York 10025

D. A. Robinson
Rutgers University
New Brunswick, New Jersey 08903

C. Grund
University of Wisconsin-Madison
Madison, WI 53706

INTRODUCTION - One objective of the FIRE Project is to validate the cloud parameters given on ISCCP tapes. ISCCP first defines whether or not a region is clear or has clouds based on two threshold algorithms. If the region has clouds, then a cloud optical depth is given as well as a cloud height. Special high-resolution ISCCP CX tapes were created for the time period of the Wisconsin FIRE experiment. These tapes did not include the cloud height product, however, other parameters used to make up the standard ISCCP C1 products were available. It is the purpose of this paper to compare the ISCCP cloud/no cloud and cloud optical depth parameters with surface-derived values for the Wisconsin FIRE region during the October 27 and 28 case study days.

DATA - A total of 6 daylight scenes on October 27 and 28 were examined. For sake of brevity, only 3 scenes are presented in this paper to illustrate typical results. Four types of images are presented for each scene as shown in figures 1 through 3.

For each figure, both images on the left side of the figure are based on instrument measurements from the surface at various ground-truth sites during the experiment. Cloud fraction and optical depth are half-hour averages shown as lines based on wind velocity and direction at cloud altitude. Cloud fraction results were obtained from hemispherical surface radiometers. Optical depth values were obtained from a narrow-beam radiometer at Ft. McCoy, a combination of shadow-band and hemispherical radiometers at Wausau, and a lidar at Madison. (See reference 1 for a more complete description of these data and instruments used for the measurements.)

The images on the right side of the figure are based on data from the special ISCCP CX tape. Data are given for pixel locations based on sampling of the basic satellite data every 30 km instead of at the ground truth sites. The pixel locations are held constant for each month, but may change from month to month. Cloud/no cloud conditions were determined using 3 parameters from the CX tapes in the same manner as used to obtain C1 cloud parameters. If the

parameter CLOUD CODE indicated clear, then the "no cloud" condition was assumed. If CLOUD CODE indicated as either undecided, mixed, or cloudy, an additional test was done. If either the VIS THRESHOLD or IR THRESHOLD codes had a value of 4 or 5, it was assumed that "cloudy" conditions existed, otherwise the sky was assumed to be clear. (Undecided clear skies existed on Oct. 27.) A zero value in the ISCCP cloud optical depth image indicates clear sky locations.

RESULTS - Figure 1 is a scene when nearly clear sky conditions existed. Surface cloud fraction values are zero for much of the scene except for the most western site (Ft. McCoy) and patches near the most southeastern site (Madison). The ISCCP data indicates totally clear skies. Review of the original 1-km satellite images indicates that clouds did exist suggesting that the ISCCP procedure may not detect some thin clouds because of either threshold or navigation errors.

Figure 2 is a cirrus cloud day at the same solar angle as figure 1. Surface data show broken or overcast cloud fractions over every site, and most ISCCP locations are indicated as cloudy. Non-zero surface cloud optical depth values are indicated at each station where ground measurements were made. At Wausau, the ISCCP optical depth at a nearby pixel is of the same magnitude as the surface measured value, but a precise comparison is impossible. The Ft. McCoy optical depth value (0.22) is probably of the same magnitude as ISCCP values (between 0 and 0.75), however, ISCCP values near Madison (1.42 - 2.55) appear much larger than the ground truth value of 0.24.

Figure 3 is a cirrus scene with a higher solar angle than figures 1 and 2. Again surface-measured cloud fraction is non-zero, and ISCCP indicates clouds over the central and eastern portions of the region. Surface-measured optical depth at Ft. McCoy is very low, explaining why ISCCP is indicating no clouds in that region. ISCCP cloud optical depth values near Madison range from 0 - 1.73 which may be near the measured value of 0.34. A large discrepancy exists at Wausau, however. ISCCP nearby-pixel values range from 1.82 to 5.45 as compared with a measured value of 0.98. Examination of the original 1-km satellite imagery indicates sharp changes in cloud reflectance around Wausau. Again the satellite pixel to ground station navigation mismatch may be the reason for the large discrepancy in cloud optical depth values.

CONCLUDING REMARKS - Satellite pixel to ground station navigation mismatch precludes a direct quantitative validation of ISCCP cloud/no cloud and cloud optical depth parameters. In a qualitative sense, ISCCP procedures seemed to predict cloud/no cloud conditions reasonably well over grassland and forests, with a slight tendency not to detect very thin clouds. It is not known how well the algorithm operates over more difficult surfaces such as snow and deserts. Accuracy of ISCCP cloud optical depth values is not known. Comparisons were inconsistent with factor of 10 differences in some cases. A revised validation strategy is desirable.

REFERENCE

1. LeCroy, S. R., Whitlock, C. H., Poole, L. R., Alvarez, J. M., Robinson, D. A., Starr, D. O'C., and Cox, S. K.: Surface Radiation Observations of Cirrus Cloud Properties During the Wisconsin FIRE/SRB Experiment. IRS 88: Current Problems in Atmospheric Radiation. A. Deepak Publishing, 1989, pp. 22-25.

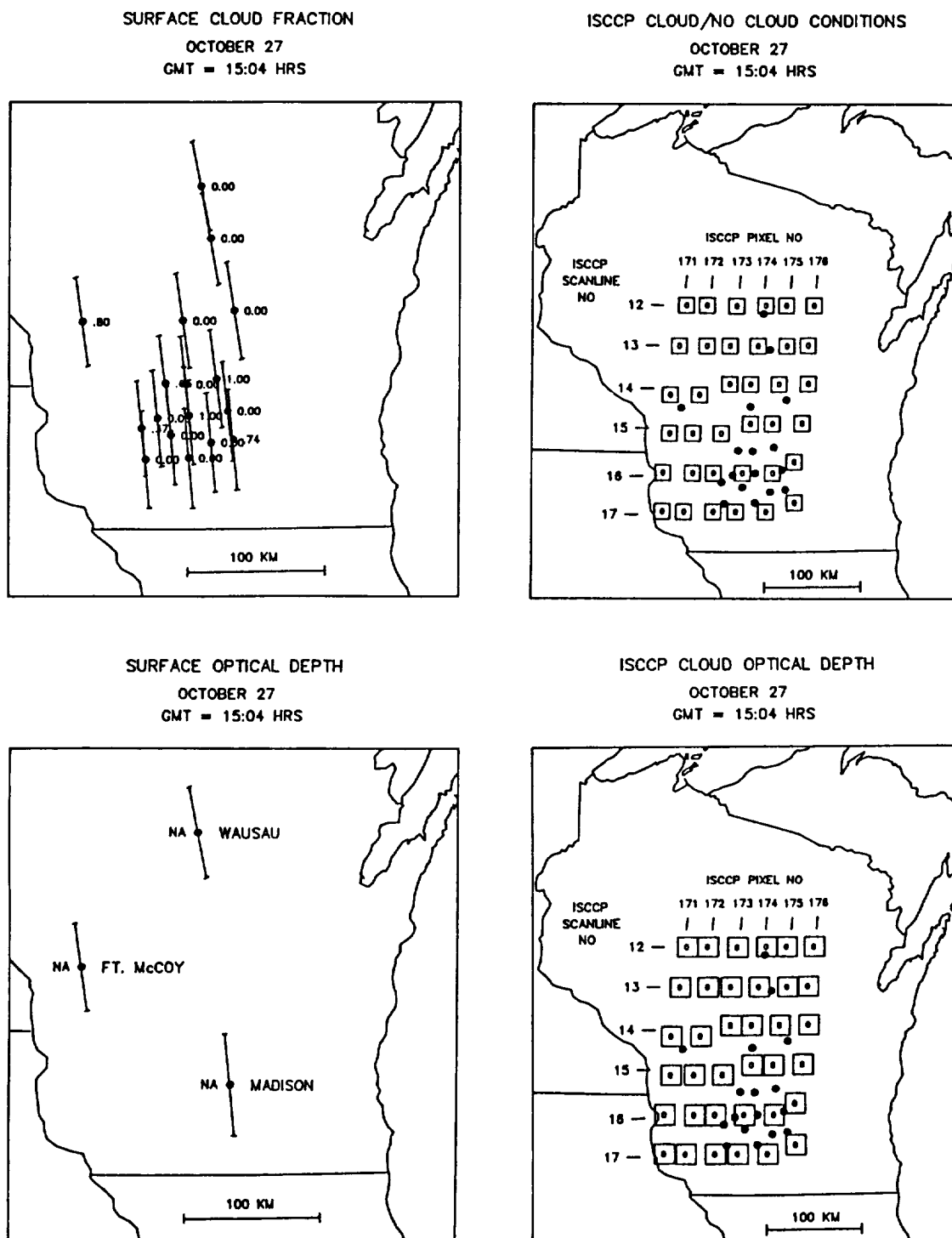
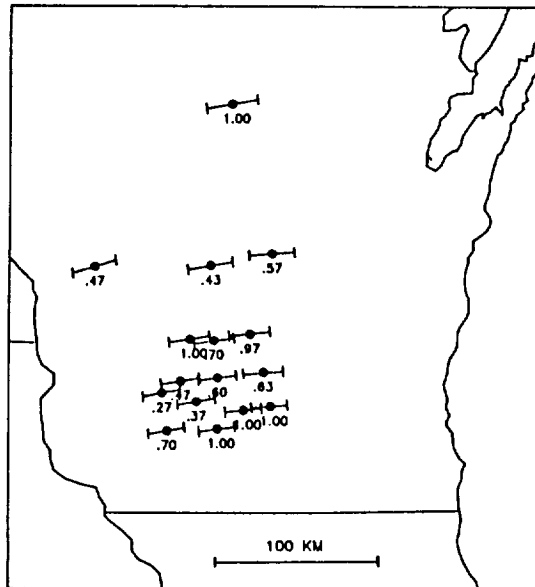
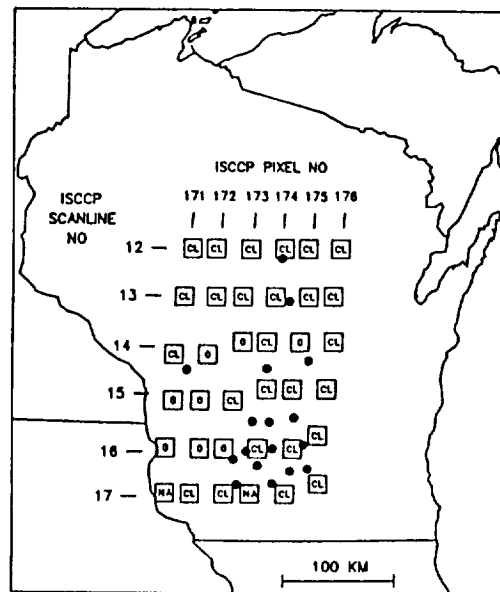


Figure 1. Surface-measured cloud fraction and cloud optical depth compared to ISCCP cloud parameters under nearly clear sky conditions with solar zenith angle = 67.3° .

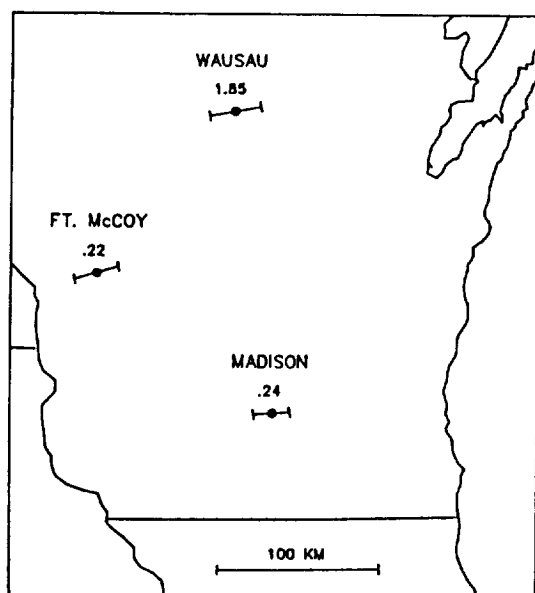
SURFACE CLOUD FRACTION
OCTOBER 28
GMT = 15:04 HRS



ISCCP CLOUD/NO CLOUD CONDITIONS
OCTOBER 28
GMT = 15:04 HRS



SURFACE OPTICAL DEPTH
OCTOBER 28
GMT = 15:04 HRS



ISCCP CLOUD OPTICAL DEPTH
OCTOBER 28
GMT = 15:04 HRS

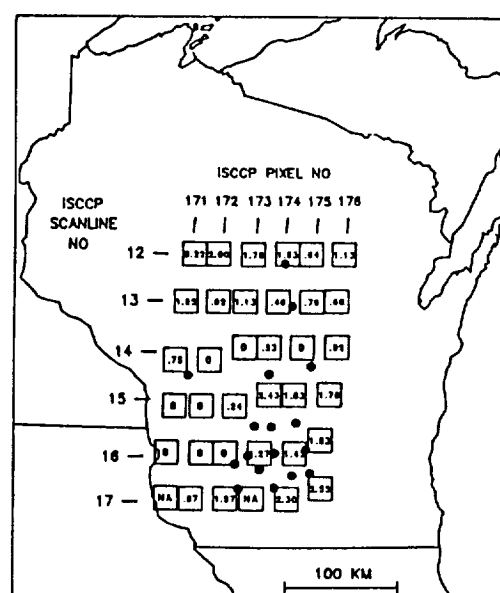
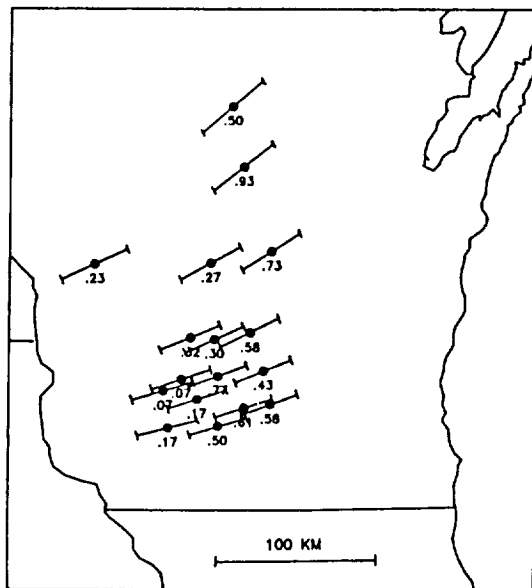


Figure 2. Surface-measured cloud fraction and cloud optical depth compared to ISCCP cloud parameters under cirrus cloud conditions with solar zenith angle = 67.7° .

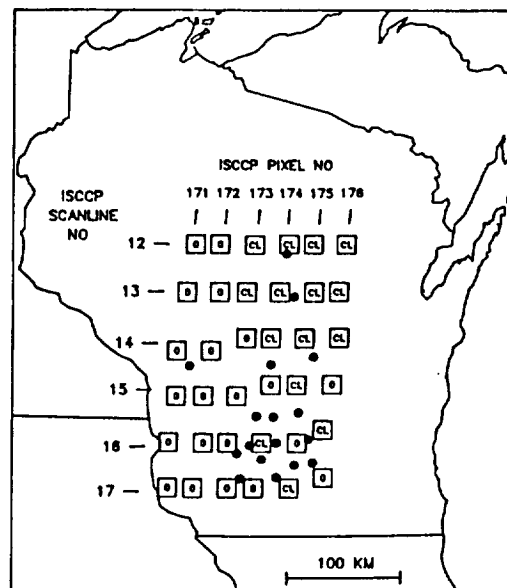
SURFACE CLOUD FRACTION

OCTOBER 28
GMT = 18:04 HRS



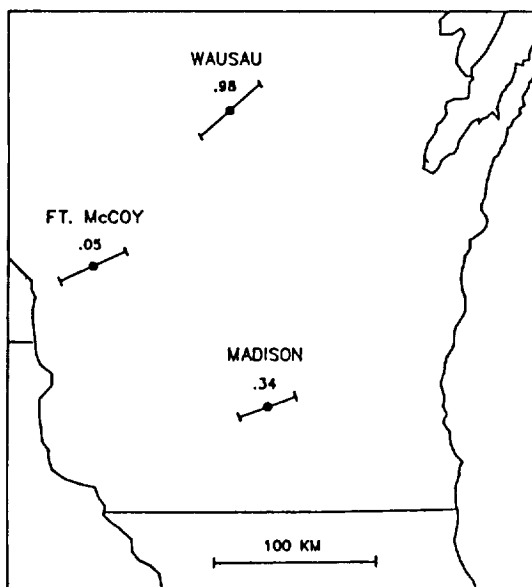
ISCCP CLOUD/NO CLOUD CONDITIONS

OCTOBER 28
GMT = 18:04 HRS



SURFACE OPTICAL DEPTH

OCTOBER 28
GMT = 18:04 HRS



ISCCP CLOUD OPTICAL DEPTH

OCTOBER 28
GMT = 18:04 HRS

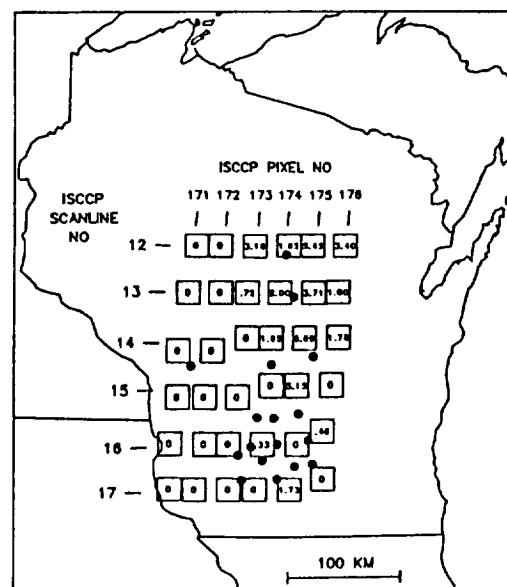


Figure 3. Surface-measured cloud fraction and cloud optical depth compared to ISCCP cloud parameters under cirrus cloud conditions with solar zenith angle = 61.3° .

**The October 27--28, 1986, FIRE Cirrus Case Study:
Cloud Microstructure**

Karen M. Miller
and
Andrew J. Heymsfield
National Center for Atmospheric Research¹
Boulder, Colorado 80307

James D. Spinhirne
NASA Goddard Space Flight Center
Greenbelt, Maryland 20771

1. Introduction

Using aircraft in situ measurements, we examined the microphysics of cirrus clouds observed on 28 October 1986 during FIRE. We present our results as one component of an extensive coordinated study of the cirrus on this day. Our study contributes to the understanding of cold clouds by (i) providing microphysical data to supplement satellite and aircraft radiometer data for investigating cirrus cloud radiative effects; (ii) providing more complete information on ice particle evolution and cloud forcing mechanisms than was available in the past, through the use of instrumentation with higher resolution and more accurate calibration; (iii) expanding our knowledge of the particle characteristics in cold liquid water clouds, through improved instrumentation and by making use of sensors on other platforms, such as lidar; and (iv) by estimating the ice nucleus concentrations active at low temperatures in the upper troposphere from the concentrations of ice particles in colloidally stable liquid water clouds.

2. Aircraft instrumentation and flight locations

The clouds were sampled on 28 October 1986 in the vicinity of Green Bay and Wausau, WI. An upper level trough and a

cold front from 400 mb to the surface were located in western Wisconsin. Details of the synoptic conditions are given by Starr and Wylie (1989).

The NCAR King Air turboprop and Sabreliner jet aircraft were used for the data collection. The period analyzed for the Sabreliner coincided with data collected from LANDSAT at 1553 UTC. The flight pattern included racetracks oriented about 30° off the mean horizontal wind direction of 260° at six altitudes from 8.6 to 11.3 km. The period analyzed for the King Air was just prior to and overlapped that for the Sabreliner. The flight pattern consisted of level traverses from 7.0 to 7.5 km.

Temperatures measured by the Rosemount sensors were accurate to $\pm 0.25^\circ\text{C}$, with a resolution of 0.006°C . Dew point temperatures were obtained from EG&G frost point hygrometers, which, at low temperatures, respond slowly and are of dubious accuracy. Liquid water (LW) was detected and the liquid water content (LWC) measured using Rosemount icing detectors (RICE). Droplet size spectra and the LWC were measured on the King Air using a Particle Measuring Systems (PMS) Forward Scattering Spectrometer Probe (FSSP) sizing from 1.5 to $46.5\ \mu\text{m}$ in $3\ \mu\text{m}$ bins beginning at $3\ \mu\text{m}$. Both aircraft were equipped with two PMS

¹The National Center for Atmospheric Research is sponsored by the National Science Foundation.

2D probes to detect ice particles larger than $25\text{--}50\text{ }\mu\text{m}$, but we will look at only the Sabreliner data here. Ice particle shapes (habits) and size spectra and estimated cloud ice water content (IWC) were derived from the 2D data and direct collections of particles on oil-coated slides.

3. Ice particle and droplet microphysics

Figure 1 depicts a vertical cross section of the attenuated backscatter observed by the ER-2 downward-looking lidar for 1552–1556 UTC as the aircraft overflowed the study area. In the region shown, there are two cloud layers. The upper cirrus layer extends from 9.0 to 11.5 km. Much or all of the lower structure of this cirrus appears to result from precipitation of ice crystals from the thin layer above 11 km. The Sabreliner traverses were conducted within this higher cloud layer. The lower cloud layer from 7 to 8 km consists of two cloud types. A low density cirrus cloud is found between 15 and 25 km distance; this

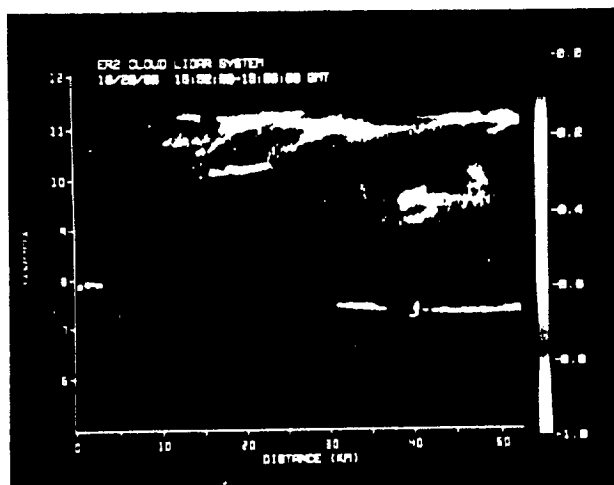


Figure 1. A vertical cross section of the attenuated backscatter observed by the ER-2 downward-looking lidar for 1552–1556 UTC as the aircraft overflowed the study area.

cloud, too, may result from precipitation of ice particles from about 8 km. An altostratus cloud less than 250 m thick is found elsewhere. Lidar depolarization data indicate that the altostratus layer was composed primarily of water droplets.

Ice particles $>150\text{ }\mu\text{m}$ sampled by the Sabreliner probes at the upper cloud levels were primarily columns and compact spatial particles with extensions; those sampled at the lower levels were primarily bullet rosettes. Possibly this effect was due to the faster growth rate of the bullet rosettes or to the growth of compact spatial particles and/or additional nucleation in a convectively unstable layer between 9.50 and 9.65 km. Particles $\leq 150\text{ }\mu\text{m}$ were compact spatial particles, but we have little confidence in the habit assignment; these particles could have been plates or even columns.

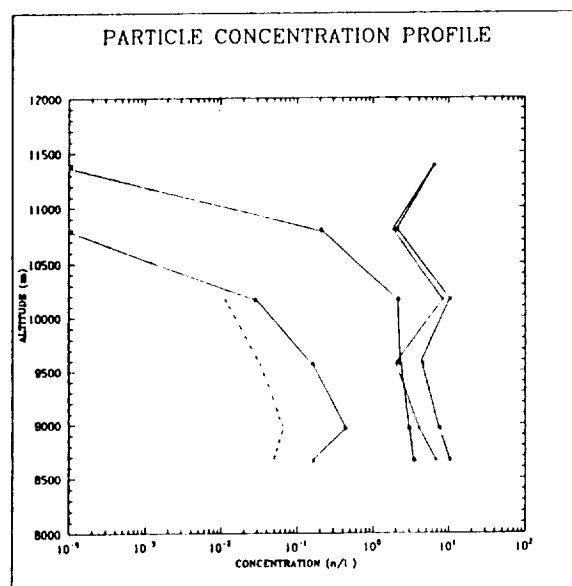


Figure 2. Ice particle concentration by size categories as a function of altitude (—: Total; - - - : $< 200\text{ }\mu\text{m}$; · · · : $200\text{--}500\text{ }\mu\text{m}$; — · : $500\text{--}1000\text{ }\mu\text{m}$).

Figure 2 shows particle concentrations by size categories as a function of alti-

tude. Concentrations decreased with increasing particle size, a spectrum typical of cirrus clouds. The total concentration was dominated by the concentration in the first size category. The concentrations in all size categories remained fairly constant with altitude; it is not known if this effect was due to particle fallout. But, notably, a sharp decrease in the concentrations of the larger particles occurred at the colder temperatures. The concentration of aggregates—particles containing two or more individual ice crystals—increased with decreasing altitude (Fig. 2, dashed line). Most of the large particles were aggregates.

The maximum ice particle dimension plotted in Fig. 3 shows a trend from smaller sizes at the cold temperatures near the cloud top to larger sizes at the base. The mass-weighted mean diameter shows a similar trend.

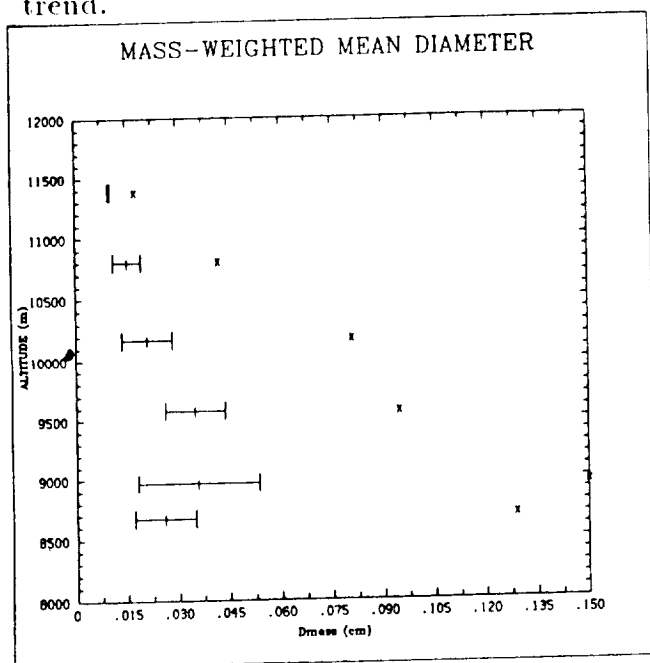


Figure 3. Maximum and mean mass-weighted ice particle dimensions as a function of altitude.

The IWC (Fig. 4) was calculated from the particle size spectra and habit percentages. The data show wide horizontal vari-

ability as indicated by the standard deviation about the mean. A dependence on north-south variability in the traverses is evident. Looking at the southern segments (traverses 1, 3, 5, from the top) and the northern segments (2, 4, 6) grouped separately, two distinct patterns of increasing IWC with decreasing altitude are seen; the value of IWC is consistently higher in the southern traverses.

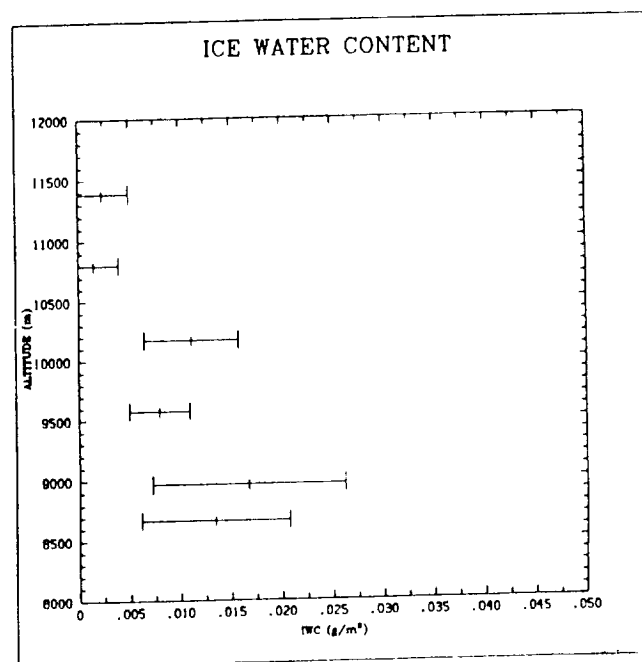


Figure 4. Ice water content as a function of altitude.

The cumulative distribution of ice mass as a function of altitude and particle size appears in Fig. 5. At the upper levels, the distribution indicates that considerable mass might be present below the minimum ice particle size detectable with the 2D-C probe. At the lower levels, probably most of the ice mass is detectable.

Liquid water was measured from the Klug Air in ten separate events at altitudes ranging from 7.30 to 7.45 km and spanning a horizontal distance of 0.5 to 7.0 km. An event was a period of continuous LW detection, that is, where no more than one consecutive second elapsed without LW detection.

The LWC averaged over each traverse was typically less than 0.005 g m^{-3} . Droplet concentrations were less than 70 cm^{-3} , and average diameters were smaller than $7 \text{ }\mu\text{m}$. Ice particle concentrations in these events were extremely low, less than 0.05 l^{-1} .

Figure 6 shows a high resolution view of the lidar backscatter within the altocumulus layer. The mean droplet diameters and the LWC observed from the King Air during an ascent through this layer are shown in Figs. 7A and 7B. The scale of horizontal variability in LWC is commensurate with the scale of changes in lidar backscatter, approximately 0.5 km . The LWC was about half the adiabatic value, and since ice mass was negligible within the layer, mixing was evidently reducing the LWC. From the temperature data, we concluded that the cloud was convectively stable, and that the cloud layer lifted from above an inversion at the base of the LW region.

4. Conclusions

We examined the microstructure of the ice and liquid water phases for the FIRE cirrus case study of 28 October, 1988, using measurements taken from two aircraft between 6 and 12 km . We characterized ice particle and droplet concentrations, and ice and liquid water contents.

Our data indicate that the cirrus resulted from weak uplift of 10 cm s^{-1} or less and the LW layer sampled at the satellite

overpass time resulted from forced ascent at 25 cm s^{-1} above a sloped temperature inversion. The LW layer was capped by a stable layer; calculated Richardson numbers were < 0.25 , suggesting that this zone may have contained Kelvin-Helmholtz waves.

The most significant microphysical finding was the persistence of liquid water clouds at temperatures about -30°C . Virtually no ice particles were detected in the cloud. Also of importance was the observation of ice crystal aggregates at temperatures as low as -56°C . Aggregation accounted for the development of most of the larger particles present, since the growth rates of aggregates are much higher than the rates for single crystals.

Acknowledgments. We thank Steve Cox for use of the Sabreliner icing probe and 2D probe data and Ken Sassen, co-principal investigator for the King Air, for his cooperation. We also thank NCAR's Research Aviation Facility for the acquisition of the King Air data, and Roelof Brientjes and Nancy Knight for collecting the ice particle and droplet samples. This analysis was supported by NASA under contract L98100B.

REFERENCES

- Starr, D. O'C., and D. P. Wylie, 1989: The October 27-28, 1986, FIRE cirrus case study: Meteorology and cloud fields. *Mon. Wea. Rev.* (in submission).

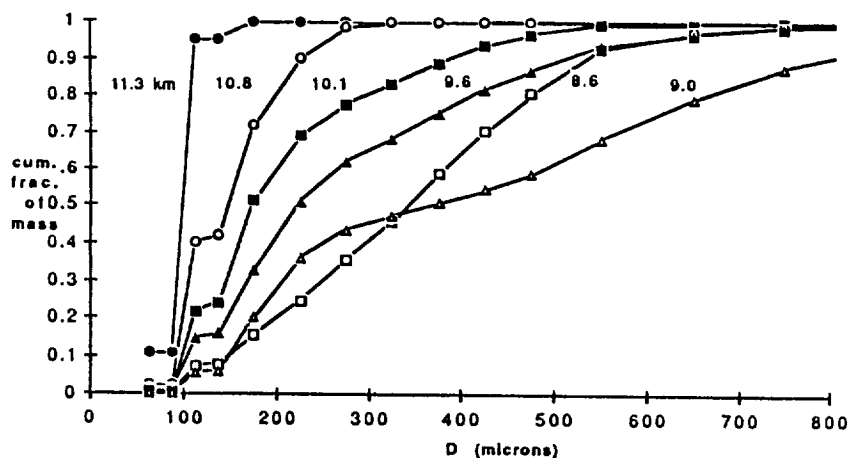


Figure 5. Cumulative distribution of ice mass as a function of altitude and particle size.

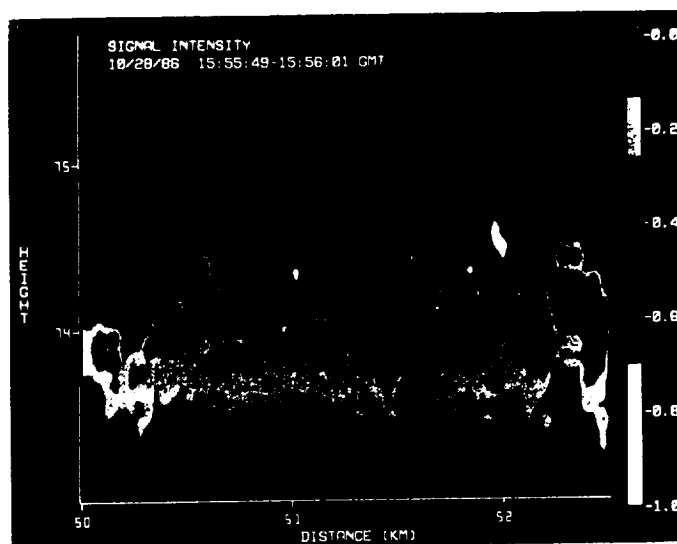


Figure 6. Lidar backscatter cross section observed by ER-2 lidar 1552–1556 UTC, showing altocumulus layer sampled by King Air. (Height is $\text{km} \times 10$.)

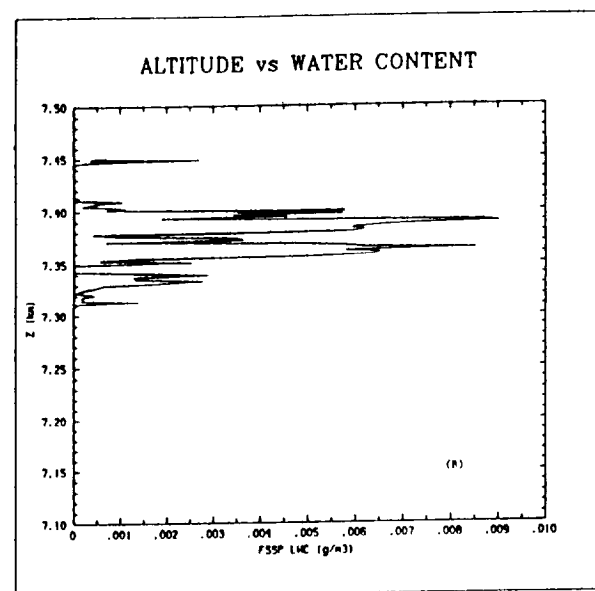
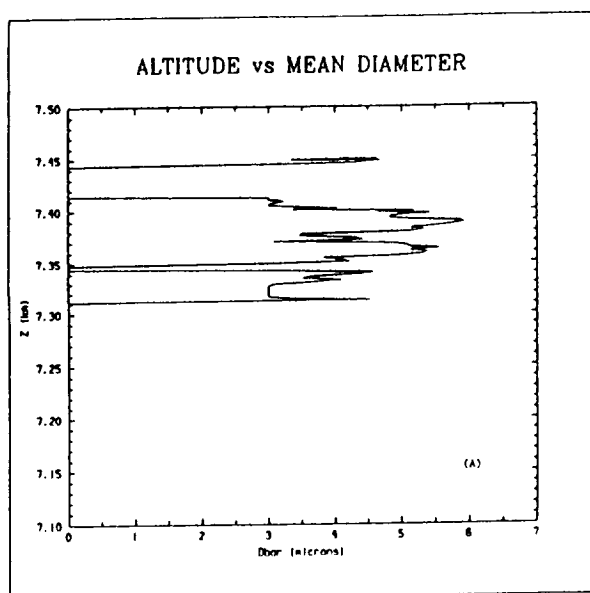


Figure 7. Data in LW region during King Air ascent 152545–152820 UTC. Panel A: Mean droplet diameter. Panel B: Liquid water content.

Cirrus Microphysics and Radiative Transfer :
Cloud Field Study on October 28th, 1986

Stefan Kinne, NASA-Ames, MS 245-3, Moffett Field, CA 94035
Thomas P. Ackerman, Dep.of Meteorology, Penn State, PA 16802
Andrew J. Heymsfield, NCAR, P.O.Box 3000, Boulder, CO 80307
Francisco P.J. Valero, NASA-Ames, MS 245-4, Mo.Field, CA 94035
Kenneth Sassen, Dep.of Meteorology, Univ.of Utah, UT 84112
James D. Spinhirne, NASA-Goddard, Greenbelt, MA 20771

1. INTRODUCTION

The radiative properties of cirrus clouds present one of the major unresolved problems in weather and climate research. Uncertainties in ice particle amount and size and, also, the general inability to model the single scattering properties of their usually complex particle shapes, prevent accurate model predictions. For an improved understanding of cirrus radiative effects, field experiments, as those of the Cirrus IFO of Fire, are necessary. Simultaneous measurements of (1) radiative fluxes and (2) cirrus microphysics at multiple cirrus cloud altitudes allow to pit calculated versus measured vertical flux profiles; with the potential to judge current cirrus cloud modeling.

2. MEASUREMENTS

As part of the detailed cirrus case study (Starr and Wylie, 1989), data are analyzed for a 75 by 50 km cirrus cloud field that moved over Wausau, WI, in the morning of October 28th, 1986. The observing systems provide simultaneous measurements of radiative broadband fluxes and cloud microphysics at altitudes of 6.1, 6.4, 7.0, 7.3, 7.6, 7.9 and 8.2km altitude within the cirrus cloud (NCAR King-air) and cloud geometry data from stratospheric (NASA ER-2) and groundbased (Wausau) remote sensing measurements. Trajectories of the two aircraft and the position of Wausau with respect to the moving cloud-field (78km/h 245°) in Figure 1 show that these measurements rarely occurred at the same cloud field position, so that flux profiles at cloud height from measurements are only realistic, if homogeneity of the cloud field can be guaranteed. Unfortunately, strong inhomogeneities are indicated by 10 μ m upwelling radiance measurements of the ER-2 and are illustrated by the contour plot of Figure 2. Equivalent blackbody temperatures of in the right half of the cloud field compared to those in the left half are lower by about 15K. Assuming an effective cloud altitude of 7.6km (240K atmospheric temperature), infrared optical depths larger than 2 for the right side and optical depths smaller than 1 for the left side of the cloud-field are detected. The groundbased lidar (Sassen, 1989) reveals an uniform cloud base at 6km altitude, while the ER-2 lidar (Spinhirne et al., 1989) detects cloud tops as high as 11km for the optically thicker right part of the cloud-field. Despite these cloud top heights, the chosen effective cloud altitude may even be lower than 7.6km (and optical depths larger), because

strong extinctions directly above the cloud base between 6.5 and 7.5km altitude generally dominate the radiative character of the cirrus cloud. The detected two natured character of the cloud-field is also supported by flux measurements, with solar and infrared optical depths of 5 and 3 for the right region being larger by a factor of 3 over those from the left cloud-field region. Thus, any comparison between measured and calculated fluxes has to treat both cloud-field domains separately.

3. MODELING

Calculations of broadband radiative fluxes are performed with an accurate 1-D spectral radiative transfer model. For the atmospheric profile, the 18 GMT Greenbay radiosonde data (Starr and Wylie, 1989), have been adjusted ($T:-3K$, water vapor saturation at cloud height) to make the sounding consistent with the King-air measurements. Humidity data above 11 km altitude and the ozone profile were taken from the US-Standard Atmosphere. Solar calculations assume a solar constant of 1360 W/m^2 and a solar zenith angle of 60° . This angle is accurate to within a few degrees with respect to local time (10.30 - 11.30 am), latitude (45°) and time of year (October 28th). A solar surface albedo of 15% was adopted, which is typical of midlatitude land surfaces. The cloud is modeled in 300 km thick layers from the cloud base at 6.1km to 8.2km altitude in the optically thinner and to 10.6km altitude in the optically thicker region of the cloud-field. Single scattering properties for ice particles, which are compact crystals with branches, bullet rosettes and hollow-ended single columns in that order (Heymsfield et al., 1989), are derived from 2-D imaging probe data. First, columns and column rosettes are modeled from measurements of cross-section area and maximum particle dimension. Then these columnar shapes are expressed by spheres of equivalent surface area, which provide in Mie calculations almost identical extinctions. Non-spherical shape effects are accounted for by reducing the solar co-single scattering albedo of spheres to 0.7 of its original value and by reducing the solar asymmetry-factor by 0.05.

4. COMPARISON

The comparison between measured and calculated fluxes suffers from the inhomogeneity of the cloud-field. Measurements at the lower cloud altitudes occurred in the optically denser right section of the cloud-field (see Figure 1 and 2), while measurements above 7.5km altitude occurred in the optically thinner left section. This makes it difficult to establish an accurate radiative flux profile. Moreover, even within these regions for each cloud altitude a wide range of flux values is detected, especially at solar wavelengths. Since it is difficult to judge the accuracy for measurements in the optically thinner cloud region with measurements at only two cloud altitudes, the comparison, here, concentrates on results for the optically denser region of the cloud-field. Horizontal bars in Figure 3 indicate ranges of flux measurements in areas of the cloud-field,

where the equivalent blackbody temperature T_B (see Figure 2) dropped below 250K. To represent this cloud-field section in calculations, particle size distributions based on 2-D imaging probe averages from the five lowest flight legs between 6.1 and 7.5 km altitude have been modeled into a cloud layer between 6.1 and 10.6km altitude. These distributions are characterized by large crystals, since particles with equivalent radii of about 70 μ m provide the largest cross-section. However, there is an uncertainty towards smaller particle sizes with radii less than 20 μ m, the instrumentation was unable to detect. Assuming a decreasing particle density from 7.5km upward towards the cloud top, the total cloud optical depth amounts to 2.6. The comparison in Figure 3 shows that measurements indicate larger optical depths, especially at solar wavelengths. Even with the microphysics from region with T_B less than 240K the smallest solar downward fluxes cannot be reproduced. Since microphysical measurements might have overlooked a possible influence of small particles, additional small particles with radii of about 3 μ m in the water and in the ice phase have been added in two different cases to the detected average size distributions near the cloud base. Their addition certainly cloud explain the disagreement between calculated and measured fluxes.

5. Conclusion

Most of the problems in this study are linked to the inhomogeneity of the cloud-field. Thus, only studies on more homogeneous cirrus cloud cases promise a possibility to improve current cirrus parameterizations. Still, the current inability to detect small ice-particles will remains as a considerable handicap.

In future experiments an instrument is needed, that can detect concentrations of ice particles for sizes between 1 and 40 μ m. Most desirable in future experiments are measurements of microphysics and radiation, which are simultaneously taken at different cloud altitudes. Due to the lack of airborne instrumentation, however, measurements along altitude legs will generally be time delayed. Then a drift with the ambient air will make cloud measurements much more useful.

REFERENCES

- Heymsfield, A.J. and K.M. Miller, 1989: October 27-28 1986 FIRE cirrus case study: Cloud microstructure.
- Sassen K. 1989: Wausau-lidar observations on October 28, 1986
- Spinhirne J.D. and W.D. Hart: ER-2 lidar and spectral radiometer cirrus observations for October 28, 1986.
- Starr D. and D.P. Wylie, 1989: The 27-28 October 1986 Fire case study: Meteorology and Cloud-Field.

all submitted to Mon.Wea.Rev.

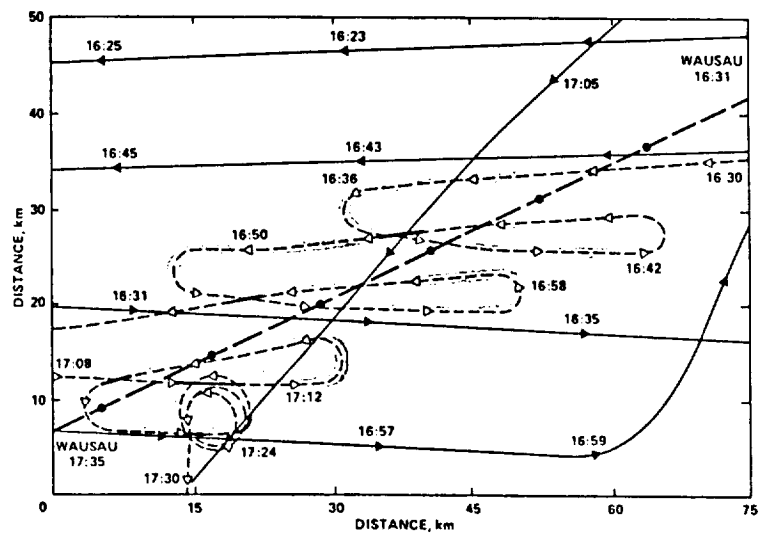


Figure 1 Analyzed 75 by 50 km cloud-field area. With respect to the movement of the cloud-field, the position of Wausau (dark dashed line, 10 min marks) and the trajectories of ER-2 (solid line, 2 min arrows) and King-air (shaded dashed line, 2 min arrows) are displayed. The King air climbed from 6.1km to 8.3km in seven constant altitude legs gaining altitude only 180° turns. The descent back to 6.1km occurred in a three loop spiral while drifting with ambient wind (displayed in the lower left corner).

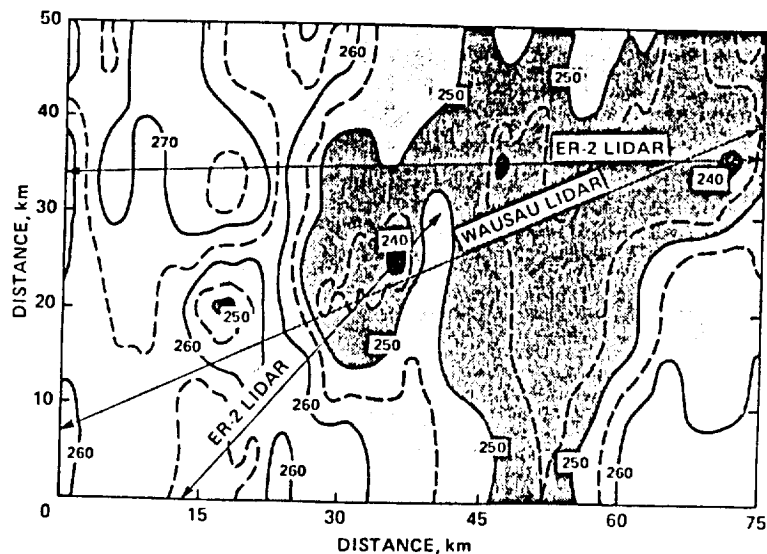


Figure 2 Contour plot of $10\mu\text{m}$ equivalent blackbody temperatures as detected by the ER-2 at 19km altitude for the selected cloud-field area of Figure 1. Double arrow lines indicate the location of vertical cloud cross-sections by stratospheric (ER-2) and groundbased (Wausau) lidar measurements.

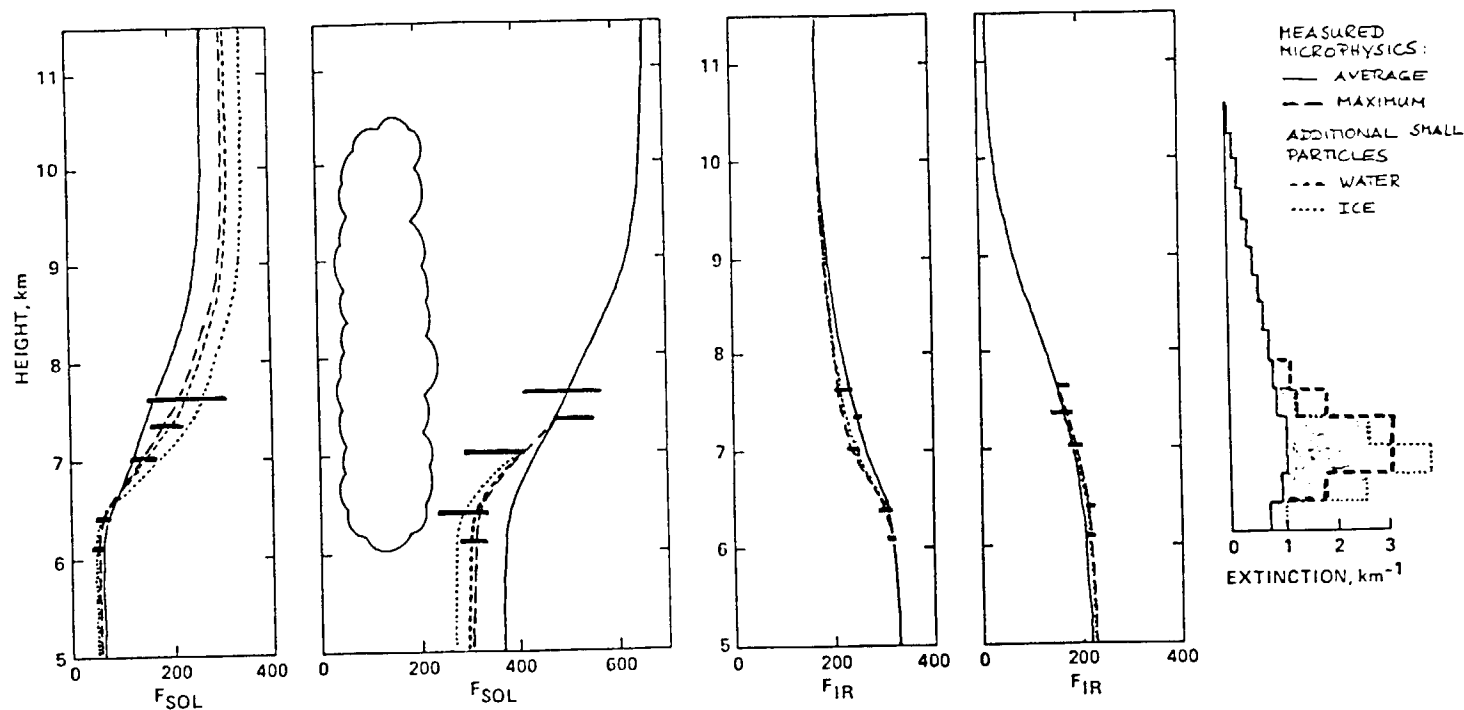


Figure 3 Comparison of measured and calculated broadband solar and infrared fluxes for the cloud-field section of large optical depths. Measurements (horizontal bars) are only available near the cloud base. Calculations (solid line, $\tau:2.6$) are based on measured microphysical averages between the cloud base at 6.1 and 7.5 km altitude. Above 7.5 km a monotonically decreasing extinction was assumed towards the cloud top at 10.6 km (solid line). Also shown are results for microphysical maxima (long dashed line, $\tau:4.4$) and calculations with added small particles in the water (short dashed line, $\tau:4.9$) and ice-phase (dotted line, $\tau:4.9$) near the cloud base. Also shown are the respective cloud extinctions at solar wavelengths, leading to the optical depths indicated above.

**THE 27-28 OCTOBER 1986 FIRE IFO CIRRUS CASE STUDY:
COMPARISON OF SATELLITE AND AIRCRAFT DERIVED PARTICLE SIZE**

Bruce A. Wielicki and J. T. Suttles
Atmospheric Sciences Division, NASA Langley Research Center
Hampton, Virginia

Andrew J. Heymsfield
National Center for Atmospheric Research, Boulder, Colorado

Ronald M. Welch
South Dakota School of Mines and Technology, Rapid City, South Dakota

James D. Spinhirne and Man-Li C. Wu
NASA Goddard Space Flight Center, Greenbelt, Maryland

David O'C. Starr
NASA Goddard Space Flight Center, Greenbelt, Maryland

Lindsay Parker and Robert F. Arduini
PRC Corporation, Hampton, Virginia

1. INTRODUCTION

Theoretical calculations predict that cloud reflectance in near-infrared windows such as those at $1.6\mu\text{m}$ and $2.2\mu\text{m}$ should give lower reflectances than at visible wavelengths (Pollack et al., 1978; Hansen and Pollack, 1970; Twomey, 1971). The reason for this difference is that ice and liquid water show significant absorption at these wavelengths, in contrast to the nearly conservative scattering at wavelengths shorter than $1\mu\text{m}$. In addition, because the amount of absorption scales with the path length of radiation through the particle, increasing cloud particle size should lead to decreasing reflectances at $1.6\mu\text{m}$ and $2.2\mu\text{m}$. Measurements at these wavelengths to date, however, have often given unpredicted results. Twomey and Cocks (1982) found unexpectedly high absorption (factors of 3 to 5) in optically thick liquid water clouds. Curran and Wu (1982) found unexpectedly low absorption in optically thick high clouds, and postulated the existence of supercooled small water droplets in place of the expected large ice particles. We will examine the implications of the FIRE data for optically thin cirrus.

2. RESULTS

The Landsat satellite has spectral bands at $0.83\mu\text{m}$, $1.65\mu\text{m}$, and $2.21\mu\text{m}$ which cover this range of variation in cloud absorption. Each pixel has a nominal spatial resolution of 28.5 meters. Figure 1 gives the region covered by the Landsat data over Lake Michigan on October 28, 1986. Figure 2 gives the Landsat measured nadir reflectance ratio $R(2.21\mu\text{m})/R(0.83\mu\text{m})$ for the 58.4 km square analysis region (solid line) in Fig. 1. At 15:38:30 UTC the King Air aircraft took a direct sample of the cloud particles on an oil covered slide. The sample is shown in Fig. 3b and is dominated by water droplets with a mean radius of about $4\mu\text{m}$. This sample corresponds to a reflectance ratio of about 0.75 found in the Landsat data at location "1" in Fig. 2. There is a time difference of 15 minutes between the King Air and Landsat observations. The liquid water regions of this cloud, however, appear to have been colloidally stable (Heymsfield et al, 1989). A second direct cloud particle sample was collected at 15:52 UTC. This sample is shown in Fig. 3a and contains only ice particles (broken spatial plates and some columns, 20 to $300\mu\text{m}$ in length). This second sample corresponds to a reflectance ratio of about 0.4 found in the Landsat data at location "2" in Fig. 2. Note that the reflectances used to derive the image in Fig. 2 are not corrected for surface reflectance. In this case the reflectance ratios are a mixture of clear and cloudy signatures.

Given this qualitative agreement between the satellite and aircraft data, the next step is to test the quantitative agreement along the King Air aircraft track. The Landsat radiance data are spatially averaged to 1 km resolution, sampled every 0.5 km along the King Air groundtrack. Cloud reflectances are then corrected for surface reflectance effects as in Platt et al (1980). The 1.65 μ m and 2.21 μ m channels are found to require less than 0.01 correction for surface reflectance. The correction for the 0.83 μ m channel is less than 0.05.

Figure 4 compares theoretical radiance calculations using the Finite Difference method (Suttles, 1981, 1985; Barkstrom, 1976) with the measured nadir cloud reflectance at 0.83 μ m and at both 1.65 μ m and 2.21 μ m along the King Air groundtrack. Calculations use a solar zenith angle of 60°. The phase function for ice particles is taken from the laboratory measurements of Volkovitskiy et al (1980). The phase function for water particles is taken from theoretical Mie calculations with an effective radius of 3.8 μ m. Figures 4a and b give results for 1.65 μ m. Figures 4c and 4d give results for 2.21 μ m. The Landsat data are shown with symbols indicating the corresponding portion of the King Air track shown in Fig. 2.

It is evident that there are two distinct populations of cloud particles along the 88 km track. The high reflectance ratio values in Fig. 2 (15:38:10-15:39:09 UTC and 15:49:40-15:50:39 UTC) appear along the diagonal of nearly equal reflectance at the two wavelengths and are consistent with water droplets or ice spheres with radius less than 7.5 μ m. The remaining data indicate larger particles of about 60 μ m radius. Examination of the 1.65 μ m versus 2.21 μ m data given in Fig. 4 indicates that the large particles are ice. An assumption of liquid water for the large particles would give inconsistent particle sizes at 1.65 and 2.21 μ m. An assumption of ice gives consistent particle size in the two wavelengths. The small particles are too small to reliably distinguish ice from liquid water phase for these optically thin clouds.

Figure 5 gives the King Air particle size distributions using the combined FSSP, 2D-C, and 2D-P probes. For the 2D-C and 2D-P probes, particle size is calculated as a sphere with cross-section area πr^2 equal to the area of the particle image in the 2-D probe. For compact non-spherical particles, this specification is similar to using equivalent volume spheres (Pollack and Cuzzi, 1980). Pollack and Cuzzi (1980) found that for large size parameter $x = 2\pi r/\lambda \gg 1$, and moderate absorption $2n''x < 1$ (where n'' is the imaginary index of refraction), equivalent volume spheres are most accurate for absorption efficiency determination. For the 1.65 μ m and 2.21 μ m spectral bands, the appropriate radius range would be from about 3 μ m to 400 μ m. Given the compact particle habits observed in the microphysical data, the use of equivalent cross-section area spheres should be reasonably accurate. Large aspect ratio particles would lead to an overestimate of the true particle volume, and therefore an overestimate in particle absorption at 1.65 and 2.21 μ m. Such particles, however, were rarely noted in the data.

Four characteristic size distributions are given in Fig. 5. The data for 15:38:10 to 15:39:09 UTC cover the high ratio of $R(2.21)/R(0.83)$ found in Fig. 2 near the location "1" in the figure. The microphysical data are dominated by small water droplets with radius about 4 μ m. The next section of the flight track (15:39:10 to 15:45:24 UTC) shows a peak at about 150 μ m, but no water droplets. The third section (15:49:40 to 15:50:39 UTC) has the smallest particle concentrations, and is taken from the high ratio of $R(2.21)/R(0.83)$ found just before the end of the King Air track in the Landsat image. The Landsat data imply small particle sizes, while the aircraft finds no small drops in the FSSP probe. Spinhirne and Hart (1989) noted from the ER-2 lidar data (ground track shown in Fig. 2) that the mixed phase cloud occurred in vertically thin layers (100 - 200 meters thick) at heights between 7.3 and 8.0 km. The lidar depolarization data at location '1' in Fig. 2 verifies the existence of a mixed ice/liquid water phase cloud layer at 7.3 km altitude (Spinhirne and Hart, 1989), the position of the King Air at 15:38:30 UTC. The King Air altitude at 15:50 UTC is 7.0 km, which is below the lidar detected altitudes for mixed phase cloud. It is likely that the King Air data at 15:50 missed the liquid water layer. We conclude that the aircraft microphysics and Landsat reflectances are in qualitative agreement, subject to uncertainties in the vertical variation of cloud microphysics and temporal evolution of the cloud field.

The quantitative comparison of aircraft and radiometrically derived particle size requires the determination of an effective mean particle radius. Figure 6 gives the Landsat 2.21/0.83 μ m cloud reflectance ratio versus effective radius r_e . We define $r_e = \int r^3 N(r) dr / \int r^2 N(r) dr$, where

$N(r)$ is the size distribution derived using the King Air microphysics data. This effective radius is a cross-section area weighted radius and has been shown useful in characterizing overall radiative properties of a particle size distribution. The number densities are averages over 5-second intervals, which results in size distributions representative of 500-meter sections of the cloud field.

Figure 6 indicates a significant but poor correlation between aircraft particle size and the $2.21/0.83\mu\text{m}$ reflectance ratio. There appear to be three clusters of data, one with r_e of about $4\mu\text{m}$, and two with r_e about $200\mu\text{m}$. The apparently anomalous data with large particle size and large reflectance ratio (15:50 UTC) are the liquid water layer missed by the King Air as discussed above. Recall that the data in Fig. 4 also clustered in two particle size groups, water droplets with radius less than 7.5 micron, and ice particles with radius about $60\mu\text{m}$. While the water droplets appear consistent between the two data sources, the ice particles are in substantial disagreement, the radiative measurements indicating a smaller particle size by about a factor of 3. In order to understand this discrepancy, the uncertainties inherent in such a comparison are examined below.

i. *Uncertain Index of Refraction: factor of 2.*

Warren (1984) estimates that the uncertainty of the imaginary index of refraction for ice in the 1.4 to $2.8\mu\text{m}$ spectral region is a factor of 2.

ii. *Uncertainty in the scattering phase function: $\approx 30\%$.*

Use of the Mie scattering phase function in place of the VPP gave particle sizes about 60% smaller than those predicted in Fig. 4. This is an extreme test of the phase function.

iii. *Uncertainty in the use of a single particle radius to represent an entire size distribution: $\approx 15\%$ at $r_e < 200\mu\text{m}$.*

Mie calculations were run to determine single scatter albedo as a function of r_e for the King Air size distributions (5 second averages) for each wavelength. These complete calculations were then compared to Mie calculations using a single particle size (as in Fig. 4).

iv. *Uncertainty in converting 2D image area to equivalent sphere: Unknown.*

The good agreement between the King Air median mass-weighted diameter determined as a function of crystal habit and $2 r_e$ determined using particle cross-section area (Fig. 6) argues that this error is of secondary importance.

v. *Inadequate microphysical sampling: Unknown.*

The size comparisons in Fig. 6 are given using the King Air measurements in the lower cloud layer at 7.3 km. Measurements of the upper cloud layer by the Sabreliner show mean particle radius decreasing from $200\mu\text{m}$ at 9 km to $40\mu\text{m}$ at 11 km. Note that a $20\mu\text{m}$ radius is the smallest particle size measured by the 2D-C probe at the Sabreliner airspeed. Many small particles in the upper cloud layer are undoubtedly missed by the 2D-C and 2D-P probes (Heymsfield et al, 1989). In support of this concern, Spinhirne and Hart (1989) estimate a mode radius of $20\mu\text{m}$ for the upper cirrus layer on October 28 using integrated lidar backscatter and $11\mu\text{m}$ emittance. For the lower cloud layer at 7-8 km, Fig. 5 shows that all of the 2-D size distributions at 7.3 km have maximum number density for the smallest particle size measured by the 2D-C probes. While the effect of these unsampled small ice particles on the determination of r_e is unknown, it seems reasonable from the size distributions shown in Fig. 5, that this effect alone might explain the discrepancy between 60 and $200\mu\text{m}$ values for r_e .

3. CONCLUSIONS

The FIRE October 28, 1986, data provide a unique opportunity to compare measured and theoretical cloud properties for cirrus clouds. Overall impressions are:

1. The lower cloud layer (7-8 km) appeared to dominate the cloud radiative properties as viewed by the ER-2 and Landsat. This result is consistent with the King Air and Sabreliner microphysical measurements and with ER-2 lidar observations.
2. Particle size inferred using Landsat cloud reflectance at $0.83\mu\text{m}$, $1.65\mu\text{m}$ and $2.21\mu\text{m}$ gave good agreement with the King Air cloud particle samples for portions of the cloud field dominated by small water droplets with $r_e = 3.8\mu\text{m}$. For the larger ice crystals, the radiation measurements determined an r_e of about $60\mu\text{m}$, compared to about $200\mu\text{m}$ determined using the King Air FSSP, 2D-C, and 2D-P probes. We conclude that the discrepancy is caused by two uncertainties. First, ice

particle sizes below about $20\mu\text{m}$ are not detected by the aircraft probes. The particle number densities are maximum at the smallest particles sensed by the 2-D probes, indicating the presence of smaller ice particles, even in the radiatively dominant lower cloud layer at 7-8 km. Second, uncertainties in the imaginary index of ice for the 1.65 and $2.21\mu\text{m}$ spectral bands causes an uncertainty of a factor of two in the Landsat derived particle size. The effect of small ice particles in the upper cirrus layer at 9-11.6 km is estimated to be of secondary importance.

3. Recommendations for future cirrus experiments include improved measurement of ice particle concentrations for sizes between 1 and $50\mu\text{m}$, improved sampling of the vertical variation of cloud microphysics, more accurate radiometric calibration of aircraft radiometers, and more accurate values for the imaginary index of ice between 1.5 and $2.5\mu\text{m}$ wavelengths.

4. REFERENCES

- Barkström, B. R., 1976: *J. Quant. Spect. Rad. Transf.*, **16**, 725-739.
 Curran, R. J. and M.-L. C. Wu, 1982: *Jour. Atm. Sci.*, **39**, 635-647.
 Foot, J. S., 1988: *Q. J. R. Meteor. Soc.*, **114**, 145-164.
 Hansen, J. E., and J. B. Pollack, 1970: *J. Atmos. Sci.*, **27**, 265-281.
 Heymsfield, A. J., and C. M. R. Platt, 1984: *J. Atmos. Sci.*, **41**, 846-855.
 Heymsfield, A. J., K. M. Miller, and J. D. Spinhirne, 1989: Submitted to *Mon. Wea. Rev.*
 Markham, B. L., and J. L. Barker, 1986: *EOSAT Landsat Technical Notes*, No. 1, August, 1986.
 Platt, C. M. R., D. W. Reynolds, and N. L. Abshire, 1980: *Mon. Wea. Rev.*, **108**, 195-204.
 Pollack, J. B., and J. N. Cuzzi, 1980: *J. Atmos. Sci.*, **37**, 868-881.
 Spinhirne, J. D., and W. D. Hart, 1989: Submitted to *Mon. Wea. Rev.*
 Suttles, J. T., 1981: Ph.D. Thesis, Old Dominion University, Norfolk, VA., 180 pp.
 Suttles, J. T., 1985: In *Radiative Transfer in Scattering and Absorbing Atmospheres*. Edited by J. Lenoble, A. Deepak Publishing.
 Takano, Y., and K-N Liou, 1989: *J. Atmos. Sci.*, **46**, 3-19.
 Twomey, S., 1971: *J. Quant. Spectros. Radiat. Transfer*, **11**, 779-783.
 Twomey, S. and T. Cocks, 1982: *J. Met. Soc. Japan*, **60**, 583-592.
 Volkovitskiy, et al., 1980: *Izvestiya, Atm. and Ocean. Phys.*, **16**, 98-102.
 Warren, S. G., 1984: *Appl. Opt.*, **23**, 1206-1225.

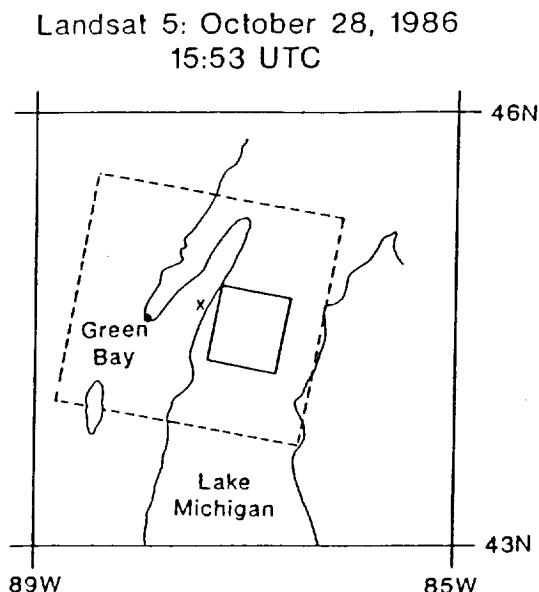


Fig. 1. Location of the Landsat image area for the study. Solid line box gives the 58.4 km square area over Lake Michigan analyzed and shown in Fig. 2.

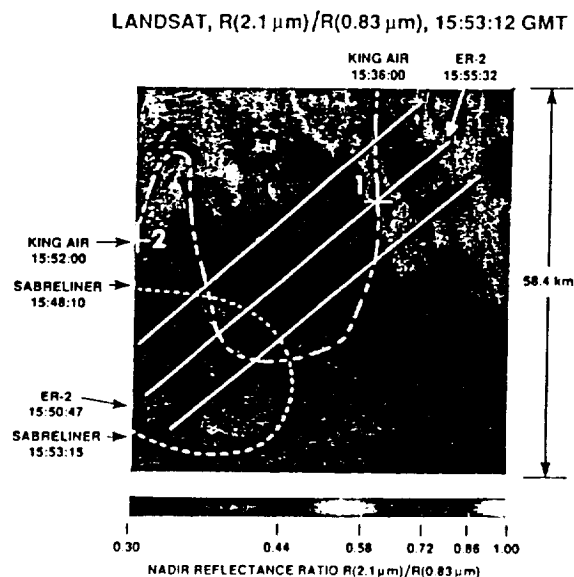


Fig. 2. Landsat reflectance ratio, $R(2.21\mu\text{m})/R(0.83\mu\text{m})$ over the analysis area. Aircraft tracks and observation times are also given in the figure. Data in Figs. 5 and 6 is taken along the King Air ground track.

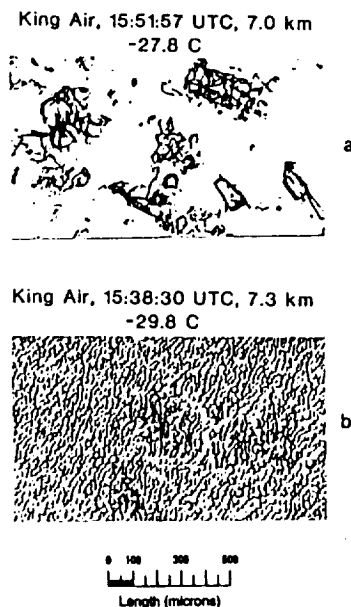


Fig. 3. Photographs of cirrus particles collected by the King Air on oil coated slides. 3a shows ice crystals collected at 15:51:57 UTC and corresponds to location "2" in Fig. 2. 3b shows water droplets collected at 15:38:30 UTC, and corresponds to location "1" in Fig. 2.

Landsat Particle Size Estimation along the King Air track

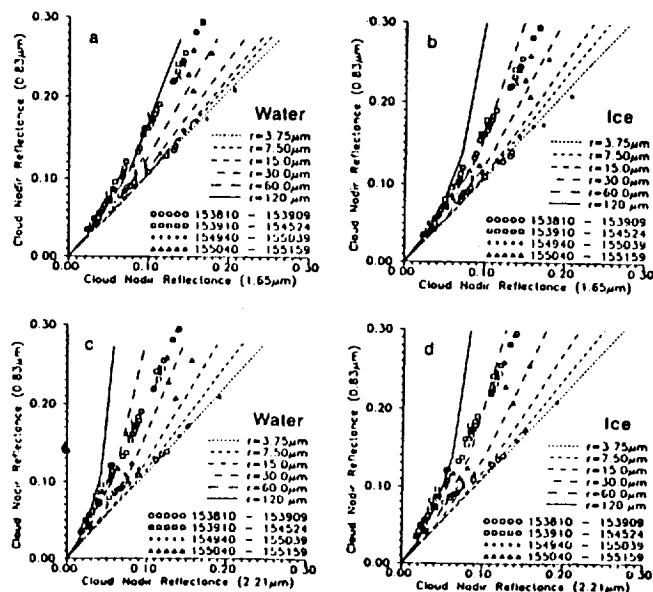


Fig. 4. Measured and calculated cloud nadir reflectance. Landsat observations are taken along the King Air ground track seen in Fig. 2. Theoretical calculations use the VPP ice scattering phase function and Mie single scatter albedos as a function of particle radius. 4a and 4b give results for $R(0.83\mu\text{m})$ vs. $R(1.65\mu\text{m})$ for liquid water (a) and ice (b) refractive index. 4c and 4d give results for $R(0.83\mu\text{m})$ vs. $R(2.21\mu\text{m})$ for liquid water (c) and ice (d) refractive index.

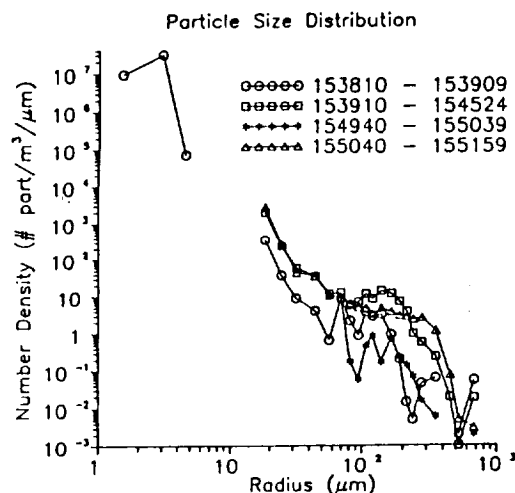


Fig. 5. King Air measured cirrus size distributions using the FSSP, 2D-C and 2D-P probes. Particle size for 2D probes is that of a sphere with equivalent cross-section area to the particle 2-D image. Size distributions are averaged over the time intervals shown in the figure.

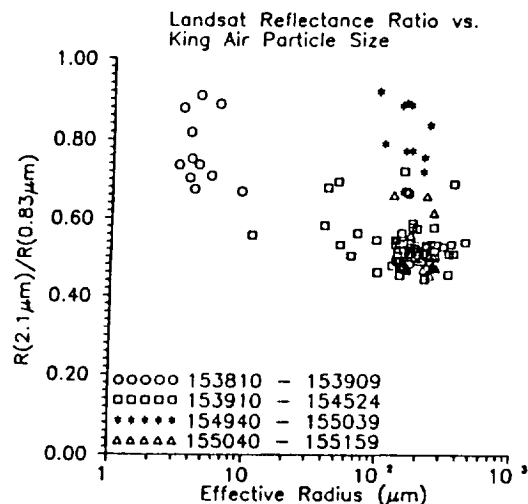


Fig. 6. Comparison of Landsat measured cloud reflectance ratio $R(2.21\mu\text{m})/R(0.83\mu\text{m})$ with the King Air determined effective radius r_e .

CIRRUS RADIATIVE CHARACTERISTICS and the RADIATIVE IMPACT of SMALL PARTICLES

Paul W. Stackhouse Jr., Grame L. Stephens and S.K. Cox

Department of Atmospheric Science, Colorado State University

Fort Collins, Colorado 80523

1 Introduction

An understanding of the way radiation interacts with clouds is vital for understanding the sensitivity of the earth's climate to both natural and anthropogenic changes in the atmosphere. Cirrus clouds are thought to be an important modulator of climate sensitivity (see Manabe and Strickler, 1964; Cox, 1973 and Stephens and Webster, 1981 among others). Stephens *et al.* (1989) show that the feedback effect of cirrus on climate can be positive or negative depending upon the microphysics and scattering properties of the cloud. These properties of cirrus clouds are not well understood partly because of their thin tenuous nature and partly because of their microphysical properties. The high altitude and cold temperatures within these clouds along with their transparency greatly increase the difficulty in which accurate measurements can be obtained and interpreted both by aircraft and remote sensing. Therefore, the understanding of the interaction of radiation in cirrus clouds is crucial to determining the ways in which these clouds interact with climate forcings.

The purpose of the present work is to examine the sensitivity of the radiative budgets of cirrus cloudiness to their microphysical composition and the environments in which they occur. Especially important is the impact of small particles on the radiative properties of cirrus. Remote sensing estimates of the effective crystal size of cirrus and *in situ* measurements show large differences up to 100 μm . Thus it becomes important to identify the sources of these differences. For this reason, simulations of actual FIRE cases are compared with the *in situ* radiative observations and inferences are made concerning the causes of the discrepancies.

2 Summary of the Radiative Transfer Model

A two stream radiative transfer band model for the solar (0.28 μm - 3.8 μm) and infrared (3.8 μm - 200.0 μm) wavelengths, is chosen and formulated in a way which allows for the consistent treatment of physical processes such as absorption and scattering by both molecules and particles which occur during the interaction of cloud and radiation (Stackhouse and Stephens, 1989). This is accomplished by solving the radiative transfer equation in terms of reflectance and transmittance coefficients and source terms dependent upon the optical depth, single scatter albedo and asymmetry factor of the optical media (Preisendorfer, 1976). The above three parameters represent the optical properties of molecules and particles for absorption and scattering processes and are weighted according to Slingo and Schrecker (1982). The particulate optical properties are determined using Mie solutions assuming equivalent diameter spheres from the particles measured during the IFO. Gaseous absorption is calculated using narrow band k-distribution data for H_2O , CO_2 , O_3 and O_2 having resolutions of 20 cm^{-1} and 50 cm^{-1} in the infrared and solar wavelengths respectively. Sum of exponential fit data is used for the ultraviolet wavelengths less than 0.68 μm . Optical paths were computed using the simple pressure temperature scaling parameterization with constants given for each gas by Chou and Arking (1980), Chou and Arking (1981), Chou and Peng (1983) and Chou (1984). Parameterizations of Rayleigh scatter (Paltridge and Platt, 1976) and e-type absorption (Kneizys *et al.*, 1982) are also included.

3 Radiation Budgets: Cirrus in Various Atmospheres

Some of the phenomenological properties of cirrus clouds are investigated by simulating cirrus clouds imbedded in various atmospheres. The atmospheres in which cirrus are imbedded include the FIRE October 28,

1986 sounding and the McClatchey *et al.* (1972) Tropical and Subarctic Winter soundings. The 3 km uniform cirrus is positioned such that cloud top corresponds to the tropopause height in each atmosphere. Figure 1a summarizes the infrared radiation budget of cirrus and shows that the net radiative effect of cirrus is largely determined by surface-cloud base temperature difference (and thus altitude) and that heating (cooling) increases with increasing (decreasing) altitude. Also the net infrared radiative effect of the cirrus is seen to be more sensitive to cloud thickness with increasing height. Infrared spectral analysis reveals that: a) radiative heating dominates in the window region (8-12 μm) while cooling is dominated more in the far infrared ($\approx 15\text{-}200\ \mu\text{m}$), and b) the heating (cooling) of the window region (far infrared) increases in both magnitude and spectral width with increasing (decreasing) altitude.

In the solar wavelengths, simulations reveal that the net solar heating of the clouds decreases with decreasing cloud top altitude, and the changes in the spectral distribution of absorption as a function of altitude were mainly confined to the 2.6 - 2.9 μm region where CO_2 is an active absorber.

The behavior of the radiative characteristics of cirrus in various atmospheres as deduced by the two-stream model agrees qualitatively to studies presented by Ackerman *et al.* (1988). Additionally, these results have profound climatological implications. It is not enough to know the amount or distribution of cirrus about the globe to understand their influence on the earth radiation budget. In order to understand the climatological effects of cirrus clouds, information regarding temperature and height as well as their distribution and microphysical characteristics must also be understood.

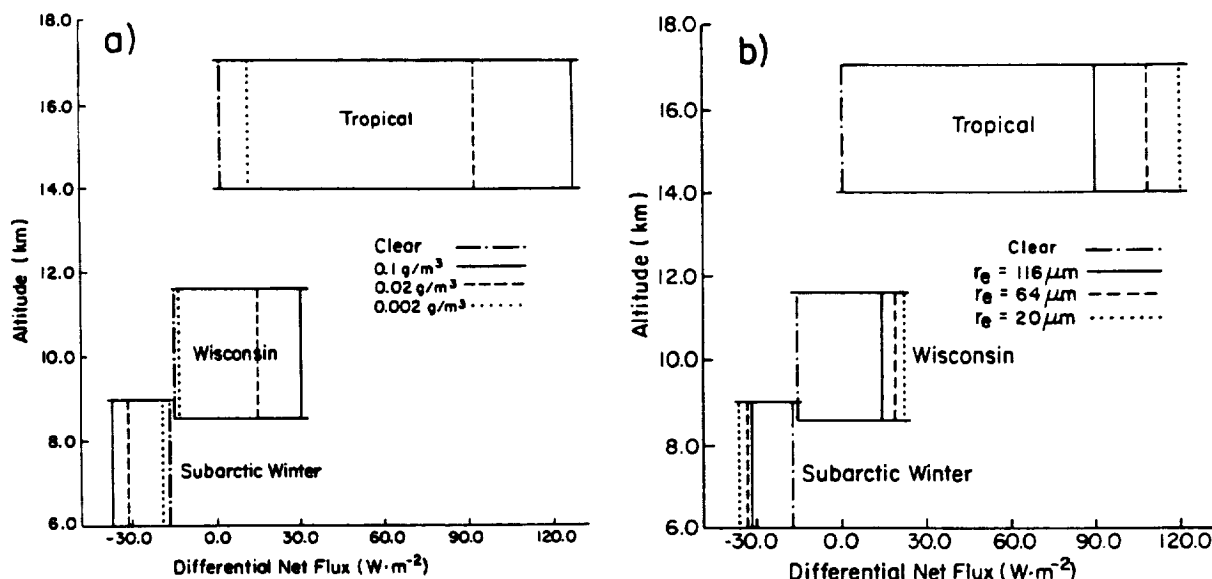


Figure 1: Schematic of the net infrared energy budgets of the three 3 km uniform cirrus clouds situated in their respective atmospheres as shown with a) each having effective radii of 116 μm for ice water contents as shown, b) each with ice water content of $0.002\ \text{g} \cdot \text{m}^{-3}$ having effective radii as shown.

4 Radiation Budgets: The Radiative Impact of Small Particles

Simulations assuming size distributions chosen from the FIRE observations and adjusted to include varying concentrations of small ice particles, are performed to evaluate the effect of these small particles on the radiative characteristics of cirrus clouds. Particles less than 50.0 μm in size were not measured during the cirrus IFO but their presence is speculated (Heymsfield and Miller, 1989). Concentrations of particles less than 100 μm in size are noted to be a source of uncertainty in understanding the radiative characteristics of cirrus clouds. To assess the importance of this uncertainty small particles are added to the observed crystal

size distributions. The sensitivities of the model to the reduction of the effective radius of the observed crystal size distribution by the addition of small particles for constant cloud ice water content (IWC) is shown in Figure 1b. This figure shows that the sensitivity of the net infrared radiative budget of the cloud to the effective radius reductions, increases with increasing altitude.

Additional simulations, where the IWC is allowed to increase with the amount of small particles added to the size distribution, show that the effect of the IWC increase on the cloud radiative characteristics is small relative to the enhanced extinction caused by the presence small particles. All simulations show that the addition of relatively small concentrations of small particles results in a substantial enhancement of cloud radiative heating and cooling rates, cloud emittances and albedos. It can be concluded that appreciable differences between observations of cirrus radiative characteristics and theoretical calculations may be partly attributable to uncertainties of the amount of small particles in the observed size distributions.

5 Comparison to Observations

Comparisons between the thin cirrus case observed during the FIRE cirrus IFO on October 28, 1986 over the vicinity of Green Bay, Wisc. and simulations of this case are shown in Figure 2. The observations are derived from the upward and downward looking pyrogeometers and pyranometers flown on board the Sabreliner for this case. The irradiances are stratified along each aircraft leg corresponding to mean, thin and thick cloud cases after Smith *et al.* (1989). In addition, it was determined that two different types of clouds were observed corresponding to the north and south legs of the racetrack flight pattern. The curves on Figure 2a and b are the result of two cloud cases one of which contains the measured size distributions from the Sabreliner flight data and the other with the same measured size distributions plus an exponential distribution of small particles less than $25\ \mu\text{m}$ in radius. The greatest amount of small particles comprising 20% of total ice water content, is assigned to the top cloud layer. This amount is decreased linearly toward cloud base where no small particles are assumed. In Figure 2c, a third cloud case corresponds to the resulting albedo when the asymmetry factor is artificially set to 0.7 for all the solar wavelengths. The comparisons shown in Figure 2a and b reveal that the simulated emittances of cirrus with the small particles added to cloud top agree most closely to the observed emittances. However, Figure 2c reveals that simulated albedos agree more closely to the observed albedoes with the addition of small particles but, the best agreement occurs when the asymmetry factor in the solar wavelengths is approximately 0.7. Thus the addition of small particles may be sufficient to explain discrepancies between the observed and simulated clouds in the infrared wavelengths but not in the solar wavelengths.

6 Conclusions

The radiative budgets of cirrus clouds are shown to be sensitive to the environment in which they are imbedded, the effective radii of the size distribution of which they are composed and their total ice water content. The comparison between the observations and simulations show that: a) underestimations of the infrared emittances are perhaps largely due to the overestimation of the effective cirrus crystal size which, may be traced to both the equivalent diameter sphere approximation and the underestimation of particles smaller than $100\ \mu\text{m}$ by observations and b) model underestimation of solar albedos is perhaps due in part to the overestimation of the asymmetry parameter as a result of the assumption of spherical particles.

It is clear from these results that the uncertainties involved in the estimation of the scattering properties of ice clouds remain one of the major hurdles that separates the agreement between the observations and simulations. Until the scattering properties of cirrus clouds are better understood, the interactions of radiation with microphysical parameters in the life cycle of these clouds will remain somewhat of a mystery. In addition, the climatic feedbacks of this radiation microphysical interaction will remain uncertain.

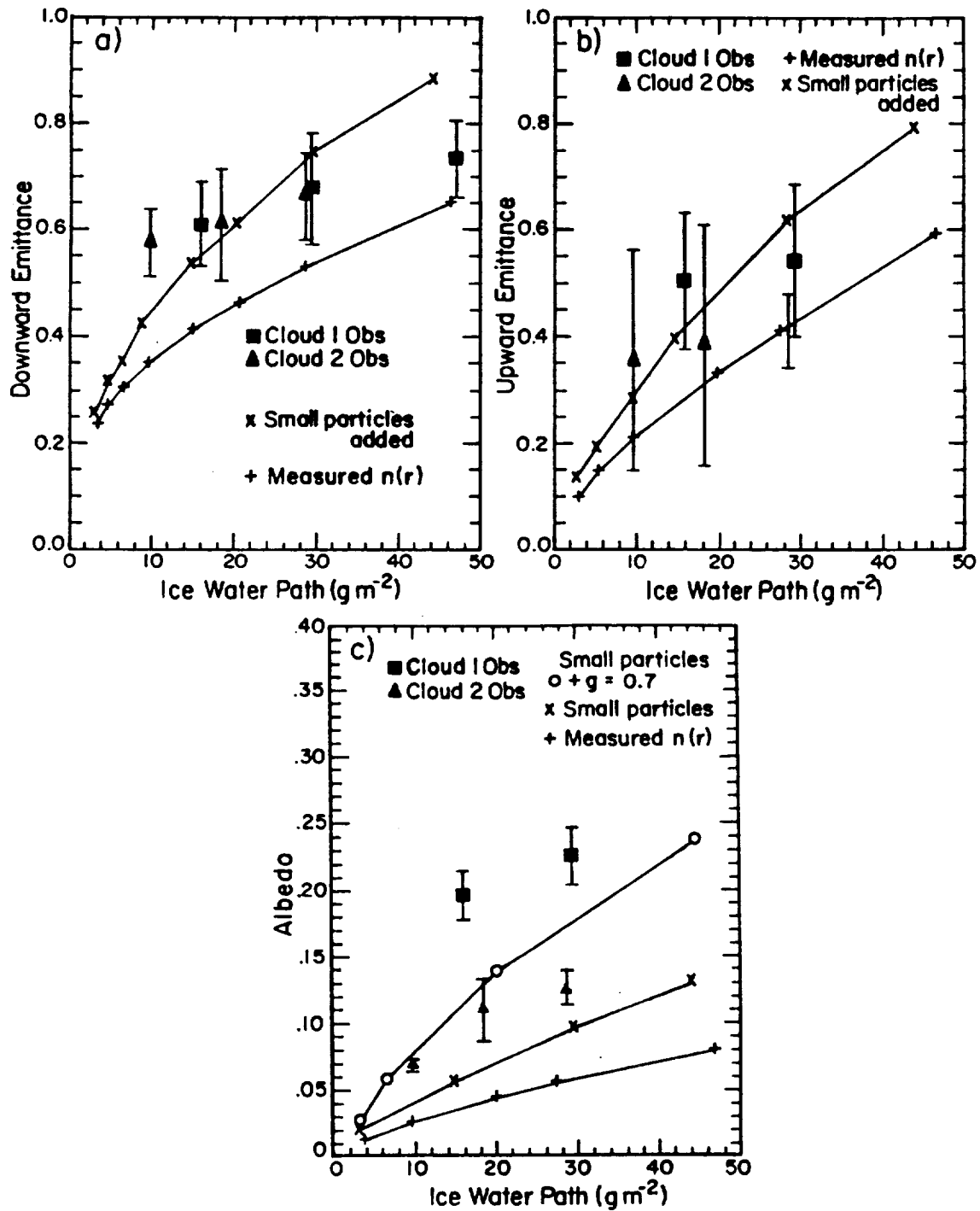


Figure 2: The variation of the downward emittance (a) the upward emittance (b) and the albedo (c) with IWP ($\text{g} \cdot \text{m}^{-2}$) computed from observed measurements for clouds 1 and 2 and the simulated emittances and albedos for the cloud cases as described in the text.

ACKNOWLEDGEMENTS

This research was supported by the Atmospheric Sciences Section of the National Science Foundation under Contracts ATM-8812353 and ATM-8519160; the Department of Defense, United States Air Force Office of Scientific Research under Grant AFOSR-88-0143; and the Department of Defense Office of Naval Research Grant N00014-87-K-0228/P00001. The Mie solution computations were performed using the super computer facilities at Colorado State University Computer Center.

REFERENCES

- Ackerman, T. P., K.-N. Liou, F. P. J. Valero and L. Pfister, 1988: Heating rates in tropical anvils. *J. Atmos. Sci.*, **45**, 1606-1623.
- Chou, M. -D., 1984: Broadband water vapor transmission functions for atmospheric IR flux computations. *J. Atmos. Sci.*, **41**, 1775-1778.
- , and A. Arking, 1980: Computation of infrared cooling rates in the water vapor bands. *J. Atmos. Sci.*, **37**, 855-867.
- , and A. Arking, 1981: An efficient method for computing the absorption of solar radiation by water vapor. *J. Atmos. Sci.*, **38**, 798-807.
- , and L. Peng, 1983: A parameterization of the absorption in the 15 μm spectral region with application to climate sensitivity studies. *J. Atmos. Sci.*, **40**, 2183-2192.
- Cox, S. K., 1973: Cirrus Clouds and the Climate. *ibid.* *J. Atmos. Sci.* **28**, 1513-1515.
- Heymsfield, A. J. and K. M. Miller, 1989: The October 27-28, 1986, FIRE cirrus case study: cloud microstructure. *submitted to Mon. Wea. Rev.*
- Kneizys, F. X., E. P. Shettle, W. O. Gallery, J. H. Chetwynd, Jr., L. W. Abreu, J. E. A. Selby, R. W. Fenn, and R. A. McClatchey, 1980: Atmospheric Transmittance/Radiance: computer code LOWTRAN 5. Report No. AFGL-TR-80-0067, Air Force Geophysics Lab, Hanscom AFB, MA., 200 pp.
- Manabe, S. and R. F. Strickler, 1964: Thermal equilibrium of the atmosphere with a convective adjustment. *J. Atmos. Sci.* **21**, 361-385.
- McClatchey, R. A., R. W. Fenn, J. E. A. Selby, F. E. Voltz, and J. S. Garing, 1972: Optical properties of the atmosphere, 3rd ed. AFCRL-72-0497, 108 pp.
- Paltridge, G. W., and C. M. R. Platt, 1976: *Radiative Processes in Meteorology and Climatology*, Elsevier, 318 pp.
- Preisendorfer, R. W., 1976: *Hydrological Optics V. Properties*, NOAA, PMEL.
- Slingo, A. and H. M. Schrecker, 1982: On the shortwave properties of stratiform water clouds. *Quart. J. Roy. Meteor. Soc.*, **108**, 407-426.
- Smith, Jr., W. L., P. F. Hein and S. K. Cox 1989: The October 27-28, 1986, FIRE cirrus case study: *in situ* observations of radiation and dynamic properties of a cirrus cloud layer. *submitted to Mon. Wea. Rev.*
- Stackhouse, Jr., P. W. and G. L. Stephens, 1989: A Theoretical and Observational Comparison of Cirrus Cloud Radiative Properties. *Atmos. Sci. Pap. No. 452*, Colorado State University, Ft Collins, 117 pp.
- Stephens, G. L. and P. Webster, 1981: Clouds and climate: Sensitivity of simple systems. *J. Atmos. Sci.*, **38**, 235-247.
- , P. W. Stackhouse, Jr., and P. J. Flatau, 1989: The relevance of the microphysical and radiative properties of cirrus clouds to climate and climatic feedback. *submitted to J. Atmos. Sci.*

Regional Conditions During The 25 October 1986 FIRE Cirrus/Alto cumulus Case Study

David O'C. Starr
NASA Goddard Space Flight Center
Greenbelt, MD 20771

Kenneth Sassen
Department of Meteorology
University of Utah
Salt Lake City, UT 84112

The regional cloud and meteorological conditions are described for this case using satellite imagery (GOES), dual polarization lidar data (from Wausau), NWS radar, NMC analyses, rawinsonde data including special soundings, and analyzed vertical motions. These observations are interpreted with respect to relationships between the observed cloud characteristics and corresponding atmospheric structure. Similarities with the 27-28 October FIRE Cirrus Case Study are noted.

Visible satellite imagery reveals overcast conditions over the upper Midwest at 2000 UTC on 25 October (Fig. 1a). Radar observations showed a band of light precipitation across southeastern Wisconsin at that time (echo tops to 7 km). Drizzle and light rain were also found to the south where the clouds were brightest. The decreased cloud albedo over southern Wisconsin indicates the presence of overlying cirrus clouds. The cirrus are more evident in the infrared imagery where a band of cold clouds stretches from western Iowa to Michigan (Fig. 1b). To the north and south of this feature, the high clouds appear more variable and were responsible for the patches of lower albedo seen over northern Illinois (Fig. 1a).

These clouds were associated with a nearly stationary occluded cyclone at the surface and closed low aloft (Fig. 2). The cyclone was centered in southern Illinois with the occluded front lying through southern Indiana and then southward to Georgia. The high clouds were located in the exit region of the upper level vortex and were bounded on the west by the interface between northerly flow (entrance) and southerly flow (exit). The northern boundary of the cirrus (Fig. 1b) lay along the transition between southerly flow out of the closed low and westerly flow in Canada. The cloud features moved steadily to the NNW during the afternoon.

Surface-based, dual-polarization lidar observations at Wausau prior to 1730 UTC detected fairly dense midlevel cirrostratus between 5.5 and 8 km (Fig. 3a). Observed polarization ratios (δ) of 0.55 to 0.65, corresponding to rimed (or very complex) ice crystals, were widespread in the lower portion of the cloud (Fig. 3b). At about 1730 UTC, cloud base height began to increase rapidly and evidence of supercooled liquid water was found between 7.8 and 8 km ($\delta \leq 0.15$). An overlying layer of cirrus between 9.5 and 11.1 km was observed at this time. Concurrent satellite observations indicate that this higher cirrus layer was present earlier but obscured by the midlevel cloud. Lidar observations after 1900 UTC may have also been significantly attenuated by the midlevel cloud layer. Subtropopause cirrus were sporadically detected above 10.5 km and another cirrus layer was observed between 8.5 and 9.8 km around 2000 UTC (Fig. 3a). Airborne observers noted the distinct clear region between this cirrostratus layer and the underlying midlevel cloud (Shanot, personal communication).

From 1900 to 2030 UTC during the King Air flight operations near Wausau, altocumulus clouds were observed between 7.8 and 8.1 km (-31 to -33 C) capping a 2.5-km deep ice cloud with a variable base around 5.5 km. Values of δ in the ice cloud were generally near 0.3 which is characteristic of some forms of cirrus. Low depolarization ratios ($\delta \leq 0.15$) in the ice cloud were likely associated with oriented plate crystals in sheared fallstreaks (in contrast to the liquid phase altocumulus layer, significantly increased δ and decreased return energy were found when the lidar was tipped off vertical by a few degrees - points labelled "x" along the bottom of Fig. 3). The strongest orientation effects were apparent below 7 km and well below the base of the altocumulus layer. This indicates that growth of the crystals to sizes greater than 200 μm , as required to maintain a stable orientation, or a change to a less complex crystal habit occurred during sedimentation. The flight crew of the King Air reported a continuous sloping cloud base during transit from Wausau, where cloud base was near 5.5 km, to Madison (2030 UTC), where the base height was about 3 km and drizzle was observed from a lower cloud layer.

Vertical velocities were estimated using the adiabatic method (three-station technique with an estimated uncertainty of $\pm 2 \text{ cm s}^{-1}$) applied to rawinsonde data from eight stations as in Starr and Wylie (1989). The location of the analyzed band of weak ascent (Fig. 4) on the 321 K isentropic surface (7.7 km at Green Bay and 8.2 km at Platteville in southwestern Wisconsin) corresponds very well to the position of the band of cold clouds (cirrus over midlevel cloud, Fig. 1b) at 0000 UTC on the 26th. Ascent rates of more than 3 cm s^{-1} were found at this level.

The corresponding vertical velocity profile computed from soundings at Green Bay (GRB), St. Cloud (STC) and Platteville (PLA) is shown in Fig. 5. The 1800 UTC profile (supplemental soundings at those stations) is consistent with upper level cloud generation at two primary levels - near the tropopause (11 km) where cirrus were detected and near the level where the altocumulus cloud layer was observed. Later, more uniform uplift is indicated throughout the upper troposphere when cirrus cloudiness was detected in the intervening layer (Fig. 3a). The fact that the maximum ascent rate at 1800 UTC was diagnosed above the altocumulus layer is not necessarily inconsistent with the observed cloud location since, as noted by Gedzelman (1988), the pre-existing vertical structure of water vapor plays a major role in determining the level of cloud formation. Rawinsonde-resolved vertical motions were quite weak below the level of the altocumulus layer where the adjoining 2.5-km deep ice cloud was observed.

Rawinsonde data from three soundings that ascended through the cloud band are shown in Fig. 6 - see Starr and Wylie (1989) for discussion of data quality. At Platteville (PLA), ice-supersaturation was observed at all levels colder than 0 C (no data at temperatures colder than -50 C), except for a layer from 8.9 to 9.7 km where relative humidity with respect to ice (RHI) decreased to 95% (Fig. 6a). Relative maxima of 102% were measured from 7.8 to 8.4 km and at the 9.9 km level (-50 C) corresponding to relative humidity with respect to pure liquid water (RH) of 73% and 64%, respectively. Greater humidities were found at lower levels (RHI = 108% at 5.5 km). The Wausau (WAU) sounding (released at 1855 UTC) exhibited more structure with RHI equal to 112% (RH = 85%) from 7.5 to 7.6 km (RHI $\geq 100\%$ from 6.8 to 7.8 km) and decreasing to 60% at -50 C and to 67% at -14 C (5.5 km). The lower vertical-resolution (standard) sounding at Green Bay (GRB) showed ice-supersaturation at 5.6 km (105%) and 7.7 km (101%) with drier but still humid conditions between these levels (RHI = 91% and 75% at 6.6 and 7.3 km, respectively) and above (91% and 86% at 8 and 8.9 km, respectively). Thus, each sounding indicates a relative humidity maximum near 7.8 km corresponding to ice-supersaturation but subsaturated with respect to the liquid phase. Both the GRB and PLA soundings show moist conditions at most levels while, except for the layer from 6.8 to 7.8 km, the WAU sounding is significantly drier. On this basis, it appears that the GRB and PLA soundings were representative of the more disturbed conditions to the south of Wausau where the base of the altocumulus-topped, midlevel, ice cloud extended to below 5.5 km.

The temperature profiles each show an inversion-capped boundary layer with a second inversion near the 3 km level at WAU and GRB (Fig. 6a). At WAU, a third inversion was found at 5 km. Tropopause heights ranged from 10.6 km at PLA to 11.2 km at WAU (11 km at GRB). The Platteville sounding is generally colder than the other two at a given height but this is mostly the result of the lower surface pressure (0.4 kPa) at PLA. Static stability structure is more evident in the potential temperature profiles (Fig. 6b). The high vertical-resolution sounding from Wausau exhibits a lot of fine structure in the upper troposphere that is not found in the PLA sounding of comparable resolution.

A striking feature of the GRB sounding is the nearly dry adiabatic stratification found from 6.6 to 7.3 km (9.4 C km^{-1}). This layer was capped by a relatively stable layer (5.8 C km^{-1}) extending to the 8 km level. There is also evidence for a statically stable layer at both Wausau (6.1 C km^{-1} from 7.7 to 8 km) and Platteville (7 C km^{-1} from 8 to 8.2 km) although the feature was weaker at those locations. The height of the stable layer corresponds closely to that of the thin, supercooled liquid phase, altocumulus layer observed over Wausau.

If the anomalously cold data point at the 7.3 km level in the GRB sounding is removed (regarding it as erroneous - possibly due to evaporative cooling of a wetted thermistor), the stable layer then extends from 7.7 to 8 km in accord with the other two soundings. In this case, the stratification below 7.7 km is also comparable in each of the soundings - lapse rates within 0.5 C km^{-1} of the ice-pseudoadiabatic lapse rate down to the 6.6 km level. The Green Bay sounding is still conditionally unstable in this layer but only slightly. Below 6.6 km, the GRB and PLA soundings become increasingly stable while the lapse rate at Wausau remains close to ice-pseudoadiabatic down to the inversion at the 5 km level. It is also of note that lapse rates were near ice-pseudoadiabatic in the layer where the overlying cirrostratus layer was observed - within 0.3 C km^{-1} from 8.5 to 9.8 km at WAU.

Upper level winds at Platteville were generally stronger than at Green Bay (Fig. 6c), especially from 8 km to the tropopause (unfortunately, the wind observations from Wausau were unusable). Of particular note is the more southerly wind directions found at GRB in the layer where the altocumulus layer and underlying ice cloud were observed (5.5 to 8 km). This may be interpreted as indicating deformation along the cloud band (see Figs. 1b and 2). The computed vertical velocity profile at 1800 UTC (Fig. 5) implies that horizontal mass convergence existed from roughly the 5 km level to near 9 km and was strongest between 7.5 and 8.5 km with divergence from 9 to 10.5 km and convergence from there to the tropopause. [Computed divergence profiles exhibited large variations depending on the stations used - probably attributable to the mesoscale character of the situation as discussed by Starr and Wylie (1989). Corresponding vertical velocity profiles computed by the kinematic method were judged to be relatively useless.] Similarly, convergence is indicated from 6.5 to 8.5 km at 0000 UTC on the 26th with divergence below.

Relatively strong wind shear was observed near the tropopause at both locations as wind direction veered from SE to SSW in the lower stratosphere. Weak veering was found near the 7 km level at PLA in association with a relative minima in wind speed. A similar feature occurred at GRB but at a lower height (near 6 km). Weak backing was found from there to 8.5 km.

In summary, regional analysis of the available rawinsonde data show that the supercooled altocumulus cloud occurred in a statically stable layer (7.8 to 8.1 km). Saturation was likely induced by adiabatic cooling due to weak ascent ($\sim 2\text{ cm s}^{-1}$) and enhanced by infrared cooling as described by Gedzelman (1988) and Starr and Cox (1985b) - solar warming was suppressed by the overlying cirrostratus cloud. Cellularity in the cloud was likely induced by infrared cooling at cloud top (see Starr, 1987b). Dynamic interaction with the adjoining 2.5-km deep ice cloud below

may also have been significant given the near ice-pseudoadiabatic stratification observed from 6.6 to 7.7 km which is consistent with weak convective overturning.

Uplift was associated with horizontal mass convergence that was strongest above 7.5 km. Given that the midlevel moisture supply associated with the convergent flow was fed by the more disturbed conditions to the south where precipitation was observed (echo tops to 7 km), the stable layer in which the altocumulus formed would be consistent with maximum detrainment of cloud water at that level in the disturbed region and maintenance of the midlevel cloud layer downstream. Furthermore, downward growth of the underlying ice cloud via ice particle sedimentation would be consistent with horizontal moisture supply near cloud top and maintenance of convective overturning (Starr and Cox, 1985a; Starr and Wylie, 1989) in the absence of significant mean ascent below the 7 km level. Maintenance of convective currents in the ice cloud would provide further moisture to the cloud by recycling vapor from evaporated particles below (Starr and Cox, 1985b).

Some notable similarities to the 27-28 October FIRE Cirrus Case Study (Starr and Wylie, 1989 - conclusions summarized in paper C02.01) are: 1) synoptic control dominated with a persistent cirrus shield maintained over a ridge axis (exit knee in the case here), 2) significant mesoscale structure was evident over a variety of horizontal scales (the long-lived 100 x 500 km altocumulus cloud band and smaller scale [10 km in width] transverse banding in cirrus here, Fig. 1a), 3) cloud generation occurred at multiple levels (optically thin subtropopause cirrus layer, an underlying cirrostratus layer and a lower altocumulus/altostratus/cirrostratus layer), and 4) relatively shallow (< 0.5 km) cloud generation layers were found.

REFERENCES

- Gedzelman, S.D., 1988: In praise of altocumulus. *Weatherwise*, 41, 143-149.
- Starr, D.O'C., and S.K. Cox, 1985a: Cirrus clouds, Part I: A cirrus cloud model. *J. Atmos. Sci.*, 42, 2663-2681.
- _____, 1985b: Cirrus clouds, Part II: Numerical experiments on the formation and maintenance of cirrus. *J. Atmos. Sci.*, 42, 2682-2694.
- _____, 1987b: Effects of radiative processes in thin cirrus. *J. Geophys. Res.*, 92, 3973-3978.
- Starr, D.O'C., and D.P. Wylie, 1989: The 27-28 October 1986 FIRE Cirrus Case Study: Meteorology and Clouds. (accepted by *Mon. Wea. Rev.*).

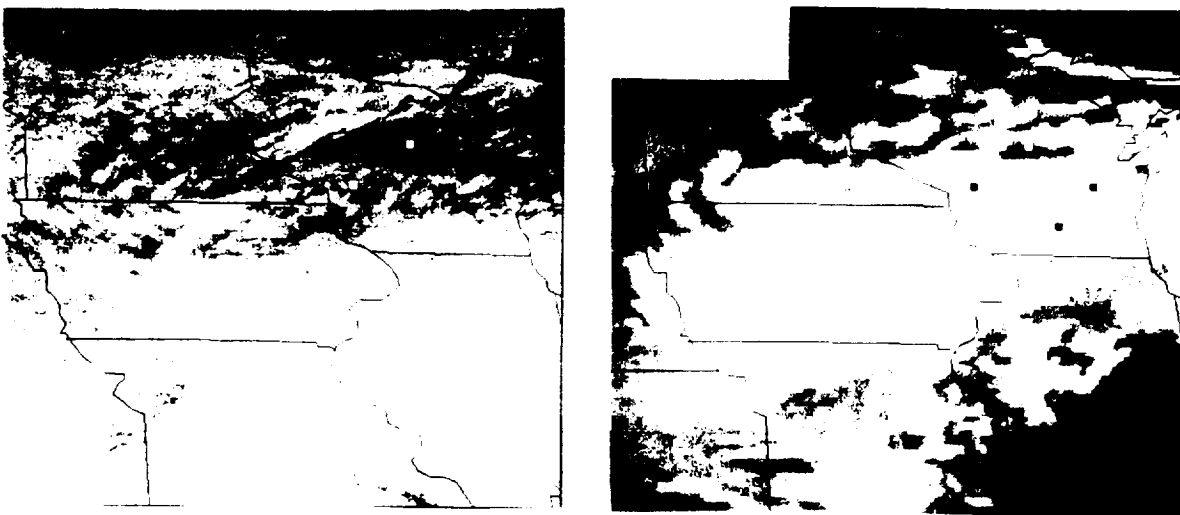


Figure 1: Visible (a) and infrared (b) satellite imagery from GOES-6 at 1800 UTC on 10-25-86.

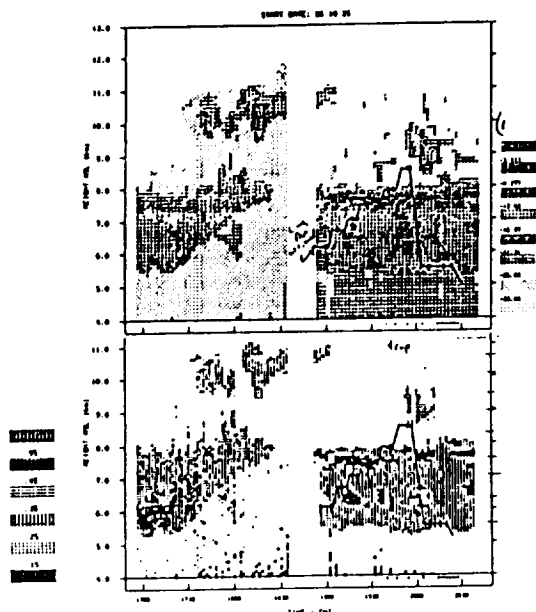


Figure 3: Time-height display of (a) range-corrected returned power (E) and (b) polarization ratio (δ) observed at Wausau by the University of Utah cloud lidar.

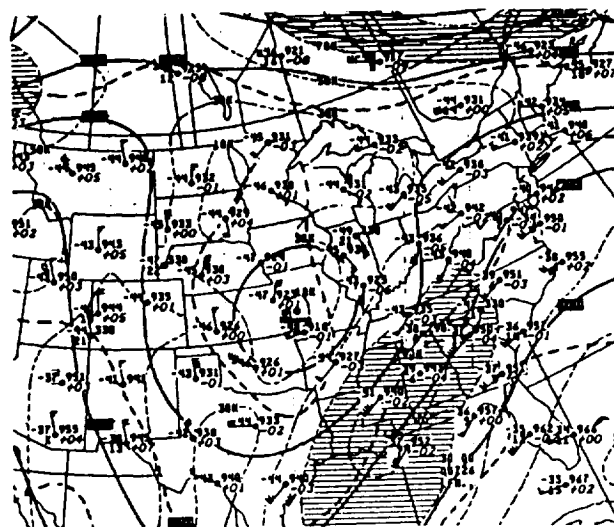


Figure 2: Upper air analyses (30 kPa) at 0000 UTC on 10-26-86.

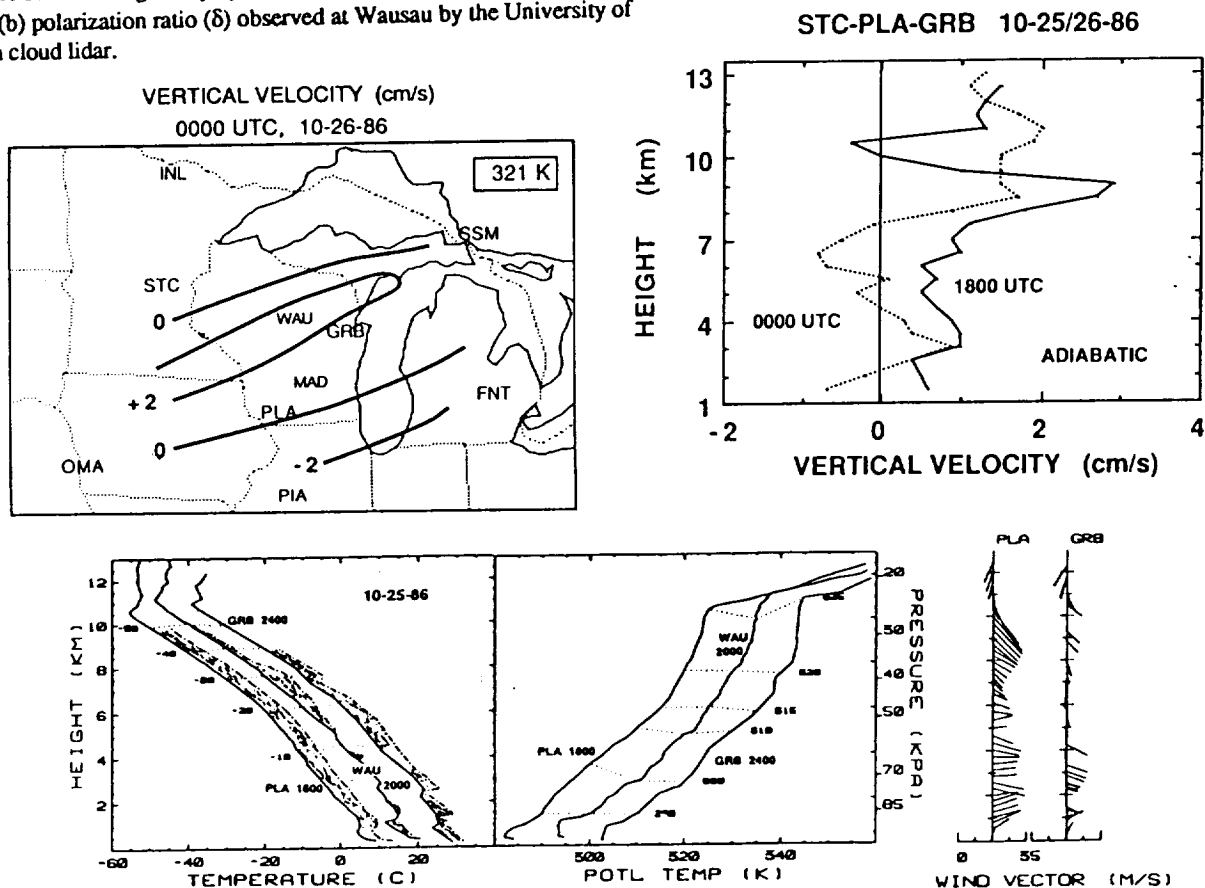


Figure 6: Rawinsonde-observed vertical profiles of a) temperature and relative humidity b) potential temperature, and c) horizontal wind vector observed at Platteville (PLA) at 1800 UTC, Wausau (WAU) at 2000 UTC on 10-25-86 and Green Bay (GRB) at 0000 UTC on 10-26-86. Temperature profiles are plotted on a scale reflecting a 10 C offset with respect to the profile to the left and similarly for potential temperature. Width of the shaded area indicates relative humidity values ranging from 50% to 100% (5°C width) or greater in the case of relative humidity with respect to ice (RHI) which is plotted at temperatures colder than -20 C.

	PAGE
C03.01 Cirrus Clouds and Climate Feedback: Is the Sky Falling and Should We Go Tell the King? Stephens, Graeme L.	389
C03.02 Low-Frequency Cloud-Radiation Interactions Randall, David A.	395
C03.03 Preliminary Simulations of the Large-Scale Environment During the FIRE Cirrus IFO <u>Westphal, Douglas L.</u> , and Owen B. Toon	401
C03.04 Microphysical Fundamentals Governing Cirrus Cloud Growth: Modeling Studies <u>Sassen, Kenneth</u> , Gregory C. Dodd, and David O'C. Starr	407
C03.05 A Scheme for Parameterizing Cirrus Cloud Ice Water Content in General Circulation Models Heymsfield, Andrew J., and Leo J. Donner	411
C03.06 Radiative Diffusivity Factors in Cirrus and Stratocumulus Clouds--Applications to Two-Stream Models Stephens, G. L., P. J. Flatau, S.-C. Tsay, and P. Hein	415

Cirrus Clouds and Climate Feedback: Is the sky falling and should we go tell the king?

Graeme L. Stephens

Dept. of Atmospheric Science, Colorado State University, Ft. Collins, CO 80523

1. Introduction

Global warming is a contemporary topic of great scientific interest. With the projected rise in sea level and the anticipated effects of climate change on agriculture among others, global warming has escalated to a major societal issue. At the grass-roots scientific level however, global warming has not yet been proclaimed as an accepted truth and it has been realized for some time that potential feedbacks via the effect of cloud on the Earth's radiation budget make nonsense of any prediction of a global temperature rise. A number of recent scientific studies have attempted to investigate the perplexing effects of cloud feedback in the context of a global warming. Some climate model results suggest that the feedback may even accentuate the warming induced by a CO_2 increase largely due to the enhancement of cirrus clouds in the models (e.g., Roeckner *et al.*; 1987).

It is a widespread belief that thin cirrus clouds act to enhance the 'greenhouse effect' owing to a particular combination of their optical properties (Manabe and Wetherald, 1967; Cox, 1971; Stephens and Webster, 1981). It is demonstrated in this study how this effect is perhaps based on inadequate resolution of the physics of cirrus clouds and that the more likely impact of cirrus to climate change remains somewhat elusive. These conclusions are developed within the context of a specific feedback mechanism incorporated into a simple 'mechanistic' climate model. A specific scientific question addressed here is whether or not the observed relationship between the ice water content and temperature of cirrus provides any significant feedback to the CO_2 greenhouse warming. A related question is also examined concerns the specific role of cloud microphysics and radiation in this feedback. This raises several pertinent issues about our understanding of cirrus clouds and their likely role in climate change as there presently exists a considerable uncertainty about the microphysics of these clouds (e.g. size and shape of ice crystals) and their radia-

tive influences.

2. Cloud microphysics and ice water content

Characterization of the shape and size of ice crystals in terms of their environmental parameters continues to be a heavily researched area of cloud physics. It is a topic crucial to the cloud climate problem. The observations of Heymsfield and Platt (1984) indicate that both the size of these ice crystals and the ice water content increases with increasing cloud temperature. Their results are reproduced in Fig. 1 together with the empirical relationship

$$w = 0.0007e^{0.041(T+60)} \quad (1)$$

where w is in $g.m^{-3}$ and T is in $^{\circ}C$. This relationship forms the basis for the ice water feedback studied in this paper.

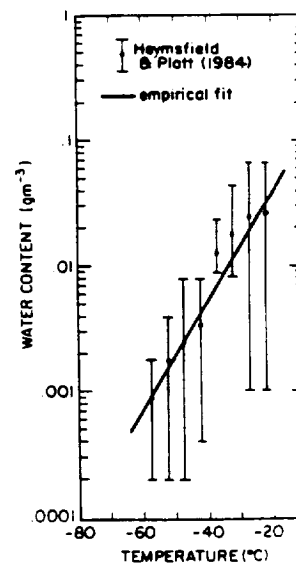


Fig. 1. The relationship between cirrus cloud ice water content and cloud temperature (after Heymsfield and Platt, 1984) and the relationship expressed by (1)

3. Cloud optical properties

The optical properties of the ice crystals were assumed to be spherical in shape and parameterized in the manner described by Stephens *et al.* (1989). A simple diffraction theory was adopted as the framework for this parameterization and the relevant properties of volume extinction and single scatter albedo were derived as functions of the effective radius of the size distribution (r_e) and the bulk absorption coefficient of ice. Typical values of r_e were chosen to be consistent with the observations reported by Platt and Harshvardhan (1988). Figure 2 shows the values of α_{obs} derived from a series of lidar-radiometer measurements (LIRAD) (e.g., Platt *et al.*, 1987) together with additional aircraft observations. Shown as curves are three relationships calculated from Mie scattering theory for a wavelength of $10.8 \mu\text{m}$ assuming an analytic size distribution with $r_e = 4, 16$ and $64 \mu\text{m}$. The three theoretical relationships included on the diagram are therefore based on the assumption that crystal size is invariant to temperature change and that the increase of ice water content with increasing cloud temperature occurs through an associated increase in total particle concentration. This is, by necessity, an overly simple assumption as already noted and a better understanding of the role of cirrus cloud microphysics in relationships like that shown in Fig. 2 is sorely needed.

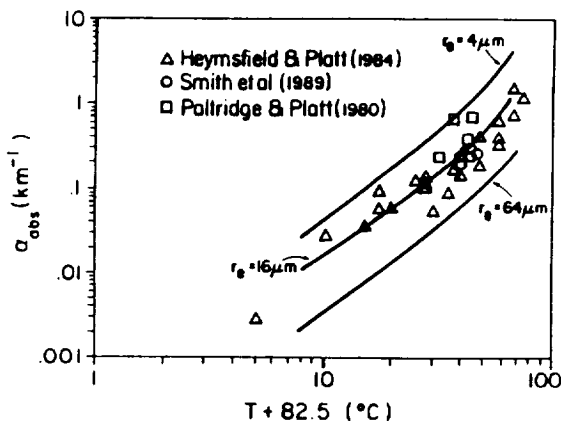


Fig. 2. The observed relationship between the volume absorption coefficient and cloud temperature taken from the sources indicated. The three curves were derived from Mie theory for the values of r_e indicated.

The asymmetry parameter was selected in the following way. Combined analyses of aircraft radiometric data and satellite data were employed to obtain

albedo (\mathcal{R})-emittance (ϵ) relationships that are then matched to theory in such a way as to provide a value of the asymmetry parameter. The values of \mathcal{R} and ϵ derived from the satellite data and the values obtained from the near coincident aircraft measurements are shown in the form of a scatter diagram in Fig. 3. Two theoretical relationships between albedo and emittance were also derived and are shown on Fig. 3. The relationship depicted by the solid curve is that derived from Mie theory with $r_e = 16 \mu\text{m}$ and the value of the solar zenith angle corresponding to the time of observation ($\mu_0 = 0.496$). The broadband average g determined from Mie theory and used to produce the solid curve is 0.87. The second relationship (dashed curve) provides a better fit to the observations and was obtained with $g = 0.7$. The difference between the Mie value of g and the value chosen to fit the observations is both significant and expected. It is straight forward to show that the reflectance of thin clouds is directly proportional to the backscatter fraction b_0 and hence a function of $1 - g$. The albedo of a cloud estimated using $g = 0.7$ is therefore greater than the albedo calculated using $g = 0.87$ (the emittance is largely independent of g). We show below that this difference in albedo significantly influences the predicted response of a climate model to the presence of cirrus cloud. It is also expected that real cirrus clouds, composed of irregularly shaped particles, have values of g that are smaller than the values of g associated with the more ideal spherical particles (e.g., Stephens, 1980).

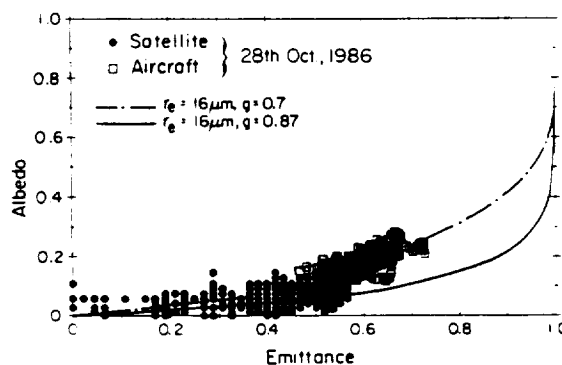


Fig. 3. The relationship between cirrus cloud albedo and emittance derived from aircraft and coincident satellite data obtained for the 28th October FIREcirrus case. For explanations of the curves consult the text.

4. The effects of cirrus optical properties in a simple climate system

The effects on a simple climate system of the cloud optical properties and their relation to ice water content on a simple climate system defined by a radiative equilibrium climate model which are examined. The radiative properties of the clouds were determined using the optical properties as specified above in a two stream model. Details are provided in Stephens *et al.* (1989).

(a) Simulations with fixed ice water

The results of a series climate equilibrium experiments are shown in Fig. 4 and 5 expressed as the difference between overcast and clear skies of the surface temperature ΔT_g , cloud temperature ΔT_c (upper panel), cloud albedo R and emittance ϵ (lower panel) as a function of r_e . The ice water path prescribed for these experiments was 3 g.m^{-2} which corresponds to a 1 km thick cloud at a temperature of 229°K . The model simulations were carried out using the two values of g mentioned above. The resultant surface warming reported in earlier studies like that of Stephens and Webster (1981) is also reproduced in this study. However, the magnitude of this warming is strongly dependent on both the value of g and the value of r_e which is assumed for R and ϵ . For example, the surface warming tendency is enhanced by either decreasing the particle size or by assuming more forwardly scattering cloud particles.

A principal driving force of the surface warming is the radiative heating of the cloud layer that results primarily from the absorption of infrared radiation. According to the analysis shown in Fig. 4, the cloud warming is more than twice the warming calculated at the surface. This is seen in the time evolution of the model solutions displayed on Fig. 5. The simulations were carried out with the following prescribed values; $r_e = 16 \text{ }\mu\text{m}$, $g = 0.7$ and $W = 4.7 \text{ g.m}^{-2}$. The simulated surface temperature undergoes a slight cooling during the first few simulation days and only significantly differs from the clear sky equilibrium value after about ten days into the simulation. By contrast, the cloud temperature systematically increases during the early stages of the simulation and after about 10 days of the simulation the increased emission from cloud base due to this temperature increase is enough

to drive a surface warming.

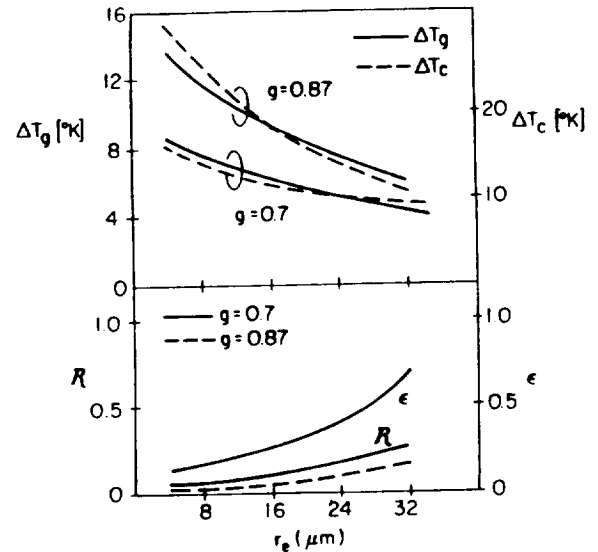


Fig. 4 The difference in equilibrium surface (T_g) and cloud (T_c) temperatures as a function of r_e for two values of g (upper panel) and the respective variation in albedo (R) and emittance (ϵ) with r_e (lower panel).

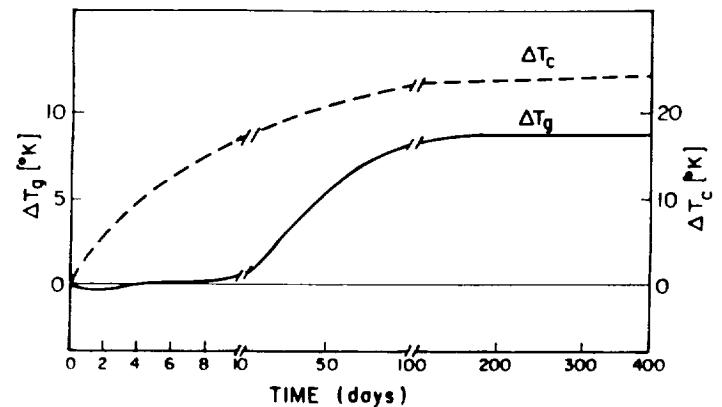


Fig. 5 Time evolution of the surface (solid) and cloud (dashed) temperatures predicted by the model.

(b) Simulations with ice water feedback

The ice water feedback was examined by analyzing pairs of control/perturbation simulations with the radiative equilibrium model. The perturbation experiment represents the simulations with twice the present day CO_2 concentration and the control simulations were run with the present day concentrations of CO_2 . The notation Δx is used to represent the difference between the perturbation and control simulations of a particular climate parameter of interest (say surface

temperature). Two pairs of perturbation/control experiments are then compared; one pair was conducted with the ice water feedback included in the model and the second pair assumed fixed values of ice water path. These comparisons are presented in terms of the parameter $\delta x = \Delta x(\text{with feedback}) - \Delta x(\text{fixed})$. Positive values of δT_g therefore indicate that the ice water feedback acts to reinforce the simulated CO_2 warming and negative values of δT_g indicate a buffering effect against such a warming.

Values of $\delta T_g, \delta T_c$ (upper panel), δW (middle panel) and $\delta \epsilon$ and δR (lower panel) are presented as a function of r_e in Fig. 6. All simulations were performed with $g = 0.7$. These results indicate that the sign of the ice water feedback varies according to the value of r_e used in the model to obtain the cloud optical properties. According to these simulations, the feedback is negative when $r_e < 24 \mu\text{m}$ and positive for larger crystal clouds. The explanation for this is revealed by comparison of δR and $\delta \epsilon$.

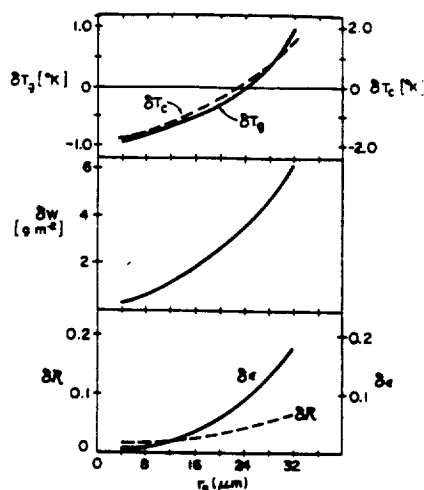


Fig. 6 The feedback parameter as defined in the text as a function of r_e .

5. Summary and Conclusions

Is the sky falling and do cirrus clouds make it worse? While the first part of this question was not explicitly addressed in this study it is clear that, from a scientific viewpoint, the potentially large but not well understood effects of cloud feedbacks cast serious doubts over any proclamations of impending climate change. The focus of this paper was directed towards the second question; is there overwhelming scientific evidence in support of a positive cirrus cloud feedback? Despite accepted wisdom to the contrary, the

results demonstrate that the sign of the cirrus feedback is uncertain, let alone its magnitude, and is influenced by cloud (microphysical and dynamical) properties that are presently neither well known nor well understood. The results also suggest that the surface warming induced by cirrus clouds as predicted previously by several others (including the author) may be model dependent and unrealistic. It was shown how the cirrus warming was governed by the radiative budget of the cloud itself. The absorbed infrared radiation gave rise to a direct warming of the cloud layer and it was shown that this warming was largely responsible for the associated surface warming. This scenario is clearly artificial as dynamical and turbulent motions, induced by the radiative warming, will likely act to alter the structure of real cirrus and perhaps even the character of the feedback. Thus an understanding of the dynamical aspects of cirrus, coupled to the microphysical and radiative properties, are likely to be important to the problem of understanding cirrus cloud feedback to climate.

6. Acknowledgements

This work was supported by the Atmospheric Sciences Section of the National Science Foundation under Contract ATM-8812353 and Office of Scientific Research of the United States Air Force under Contract AFOSR-88-0143.

7. References

- Cox, S. K., 1971: Cirrus clouds and climate. *J. Atmos. Sci.*, **28**, 1513-1515.
- Heymsfield, A. J., and Platt, C.M.R., 1984: A Parameterization of the Particle Size Spectrum of Ice Clouds in Terms of the Ambient Temperature and Ice Water Content. *J. Atmos. Sci.*, **41**, 846-855.
- Manabe, S. and R. T. Wetherald, 1967: Thermal equilibrium of the atmosphere with a given distribution of relative humidity. *J. Atmos. Sci.*, **24**, 241-259.
- Platt, C.M.R., J. S. Scott and A. C. Dilley, 1987: Remote Sounding of High Clouds. Part VI: Optical Properties of Midlatitude and Tropical Cirrus. *J. Atmos. Sci.*, **44**, 729-747.
- Platt, C.M.R. and Harshvardhan, 1988: Temperature dependence of Cirrus Extinction: Implications for climate feedback. *J. Geophys. Res.*, **93**, 11,051-11,062.

- Roeckner, E., U. Schlese, J. Biercamp and P. Loewe, 1987: Cloud optical depth feedback and climate modeling. *Nature*, 138-140.
- Stephens, G. L., 1980: Radiative Properties of Cirrus Clouds in the Infrared Region. *J. Atmos. Sci.*, **37**, 435-446.
- Stephens, G. L. and P. J. Webster, 1981: Clouds and Climate: Sensitivity of Simple Systems. *J. Atmos. Sci.*, **38**, 235-247.

Paper prepared for the FIRE Science Team Meeting, Monterey, California
July 1989

LOW-FREQUENCY CLOUD-RADIATION INTERACTIONS

David A. Randall

Department of Atmospheric Science
Colorado State University
Fort Collins, Colorado 80523

1. Introduction

The observed 30-60 day oscillation of the tropical winds (Madden and Julian, 1971), often referred to as the Madden-Julian oscillation, has excited considerable interest in recent years, because its existence suggests the possibility that the behavior of the atmosphere is at least partially predictable on such relatively long time scales. Most theories of the Madden-Julian oscillation have been based on wave-instability theories, such as wave-CISK. As discussed by Hu and Stevens (1989; hereafter HS), these theories have not yet satisfactorily explained the observations.

Recently, HS have suggested that the Madden-Julian oscillation is actually a *forced response* to periodic heating. They suggested that the oscillatory forcing originates in the hydrologic cycle, without the active participation of large-scale dynamics. They constructed a very simple model to support their hypothesis. According to their model, the oscillation originates in a progressive build-up of atmospheric water vapor, which continues until a (prescribed) threshold is reached, after which precipitation begins and rapidly dries the atmosphere. The drying due to a precipitation episode is followed by renewed gradual moistening, and the cycle continues indefinitely in this way.

In this paper we present preliminary results from a one-dimensional (1-D) version of the UCLA / CSU GCM (Randall *et al.*, 1989), which lend further support to the ideas of HS (1989). The present 1-D results also differ in important ways from those of HS, however. In particular, *cloud-radiation effects are essential for the oscillatory behavior of our model*, although they are not essential in the model of HS.

2. Model description

The 1-D model incorporates the full radiation and moist physics parameterizations of the GCM, including interactive cloudiness (Harshvardhan *et al.*, 1989).

In some of the simulations, the 1-D atmospheric model is coupled to a slab ocean of fixed depth. For simplicity, the slab does not exchange energy with the "deep ocean;" its temperature is controlled entirely by the surface energy flux.

In each of the simulations discussed below, the daily-mean incident solar radiation at the top of the atmosphere is set to the observed globally averaged value for the Earth. The model is

spun up for 1000 simulated days in order to reach statistical equilibrium, and then is run for an additional 2000 simulated days to produce results for analysis.

3. Results

When the sea surface temperature (SST) is fixed, the model produces strong oscillations of the precipitation rate, cloudiness, and surface energy flux, with a period of about 66 days. The only other spectral peak is diurnal. Figs. 1 and 2 show the time histories of the precipitation and surface solar radiation, for a particular 500 day segment. Fourier analysis (e.g., Fig. 3) shows that the 66-day spectral peak is both strong and sharp. In the following, we refer to this as the "control run."

As an experiment, we performed a simulation with fixed atmospheric radiative heating profiles, prescribed to be the same as the 2000-day average radiative heating profiles in the control run. No oscillations occurred in this "fixed-cloud" run. This indicates that cloud-radiation interactions are necessary to produce the oscillations.

To gain an understanding of the mechanism by which the oscillations are generated, we have examined in detail individual cycles of the oscillations produced in the control run. The results show that during periods of weak precipitation the upper troposphere is relatively warm, so that the static stability is relatively high. The warming of the upper troposphere is due primarily to the absorption of upwelling infrared radiation by the clouds, and to a lesser extent to the absorption of solar radiation.

When run with an ocean mixed-layer with a depth of 60 m, the model produces oscillations of the SST, with an amplitude of 0.4 K, and a period of 60 days. These are forced by the oscillations of the net surface energy flux, which are due to changes in the absorbed solar radiation; these are controlled, in turn, by the cloudiness fluctuations. The amplitude of the precipitation oscillation is slightly greater when the SST is allowed to vary. This may be because the ocean is relatively cool during the periods of weak precipitation, and relatively warm during periods of strong precipitation; the SST fluctuations thus act to reinforce the precipitation fluctuations.

4. Conclusions

Our results show that an atmospheric heating oscillation with a period of about 60 days can be generated by cloud-radiation interactions, without the participation of large-scale dynamical processes. This suggests the possibility that the observed Madden-Julian oscillation of the tropical winds is a passive dynamical response to such oscillatory forcing. A logical next step would be to explain why the observed oscillation originates near the maritime continent; there may be some reason why the oscillatory forcing is particularly strong in that region.

ACKNOWLEDGEMENTS

Support for this research was provided by NASA's Climate Program under Grant NAG-1-893.

REFERENCES

- Harshvardhan, D. A. Randall, T. G. Corsetti, and D. A. Dazlich, 1989: Earth radiation budget and cloudiness simulations with a general circulation model. *J. Atmos. Sci.* (to appear).
- Hu, Q., and D. E. Stevens, 1989: A mechanism for tropical ocean-atmosphere interaction on the intraseasonal time scale. Submitted to *Dyn. Atmos. and Oceans*.
- Madden, R. A., and P. R. Julian, 1971: Detection of a 40-50 day oscillation in the zonal wind in the tropical Pacific. *J. Atmos. Sci.*, **28**, 702-708.
- Randall, D. A. Harshvardhan, T. G. Corsetti, and D. A. Dazlich, 1989: Interactions among clouds, radiation, and convection in a general circulation model. *J. Atmos. Sci.* (to appear).

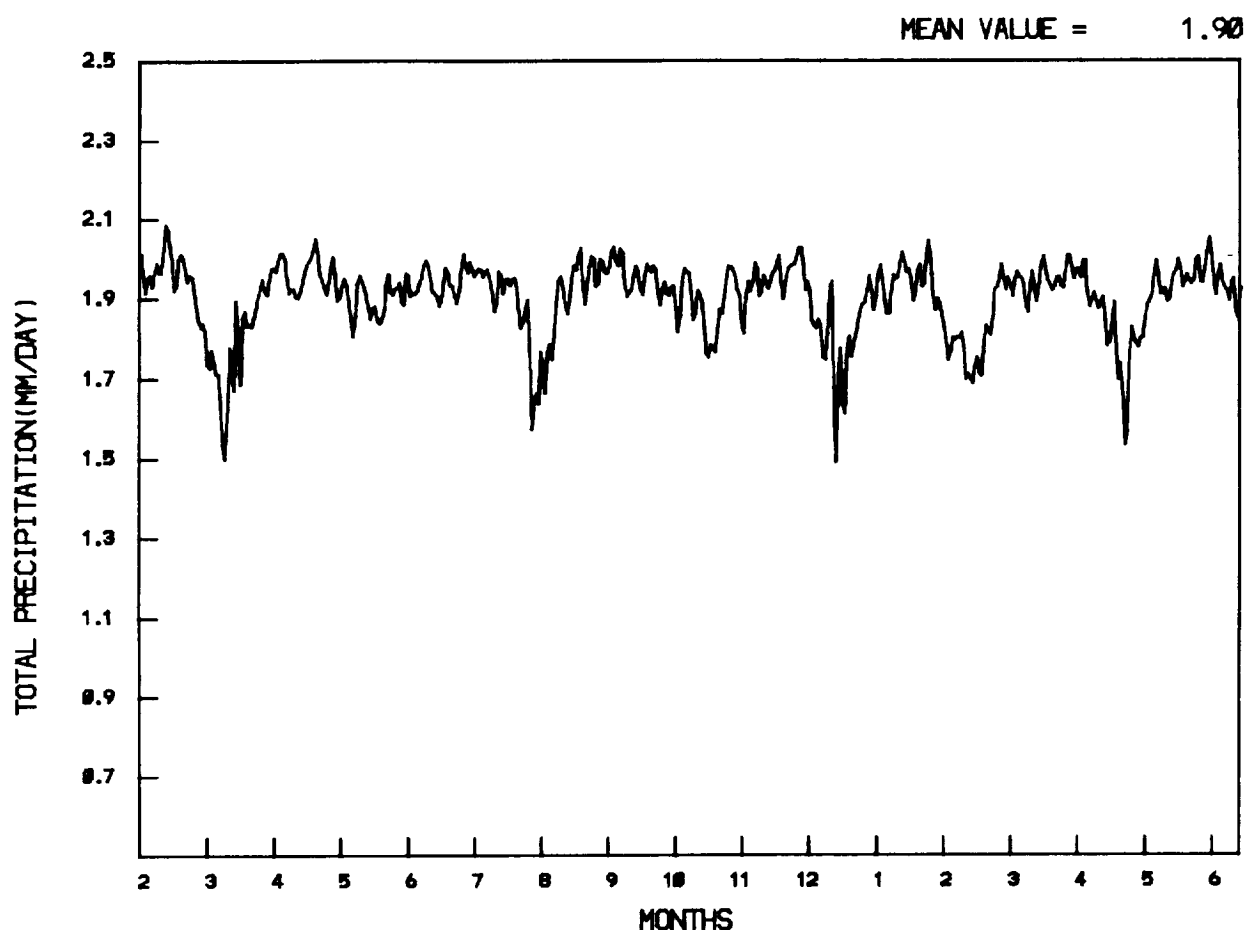


Figure 1 The time history of the precipitation, for a particular 500 day segment of the control run.

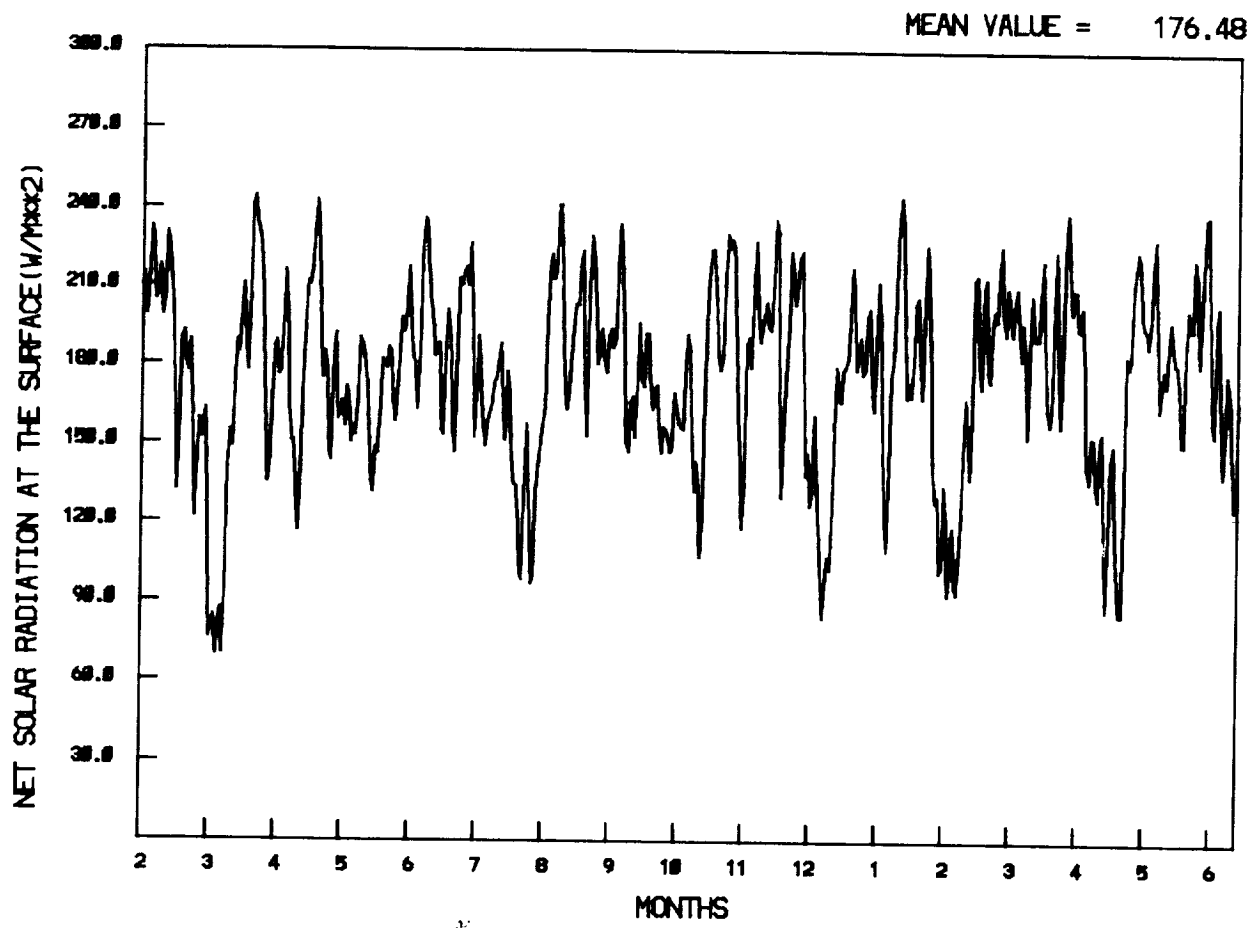


Figure 2: Same as Fig. 1, but for the solar radiation absorbed at the Earth's surface.

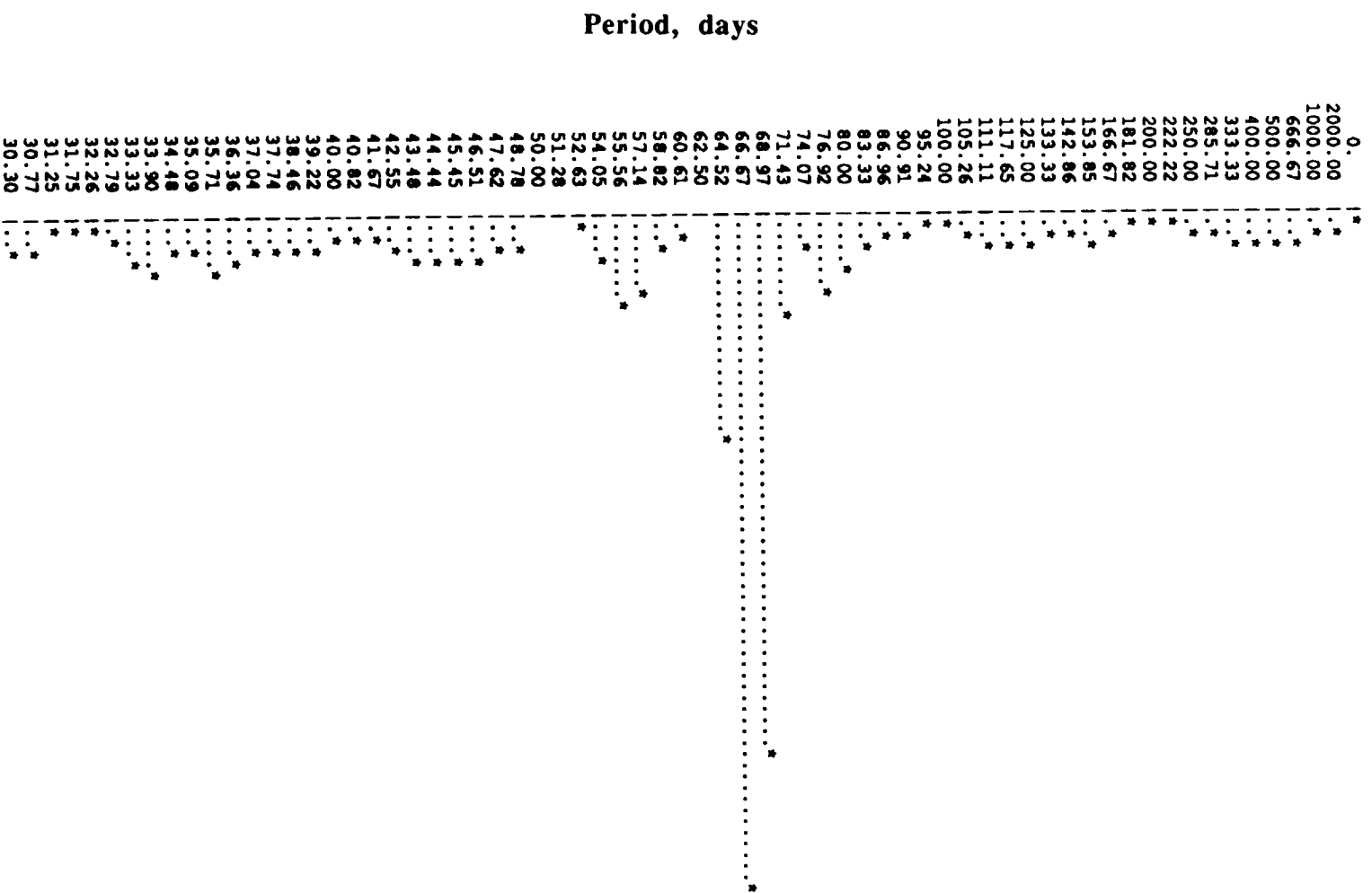


Figure 3: Square of the amplitude of the Fourier harmonics of the precipitation in the control run. The peak at about 66 days represents an amplitude of 0.3 mm day⁻¹.

PRELIMINARY SIMULATIONS OF THE LARGE-SCALE ENVIRONMENT DURING THE FIRE CIRRUS IFO

Douglas L. Westphal and Owen B. Toon
NASA Ames Research Center
Moffett Field, CA 94035

INTRODUCTION

Large-scale forcing (scales greater than 500 km) is the dominant factor in the generation, maintenance, and dissipation of cirrus cloud systems. However, the analyses of data acquired during the first Cirrus IFO have highlighted the importance of mesoscale processes (scales of 20 to 500 km) to the development of cirrus cloud systems (Starr and Wylie, 1989). Unfortunately, Starr and Wylie found that the temporal and spatial resolution of the standard and supplemental rawinsonde data were insufficient to allow an explanation of all of the mesoscale cloud features that were present on October 27-28, 1986. Below we will describe how dynamic initialization, or four-dimensional data assimilation (FDDA), can provide us with a method to address this problem. Then we will describe our first steps towards application of FDDA to FIRE.

FOUR-DIMENSIONAL DATA ASSIMILATION

In FDDA, asynoptic data are allowed to modify a numerical forecast by adding additional terms to the equations in the model which will force, or 'nudge', the model state towards the observations. The additional terms are weighted according to the proximity, both in time and space, of the observation to the model grid point. In this manner, the resultant modeled state reflects the observations in the vicinity where they were taken, and utilizes the model's forecast ability to determine the atmospheric state in data-sparse regions. For FIRE, the supplemental rawinsonde network data from the first Cirrus IFO and the anticipated time-continuous profiler data from the second Cirrus IFO can be systematically processed to form four-dimensional datasets describing the IFO's.

The FDDA method has been successfully applied to the Penn State/NCAR mesoscale model in studies of tropical cyclones (Anthes, 1974), severe weather (Kuo and Guo, 1989), terrain-induced flow (Stauffer and Seaman, 1987), and developing continental cyclones (Stauffer and Seaman, 1988). The study by Kuo and Guo has particular relevance to the Kansas IFO since they studied the impact, on mesoscale simulations, of FDDA of a network of 77 *simulated* wind profilers. Assimilation of the profiler data was effective in recovering mesoscale circulations which were not resolved by the conventional analyses of the rawinsonde data. In particular, the divergence field, which is critical for vertical motions, clouds, and precipitation, was significantly improved. Kuo and Guo suggest that even a small network of profilers, such as that which will be available in 1990, will improve the analyses; however, the impact is greatest in the region covered by the profilers.

PSU/NCAR MESOSCALE MODEL

As a first step towards applying FDDA to the FIRE IFO's, we have made a preliminary simulation over the continental United States from 0000 to 1200 UT, November 1, 1986 with the basic version of the PSU/NCAR mesoscale model *without* FDDA.

The PSU/NCAR mesoscale model used here is described in detail by Anthes *et al.* (1987). It is a hydrostatic, three-dimensional, primitive-equations model with a terrain-following vertical coordinate (σ). The model has a sophisticated multi-level planetary boundary layer parameterization and simple diagnostic parameterizations of convective and non-convective precipitation. The experiment described here was performed on a 61X46 grid with a 70-km mesh. We define the model top at 100 mb and the boundaries of the vertical levels at $\sigma = 1.0, 0.99, 0.95, 0.9, 0.8, 0.7, 0.6, 0.5, 0.43, 0.36, 0.29, 0.22, 0.15, 0.1$ and 0.0. These midpoint of these layers are approximately at 995, 970, 930, 865, 775, 685, 595, 520, 455, 390, 330, 265, 210, and 145 mb.

NOVEMBER 1, 1986 STUDY

We use NMC 2.5° analyses, interpolated to our grid, to initialize the model at 0000 UT November 1, 1986 (Fig. 1a). During this period a ridge lies to the east of Wisconsin and a trough to the west. Wisconsin is in generally WSW flow at 0000 UT and nearly zonal flow at 1200 UT. We then carry out a 12-hour simulation.

The results of this simple experiment demonstrate the ability of even a simple version of the mesoscale model to develop mesoscale features starting from the initial highly smoothed NMC analyses. As an example, we show in Figs. 1a-c the 0000 UT and 1200 UT analyses, and the 1200 UT simulation of 325 mb relative humidity. Both analyses show a smooth field with high values of relative humidity aligned parallel with the large-scale wave. In the 1200 UT simulation the horizontal gradients are sharper, especially along the northern boundary, and the separation in the moisture field over Wisconsin is more distinct than in the analyses. In Figs. 2a-c we show the 0000 UT and 1200 UT analyses and the 1200 UT simulation of relative humidity and potential temperature along a cross-section running southeast from the point A in Fig. 1 just north of International Falls, through Wisconsin, to the point B on the Indiana-Ohio border. A comparison with the 0000 UT and 1200 UT analyses (Fig. 2a-b) indicates that dry air at mid-levels has descended north of the front and that the relative humidity has increased at upper-levels directly above and south of the front. The 1200 UT simulated thermal structure (Fig. 2c) is nearly identical to the 1200 UT analyses. The 1200 UT simulated relative humidity exhibits the same trends seen in the analyses. However, the horizontal and vertical gradients of relative humidity are sharper and three maxima in the relative humidity field, not found in the NMC analyses, have developed between 300 and 200 mb (9.5 and 12 km). At the southern two maxima, the model has injected moisture above the tropopause. This is unrealistic and probably related to the simple moisture physics used for this experiment and to the coarse vertical resolution at the model top. Nevertheless, the model has developed vertical and horizontal structure in the moisture fields with scales of order 200 km that were not found in the NMC analyses. We are currently comparing both the analyses and the simulation with the observations.

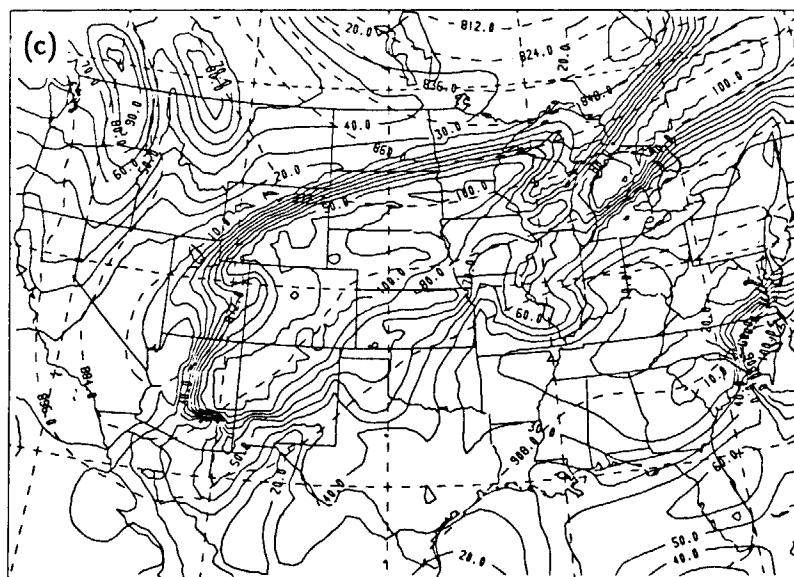
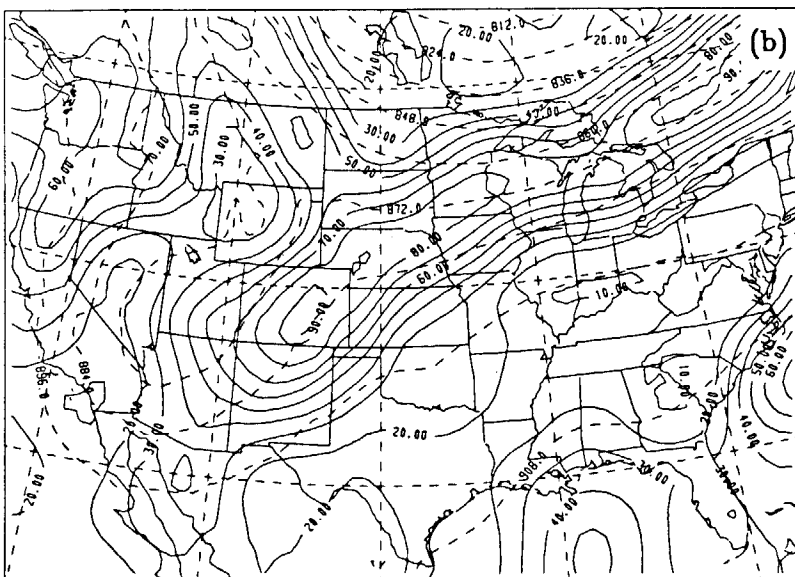
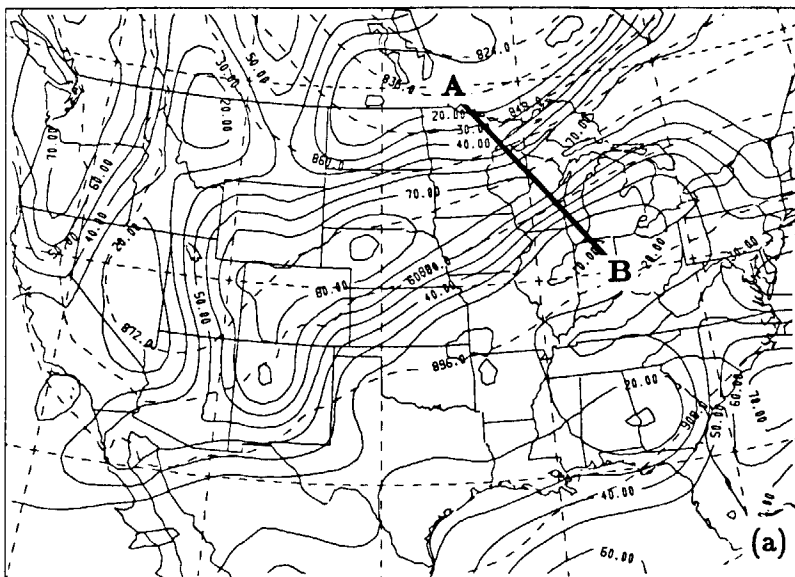
FUTURE APPLICATIONS

The general structure of the PSU/NCAR mesoscale model and its widespread use allow us to easily optimize the model for this study. In subsequent runs we will increase model resolution to 40 km in the horizontal and to 0.5 km in the vertical in the upper half of the troposphere and in the vicinity of the tropopause. We will improve the initial conditions by using the rawinsonde data to *desmooth* the NMC analyses. Then we will use the FDDA scheme to produce a four-dimensional dataset for the first Cirrus IFO. We will then have the capability and experience required for handling the large amount of profiler data that is expected during the second Cirrus IFO. We have long-range plans to replace the model moisture scheme with an explicit prediction scheme (Toon *et al.*, 1988) that will resolve the spectra of ice particles. We will also add a detailed radiative transfer scheme (Toon *et al.*, 1989). A discussion of these topics, however, is beyond the scope of this paper.

REFERENCES

- Anthes, R. A., 1974: Data assimilation and initialization of hurricane prediction models. *J. Atmos. Sci.*, **31**, 702-719.
- Anthes, R. A., E.-Y. Hsie, and Y.-H. Kuo, 1987: Description of the Penn State/NCAR Mesoscale Model Version 4 (MM4). NCAR Technical Note, NCAR/TN-282+STR, National Center for Atmospheric Research, P.O. Box 3000, Boulder, CO 80307.
- Kuo, Y.-H., and Y.-R. Guo, 1989: Dynamic initialization using observations from a hypothetical network of profilers. Submitted to *Mon. Wea. Rev.*
- Starr, D. O'C., and D. P. Wylie, 1989: The 27-28 October 1986 FIRE cirrus case study: meteorology and cloud fields. Submitted to *Mon. Wea. Rev.*
- Stauffer, D. R., and N. L. Seaman, 1987: A real-data numerical study and four-dimensional data assimilation application for mesobeta-scale flow in complex terrain. In *Proc. Symp. Mesoscale Analysis and Forecasting*, Vancouver, Canada, 17-19 August 1987.
- Stauffer, D. R., and N. L. Seaman, 1988: Use of four-dimensional data assimilation to limit error growth in a mesoscale numerical model simulation. In *Preprints of the Eighth Conference on Numerical Weather Prediction*, Baltimore, MD, 22-25 February, 1988.
- Toon, O.B., R.P. Turco, D.L. Westphal, R. Malone, and M.S. Liu, 1988: A multidimensional model for aerosols: Description of Computational Analogs. *J. Atmos. Sci.*, **45**, 2123-2143.
- Toon, O.B., C.P. McKay, T.P. Ackerman, and K. Santhanam, 1989: Rapid calculation of radiative heating rates and photodissociation rates in inhomogeneous multiple scattering atmospheres. Submitted to *J. Geophys. Res.*

Fig. 1: 325 mb fields of relative humidity (solid lines, contour interval of 10%) and geopotential height (dashed lines, contour interval of 12 dam) for November 1, 1986. (a) 0000 UT NMC analysis and model initial condition; (b) 1200 UT NMC analysis; and (c) 1200 UT PSU/NCAR mesoscale model simulation. The line A-B denotes the location of the cross-section shown in Fig. 2.



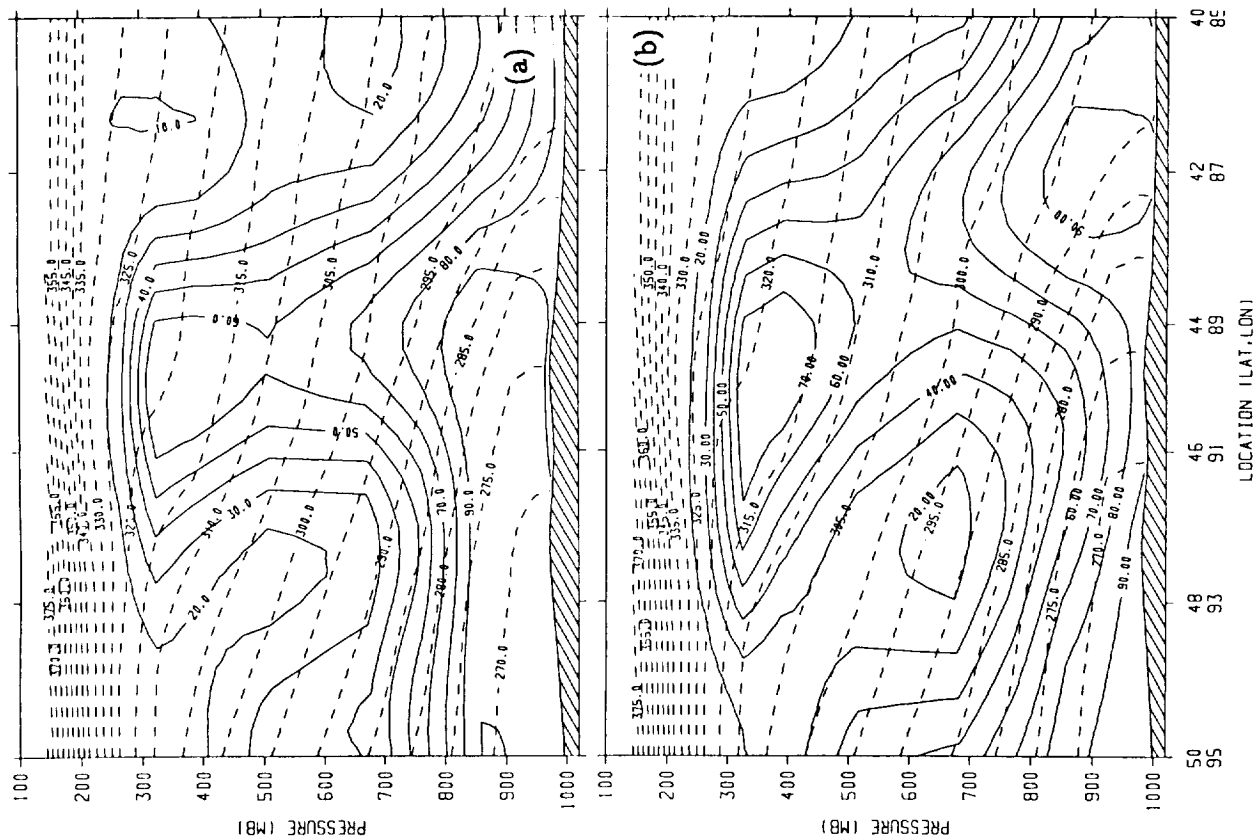


Fig. 2: Cross-sectional analysis of relative humidity (solid lines, contour interval of 10%) and potential temperature (dashed lines, contour interval of 6K) for November 1, 1986 along the line denoted by A-B in Fig. 1. (a) 0000 UT NMC analysis and model initial condition; (b) 1200 UT NMC analysis; and (c) 1200 UT PSU/NCAR simulation.

Microphysical Fundamentals Governing Cirrus
Cloud Growth: Modeling Studies

Kenneth Sassen and Gregory C. Dodd

Department of Meteorology, University of Utah
Salt Lake City, Utah 84112

David O'C. Starr

NASA Goddard Space Flight Center
Greenbelt, MD 20771

ABSTRACT

For application to Global Climate Models, large-scale numerical models of cirrus cloud formation and maintenance need to be refined to more reliably simulate the effects and feedbacks of high level clouds. A key aspect is how ice crystal growth is initiated in cirrus, which has triggered a cloud microphysical controversy between camps either believing that heterogeneous (Detwiler 1989) or homogeneous (Sassen 1989) drop freezing is predominantly responsible for "cold" (i.e., $\leq -35^{\circ}\text{C}$) cirrus ice crystal nucleation. In view of convincing evidence for the existence of highly supercooled cloud droplets in the middle and upper troposphere, however, we conclude that active ice nuclei are rather scarce at cirrus cloud altitudes, and so a new understanding of cirrus cloud formation is needed.

Previously, in the large-scale cirrus model of Starr and Cox (1985), for example, ice mass increases were linked to the maintenance of a relative humidity with respect to ice (RH_i) of 105%. Any growth above 105% occurred with regard to both the introduction of new crystals and the increase in mass of existing crystals, according to generalized cloud microphysical parameters. Where the cirrus cloud was absent, an RH_i of 120% was required to produce new ice crystals regardless of an understanding of ice nucleation mechanisms. The consequences of this simplified treatment cannot be evaluated without specific knowledge of cirrus ice crystal nucleation, which is considered here on the basis of detailed cloud microphysical modeling studies.

Our model, as described in Sassen and Dodd (1989), treats ice crystal nucleation and fallout in uniform $0.1\text{-}0.25\text{ m s}^{-1}$ updrafts embedded in a "cold" cirrostratus environment displaying vertical wind shear. Ice crystal nucleation occurs exclusively from the homogeneous freezing of haze particles composed of ammonium sulfate solutions using the freezing rate derived in Sassen and Dodd (1988) from cirrus cloud observations, which has been shown to be in good agreement with the theoretical and experimental results of Heymsfield and Sabin (1989) and DeMott (personal communication), respectively. Although the one-dimensional framework of the model limits large-scale model applications in some respects, the results are useful for comprehending basic cirrus cloud nucleation and laser scattering properties, for example (see Sassen and Dodd 1989).

A chief finding is that, even in a uniform updraft, ice particle generation in deep cirrus is accomplished in a pulse-like fashion due to the water vapor competition effects between growing haze particles and the initial ice crystals nucleated homogeneously. Figure 1 illustrates this basic characteristic in terms of relative humidity with respect to water (RH_w) and nucleated ice crystal concentrations within an impulse rising at 0.1 m s^{-1} in an environment with a $5 \text{ m s}^{-1} \text{ km}^{-1}$ wind shear. The cloud base temperature is -40°C , and the 0, 1, and 5 l^{-1} curves refer to the background ice crystal concentrations allowed to be entrained into the updraft. What is more important than the predicted frequencies of the ice generating pulses, which are influenced by the model framework, is the temperature dependency in the RH_w peaks. In particular, rather consistent results are generated over a range of likely cirrus conditions, suggesting that cirrus ice crystal nucleation occurs under reasonably predictable conditions.

The domain in the temperature/humidity field where the model simulations indicate that new cirrus ice particle generation is possible is depicted in Fig. 2. The symbols denote the results of tests using different maximum ammonium sulfate CCN masses, compared with results from basic theoretical homogeneous freezing considerations (the solid lines labeled by the CCN mass in grams). It is clear that to produce ice crystals within the homogeneous haze particle freezing regime, the required RH_w decreases with decreasing temperature, and water saturation is not required for temperatures $\leq -35^\circ\text{C}$. In effect, cold cirrus cloud processes follow an adjusted pseudoadiabatic affecting fundamental thermodynamic and microphysical processes.

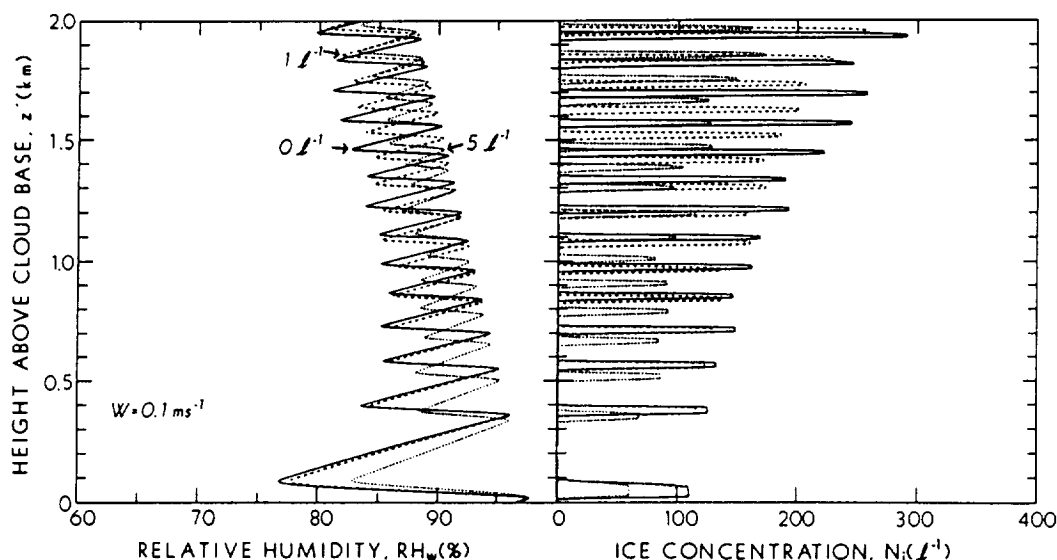


Fig. 1 Cirrus cloud microphysical model predictions of relative humidity RH_w and the concentrations of ice crystals N_i nucleated from freezing haze particles in a uniform updraft of $W = 0.1 \text{ m s}^{-1}$. With increasing background crystal concentrations of 0, 1, and 5 l^{-1} , N_i in each nucleation pulse decrease due to increasing vapor competition effects between haze particles and the total number of crystals present.

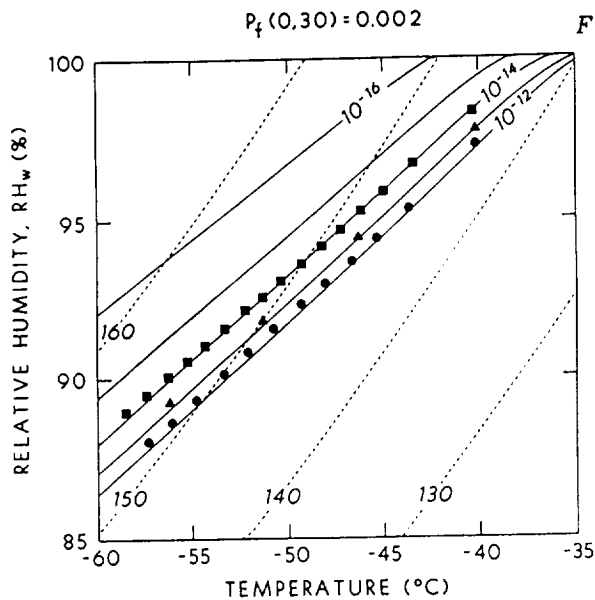


Fig. 2 The temperature/humidity dependence of cirrus ice nucleation computed from the homogeneous nucleation rate P_f at top and on the basis of model simulations (lines and symbols, respectively). A linear fit to the "•" symbols was used for Eq. (1).

On the basis of the model findings, we offer the following formula to describe the approximate temperature dependency in RH_w needed to introduce new ice crystals in large-scale cirrus cloud models:

$$RH_w = 5.36 \times 10^{-3} T(K) - 0.276 \quad . \quad (1)$$

This relation offers a considerable improvement over earlier attempts to parameterize cold cirrus cloud growth, as exemplified earlier, but at the same time further research is clearly needed to describe cirrus ice particle generation at temperatures warmer than about -35°C , where homogeneous nucleation would likely be ineffective. As a first step, however, available large-scale cirrus models should incorporate these findings to compare and evaluate the impacts of ice particle generation based on realistic microphysical considerations.

Acknowledgments. This research has been supported by Grant ATM-85 13975 from the National Science Foundation.

References

- Detwiler, A., 1989: Comments on "Homogeneous nucleation rates for highly supercooled cirrus cloud droplets." *J. Atmos. Sci.*, **46**, 2344-2345.
- Heymsfield, A. J., and R. M. Sabin, 1989: Cirrus nucleation by homogeneous freezing of solution droplets. *J. Atmos. Sci.*, **46**, 2252-2264.
- Sassen, K., 1989: Reply. *J. Atmos. Sci.*, **46**, 2346-2347.
- Sassen, K., and G. C. Dodd, 1988: Homogeneous nucleation rate for highly supercooled cirrus cloud droplets. *J. Atmos. Sci.*, **45**, 1357-1369.
- Sassen, K., and G. C. Dodd, 1989: Haze particle nucleation simulations in cirrus clouds, and applications for numerical and lidar studies. *J. Atmos. Sci.*, **46**, 3005-3014.
- Starr, D. O'C., and S. K. Cox, 1985: Cirrus clouds. Part I: A cirrus cloud model. *J. Atmos. Sci.*, **42**, 2663-2681.

A SCHEME FOR PARAMETERIZING CIRRUS CLOUD ICE WATER CONTENT IN GENERAL CIRCULATION MODELS

by

Andrew J. Heymsfield
National Center for Atmospheric Research
P.O. Box 3000
Boulder, Colorado 80307

Leo J. Donner
Department of Geophysical Sciences
University of Chicago
Chicago, Illinois 60637

1. INTRODUCTION

Clouds strongly influence the earth's energy budget. They control the amount of solar radiative energy absorbed by the climate system, partitioning the energy between the atmosphere and the earth's surface. They also control the loss of energy to space by their effect on thermal emission. Cirrus and altostratus are the most frequent cloud types, having an annual average global coverage of 35% and 40%, respectively. (Compiled from Hahn, et al., 1984, who used surface synoptic observations for the period 1971-1980). Cirrus is composed almost entirely of ice crystals and the same is frequently true of the upper portions of altostratus since they are often formed by the thickening of cirrostratus and by the spreading of the middle or upper portions of thunderstorms. Thus, since ice clouds cover such a large portion of the earth's surface, they almost certainly have an important effect on climate. With this recognition, researchers developing climate models are seeking largely unavailable methods for specifying the conditions for ice cloud formation, and quantifying the spatial distribution of ice water content, IWC, a necessary step in deriving their radiative characteristics since radiative properties are apparently related to IWC (e.g. Griffith, et. al., 1980). This study develops a method for specifying ice water content in climate models, based on theory and measurements in cirrus during FIRE and other experiments.

2. APPROACH

A conceptual model of the production of ice within a lifting layer is illustrated in Fig. 1. The horizontal extent of the layer is commensurate with one GCM grid, ≥ 100 km, and in the vertical it is 1 km. The parameterization will generate mean IWC for this layer, whose horizontal dimensions do not enter the parameterization, and whose vertical dimensions enter only weakly. The layer lifts at constant velocity, w (taken as the large-scale vertical velocity prognosed by the GCM or obtained from aircraft data in the verification experiments), from some initial state characterized by temperatures T_i and \bar{T}_i , and pressures p_i and \bar{p}_i , at its base and top, respectively. The relative humidity is assumed to be at ice saturation. After lifting for time t , the layer contains an ice water content given by the difference between the vapor mass sublimated onto the ice crystals and the net fallout of ice mass from the layer. Fallout must be considered since ice crystals have terminal velocities of tens of cm s^{-1} , much more than synoptic scale vertical velocities.

In this section the theoretical development of this conceptual view is given, and a discussion of aircraft flights used to characterize the ice mass distribution in deep ice clouds will be presented. The IWC's from the aircraft measurements are enhanced in some instances by horizontal advection of ice formed above and outside of the layers in cirrus convective cells, a factor which must be considered in comparing the measurements to the model results.

A. Theoretical Development

The total water mass in a layer undergoing ascent and cooling is constant, except for the accumulated mass which settles out of the layer:

$$X_{s,s}(1 + S_s) + X_s = C - F, \quad (1)$$

where $X_{s,s}$ is the mixing ratio of the vapor at saturation with respect to the solid (ice), X_s is the ice mass mixing ratio, S_s is the supersaturation with respect to ice, C is the initial water mass, and F is the mass mixing ratio of ice which has settled out of the layer.

The mass settled out of the layer (in a Lagrangian framework) is given by the vertical divergence of the ice mass mixing ratio integrated over the time of the parcel's ascent:

$$\begin{aligned} F &= \int_0^t \frac{1}{\rho} \frac{\partial}{\partial z} \left[\int_0^{D_{max}} N(D, t') m(D, t') V_t(D, t') dD \right] dt' \\ &= \int_0^t \frac{1}{\rho} \frac{\partial}{\partial z} [\rho X_s \bar{V}_t] (p_i, t') dt', \end{aligned} \quad (2)$$

where ρ is the density of air, z is the height, p is the pressure, t is the time, N , m , and V_t the concentration, mass and terminal velocity of ice crystals of dimension D , and \bar{V}_t the mean mass-weighted terminal velocity. The bracketed term on the right-hand side of Eq. (2) is the precipitation mass flux (or precipitation rate) relative to the lifting layer.

Taking the time differential of Eq. (2), using the Clausius-Clapeyron and hydrostatic equations, and taking $\frac{d}{dt} = w \frac{d}{dz}$, where w is the layer ascent velocity, the following is obtained²:

² We have denoted Lagrangian derivatives as total derivatives, although strictly speaking these are partial time derivatives with the initial position of the layer held constant, as noted explicitly in Eq. (2).

¹ The National Center for Atmospheric Research is sponsored by the National Science Foundation.

ICE PRODUCTION IN LIFTING LAYER

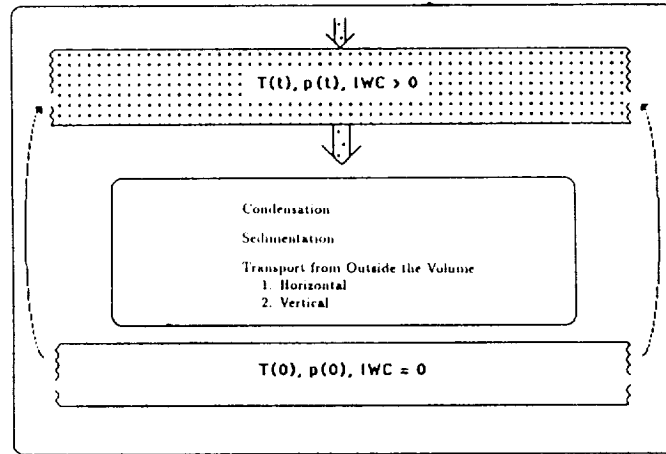


Figure 1. A conceptual model of the production of condensate in an ice cloud.

$$\frac{dX_s}{dt} = \underbrace{-(1 + S_s) w X_s \left(\frac{L_s}{R_v T^2} \frac{dT}{dz} + \frac{g}{R_d T} \right) - X_{vs} \frac{dS_s}{dt}}_{\text{supply}} - \underbrace{X_s \bar{V}_t \left[\frac{1}{\bar{V}_t} \frac{d\bar{V}_t}{dz} + \frac{1}{X_s} \frac{dX_s}{dz} - \frac{1}{T} \frac{dT}{dz} - \frac{g}{R_d T} \right]}_{\text{sedimentation}}, \quad (3)$$

where L_s is the latent heat of sublimation, R_v and R_d are the ideal gas constants for water vapor and dry air, T is the air temperature, and g is the gravitational acceleration constant. The change in temperature is computed on the basis of dry adiabatic ascent and latent heat released due to vapor deposition onto ice crystals:

$$\frac{dT}{dz} = -\frac{g}{c_p} - \frac{L_s}{c_p} \frac{d}{dz} [(1 + S_s) X_{vs}]. \quad (4)$$

If supersaturation with respect to ice S_s is known³ as a function of z , Eq. (4) provides an expression for $\frac{dT}{dz}$ for use in Eq. (3).

The \bar{V}_t is evaluated from calculations of the ice mass precipitation rate in deep ice clouds by Heymsfield (1977). Converting to the terms used here,

$$\bar{V}_t = 1.09 (\rho X_s)^{0.16}, \quad (5)$$

where V_t is in units of m s^{-1} , ρ is in units of g m^{-3} , and X_s is unitless. Values predicted from this equation are in accord with estimated particle terminal velocities of 0.3 to 2.0 m s^{-1} in virga falling from ice and snow generating cells (e.g., cirrus uncinus).

³ Our calculations assume an ice-saturated mixing ratio through the cloud depth.

Fig. 2 illustrates the ice water content for several layers undergoing ascent for $t=10,000$ sec., obtained by solving Eq. (3). Temperatures indicated are those at the end of the time period, and vertical velocity is held constant throughout. A common characteristic is a phase during which IWC increases with time, followed by a phase during which it decreases. Ice mass first increases in the layer by condensation; as the ice content increases, settling becomes increasingly important in removing ice, eventually dominating as the layer continues to cool moist adiabatically and the condensation rate decreases. Thus,

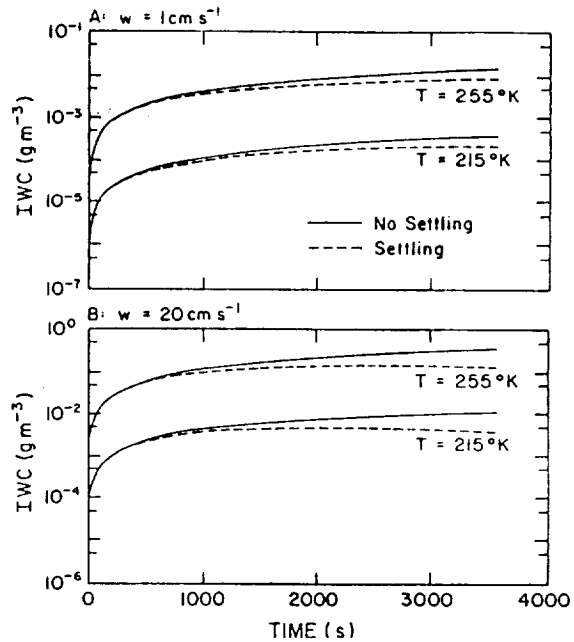


Figure 2. The ice water content as a function of time for several layers undergoing ascent for various temperatures (at the end of the ascent) and vertical velocities. A: $w = 1 \text{ cm s}^{-1}$. B: $w = 20 \text{ cm s}^{-1}$

the ice content of a layer depends on its ascent time. In later comparisons with aircraft measurements the ice content for a fully developed ice cloud will be taken as the maximum value during the layer ascent. These contents are appropriate for comparison with ice contents measured in clouds by aircraft which typically sample the densest regions of clouds undergoing penetration.

Later in this paper we will be comparing data from aircraft taken at particular temperatures and pressures with those predicted from Eq. (3). The comparison should be for the time the maximum IWC is reached in the parcel. Therefore, the history of parcel ascent must be reconstructed so that the initial conditions of the parcels ascent can be deduced. An estimate of the ascent time to maximum ice content for the conditions at the end of the parcel's ascent is made by tracing a parcels ascent backwards in time. The estimated initial temperature and pressure is iterated using the ascent times to maximum ice content until the cycle does not change the ice content significantly.

B. Aircraft Data Collection

Data were collected by aircraft in cold clouds over the continental United States in the mid-1970's during the Environmental Definition Program (EDP) (Heymsfield, 1977) and from the FIRE cirrus IFO. Measurements in the twenty EDP flights were acquired in the densest (visually) regions of deep winter- and springtime ice clouds associated with warm frontal overrunning systems, warm frontal occlusions, closed lows aloft, and jet stream bands. Sampling patterns consisted of 25-km-long constant altitude legs oriented parallel to the wind direction, beginning at the cloud top (8.5 to

11.0 km), and descending in 600-m steps to below cloud base (1 to 5 km). Four of the flights were coincident with single Doppler radar measurements. The FIRE data reported here were collected during eight flights by the NCAR King Air aircraft in visually dense cloud during spiral descents which began near cloud top (8 to 9 km) and ended at or below cloud base (5 to 6 km). The aircraft drifted with the wind and descended at a rate of about 2 m s^{-1} to follow approximately the fallout of the ice particles. The flights occurred on 19 October, 22 October, 25 October (2 flights), 28 October (2 flights), 1 November, and 2 November 1986. Horizontal distances covered by each loop of the spiral were from 5 to 10 km. Synoptic systems sampled were the same as those discussed above for the EDP data.

Aircraft size spectra measurements were used in conjunction with the ice crystal shape data to calculate the ice water content and precipitation rate. Vertical air velocity was calculated by equating the change in the calculated precipitation rate between two sampling levels to the vertical flux of moisture producing this change (Heymsfield, 1977).

3. RESULTS

The variation of ice water content with temperature and vertical velocity from the parameterization is illustrated by the lines in Fig. 3. These curves are computed by assuming ice-saturated ascent in Eq. (4) over times required for condensation and settling to balance (about 1800 to 4000 seconds). Pressure at the end of the ascent time is taken as the average for a specified vertical velocity from the aircraft data. The IWC depends primarily upon T , varying by four orders of magnitude over temperatures found in the troposphere. Increasing

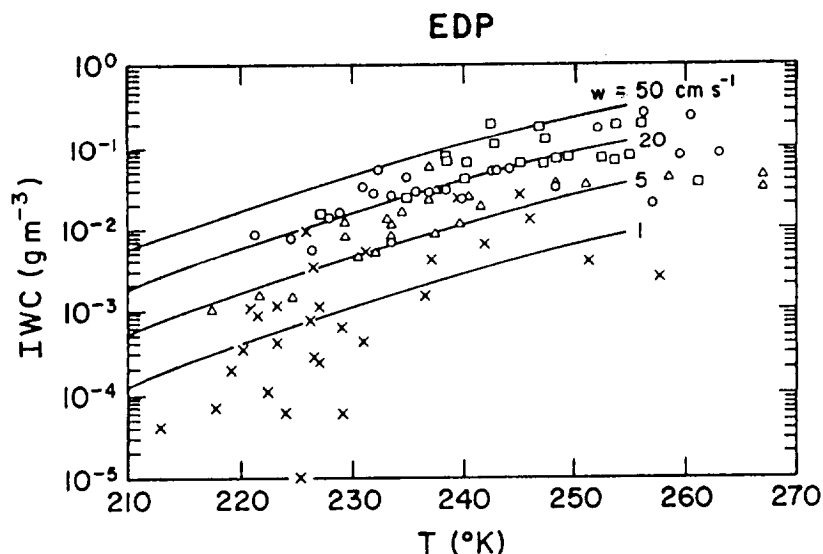


Figure 3. IWC values for each constant altitude penetration from the EDP data, plotted against temperature and partitioned into vertical air velocity intervals. Curves for the mid-point of the vertical velocity intervals from the parameterization are shown with dashed lines. Crosses: 0 to 2.5 cm s^{-1} ; triangles: 2.5 to 10 cm s^{-1} ; circles: 10 to 33 cm s^{-1} ; squares: $>33 \text{ cm s}^{-1}$.

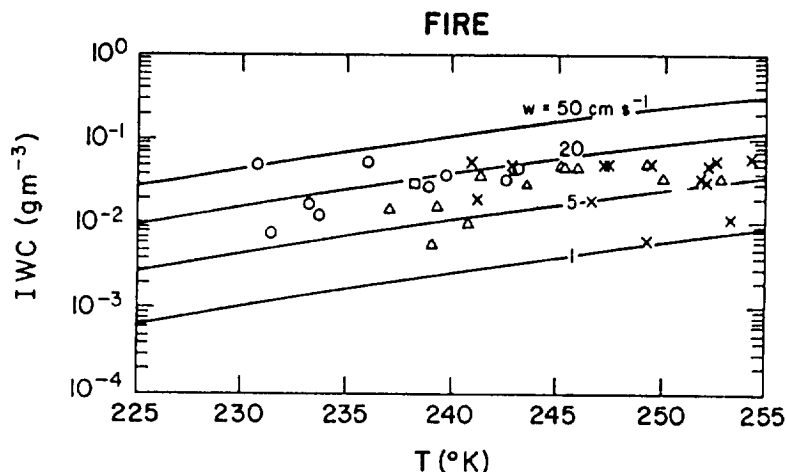


Figure 4. Same as Fig. 3, except for the FIRE measurements. Each data point is from the mid-altitude of a loop during a Lagrangian spiral descent.

w produces less than linear increases in IWC , because the ascent times required to reach equilibrium between settling and condensation are less at higher values of w .

Individual IWC from the EDP and FIRE data sets are partitioned into vertical velocity intervals bounding those from the parameterization and plotted against temperature in Figs. 3-4. The curves from Fig. 3 are reproduced in Fig. 4. In general, the parameterization has reasonably captured the variation of IWC with temperature and vertical velocity. The FIRE data at low w does not compare as favorably with the parameterization as the other methods; this might possibly be due to the small horizontal distances over which this data was averaged.

4. CONCLUSIONS

A simple parameterization for atmospheric ice water content can account reasonably well for ice water contents observed by aircraft in numerous synoptic contexts in mid-latitude and tropical areas. The physical processes are idealized condensation and crystal settling. Starr and Cox (1985) constructed a model in which many of the processes contributing to ice-cloud formation, as well as the circulation in which the cloud formed, were calculated explicitly over the development history of the cloud; phase changes, crystal settling, and radiative processes were the key elements in their model. The parameterization developed here is intended for use in large-scale models in which atmospheric ice distribution is sought diagnostically as a function of an instantaneous atmospheric state, so some of the details of the Starr and Cox model cannot be included. Atmospheric ice water content in large-scale models will, of course, interact with the radiative field, so feedbacks, which are likely to be significant, will develop between the cloud field and atmospheric dynamics and thermodynamics. This parameterization is essentially a simplification for the solution of large-scale equations for atmospheric ice, analogous to those for water vapor, which could be added to large-scale models as a more explicit means of treating

ice clouds (or atmospheric liquid water in general). Since the history of atmospheric ice which would be contained in such large-scale equations is absent, the parameterization has adopted assumptions to permit diagnostic solution.

ACKNOWLEDGMENTS

This analysis was partially supported by NASA under contracts L98100B (AJH) and NAG5-1056 (LJD).

REFERENCES

- Cox, S. K., D. S. McDougal, D. Randall, and R. Schiffer, 1987: FIRE- The First ISCCP Regional Experiment. *Bull. Amer. Meteor. Soc.*, **67**, 114-118.
- Griffith, K. T., S. K. Cox and R. G. Knollenberg, 1980: Infrared radiative properties of tropical cirrus clouds inferred from aircraft measurements. *J. Atmos. Sci.*, **37**, 1077-1087.
- Hahn, C. J., S. Warren, J. London, B. Chervin, and R. Jenne, 1984: Atlas of simultaneous occurrence of different cloud types over land. *National Center for Atmospheric Research Technical Note*, 241+STR, 209 p.
- Heymsfield, A. J., 1977: Precipitation development in stratiform ice clouds: A microphysical and dynamical study. *J. Atmos. Sci.*, **34**, 367-381.
- Ramanathan, V., E. J. Pitcher, R. C. Malone, and M. L. Blackmon, 1983: The response of a spectral general circulation model to refinements in radiative processes. *J. Atmos. Sci.*, **40**, 605-630.
- Starr, D. O'C., and S. K. Cox, 1985: Cirrus clouds. Part I: A cirrus cloud model. *J. Atmos. Sci.*, **42**, 2663-2681.

RADIATIVE DIFFUSIVITY FACTORS IN CIRRUS AND STRATOCUMULUS CLOUDS — APPLICATION TO TWO-STREAM MODELS

G. L. Stephens, P. J. Flatau, S.-C. Tsay, and P. Hein

Colorado State University, Department of Atmospheric Science, Fort Collins, Co. 80523

1. Introduction

A diffusion-like description of radiative transfer in clouds and the free atmosphere is often employed. The two stream model is probably the best known example of such a description.^{6,12,9} The main idea behind the approach is that only the first few moments of radiance are needed to describe the radiative field correctly. Integration smooths details of the angular distribution of specific intensity and it is assumed that the closure parameters of the theory (diffusivity factors) are only weakly dependent on the distribution. In this paper we investigate the diffusivity factors using the results obtained from both Stratocumulus and Cirrus phases of FIRE experiment. A new theoretical framework is described in which two (upwards and downwards) diffusivity factors are used and a detailed multi-stream model is used to provide further insight about both the diffusivity factors and their dependence on scattering properties of clouds.

2. Diffusivity factors

There are many diffusion-like approximations in radiative transfer theory.¹⁰ The most intuitive being

$$\mathbf{F} = \hat{\mathbf{D}} \frac{d\mathbf{U}}{d\tau} + \mathbf{S}' \quad (2.1)$$

where flux and scalar irradiance vectors

$$\mathbf{F} = \begin{pmatrix} F^+ \\ F^- \end{pmatrix}, \quad \mathbf{U} = \begin{pmatrix} U^+ \\ U^- \end{pmatrix} \quad (2.2)$$

are defined by the following hemispheric averages

$$F^+ = \int_{-1}^0 \mu I(\tau, \mu) d\mu \quad F^- = \int_0^1 \mu I(\tau, \mu) d\mu \quad (2.3a)$$

$$U^+ = \int_{-1}^0 I(\tau, \mu) d\mu \quad U^- = \int_0^1 I(\tau, \mu) d\mu \quad (2.3b)$$

of specific intensity $I(\tau, \mu)$. Vector \mathbf{S}' is related to the source term. The sign convention is as follows: the instrument located on a airplane and facing the Earth's surface will measure the upward flux of radiation, here indicated by the + sign, the corresponding θ values are between $(\pi/2, \pi)$ and $\mu \in (0, -1)$. The instrument facing skywards will measure downward flux, here indicated by the - sign, the corresponding θ values are between $(0, \pi/2)$ and $\mu \in (1, 0)$.

Equation (2.1) is a direct analog to the Fickian diffusion law where the flux quantity is related to the *gradient* of a scalar quantity (scalar irradiance) through the diffusivity matrix $\hat{\mathbf{D}}$. In oceanography¹¹ and atmospheric science² another diffusivity matrix is often employed

$$\mathbf{U} = \mathbf{D}\mathbf{F} \quad (2.4)$$

where \mathbf{D} is the 2×2 matrix

$$\mathbf{D} = \begin{pmatrix} D^+ & 0 \\ 0 & D^- \end{pmatrix} \quad (2.5)$$

and the diffusivities D^- and D^+ are defined as

$$D^- = \frac{U^-(\tau)}{F^-(\tau)} \quad \text{and} \quad D^+ = \frac{U^+(\tau)}{F^+(\tau)} \quad (2.6)$$

It can be seen that (2.6) involves the first two moments of angular radiance dependence. These quantities are used to close the set of hierarchy of equations for various moments of radiance. The resulting set of equations is called the two-stream approximation.

3. Measured diffusivities from the CSU bug-eye

The Marine Stratocumulus Intensive Field Observations (MSIFO) of the First ISCCP(International

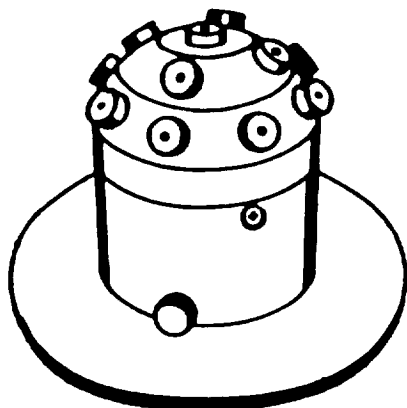


Figure 1: CSU bugeye instrument

Satellite Cloud Climate Program) Regional Experiment (FIRE) was conducted off the coast of California at and in the vicinity of San Nicolas Island in July 1987. On San Nicolas Island, a tethered balloon with radiometric instrumentation from Colorado State University (CSU) probed the marine stratocumulus.⁷ The shortwave radiometric instrumentation measured both the downwelling and upwelling irradiances, and consisted of four Epply pyranometers (measuring wavelengths from 0.3 to 2.8 μm and from 0.7 to 2.8 μm), and two CSU bugeyes. The bugeye measurements will be used to derive the radiative diffusivities.

The Bugeye, the CSU Multidirectional Photodiode Radiometer⁴ measures the angular distribution of the radiance field. It consists of a hemispherical array of thirteen silicon photodiodes and associated electrical circuitry mounted on an aluminum housing (Fig. 1). The upward looking bugeye had diodes with a 10° field of view. Each diode of the downward looking bugeye had a 50° field of view. The spectral range of both bugeyes is from 0.36 to 1.10 μm but the diodes of the downward looking bugeye were covered with a blue tinted Schott glass filters. Figure 2 shows the spectral response of the downward looking bugeye (solid line) and the upward looking bugeye (dashed line). The peak sensitivity of the downward looking bugeye is at 0.40 μm while the upward looking bugeye has a peak sensitivity at about 0.93 μm . The bugeye voltages are actually irradiances seen within each bugeye diode's field of view. These voltages were normalized to the sensitivity of the first diode after being corrected for a zero offset. A field of view correction was then applied to each diode voltage to provide the proper steradian weighting on the hemisphere. A correction for the pitch and roll of the platform was also accounted for. From the 13 diode measurements, the

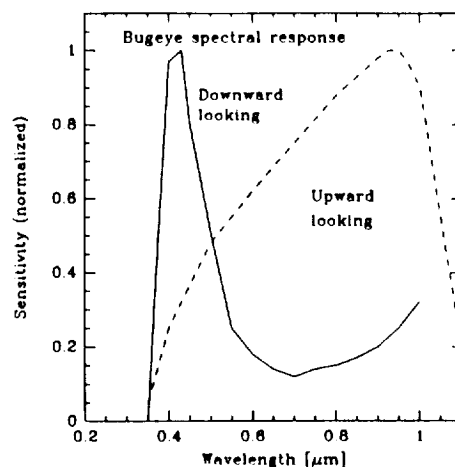


Figure 2: Spectral response of CSU Bugeyes

diffusivity factor was deduced as

$$D = \frac{\sum_{i=1}^{13} V_i A_i(\text{hemi})/A(\text{diode})}{\sum_{i=1}^{13} V_i A_i(\text{hemi})/A(\text{diode}) \cos \theta_i} \quad (3.1)$$

where V_i is the voltage of diode i , $A(\text{diode})$ is the steradian field of view of each diode, $A_i(\text{hemi})$ is the steradian area that diode i voltage represents, and θ_i is the zenith/nadir angle (accounting for the pitch and roll of the platform) of diode i . Comparison of (3.1) to (2.6) and (2.3) emphasizes the approximations used to integrate over angle. To test the approximation, the irradiances obtained from summation of the diode measurements (the denominator of (3.1)), were compared to the shortwave irradiances obtained directly from the Epply pyranometer. An excellent relationship (not shown) between these measurements was obtained despite the different spectral characteristics of the bugeyes and pyranometers. The diffusivities for the downwelling radiation (D^-) and for the upwelling radiation (D^+) are shown in Figure 3 for a Sc cloud sampled on the morning of Julian Day 189 (8 July 1987). The diffusivity values average about 1.62 with D^+ being slightly larger than D^- . Cloud base is at about 970 mb and cloud top is at about 930 mb. As the bugeye entered the base of the cloud the value of D^+ rapidly increases until D^+ assumes a in-cloud profile and then decreases through out the cloud. D^- increases with height through the cloud to cloud top where it has the same value as D^+ .

We also performed some preliminary calculations of diffusivities for the downward looking (and only) aircraft bugeye from FIRE Cirrus, Oct. 28, 1986. The results for several passes through two cirrus samples give results of $D^+ \approx 1.7$.

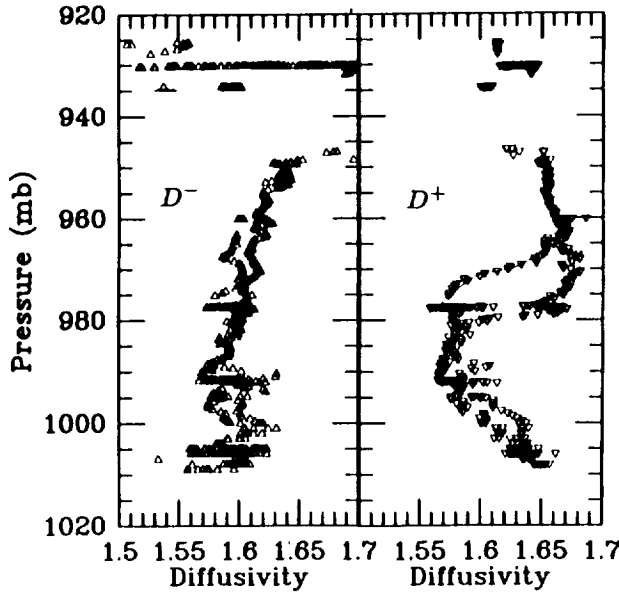


Figure 3: Diffusivity coefficient. Marine stratocumulus. FIRE 8 July 1987

4. Model results

A. Diffusivity factors from the detailed radiative transfer code

To demonstrate further the structure and dependency of diffusivity factors under various conditions, we have employed a comprehensive radiation model¹³ which includes scattering and absorption by molecules, as well as by particles. The midlatitude summer⁸ atmospheric profile is employed in which a cloud layer of 1 km thick is located with a base 1 km above the surface. The cloud layer is assumed to be homogeneous with a mean liquid water content of 0.2gm^{-3} and a mean effective radius of $10\mu\text{m}$. Three spectral bands of $0.52-0.57\mu\text{m}$, $1.28-1.53\mu\text{m}$, and $2.38-2.91\mu\text{m}$ are selected, respectively to represent the cases of no, moderate and strong absorption by water droplets. Three solar zenith angles of 0° , 30° and 75° are also chosen to investigate the angular dependence of diffusivity factor. The results of these calculations are shown in Fig. 4. These calculations clearly demonstrate the dependence of D^+ and D^- on absorption strength, solar zenith angle, and optical depth. The diffusion domain in which $D^+(\tau, \mu_0) = D^+$ and $D^-(\tau, \mu_0) = D^-$ is also apparent for large τ . The results also indicate that the diffusivity is highly variable for clouds of $\tau < 1$.

B. Two-stream approximation

The azimuthally and hemispherically averaged monochromatic radiative transfer equation for diffuse radiation, $I(\tau, \mu)$, in a plane-parallel, horizontally homogeneous medium which scatters, emits and absorbs can be written as

$$\frac{dF^+(\tau)}{d\tau} = U^+(\tau) - \tilde{\omega}_0 \int_0^1 \beta(\mu) I(\tau, \mu) d\mu - \tilde{\omega}_0 \int_0^1 \varphi(\mu) I(\tau, -\mu) d\mu - S^+(\tau) \quad (4.1)$$

$$\frac{dF^-(\tau)}{d\tau} = -U^-(\tau) + \tilde{\omega}_0 \int_0^1 \beta(\mu) I(\tau, -\mu) d\mu + \tilde{\omega}_0 \int_0^1 \varphi(\mu) I(\tau, \mu) d\mu + S^-(\tau) \quad (4.2)$$

where the backscatter fraction is

$$\beta(\mu) = \frac{1}{2} \int_0^1 P(\mu, -\mu') d\mu' \quad (4.3)$$

and the forward scattering fraction

$$\varphi(\mu) \equiv 1 - \beta(\mu) = \frac{1}{2} \int_0^1 P(\mu', \mu) d\mu' \quad (4.4)$$

Equation (4.1-4.2) doesn't involve any approximations. Unfortunately it is a system of 2 equations and 6 unknowns: F^+ , U^+ , F^- , U^- and 2 independent integrals involving scattering fraction. To overcome this difficulty all two-stream models introduce some kind of closure hypothesis.^{9,1} The particular choice below follows the discussion given in Preisendorfer¹¹ and Buglia.¹ To close the system of equation we need the relationships between F , U (eq. 2.1 or 2.1, for instance), and the integrals involving backscatter. For this purpose we introduce diffusivities as defined by (2.6) and assume that the back and forward scatter fractions are independent of angle. It follows that

$$\frac{d\mathbf{F}}{d\tau} = \mathbf{A}\mathbf{F} + \mathbf{S} \quad (4.5)$$

where \mathbf{A} is the 2×2 matrix

$$\mathbf{A} = \begin{pmatrix} \gamma_1^+ & -\gamma_2^- \\ \gamma_2^+ & -\gamma_1^- \end{pmatrix} \quad (4.6)$$

and

$$\gamma_1^+ = D^+ (1 - \tilde{\omega}_0 \varphi), \quad \gamma_1^- = D^- (1 - \tilde{\omega}_0 \varphi) \quad (4.7a)$$

$$\gamma_2^+ = D^+ \tilde{\omega}_0 \beta, \quad \gamma_2^- = D^- \tilde{\omega}_0 \beta \quad (4.7b)$$

and

$$\mathbf{F} = \begin{pmatrix} F^+ \\ F^- \end{pmatrix}, \quad \mathbf{S} = \begin{pmatrix} -S^+ \\ -S^- \end{pmatrix} \quad (4.8)$$

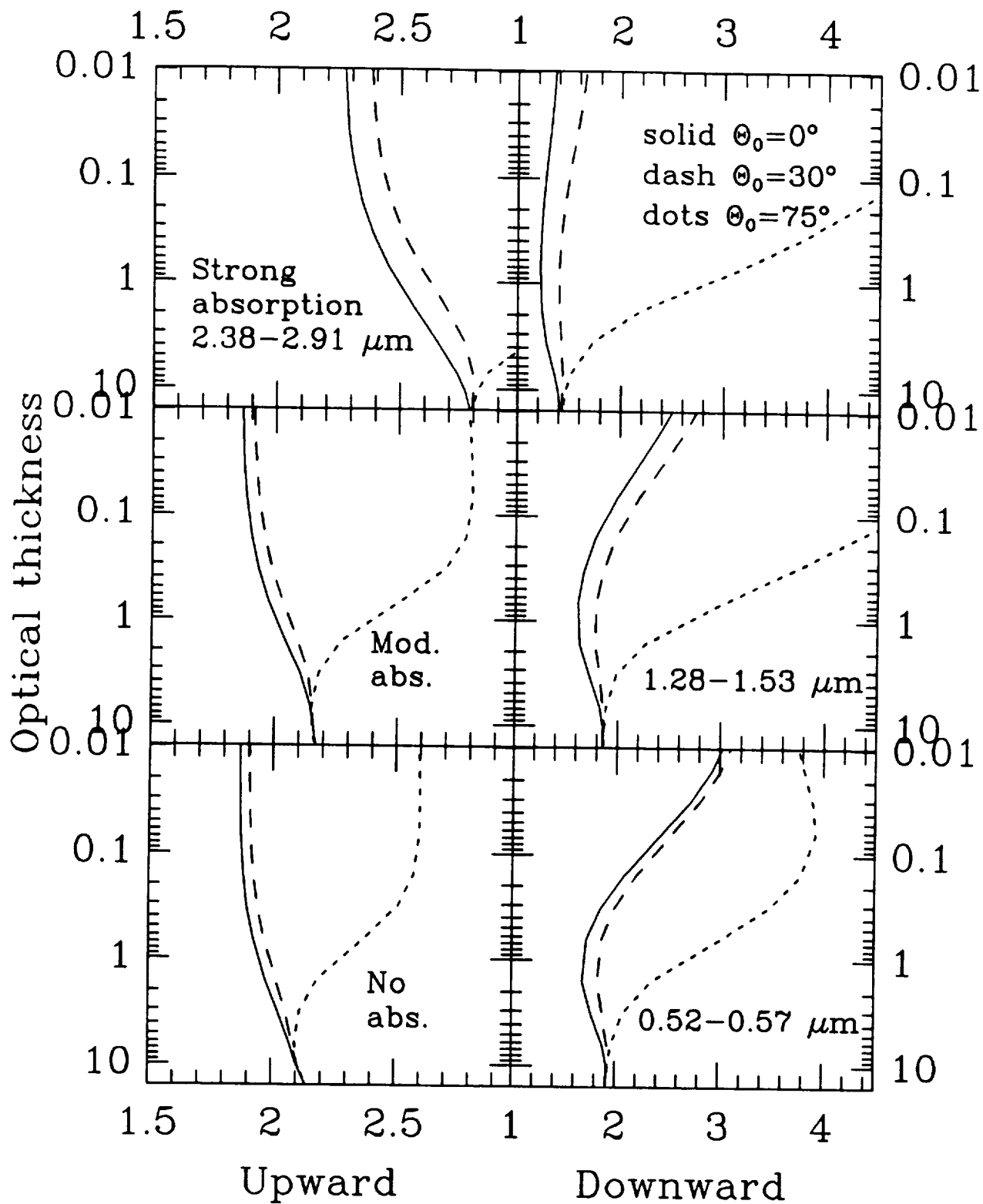


Figure 4: Diffusivity factors from detailed radiative transfer model

Matrix \mathbf{A} depends on local optical properties of the atmosphere (such as the single scattering albedo $\tilde{\omega}_0$ and the asymmetry parameter g). With the typical assumption that $D^+ = D^- = D$, i.e. that the properties of the homogeneous layer are radiatively isotropic, we write scalars γ_1 and γ_2 as

$$\gamma_1 = D(1 - \tilde{\omega}_0\varphi) \quad (4.9a)$$

$$\gamma_2 = D\tilde{\omega}_0\beta \quad (4.9b)$$

For the case $D^+ = D^-$, the matrix \mathbf{A} exhibits specific structure and is defined by two scalars. It is this fact which allows us to introduce only two physical parameters defining the homogeneous and isotropic medium: transmittance t and reflectance r . For the anisotropic (but homogeneous) layer, for which $D^+ \neq D^-$, the matrix structure (4.6) is defined by four scalar entries and two transmittances and two reflectances are needed to define the system. The apparent¹¹ anisotropy of the medium is forced by differences in the distributions of the intensity incident at cloud top and base. The solution of (4.5) may be written in the form⁵

$$\mathbf{F}(\tau) = \mathbf{P}\mathbf{F}(\tau_t) \quad (4.10)$$

where \mathbf{P} is a 2×2 fundamental solution matrix. The propagator for a homogeneous atmosphere, i.e. for constant \mathbf{A} , is

$$\mathbf{F}(\tau) = e^{\mathbf{A}(\tau - \tau_t)}\mathbf{F}(\tau_t) \quad (4.11)$$

for a layer of thickness $\tau - \tau_t$. For the case of a two-stream model and we can represent the propagator as

$$\mathbf{P}_{\text{exp}} = \frac{1}{\lambda_1 - \lambda_2} [e^{\lambda_1\tau}(\mathbf{A} - \lambda_2\mathbf{1}) - e^{\lambda_2\tau}(\mathbf{A} - \lambda_1\mathbf{1})] \quad (4.12)$$

where $\mathbf{1}$ is the 2×2 identity matrix. The eigenvalues λ_1 and λ_2 are roots of the characteristic equation

$$\lambda^2 - p\lambda + q = 0 \quad (4.13)$$

and

$$p = \text{tr}\mathbf{A} = \gamma_1^+ - \gamma_1^- \quad (4.14a)$$

$$q = \det \mathbf{A} = \gamma_2^+\gamma_2^- - \gamma_1^+\gamma_1^- \quad (4.14a)$$

It can be shown that the reflectances and transmittances are directly related to the propagator

$$\begin{pmatrix} r^+ & t^+ \\ t^- & r^- \end{pmatrix} = \frac{1}{p_{11}} \begin{pmatrix} -p_{12} & 1 \\ p_{11}p_{22} - p_{21}p_{12} & p_{21} \end{pmatrix} \quad (4.15)$$

where

$$p_{11} = \frac{1}{l} [e^{\lambda_1\tau}(\gamma_1^+ - \lambda_2) - e^{\lambda_2\tau}(\gamma_1^+ - \lambda_1)] \quad (4.16a)$$

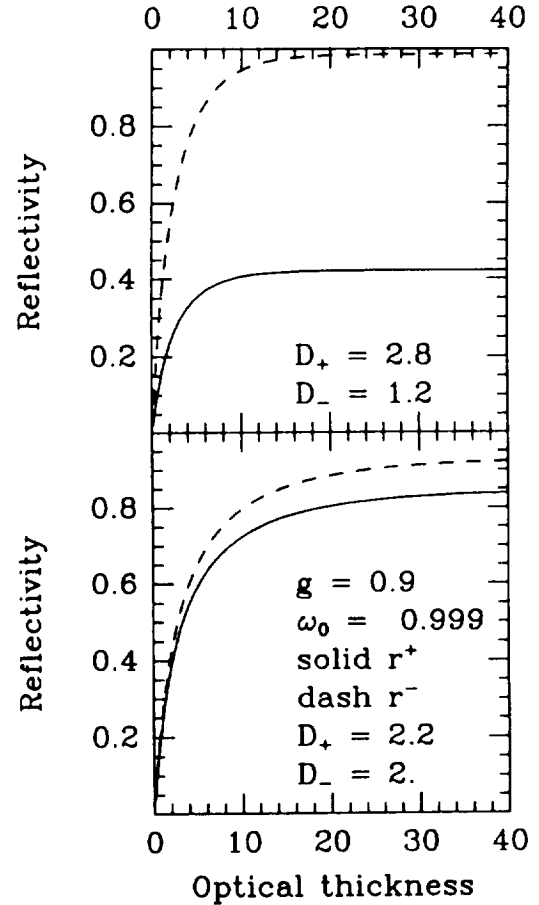


Figure 5: Reflectivities from the four parameter two-stream model

$$p_{12} = -\frac{1}{l}\gamma_2^- (e^{\lambda_1\tau} - e^{\lambda_2\tau}) \quad (4.16b)$$

$$p_{21} = \frac{1}{l}\gamma_2^+ (e^{\lambda_1\tau} - e^{\lambda_2\tau}) \quad (4.16c)$$

$$p_{22} = -\frac{1}{l} [e^{\lambda_1\tau}(\gamma_1^- + \lambda_2) - e^{\lambda_2\tau}(\gamma_1^- + \lambda_1)] \quad (4.16d)$$

and $l = \lambda_1 - \lambda_2$. Figure 5 presents results for two sets of diffusivities. First $D^+ = 2.2$, $D^- = 2$ which corresponds to the no absorption case (compare Fig. 4). The second set $D^+ = 2.8$, $D^- = 1.2$ is more typical of the absorption case. The results indicate that the medium becomes anisotropic ($r^+ \neq r^-$) and that reflectances and transmittances of the cloud are sensitive to changes in the diffusivity matrix.

5. Summary

The diffusivity factor has been studied in the context of two-stream approximation of the radiative transfer equation using data obtained from both Stratocumulus and Cirrus phases of FIRE project. De-

tailed radiative transfer calculations have been employed. The theoretical framework of the two-stream model for homogeneous but anisotropic (anisotropy being forced by the boundary conditions) atmospheric layer is described. It is shown that the total extinction matrix is defined by four components. Preliminary results indicate that the diffusion coefficients depend on the specific spectral region under consideration, absorption strength, optical thickness and solar zenith angles. In the strong absorption case, upward and downward diffusivities separate and the two-stream model predicts large differences in upward and downward reflectances and transmittances for such a case. Model results indicate the existence of a diffuse region in which the diffusion matrix doesn't vary with respect to solar zenith angle and/or increased optical thickness. Experimental data indicate the variability with the sun's zenith angle of the downward diffusivity in the free air overlying the cloud. In the cloud layer the upward diffusivity is larger than the downward diffusivity which is in agreement with the strong absorption case obtained from the numerical model. Downward diffusivity is fairly constant throughout the cloud and below the cloud layer. The upward diffusivity adjusts rapidly to the existence of the cloud layer. Model results indicate that a 'skin' layer in which rapid changes in diffusivity occur is of the order of $\tau = 1$. Thus constant- D models may not be suitable for thin cirrus clouds.

Acknowledgments

The research presented in this paper has been supported in part by the grant from the Air Force AFOSR-88-0143 and in part by the NSF grant ATM-8812353 and Office of Naval Research, Grant N00014-87-K-0288/P00002.

References

- ¹J. J. Buglia. *Introduction to the theory of atmospheric radiative transfer*. Reference publication 1156, NASA, Langley Research Center, Hampton, Virginia, July 1986.
- ²J. C. Ceballos. On two-stream approximations for shortwave radiative transfer in the atmosphere. *Beitr. Phys. Atmosph.*, 61:10—22, 1988.
- ³W. R. Cotton, P. J. Flatau, G. L. Stephens, and P. W. Stackhouse. *Numerical modeling of middle and high level clouds with the Colorado State University Regional Atmospheric Modeling System*. Annual Tech. Rep., Colorado State University, Fort Collins, Colo. 80523, 1989.
- ⁴J. M. Davis, C. Vogel, and S. K. Cox. Multidirectional photodiode array for measurement of solar radiances. *Rev. Sci. Instrum.*, 53:667—673, 1982.
- ⁵P. J. Flatau and G. L. Stephens. On the fundamental solution of the radiative transfer equation. *J. Geophys. Res.*, 93(D9):11037—11050, 1988.
- ⁶J. F. Geleyn and A. Hollingsworth. An economical analytical method for the computation of the interaction between scattering and line absorption of radiation. *Contrib. Atmos. Phys.*, 52:1—16, 1979.
- ⁷P. F. Hein, S. K. Cox, W. H. Schubert, C. M. Johnson-Pasqua, D. P. Duda, T. A. Guinn, M. Mulloy, T. B. McKee, W. L. Smith, and J. D. Kleist. *The CSU tethered balloon data set of the FIRE marine stratocumulus IFO*. Technical Report 432, Colorado State University, Fort Collins, Colo. 80523, 1988. FIRE Series 6.
- ⁸R. A. McClatchey, R. W. Fenn, J. E. Selby, F. E. Volz, and J. S. Garing. *Optical properties of the atmosphere*. Technical Report AFCRL-72-0497, Air Force Cambridge Research Laboratories, 1972. 108pp.
- ⁹W. E. Meador and W. R. Weaver. Two-stream approximation to radiative transfer in planetary atmospheres: A unified description of existing methods and a new improvement. *J. Atmos. Sci.*, 37:630—643, 1980.
- ¹⁰G. C. Pomraning. *The equations of radiation hydrodynamics*. Pergamon Press, Oxford, New York, 1973.
- ¹¹R. W. Preisendorfer. *Hydrologic optics. Volume V. Properties*. U.S. Dept. Commerce, NOAA, Honolulu, Hawaii, 1976. Environmental Research Laboratories, Pacific Marine Environmental Labs.
- ¹²O. B. Toon, C. P. McKay, and T. P. Ackerman. Rapid calculation of radiative heating rates and photodissociation rates in inhomogeneous multiple scattering atmospheres. 1988. submitted to *J. Geophys. Res.*
- ¹³S. C. Tsay, K. Stamnes, and K. Jayaweera. Radiative energy balance in the cloudy and hazy Arctic. *J. Atmos. Sci.*, 46:1002—1018, 1989.

	PAGE
C04.01 A Comparative Study of Infrared Radiance Measurements by an ER-2 Based Radiometer and the Landsat 5 Thematic Mapper (TM-6) <u>Hammer, Philip D.</u> , Francisco P. J. Valero, and Stefan Kinne	423
C04.02 Radiative Properties of Cirrus Clouds Inferred from Broadband Measurements During FIRE <u>Smith, Jr., William L.</u> , and Stephen K. Cox	429
C04.03 Remote Sounding Through Semi-Transparent Cirrus Cloud <u>Smith, William L.</u> , Steven A. Ackerman, and Allan H.-L. Huang	435
C04.04 IR Spectral Characteristics of Cirrus Clouds <u>Ackerman, Steven A.</u> , and William L. Smith	441
C04.05 Airborne Lidar/Radiometric Measurements of Cirrus Cloud Parameters and Their Application to Lowtran Radiance Evaluations Uthe, Edward E.	447

A Comparative Study of Infrared Radiance Measurements by an ER-2 Based Radiometer and the Landsat 5 Thematic Mapper (TM-6)

Philip D. Hammer, Francisco P. J. Valero, and Stefan Kinne
NASA Ames Research Center, Moffett Field, CA 94035

1 Introduction

Infrared radiance measurements were acquired from a radiometer on the NASA ER-2 during a coincident Landsat 5 overpass on October 28, 1986 as part of the FIRE Cirrus IFO in the vicinity of Lake Michigan. A comparative study is made to infer microphysical properties of the cirrus cloud field. Radiances are derived from the image by convolving the ER-2 radiometer's effective field of view along the flight path. A multistream radiative transfer model is used to account for the differences in spectral bandwidths, 10.40-12.50 μm for the Landsat band and 9.90-10.87 μm for the radiometer.

2 Instruments

The primary aircraft based instrument employed for this study is a two spectral channel narrow field of view radiometer (NFOV). This instrument was mounted within a pod attached to the fuselage of the NASA ER-2 aircraft. Both channels detect upwelling infrared radiation within a conical field half-angle of 8.3 degrees. The optically sensitive components are electrically calibrated pyroelectric detectors (Valero et al. 1982; Geist and Blevin 1973). A reflective chopper operating at 18 hz alternately exposes the detectors to external radiation and a liquid nitrogen cooled zero-radiation reference. The temperature corrected spectral bandwidths (full width at half maximum) of the interference filters are 6.14-7.14 and 9.90-10.87 μm . In this study only the 10 μm channel bandwidth overlapped one of the Landsat 5 bands: TM-6.

The basic operation principles of the Landsat thematic mapper are described elsewhere (Engel and Weinstein 1983). Standard relations were used for converting the digital pixel counts to radiance and brightness temperature (Markham and Barker 1986). The Landsat 5 TM6 band has an equivalent rectangular spectral bandpass of 10.40-12.50 μm (Wielicki and Parker 1987). Radiances derived from the Planck function integrated over this bandpass agree very well with the Markham and Barker formulas for which this integral is approximated by a simple analytic expression.

3 Analysis

In order to make meaningful comparisons between our NFOV ER-2 radiometer and Landsat image data, a systematic procedure was used to prepare both data sets. First, a geometrically registered satellite image was obtained. Next, the aircraft flight tracks derived from navigational data were adjusted for cloud level winds. Radiances were determined from the image by convolving the ER-2 radiometer's effective field of view with image pixel values along the flight track. The previous two steps require an estimate of the altitude of the optically dominant cirrus layer; this was aided by lidar data. The resulting signals were expressed in spectral bandpass independent units of

brightness temperature versus aircraft coordinates. Finally the two sets of radiance measurements were prepared for a 2 channel radiance correlation plot for comparison to model calculations.

4 Model

A discrete ordinates radiative transfer code designed for multi-layered plane-parallel media (Stamnes et al., 1988) was used to calculate radiance values at the corresponding altitudes of the measurements, 19.1 km for the ER-2 and >70 km for Landsat. The number of computational polar angles (streams) was set to 8, as larger values did not generally yield significant differences in the results. 17 atmospheric layers were chosen so as to achieve reasonable homogeneity in temperature (less than 10°K variation) and particle composition within each layer. The upwelling radiance was evaluated at a polar angle of 0 degrees to correspond to the conditions of the measurements.

The assumed ice particle size distributions are described in terms of Mie spheres of a single equivalent radius. Mie calculations were done for a selection of water and ice sphere radii using experimentally determined values for the complex index of refraction of ice (Warren, 1984) and water (Downing and Williams, 1975). Particle concentrations were chosen to yield the desired zero zenith angle optical depths for extinction through all the cloud layers at a reference wavelength of 11.4 μm .

The atmospheric profile input to the model was derived from the 1500 GMT Greenbay radiosonde. Since direct measurements of the Lake Michigan surface temperature were not available the Greenbay surface temperature was used: $T_s = 281.9^\circ\text{K}$. The lake surface was assumed to be Lambertian with a wavelength independent albedo of 0.04. ER-2 based lidar measurements (Spinhrne et al. 1988) indicate that there are two distinct cloud layers over most of the Landsat image extract, with altitude ranges of about 7 to 8 km and 9 to 11 km.

5 Results and Conclusions

Fig. 1a is the Landsat image extract. Fig. 1b shows the ER-2 radiometer and Landsat signals along the flight track in units of brightness temperature. Figs. 2 and 3 are correlation plots. The ER-2 and satellite scales are expressed in radiance units ($\text{Wm}^{-2}\text{sr}^{-1}$) for the instruments' respective bandpasses. The measured data points of Fig. 2 (represented as small dots in Fig. 3) are derived from the data represented in Fig. 1b. Data is distinguished as to ice or water according to the lidar plot of Fig. 1c.

The model calculations are plotted as connected sets of specific symbol types. Each set corresponds to radiance results for a range of optical depths using particles with particular radius selections. Beginning at the upper right convergence point the optical depth values (referenced at 11.4 μm) are 0, 0.125, 0.25, 0.375, 0.5, 0.625, 0.75, 1.0, 1.25, 1.5, and 2.0. For the standard model (connected unfilled symbols in Fig. 2 and solid symbols in Fig. 3) a two layer cloud profile was chosen with ice spheres in the upper layer having about half the effective radius of spheres in the lower layer. The 11.4 μm optical depths of the lower and upper layers were set equal. Unfilled symbols in Fig. 3 represent a profile with water drops present in the lower layer and nothing in the upper. The following conclusions are based on comparisons of measured radiances with model results on the correlation plots:

1. Assuming the above standard model, ice particles with equivalent sphere radii of 8 to 15 μm for the upper layer and 15 to 30 μm for the lower layer may be inferred. This contrasts with particle sizes typically greater than 100 μm determined by in-situ measurements. The lack of sensitivity of the in-situ probes to small ice crystals and the uncertainties in ice-water content determinations causes difficulties in resolving whether a large number of small particles are actually present as opposed to complex large particles with small protrusions. The combined cloud extinction optical depth for both layers at the reference wavelength of 11.4 μm ranges from about 0.3 to 2.

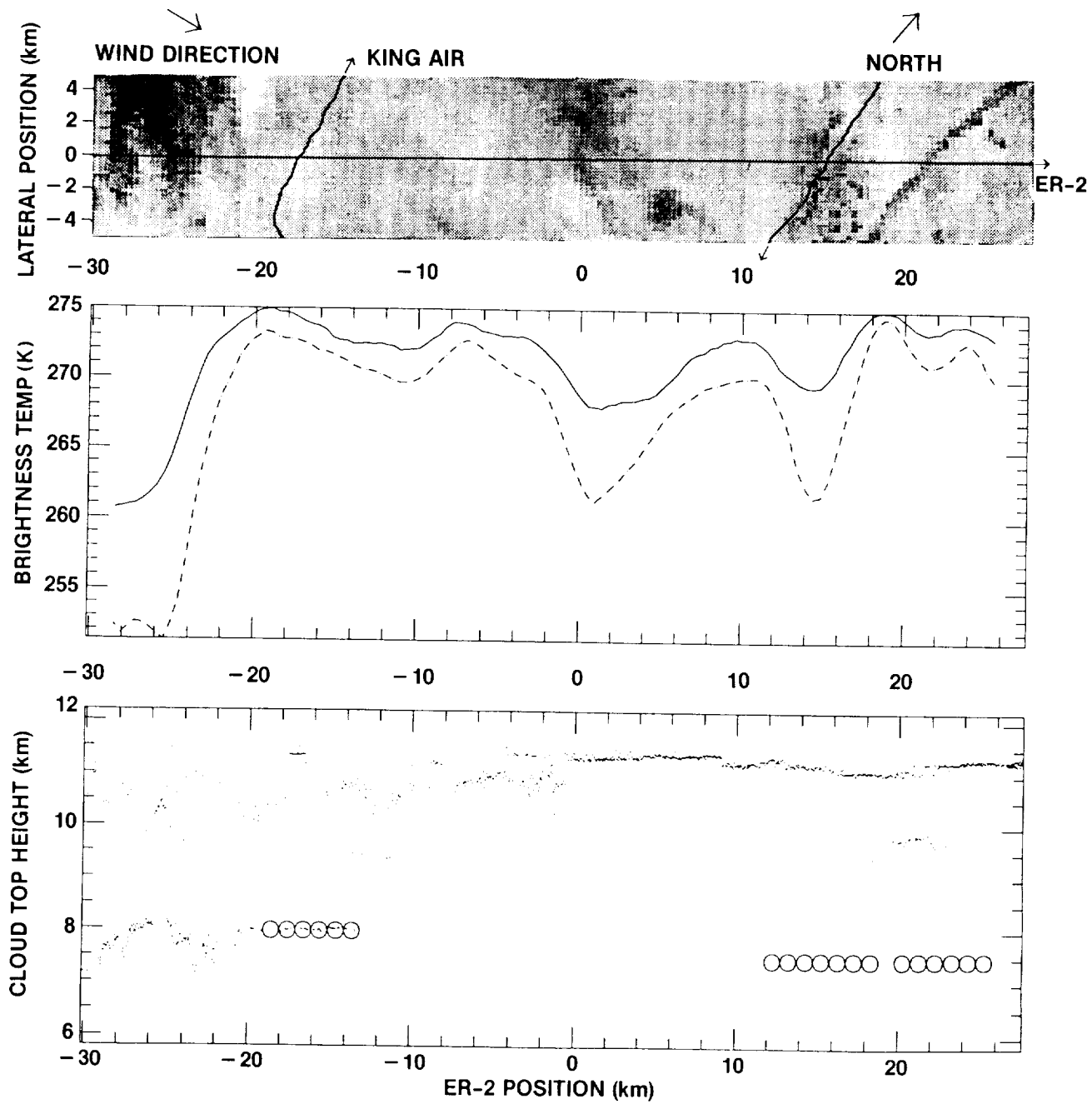
2. Assuming a 1-layer lower water cloud yields results consistent with approximately 8 μm radii water droplets. This compares with in-situ measurements of radii about 4 μm . Distinguishing measurements made with water clouds present from those made for just ice clouds gives no apparent

separation on the correlation plots. Thus water and ice clouds cannot be distinguished from the correlation plots alone under the conditions of this case study. The optical depth scale is only moderately changed ($< 20\%$) from the 2-layer ice model results.

3. Limits on the estimated instrument error may be established by means of self-consistency of the model results. Specifically, if Landsat radiances values were too high, the inferred water cloud droplet sizes would be unrealistically large. Thus our retrieval of relatively small ice crystals cannot be attributed to a Landsat (nor an ER-2 radiometer) calibration error.

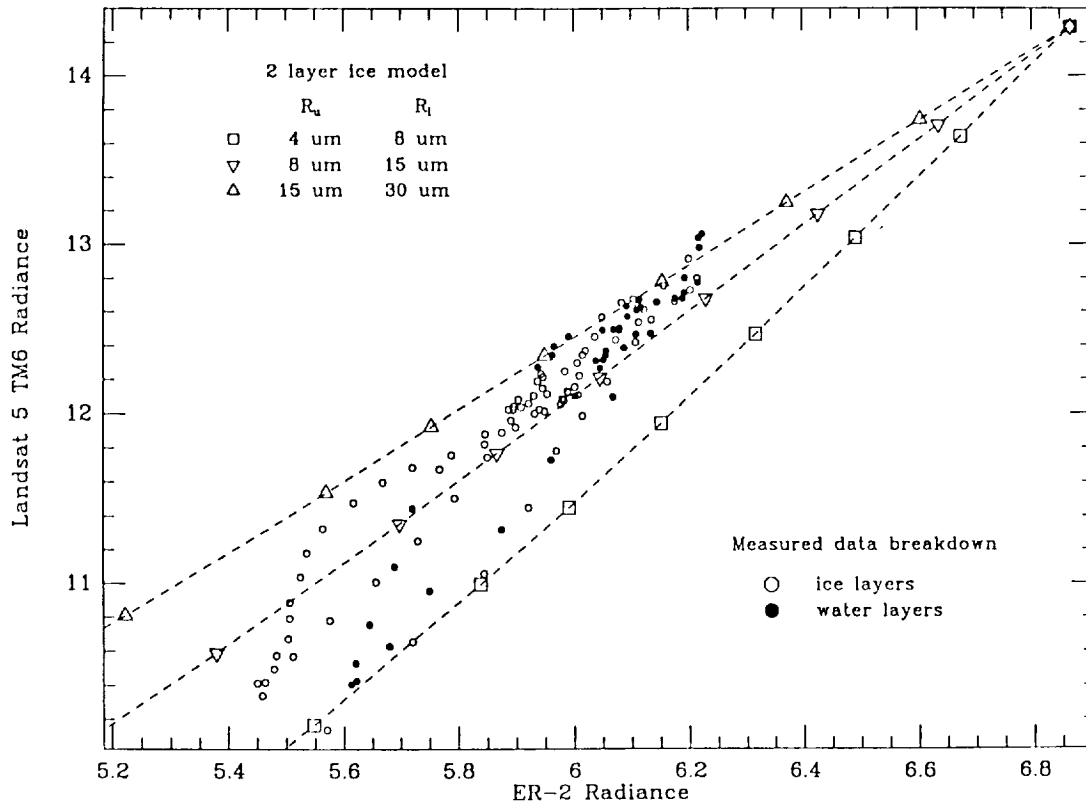
References

- [1] Downing, H. D. and D. Williams, 1975: Optical constants of water in the infrared. *J. Geophys. Res.*, **80**, 1656-1661.
- [2] Engel, J. L. and O. Weinstein, 1983: The Thematic Mapper - An Overview. *IEEE Trans. Geosci. Remote Sensing*, Vol. GE-21, No. 3: 258-265.
- [3] Geist, J. and W. R. Blevin, 1973: Chopper-stabilized null radiometer based upon an electrically calibrated pyroelectric detector. *Appl. Opt.*, **12**, 2532-2535.
- [4] Markham, B. L., and J. L. Barker, 1986: Landsat MSS and TM post-calibration dynamic ranges, exoatmospheric reflectances and at-satellite temperatures. *EOSAT Landsat Technical Notes*, August 1986, 3-8.
- [5] Spinhirne, J. D., D. L. Hlavka, W. D. Hart, 1988: ER-2 lidar observations from the October 1986 FIRE cirrus experiment. *NASA Technical Memorandum 100704*, NASA Goddard Space Flight Center, June 1988, 49pp.
- [6] Stamnes, K., S. C. Tsay, W. J. Wiscombe and K. Jayaweera, 1988: A general-purpose numerically stable computer code for discrete-ordinate-method radiative transfer in scattering and emitting layered media. *International Radiation Symposium Abstracts, Lille, France*, August 18-24, p. 186.
- [7] Valero, F. P. J., W. J. Y. Gore, and L. P. M. Giver, 1982: Radiative flux measurements in the troposphere. *Appl. Opt.*, **21**, 831-838.
- [8] Warren, S. G., 1984: Optical constants of ice from the ultraviolet to the microwave. *Appl. Opt.*, **23**, 1206-1225.
- [9] Wielicki, B. A. and L. Parker, 1987: Intercalibration of landsat thematic mapper (TM) and ER-2 MAMS during the FIRE cirrus IFO-I October 28, 1986. *NASA Langley Technical Report*
- [10] Wielicki, B. A., J. T. Suttles, A. J. Heymsfield, R. M. Welch, J. D. Spinhirne, L. Parker, and R. F. Arduini, 1988: FIRE cirrus on 10/28/86: Landsat; ER-2; King air; theory. FIRE Science Team Workshop, Vail CO, July 1988.



ORIGINAL PAGE IS
OF POOR QUALITY

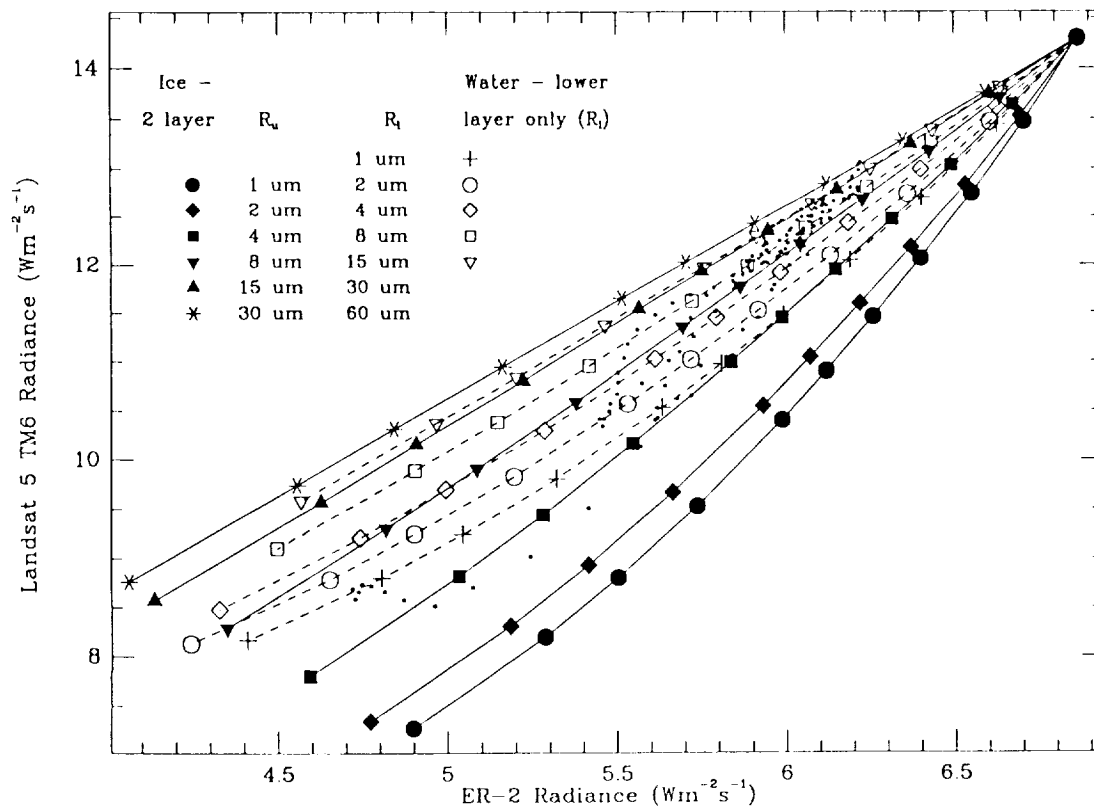
FIG 2



NASA-Ames

7-JUL-1989 16:10:39

FIG 3



Radiative Properties of Cirrus Clouds Inferred from Broadband Measurements During FIRE

William L. Smith, Jr. and Stephen K. Cox

Colorado State University
Department of Atmospheric Science
Fort Collins, Colorado 80523

June 1989

1. Introduction

It is well known that clouds are significant modulators of weather and climate because of their effects on the radiation field and thus on the energy balance of the earth-atmosphere system. As a result, the accurate prediction of weather and climate depends to a significant degree on the accuracy with which cloud-radiation interactions can be described.

It is the purpose of this investigation to report the broadband radiative and microphysical properties of five cirrus cloud systems, as observed from the NCAR Sabreliner during the FIRE first Cirrus IFO, in order to better understand cirrus cloud-radiation interactions. A broadband infrared (BBIR) radiative transfer model is employed to deduce BBIR absorption coefficients in order to assess the impact of the cirrus clouds on infrared radiation. The relationships of these absorption coefficients to temperature and microphysical characteristics are explored.

2. Flight and Data Description

The analysis presented here was conducted for five cirrus systems that were penetrated by the NCAR Sabreliner during the first Cirrus IFO in the fall of 1986. Broadband, infrared (4-50 μm) and shortwave (0.3-2.8 μm) fluxes were obtained from measurements made by pyrgeometers and pyranometers manufactured by Eppley Laboratories Inc. For a description of these radiometers and calibration procedures, see Albrecht and Cox (1976, 1977) and Smith, Jr., *et al.*, (1988). In addition, the shortwave irradiances were corrected to a horizontal plane and normalized to common time for each flight by taking into account Sabreliner flight information (i.e. pitch, roll, and heading), as well as the sun-earth geometry (Rockwood and Cox 1976; Ackerman and Cox 1981). The microphysics data were obtained from the Particle Measuring System, Inc. (PMS) 2-D probes. These data are described by Heymsfield and Miller (1989). For a description of the Sabreliner data set, see Hein, *et al.*, (1987). A brief description of

each of the four flights and the associated synoptic conditions are given in Smith, Jr., and Cox (1989).

3. Broadband Infrared Radiative Transfer Model

In order to assess the impact of the cloud layers on infrared radiation, the broadband (4-50 μm) irradiance data were analysed utilizing a broadband infrared radiative transfer model similar to that described by Cox and Griffith (1979). For clear sky, this model is capable of reproducing broadband divergence values which agree with observations (Albrecht, *et al.*, 1974). This model has been modified to include the effects of clouds and is described in detail by Smith, Jr., and Cox (1989). In this model, the cloud is treated as a greybody where

$$\epsilon_{\text{cld}} = 1 - e^{-\tau_{\text{cld}}} \quad (1)$$

and

$$\tau_{\text{cld}} = \sum_i (K_i \cdot \overline{IWC}_i \cdot \Delta Z_i) = \sum_i \sigma_i \cdot \Delta Z_i \quad (2)$$

In (5), K_i is the greybody mass absorption coefficient, \overline{IWC}_i is the mean ice water content, σ_i is the broadband absorption coefficient (units m^{-1}) and ΔZ_i is the thickness for the i^{th} cloud layer. Paltridge (1974) and Stephens (1978) have shown that when employing a constant value of K , (5) is a good descriptor of the radiative properties of water clouds. Griffith, *et al.*, (1980) successfully employed this relationship, assuming a constant value of K , to fit irradiance observations of cirrus obtained during GATE, although to date, there is no theoretical basis supporting the assumption that the broadband cloud transmittance through cirrus is an exponential function of optical depth. Therefore, we have adopted (5), but with the assumption that K may be variable through the cirrus layer. This parameterization of cloud emittance permits us to retrieve profiles of K that yield calculated irradiance profiles that precisely match the measured infrared irradiance profiles (Fig. 1) through the cirrus clouds. Vertical profiles of

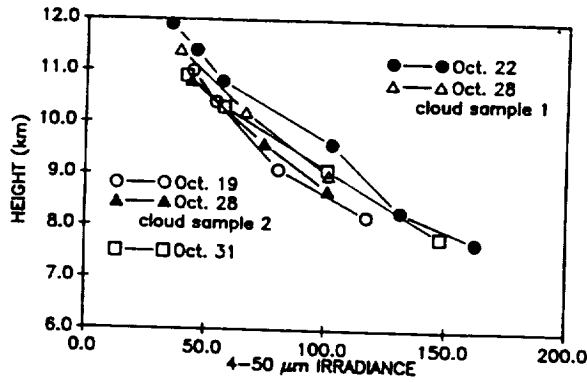


Figure 1.: Vertical profiles of downwelling 4-50 μm irradiance for five cirrus systems penetrated by the NCAR Sabreliner.

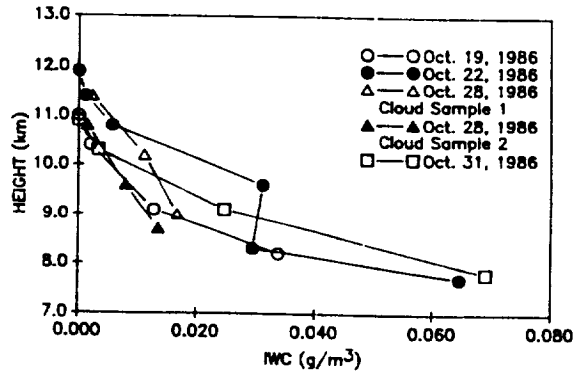


Figure 2: Vertical profiles of Ice Water Content (IWC) through five cirrus cloud systems.

mean IWC deduced from the 2-D PMS probe measurements are shown in Fig. 2 for the four flights analyzed here. The IWC generally increases with decreasing altitude (increasing temperature) as expected. These values are generally lower than those measured in tropical cirrus systems (i.e. Griffith, *et al.*, 1980) and range from 0.0 in clear regions to about 0.07 near the base of the cirrus cloud sampled on 22 October.

Platt and Harshvardhan (1988), hereafter referred to as PH, discuss the relationship between cirrus cloud absorption and ice water content and provide insight as to why the mass absorption coefficient, K , may not be a constant through a cirrus cloud of variable ice particle size distribution. As in PH, K may be considered as:

$$K = \frac{\sigma}{IWC} \approx \beta \frac{\bar{Q}_a}{r_e}, \quad (3)$$

where \bar{Q}_a is the "effective absorption efficiency", r_e the "effective radius" for the size distribution and β is a constant which includes the density of ice and an ice particle orientation factor. Theoretical computations of the absorption efficiency Q_a (or extinction efficiency) as a function of size parameter have been carried out by Herman (1962), Pinnick, *et al.*, (1979) and others. For incident energy in the infrared wavelengths, $Q_a \approx c \cdot r_e$ (c is some constant) for size parameters typically found in fogs and

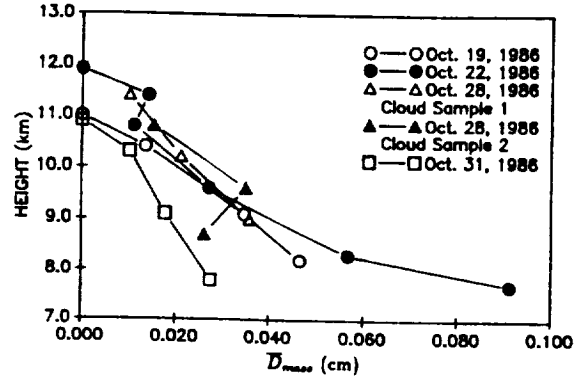


Figure 3: Vertical profiles of $\bar{D}_{m...}$ (see text for description).

stratiform water clouds and thus K is approximately constant. However, for ice clouds where typical ice crystal dimensions are known to be an order of magnitude larger than the water droplet dimensions found in stratiform clouds, the absorption efficiency approaches a value of unity so that K cannot be treated as a constant through cirrus unless r_e remains constant. This is clearly not the case for the cirrus clouds observed during the FIRE first cirrus IFO. Fig. 3 shows the parameter $\bar{D}_{m...}$ varying as a function of height for the five cirrus systems described here where $\bar{D}_{m...}$ is the median mass weighted ice particle dimension as defined by Heymsfield and Miller (1989).

4. Results

In order to deduce the impact of cirrus clouds on infrared radiation, the data sampled in five cirrus systems were analyzed to infer cloud emittances (ϵ_{cid}) and broadband, infrared absorption coefficients (K). The relationship of the absorption coefficients to temperature and microphysical characteristics of the clouds are explored. Because only one aircraft was used, measurements at different levels in the cloud were not made simultaneously. As a result, sampling errors may occur due to the nonsteady state of the cloud field and/or due to the possibility that the flight legs were not flown directly above or below each other. To minimize these errors and in an attempt to set some limits on the observed radiative properties (ϵ_{cid} and K), the downwelling irradiance and IWC data for each flight leg were stratified in the following ways:

MEAN: Average using every measurement along the flight leg to determine a mean value for the cirrus cloud field.

THINNER: Average the lowest 30% of the irradiance measurements and the lowest 30% of the IWC data to represent the optically thinner part of the cloud field.

THICKER: Same as above but for the highest 30% to represent the optically thicker part of the cloud field.

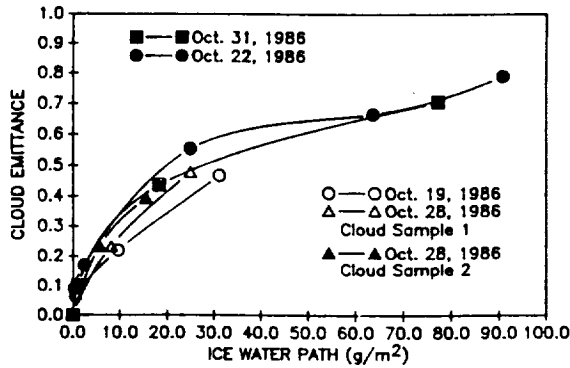


Figure 4: Model deduced cloud emittance (ϵ_{cl}) for five cirrus cloud systems as a function of ice water path (IWP).

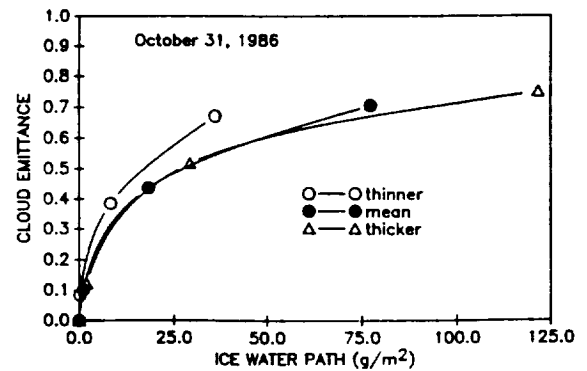


Figure 5: Model deduced cloud emittance (ϵ_{cl}) for the stratified data of October 31, 1986.

4.1 Radiative Properties

The model deduced cloud emittances, that is, the emittances due to the cloud ice (water) itself, are shown in Fig. 4 as a function of ice water path (IWP) for the five cirrus clouds for the case using the flight leg means. For the geometrically thinner clouds (19 Oct., 28 Oct.) the emittance approaches about 0.4-0.5 while for the geometrically thicker clouds (22 Oct., 31 Oct.) the emittance approaches 0.7-0.8. This figure suggests that ϵ_{cl} is a similar function of IWP for these 5 cirrus clouds sampled during FIRE.

Fig. 5 depicts the resulting cloud emittances for the stratified irradiance and IWC profiles of 31 October. For the case of 31 October, ϵ_{cl} was about 0.67 for the thinner cloud and 0.75 for the thicker cloud. It is interesting to note that the functional dependencies of the cloud emittance on IWP are similar between the mean and thicker cloud, but not for the thinner cloud. This occurred in the other cirrus cloud systems as well. It is possible that when stratifying the data as described above, the infrared radiative properties of the thinner clouds are being significantly modulated by unmeasured small particles.

Stackhouse (1989) has shown that small particles ($d < 50 \mu\text{m}$) can significantly modulate the transfer of infrared radiation. Furthermore, Prabhakara, *et al.*, (1988) and Ackerman, *et al.*, (1989) have demonstrated that a unique spectral signature which occurs across the infrared window region ($8\text{--}12 \mu\text{m}$) due to cirrus clouds is consistent with radiative transfer calculations for ice particle size distributions with effective radii less than $40 \mu\text{m}$. Unfortunately, small particles ($d < 36 \mu\text{m}$) were not measured during the FIRE first cirrus IFO and have not been measured anywhere in high altitude cirrus clouds. This shortcoming must be dealt with in the future in order to understand the relationship between small particles and the measured radiative properties of cirrus clouds. Broadband mass absorption coefficients (K in units of m^2/kg) have been deduced and are shown for the five cirrus clouds investigated here and for the different cloud stratifications in Fig. 6 versus the parameter \bar{D}_{mass} . Fig. 6 shows the K values retrieved from the mean irradiance and IWC

profiles. As expected from the theoretical considerations in Section 3, K is shown to decrease with increasing particle size. The magnitude of K is shown to vary by about two orders from about 0.48 to 0.007. Griffith *et al.*, (1980) deduced K values of 0.096, 0.080 and 0.076 to fit irradiance observations of three cirrus clouds observed during a tropical eastern Atlantic experiment (GATE). Those cirrus systems were anvils very close to deep convection. Paltridge and Platt (1981) deduced a K value of 0.056 to fit irradiance observations of cirrus cloud decks over New Mexico. This investigation is the first which attempts to deduce profiles of K through cirrus clouds. The physical significance of K as it is defined in Eqn. 2 may best be described as a coefficient which relates the IWP to all other microphysical characteristics important to the modulation of the incident irradiance. These other microphysical characteristics probably include, but are not limited to, the effects of small particles, particle orientation and ice crystal habit. The functional dependence of K on the parameter \bar{D}_{mass} shown in Fig. 6 appears to be somewhat dissimilar from one cirrus cloud to the next although the general negative slope is common to all cases. This may indicate that the microphysical properties that the K values characterize in Eqn. 2 are dissimilar from one cirrus cloud to the next. Fig. 7 depicts the retrieved K values for 31 October for the different cloud stratifications. As in the case of the cloud emittance, the functional dependence of K for the mean and thicker stratifications are similar to each other but rather different from that of the thinner clouds. It is likely that the data stratified into the thinner clouds are more effectively characterized by small particles. In other words, the thinner clouds represent data with lower IWC and lower irradiances, however the high values of K that are retrieved from this data indicate the significant effect of some unmeasured microphysical characteristic (i.e. small particles) on the radiative properties of the cirrus.

Platt and Harshvardhan (1988) (hereafter referred to as PH) discuss the temperature dependence of cirrus infrared extinction based on data obtained by Platt, *et al.*, (1987) and Heymsfield and Platt (1984). The beam volume absorption coefficients ($10\text{--}12 \mu\text{m}$) deduced from

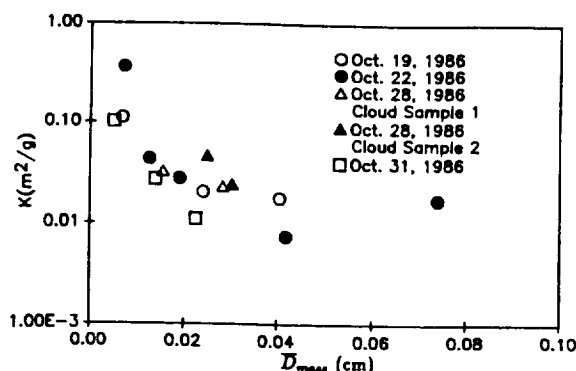


Figure 6: Mass absorption coefficients (K) as a function of the parameter \bar{D}_{mass} for five cirrus cloud systems.

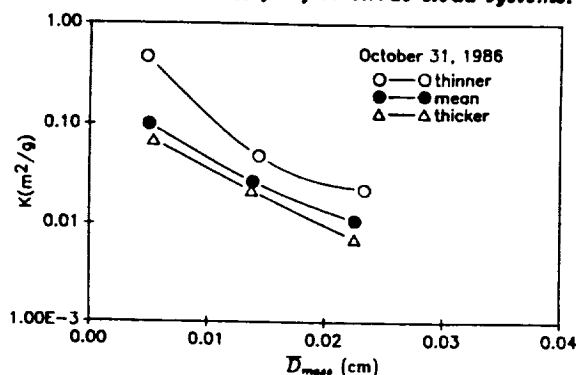


Figure 7: Mass absorption coefficients (K) as a function of the parameter \bar{D}_{mass} for the stratified data of October 31, 1986.

these two independent data sets were found to be similar functions of temperature. Broadband volume absorption coefficients (σ) have been computed where

$$\sigma = K \cdot IWC \quad (8)$$

for the five cirrus clouds examined here and for the mean cloud cases. σ is plotted as a function of temperature in Fig. 8 against two regression lines for the data in PH. The solid line fits the beam absorption coefficients as presented in PH while the dashed line fits these same values multiplied by a diffusivity factor of 1.66. The agreement between the σ values and the regression lines from PH is very good. It should be noted that the data of PH were obtained by first deducing a single volume absorption coefficient from ground-based radiometer and lidar observations of a cirrus cloud with some mid-cloud temperature. The absorption coefficients were then averaged for many clouds with similar mid-cloud temperatures. Here, volume absorption coefficients have been determined as a function of depth through cirrus clouds and have been related to the mean temperature of the appropriate layer. The degree with which these two data sets compare may suggest that the bulk infrared properties of cirrus may be adequately parameterized as a function of temperature.

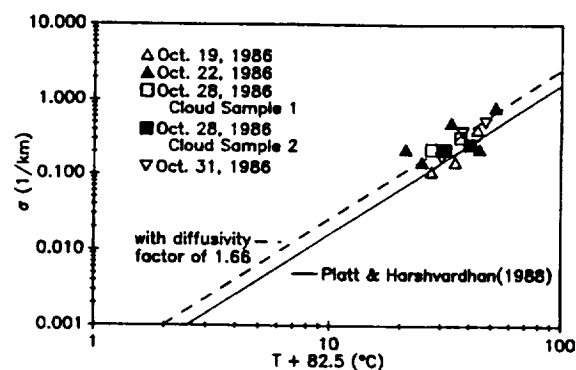


Figure 8: Broadband absorption coefficients (σ) as a function of temperature. The dashed line is from the data of Platt and Harshvardhan (1988) multiplied by a diffusivity factor of 1.66.

6. Acknowledgements

This research has been supported by the National Aeronautics and Space Administration Contract NAG 1-554, the Office of Naval Research Contract N00014-87-K-0228/P00002 and the Army Research Office Contract DAAL03-86-K-0175, P00010.

7. References

- Ackerman, S. A., and S. K. Cox, 1981: Aircraft observations of the shortwave fractional absorptance of non-homogeneous clouds. *J. Appl. Meteor.*, **20**, 128-133.
- Ackerman, S. A., W. L. Smith, J. Spinhirne and H. E. Revercomb, 1989: The 27-28 October 1986 FIRE cirrus case study: Spectral properties of cirrus clouds in the 8-12 μ m window. Submitted to *Monthly Weather Review*.
- Albrecht, B. A., M. Poellot and S. K. Cox, 1974: Pyrgeometer measurements from aircraft. *Rev. Sci. Instrum.*, **45**, 33-38.
- Albrecht, B., and S. K. Cox, 1976: Radiation data reduction procedures for Sabreliner, C-10 and DC-6 aircraft during GARP Atlantic Tropical Experiment. *Atmos. Sci. Pap. No. 244*, Colorado State University, Ft. Collins, 100 pp. [Available from the Department of Atmospheric Science, Colorado State University, Fort Collins, CO 80523].
- Albrecht, B., and S. K. Cox, 1977: Procedures for improving pyrgeometer performance. *J. Appl. Meteor.*, **16**, 188-197.
- Cox, S. K. and K. T. Griffith, 1979: Estimates of radiative divergence during phase III of the GARP Atlantic Tropical Experiment: Part I. Methodology. *J. Atmos. Sci.*, **36**, 575-585.
- Griffith, K., S. K. Cox, and R. G. Knollenberg, 1980: Infrared radiative properties of tropical cirrus clouds inferred from aircraft measurements. *J. Atmos. Sci.*, **37**, 1077-1087.
- Herman, B. M., 1962: Infrared absorption, scattering, and total attenuation cross-sections for water spheres. *Q. J. R. Meteorol. Soc.*, **88**, 143-150.

- Hein, P. F., S. K. Cox and C. M. Johnson-Pasqua, 1987: The Sabreliner data set of the FIRE Cirrus IFO: FIRE Series No. 1. *Atmos. Sci. Pap. No. 418*, Colorado State University, Ft. Collins, 52 pp. [Available from the Department of Atmospheric Science, Colorado State University, Fort Collins, CO 80523]
- Heymsfield, A. J. and C. M. R. Platt, 1984: A parameterization of the particle size spectrum of ice clouds in terms of the ambient temperature and the ice water content. *J. Atmos. Sci.*, **41**, 846.
- Heymsfield, A. J. and K. M. Miller, 1989: The 27-28 October 1986 FIRE IFO cirrus case study: Cloud structure and composition from in-situ measurements. Submitted to *Mon. Wea. Rev.*
- Paltridge, C. W., and C. M. R. Platt, 1981: Aircraft measurements of solar and infrared radiation and the microphysics of cirrus clouds. *Quart. J. Roy. Meteor. Soc.*, **107**, 367-380.
- Paltridge, G. W., 1974: Infrared emissivity, shortwave albedo and the microphysics of stratiform water clouds. *J. Geophys. Res.*, **79**, 4053-4058.
- Pinnick, R. G., S. G. Jennings, P. Chylek and H. J. Auverman, 1979: Verification of a linear relation between IR extinction, absorption and liquid water content of fogs. *J. Atmos. Sci.*, **36**, 1577-1586.
- Platt, C. M. R., J. C. Scott, and A. C. Dilley, 1987. Remote sounding of high clouds. VI. Optical properties of midlatitude and tropical cirrus. *J. Atmos. Sci.*, **44**, 729-747.
- Platt, C. M. R., and Harshvardhan, 1988: Temperature dependence of cirrus extinction: implications for climate feedback. *J. Geophys. Res.* **93**, 11,051-11,058.
- Prabhakara, C., R. S. Fraser, G. Dalu, Man-Li C. Wu, R. J. Curran and T. Styles, 1988: Thin cirrus clouds: Seasonal distribution over oceans deduced from Nimbus-4 IRIS. *J. Appl. Meteor.*, **27**, 379-399.
- Rockwood, A. A. and S. K. Cox, 1976: Satellite inferred albedo over northwestern Africa. *Atmos. Sci. Pap. No. 262*, Colorado State University, Ft. Collins, 64 pp. [Available from the Department of Atmospheric Science, Colorado State University, Fort Collins, CO 80523]
- Smith, Jr., W. L., S. K. Cox and V. Glover, 1988: Temperature sensitivity of Eppley broadband radiometers. *Atmos. Sci. Pap. No. 423*, Colorado State University, Ft. Collins, 12 pp. [Available from the Department of Atmospheric Science, Colorado State University, Fort Collins, CO 80523]
- Smith, Jr., W. L., P. F. Hein and S. K. Cox, 1989: The 27-28 October 1986 FIRE IFO cirrus case study: In situ observations of radiation and dynamic properties of a cirrus cloud layer. Submitted to *Mon. Wea. Rev.*
- Smith, Jr., W. L., and S. K. Cox, 1989: Broadband radiative properties of cirrus clouds deduced from aircraft measurements during FIRE. *Atmos. Sci. Pap. No. 448*, Colorado State University, Ft. Collins [Available from the Department of Atmospheric Science, Colorado State University, Fort Collins, CO 80523]
- Stackhouse, P.W., Jr. A Theoretical and observational comparison of cirrus cloud radiative properties. M.S. Degree, 117 pp. Department of Atmospheric Science, Colorado State University, Ft. Collins, CO. July, 1989.
- Stephens, G. L., 1978: Radiation profiles in extended water clouds, II. Parameterization schemes. *J. Atmos. Sci.*, **35**, 2123-2132.
- Stephens, G. L., Paul W. Stackhouse and Piotr J. Flatau 1989: The relevance of the microphysical and radiative properties of cirrus clouds to climate and climatic feedback. Submitted to *J. Atmos. Sci.*

REMOTE SOUNDING THROUGH SEMI-TRANSPARENT CIRRUS CLOUD

William L. Smith, Steven A. Ackerman, and Allan H.-L. Huang

Cooperative Institute for Meteorological Satellite Studies
 Space Science and Engineering Center
 1225 West Dayton Street
 Madison, Wisconsin 53706

1. Introduction

A large part of the earth is covered by thin semi-transparent cirrus cloud (Wylie et al., 1989). The cirrus results from the natural injection of moisture into the upper troposphere by deep convection (i.e., anvils) and from man-made moisture injected into the upper troposphere by jet aircraft. Although most cirrus cloud is semi-transparent to infrared wavelengths, their heights, thicknesses, and spectral absorption properties must be known in order to retrieve atmospheric temperature and moisture profiles from the data.

In this paper, an algorithm is developed for accounting for the radiative properties of semi-transparent cloud in the retrieval of vertical temperature and moisture profiles. The algorithm is to be applied to the NASA ER2 HIS data collected during the FIRE cirrus field program. The results of its application will be reported at the second FIRE Annual Meeting to be held July 10-14, 1989 in Monterey, California.

2. The Cloud Algorithm

The retrieval of temperature and moisture profiles from spectral measurements of upwelling radiances are most efficiently achieved through the simultaneous solution of the radiative transfer equation of the form (Smith et al., 1989)

$$\delta I(\nu_j) = \delta T_s f_j^o \tau_s^o(\nu_j) - \sum_{i=1}^N \int_{p^*}^{p_s} \delta T_i(p) f_j^o \tau^o(\nu_j) \frac{d \ln \tau_i^o(\nu_j)}{dp} dp \quad (1)$$

where I is spectral radiance, ν is wavenumber, T is temperature, f is the derivative of Planck radiance with respect to temperature computed for a "guess" temperature profile condition, τ^o is the total atmospheric transmittance (i.e., the transmittance due to all absorbing constituents) for the "guess" atmospheric conditions, τ_i^o is the transmittance due to individual absorbing constituents (e.g., CO_2 , H_2O , and cloud). The subscript "s" denotes the surface value, N the number of individual absorbers to be considered, and the transmittance function is understood to pertain to the atmosphere between the instrument level (p^*) and the level of interest (p).

The symbol δ denotes a perturbation from the "guess" condition. For a constituent whose concentration is known a priori, δT_i represents the deviation of the actual temperature profile from the "guess" profile. For all other constituents,

$$\delta T_i = \delta T - \frac{\partial T}{\partial U_i^0} (U_i - U_i^0) \quad (2)$$

where $\delta T = T - T^0$, U_i is the total path length of the gas between the instrument and the level of interest. The significance of Eq. (1) is that it is linear, the only unknowns are the temperature perturbations, $\delta T_i(p)$ and they can be determined by the linear inverse of (1).

Neglecting scattering, clouds can be treated in the very same manner as a molecular absorber, provided its spectral dependence is known. In this case, the total transmittance $\tau^0(\nu_j)$ is given by

$$\tau^0(\nu_j) = \prod_i \tau_i^0(\nu_j)$$

where the "guess" cloud transmittance (e.g., $i=3$) has the form

$$\tau_{cd}(\nu_j) = \tau_3^0(\nu_j) = \text{EXP} \left(-\alpha f(\nu_j, r^0) \left(\frac{P - P_t}{P_b - P_t} \right) \right) \quad (3)$$

In (3), α is a constant dependent upon the total ice or water content of the cloud, $f(\nu, r^0)$ is a spectral function dependent on the effective radii, r^0 , of the absorbing particles (ice or liquid water drops), P_t and P_b are the top and base pressures of the cloud. Assuming that the cloud is purely absorbing, a good approximation for $f(\nu, r^0)$ can be obtained by the Modified Anomalous Diffraction Theory (MADT) presented by Ackerman and Stephens (1987). In this case,

$$f(\nu, r^0) = Q_{\text{ABS}} = 1 + \frac{m^2}{2\chi n_i} e^{-4\chi n_i} \left(1 + \frac{1}{4\chi n_i} \right) - \frac{m}{2\chi n_i} e^{-4\chi n_i \sqrt{1-m^2}} \left(\sqrt{m^2-1} + \frac{m}{4\chi n_i} \right) \quad (4)$$

where Q_{ABS} is the absorption efficiency, χ is the size parameter $2\pi r^0/\lambda$, where r^0 is the effective particle radius and λ is the wavelength, m is the index of refraction, and n_i is the complex part of the index of refraction. Figure 1 shows a comparison between the absorption efficiency computed for ice clouds using modified anomalous diffraction theory and Mie theory. It can be seen that the difference in spectral dependence for large and small particles is explained with MADT. In fact, if the effective radius is a free parameter, as it is in the retrieval problem, an effective radius for Eq. (4) can be chosen which provides an even closer fit to the Mie calculations.

Thus, given (3) and (4), one has the following four cloud parameters, α , r^0 , P_t , and P_b . If we consider the cloud term of Eq. (1), we can write

$$- \int_{p_*}^{P_s} \delta T_{cd} r^0(\nu_j) \frac{d \ln \tau_{cd}(\nu_j)}{dp} dp = \beta^0 f(\nu_j, r^0) \int_{p_*}^{P_s} \delta T_{cd} f_j r^0(\nu_j) dp \quad (5)$$

where $\beta = \alpha/(P_b - P_t)$. Thus, given an initial guess of α , r^0 , P_t , and P_b from which $r^0(\nu_j)$ can be specified, one could solve for the profile

$$\delta T_i = \delta T_{cd} = (T_{cd} - T) \quad p_t \leq p \leq p_b$$

As with the molecular absorber

$$T_{cd} - T = - \frac{\partial T}{\partial U_{cd}^0} (U_{cd} - U_{cd}^0)$$

Since

$$U_{cd} = \beta(p - p_t)$$

Then,

$$T_{cd} - T = - \frac{\partial T}{\partial p} \left[\delta \beta \left(\frac{p - p_t^0}{\beta^0} \right) - \delta p_t \right] \quad (6)$$

If the true temperature profile, T , and the cloud temperature profile, T_{cd} , are known from the increase solution of Eq. (1), Eq. (6) can be solved for $\delta \beta$ and δp_t . Given $\delta \beta$ and δp_t , a new base pressure can be defined from

$$P_b \approx P_t + \frac{\alpha^0}{\beta} = (p_t^0 + \delta p_t) + \frac{\alpha^0}{\beta^0 + \delta \beta} \quad (7)$$

The solution for the absorber temperature profiles and cloud parameters depend upon an initial estimate of the particle radius r^0 and the particle concentration variable α^0 . It can be shown that for an isothermal cloud, and at a wavenumber void of molecular absorption (i.e., a "window")

$$f(\nu_o, r^o) \alpha^o = \ln \left(\frac{I(\nu_o) - B[T^o(p_t^o)]}{B(T_s^o) - B[T^o(p_t^o)]} \right) . \quad (8)$$

In order to solve (8) for r^o and α^o , the initial cloud top pressure can be defined using the CO₂ slicing technique (Menzel, 1986; Smith and Frey, 1988). Given the product $f(\nu_o, r^o)\alpha^o$ for two window wavelengths whose cirrus optical properties are expected to differ (e.g., 8.5 and 11.5 μm as shown in Fig. 1), r^o can be defined from the ratio of Eq. (8) applied to the two wavelengths since α^o cancels. Once r^o is known, α^o can then be obtained from Eq. (8) applied to either one of the two window wavelengths. Given α^o an estimate of β^o can be obtained from an initial guess of cloud-base altitude, p_b^o (i.e., $\beta^o = \alpha^o/(p_b^o - p_t^o)$).

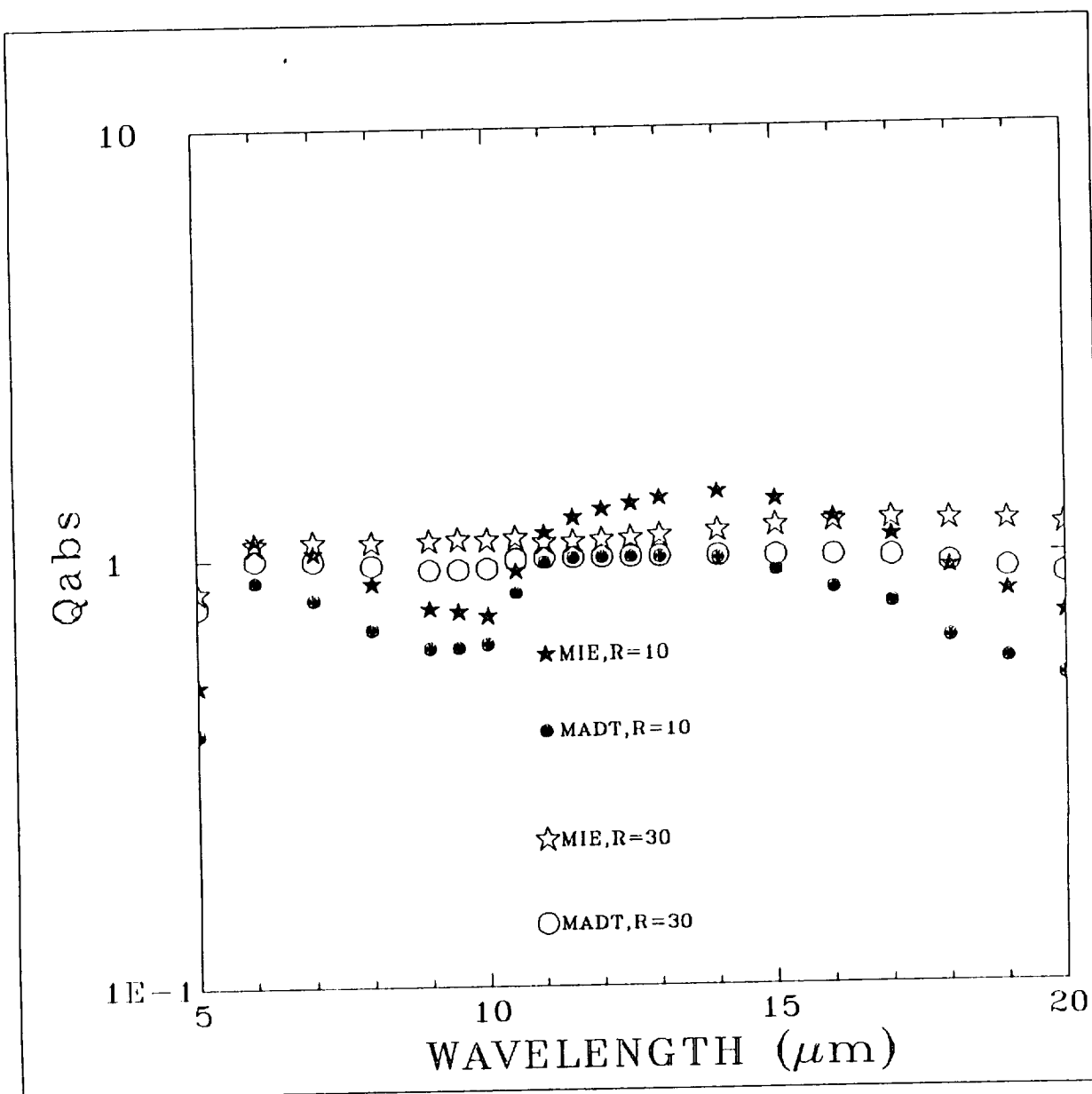
In summary, the following steps can be taken to solve simultaneously for temperature and water vapor profiles and cloud parameters from cirrus cloud contaminated radiance spectra:

- (1) Using the CO₂ slicing technique with the guess temperature profile, solve for an initial cloud top pressure, p_t^o .
- (2) Using the 8.5 μm and 11.5 μm window radiances and the initial guess surface and cloud temperature conditions, use Eq. (8) to determine the ratio $f(8.5\mu\text{m}, r^o)/f(11.5\mu\text{m}, r^o)$. Use (4) to determine r^o and then Eq. (8) applied to one of the two window wavelengths to determine α^o . This step yields the initial guess cloud parameters α^o , β^o , p_b^o .
- (3) Specify the initial guess cloud transmission profile using Eq. (3) where $f(\nu_j, r^o)$ is calculated using Eq. (4).
- (4) Solve for the profiles δT_i through the linear matrix inverse solution of Eq. (1).
- (5) Use Eq. (6) to solve for $\delta\beta$ and δp_t .
- (6) Use Eq. (7) to provide p_b .

The entire process could be iterated until the cloud parameters cease to change from one iteration to the next.

3. Summary

A method for direct and simultaneous solution for temperature and moisture profiles and cloud parameters is outlined. The method takes into account the spectral dependence of cloud emissivity/transmissivity which has been found to be a function of particle size. The results of the application of this technique to cirrus radiance spectra achieved with the HIS interferometer flown on the NASA ER2 during the FIRE will be reported at the meeting.



July 1989

Ackerman and Smith

IR Spectral Characteristics of Cirrus Clouds

Steven A. Ackerman and William L. Smith*Cooperative Institute for Meteorological Satellite Studies**Space Science and Engineering Center, 1225 West Dayton St.**University of Wisconsin-Madison, Madison, WI. 53706*

(July 1989)

The recent focus of parameterizations of the radiative properties of clouds has been to include the microphysical properties of the cloud. A variety of parameterizations have been developed for both the shortwave and the longwave. In parameterizing the longwave properties of clouds, it is useful to consider the two stream solution of the radiative transfer equation appropriate for a thermal source. While various solutions exist, here we consider the form

$$\begin{bmatrix} F^+(\tau_b) \\ F^-(\tau_t) \end{bmatrix} = \begin{bmatrix} t & r \\ r & t \end{bmatrix} \begin{bmatrix} F^+(\tau_t) \\ F^-(\tau_b) \end{bmatrix} + \begin{bmatrix} s-t & 1-s-r \\ 1-s-r & s-t \end{bmatrix} \begin{bmatrix} B(\tau_t) \\ B(\tau_b) \end{bmatrix} \quad (1)$$

where

$$r = \frac{\rho(1 - e^{-\tau_{eff}})}{1 - \rho^2 e^{-\tau_{eff}}} \quad (2)$$

$$t = \frac{e^{-\tau_{eff}}(1 - \rho^2)}{1 - \rho^2 e^{-\tau_{eff}}} \quad (3)$$

$$s = \frac{(1 - t + r)}{\bar{\mu}(1 - \omega_0 + 2\omega_0\bar{\beta})\tau} \quad (4)$$

$$K = \sqrt{1 - 2\omega_0 + \omega_0^2 + 2\omega_0\bar{\beta} - 2\omega_0^2\bar{\beta}} \quad (5)$$

$$\tau_{eff} = \bar{\mu}K\tau = \pi\bar{\mu} \int \int K Q_{ext} n(r) r^2 dr dz \quad (6)$$

$$\rho = \frac{\omega_0\bar{\beta}}{1 - \omega_0 + \omega_0\bar{\beta} + K} \quad (7)$$

where B is the Plank function $\bar{\beta}$ is the backscatter coefficient and $\bar{\mu}$ is the diffusivity factor ($\bar{\mu} \approx 1.66$). For an isothermal cloud, $B(\bar{r})$, equations (12)-(18) indicate the necessity to parameterize two variables, ρ and KQ_{ext} . Physically, ρ is the reflectance for an infinitely thick cloud. The value of ρ as a function of wavelength is shown in figure 1 for ice spheres. For wavelengths between 10 and $13\mu\text{m}$, ρ is a weak function of the particle size and $\rho < 0.08$. ρ can become large for small particles for regions outside this window.

To parameterize KQ_{ext} we consider the ratio of KQ_{ext} to Q_{abs} . This ratio (Figure 2) displays a similar dependency on wavelength and particle size as that depicted by ρ , with a strong dependency on particle size outside the window region. For wavelengths between 10 and $13\mu\text{m}$, $KQ_{ext} \approx Q_{abs}$. In parameterizing the longwave properties of clouds in the 10-13 μm window region, it is therefore useful to parameterize Q_{abs} . An appropriate parameterization of Q_{abs} is that of the modified anomalous diffraction theory. Figure 3 depicts the relations between wavelength and Q_{abs} for two different droplet sizes. The stars represent Mie calculations while the circles denote the approximation of equation (9). The open symbols are for a $30\mu\text{m}$ particle while the solid symbols represent the calculations for a $1\mu\text{m}$ droplet. The approximation is excellent, even for droplets as small as $1\mu\text{m}$.

The dependence of effective emittance on the particle size can be expressed to second order using MADT as

$$\epsilon = 1 - \exp \left(\bar{\mu}\pi \int \int n(r) \left\{ \frac{4}{3}m^2r^3\kappa \left[1 - (1 - m^{-2})^{3/2} \right] dr + r^4\kappa^2m^2 \left[1 - (1 - m^{-2})^2 \right] \right\} drdz \right)$$

where $\kappa = 4\pi n_i/\lambda$ is the absorption coefficient of water/ice. The first term of the exponential represents the dependency on the water content of the cloud, while the second term displays a dependency on the fourth moment of the size distribution. As an estimate of the particle size at which the emissivity becomes dependent on the droplet size we consider the radius at which

$$\frac{4}{3}m^2\kappa \left[1 - (1 - m^{-2})^{3/2} \right] = R\kappa^2m^2 \left[1 - (1 - m^{-2})^2 \right] \quad (9)$$

Figure 4 depicts this radius, R , as a function of wavelength for water (solid lines) and ice (dashed lines) spheres. A cloud with a monomodal distribution of particles of size R or greater will display a sensitivity to droplet size. For example, if we have two water clouds, one with a monomodal size distribution of $12\mu\text{m}$ particle and the other with a $8\mu\text{m}$ droplet distribution, the cloud emissivity in the $8\text{--}11.5\mu\text{m}$ band will be sensitive primarily to the LWP, while the 11.5 to $14\mu\text{m}$ band emissivity would also display a sensitivity to the size distribution. This is in agreement measurements and calculations of fogs. In the the case of ice clouds, the $11\text{--}13\mu\text{m}$ band will display a dependency on the size distribution for particles greater than $4\mu\text{m}$.

In summary, high spectral resolution measurements in the $8\text{--}13\mu\text{m}$ "window" region are appropriate for remotely sensing the microphysical properties of ice clouds as: windows in gaseous absorption are available; this is the most sensitive region to particle size; the value of ρ is small compared to other wavelengths; and $KQ_{ext} \approx Q_{abs}$.

To demonstrate this dependency of particle size on IR observations, we consider the spectral variation of the equivalent blackbody temperatures in the "window" region, four spectral bandwidths: $8\mu\text{m}$ ($8.3\text{--}8.4$), $10\mu\text{m}$ ($10.07\text{--}10.173$), $11\mu\text{m}$ ($11.062\text{--}11.249$) and $12\mu\text{m}$ ($11.93\text{--}12.063$). The equivalent blackbody temperature observations were made with the HIS (High resolution Interferometer Spectrometer) aboard the NASA ER2 during FIRE on 2 November, 1986. Figure 5 is a scatter diagram of the $BT_8\text{--}BT_{11}$ versus $BT_{11}\text{--}BT_{12}$. Each symbol in figure the figure represents a range in the BT_{11} as noted in the legend. The differences in the brightness temperatures observed in these channels are very useful in detecting the presence of cirrus clouds. The cloud free regions have negative differences in $BT_8\text{--}BT_{11}$ due to absorption by water vapor. While cirrus clouds have positive differences owing to the optical properties of ice. The cirrus $BT_8\text{--}BT_{11}$ are greater than the $BT_{11}\text{--}BT_{12}$ as expected from figure 3.

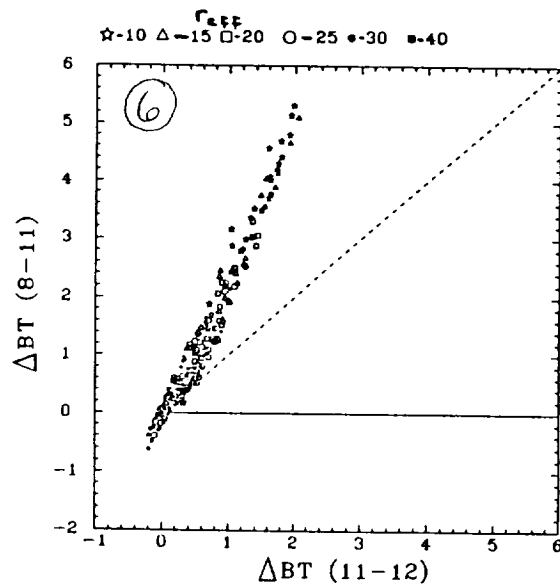
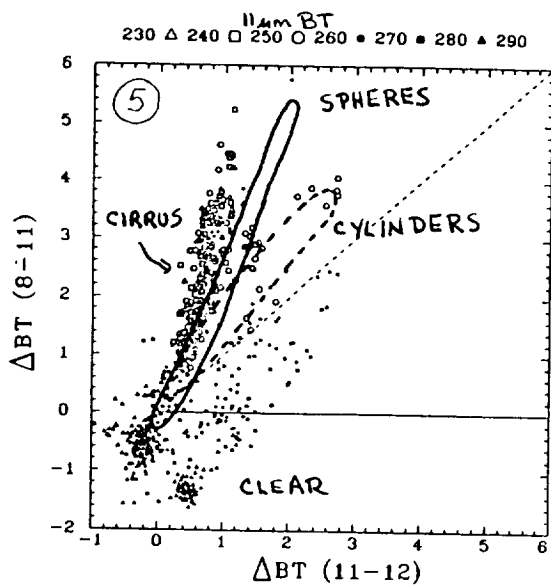
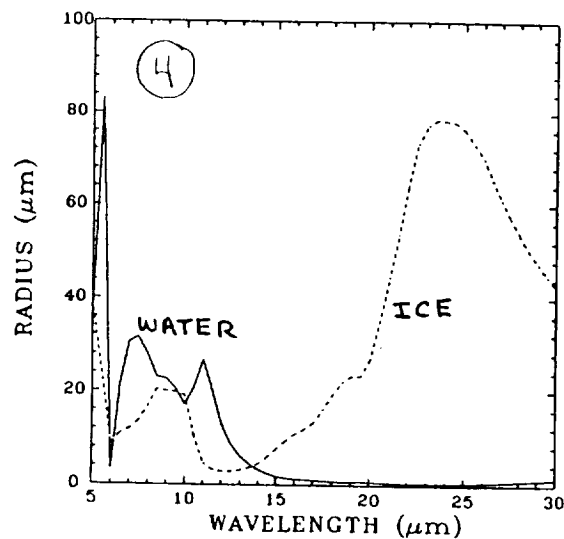
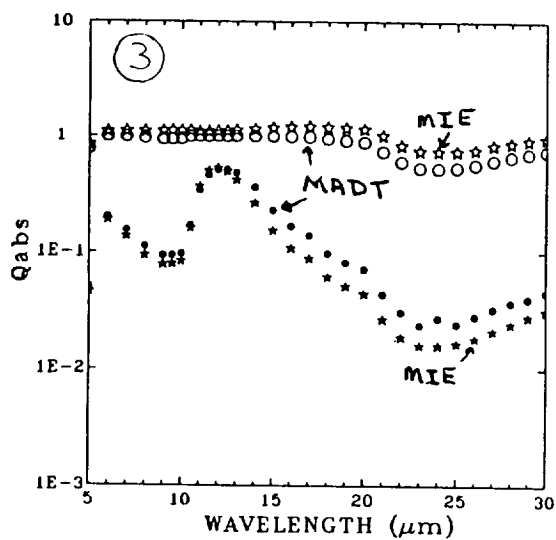
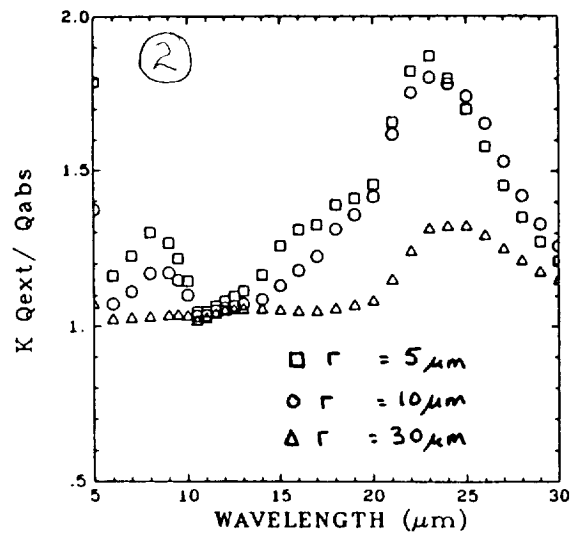
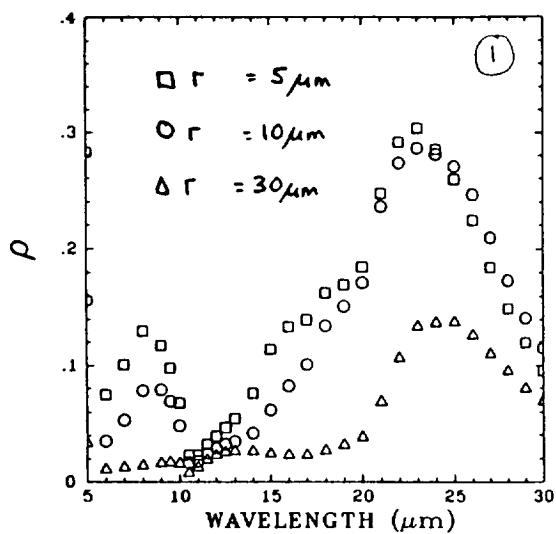
The magnitude of the HIS measured BT differences is related to the cloud particle size distribution. This is demonstrated in figure 6 where the brightness differences are determined with theoretical radiative transfer calculations using a doubling/adding model and assuming various surface temperatures, cloud top temperatures, and different ice water content and geometric thick-

nesses. The cloud is assumed to have a lapse rate of $-6\text{ }^{\circ}\text{K km}^{-1}$ and is homogeneous. The cloud particles are assumed to be spheres with a gamma size distribution and effective radii as denoted in the symbol legend. These calculations demonstrate that the ice cloud with the smaller r_{eff} (stars) display the large BT differences observed by the HIS while the ice cloud with the larger r_{eff} do not. The magnitude of the ΔBT is also related to the IWP (e.g. very thin clouds are similar to the clear sky values).

The envelope of the calculations is depicted on figure 5 by the solid line. Differences between the theory and observations are seen at the larger $\text{BT}_8\text{-BT}_{11}$ values. This difference may be attributed to particle shape, or to a non-homogeneous vertical/horizontal distribution of the particles. The effect of particle shape is demonstrated by the dashed line which is the envelop for a cirrus cloud consisting of small ice cylinders.

4. SUMMARY

- The HIS spectra show spectral variations in equivalent blackbody temperatures in the window region of greater than 5°C , for a given cirrus cloud.
- The brightness temperature differences between 8 and $11\text{ }\mu\text{m}$ and 11 and $12\text{ }\mu\text{m}$ are useful parameters for detecting the presence of cirrus clouds.
- Theoretical calculations indicate that the magnitude of the spectral variation in brightness temperature is related to the particle size. The smaller particles are associated with larger brightness temperature differences.
- The magnitude of the brightness temperature differences are also related to the particle shape. Calculations assuming spherical particles are in better agreement with the majority of HIS observations than similar calculations assuming cylindrical particles.



AIRBORNE LIDAR/RADIOMETRIC MEASUREMENTS OF CIRRUS CLOUD PARAMETERS AND THEIR APPLICATION TO LOWTRAN RADIANCE EVALUATIONS

Edward E. Uthe
Geoscience and Engineering Center
SRI International
Menlo Park, CA 94025 USA

EXTENDED ABSTRACT

SRI has assembled an airborne lidar/radiometric instrumentation suite for mapping cirrus cloud distributions and analyzing cirrus cloud optical properties. Operation of upward-viewing infrared radiometers from an airborne platform provides the optimum method of measuring high-altitude cold-cloud radiative properties with minimum interference from thermal emission by the earth's surface and lower atmospheric constituents. Airborne installed sensors can also operate over large regional areas including water, urban and mountain surfaces and above lower atmospheric convective clouds and haze layers.

Figure 1 illustrates currently available sensors installed on the SRI Queen Air aircraft. The upward-viewing lidar (ALPHA-2) transmits energy pulses at two wavelengths (0.53 and $1.06\ \mu\text{m}$) at pulse rates to 10/sec. Backscattered energy is collected in a 14-inch diameter telescope and is wavelength separated into two independent detector systems that produce range-dependent lidar signatures representing a profile of the scattering medium above the aircraft. Because an upward-viewing airborne radiometer views a low-radiance background in the absence of clouds, radiance perturbations introduced by low-density aerosol and cloud layers may be detected by a high-sensitivity infrared radiometer. The upward-viewing 8- to $14\text{-}\mu\text{m}$ infrared radiometer is calibrated for equivalent blackbody temperatures as low as -80°C .

Lidar and radiometric data records are processed for real-time viewing on a color video screen. Figure 2 presents a cirrus cloud data example as a black-and-white reproduction of a color display. Upward-viewing lidar backscatter signatures are plotted as an altitude/distance intensity-modulated display with relative density scale shown to the right of the lidar data display. Aircraft latitude data are overplotted on the lidar display between 10,000 and 15,000 ft. Longitude data are overplotted between 15,000 and 20,000 ft. Downward-viewing solar flux radiometer data are overplotted between 20,000 and 25,000 ft. Downward-viewing infrared radiometer data are overplotted between 25,000 and 30,000 ft. Upward-viewing solar-flux radiometer data are overplotted between 45,000 and 50,000 ft. Upward-viewing infrared radiometer data are overplotted between 50,000 and 55,000 ft.

The data presented in Figure 2 show that at the aircraft altitude of 12,000 ft, the 8- to $14\text{-}\mu\text{m}$ atmospheric radiation background was equivalent to a blackbody temperature of about -60°C and, therefore, the radiometer did not respond strongly to low-density cirrus cloud concentrations detected by the lidar. At an altitude of about 20,000 ft, the radiation background was near -80°C and the radiometric temperature of low-density cirrus clouds could better be measured. For the sensitivity of the radiometer flown on the Queen Air aircraft, an altitude of at least 20,000 ft is required for making optimum cirrus cloud radiance measurements.

Figure 3 presents cloud blackbody temperatures (observed by radiometer) plotted against midcloud temperatures (derived from lidar-observed cloud heights and supporting temperature profiles) for data collected on 30 June and 28 July. The radiation temperatures for 30 June were generally warmer (5°C) than cloud temperatures, indicating an effective cloud emissivity greater than 1.0. Data from optically dense clouds observed on 28 July agree with the 30 June results; while radiation temperatures were significantly lower than cloud temperatures for optically thin clouds, indicating cloud effective emissivities were substantially less than 30 June radiation temperatures were related to cloud base height, while the 28 July radiation temperatures were related to cloud thickness.

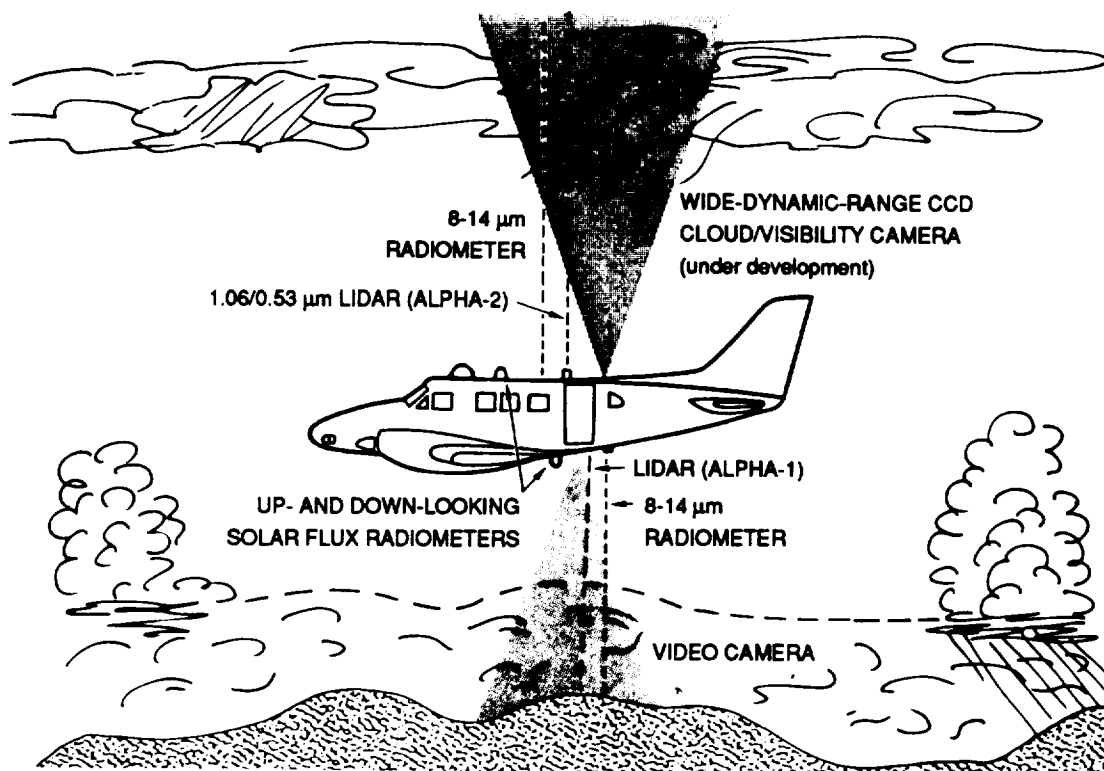


FIGURE 1 SRI QUEEN AIR AND INSTRUMENTS USED FOR OPTICAL CLOUD MAPPING

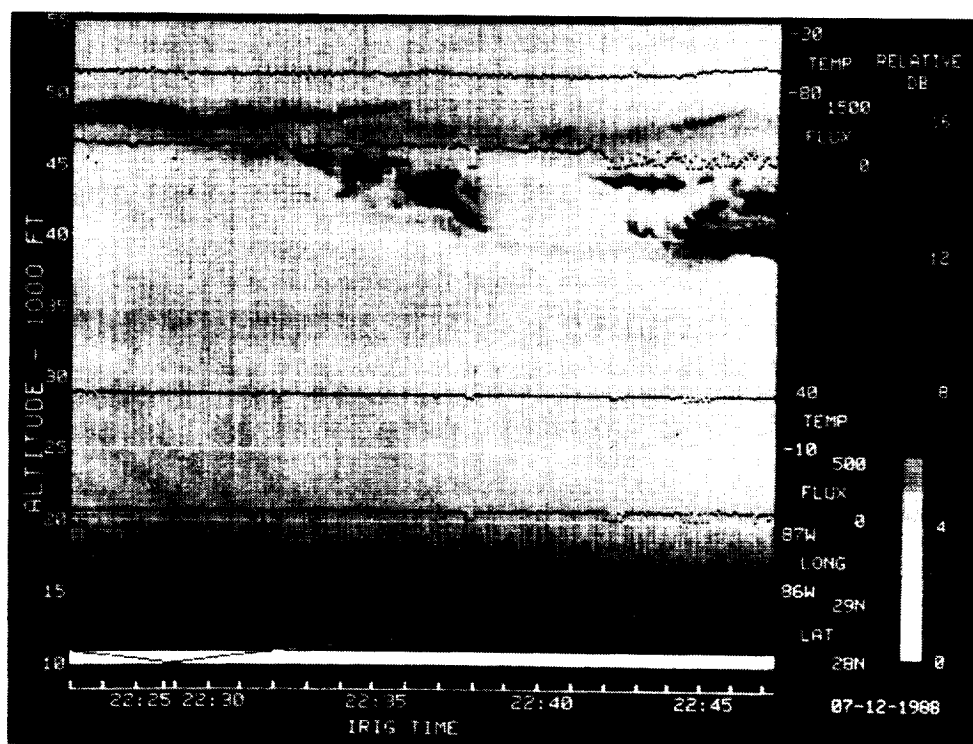


FIGURE 2 AIRBORNE LIDAR RADIOMETRIC CLOUD DATA COLLECTED ON 12 JULY 1988

Table 1
LOWTRAN-7 INPUT PARAMETERS

PARAMETER (WAVELENGTH)	SYMBOL	SOURCE	PARAMETER VALUES		
			30 JUNE (1855 IRIG)	14 JULY (2235 IRIG)	28 JULY (2233 IRIG)
CLOUD BASE ALTITUDE	Z_C	LIDAR	11.9 km	12 km	8.4 km
CLOUD THICKNESS	ΔZ_C	LIDAR	3.0 km	1.5 km	2.1 km
TEMPERATURE PROFILE	$T(Z)$	SOUNDING	2100 IRIG	2400 IRIG	2400 IRIG
WATER VAPOR PROFILE	$W(Z)$	SOUNDING	2100 IRIG	2400 IRIG	2400 IRIG
BOUNDARY TEMPERATURE (PRT-5)	T_B	DOWN-VIEWING RADIOMETER	302° K	304.5° K	306° K
CLOUD EMISSIVITY (PRT-5)	ϵ	UP-VIEWING RADIOMETER/ LIDAR/CLEAR AIR LOWTRAN-7	0.80	0.099	0.62
CLOUD ABSORPTION OPTICAL DEPTH (PRT-5)	u_B	$u_B = -\ln(1 - \epsilon)$	1.59	0.10	0.97
SINGLE-SCATTERING ALBEDO (11 μm)	ω	PLATT AND STEPHENS (1980)	0.53	0.53	0.53
CLOUD TOTAL OPTICAL DEPTH (PRT-5)	u	$u = u_B / (1 - \omega)$	3.38	0.21	2.06
EXTINCTION COEFFICIENT (PRT-5)	σ_B	$\sigma_B = u / \Delta Z_C$	1.13 km ⁻¹	0.14 km ⁻¹	0.98 km ⁻¹
ASYMMETRY PARAMETER (11 μm)	g	PLATT AND STEPHENS (1980)	0.70	0.70	0.70

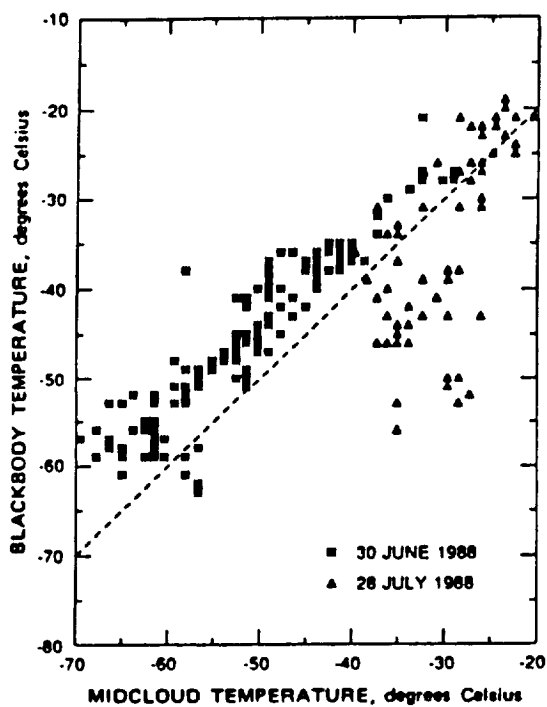


FIGURE 3 OBSERVED CLOUD BLACKBODY TEMPERATURES PLOTTED AGAINST
MIDCLOUD TEMPERATURES DERIVED FROM LIDAR CLOUD HEIGHTS
AND OBSERVED TEMPERATURE PROFILES

Actual cloud emissivities were evaluated from the measured effective emissivities by applying corrections for (1) clear-air thermal emission from the intervening aircraft-to-cloud base layer as computed from the LOWTRAN-7 radiance code using measured temperature and water vapor profiles as model input and (2) reflection by the cloud of upwelling infrared radiation emitted by the earth's surface and lower atmospheric constituents. The cloud base altitude, cloud thickness, and cloud emissivity can be used as LOWTRAN-7 model inputs to evaluate cloud effects on atmospheric radiances. The LOWTRAN-7 code is attractive as it incorporates wavelength-dependent absorption and scattering parameters, multiple-scattering parameterization, and two new cirrus cloud models. The code is widely used to evaluate atmospheric effects on electro-optical systems. Table 1 presents model parameters derived for three airborne lidar/radiometric measurement periods. It should be noted that the lidar data are used only for deriving cloud height and thickness and not for estimating cloud optical parameters. Because of uncertainties introduced by scattering from the irregularly shaped ice crystals, optical analysis of lidar signatures in terms of cloud optical properties is believed to be less desirable than derivation of cloud emissivity based on radiometer readings. The method of deriving cloud parameters from lidar/radiometer observations has been extensively discussed in a series of papers by Platt (1973).

Figure 4 presents an example of LOWTRAN-7 model simulations for infrared radiometer measurements of the cloud/atmospheric conditions observed on 30 June 1989. In this case, the standard LOWTRAN-7 cirrus cloud model, in which cloud emissivity is based on cloud thickness, gives about half the radiance of the LOWTRAN-7 model using the parameters listed in Table 1. The LOWTRAN-6 model gives radiances about halfway between the two LOWTRAN-7 model results. Using the standard LOWTRAN-7 cloud single-scattering albedo and asymmetry parameters based on spherical scattering particles rather than parameters based on scattering cylinders (Platt and Stephens, 1980) results in lower radiance as observed by the upward-viewing radiometer. The radiometer measurement supports the standard LOWTRAN-7 model, although other cases support the modified LOWTRAN-7 model.

A methodology of applying airborne lidar and radiometer measurements for deriving LOWTRAN-7 radiance model parameters and for predicting cloud effects on atmospheric radiances has been illustrated. This study was supported by the U.S. Air Force, Aeronautical Systems Division, Wright-Patterson AFB.

REFERENCES

- Platt, C.M.R., 1973: Transfer of Solar Irradiance through Cirrus Cloud Layers. *J. Atmos. Sci.*, **30**, pp. 1191-1203.
- Platt, C.M.R. and G.L. Stephens, 1980: The Interpretation of Remotely Sensed High Cloud Emissivities. *J. Atmos. Sci.*, **37**, pp. 2314-2322.

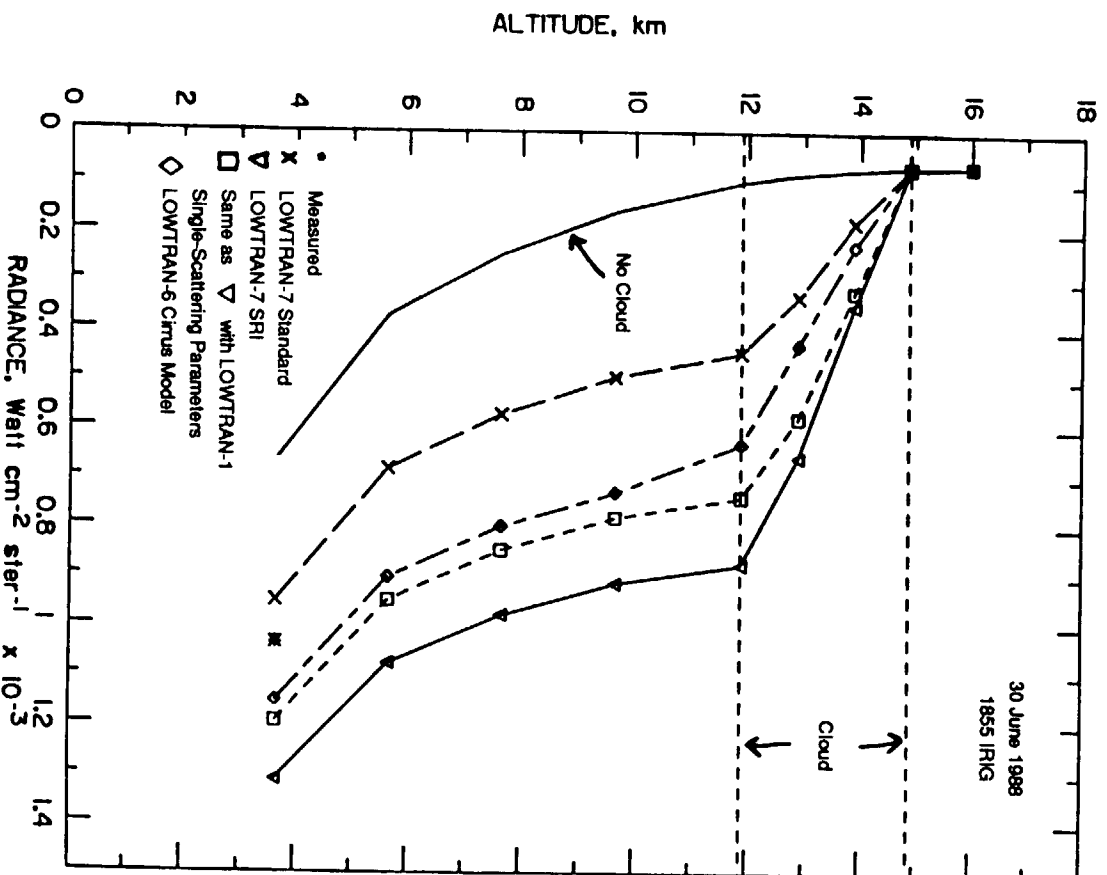


FIGURE 4 RADIANCE SIMULATIONS FOR UPWARD-VIEWING PRT-5 RADIOMETER AS A FUNCTION OF RADIOMETER ALTITUDE.

Simulations are for various LOWTRAN models of cloud conditions observed during a flight test on 30 June 1988.

CIRRUS
SESSION C05: FIRE Phase II
CHAIRMAN: Stephen K. Cox

Thursday, July 13, 1989

	PAGE
C05.01 Objectives Cox, Stephen K.	***
C05.02 Future Plans Cox, Stephen K.	***

	PAGE
C06.01 The May-June 1989 Wisconsin Focused IFO Eloranta, Edwin W., Christian J. Grund, and Donald Wylie	***
C06.02 The Colorado/Missouri 1989 Mini Cirrus IFO Heymsfield, Andrew J., and Donald Hagen	457
C06.03 The Central Pennsylvania Focused IFO: Utilization of a Surface-Based Cloud Observing System Ackerman, Thomas P., Bruce A. Albrecht, and Christopher W. Fairall	***
C06.04 Utah Focused IFO Sassen, Kenneth	***
C06.05 TOGA Stephens, Graeme L.	***
C06.06 A Tropical Cirrus Mini IFO at Kwajalein, Marshall Islands Heymsfield, Andrew J.	***
C06.07 General Discussion Cox, Stephen K.	***

The Colorado/Missouri 1989 Cirrus Mini IFO

Andrew J. Heymsfield
National Center for Atmospheric Research¹
Boulder, Colorado

and Donald Hagen
University of Missouri
Rolla, Missouri

A series of experiments with aircraft are planned for November and December 1989 to study cirrus ice crystal nucleation mechanisms and to test new aircraft instrumentation. The measurements will be conducted using the NCAR Sabreliner (Drs. Don Hagen and Andy Heymsfield) and King Air (Dr. Al Cooper). Sampling will be conducted near Boulder, Colorado, in lenticular (mountain wave) clouds, and over Missouri in cirrus generating cells. Field samples of aerosol and ice crystal replicas and melt-water from these cirrus clouds will be collected and studied in Prof. Hagen's laboratory.

One of the limitations of FIRE Phase I was the inability to collect particles from the Sabreliner and estimate their shape; shape is important for estimating ice water content and ice particle scattering properties. A sampler similar to that used on the King Air during FIRE Phase I (a rod containing a coated slide) will be extended through the skin of the Sabreliner. Owing to the comparatively high speed of the Sabreliner, the collection area is reduced from the probe used on the King Air to improve collection efficiency. Our initial tests of this collection apparatus indicates that oil on the slides is stripped-off in the high velocity air. Therefore, we will use other collection media. Soot-coated slides will be used as the impressions can be used to discern particle phase (Fig. 1A, particles in cirrus from the Sabreliner, Fig. 1B, water droplets in the laboratory, courtesy Nancy Knight). (Water droplets cause soot to concentrate at their centers and leave diffuse edges, ice particles leave streaked impressions). Gelatin-coated slides containing dye can also be used to

decipher phase. We will also use replication techniques as these proved to provide high quality images of ice particles during FIRE phase I. Collections will also be made from the King Air, as was done during FIRE Phase I.

A major limitation of the FIRE Phase I microphysical data set was the lack of measurements of particles below 50 microns with the Sabreliner and below 25 microns with the King Air. A new instrument currently being fabricated which collects particles in oil on a continuously moving belt and then photographs them with a video camera will be tested on the King Air and possibly the Sabreliner as well. The minimum detectable crystal size is about 7 microns, with 1 micron resolution. The device will fit within a Particle Measuring Systems (PMS) 2D probe cannister and thus will be interchangeable between aircraft. (However, removal of a 2D probe is required, and consequently 2D data from will be lost). A photograph of a prototype of the instrument appears in Fig. 2 and imaged ice crystals in the laboratory appear in Fig. 3. We hope to obtain ice particle concentration data continuously down sizes much smaller than previously possible with aircraft.

Relative humidity, crucial to understanding ice particle growth and vertical motion in cirrus, was poorly measured by aircraft during FIRE Phase I. A new cryogenic hygrometer which is purported to provide high accuracy relative humidity measurements down to temperatures below -50°C will be tested. This instrument has been fabricated at NCAR using a design developed by NOAA to measure relative humidity from balloons. The instrument is contained within the aircraft cabin, and air

¹ The National Center for Atmospheric Research is sponsored by the National Science Foundation.

is drawn in to the sensing area using a metal bellows pump. Flights in lenticular clouds are ideal to test the accuracy of this device since the leading edge of the cloud will contain water droplets (approximately 100% relative humidity) and humidities upwind of the cloud are easily calculable. Flights in and below cirrus generating cells which contain liquid water can also be used to test the accuracy of the measurement.

Improved methods for measuring the vertical velocity from the aircraft will be tested as vertical velocities during FIRE Phase I could only be reliably measured to 50 cm s^{-1} . The

method involves using Lagrangian-type spiral descents. The horizontal velocity lateral to the aircraft is measured in each loop of the spiral. Divergence values are found for each loop, and the equation of continuity is integrated to find the vertical velocity distribution with altitude. It is necessary to define the boundary conditions at the cloud top before integrating the equation of continuity. We hope to test various methods for obtaining the upper boundary condition, possibly by making a circular, constant altitude track immediately at or immediately above cloud top from which a divergence value can be obtained.



Figure 1. Microphotographs of images of particles collected in soot-covered slides **A:** Ice particles with the Sabreliner in cirrus. Note the columnar images at the center of the each impression. These particles were about 120 microns. **B:** Water droplets in the laboratory. The droplets forming these impressions were 10 to 50 microns diameter. This data is courtesy Nancy Knight.

Ice Crystal Collection Area

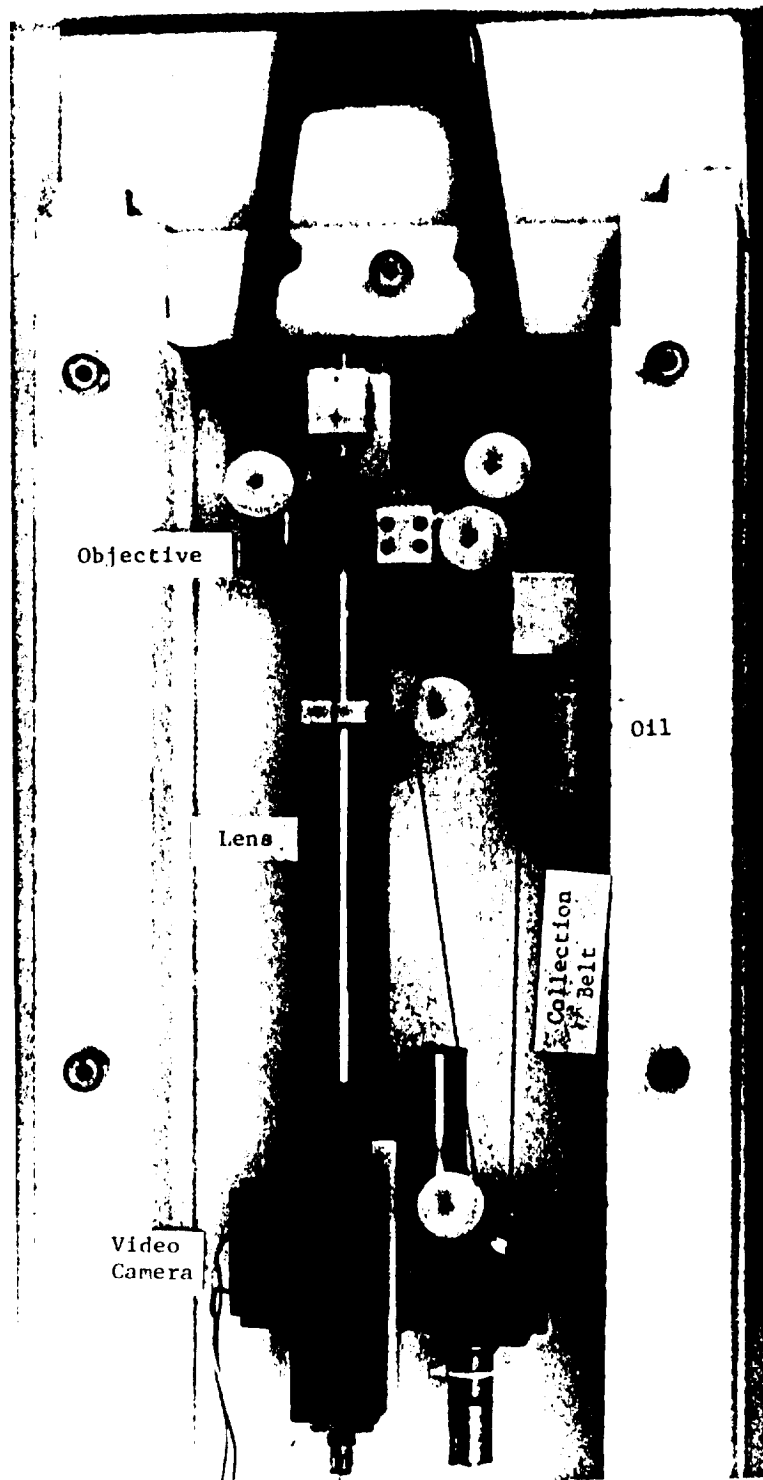


Figure 2. Prototype of continuous ice particle sampler.

Another unknown from FIRE Phase I was the cloud condensation nucleus (CCN) spectra and nuclei composition; further understanding of cirrus crystal nucleation and cirrus crystal concentrations requires such knowledge. Air samples will be collected in mylar bags from the aircraft. Air will be pumped (metal bellows pumps) into the aircraft through a manifold

with an inlet beyond the aircraft's sphere of influence. Following sample collection, the bags will be transported rapidly to the Rolla airport and the CCN spectrum and composition will be characterized. Decay of the CCN spectrum due to collection on the walls of the bag, expected to be small, will be evaluated by experiments.

ORIGINAL PAGE
BLACK AND WHITE PHOTOGRAPH

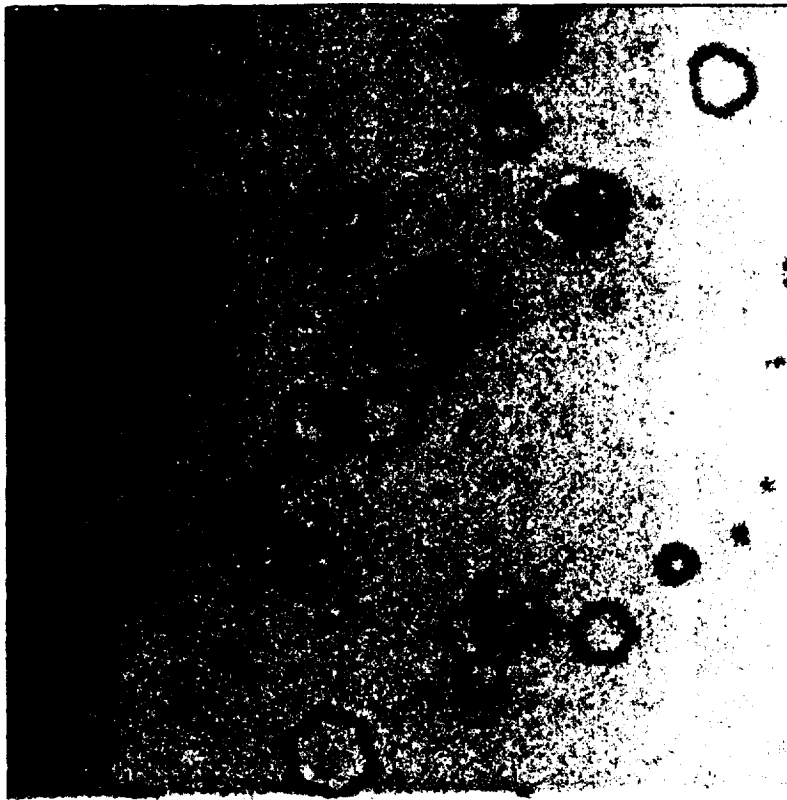


Figure 3. Photograph of ice particles imaged with sampler in the laboratory.

Crystals are approximately 20 microns diameter.

ORIGINAL PAGE IS
OF LOW QUALITY

	PAGE
C07.01 Summary of Results and Conclusions Based on Analysis of Volume Imaging and High Spectral Resolution Lidar Data Acquired During FIRE Phase I: Part II Grund, C. J., and <u>E. W. Eloranta</u>	463
C07.02 A System for Recording Physical Properties of Clouds Purgold, G. C., and C. H. Whitlock	467
C07.03 Cirrus Parameterization from the FIRE ER-2 Observations Spinhirne, J. D.	473
C07.04 1973-1974 Lidar Observations of Cirrus Clouds at Kwajalein Uthe, Edward E.	477
C07.05 The Use of an Airborne Lidar for Mapping Cirrus Clouds in FIRE II Radke, Lawrence F., and Peter V. Hobbs	481
C07.06 On the Use of IR Lidar and Ka-Band Radar for Observing Cirrus Clouds <u>Eberhard, Wynn L.</u> , R. Michael Hardesty, and Robert A. Kropfli	487
C07.07 Intercomparison of Standard Resolution and High Resolution TOVS Soundings with Radiosonde, Lidar, and Surface Temperature/Humidity Data Wheeler, R. J., C. H. Whitlock, J. M. Alvarez, D. O'C. Starr, and D. P. Wylie	491
C07.08 The October 27-28, 1986 FIRE Case Study: A Lidar Compendium from Fort McCoy Alvarez, J. M., W. H. Hunt, J. G. Moore, and M. A. Vaughn	***

Summary of Results and Conclusions Based on Analysis of Volume Imaging and High Spectral Resolution Lidar Data Acquired During FIRE Phase I: Part II

C. J. Grund and E. W. Eloranta

University of Wisconsin
Department of Meteorology
1225 West Dayton St.
Madison, WI 53706

NOTE: Continuation from part I... see Grund and Eloranta in oral presentation section.

IV. Summary

Since the fall of 1986, we have observed cirrus clouds with backscatter cross sections ranging from $<1 \cdot 10^{-7}$ - $4.2 \cdot 10^{-5} \text{ m}^{-1} \text{ sr}^{-1}$, optical thicknesses ranging from $<.003$ to >2.7 , and bulk average backscatter phase functions from $.02$ - $.065 \text{ sr}^{-1}$. We have recorded cirrus cloud structures ranging in vertical extent from 0.1 to 8 km, having horizontal scales from 10's of meters to 266 km, and exhibiting aspect ratios of from 1:5 to 1:100.

The altitude relationship between cloud top and bottom boundaries and the optical center of the cloud is influenced by the type of formation observed. Altocumulus and uncinus generating regions tend to concentrate attenuation in regions of less than 200 m thickness which dominate the vertical extinction profile, even when the generating cell caps an extended column of virga. Virga exhibits complicated fine scale structure, often lying in interleaved, sheared sheets. In cirrostratus, imbedded vertically developed cells frequently occupy a significant altitude range and create large spatial inhomogeneities in optical properties.

Cirrus morphology and generation processes appear to be related to the wind field. Better temporal and spatial resolution in wind measurements in future experiments would aid the understanding of cirrus generation and dissipation mechanisms.

The characterization of the microphysical, morphological and optical properties on satellite footprint and model grid sized areas could be improved in future experiments by characterizing the 3D volume in which the insitu measurements are acquired. High spatial resolution characterization of the distribution of cirrus could be profitably used to shed light on the relationship between aircraft measurements and cirrus formations.

The HSRL has been successfully adapted to the task of cirrus cloud optical property measurement. The HSRL data reported here were collected with the CuCl_2 transmitter producing 50 mW of output power, achieving eye-safe, direct optical depth and backscatter cross section measurements with 10 minute averaging times. A continuously pumped, injection seeded, doubled Nd:YAG laser has just been installed and has increased temporal resolution by a factor of ~ 20 , while improving the aerosol-molecular signal separation capabilities and wavelength stability of the instrument. We expect considerable further improvements as we fine tune the system.

We are just beginning a several week long field experiment in which the VIL will be operated from a site just west of Madison while the HSRL produces vertical optical property measurements. By scanning the VIL in two approximately cross wind planes, we expect to deduce high resolution winds when cirrus are present (by a time lag structural correlation technique), and to characterize the 3D context for cirrus optical properties deduced from HSRL measurements. We will be launching radiosondes in support of this effort. Satellite data acquired by Don Wylie will be subsequently used to

compare passive retrievals to the HSRL optical properties and the VIL contextual information.

Acknowledgements

Funding for VIL construction was provided under ARO grant DAAG29-84-G-0028. HSRL and VIL instrument development and data analysis with regard to cloud statistics has been supported under ARO grant DAAG29-84-K-0069 and ONR contract N00014-87-K-0436. Support for the development of VIL wind measurement capabilities has been provided under ARO grant DAAL03-86-K-0024. Recent algorithm development, and studies of the correlation between wind and backscatter are supported under AFGL contract F19628-87-0056.

References

1. Grund, C.J., and E.W. Eloranta 1989: The 27-28 October 1986 FIRE IFO cirrus cloud study: Cloud optical properties determined by the High Spectral Resolution Lidar. *Mon. Wea. Rev.* **117**, in review.
2. Grund, C.J., E.W. Eloranta, and D.P. Wylie 1989: Lidar validation of VAS Cirrus Cloud Height Determinations. 27th Aerospace Sciences Meeting Jan. 9-12, Reno, NV. *AIAA pub.* **89-0804**.
3. Sassen, K., D.O'C. Starr, and A.J. Heymsfield, 1989: The 27-28 October 1986 FIRE IFO cirrus cloud study: An experiment summary. *Mon. Wea. Rev.* **117**, in review.
4. Sassen, K., C.J. Grund, J.M. Spinhirne, M.J. Hardesty, and J.M. Alvarez 1989: The 27-28 October 1986 FIRE IFO cirrus cloud study: A five lidar overview of cloud structure and evolution. *Mon. Wea. Rev.* **117**, in review.
5. Starr, D.O'C. , and D.P. Wylie 1989: The 27-28 October 1986 FIRE IFO cirrus cloud study: Meteorology and clouds. *Mon. Wea. Rev.* **117**, in review.

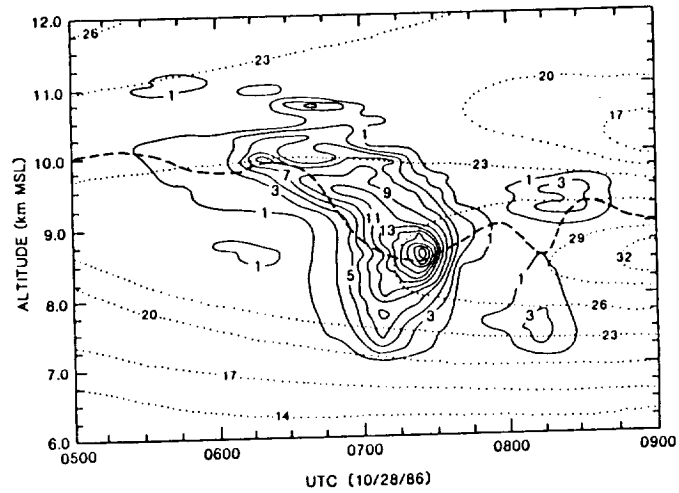


Fig. 3 Mesoscale uncinus complex. Average optical thickness between 0600 and 0750 was .58 (minimum .09 at 0750, maximum 1.1 at 0718), bulk backscatter phase function .042 sr^{-1} . Backscatter cross section (—) in $10^{-6} \text{ m}^{-1} \text{ sr}^{-1}$, optical mid-cloud altitude (---), wind speed (· · ·) in m/s. The MUC passed over Madison just ahead of a mesoscale wind jet.

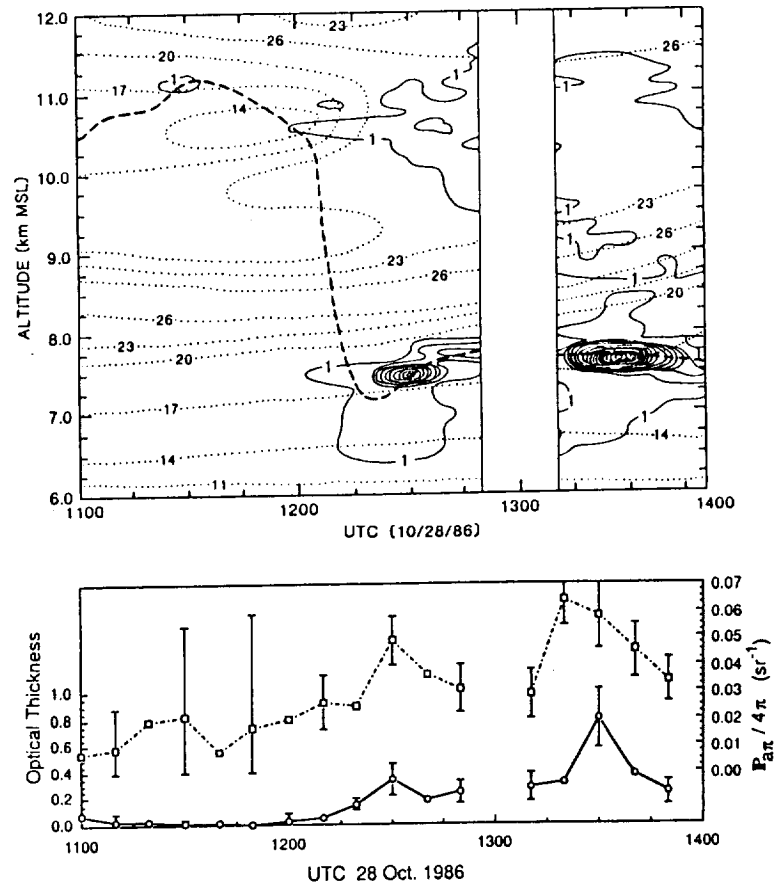


Fig. 4 (Top) Time height backscatter cross section (—, $10^{-6} \text{ m}^{-1} \text{ sr}^{-1}$, interval: $7 \cdot 10^{-6} \text{ m}^{-1} \text{ sr}^{-1}$) mapping of an Allocumulus - cirrus formation with isotachs (· · ·, in m/s) and optical mid-cloud altitude (---). Fig. 5 (Bottom) Corresponding cloud optical depth (—) and normalized bulk backscatter phase function (---, sr^{-1}). Note peaks in backscatter phase function coincide with ACu.

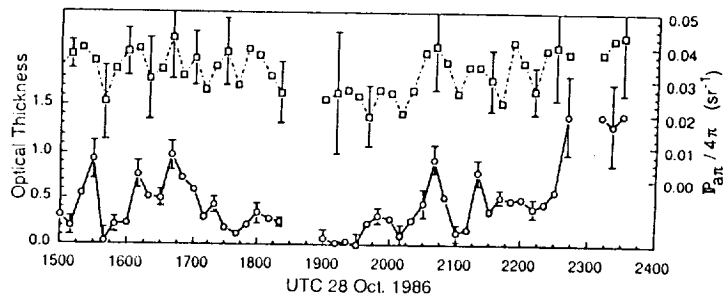
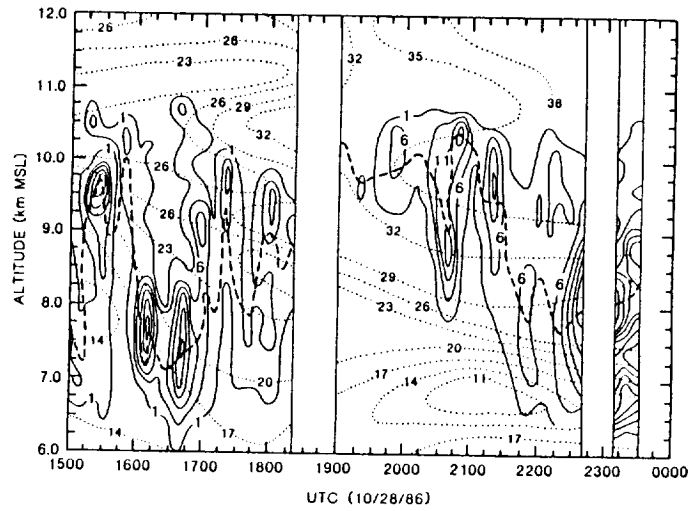


Fig. 6 (Top) Time height backscatter cross section (—, $10^{-6} \text{ m}^{-1} \text{ sr}^{-1}$) mapping of an cirrostratus formation with isotachs (---, in m/s). Optical mid-cloud altitude (---) tends to follow regions of intensified backscatter independent of cloud top and bottom altitudes. Fig. 7 (Bottom) Corresponding cloud optical depth (—) and normalized bulk backscatter phase function (---, sr^{-1}).

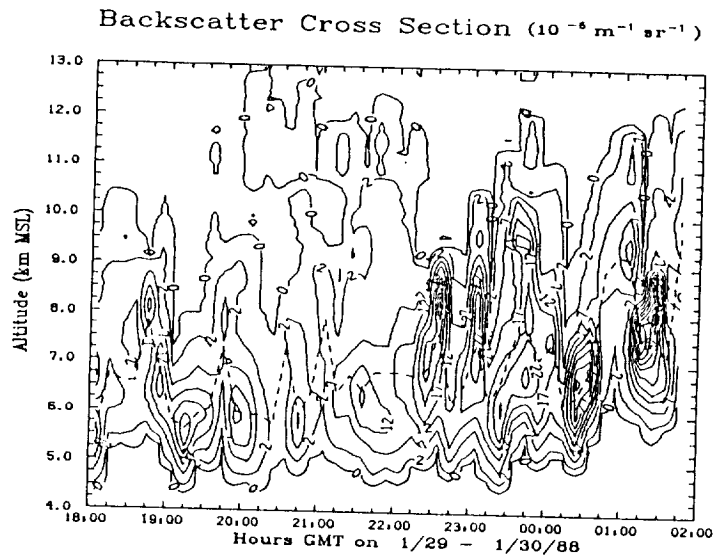


Fig. 8 Time height backscatter cross section (—, $10^{-6} \text{ m}^{-1} \text{ sr}^{-1}$, 0–5, 10–7 $\text{m}^{-1} \text{ sr}^{-1}$) mapping of an cirrostratus formation with isotachs (---, in m/s) and optical mid-cloud altitude (---). Repeated overlapping cell structure is inclined $\sim 7^\circ$ from horizontal.

A SYSTEM FOR RECORDING PHYSICAL PROPERTIES OF CLOUDS

G. C. Purgold and C. H. Whitlock
Atmospheric Sciences Division
NASA Langley Research Center
Hampton, Virginia 23665-5225

INTRODUCTION - Characterization of the physical properties of clouds is an important objective of the FIRE Project intensive field operations (IFO) planned for 1990 thru 1992. Physical properties observed from satellites will be directly compared to ground based observations during this period. It is the purpose of this paper to provide the technical information required to record local cloud parameters such as type of clouds, direction of travel, layering, and cloud fraction data. Such information should be very useful in analyzing other cloud and meteorological data. A system of the type described in this paper was successfully deployed as part of the First Global Surface Radiation Budget Experiment in April 1989.

HARDWARE DESCRIPTION - A video-based system to monitor and record cloud properties during daylight hours was developed around state-of-the-art video equipment, a time-lapse format video recorder, and off-the-shelf optical hardware shown in figures 1, 2, 3, and 4. The optical system consists of a 28 mm auto-iris lens, and a mirrored acrylic hemispherical dome. The outdoor physical set-up, shown in figure 2, includes a tripod to support the solid-state video camera and it's weather proof housing. The electronic hardware including the ac power adapter, time-lapse recorder, and video monitor, should be located in a normal indoor environment.

Long term recording of video images of cloud movements is accomplished using an off-the-shelf video time-lapse recorder as shown in figure 3. This recorder uses standard VHS format video cassettes which are the same as used on home video cassette recorders. Recording speeds from 2 to 480 hours in 8 steps are possible on the AG-6050, however the 480 hour range has proven to be the most effective for recording cloud movements.

The solid state video camera, shown in figure 4, was selected for it's small size and automatic gain control feature. Equally important was the auto-iris lens which is available for this type of camera. The auto-iris automatically compensates for the wide range of light levels which will be encountered over a 14 hour data collection period. The combination of the auto-iris lens and the automatic gain control feature enable the camera to adjust to all light levels from early dawn, or heavy overcast conditions, to very bright sunlight.

Recording images of cloud movements over an entire local hemisphere required a "fish-eye" type view of the sky. This implied a set-up where the camera would be looking skyward. This was undesirable because relatively small droplets or other

contaminants could obstruct the cameras view and therefore would require frequent cleaning. To minimize these effects, an inverted camera and a dome shaped reflector were used.

FIELD EXPERIMENT AND OPERATION - The cloud imaging system was operated continuously for a period of 35 days in support of the First Global Surface Radiation Budget Experiment in April, 1989. The entire cloud imaging system was co-located with a cloud lidar ranging system. The cloud camera setup was installed on an elevated platform, shown in figure 2, to allow an unobstructed view of the hemisphere 10 degrees above the horizon. This prevented local site activity and buildings from blocking the cameras view above 10 degrees and also provided a measure of physical security for the system. The dome and camera window required cleaning only once a week and then only as a prudent operational requirement. Occasional bird droppings on the dome were seen, but only obscured a minute portion of the whole sky image. Salt spray build-up was not a problem from a video imaging standpoint but could be detected by visual inspection when cleaning the dome.

The format employed by the time-lapse recorder is not compatible with a standard VHS video cassette player. However, images recorded on the time-lapse recorder may be played back from that machine and re-recorded on a standard VHS machine for general distribution. The limitation to this procedure is that the playback speed must be chosen prior to conversion, and the multi-speed viewing capability of the time-lapse recording is not transferable to the VHS format. However, all playback features normal to a standard VHS player such as slow motion, stop action, and copying, will still be possible with the converted tapes. The time-lapse recorder can be programmed to turn itself on and off at pre-selected times which is a valuable feature for conserving tape and increasing storage capacity. The 480 hour recording rate combined with the on-off timer mode will allow over one month of sky data to be recorded on a standard T-120 two hour video cassette tape.

CONCLUDING REMARKS - Results are currently being studied and initial indications are that the system provided excellent data on cloud movements, multiple layers, and surface conditions such as dew, rain, and sea spray. When combined with lidar cloud height data, this system can also yield quantified estimates of cloud fraction at a spatial resolution similar to that of the satellite pixel. A graphic representation of this approach is shown in figure 5. The system is first calibrated to determine angular distribution within the near-hemispherical image. If the satellite view angle is known, the pixel centerline can be located on the video image. If cloud base is known along with satellite pixel size, trigonometry can be used to calculate the solid angle about the centerline which defines the effective satellite viewing area. The portion of clouds in this angular area of the image is then an indicator of cloud fraction in the same region of the sky as being viewed by the satellite.

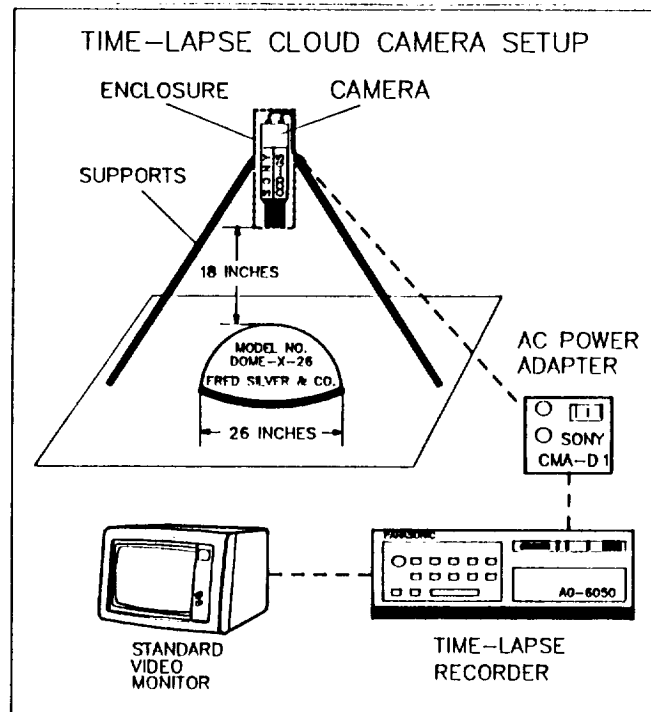


Figure 1. Video equipment and associated hardware.

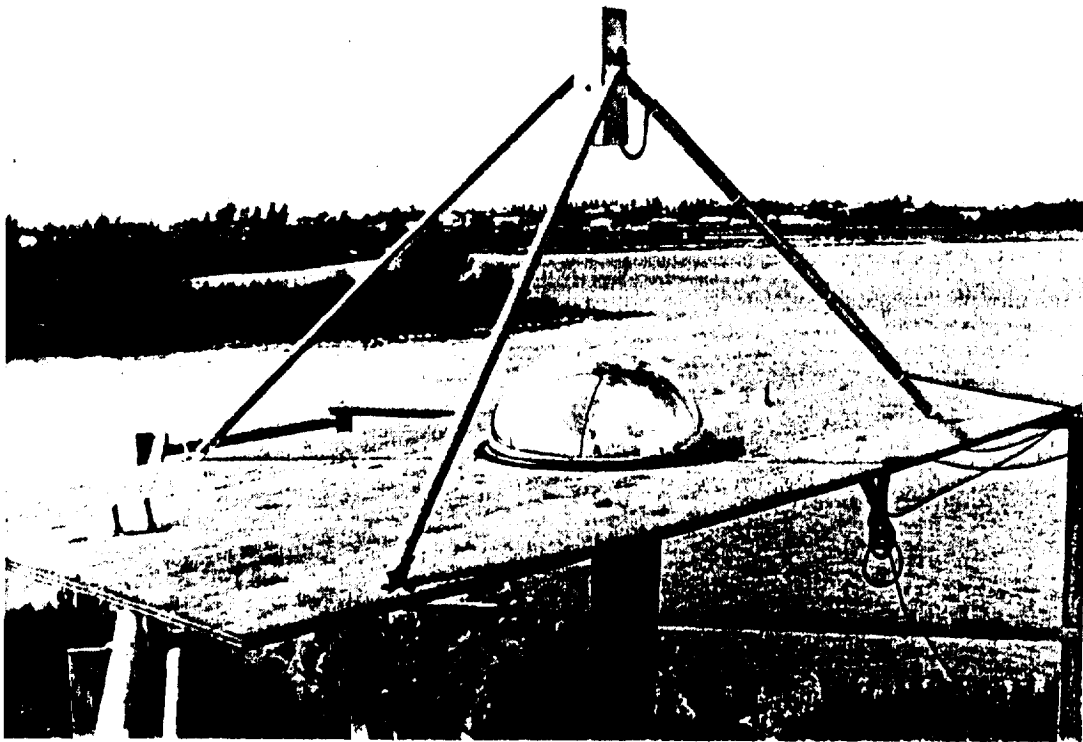


Figure 2. Outdoor physical set-up of camera and dome.

ORIGINAL PAGE
BLACK AND WHITE PHOTOGRAPH



Figure 3. Panasonic time-lapse recorder model AG-6050.

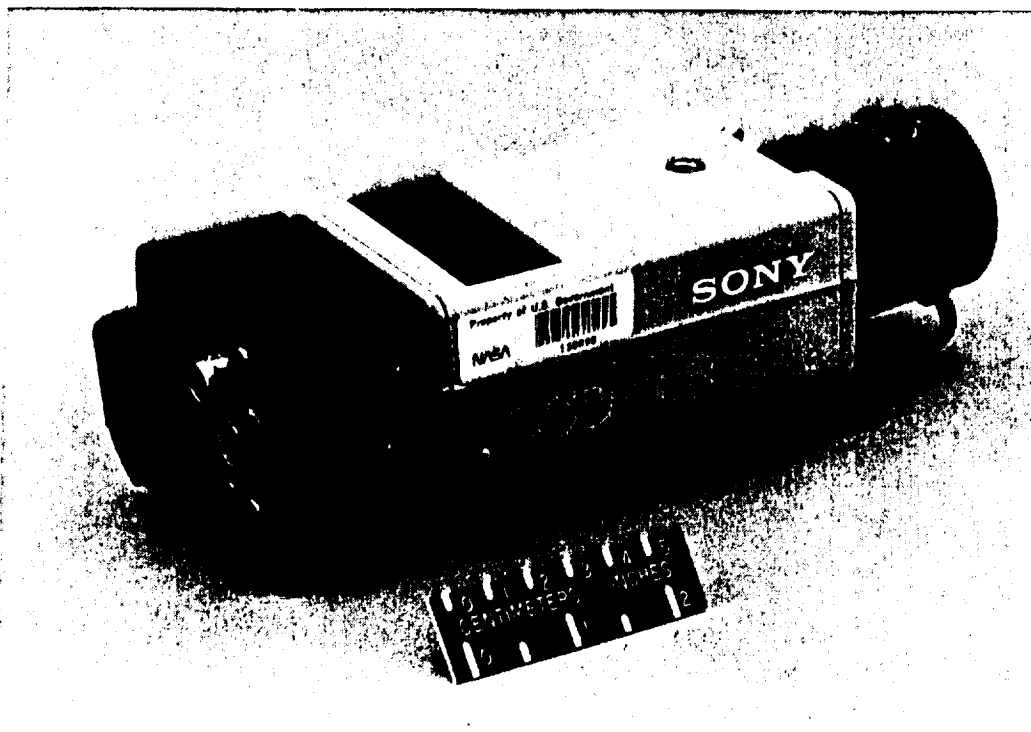
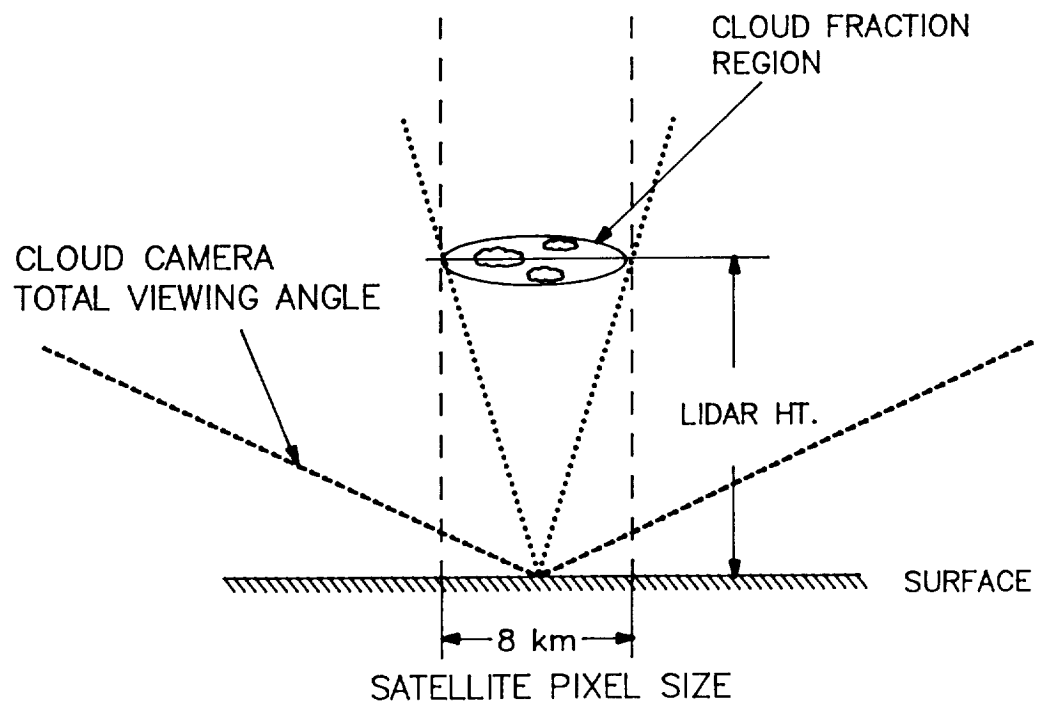


Figure 4. Sony solid-state camera model CCD-G5.

POSSIBLE CLOUD FRACTION APPROACH



VIDEO IMAGE

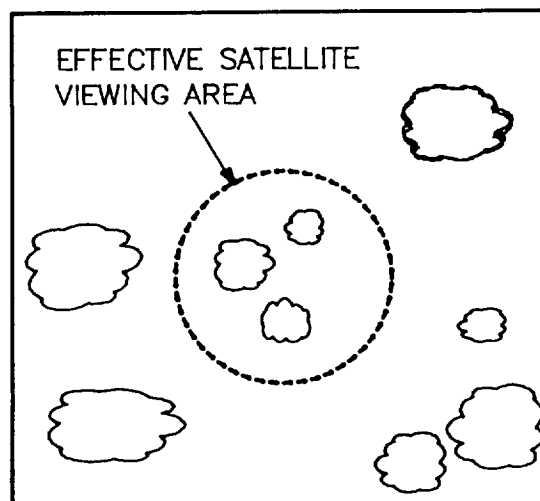


Figure 5. Graphic representation of cloud fraction approach.

Cirrus Parameterization from the FIRE ER-2 Observations

J. D. Spinhirne
 Laboratory for Atmospheres
 NASA Goddard Space Flight Center
 Greenbelt, MD 20771

Primary goals for the FIRE field experiments were validation of satellite cloud retrievals and study of cloud radiation parameters. The radiometer and lidar observations which were acquired from the NASA ER-2 high altitude aircraft during the FIRE cirrus field study may be applied to derive quantities which would be applicable for comparison to satellite retrievals and to define the cirrus radiative characteristics. The analysis involves parameterization of the vertical cloud distribution and relative radiance effects. An initial case study from the October 28, 1986 cirrus experiment has been carried out, and results from additional experiment days are to be reported.

The meaning of cloud parameters retrieved from remote sensing are to an extent defined by the observation and analysis technique by which the parameter is derived. Satellite retrievals such as the ISCCP products which involve observations at limited wavelength channels and large spatial averages are in particular subject to interpretation. The ER-2 observations included combined active and high

resolution passive observations. Due to the large difference in observational scales and techniques, the eventual comparison between the aircraft and satellite derived parameters is of interest. A discussion of analysis procedures and the parameterization from the aircraft observations is given in more detail by Spinhirne and Hart (1989).

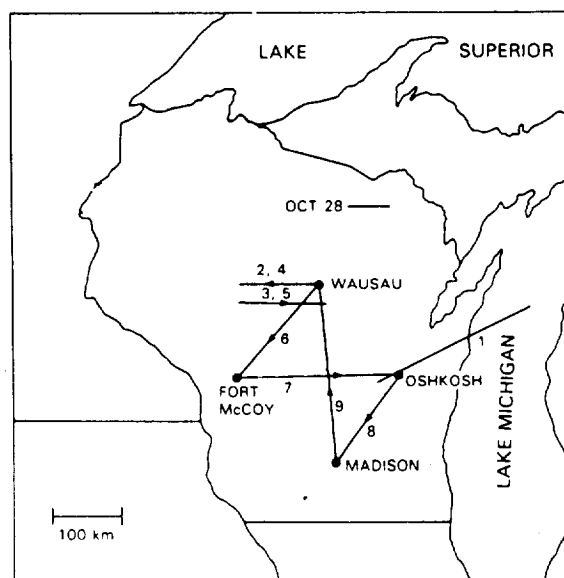


Fig. 1 ER-2 flight line map for October 28 1986.

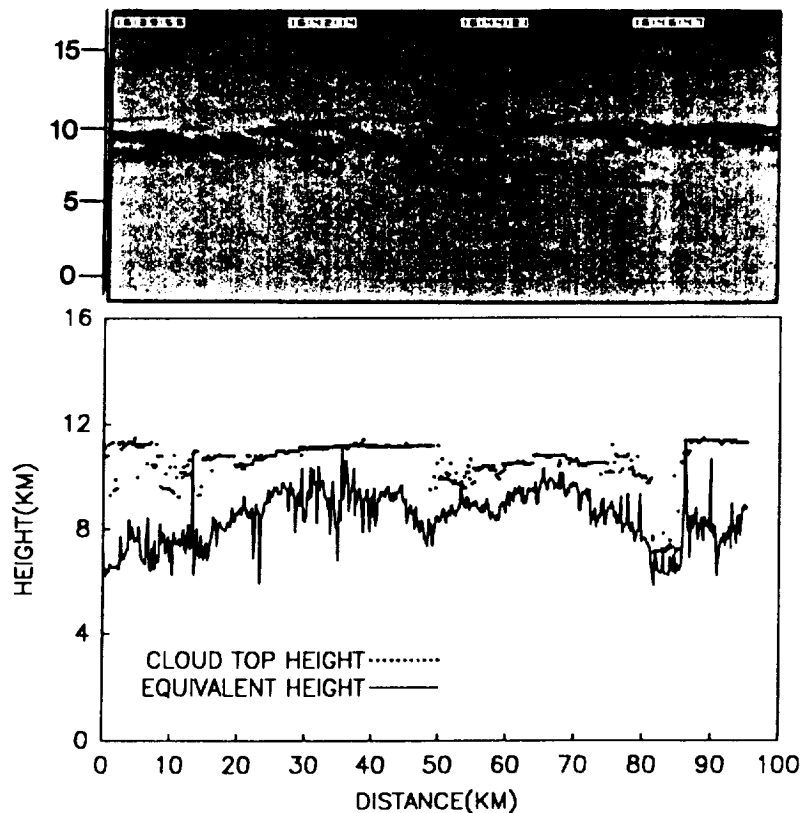


Fig. 2 The lidar observed vertical cloud structure for the fourth flight line of October 28 and the calculated equivalent cloud height.

I. Cloud Height and Vertical Structure

Cloud height is an important variable for satellite cloud retrievals and for the general meteorological description of clouds. The cloud top height z_t detected by lidar is very sensitive to even small increases of scattering above clear air levels, and the top of even thin subvisible cirrus is accurately found. However cirrus layers may be many kilometers thick and the top height is not a singularly meaningful description. An alternate cloud height level may be defined for cirrus which more closely relates to satellite observations and radiative influence. The equivalent height z_e may be defined such that

$$\epsilon = \frac{L_m - L_s}{b(T(z_e)) - L_s}$$

where ϵ is the emittance derived from a calculation procedure that makes use of the distributed vertical structure of the cirrus cloud as obtained from the lidar measurements. The radiance L_m and L_s are the measured cloud top and cloud base values. The equivalent height is thus the weighted level which would define the upward radiance of an isothermal layer of the lidar defined effective emittance.

On a typical FIRE field experiment day ER-2 observations were acquired over a 1500 km operational distance. The flights were broken into a series of approximately ten flight lines. A map of

flight lines for October 28 is shown in the first figure. Lidar backscatter data for the fourth flight line is shown Fig. 2. In the figure is also given the comparison between the lidar derived true cloud top and the calculated equivalent cloud height. The equivalent height is several kilometers lower than the cloud top height in most instances. In some areas where the cloud density increased toward the cloud base the equivalent height is closer to the cloud base height than to the actual cloud top.

From the combined lidar and radiometer data analysis, an average vertical structure may be defined for the cloud field which was overflown. The analysis involves a correction for attenuation for the lidar data and an iterative solution for radiation parameters. The averaged vertical distribution of the derived infrared absorption cross section ($10.8 \mu\text{m}$) for the entire data set of October 28 is shown in Fig. 3. The averaged vertical source function, defined as the relative contribution to the upward $10.8 \mu\text{m}$ radiation, is also given. The cloud layers extend over a six kilometer altitude range. The lower cloud layers are seen to have dominated the infrared radiative effects, but for the overall observations of October 28, the upper cirrus layers remain significant. The cirrus heating and cooling influence would have been important for this case from cloud bases at 6 km to the tropopause at 11.4 km.

II. Visible reflectance and infrared emittance

An important aspect of cirrus are the relative visible and thermal radiative influence. An initial parameterization to study the relative influence is the relation

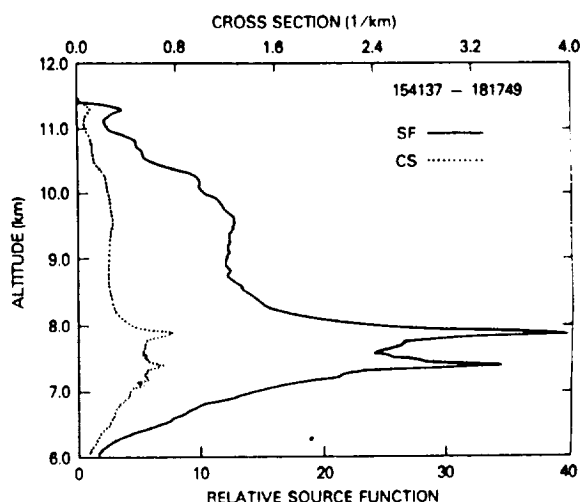


Fig. 3 Average vertical structure of infrared absorption cross section and upward source function.

between visible reflectance and infrared emittance at selected wavelengths. The relation of reflectance and emittance is also a key factor for satellite cloud retrievals such as the ISCCP algorithm. The ER-2 data permits a direct correlation between reflectance and emittance over a small field of view. The relative visible reflectance at $0.76 \mu\text{m}$ and emittance at $10.8 \mu\text{m}$ for October 28 is shown in Fig. 4. The two main groupings of points for the scatter diagram are the result of the difference of surface reflectance for the lake and land surface which were over flown on the first flight line. The dispersion of points for the land surface grouping is also primarily due to the variability of surface reflectance. In general the dispersion of the cirrus reflectivity and emittance relation is not, in comparison, strongly influenced by the variation of cloud type that was found to occur.

For satellite observations the surface

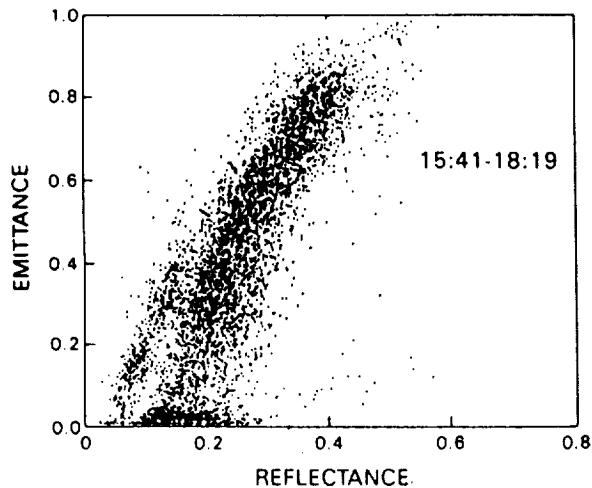


Fig. 4 Emittance and reflectance for the entire October 28 data set.

reflectivity may be obtained from previous clear air observations of a scene and a correction to the cloud reflectivity estimated. That is not possible from the aircraft observations. However an overall surface reflectivity for a scene type may be estimated by extrapolating the data as in Fig. 5 to zero emittance. Using the lidar derived effective beam transmittance, the influence of the surface reflectance on the total reflectance may be estimated for a pixel and a normalized cirrus reflectance derived. If a parameterization for cirrus bidirectional reflectance is assumed, a

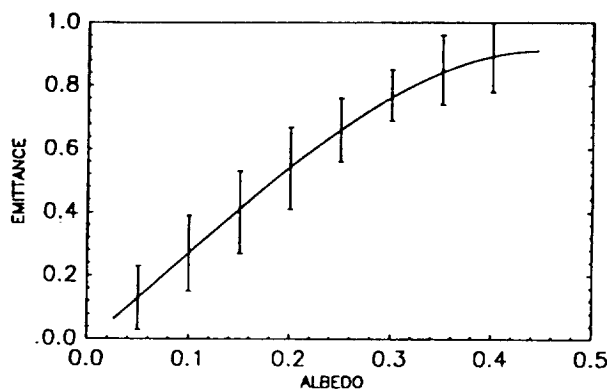


Fig. 6 Functional fit and variance of overall values of the cirrus emittance and defined albedo.

defined visible albedo for the cirrus may be obtained from the normalized reflectance. A significant dispersion to emittance values is still found which would most probably result from the average nature of the surface reflection correction and inhomogeneity and shadow effects for the cirrus.

The calculated emittance and albedo relation for the entire October 28 data set is summarized Fig. 5. A third order polynomial was fitted to the scatter of measurement to give the line shown, and the error bars in Fig. 5 represent two standard deviations of the emittance for an average over 0.05 albedo intervals. The functional line fit for the overall effective emittance and defined cirrus albedo a may be reproduce by the equation below up to the limit of $a=0.45$.

$$\epsilon = 2.709a + 1.603a^2 + 6.870a^3$$

III. Summary

The observations reported in this abstract are for one day. Analysis of the many other cirrus observation cases from the FIRE study show variability of results. In addition, only a fraction of the spectral and other data that was collected for this one case has been studied. Additional parameterization of cirrus properties from the aircraft remote sensing data and comparison to satellite retrievals are planned.

Reference.

Spinhirne, J. D. and W. D. Hart, 1989: Cirrus structure and radiative parameters from airborne lidar and spectral radiometer observations: the 28 October 1986 FIRE study. (submitted to *Mon. Wea. Rev.*).

1973-1974 LIDAR OBSERVATIONS OF CIRRUS CLOUDS AT KWAJALEIN

Edward E. Uthe
 Geoscience and Engineering Center
 SRI International
 Menlo Park, CA 94025 USA

EXTENDED ABSTRACT

A series of surface-based lidar measurements was made in support of reentry tests at Kwajalein (9° 6'N, 167° 43'E). The measurement periods were conducted during May-June 1973, August 1973, December 1973 and March-April 1974. The lidar used was the SRI Mark IX, a ruby lidar (694.3 nm wavelength) installed within a van complete with its own power supplies, azimuth and elevation scanning capabilities and real-time digital data recording, processing and display system (Uthe and Allan, 1975). The digital data system was used to estimate cirrus cloud equivalent ice-water content as the cloud was being observed. Other supporting equipment included an instrumented WB-57 aircraft used for sampling cirrus cloud ice crystals (Jahnsen et al., 1974).

Figure 1 presents an altitude-time intensity modulated video display of cirrus cloud structure observed on 17 December 1973. The cloud is seen to consist of multiple thin layers that show horizontal density variations as the cloud traversed the lidar site. The cloud was subvisible to surface observers and was visible to the WB-57 pilot only when the aircraft operated above the cloud and the pilot observed downward in the direction of the sun. The equivalent ice-water content of the cloud was estimated from the lidar backscatter signature by deriving absolute backscatter coefficients based on normalizing clear-air lidar returns to standard tropical atmospheric density data and using the following expressions:

$$\sigma = \text{volume extinction coefficient} = \frac{4 \pi \beta}{0.25}$$

$$N = \text{crystal number density} = \frac{\sigma}{2\pi a^2}$$

$$W = \text{ice-water content} = 4/3 \pi a^2 \rho N$$

where β = volume backscatter coefficient

a = particle radius

ρ = ice density

N = particle number density.

The particle size (a) assumed was based on previously collected aircraft data that indicated particle size decreases with altitude. For the data shown in Figure 1 the maximum ice-water content derived from the lidar records was 10^{-4} g/m^3 and agreed with the aircraft cloud density measurements. During the course of the measurement program, lidar-observed clouds were inferred to have a maximum ice-water content ranging from 10^{-5} to 2 g/m^3 . Although a wide range of cloud densities was observed, the aircraft and lidar-derived values normally agreed to within a factor of ± 2 when particle size was taken from the aircraft measurements. When particle size was based on previously collected data, uncertainties of the lidar derived ice-water content were increased by an additional factor of ± 2 . Other results are given by Uthe and Russell (1977). This paper will present several data examples illustrating the high-altitude low-density and persistent nature of cirrus clouds over the Kwajalein area. The clouds were found to be more reflective of lidar energy than for

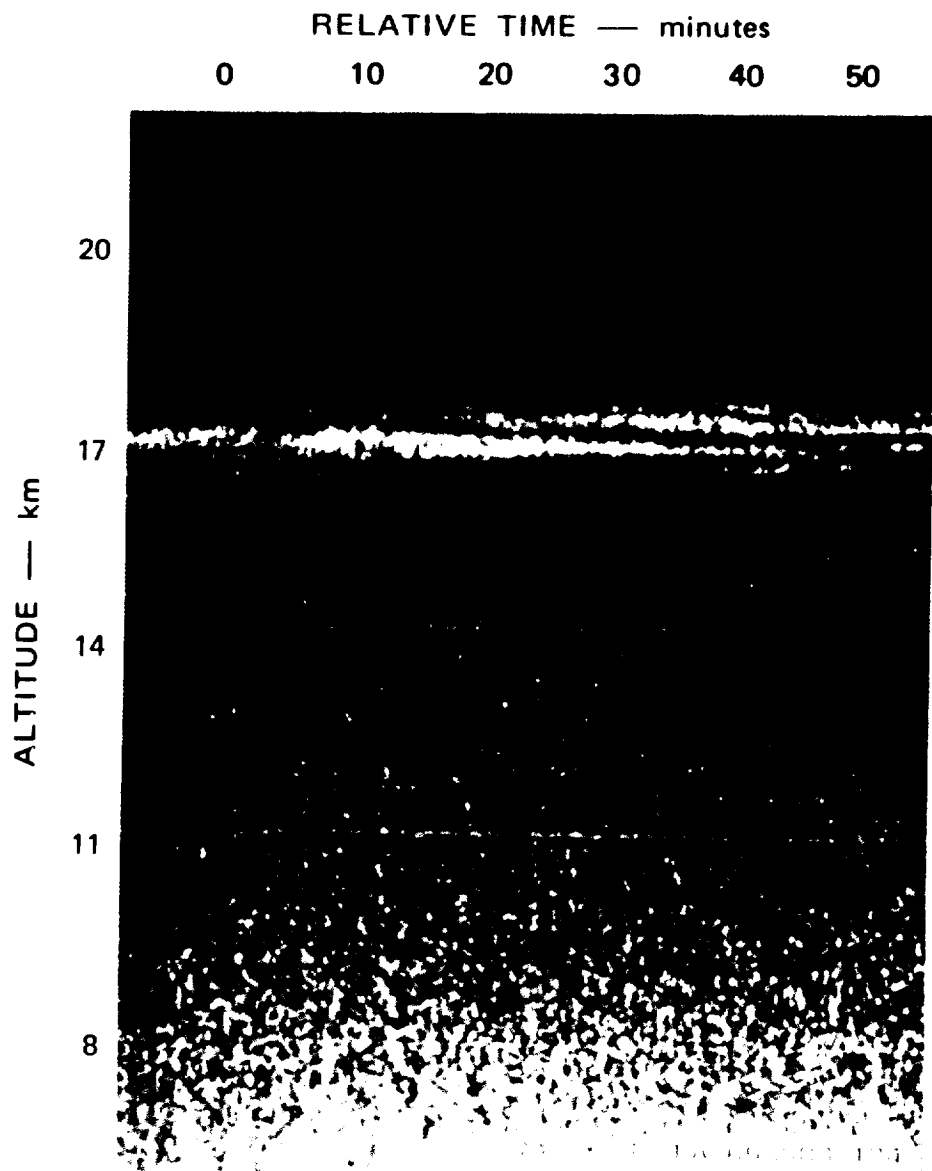


FIGURE 1 EXAMPLE OF HIGH-ALTITUDE LOW-DENSITY CIRRUS CLOUD OBSERVED OVER KWAJALEIN WITH THE MARK IX RUBY LIDAR SYSTEM (17 DECEMBER 1973, 1220-1330 LOCAL TIME). The maximum cloud density was computed as $2 \times 10^{-4} \text{ g/m}^3$.

equivalent spherical particle clouds although backscattering from cylinders is expected to be significantly less than from equivalent volume spheres (Liou, 1972). Therefore, reflection of incoming solar energy and outgoing infrared energy emitted from the earth's surface and lower atmospheric constituents could serve as important climatic change mechanisms.

REFERENCES

- Jahnsen, L.J., A.J. Heymsfield, and R.E. Carbone, 1974: PVM-5 Mission and WB-57F Instrumentation and Cloud Particle Measurements. Final Report, Contract DNA-001-73-C-0233. Meteorology Research, Inc., Altadena, California 91001 (MRI 74 R-1230).
- Liou, K.N., 1972: Light Scattering by Ice Clouds in the Visible and Infrared: a Theoretical Study. J. Atmos. Sci., 29, pp 524-536.
- Uthe, E.E., and R.J. Allen, 1975: A Digital Real-Time Lidar Data Recording, Processing and Display System. J. Optical and Quantum Electronics, 7, pp. 121-129.
- Uthe, E.E. and P.B. Russell, 1977: Lidar Observations of Tropical High-Altitude Clouds. Radiation in the Atmosphere, H.J. Bolle, editor, Science Press, Princeton, pp. 242-244.

THE USE OF AN AIRBORNE LIDAR FOR MAPPING CIRRUS CLOUDS IN FIRE PHASE II

Lawrence F. Radke and Peter V. Hobbs

*Atmospheric Sciences Department, AK-40, University of Washington,
Seattle, WA 98195*

The University of Washington and Georgia Tech have recently built a dual-wavelength airborne lidar for operation on the University of Washington's Convair C-131A research aircraft. This lidar has been used successfully in studying aerosols and clouds. These studies have demonstrated the utility of airborne lidar in a variety of atmospheric research and prompt our suggestion that this facility be included in the next FIRE cirrus experiment.

The vertically-pointing airborne lidar would be used as a complement to ground-based lidars. The airborne lidar would ensure extended coverage of IFO cases that develop upwind of the surface lidars or which miss the ground-based lidars while still being the focus of satellite and aircraft in situ studies. The airborne lidar would help assure that cirrus clouds were simultaneously viewed by satellite, sampled by aircraft, and structurally characterized by lidar.

Table 1 lists system specifications and Figure 1 shows a schematic of the lidar system aboard the C-131A. Polarized, incoherent, monochromatic light is emitted from the neodymium-doped yttrium aluminum garnet (Nd:YAG) laser simultaneously at both the primary ($1.064\ \mu\text{m}$) and frequency-doubled ($0.532\ \mu\text{m}$) wavelengths. The beam is reflected by a mirror 90° toward the center line of the telescope assembly. The beam is then reflected by another mirror and is emitted upward along the axis of the telescope. Alignment of the laser beam with the telescope is controlled by adjusting the second mirror. The emitted laser pulse, which has a pulse width of 20 ns (or 6 m) and energies of 70 mJ at $1.064\ \mu\text{m}$ and 45 mJ at $0.532\ \mu\text{m}$, travels upward while diverging at an angle of approximately 1 mrad. The laser pulse interacts with gas molecules, aerosol and cloud particles, returning a small fraction of the energy as backscattered light at the same wavelengths. This return pulse is received and focused by the 0.356 m (14 in.) Cassegrainian telescope.

After the light passes through the telescope, it strikes a dichroic mirror. This beamsplitting device allows the infrared wavelength to pass without reflection; the visible light is reflected 90° . The $1.064\ \mu\text{m}$ beam is detected by a silicon avalanche photodiode (APD), while the visible light is sensed with a photomultiplier tube

TABLE 1

THE UNIVERSITY OF WASHINGTON-GEORGIA TECH LIDAR SYSTEM

Specifications

A) Laser

Type: Neodymium-doped Yttrium Aluminum Garnet (Nd-YAG)
Wavelengths: 1.064 and 0.532 μm
Energies: 70 and 45 mJ
Pulse width: 20 ns
Beam divergence: 1 mrad

B) Telescope

Type: Cassegrainian
Diameter: 0.356m (14 in)

C) Detection

Polarizing filters: selectable for parallel and perpendicular polarizations
Detectors: 1.064 μm
Type: Silicon Avalanche Photodiode
0.532 μm
Type: Photomultiplier tube

D) Data acquisition/control system

Data input and shot summing
Type: CAMAC crate
Manufacturer: DSP Technologies, Inc.
Digitization rate: 50 ns

Control/display computer: 20 MHz AT-compatible microcomputer
Data display: VGA monitor, 640 x 480 resolution
Data storage: 80 megabyte hard disk and
2.2 gigabyte mini-video cassettes

A schematic of the lidar system is shown in Fig. 1

(PMT). The signals from each of these detectors pass through separate pre-amplifiers (to convert current to voltage) and logarithmic amplifiers. The logarithmic amplifiers are needed to detect a wide range of signal strengths without electronic saturation.

The amplifier outputs are received by a data acquisition system (DAS, DSP Technologies, Inc.), which has a variable signal digitization rate of 25 or 50 ns, corresponding to vertical resolutions of 7.5 and 15 m, respectively. The data are summed in the DAS for a user-specified number of laser shots, and are then dumped to an IBM clone 20 Mz/80386 AT microcomputer through an input board supplied with the DAS. An Exabyte 8mm cartridge tape (2.1 gigabyte) recorder is used to log the data. The microcomputer also displays both wavelengths in a false color vertical cross-section (at half resolution) in real-time aboard the aircraft. As an example we show in Fig. 2 a gray-scale depiction of thin altostratus clouds some 4-6 km above the lidar and higher and rather complex cirrus clouds near the tropopause. Despite modest transmitted energies, the lidar has demonstrated more than sufficient sensitivity for cirrus measurements in a full daylight environment.

With the lidar's laser aboard the C-131A aircraft pulsing at 20 Hz (maximum rate), we can achieve a horizontal resolution of 4 m and a vertical resolution of 7.5 m (at a maximum range of 7.5 km) or 15 m (at a maximum range of 15 km). The aircraft would have a mission endurance of ~7 hr at a flight elevation of 3 km MSL.

This lidar, combined with the aircraft's radiometric and cloud physics instrumentation, as well as a vertically-pointing (up or down) 8.6 mm radar, would be of significant utility in FIRE Phase II.

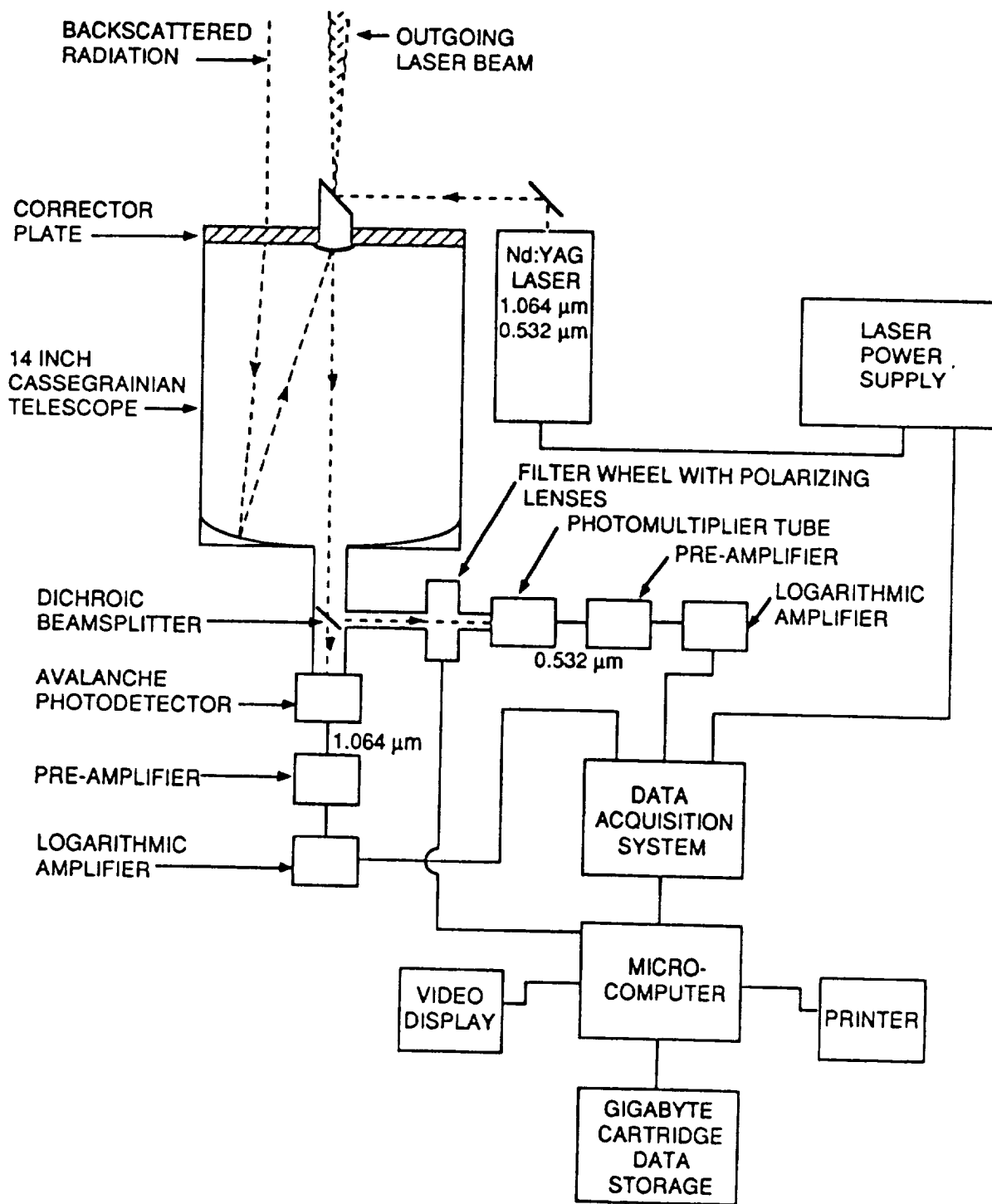


Figure 1. Schematic of the University of Washington-Georgia Tech Lidar System aboard the University of Washington's Convair C-131A aircraft.

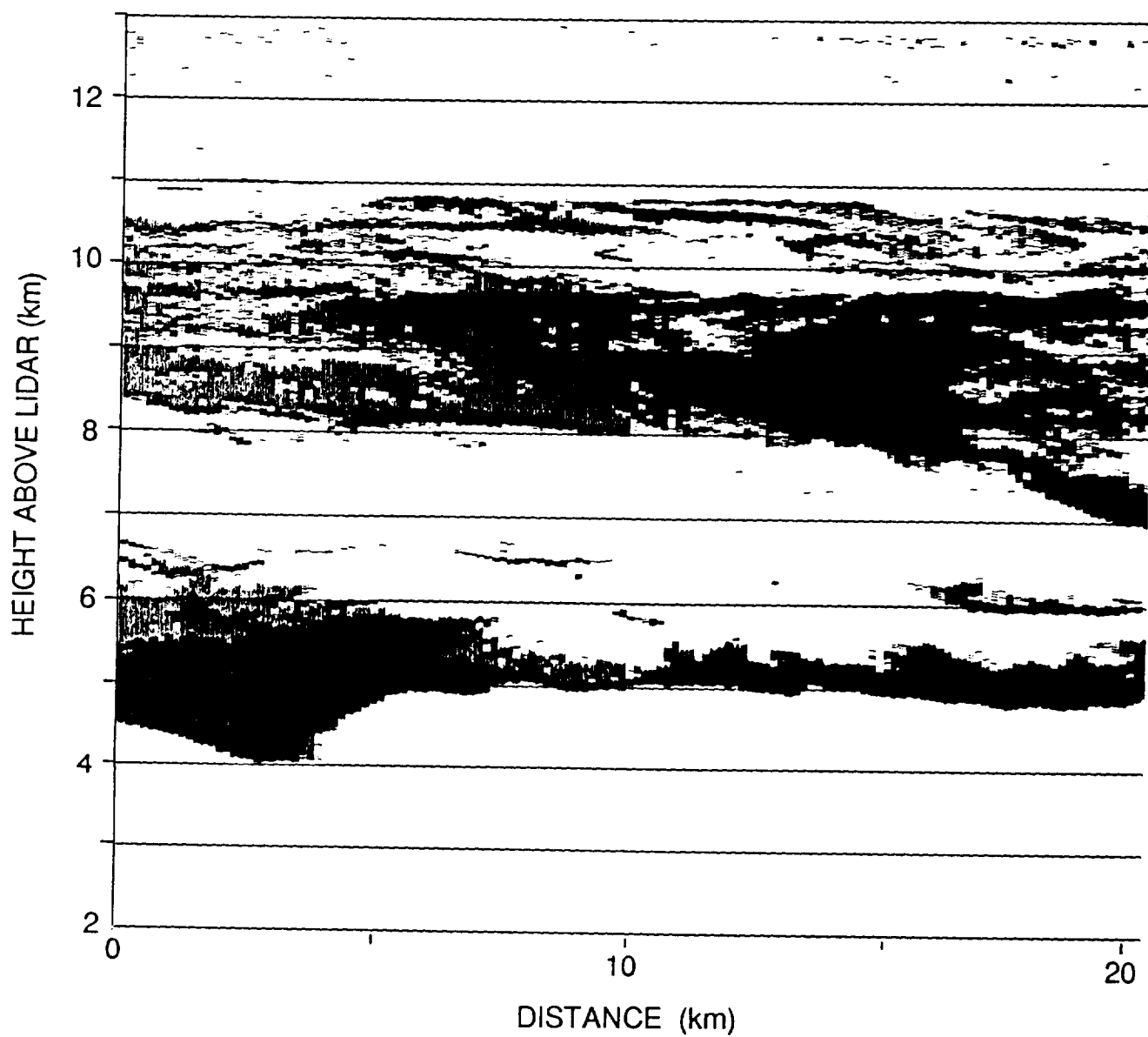


Figure 2. Lidar backscatter cross-section (at $\lambda = 1.06 \mu\text{m}$) of altostratus and cirrus clouds obtained with the lidar aboard the University of Washington's Convair C-131A research aircraft.

ON THE USE OF IR LIDAR AND K_a-BAND RADAR FOR OBSERVING CIRRUS CLOUDS

Wynn L. Eberhard, R. Michael Hardesty, and Robert A. Kropfli

NOAA Wave Propagation Laboratory
325 Broadway
Boulder, Colorado 80303

I. Introduction

Advances in lidar and radar technology have potential for providing new and better information on climate-significant parameters of cirrus. Consequently, the NOAA Wave Propagation Laboratory is commencing CLARET (Cloud Lidar And Radar Exploratory Test) to evaluate the promise of these new capabilities. Parameters under investigation include cloud particle size distribution, height of cloud bases, tops, and multiple layers, and cloud dynamics revealed through measurement of vertical motions. The first phase of CLARET is planned for September 1989 at the Boulder Atmospheric Observatory (BAO) near Erie, Colorado.

II. Lidar and Radar Capabilities

The CO₂ coherent lidar operating at 10.6 μ m wavelength is a relative newcomer in the arsenal of cirrus remote sensors. It differs from the other lidars commonly used for cirrus studies in several important respects. First, its wavelength is an order of magnitude larger, so size parameters for scattering are smaller. Second, absorption by cloud particles is substantial. Third, the CO₂ lidar operates in the atmospheric window, whereas others are in or near the visible. And fourth, it has Doppler capability for observing cirrus dynamics. Some introductory research on cirrus with this lidar has already been accomplished (Gross et al., 1984; Hall et al., 1988; Sassen et al., 1990). Recently, however, the stability of the transmitter frequency has been improved for better Doppler estimates, and the pulse can now be shortened to approximately 50 m range resolution instead of exceeding 300 m (Eberhard et al., 1989). This eyesafe instrument is now much more suited to cirrus measurements.

The longer wavelength of a sensitive radar can provide a somewhat different perspective on cirrus. The ice content can be estimated from the backscatter, but depends strongly on size distribution (Sassen, 1987). A radar can penetrate optically thick clouds to reveal the height of cloud top and the presence of multiple layers. During the first phase of CLARET we are limited to the use of an X-band radar (3.2 cm wavelength), but we will use extensive coherent averaging to detect weak signals. Preliminary data sets have shown that this radar can detect some cirrus. Our considerably more sensitive K_a-band radar (0.86 cm wavelength) will be available after renovation and testing are completed within a year. Both radars have Doppler capability to study the dynamic structure of cirrus clouds.

CLARET will explore what new kinds of information on cirrus can be extracted from measurements by these two instruments operating individually and in combination with each other and with more common instruments.

III. CLARET Experiment

The CO₂ lidar and the X-band radar will operate in a coordinated fashion when cirrus appears. They will be joined by a ruby lidar (694 nm wavelength; Eberhard and McNice, 1986) with polarization discrimination and perhaps an additional 347 nm wavelength.

Other instruments at the BAO site will include a microwave radiometer that measures integrated liquid water and precipitable water. Radiation data from a pyranometer, pyrgeometer, and pyrheliometer (shortwave and longwave channels) will help in interpreting the results. A narrow-field radiometer with bandpass centered at 10.7 μ m will point parallel to the lidars so the LIRAD (Platt et al., 1987) method can be applied. Time-lapse pictures with an all-sky camera are also planned. Data from twice-daily radiosonde launches from Stapleton Airport 30 km away will be collected.

Data sessions will be coordinated as much as practical with overpasses of the NOAA polar orbiter, and corresponding AVHRR and TOVS data will be stored. Winds at cloud height are needed for using advection to connect satellite data with the ground-based data. The wind profiler at Stapleton, Doppler lidar or radar, and all-sky movies will be used to accomplish this correctly. The cloud signals from the lidars and radar can therefore be compared with the clouds' effects on radiative transfer as measured at the surface and from space.

IV. Parameters to be investigated

The main cloud and instrumental parameters under evaluation in CLARET are as follows.

1) SENSITIVITY FOR DETECTING THIN CIRRUS

Visible lidars have demonstrated detection of optically thin cirrus, including subvisual clouds not observable by eye. The ability of the CO₂ lidar, operating with the short pulse at reduced power (maximum 100 mJ pulse energy), for detecting diffuse cirrus will be compared to that of the ruby lidar. The detection threshold of the radar will be compared to those of lidars and radiation instruments.

2) SIZE DISTRIBUTION FROM MULTIWAVELENGTH BACKSCATTER

The widely varied wavelengths of the two lidars and radar are expected to be sensitive to different parts of a cirrus particle size distribution. We therefore anticipate that simultaneous measurements will give information on the cloud particle size distribution. Another perspective is that the three instruments can indicate the size-dependent balance between ice content, longwave radiation, and shortwave attenuation.

CLARET will provide an opportunity to evaluate this possibility in a preliminary way. The wavelength dependence of the backscatter measured by the two lidars and the radar will be examined for correlation with other indicators of particle size, such as cloud temperature. A first-cut analytical study, using Mie scattering and published results on scattering from nonspherical particles, will also search for size-dependent signatures. Because the radar backscatter cross section of complex-shaped ice particles is nearly equal to the cross section of an ice sphere of equal mass (Marshall and Gunn, 1952), the Rayleigh scatter approximation will easily apply to the radar scatter. If the outcome is positive, further research should ensue using *in situ* size distribution measurements and perhaps new scattering calculations for nonspherical particles to verify the lidar-radar results.

3) EMISSION PROFILE FROM IR PROFILE OF BACKSCATTER

The absorbing character and large-sized, complicated shapes of ice particles may cause the backscatter of the CO₂ lidar to be related to the effective volume at which the particles radiate in the longwave. If so, the backscatter and temperature profiles could give the emission profile of cirrus. This suggestion will be tested empirically by vertically

integrating the backscatter from the CO₂ lidar and comparing this with the emissivity obtained from measurements by the narrow-field IR radiometer.

4) DEPOLARIZATION OF IR BACKSCATTER

The degree of depolarization at visible wavelengths is a useful tool for determining the phase of the cloud particles (Sassen et al., 1989). Depolarization for an IR lidar may be somewhat different because of a smaller size parameter and substantial absorption. Multiple scatter, which contaminates the measurement by most visible lidars, is negligible in the coherent CO₂ lidar. Depolarization at CO₂ and ruby wavelengths will be compared to find what information may be available from the CO₂ lidar data alone and in combination with visible lidar depolarization.

5) WAVELENGTH DEPENDENCE OF ANGULAR WIDTH OF SPECULAR PEAK

The angular width of the enhanced backscatter from oriented ice crystals is believed to depend on the size of the particles through diffraction effects and on the extent of their fluttering motion (Platt, 1978). We will compare the magnitude and angular widths of such scatter at visible and IR wavelengths. Differences may allow a separation of size and flutter effects.

6) VERTICAL DOPPLER MEASUREMENTS

Velocity measurements from the Doppler lidar and radar pointed at the zenith will be examined for consistency, which will show that both are trustworthy. Case studies of small-scale vertical motions and the corresponding cloud structure should provide valuable insights about the mechanisms involved in the various stages of cloud evolution.

7) IR EXTINCTION-TO-BACKSCATTER RATIO

The range-averaged ratio of extinction-to-backscatter for a lidar can be obtained from range-integrated measurements on optically thick clouds (Platt, 1979). This method should be particularly straightforward for the coherent CO₂ lidar because multiple scatter is very small. One use of this ratio is to obtain optical depth from the measured profile of backscatter.

8) ECLIPS

CLARET will also be a component of ECLIPS (Experimental Cloud Lidar Pilot Study; WCRP, 1988). The extent of data acquisition and archival will depend on the amount of financial resources that become available.

V. Summary

The CO₂ coherent Doppler lidar and the sensitive K_a-band radar hold considerable promise for providing valuable information on cirrus that is beyond the grasp of current visible lidars.

Some of the possibilities are particularly noteworthy. First, the effective size distribution is a critical parameter in understanding the climate effects of cirrus. A multiwavelength measurement may be able to provide such information as a function of height. Second, a CO₂ lidar can reveal cloud height, probably the phase, and perhaps the long-wave emission profile. If so, addition of these measurements to the proposed space-borne Laser Atmospheric Wind Sounder would be extremely cost-effective and should have high priority. Third, the sensitive K_a-band radar is expected to detect cirrus often, including cloud top and multiple layers. And fourth, the vertical motion and structure information from zenith-pointing Doppler lidar or radar is expected to reveal much about formation and maintenance of cirrus clouds.

These possibilities will be explored in CLARET. Successful methods can be used in Phase II of cirrus FIRE and similar intensive field programs. A suite of lidar(s), radar, and radiation instruments may also be ideal for extended observations of clouds to study their climatic influences.

VI. References

- Eberhard, W.L., R.E. Cupp and K.R. Healy, 1989: Doppler lidar measurement of profiles of turbulence and momentum flux. J. Atmos. Oceanic Technol., **6**, 809-819.
- Eberhard, W.L., and G.T. McNice, 1986: Versatile lidar for atmospheric studies, including plume dispersion, clouds, and stratospheric aerosol. J. Atmos. Oceanic Technol., **3**, 614-622.
- Gross, A., M.J. Post and F.F. Hall, Jr., 1984: Depolarization, backscatter, and attenuation of CO₂ lidar by cirrus clouds.
- Hall, F.F., Jr., R.E. Cupp and S.W. Troxel, 1988: Cirrus cloud transmittance and backscatter in the infrared measured with a CO₂ lidar. Appl. Opt., **27**, 2510-2516.
- Marshall, J.S., and K.L.S. Gunn, 1952: Measurement of snow parameters by radar. J. Meteor., **9**, 322-327.
- Platt, C.M.R., 1978: Some microphysical properties of an ice cloud from lidar observation of horizontally oriented crystals. J. Appl. Meteor., **17**, 1220-1224.
- Platt, C.M.R., 1979: Remote sounding of high clouds. I: Calculations of visible and infrared optical properties by laser backscattering and extinction measurements. J. Appl. Meteor., **18**, 1130-1143.
- Platt, C.M.R., J.C. Scott and A.C. Dilley, 1987: Remote sounding of high clouds. Part IV: Optical properties of midlatitude and tropical cirrus. J. Atmos. Sci., **44**, 729-747.
- Sassen, K., 1987: Ice cloud content from radar reflectivity. J. Climate Appl. Meteor., **26**, 1050-1053.
- Sassen, K., C.J. Grund, J. Spinhirne, R.M. Hardesty and J.M. Alvarez, 1990: The 27-28 October 1986 FIRE IFO cirrus case study: A five lidar view of cirrus cloud structure and evaluation. Submitted to Mon. Wea. Rev.
- Sassen, K., D.O. Starr, and T. Uttal, 1989: Mesoscale and microscale structure of cirrus clouds: Three case studies. J. Atmos. Sci., **46**, 371-396.
- WCRP, 1988: An Experimental Cloud Lidar Pilot Study (ECLIPS): Report of the WCRP/CSIRO Workshop on Cloud Base Measurement. WCRP-14 and WMO/TD-No. 251, available from T.L. Owens, MS483, NASA Langley Research Center, Hampton, Virginia 23665.

INTERCOMPARISON OF STANDARD RESOLUTION AND HIGH RESOLUTION TOVS SOUNDINGS
WITH RADIOSONDE, LIDAR, AND SURFACE TEMPERATURE/HUMIDITY DATA

R. J. Wheeler
Aerospace Technologies Division, Planning Research Corporation
Hampton, Virginia 23666

C. H. Whitlock and J. M. Alvarez
Atmospheric Sciences Division, NASA Langley Research Center
Hampton, Virginia 23665-5225

D. O'C. Starr
Laboratory For Atmospheres, NASA Goddard Space Flight Center
Greenbelt, Maryland 20771

D. P. Wylie
Space Science and Engineering Center, University of Wisconsin-Madison
Madison, Wisconsin 53706

INTRODUCTION - One objective of the FIRE Cirrus IFO is to characterize relationships between cloud properties inferred from satellite observations at various scales to those obtained directly or inferred from very high resolution measurements.¹ It is the purpose of this paper to compare satellite-derived NOAA-9 high and standard resolution TOVS soundings with directly measured lidar, surface temperature, humidity, and vertical radiosonde profiles associated with the Ft. McCoy site. The results of this intercomparison should be useful in planning future cloud experiments.

DATA - Satellite derived results were obtained by two methods. First, standard resolution (250 x 293 km subsatellite pixel size) TOVS sounding values were obtained from NOAA in the form of their standard product.² Second, a special high-resolution (18 x 18 km subsatellite pixel size) sounding product was created by the University of Wisconsin using only HIRS/2 instrument raw data.³

Radiosonde temperature and geopotential height data were extracted from the FIRE Cirrus radiosonde data set for Ft. McCoy in NASA's Climate Data System. Precipitable water amounts were calculated from raw radiosonde profiles using a method suggested by Charlack⁴, integrating all possible 1.5 second reporting levels in each layer. A total of 9 cases were examined in this study. In 8 of the 9 cases radiosonde data from Ft. McCoy had launch times sufficiently close (within 3 hours of NOAA-9 overpass) as to permit a reasonable intercomparison.

Surface lidar measured cloud base altitudes for mid- and upper-altitude clouds. These data were averaged over time periods which were consistent with standard and high resolution TOVS-product pixel sizes. Additional surface observations in the form of thermograph and hydrograph data were taken on a continuous basis throughout the study period.

RESULTS - Figures 1 and 2 show that typical temperature soundings from both standard- and high-resolution TOVS compare reasonably well with the radiosonde trace. TOVS Surface temperatures displayed, in figure 3, are generally within 2 to 3°K of radiosonde and/or thermograph results except on October 17th and 24th. This was also the case in the mid-tropospheric levels; however, temperatures at the 925 millibar level often displayed the greatest differences in the vertical profile.

In figures 4, 5, and 6; precipitable water amounts from both TOVS products under-estimate observed radiosonde values in the lower atmosphere while over-

estimating in the 500 to 300 millibar layer. Estimates for the 700 to 500 millibar layer are split with high-resolution TOVS over-estimating and standard-resolution TOVS under-estimating precipitable water amounts.

Comparisons between lidar-measured cloud base altitudes and cloud top altitudes derived from the two TOVS products show considerable disagreement as is evident in figures 7 and 8. With the exception of October 22nd, TOVS cloud top heights were at or below measured cloud base altitudes. Of the two, the standard-resolution TOVS cloud tops display the greatest errors (approximately 5 km on average) compared to only 2.3 km for the high-resolution product.

Figure 9 compares cloud fractions from standard and high resolution products. Combining these data with cloud observation histories indicates that the cloud fraction comparisons are closest during periods approaching total overcast, while the greatest discrepancies exist with reported clear or scattered conditions. High resolution TOVS results are particularly poor on October 16th, 17th, and 18th.

CONCLUSIONS - Standard and high resolution TOVS temperatures compare reasonably well with both surface and radiosonde observations. The greatest differences occurred at the 925 millibar level. At no time are differences more than 6°K and generally temperatures measured by TOVS were within 2 to 3°K of the radiosonde observed values.

Precipitable water, cloud top altitudes, and cloud fractions do not compare well, or with any consistency, either with observed radiosonde values or between the TOVS products themselves. In the case of precipitable water, it appears that both TOVS products show wide scatter compared to radiosonde observed conditions. The high-resolution product appeared to give the better estimate of cloud top altitude even though its cloud top value was less than lidar-observed cloud base for some days. For cloud fraction determination, high-resolution TOVS appears to be biased toward either clear or overcast cloud fractional amounts, while the standard-resolution TOVS fractions more closely reflect actual conditions.

REFERENCES

1. Starr, D. O'C., 1987: A Cirrus-Cloud Experiment: Intensive Field Observations Planned for FIRE. Bull. American Meteorological Society, Vol. 68, Number 2, 119 - 124.
2. Whitlock, C. H., S. R. LeCroy, and W. L. Darnell: Standard Resolution TOVS Observations for the FIRE/SRB Wisconsin Experiment Region from October 9 Through November 2, 1986. NASA TM 89151, May 1987.
3. Whitlock, C. H., D. P. Wylie, and S. R. LeCroy: High-Spatial-Resolution TOVS Observations for the FIRE/SRB Wisconsin Experiment Region from October 14 Through November 2, 1986. NASA TM 100522, January 1988.
4. T. P. Charlock, NASA Langley Research Center, Personal Communications, April 1989.

FIGURE 1. RADIOSONDE VERSUS
STANDARD AND HIGH RESOLUTION
TOVS TEMPERATURE SOUNDING
OCTOBER 15, 1986 1957 GMT.

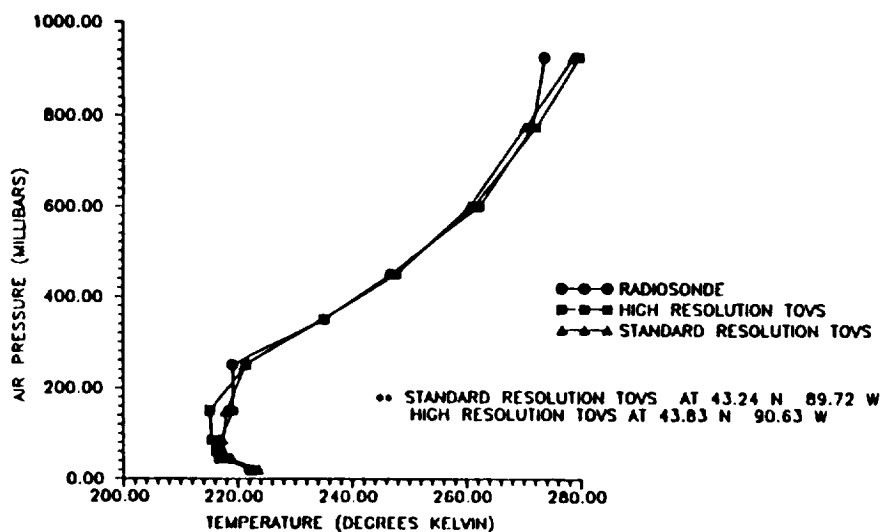


FIGURE 2. RADIOSONDE VERSUS
STANDARD AND HIGH RESOLUTION
TOVS TEMPERATURE SOUNDING
OCTOBER 21, 1986 2033 GMT.

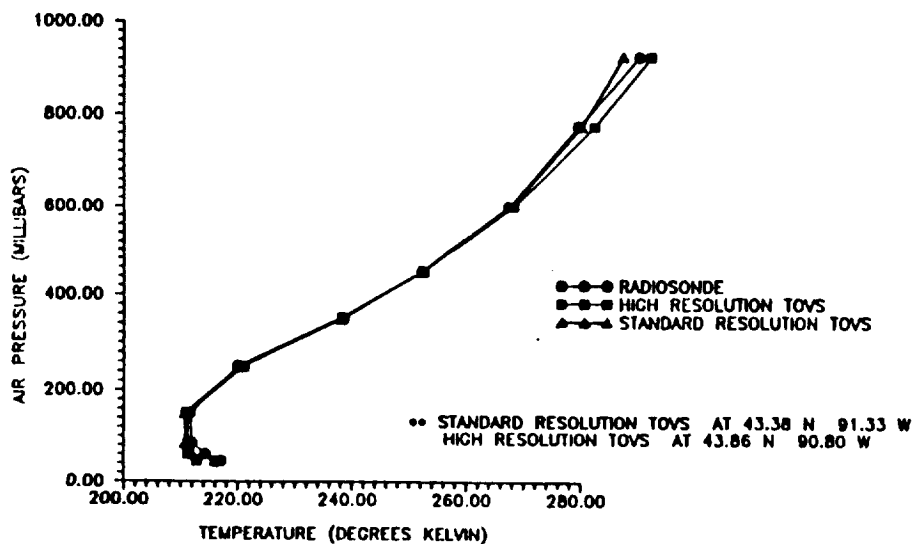


FIGURE 3. FORT McCOY
SURFACE TEMPERATURES
14 OCTOBER - 2 NOVEMBER 1986.

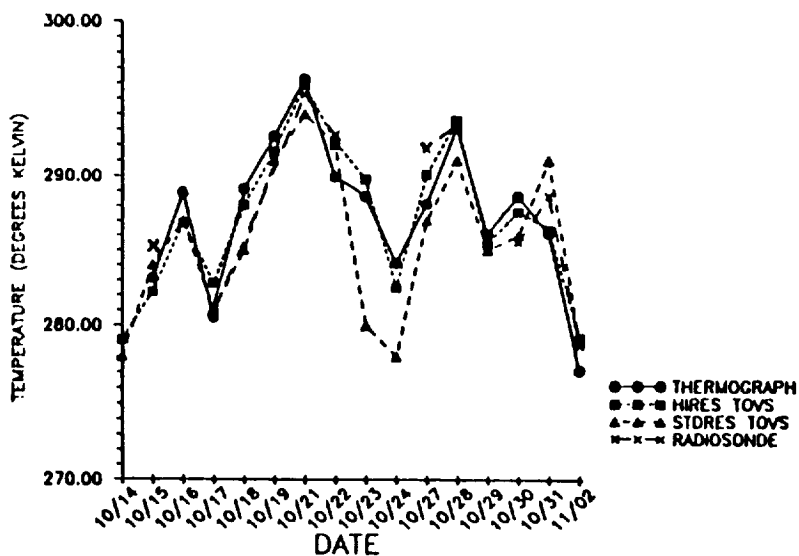


FIGURE 4. RADIOSONDE VERSUS
STANDARD AND HIGH RESOLUTION
TOVS SURFACE TO 700 MILLIBAR
PRECIPITABLE WATER.

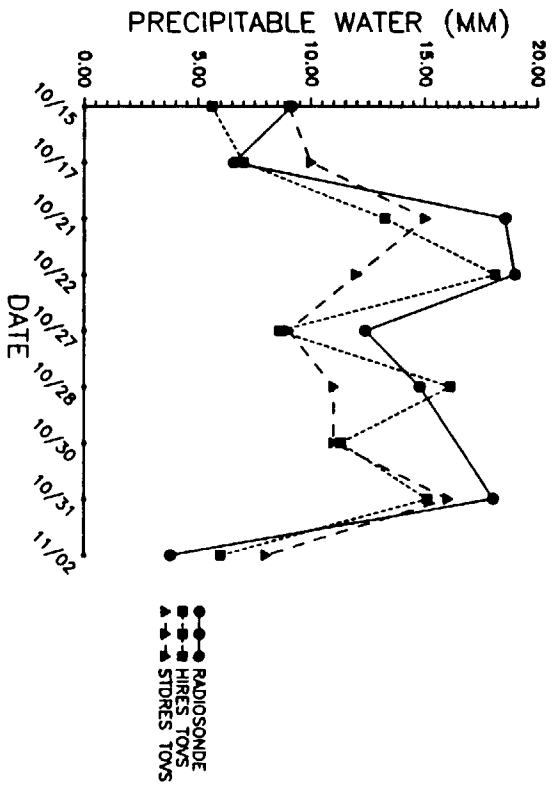


FIGURE 5. RADIOSONDE VERSUS
STANDARD AND HIGH RESOLUTION
TOVS 700 TO 500 MILLIBAR
PRECIPITABLE WATER.

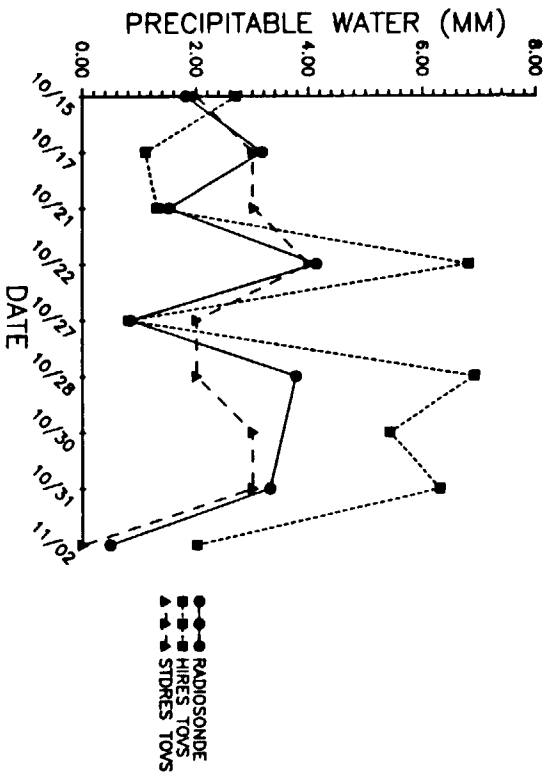


FIGURE 6. RADIOSONDE VERSUS
STANDARD AND HIGH RESOLUTION
TOVS 500 TO 300 MILLIBAR
PRECIPITABLE WATER.

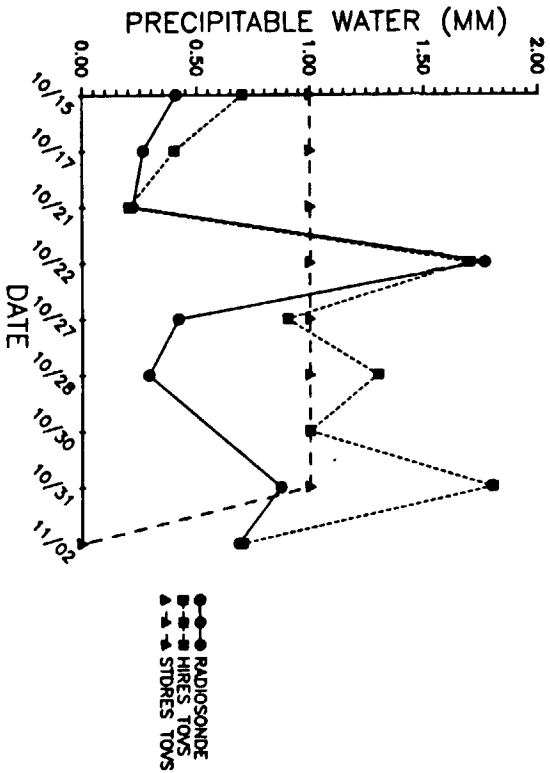


FIGURE 7. 5 HOUR AVERAGE LIDAR CLOUD BASE VERSUS STANDARD RESOLUTION TOVS CLOUD TOP ALTITUDES.

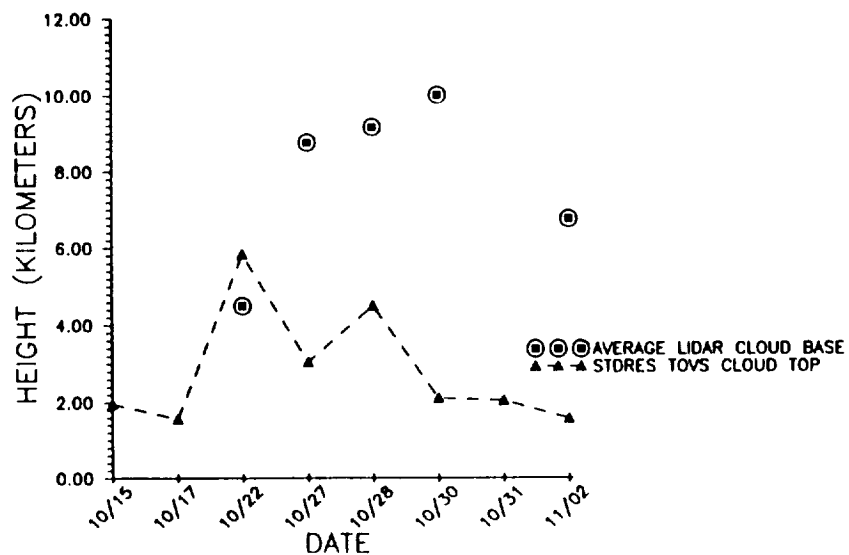


FIGURE 8. 30 MINUTE AVERAGE LIDAR CLOUD BASE VERSUS HIGH RESOLUTION TOVS CLOUD TOP ALTITUDES.

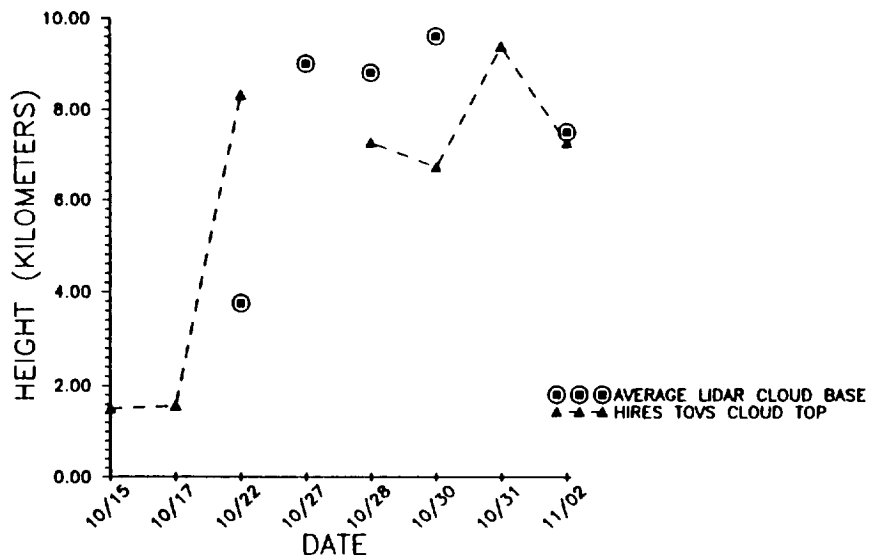
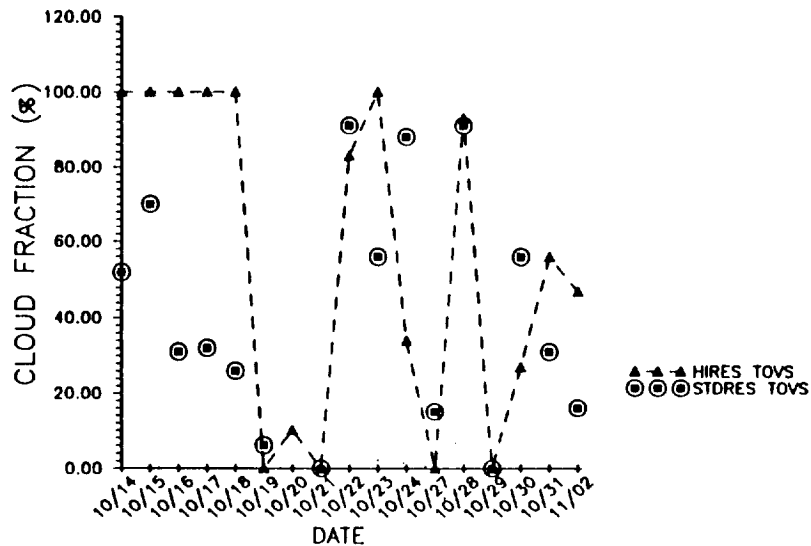


FIGURE 9. HIGH AND STANDARD RESOLUTION TOVS CLOUD FRACTIONS.



CIRRUS
SESSION C08: Midlatitude Cirrus IFO
CHAIRMAN: David O'C. Starr

Friday, July 14, 1989

	PAGE
C08.01 Objectives Cox, Stephen K.	***
C08.02 Climatology Wyllie, Donald	***
C08.03 Methodology Starr, David O'C.	***
C08.04 General Discussion Starr, David O'C.	***

AUTHOR INDEX

<u>Author</u>	<u>Session</u>	<u>Paper No.</u>	<u>Page</u>
Ackerman, Steven A.	Case Studies	C04.03	435
	Radiative/Optical Properties	C04.04	441
Ackerman, Thomas P.	Case Studies	C02.05	363
	Focused IFO's	C06.03	***
Albrecht, Bruce A.	Physical Properties	M01.02	009
	Physical Properties	M01.06	033
	Dynamic/Thermodynamic Properties	M04.04	125
	Focused IFO's	C06.03	***
Alvarez, J. M.	Physical/Microphysical Properties	C01.02	317
	Poster Session	C07.07	491
	Poster Session	C07.08	***
Ardiuni, R. F.	Case Studies	C02.06	369
Arking, Albert	Satellite Studies	E01.03	***
Austin, Philip	Dynamic/Thermodynamic Properties	M04.03	119
Baker, Marsha B.	Dynamic/Thermodynamic Properties	M04.01	107
Barlow, Roy W.	Physical Properties	M01.02	009
	Transport Mechanisms and Modeling	M06.03	185
Bell, K. L.	Case Studies	C02.03	351
Betts, Alan K.	Transport Mechanisms and Modeling	M06.06	203
Blaskovic, M.	Physical Properties	M01.06	033
Boers, Reinout	Physical Properties	M01.07	039
	Radiative Properties	M03.02	101
	Transport Mechanisms and Modeling	M06.06	203
	Poster Session	M08.03	***
Bretherton, Christopher	Dynamic/Thermodynamic Properties	M04.01	107
Briegleb, B. P.	Optical Properties	M02.01	071
Cahalan, Robert F.	Physical Properties	M01.04	021
Cawley, Robert	Poster Session	M08.06	241

AUTHOR INDEX

<u>Author</u>	<u>Session</u>	<u>Paper No.</u>	<u>Page</u>
Coakley, James A.	Optical Properties	M02.01	071
	Optical Properties	M02.02	075
	Microphysical Properties	M05.04	163
	Physical/Microphysical Properties	C01.03	323
Cox, Stephen K.	Radiative Properties	M03.03	103
	FIRE Phase II	M07.05	***
	Physical/Microphysical Properties	C01.01	311
	Case Studies	C02.07	375
	Radiative/Optical Properties	C04.02	429
	FIRE Phase II	C05.01	***
	FIRE Phase II	C05.02	***
	Focused IFO's	C06.07	***
	Midlatitude Cirrus IFO	C08.01	***
Davidson, K. L.	Transport Mechanisms and Modeling	M06.04	191
Davies, Roger	Physical Properties	M01.06	033
de Leeuw, G.	Transport Mechanisms and Modeling	M06.04	191
Dodd, G. C.	Large-Scale Environment and Modeling	C03.04	407
Donner, Leo J.	Large-Scale Environment and Modeling	C03.05	411
Duda, David	Radiative Properties	M03.03	103
Durkee, Philip A.	Microphysical Properties	M05.02	151
Eberhard, Wynn L.	Poster Session	C07.06	487
Eloranta, Edwin W.	Physical/Microphysical Properties	C01.04	327
	Focused IFO's	C06.01	***
	Poster Session	C07.01	463
Fairall, Christopher W.	Physical Properties	M01.05	027
	Physical Properties	M01.09	051
	Physical Properties	M01.10	057
	Focused IFO's	C06.03	***
Flatau, Piotr	Large-Scale Environment and Modeling	C03.06	415
Frei, Allan	Surface Based Studies	E02.02	275
Gatham, S. G.	Transport Mechanisms and Modeling	M06.04	191
Gerber, Hermann E.	Microphysical Properties	M05.01	145
Gibson, Gary G.	Satellite Studies	E01.01	257
	Case Studies	C02.02	345

AUTHOR INDEX

<u>Author</u>	<u>Session</u>	<u>Paper No.</u>	<u>Page</u>
Gordon, Tony	Large-Scale Environment and Modeling	E03.04	301
Grund, Christian J.	Physical/Microphysical Properties	C01.02	317
	Physical/Microphysical Properties	C01.04	327
	Case Studies	C02.03	351
	Focused IFO's	C06.01	***
	Poster Session	C07.01	463
Guinn, Thomas A.	Transport Mechanisms and Modeling	M06.02	179
Gultepe, Ismail	Physical/Microphysical Properties	C01.05	333
Haack, Tracy	Transport Mechanisms and Modeling	M06.05	197
Hagen, Donald	Focused IFO's	C06.02	457
Hammer, Phillip D.	Radiative/Optical Properties	C04.01	423
Hanson, Howard P.	Physical Properties	M01.01	003
	Physical Properties	M01.08	045
	Poster Session	M08.04	***
Hardesty, R. Michael	Poster Session	C07.06	487
Hare, J. E.	Physical Properties	M01.09	051
Harrison, Edwin F.	Radiative Properties	M03.01	095
	Satellite Studies	E01.01	257
	Case Studies	C02.02	345
Harshvardhan	Large-Scale Environment and Modeling	E03.03	295
Hart, W. D.	Radiative Properties	M03.02	101
Heck, P.	Satellite Studies	E01.01	257
	Case Studies	C02.02	345
Hein, Paul F.	Physical/Microphysical Properties	C01.01	311
	Large-Scale Environment and Modeling	C03.06	415
Herbster, Chris	Poster Session	M08.09	247
Heymsfield, Andrew J.	Physical/Microphysical properties	C01.05	333
	Case Studies	C02.04	357
	Case Studies	C02.05	363
	Case Studies	C02.06	369
	Large-Scale Environment and Modeling	C03.05	411
	Focused IFO's	C06.02	457
	Focused IFO's	C06.06	***

AUTHOR INDEX

<u>Author</u>	<u>Session</u>	<u>Paper No.</u>	<u>Page</u>
Hignett, Phillip	Dynamic/Thermodynamic Properties	M04.06	137
Hobbs, Peter V.	Optical Properties	M02.03	079
	Microphysical Properties	M05.04	163
	Poster Session	M08.08	***
	Poster Session	C07.05	481
Huang, Allan H.-L.	Case Studies	C04.03	435
Hudson, James G.	Microphysical Properties	M05.03	157
Hunt, W. H.	Poster Session	C07.08	***
Jensen, D. R.	Transport Mechanisms and Modeling	M06.04	191
Kessler, Bernard V.	Poster Session	M08.06	241
Khalsa, Siri Jodha Singh	Dynamic/Thermodynamic Properties	M04.05	131
King, Michael D.	Optical Properties	M02.03	079
	Optical Properties	M02.04	085
	Microphysical Properties	M05.04	163
	Microphysical Properties	M05.05	165
	Poster Session	M08.08	***
Kinne, Stefan	Case Studies	C02.05	363
	Radiative/Optical Properties	C04.01	423
Kloesel, Kevin A.	Physical Properties	M01.11	063
	Transport Mechanisms and Modeling	M06.07	211
	Poster Session	M08.02	***
Kropfli, Robert A.	Poster Session	C07.06	487
Kukla, George	Surface Based Studies	E02.02	275
Laufersweiler, M. J.	Dynamic/Thermodynamic Properties	M04.02	113
	Poster Session	M08.01	***
LeCroy, Stuart R.	Case Studies	C02.03	351
Lenschow, Donald H.	Transport Mechanisms and Modeling	M06.08	213
McDougal, David S.	FIRE Phase II	M07.03	***
Miller, Karen M.	Case Studies	C02.04	357

AUTHOR INDEX

<u>Author</u>	<u>Session</u>	<u>Paper No.</u>	<u>Page</u>
Minnis, Patrick	Physical Properties	M01.05	027
	Physical Properties	M01.06	033
	Radiative Properties	M03.01	095
	Satellite Studies	E01.01	257
	Physical/Microphysical Properties	C01.02	317
	Case Studies	C02.02	345
Moeng, Chin-Hoh	Transport Mechanisms and Modeling	M06.09	219
Moore, J. G.	Poster Session	C07.08	***
Nakajima, Teruyuki	Optical Properties	M02.04	085
	Radiative Properties	M03.02	101
	Microphysical Properties	M05.05	165
Nicholls, Stephen	Transport Mechanisms and Modeling	M06.03	185
Nucciarone, J. J.	Dynamic/Thermodynamic Properties	M04.04	125
Olsen, Lola M.	FIRE Phase II	M07.04	***
Paluch, Ilga	Transport Mechanisms and Modeling	M06.08	213
	Transport Mechanisms and Modeling	M06.09	219
Parker, L.	Satellite Studies	E01.02	263
	Case Studies	C02.06	369
Poole, Lamont R.	Case Studies	C02.03	351
Purgold, Gerald C.	Poster Session	C07.02	467
Radke, Lawrence F.	Optical Properties	M02.03	079
	Microphysical Properties	M05.04	163
	Poster Session	M08.08	***
	Poster Session	C07.05	481
Randall, David A.	Transport Mechanisms and Modeling	M06.01	173
	FIRE Phase II	M07.01	***
	FIRE Phase II	M07.02	***
	Large-Scale Environment and Modeling	E03.01	283
	Large-Scale Environment and Modeling	C03.02	395
Robinson, David A.	Surface Based Studies	E02.02	275
	Case Studies	C02.03	351
Rossow, William B.	Case Studies	C02.03	351
Rotunno, Richard	Transport Mechanisms and Modeling	M06.09	219

AUTHOR INDEX

<u>Author</u>	<u>Session</u>	<u>Paper No.</u>	<u>Page</u>
Sassen, Kenneth	Surface Based Studies	E02.01	271
	Physical/Microphysical Properties	C01.02	317
	Case Studies	C02.05	363
	Case Studies	C02.08	381
	Large-Scale Environment and Modeling	C03.04	407
	Focused IFO's	C06.04	***
Schubert, Wayne H.	Transport Mechanisms and Modeling	M06.02	179
Seze, Genevieve	Physical Properties	M01.03	015
	Poster Session	M08.07	***
Shirer, Hampton N.	Dynamic/Thermodynamic Properties	M04.02	113
	Transport Mechanisms and Modeling	M06.05	197
	Poster Session	M08.01	***
Shy, Shenqyang S.	Transport Mechanisms and Modeling	M06.10	225
	Poster Session	M08.05	235
Siems, Steven T.	Dynamic/Thermodynamic Properties	M04.01	107
Smith, Jr., William L.	Radiative/Optical Properties	C04.02	429
Smith, L. A.	Physical Properties	M01.03	015
	Poster Session	M08.07	***
Smith, William L.	Case Studies	C04.03	435
	Radiative/Optical Properties	C04.04	441
Snider, Jack B.	Physical Properties	M01.04	021
	Physical Properties	M01.09	051
	Optical Properties	M02.02	075
Spinhirne, James D.	Physical Properties	M01.07	039
	Radiative Properties	M03.02	101
	Poster Session	M08.03	***
	Case Studies	C02.04	357
	Case Studies	C02.05	363
	Case Studies	C02.06	369
	Poster Session	C07.03	473
Stackhouse, Paul	Case Studies	C02.07	375
Stage, Stephen A.	Poster Session	M08.09	247

AUTHOR INDEX

<u>Author</u>	<u>Session</u>	<u>Paper No.</u>	<u>Page</u>
Starr, David O'C.	Case Studies	C02.01	341
	Case Studies	C02.06	369
	Case Studies	C02.08	381
	Large-Scale Environment and Modeling	C03.04	407
	Poster Session	C07.07	491
	Midlatitude Cirrus IFO	C08.03	***
	Midlatitude Cirrus IFO	C08.04	***
Stephens, Graeme L.	Radiative Properties	M03.03	103
	Case Studies	C02.07	375
	Large-Scale Environment and Modeling	C03.01	389
	Large-Scale Environment and Modeling	C03.06	415
	Focused IFO's	C06.05	***
Suttles, James D.	Case Studies	C02.06	369
Thomson, Dennis W.	Physical Properties	M01.10	057
Toon, Owen B.	Large-Scale Environment and Modeling	C03.03	401
Tsay, S.-C.	Large-Scale Environment and Modeling	C03.06	415
Uthe, Edward E.	Radiative/Optical Properties	C04.05	447
	Poster Session	C07.04	477
Valero, Francisco P. J.	Case Studies	C02.05	363
	Radiative/Optical Properties	C04.01	423
Vaughn, M. A.	Poster Session	C07.08	***
Welch, Ronald M.	Case Studies	C02.06	369
Westphal, Douglas L.	Large-Scale Environment and Modeling	C03.03	401
Wheeler, R. J.	Poster Session	C07.07	491
White, Allen B.	Physical Properties	M01.10	057
Whitlock, Charles H.	Case Studies	C02.03	351
	Poster Session	C07.02	467
	Poster Session	C07.07	491
Wielicki, Bruce A.	Satellite Studies	E01.02	263
	Case Studies	C02.06	369
Wu, Man-Li	Case Studies	C02.06	369

AUTHOR INDEX

<u>Author</u>	<u>Session</u>	<u>Paper No.</u>	<u>Page</u>
Wylie, Donald	Large-Scale Environment and Modeling	E03.02	289
	Case Studies	C02.01	341
	Focused IFO's	C06.01	***
	Poster Session	C07.07	491
	Midlatitude Cirrus IFO	C08.02	***
Young, David F.	Physical Properties	M01.05	027
	Physical Properties	M01.06	033
	Radiative Properties	M03.01	095
	Satellite Studies	E01.01	257
	Physical/Microphysical Properties	C01.02	317
Young, George S.	Dynamic/Thermodynamic Properties	M04.04	125

1. Report No. NASA CP-3079		2. Government Accession No.		3. Recipient's Catalog No.	
4. Title and Subtitle FIRE Science Results 1989				5. Report Date July 1990	
				6. Performing Organization Code	
7. Author(s) David S. McDougal, Editor				8. Performing Organization Report No. L-16792	
				10. Work Unit No. 672-22-10-70	
9. Performing Organization Name and Address NASA Langley Research Center Hampton, VA 23665-5225				11. Contract or Grant No.	
				13. Type of Report and Period Covered Conference Publication	
12. Sponsoring Agency Name and Address National Aeronautics and Space Administration Washington, DC 20546-0001				14. Sponsoring Agency Code	
15. Supplementary Notes Presented at the FIRE Science Meeting, Monterey, California, July 10-14, 1989. Co-sponsored by National Science Foundation, Office of Naval Research, Department of Energy, Air Force Geophysical Laboratory, and National Oceanic and Atmospheric Administration.					
16. Abstract FIRE (First ISCCP Regional Experiment) is a U.S. cloud-radiation research program formed in 1984 to increase the basic understanding of cirrus and marine stratocumulus cloud systems, to develop realistic parameterizations for these systems, and to validate and improve ISCCP cloud product retrievals. A FIRE Science Meeting was held in Monterey, California, July 10-14, 1989, to highlight presentations of results culminating the first 5 years of FIRE research activities. This Conference Publication contains the full text of the papers presented at the FIRE Science Meeting. The papers describe important elements of the 1986 Cirrus Intensive Field Observations (IFO), the 1987 Marine Stratocumulus IFO, the Extended Time Observations (ETO), and modeling activities. A number of papers describe collaborative efforts involving the comparison of multiple data sets (i.e. satellite, airborne, and surface), incorporation of data measurements into modeling activities, validation of ISCCP cloud parameters, and development of parameterization schemes for GCMs.					
17. Key Words (Suggested by Author(s)) FIRE Cirrus ISCCP Marine Stratocumulus Cloud-Radiation			18. Distribution Statement Unclassified - Unlimited Subject Category - 47		
19. Security Classif. (of this report) Unclassified		20. Security Classif. (of this page) Unclassified		21. No. of pages 521	
				22. Price A22	

